AGARD
ADVISORY GROUP FOR AEROSPACE RESEARCH & DEVELOPMENT
64 RUE DE VARENNE PARIS 7E FRANCE

Fluid Physics of Hypersonic Wakes

VOLUME 2

★

MAY 1967

NORTH ATLANTIC TREATY ORGANIZATION

CONFERENCE PROCEEDINGS No. 19

NORTH ATLANTIC TREATY ORGANIZATION

ADVISORY GROUP FOR AEROSPACE RESEARCH AND DEVELOPMENT

(ORGANISATION DU TRAITE DE L'ATLANTIQUE NORD)

FLUID PHYSICS OF HYPERSONIC WAKES

Published in Two Volumes

VOLUME 2

Papers presented at a Specialists' Meeting of the
Fluid Dynamics Panel of AGARD held at the
Colorado State University, Fort Collins, Colorado, U.S.A.,
10-12 May 1967

The material in this publication has been reproduced directly from copy supplied by each author.

Printed by Technical Editing and Reproduction Ltd
Harford House, 7-9 Charlotte St. London. W. 1.

VOLUME 2

Experimental Studies of Turbulence Characteristics in the Hypersonic Wake of a Sharp Slender Cone

by

A.G. Boyer

E.P. Muntz

General Electric Company
Space Sciences Laboratory
Valley Forge, Pennsylvania

SUMMARY

This paper presents the results of an experimental investigation of the turbulence characteristics in the wake of a sharp slender cone. The investigation was conducted in a hypersonic shock tunnel and employed a new application of the electron beam excitation technique to measure directly the scale and velocity of the turbulent density and temperature fluctuations and to monitor their axial history in the wake of a sharp 10° half-angle cone model free flying in a Mach 12.6 flow.

The use of the electron beam excitation technique for the investigation of turbulent flows has been analyzed. While the gas densities in turbulent wake experiments tend to be higher than those within the normal operating range of this technique, it is possible to use the technique in turbulent wakes generated in a shock tunnel. In fact the electron beam technique and a shock tunnel is demonstrated to be an important combination in the study of turbulent hypersonic wakes.

The new application of the beam technique incorporates a linear deflection system at the exit orifice to sweep the electron beam in the axial flow direction. The beam is collected in a special elongated receiver of precise dimensions which also serves as a timing device to accurately measure the axial velocity of the sweeping beam from the collected beam current waveform.

By sweeping the beam as two well separated sweep rates, direct measurements of the scale and velocity of the turbulent fluctuations have been made. With the sweep rate adjusted to the measured velocity, a turbulent fluctuation can be tracked in the axial distance (.78 ins.) observed by the 10-channel image dissector of density package optical system. Extensive measurements have been made at various radial and axial positions in the wake.

All the tests were run at the same conditions: M = 12.6; stagnation temperature of 1200°K, freestream Reynolds number of 1.3×10^6/ft., freestream density equivalent to a pressure of 5.7 mm Hg at room temperature, and freestream velocity of 5660 fps. Dry nitrogen was used as the test gas. The flow thus closely approximated a perfect gas flow since nitrogen vibration is not significantly excited for these stagnation conditions.

RESUME

Les auteurs de cet exposé présentent les résultats d'une étude expérimentale portant sur les caractéristiques de turbulence apparaissant dans le sillage d'un cône fuselé et effilé. Au cours de l'expérience, on a eu recours à une nouvelle application de la technique d'excitation par faisceau d'électrons pour mesurer directement l'échelle et la vitesse des fluctuations de densité et de température en régime turbulent, et pour contrôler leur comportement axial dans le sillage d'une maquette en forme de cône effilé au demi-angle de 10°, évoluant en vol libre à une vitesse de Mach 12,6.

On a analysé l'utilisation de la technique d'excitation par faisceau électronique dans l'étude des écoulements turbulents. Dans les expériences portant sur les sillages turbulents, les densités gazeuses tendent à être supérieures à celles qui caractérisent le domaine normal d'application de cette technique; on peut toutefois utiliser cette dernière dans les sillages turbulents engendrés dans une soufflerie à ondes de choc. On démontre, en fait que la technique du faisceau électronique s'allie à l'emploi d'une soufflerie à ondes de choc pour constituer un facteur important dans l'étude des sillages turbulents hypersoniques.

Dans sa nouvelle application, la technique du faisceau comporte, à l'orifice de sortie, un système de déflexion linéaire destiné à orienter le balayage du faisceau d'électrons dans la direction de l'écoulement axial. On recueille le faisceau dans le récepteur spécial, de forme allongé et de dimensions précises, qui sert également de dispositif de chronométrage pour mesurer avec exactitude la vitesse axiale du faisceau balayeur à partir de la forme d'onde du courant du faisceau recueilli.

En choisissant pour le faisceau, deux fréquence de balayage bien distinctes, on a mesuré directement l'échelle et la vitesse des fluctuations turbulentes. En ajustant la fréquence de balayage à la vitesse telle qu'elle est donnée par les mesures, on peut suivre une fluctuation turbulente à la distance axiale (0,78 pouces) observée par le dissecteur d'image à 10 canaux d'un système optique à unité compacte de mesure de densité. On a procédé à toute une série de mesures en divers points radiaux et axiaux du sillage.

Tous les essais ont été effectués dans les mêmes conditions: Mach = 12,6 température d'arrêt de 1200°K, nombre de Reynolds en écoulement libre de $1,3 \times 10^6$ par pied, densité en écoulement libre équivalent à une pression de 5,7 mm Hg à température ambiante, et vitesse d'écoulement libre de 5660 pieds par seconde. Le gaz utilisé était l'azote sec. L'écoulement se rapprochait donc beaucoup de celui d'un gaz parfait, puisque, dans ces conditions d'arrêt, aucune vibration importante n'est suscitée au sein de l'azote.

BLANK PAGE

1. Introduction

In the preceding half decade there has been collected a large assortment of Schlieren, shadowgraph, self luminosity, race track, interferometer and other photographs of hypersonic turbulent wakes in ballistic ranges (c.f. Refs. 1 - 8 and many others).

Despite this mass of data there has been little if any information relating to many of the important physical characteristics of hypersonic turbulent wakes. While wake growth and edge statistics are readily found from Schlieren flow photographs, density and temperature fluctuations are another matter. Using unfolding techniques the apparent density fluctuations have been measured in a few cases. However, because of moderately complicated unfolding procedures and associated necessary assumptions this type of measurement is unsatisfactory. It would be desirable to have direct, point measurements of the density fluctuations at least in enough situations to validate the unfolding procedures and other assumptions required to obtain densities from Schlieren photographs. Additionally, direct temperature measurements would be useful.

The need for direct point measurements has of course been obvious for a long time. Hot wire experiments provide spatially resolved measurements but are difficult to interpret in terms of density or temperature fluctuations. Recently an attempt has been made at the Avco Everett Research Laboratory to measure point densities in the wake of a sphere using Rayleigh scattered light. The light source is a ruby laser with the

output focussed at the point of interest in the wake. This technique which in principle is very appealing currently has operational difficulties (as do all new techniques). These, however, will undoubtedly be overcome. Rayleigh scattering also offers the possibilities of temperature measurements through the medium of the Raman effect.

There is at least one other technique that offers the possibility of simultaneous point measurements of density and temperature. This is the electron beam excitation technique. While the gas densities in turbulent wake experiments tend to be higher than those within the normal operating range of this technique it turns out to be possible to use it in the turbulent wakes generated in a shock tunnel. The application of the beam probe to turbulent property measurements is discussed in the next section of this paper. The results of turbulent density measurements in the wake of 0.01 nose bluntness ratio, 10° half-angle sphere cones are presented in the third section.

2. Experimental Arrangement and Techniques

2.1 Flow and Model Details

For all the experiments discussed here the Space Sciences Laboratory's 54-inch exit diameter nozzle shock tunnel was used. This tunnel has a large "parallel flow" nozzle designed for Mach 20. It can be run off condition, and for the present experiments the Mach number was 12.6 with a Mach number gradient of about 0.09/ft. There are approximately 150 ins.

of good flow at the nozzle center line. All the tests were run at the same condition; M = 12.6, stagnation temperature of 1200°K, free stream Reynolds number of 1.3×10^6/ft., free stream density equivalent to a pressure of 5.7 mm Hg at room temperature, and free stream velocity of 5660 fps. The gas used was bottled nitrogen, the flow thus closely approximated a perfect gas flow since nitrogen vibration is not significantly excited for these stagnation conditions. There is good flow in the shock tunnel for longer than 10 msec. after the starting shock wave enters the test section. The tunnel flow plus the wake flow took about 4 msec. to establish under the present conditions. The wakes were sampled either for 0.5 or 1 msec. in all the experiments, beginning 8 msec. after the starting shock's arrival. Knowledge of test section conditions is based on nozzle calibration with pitot pressure surveys.

Two models were used in the experiments. These were 1.00-in. and 3.00-in. base diameter 10° half-angle cones with a .01 nose bluntness ratio. In all the experiments the models were suspended on light threads. The instrumentation remained fixed in the test section and various locations in the wake were examined by suspending the model at appropriate positions upstream of the measuring station. The model suspension was such that the starting shock wave propagating over the model sheared off the suspending threads at the model surface and swept them away. The model was thus left flying freely in the shock tunnel. It was sufficiently heavy

such that its motion was negligible during the approximately 9 msec. before the end of the sampling time. In terms of support interferences, then, the shock tunnel test is similar to a range experiment in that for each the models are freely flying.

2.2 The Electron Beam Excitation Technique Applied to Turbulence Measurements in a Shock Tunnel

The electron beam excitation technique has been used for a number of years at the Space Sciences Laboratory to measure density and temperature in a variety of shock tunnel flows (12 - 15). As set up in a shock tunnel this equipment is shown in Fig. 1. A beam of 35 kv electrons is passed from the electron gun through a small (2 mm dia.) orifice into the flow. The beam is collected by the receiver shown in the figure.

The electrons excite emission from the nitrogen molecules. The intensity of the emission at points along the path of the beam is related to the local gas density at these points (16). Also, the intensity distribution in the rotational fine structure of the first negative system of nitrogen, which is one of the systems excited by the beam electrons, can be related to the rotational temperature of the nitrogen molecules prior to their excitation (17). To observe the overall emission intensity and the spectral distribution the instruments shown in Fig. 1 are used. The total emission is monitored by the instrument marked "density package". The lens system forms an image of the beam

excited emission on a ten channel image dissector consisting of a pile of fiber optic bundles, each bundle leading to a photomultiplier tube. The height of each bundle is such that light corresponding to a 1.5 mm length along the beam is selected from the image. Also in the optical path is a filter that transmits from about 4800 Å down to glass cut-off.

The rotational temperature apparatus, on the other side of the shock tunnel, is used to measure flow static temperature at any point along the length of the beam. It has been described in previous publications (18) to which the reader is referred.

For previous shock tunnel measurements with the electron beam system gas densities were generally below that equivalent to a pressure of 500 μHg at room temperature (equivalent pressure). At these densities the electron beam excited emission intensity is very nearly a linear function of gas density. In the present turbulent wake measurements the densities were rather higher, varying from equivalent pressures of 1 to 4 mm Hg. As discussed in Ref. 11, this can cause difficulties since the electron beam excited emission intensity becomes a noticeably non-linear function of gas density. It remains to be seen whether temperature measurements are also severely affected by high gas densities.

The anticipated difficulties involved in applying the excitation technique to the investigation of wake turbulence were the following:

there should be sufficient emission intensity such that for the required sampling time enough photons reach the detectors to give a reasonable statistical accuracy; the relationship between emission intensity and gas density must be known, including any effects of temperature on this non-linear relationship; the high flow densities also introduce the problem of beam scattering or spreading which must be kept small; and finally, the spatial resolution should be such that the minimum disturbance size that can be detected has a characteristic dimension only a few percent of the model base diameter.

Of these problems the most worrisome is that of the non-linear relationship between emission intensity and density. At low densities (less than 500 μ Hg equivalent pressure) the emission intensity from nitrogen is predominantly in the first negative system. It is closely proportional to the gas density and the electron beam current. However, as the gas density is increased the curve of emission intensity versus gas density at a constant beam current becomes noticeably non-linear due to collisional quenching of the radiating species. For pure nitrogen the quenching is significantly less severe than for air (19); thus, using nitrogen as the test gas has advantages other than to maintain perfect gas flow conditions.

The quenching curves have not been particularly well defined. Variation of quenching collision cross section with relative velocity of

collisions, or temperature, is not known. There is some evidence to suggest that the cross section varies approximately as $\left(\sqrt{T}\right)^{-1}$ (20, 21) at least for foreign gas quenching of resonance radiation. Since collision frequency varies as $\sqrt{T}$ a quenching curve for a $\left(\sqrt{T}\right)^{-1}$ cross section variation with temperature would have no temperature sensitivity. Also, in the measurement of density with the system shown in Fig. 1 the filter selects a wide range of wavelengths (approximately 4800 Å to 3900 Å). For the low densities this allows light from the 0-0, 0-1 and 0-2 vibrational bands of the beam excited first negative system of nitrogen to reach the detector. However, as the gas density is increased the intensity of the beam excited second positive system relative to the first negative increases (22). A large number of the bands in this system are also passed by the filter. Thus, in order to establish the form of the relationship between gas density and emission intensity for the detecting system used in the tests it is important that the same filter be used. This was done. The results are shown in Fig. 2, where observed emission intensity for a constant beam current is plotted against density in terms of equivalent pressure at room temperature. Experiments were completed at two temperatures with the gas flow velocity in the calibration experiments as noted on the figure. The range of temperatures in the turbulent wake flows was from 50 to 300°K, with flow velocities up to about 5000 fps. Conditions in the calibration

experiments thus covered a reasonable proportion of this temperature and velocity range (80 to 210°K at 1300 and 2100 fps), although by no means exhaustively. It can, however, be concluded that at least for the conditions of the present experiments the calibration curve is independent of gas temperature and has a reasonable sensitivity throughout the density range of interest (1-4 mm Hg equivalent pressure). All observations both for calibration and in the actual tests were made perpendicular to the flow velocity.

It is important to note that changing the filter band pass significantly alters the shape of the calibration curve. Isolating the first negative system produces a curve that demonstrates much greater quenching and a small but measurable sensitivity to temperature.

The calibration curve shown in Fig. 2 was used to reduce the experimental light intensity measurements to density fluctuation. This was accomplished in the following manner. The wake densities ranged from 1 to 4 mm Hg equivalent pressure. In this range select any point on the calibration curve, draw a straight line through it and the origin, and a tangent to the calibration curve at the same point (dashed lines in Fig. 2). It turns out that the slopes of the two lines are such that the tangent to the curve has very closely 1.3 times less sensitivity than a linear relationship at that point (as indicated by the straight dashed line to the origin). This 1.3 factor is constant to within about 3% for the 1 mm Hg to 4 mm

Hg range. Consequently, when examining detector outputs, any light intensity oscillations about some average level implies a density fluctuation approximately 1.3 times as great.

For the reduction of the experimental results the technique just described for approximating the calibration curve was used. Since the density oscillations were at most not greater than ±50% of the average density level in any measurement, the approximation did not introduce a serious error.

The other problems associated with the turbulence measurements are of a less exacting nature. To prevent unacceptable scattering of the electron beam, and thus loss of spatial resolution, the hardware generating the beam and the beam receiver were placed only 3 in. apart in the flow. This did not disturb the flow at the measuring station since the wake is well supersonic everywhere that the apparatus was placed (the hardware is not large enough to cause serious blockage effects to the tunnel flow). The fact that the wake becomes supersonic very rapidly has been shown by the wind tunnel measurements of Cresci and Zakkay (23).

For all the experiments the beam energy was 35 kv. This gave a scattering outside of a 2 mm diameter of about 1% of the beam current at a distance of 1.5 in. from the beam generator (measuring point). This was for a density equivalent to a pressure of 3 mm Hg at room

temperature.

The nominal beam diameter (as defined by the exit orifice from the beam generating chamber to the flow field) was 2 mm for these experiments. Because of scattering the effective diameter was certainly no larger than 2.3 mm. Thus, roughly, the spatial resolution is equivalent to a volume defined by the 2.3 mm beam diameter and whatever length of beam is observed with the monitoring optical system, say 2 mm. Accordingly, the spatial resolution may be quoted as being no worse than that equivalent to a 2.3 mm cube. The spatial resolution corresponds to 3% of the base diameter for the 3.00 in. base diameter cone. In the experiments, only disturbances several times larger than about 3% of the 3.00 in. base diameter model could have their density profiles measured with any accuracy. The beam technique will likely be able to produce a resolution equivalent to about 0.5 mm in the future. The present measurements however were all made with the 2.3 mm resolution.

It must always be remembered that the measurements in a shock tunnel involve the passage of the flow past the measuring station. In the very far wake the turbulent structure will be convected through the beam at essentially the freestream velocity. Thus, the time response of the entire system must be such that accurate measurements can be obtained in times equal to that required to convect disturbance with a say 2 mm characteristic size through the beam. Using 5000 fps a time

response of about 1.3 μsec. is required. To accomplish this two things are necessary. First the photomultiplier circuits must have sufficient response characteristics. This is no problem and can be easily accomplished. Secondly, the light intensity of the electron beam excited emission must be sufficient to provide enough photons to the detecting photomultiplier so that during 1.3 μsec. a statistically accurate measurement can be obtained. As an example, for the f-5 optical system used in the present experiments, observation of a 2 mm length of beam, and using data from Ref. 11, the amount of light received by the photomultiplier measuring the density was approximately 13,000 photons in 1.3 μsec. Since the photocathode efficiency is about 10% this leaves 1300 photo-electrons. Thus a measurement with a probable error of $\pm$ 4% can be made in 1.3 μsec. This was satisfactory for the present work.

For temperature measurements, an increase in the beam excited emission intensity is required. Because the available light is split into two channels in the Rotational Temperature Apparatus (right hand side of Fig. 1), each channel incorporating narrow band pass filters, relatively high beam currents must be generated in the test flow in order to produce adequate signal levels. Temperature fluctuations are presently under investigation with beam currents up to 15 ma.

An important feature of the electron beam and recording techniques

is the ability to make simultaneous density and temperature measurements, permitting direct comparison and phase relation studies. Pressure fluctuations can also be deduced from the measurements. Further, with the density package yielding simultaneous records of the density fluctuations at ten radial positions, radial correlation coefficients can be measured. To obtain the axial correlation coefficient, however, another beam would be required.

In addition to the density and temperature studies, a sweeping electron beam technique has been developed to measure the scale and local mean velocity of wake turbulence. This is a new application of the beam technique incorporating a linear deflection system at the exit orifice of the electron gun to sweep the beam in the axial flow direction behind the model.

With the sweeping beam, the image dissector of the density package is aligned in the axial flow direction, and a time-resolved picture in ten segments of the turbulent density fluctuations obtained during one pass of the beam across the field-of-view of the fiber optic bundles. The beam is collected in a special elongated receiver of precise dimensions which also serves as a timing device to accurately measure the axial velocity of the sweeping beam from the collected beam current waveform and the known geometrical arrangement.

This type of sweeping beam record will stretch out the fluctuations in

proportion to the reduced relative velocity of the beam and turbulence. With the known axial velocity of the beam, combining such results with stationary beam records affords a direct measurement of both scale size and local mean velocity of the turbulence. Alternatively, sweeping the beam at a constant velocity with and against the flow will provide a suitable change in relative velocity and yield two sets of data from which the unknown scale and mean velocity can be determined.

Figure 3 illustrates the sweeping beam technique and shows oscilloscope traces of the photomultiplier outputs recorded with an axial beam velocity of 1000 fps. To conserve our instrumentation requirements, the ten photomultiplier tubes of the density package are coupled in pairs so each oscilloscope trace records the output from two channels as the beam passes. The windows of each pair are spaced far enough apart so that the beam has cleared one window before it reaches its partner. By piecing together the approximately 5 μ secs. of peak signal information from each output, a density-time record of the turbulent fluctuations is obtained. The particular traces shown in the figure, however, were obtained during calibration and system check in a nitrogen free jet facility. The decaying peak signal level is due to the strong streamwise density gradient as indicated in the figure.

Measurements of scale and local mean velocity of wake turbulence are planned for future experiments.

3. Turbulent Wake Experiments

3.1 Procedure

The measurements were conducted in the Space Sciences Laboratory's large shock tunnel that has been described previously. Models were suspended upstream in the nozzle at varying distances depending on the axial and radial position under study in the wake. The electron beam was passed vertically through the geometric wake axis (suspension accuracy is such that the beam can be placed within $\pm$ 0.015 in. of the geometric wake center line with the model having 0^{o} angle of attack to within $\pm 0.1^{o}$). Radial profiles of the wake were obtained using the fiber optics arrangement that has been described before. For the 3.00 in. model, to obtain a complete radial profile of the wake at one axial position required up to three runs with the model being moved off the nozzle axis in a vertical plane.

Signals from the photomultipliers attached to the individual fiber bundles were recorded on oscilloscopes. Two sets of data were obtained, one with a circuit response time of 10 μsec., the other with a response time of 1 μsec. In the first case the wake density was sampled for 1 msec. from 8.0 to 9.0 msec. after flow initiation in the shock tunnel test section. In the latter case the sample was for 500 μsec. beginning at 8.0 msec. Some larger sampling time runs were made to observe the flow establishment and help select an appropriate time during

the run to study the turbulent wake.

For the stagnation or reservoir condition of these shock tunnel runs there is a characteristic decreasing pressure and temperature. However, at 8 msec. after flow initiation relatively constant stagnation conditions are achieved. In this connection it is worthwhile remembering that in 1 msec. the freestream flow will travel approximately 6 ft. Thus, it seems reasonable to look at variations in stagnation conditions no more than one or two milliseconds ahead of the sampling period. Also as has been shown by previous work (14) the response time of these particular wakes seem to be of the order of one millisecond. One is thus only concerned with flow gradients from say 6 to 8.5 msec. The variation in stagnation conditions is not severe for this interval. At 6 msec. the flow density is equivalent to a pressure of 6.3 mm Hg at room temperature while at 8 msec. the corresponding density is 5.7 mm Hg. About a 9% change. The corresponding change in Reynolds number is about 2% (the stagnation temperature also varies slightly, this results in a reduced variation in the Reynolds number). This variation is not considered significant in terms of say a changing transition distance.

Some of the features of the experiments have been discussed. It is now appropriate to begin a discussion of the results.

3.2 Results

There were two objectives for these experiments. The first was to

establish that a shock tunnel can be used to study some aspects of turbulent wake flows. The second was to investigate a few of the properties of the density fluctuations in the turbulent wake of the 3.00 in. base diameter 10^{o} half angle cone described previously.

The observation of transition in a shock tunnel wake is well demonstrated by the traces in Fig. 4. These traces are for positions as noted in the figure. The model was the 1.00 in. base diameter cone. At five base diameters the oscilloscope trace of observed emission intensity versus time has no large light output fluctuations. The steadily decreasing light output with increasing time for this trace is due to a decaying electron beam current. In contrast to the trace at five base diameters, the light intensity at $X/D_B = 30$ shows large density fluctuations.

The low level fluctuations at five base diameters are no greater than those observed in the freestream of the shock tunnel. This type of trace will be associated with laminar flow. The obvious fluctuations at $X/D_B = 30$ are associated with turbulent flow. Also, at $X/D_B = 30$ the intensity of the fluctuations were fairly constant as a function of radius in the wake. As will be mentioned later in describing experiments with the 3.00 in. cone this is not characteristic of all axial positions during transition.

The 3.00 in. cone wake was studied in some detail. A limited survey of the region between 5 and 20 base diameters was obtained. In this

work the photomultiplier circuit response time was 10 μsec. This response time was used for most of the tests in an effort to simplify the traces in this first look at turbulent shock tunnel wakes. The 10 μsec. response time corresponded to a length of 9 mm, or about 10% of the base diameter, if a local flow velocity one-half of the freestream velocity is assumed. Thus, any disturbance many times smaller than this would not be detected. The observed root mean square density fluctuations are shown in Fig. 5 plotted numerically and appearing unbracketed in the position to which they apply. The bracketed numbers are discussed below.

First, it is important to discuss the effect of the 10 μsec. response time. Some runs were also conducted with a 1 μsec. response time. A trace from one of these is shown in Fig. 6 for the $X/D_B = 20$ position in the wake and at $Y/R_B = 0.5$. The average distance between the maximum and minimum of major density excursions (those greater than 5% of mean) was found to be around 18 μsec. For the same position but with the 10 μsec. response (and a different run) the same average comes to 16 μsec. This type of comparison leads one to believe that the 10 μsec. circuitry did not miss any major density disturbances. On the other hand the 1 μsec. response circuit gave larger root mean square density fluctuations than the 10 μsec. circuit. The 1 μsec. results are shown with brackets in Fig. 5. Going to a faster response

time than 1 μsec. would produce no better results because of the finite size of the electron beam.

Close to the base of the cone, say at 10 base diameters, the major density disturbances were large in size as indicated by an average distance between major excursions of about 35 μsec. for this station. This also applies at $X/D_B = 7.5$. At both these stations the large off axis root mean square fluctuations (see Fig. 5) are caused by fluctuations with a "wavelength" of about 70 μsec. (twice average distance between maximum and minimum). At $Y/R_B = 0.6$ the disturbances are most intense. If a stream velocity of 0.8 times freestream is assumed the "wavelength" is 3.2 in. or about one base diameter. Towards the wake center the disturbances become both smaller and more frequent.

For the measurements in the first ten base diameters it is felt that the 10 μsec. time response measurements provide an adequate description of major density fluctuations. It appears that major fluctuations in this region are concentrated off the wake axis and have a "wavelength" transit time of about 70 μsec. At 20 base diameters the wavelength transit time is only about 35 μsec. and the faster time response of 1 μsec. is necessary.

Several other general observations can be made. At $X/D_B = 5.0$ the density fluctuations are only slightly above what would be termed laminar for the shock tunnel measurements. Freestream measure-

ments in the tunnel give a root mean square oscillation of about 2.5%. Some disturbances in excess of this "noise" level are detectable around $Y/R_B = 0.7$ at five base diameters.

One final qualitative observation resulting from eye examination of the traces. For the radial profiles there seem to be three sometimes more, sometimes less, distinct regions as one proceeds radially outward from the wake center. Near the wake center it was noticed that the density excursions are quite clearly high density areas in a lower density background. This changes to a mixed region and then finally to a region of low density disturbances embedded in a high density background.

4. Conclusions

The electron beam excitation technique and a shock tunnel show promise of being an important combination in the study of turbulent hypersonic wakes.

Transition was observed in the shock tunnel generated wakes. The observed transition distances were consistent with predictions based on Waldbusser's (24) correlation of range firings.

The observed root mean square percentage density fluctuations at $X/D_B = 20$ behind a 3.00 in. base diameter, 10° half angle cone, at $M = 12.6$ and freestream unit Reynolds number of 1.3×10^6/ft. was about 30%. This is approximately one-half of the root mean square fluctuation intensity found by Slattery and Clay (1).

References

1. Slattery, R.E. and Clay, W.G., "The Turbulent Wake of Hypersonic Bodies", A.R.S. preprint 2673-62, Nov. 1962.

2. Lyons, W.C., Brady, J.J. and Levensteins, Z.J., "Hypersonic Drag; Stability and Wake Data for Cones and Spheres", AIAA preprint 64-44, January 1964.

3. Levensteins, Z.J. and Krumins, M.V., "Experimental Study of Aerodynamics Characteristics of Hypersonic Wakes", AIAA Paper 66-53, January 1966.

4. Pallone, A.J., Erdos, J.I., Eckerman, J. and McKay, W., "Hypersonic Laminar Wakes and Transition Studies", AIAA preprint 63-171, June 1963.

5. Clay, W.G., Hermann, J. and Slattery, R.E., "Statistical Properties of the Turbulent Wake Behind Hypervelocity Spheres", Phys. of Fluids, 8, 10, 1792, October 1965.

6. Schapker, R.L., "Statistics of High-Speed Turbulent Wake Boundaries", AIAA Paper 65-808.

7. Goldburg, A. and Fay, J.A., "Vortex Loops in the Trails Behind Hypervelocity Pellets", Avco-Everett Research Laboratories AMP 75, February 1962.

8. Washburn, W.K. and Keck, J.C., "The Race Track Flow Visualization of Hypersonic Wakes", Avco-Everett Research Laboratory, Research Report 131, March 1962

9. Ladenburg, R.W., Lewis, B., Pease, R.N. and Taylor, N.S., eds. "Physical Measurements in Gas Dynamics and Combustion", Article F, 2 p. 219, Princeton Univ. Press, 1954.

10. Camac, M., Locke, E.V. and Rose, P.H., "A Technique for Measuring Wake Densities by Rayleigh Scattering", Avco-Everett Research Laboratory, AMP 181, November 1965.

11. Muntz, E.P., Abel, S.J. and Maguire, B.L., "The Electron Beam Fluorescence Probe in Experimental Gas Dynamics", Supplement to IEEE Transaction on Aerospace, p. 210, June 1965.

12. Zempel, R.E. and Muntz, E.P., "Slender Body Near Wake Density Measurements at Mach Numbers Thirteen and Eighteen", GE MSD TIS R63SD55, July 1963 (also AIAA Paper 63-272).

13. Kaegi, E.M. and Muntz, E.P., "Driver-Driven Gas Mixing and Its Effect on Shock Tunnel Test Time", 3rd Hypervelocity Techniques Symposium, Denver, Colorado, March 1964.

14. Muntz, E.P. and Softley, E.J., "An Experimental Study of Laminar Near Wakes", GE MSD TIS R65SD6, April 1965.

15. Softley, E.J., Zempel, R.E. and Muntz, E.P., "Experimental Determination of Pressure, Temperature and Density in Some Laminar Hypersonic Near Wakes", GE MSD TIS R64SD35, May 1964.

16. Schumacher, B.W. and Gadamer, E.O., "Electron Beam Fluorescence Probe for Measuring the Local Gas Density in a Wide Field of Observation", Can J. Phys. 36, 654, 1954.

17. Muntz, E.P., "Static Temperature Measurements in a Flowing Gas", Phys. of Fluids, 5, 1, 80, January 1962.

18. Muntz, E.P. and Abel, S.J., "The Direct Measurement of Static Temperature in Shock Tunnel Flows", GE TIS R64SD25, 1964.

19. Muntz, E.P. and Marsden, D.J., "Electron Excitation Applied to the Experimental Investigation of Rarefied Gas Flows", Rarefied Gas Dynamics Vol. II, 495-526 (ed. J.A. Laurmann) Academic Press, 1963.

20. Mitchell, A.C.G. and Zemansky, "Resonance Radiation and Excited Atoms", Cambridge University Press, 1934.

21. Hasted, J.B., "The Physics of Atomic Collision", Chapter 13, Butterworths 1964.

22. Davidson, G. and O'Neil, R., "The Fluorescence of Air and Nitrogen by 50 Kev Electrons", AFCRL-64-466, May 1964.

23. Cresci, R.J. and Zakkay, V., "An Experimental Investigation of the Near Wake of a Slender Cone at M = 8 and 12", ARL 65-87, May 1965.

24. Waldbusser, E., "Relationship of Laminar Wake Width to Wake Transition Distance", AIAA Journal 3, 10, 1965, October 1965.

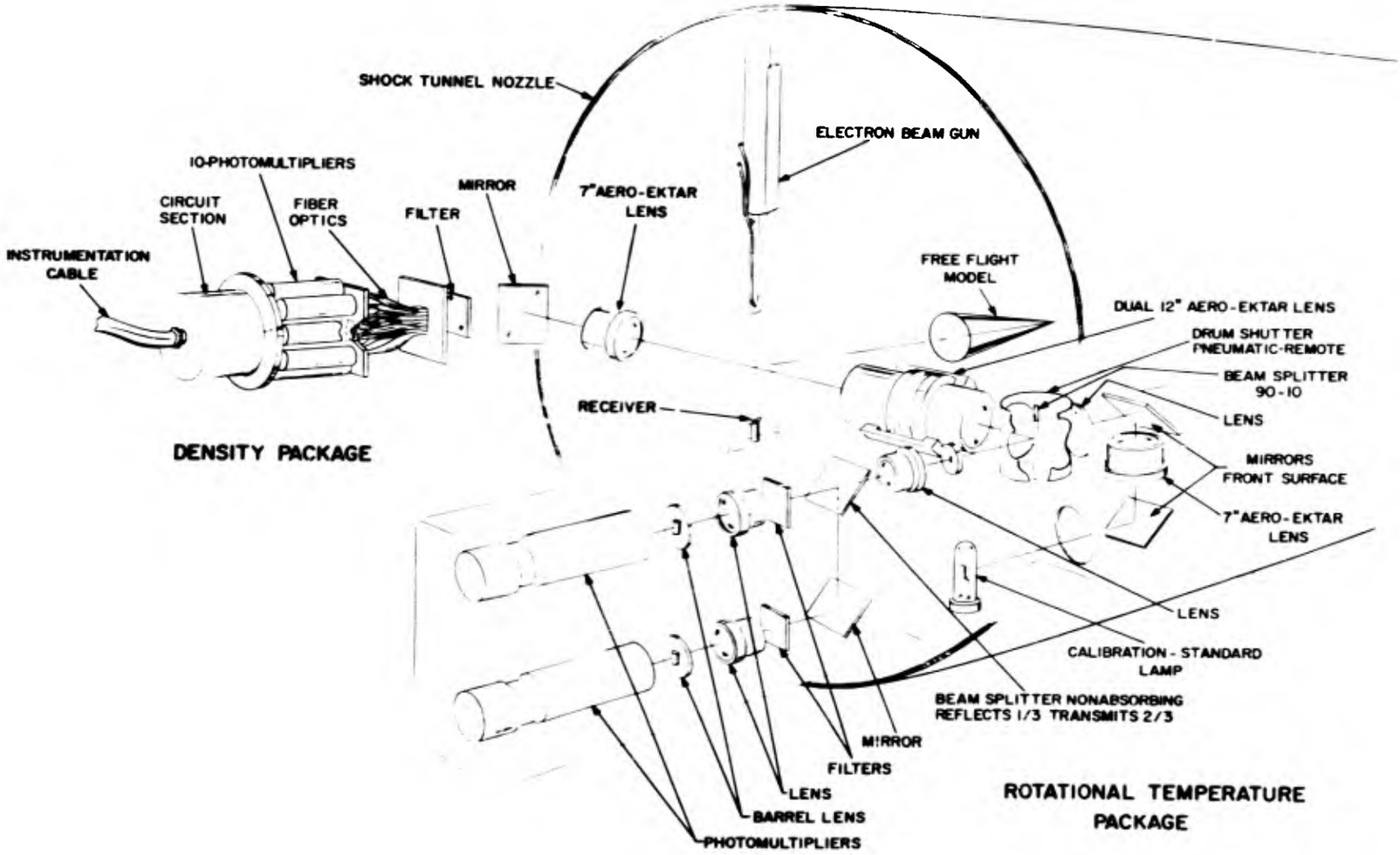

FIGURE 1. EXPERIMENTAL ARRANGEMENT IN THE SHOCK TUNNEL

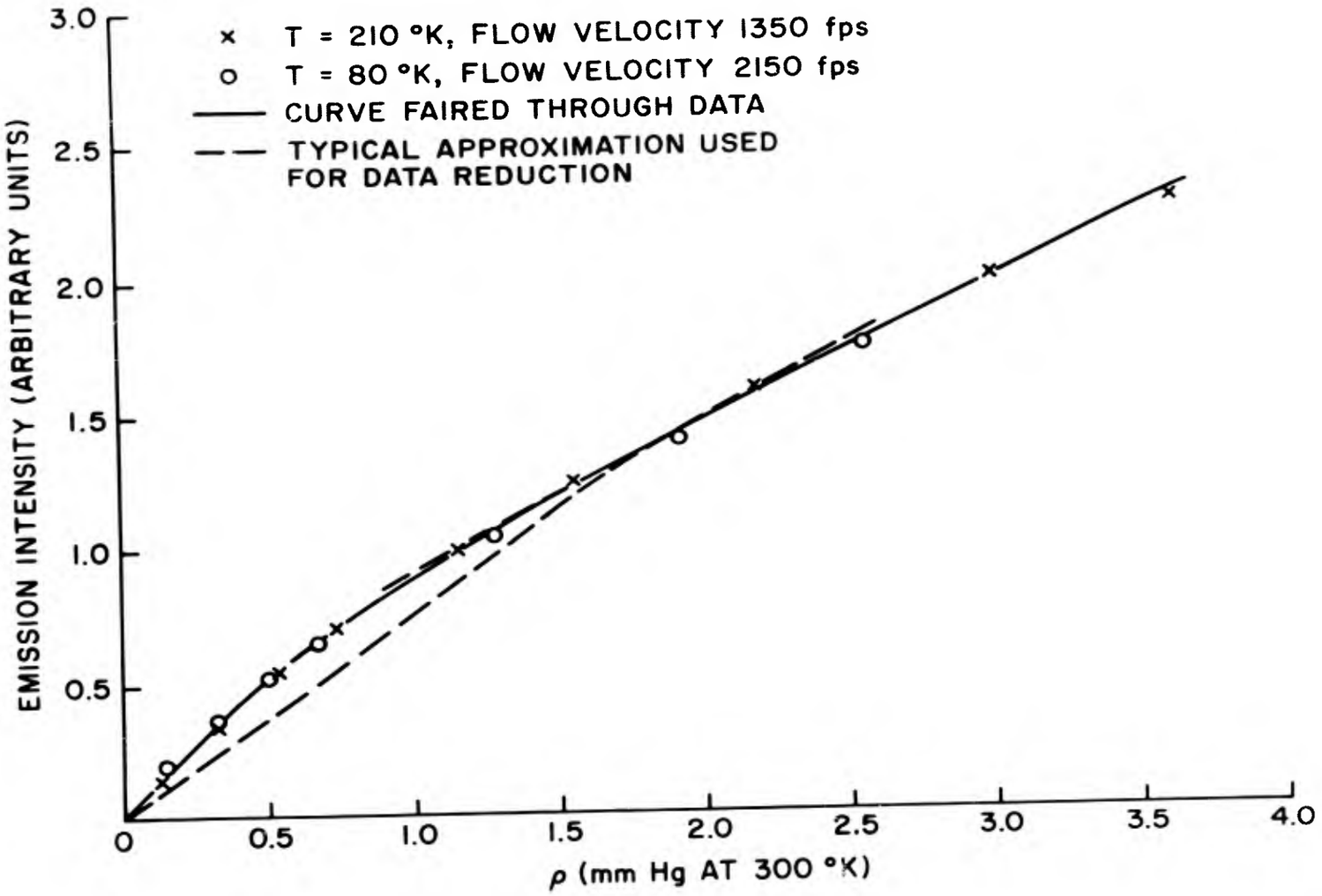

FIGURE 2. CALIBRATION CURVE FOR DENSITY MEASUREMENTS

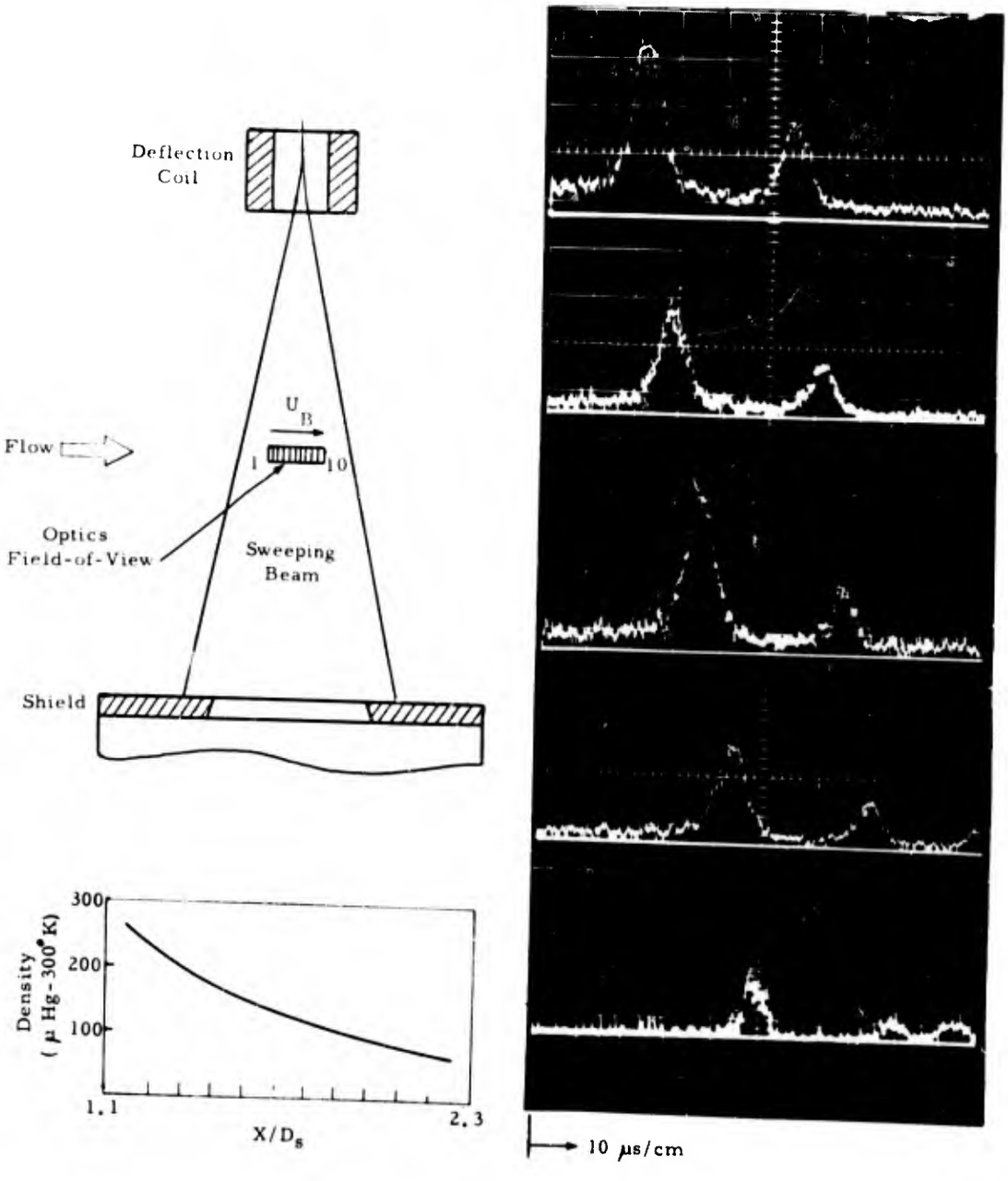

FIGURE 3. OSCILLOSCOPE TRACES OF PHOTOMULTIPLIER OUTPUTS WITH AN AXIAL BEAM VELOCITY U_B = 1000 FT/SEC

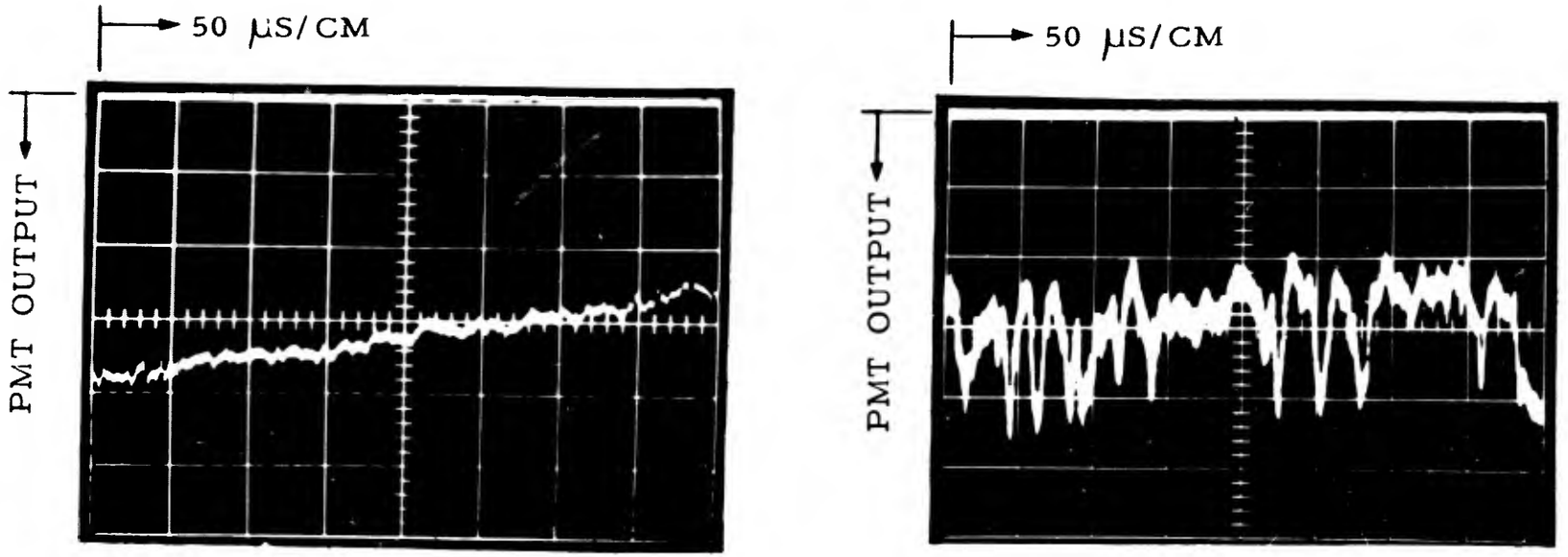

$X/D_B = 5$
$Y/R_B = 0.5$

SMALL FLUCTUATIONS
LAMINAR FLOW

$X/D_B = 30$
$Y/R_B = 0.5$

LARGE FLUCTUATIONS
TURBULENT FLOW

FIGURE 4. OSCILLOSCOPE TRACES OF PHOTOMULTIPLIER OUTPUTS AT TWO POSITIONS IN A HYPERSONIC WAKE

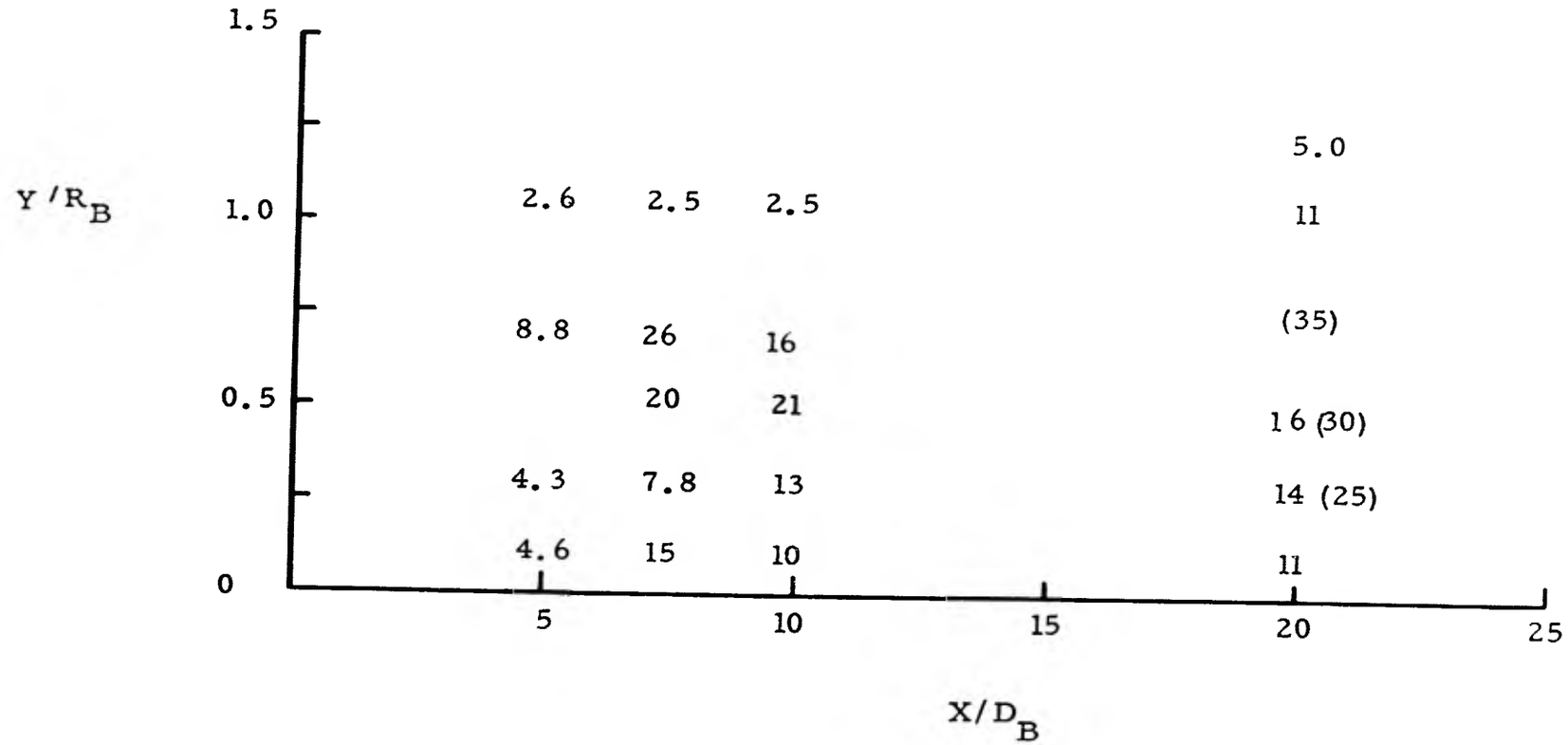

FIGURE 5. ROOT MEAN SQUARE PERCENTAGE DENSITY FLUCTUATIONS AT POSITIONS IN A HYPERSONIC WAKE

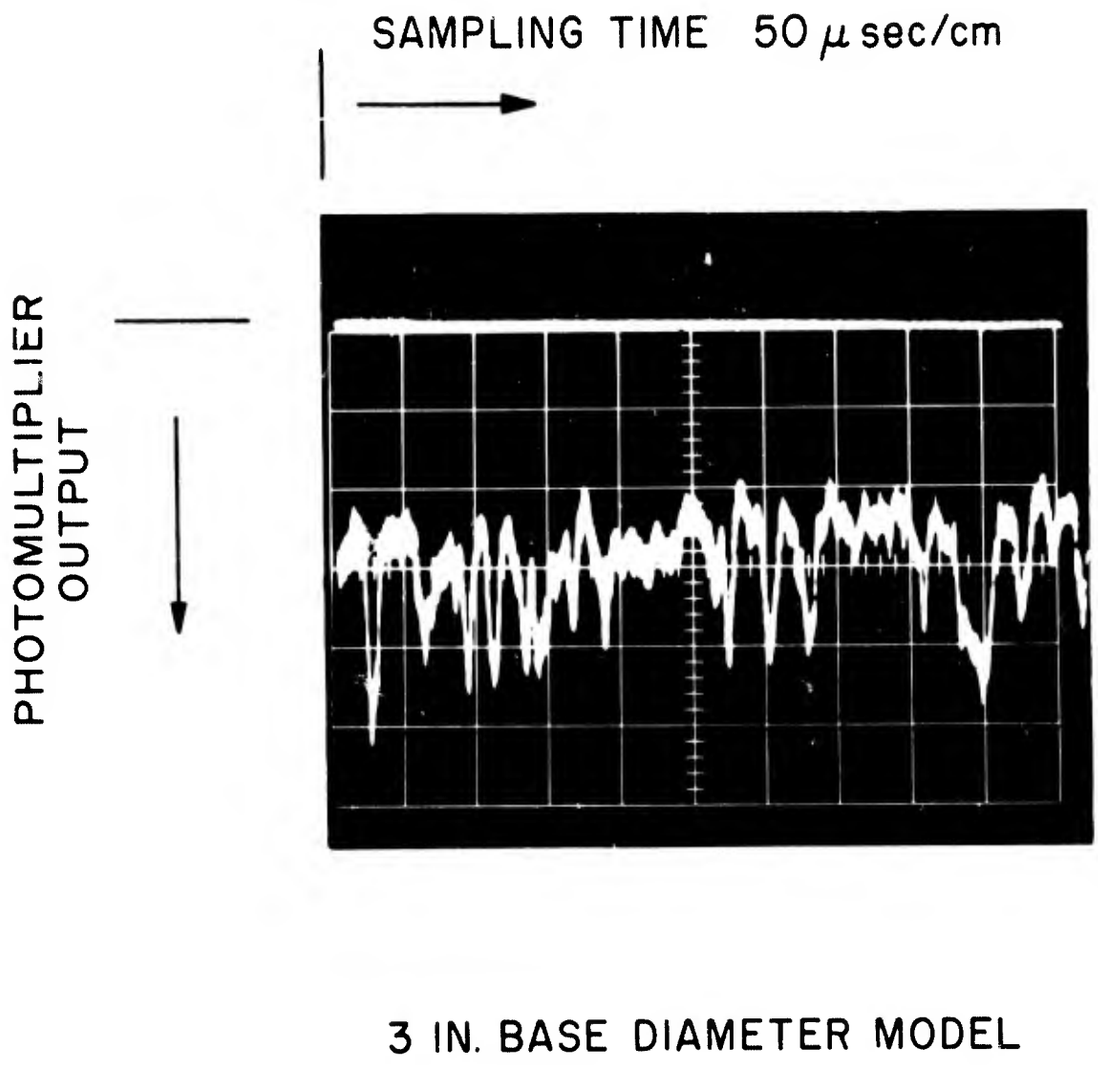

FIGURE 6. FAST RESPONSE PHOTOMULTIPLIER OUTPUT IN THE TURBULENT WAKE, $X/D_B = 20$, $Y/R_B = 0.5$

STUDIES OF TURBULENCE IN THE WAKES OF HYPERSONIC SPHERES UNDER SIMULATED REENTRY CONDITIONS.

By

D. Ellington* and G. Trottier**

Canadian Armament Research and Development Establishment,

Valcartier, Québec, Canada.

* Group Leader, Hypersonic Gas Dynamics Group

** Defence Scientific Service Officer

Paper presented at the AGARD Specialists' Meeting on "Fluid Physics of Hypersonic Wakes", Colorado State University, Fort Collins, Colorado, USA, May 10-12, 1967.

SUMMARY

The techniques of cooled-film anemometry have been applied to the study of mean and fluctuating quantities in the hypersonic wakes of free flight spheres launched in the CARDE ranges. The measurements have yielded information on the temperature and velocity field over an extended length of wakes. Statistical analysis of this data in terms of correlation function and power spectral density has also been undertaken. This information is compared with results of measurements of other wake parameters such as mass and electron density.

RESUME

On a appliqué la technique des anémomètres à pellicule refroidie à l'étude des quantités moyennes et fluctuantes caractérisant le sillage hypersonique de sphères lancées en vol libre dans les installations balistiques du CARDE. Ces mesures ont permis d'obtenir des données sur les champs de température et de vitesse pour une portion étendue du sillage. On a également entrepris l'analyse statistique de ces données du point de vue de la fonction de corrélation et de la densité du spectre de force. Les auteurs comparent enfin ces données avec les résultats de mesures portant sur d'autres paramètres du sillage, tels que masse et densité électronique.

INTRODUCTION

The first application of hot wire anemometry to the study of the turbulent characteristics of projectiles in free flight was made by Fox, Webb, Jones and Hammitt (1). They employed a constant temperature anemometer to study the wake of 0.22 calibre rifle bullet travelling at supersonic speed in a ballistic range. These measurements were aimed primarily at determining the frequency content of the wake and from the measured power spectral density the micro scale and integral scale of the turbulence were inferred as functions of axial distance downstream.

Early in 1966, studies were initiated at CARDE to investigate the turbulence characteristics of the hypersonic wake behind free-flight projectiles. One of the experimental techniques employed was that of the application of the two-temperature method, using cooled-film anemometers, to determine temperature and velocity histories.

EXPERIMENTAL

The cooled-film constant temperature anemometer developed by Fingerson of Thermosystems, Inc., (2) was chosen as the operational tool for these studies. The sensing element consists of a Pyrex-U-tube, 0.006" in diameter through which a cooling fluid can be circulated. On one limb of this U-tube a platinum film, less than one micron thick and about 0.040" long, is deposited and electrical contact is provided by means of a gold coating on the rest of the tube. A photograph of the sensing element is shown in Fig. 1. With the coolant circulating through the sensor, the platinum film is maintained at constant resistance (and hence constant temperature) by means of a bridge circuit, of

which the sensor forms a part, utilizing a feedback system which comprises voltage and power amplifiers to maintain bridge balance. The frequency response of this heat flux system is rated at 500 Kcps. A schematic of the circuit is shown in Fig. 2.

In the absence of any heat transfer between the film and the environment the electrical power supplied to the film element is dissipated by the coolant circulating through the sensor. When this element is exposed to environmental conditions such that a power transfer between the environment and the element occurs, the power supplied to the element by the heat flux system is adjusted so that the power dissipation to the coolant is unaltered. In this way fluctuations in bridge voltage are indicative of changes in the environmental conditions. The power balance for hot film and cooled film constant temperature operation is illustrated in Figs. 3 and 4.

In our present work at CARDE the recording of these bridge voltage fluctuations is effected by means of oscilloscopes viewed by Wollensak Fastax cameras. The signal is displayed on the vertical axis of an oscilloscope with a short persistance phosphor screen and recorded as a trace on a horizontally-moving film. This film, after development, is scanned by an electronic data reader which digitizes on punched paper tape the amplitude of the analog signal. Sampling can be made by the present data reader at frequencies up to 350 Kcps.

The CARDE hypersonic range No. 5 facility shown in Fig. 5 consists of a light gas gun with a 4" barrel capable of launching projectiles into a depressurized tank of 400 ft length at velocities in excess of 15,000 ft/sec.

ANALYSIS

For the determination of wake temperature and velocity histories the two-temperature method is employed. Two sensing elements, each controlled by its own heat flux system, are placed in close proximity to each other and situated close to the predicted flight path of the projectile as shown in Figs. 6 and 7. The sensing elements are maintained at two different but constant temperatures and the two outputs are recorded simultaneously on the same Fastax film. The heat flux systems and coolant supply is shown in Fig. 8. The signals from the two probes can then be analysed to yield wake temperature and velocity as functions of distance behind the projectile.

The analysis involves the use of an empirical relation between Nusselt Number, N_u, and Reynolds number R_e of the cylinder, and the assumption of constant pressure wake. One such relationship which may be employed is that due to Collis and Williams (3), which was obtained for the cooling of heated cylinders at relatively low environment temperatures and under subsonic incompressible flow conditions in undissociated air. This relationship reads

$$Nu_f \left(\frac{T_e}{T_f}\right)^m = a + b\left(Re_f\right)^n \qquad (1)$$

where subcript f refers to film conditions (the film temperature T_f is usually taken as the mean of the sensor and environment temperatures), T_e is the environment temperature and a, b, m and n are empirical constants.

Recently Ahmed (4) has investigated the heating of internally cooled cylinders in a high temperature environment. His experiments were performed in the CARDE plasma-jet facility using various mixtures of monatomic, diatomic and triatomic gases. Ahmed's correlation is similar to that of Collis and Williams except that he uses a kinematic viscosity loading factor instead of a temperature loading factor. His correlation reads:

$$Nu_f \left(\frac{\nu_e}{\nu_f}\right)^m = a + b\,(Re_f)^n \qquad (2)$$

Values of the empirical constants for these two correlations are listed below:

CORRELATION	Re_f	a	b	m	n
Collis & Williams	0.02 - 44	0.24	0.56	0.17	0.45
Collis & Williams	44 - 140	0	0.48	0.17	0.51
Ahmed	5 - 40	0.2068	0.4966	0.15	0.45

A comparison of the Ahmed correlation with those of Kramer (5), Van Der Hegge Zijnen (6), Collis and Williams (3), Hilpert (7), is shown in Fig. 9.

In terms of the Ahmed correlation we have

$$Nu_f = \frac{h_c d}{k_f} = \left(a + b\,Re_f^n\right)\left(\frac{\nu_f}{\nu_e}\right)^m \qquad (3)$$

where h_c is the heat transfer coefficient corrected for slip effects,

defined according to Collis and Williams (2) by

$$\frac{1}{h_c} = \frac{1}{h} - \frac{2\lambda_s}{k_s} \tag{4}$$

and where h, the heat transfer coefficient, is given by

$$h = \frac{Q}{\pi d l (T_e - T_s)} \tag{5}$$

Here

d is the cylinder diameter,

l is the cylinder length,

k_f is the thermal conductivity of the environment fluid evaluated at film temperature, T_f,

k_s is the thermal conductivity of the environment fluid evaluated at sensor temperature, T_s,

λ_s is the mean free path of the environment fluid at sensor temperature, T_s,

Q is the power transfer from the environment to the sensor.

From Eq. (3) and (4)

$$Nu_f = \frac{h d k_s}{k_f (k_s - 2 Kn . h d)} = \left\{ a + b (Re_f)^n \right\} \left(\frac{\nu_f}{\nu_e} \right)^m$$

where $Kn = \frac{\lambda_s}{d}$ is the Knudsen number evaluated at sensor temperature.

Then from Eq. (5)

$$\left\{a + b(Re_f)^n\right\}\left(\frac{\nu_f}{\nu_e}\right)^m = \frac{Q k_s}{k_f\left\{\pi \ell (T_e - T_s) k_s - 2 Kn . Q\right\}} \tag{6}$$

whence

$$V = \frac{\nu_f}{d}\left[\frac{1}{b}\left\{\frac{Q}{\left[\pi \ell k_f (T_e - T_s) - 2\frac{k_f}{k_s} Kn . Q\right]\left(\frac{\nu_f}{\nu_e}\right)^m} - a\right\}\right]^{\frac{1}{n}} \tag{7}$$

where V is the fluid velocity past the sensor.

For two sensors operating at the same point in the fluid, but at differe constant temperatures denoted by subscripts 1 and 2, two equations of the form of Eq. (7) pertain.

V may be eliminated between them and the resulting equation solved for the environment temperature T_e . Explicity there results a quadratic

$$A T_e^2 + B T_e + C = 0 \tag{8}$$

where A, B and C are weak functions of T_e , given by

$$A = a\pi^2 \ell_1 \ell_2 k_{f_1} k_{f_2} \left(\frac{\nu_{f_1}}{\nu_e}\right)^m \left(\frac{\nu_{f_2}}{\nu_e}\right)^m \left\{(\nu_{f_2} d_1)^n - (\nu_{f_1} d_2)^n\right\}$$

$$B = Q_1 \pi \ell_2 k_{f_2} \left(\frac{\nu_{f_2}}{\nu_e}\right)^m (\nu_{f_1} d_2)^n - Q_2 \pi \ell_1 k_{f_1} \left(\frac{\nu_{f_1}}{\nu_e}\right)^m (\nu_{f_2} d_1)^n - A(T_{s_1} + T_{s_2})$$
$$+ 2a k_{f_1} k_{f_2} \left(\frac{\nu_{f_1}}{\nu_e}\right)^m \left(\frac{\nu_{f_2}}{\nu_e}\right)^m \left(Q_1 \frac{Kn_1}{k_{s_1}} \pi \ell_2 - Q_2 \frac{Kn_2}{k_{s_2}} \pi \ell_1\right) \left\{(\nu_{f_1} d_2)^n + (\nu_{f_2} d_1)^n\right\}$$

$$C = A\left(T_{s_1} T_{s_2} - Q_1 Q_2 \frac{4 Kn_1 Kn_2}{\pi^2 \ell_1 \ell_2 k_{s_1} k_{s_2}}\right)$$
$$+ 2a \left(\frac{\nu_{f_1}}{\nu_e}\right)^m \left(\frac{\nu_{f_2}}{\nu_e}\right)^m k_{f_1} k_{f_2} \left(Q_2 T_{s_1} \frac{Kn_2}{k_{s_2}} \pi \ell_1 - Q_1 T_{s_2} \frac{Kn_1}{k_{s_1}} \pi \ell_2\right) \left\{(\nu_{f_2} d_1)^n + (\nu_{f_1} d_2)^n\right\}$$
$$- (\nu_{f_1} d_2)^n \left(\frac{\nu_{f_2}}{\nu_e}\right)^m Q_1 k_{f_2} \left(\pi \ell_2 T_{s_2} + 2 Q_2 \frac{Kn_2}{k_{s_2}}\right) + (\nu_{f_2} d_1)^n \left(\frac{\nu_{f_1}}{\nu_e}\right)^m Q_2 k_{f_1} \left(\pi \ell_1 T_{s_1} + 2 Q_1 \frac{Kn_1}{k_{s_1}}\right)$$

The solution consists in using a preliminary estimate of T_e in order to evaluate the coefficients A, B and C. The Eq. (8) is then solved for a new estimate of T_e and the procedure repeated iteratively until the solution converges. V may then be calculated from Eq. (7).

The above method has been programmed for solution using a digital computer, a pair of values (T_e, V) being computed from each input pair (Q_1, Q_2).

ERROR ANALYSIS

It became evident at an early stage that the method suffered from inaccuracies introduced in the calibration, measurement, recording, reading and analysis phases of the experiment. These inaccuracies were such as to produce an unacceptably large cumulative error in the final determination of wake temperature and velocity.

For ease of performing an error analysis Eq. (6) was simplified to read

$$Q_1 = (T_e - T_{s_1}) \left(\frac{V}{Z_1}\right)^{1/2} \qquad (9)$$

$$Q_2 = (T_e - T_{s_2})\left(\frac{V}{Z_2}\right)^{1/2} \tag{10}$$

for the two sensors respectively.

This representation corresponds to the Collis and Williams correlation for $44 < Re_f < 140$. $Z_{1,2}$ is defined

$$Z_{1,2} = \frac{\nu_{f_{1,2}}}{d_{1,2}\, b^2 \pi^2 \ell_{1,2}^2 k_{f_{1,2}}^2 \left(\frac{T_{f_{1,2}}}{T_e}\right)^{0.34}} \tag{11}$$

For a given ambient pressure, over the range of realizable values of T_{s_1}, and T_{s_2}, the values of Z does not vary by more than a few percent for typical values of T_e likely to be encountered in the hypersonic wake. Thus we take:

$$Z_1 = Z_2 = Z \quad , \quad \text{say}$$

From Eq. (9) and (10) we obtain

$$T_e = \frac{Q_1 T_{s_2} - Q_2 T_{s_1}}{Q_1 - Q_2} \tag{12}$$

and,

$$V = \frac{Z\,(Q_1 - Q_2)^2}{(T_{s_2} - T_{s_1})^2} \tag{13}$$

Defining a parameter

$$K = \frac{Q_1}{Q_2} = \frac{T_e - T_{s_1}}{T_e - T_{s_2}} \tag{14}$$

we find that a fractional error in K is related to fractional errors in Q_1 and Q_2 as follows

$$\frac{\Delta K}{K} = \frac{\Delta Q_1}{Q_1} - \frac{\Delta Q_2}{Q_2} \tag{15}$$

Assuming that $\left|\frac{\Delta Q_1}{Q_1}\right| = \left|\frac{\Delta Q_2}{Q_2}\right| = \left|\frac{\Delta Q}{Q}\right|$, say,

the maximum error in K occurs for

$$\frac{\Delta Q}{Q} = \frac{\Delta Q_1}{Q_1} = -\frac{\Delta Q_2}{Q_2}$$

or, $$\frac{\Delta Q}{Q} = -\frac{\Delta Q_1}{Q_1} = \frac{\Delta Q_2}{Q_2}$$

whence from Eq. (15),

$$\frac{\Delta K}{K} = \pm 2 \frac{\Delta Q}{Q} \tag{16}$$

The resultant errors $\frac{\Delta T_e}{T_e}$ and $\frac{\Delta V}{V}$

are obtained from Eq. (12) and (13) as follows

$$\frac{\Delta T_e}{T_e} = \pm 2 \frac{\Delta Q}{Q} \left(\frac{K T_{s_2}}{K T_{s_2} - T_{s_1}} - \frac{K}{K-1} \right) \tag{17}$$

$$\frac{\Delta V}{V} \quad \mp 2 \frac{\Delta Q}{Q} \left(\frac{K+1}{K-1} \right) \tag{18}$$

Further, for T_{s_1}, T_{s_2} and K specified, the value of T_e is uniquely determined from Eq. (12) as

$$T_e = \frac{K T_{s_2} - T_{s_1}}{K-1} \tag{19}$$

$\left(\frac{\Delta T_e}{T_e} \Big/ \frac{\Delta Q}{Q}\right)$ and $\left(\frac{\Delta V}{V} \Big/ \frac{\Delta Q}{Q}\right)$ have been evaluated from Eq. (17) and (18) as functions of K for two pairs of sensor temperatures and are shown in Figs. 10 to 12, together with a scale of T_e as evaluated from Eq. (19).

Fig. 10 is appropriate to sensor temperatures T_{s_1} = 400°K, T_{s_2} = 500°K and Fig. 11 to T_{s_1} = 600°K, T_{s_2} = 800°K. It will be seen that for wake temperatures T_e typically of the order of 1000°K , the values of $\left(\frac{\Delta T_e}{T_e}\Big/\frac{\Delta Q}{Q}\right)$ and $\left(\frac{\Delta V}{V}\Big/\frac{\Delta Q}{Q}\right)$ increase sharply for values of K less than about 2.

DISCUSSION

With distilled water as a coolant, the maximum realizable value of K under hypersonic wake environmental conditions of $T_e \sim 1000°K$ is about 1.2, corresponding to T_{s_1} = 400°K and T_{s_2} = 500°K. Under these conditions, as will be seen from Figs. 10 and 12, a 10% error in $Q_{1,2}$ will result in a maximum error of 60% in T_e and a maximum error of 220% in V. The reasons for such a low maximum value of K when distilled water is used as a coolant are twofold. First, for a laminar flow of water through the sensor a maximum sensor temperature of about 500°K is realizable before the water boils. If the mass flow of water through the sensor is increased to accomodate a higher sensor temperature, the water flow becomes transitional or turbulent and the resultant electronic noise increases from its value under laminar coolant flow conditions by at least an order of magnitude. Second, the minimum sensor temperature is determined by the condition that the power transfer to the coolant should exceed the power transfer from the environment to the sensor, in order to avoid saturation.

Recent experiments at CARDE have shown that the maximum sensor temperature can be increased by using a coolant fluid of higher viscosity than that of water. One may thus increase the mass flow through the sensor before the coolant flow becomes turbulent, and sensor tempe- temperatures in excess of 800°K have been obtained with the use of

such fluids as Silicon oil 704 and Fluorolube FS. These fluids are safe, odourless, and have flash points in excess of 500°K. Also they are clean, do not coagulate, and thereby do not produce blockage of the sensor. Values of K in excess of 2 may thus be obtained using these or similar fluids as coolants. With K= 2, Figs. 11 and 12 indicate that a 10% error in $Q_{1,2}$ will result in maximum error of 8% in T_e and a maximum of 60% in V, for environmental conditions corresponding to T_e = 1000°K.

SOURCES OF ERROR

Some of the main sources of experimental error which contribute to $\Delta Q/Q$ may be mentioned;

(a) Calibration

The errors introduced in the measurement of sensor length and diameter, of sensor holder and cable resistances and of absolute resistances in the compensating bridge circuitry can generally be minimised by the use of standard calibration techniques. The relationship between sensor resistance and sensor temperature is however one which is difficult to ascertain. Measurements made using a high resolution infrascope (Huggins Lab. MkI) have indicated that significant departures from uniformity of temperature along the length of the sensing element can exist under certain operating conditions. The effects of temperature loading non-uniformity have previously been discussed by Betchov (8) and Betchov and Welling (9), and more recently by Champagne, Sleicher and Wehrmann(10).

Since a known environment approximating hypersonic wake conditions is extremely difficult to simulate in the laboratory for periods of time sufficiently long to permit calibrations to be performed,

one must rely on the ad hoc hypothesis that the shape of the temperature distribution under operating conditions is not significantly different from that measured in the laboratory. It may be argued that this hypothesis could hold providing that the power transfer to the supports is significantly less than the power transfer to the coolant, but so far there is no data to substantiate this argument.

At present the relationship between sensor temperature and sensor resistance is established by a calibration procedure involving the use of a black-body, a chromel-alumel thermocouple and a high precision digital voltmeter. The calibration is extended above 500°K using a constant current source and a high resolution infrascope.

(b) Measurement

In order to determine the power transfer to the coolant, it has been assumed that, prior to the arrival of the hypersonic environment of the projectile, the electrical power supplied to the sensing element is entirely dissipated by the coolant. The effects of free convection under these static conditions have been neglected, since laboratory tests conducted so far at CARDE have failed to establish their importance.

Another factor is the mutual interference of the two sensing elements when placed in close proximity to each other. There exists the possibility of mutual interference between them due to thermal gradients and boundary layer interaction. These effects have not been investigated in our laboratory. It is evident that the resolution of

the smallest turbulent eddy depends not only on the finite sensing element size but also on the physical spacing between the sensors. Experiments to date have been made with spacings of the order of 0.050", or about $\frac{1}{50}$th of the projectile size.

As is common to all anemometry techniques there exist thermal losses from the sensor to the supports. Because of the non-uniformity in the sensor temperature distribution these effects are difficult to assess.

It has been observed also that the sensor at higher temperature exhibits a higher frequency response than the one at lower temperature. Under operating conditions, of course, the overall frequency response of the system is limited by the dynamic response of the sensing element, which is about one order of magnitude less than the frequency response of the electronic feedback system. This difference in frequency response between the sensors complicated the synchronization problem. At first, smoothing techniques were employed to reduce the frequency content of the higher temperature sensor signal so that it became compatible with that of the lower temperature sensor signal. It appears however that this problem is less acute when oils are used as coolants rather than water, since the absolute temperatures of the sensors are somewhat higher, and also it is possible by a judicious choice of sensor temperatures to match the dissipation to two different coolants, and hence to match the frequency response of the two sensors.

It must be recognized also that the boundary layer characteris-

tics of the two sensors are likely to be different, as are the points of boundary layer separation. The latter effect implies that the effective heat transfer areas of the sensors are different. No allowance for these effects have so far been made in our analysis.

There exists also the possibility that in the hypersonic wake environment the catalytic effects of the sensors may become important. Recombination of dissociation products in the wake may occur with the sensor acting as a third body. From our present limited knowledge of the hypersonic wake we calculate that these effects are minimal, although experimental verification is much needed.

Finally, as in the case with all electronic systems, the measurements suffer from the effects of electronic noise. For laminar coolant flow this noise is of the order of a few millivolts but increases by an order of magnitude for transitional or turbulent coolant flow. These values are to be compared with a signal level of the order of a tenth of a volt in environmental conditions for which the ambient pressure is one tenth of an atmosphere. At lower ambient pressures the signal level decreases and so correspondingly does the signal to noise ratio.

(c) Recording

With an analog recording system, such as we have previously described, errors are introduced in the absolute calibration of the recording oscilloscopes and by their non-linearity. Additionally the magnification of the Fastax cameras amy deviate from their nominal values. The effects of these errors are minimized by employing a voltage

"staircase" generator which calibrates the Fastax film a few milliseconds prior to the arrival of the signal from the projectile environment. A major difficulty is that associated with the finite spot size resulting from impact of the electron beam on the oscilloscope phosphor. This results in a finite trace width on the film which is much larger than the scanning spot of the data reader.

All of these errors may be eliminated by the use of a digital recording system. Such a system is under development at CARDE. The analog signals from the sensors are first digitized by analog to digital conversion units which produce twelve bits of binary information corresponding to the analog signal. For most hypersonic range applications the system is capable of covering the full dynamic range of operation at a conversion rate of about 60 Kcps. The binary information is then recorded on Fastax film through Z modulation of the oscilloscope beam. The developed film is then passed on the data reader which transfers the information to punched paper tape.

(d) Reading

In reading an analog signal the data reader operates on the basis of discrete steps, or counts, rather than on a continuous basis. Backlash in the mechanical drive and film imperfections can result in spurious readings.

These problems are likely to be overcome with the use of a digital recording system.

(e) Analysis

For ease of analysis it has been assumed that the pressure

fluctuations associated with compressible turbulence are small in the hypersonic wake. Close to the projectile this assumption is almost certainly invalid. Further, in this same region where the flow is at least transonic past the sensors, there exists no established correlation between Nusselt number and Reynolds number. Such correlations as do exist pertain to wholly subsonic or wholly supersonic flow, which is considerably different, both chemically and thermodynamically from a hypersonic wake flow.

OBSERVATIONS

Investigations concerned with the decay of turbulent energy in low speed two dimensional wake flows have been conducted by Townsend (11,12). The low speed axially symmetric wake problem has been investigated experimentally by Cooper and Lutzky (13) and by Hwang and Baldwin (14). The latter two references indicate that similarity considerations can accurately predict the characteristics of low speed turbulent axisymmetric wakes.

The high speed turbulent axisymmetric wake has been considered by Schapker (15) based on results obtained at the Ballistics Research Laboratory and the Naval Ordnance Laboratory in the United States. He concludes that similarity behaviour is not exhibited until at least one thousand body diameters downstream in the case of a sphere. Slattery (16), on the other hand, has observed similarity in sphere wakes at downstream distances less than a thousand body diameters, a finding which appears to have been substantiated by Fox, et al (1).

Since the two-temperature method yields wake velocity directly as one of the variables, power spectral densities may be transposed immediately to the wave number domain to provide Eulerian integral and micro-scales.

It is hoped then that the present investigations will shed light on the question of self-similarity at high speeds, that the important cross correlation between wake temperature and velocity may be established as a function of axial

distance downstream (Lykoudis (17)), and further that some information may be obtained regarding the laws of turbulent transport in the hypersonic wake.

Results obtained so far at CARDE are of a preliminary nature, but are indicative of the feasibility of the experiment.

CONCLUSIONS:

The technique of cooled film anemometry may be applied to the study of the turbulent characteristics of hypersonic wakes in free-flight ranges. The two-temperature method, however, suffers from limitations associated with the uncertainties in suitable heat transfer correlations under transonic flow conditions, the effects of free convection, surface catalysis, boundary layer separation, mutual interference, and the effects of compressibility.

Measurements are complicated by such effects as non uniformity in sensor temperature distribution, thermal losses, frequency response and electronic noise in the system. Nevertheless some progress has been made in the measurement by such means as the use of different coolants and the development of a digital, instead of analog, recording system.

In summary, it is felt that in view of the fact that our knowledge of the turbulent characteristics of hypersonic wakes is so inadequate, that such techniques can be applied successfully to yield a better understanding of the phenomena observed. In particular, the method can yield information on both the mean and fluctuating components of wake temperature and velocity, the important cross correlation between these parameters, and some measure of the turbulence scales. It should be possible also to make some definitive statements on the extent to which considerations of isotropy, local homo geneity and local similarity can be applied to our model of the hypersonic wake and to improve our understanding of the turbulent transport processes involved.

ACKNOWLEDGEMENTS

This work is sponsored under the joint CARDE-ARPA reentry physics program of ARPA Order 133. Thanks are due to the Chief Superintendent of CARDE for permission to publish this paper, and to the supervisors and staff of Aerophysics Wing for their support, in particular Mr. G.H. Tidy, Major T.E. Bearden, Dr. A. Lemay, Dr. E. Léger and Mr. P. Solnoky.

We wish to acknowledge the cooperation of Messrs J. Holland and L. Moir for instrumentation design and development.

We are indebted to Prof. S. Mölder and Mr. A.M. Ahmed of McGill University for their active support and to Prof. C.I.H. Nicholl of Laval University and Dr. L. Fingerson of Thermosystems Inc., for helpful discussions.

Finally we recognize gratefully the efforts of our two technicians, Messrs. P. Desjardins and M. Paquin for their invaluable assistance in the experimental phases of our work.

REFERENCES

1. Fox, J.
   Webb, W.H.
   Jones, B.G.
   Hammitt, A.G.
   Hot Wire Measurements of Wake Turbulence in a Ballistic Range
   AIAA Journal 5, 1, pp 99-102 January 1967

2. Fingerson, L.
   Instruction Manual, Heat Flux System Model 1000A. Thermosystems Inc., St. Paul, Minnesota.

3. Collis, D.C.
   Williams, M.J.
   Two Dimensional Convection from Heated Wires at Low Reynolds Numbers.
   J. Fluid Mech 6, 3, pp 357-384 - October 1959.

4. Ahmed, A.M.
   Forced Convection Heat Transfer to Cooled Cylinders at Low Reynolds Numbers and with Large Temperature Differences.
   Journal of Heat and Mass Transfer
   (To be submitted for publication)

5. Kramer, H.
   Physica, 12, No. 2-3, 61 (1946)

6. Vander Hegge Zijnen, B.G.
   Appl. Sci. Research A, 6 , 129 (1956)

7. Hilpert, R.
   Forsch Gebiete Ingenieurw, 4, 215 (1933)

8. Betchov, R.
   Nonlinear Theory of a Hot Wire Anemometer
   NACA TM 1346 (July 1952)

9. Betchov, R.
   Welling. W.
   Some Experiences regarding the Nonlinearity of Hot Wires.
   NACA TM 1223 (June 1952)

10. Champagne, F.H., Sleicher, C.A., Wehrmann, O.H. — "Turbulence Measurements with Inclined Hot-Wires" J. Fluid Mech 28, 1 pp 153-182 (April 1967)

11. Townsend, A.A. — "Measurements in the Turbulent Wake of a Cylinder" Proc. Roy. Soc. A. 190, 1023, pp. 551-561 (Sept. 1947).

12. Townsend, A.A. — "The fully Developed Turbulent Wake of a Circular Cylinder". Aug. J. Sci. Res., A, 2, pp. 451-468 (1949)

13. Cooper, R.D. — "Exploratory Investigation of the Turbulent Wakes Behind Bluff Bodies". David Taylor Model Basin Re. 963 (NS 715-102) (Oct. 1955).

14. Hwang, N.H.C. Baldwin, L.V. — "Decay of Turbulence in Axisymmetric Wakes". Amer. Soc. Mech. Eng., Paper No. 65-FE-8 (June 1965)

15. Schapker, R.L. — "Statistics of High-Speed Turbulent Wake Boundaries". AIAA Journal, 4, 11, pp. 1979-1987. (Nov. 1966).

16. Slattery, R. — Private Communication (MIT Lincoln Labs) (April 1967)

17. Lykoudis, P.S. — "Recent Developments in the Fluid Mechanics of Hypersonic Wakes". Paper presented at the XVIIth International Aeronautical Congress, Madrid, (Oct. 1966).

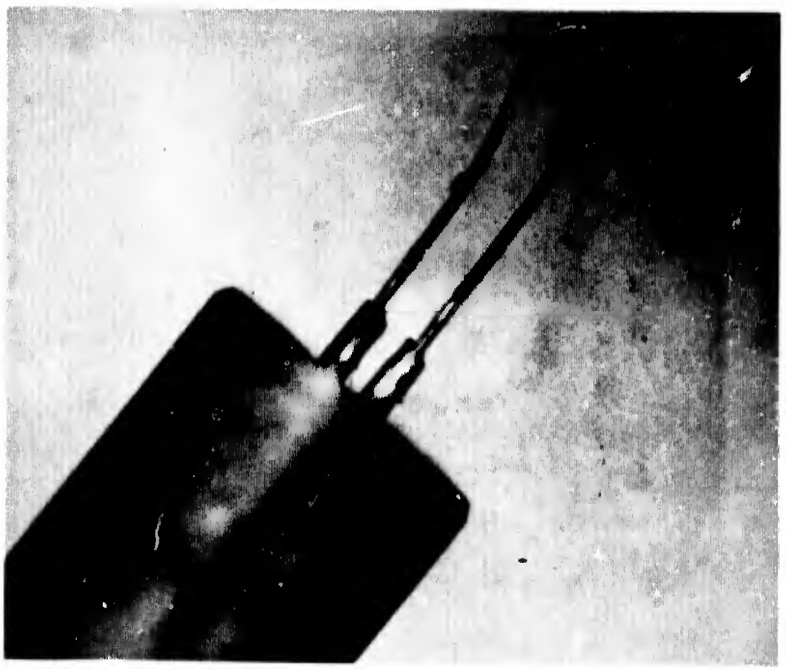

Fig.1 Photograph of sensing element

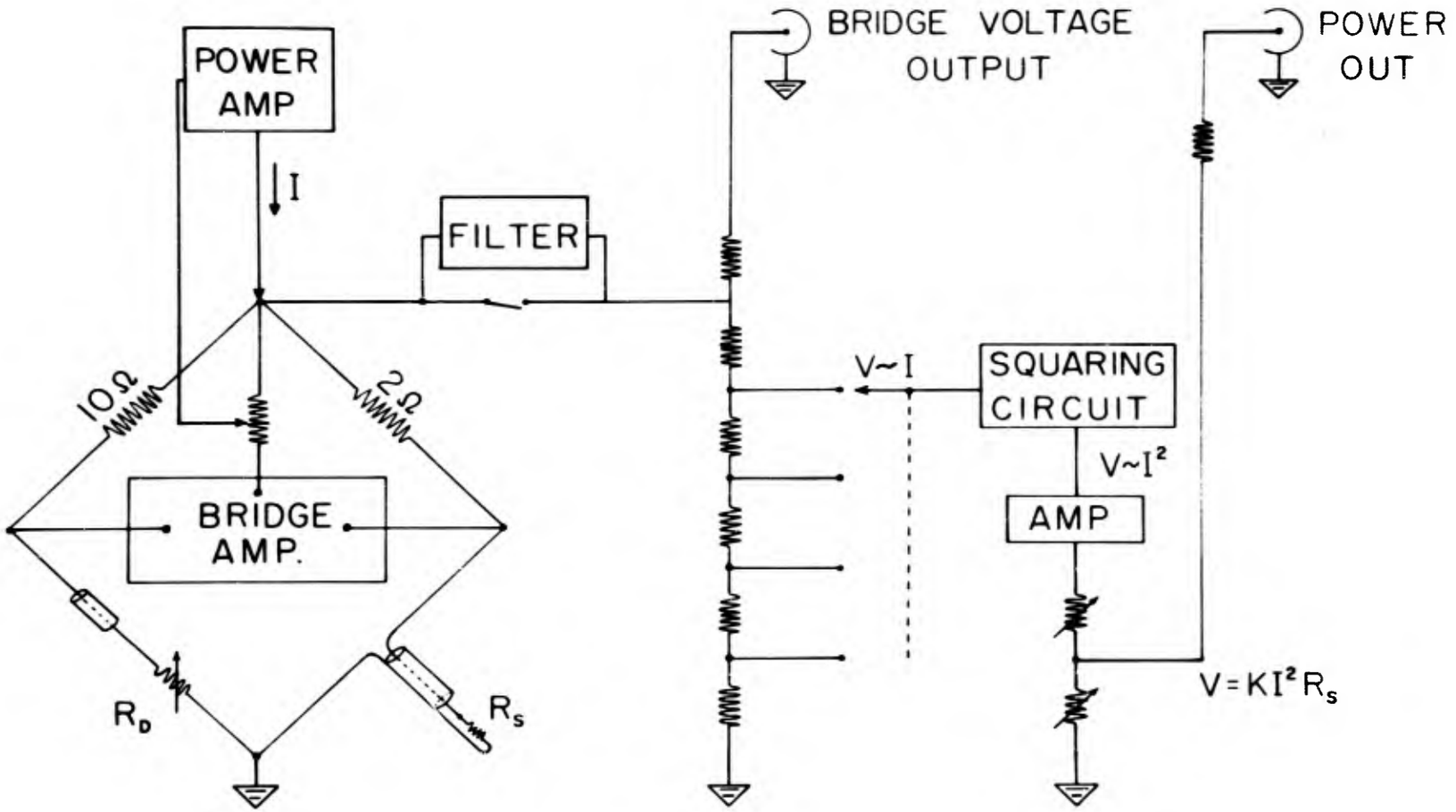

Fig. 2 Functional schematic of circuit

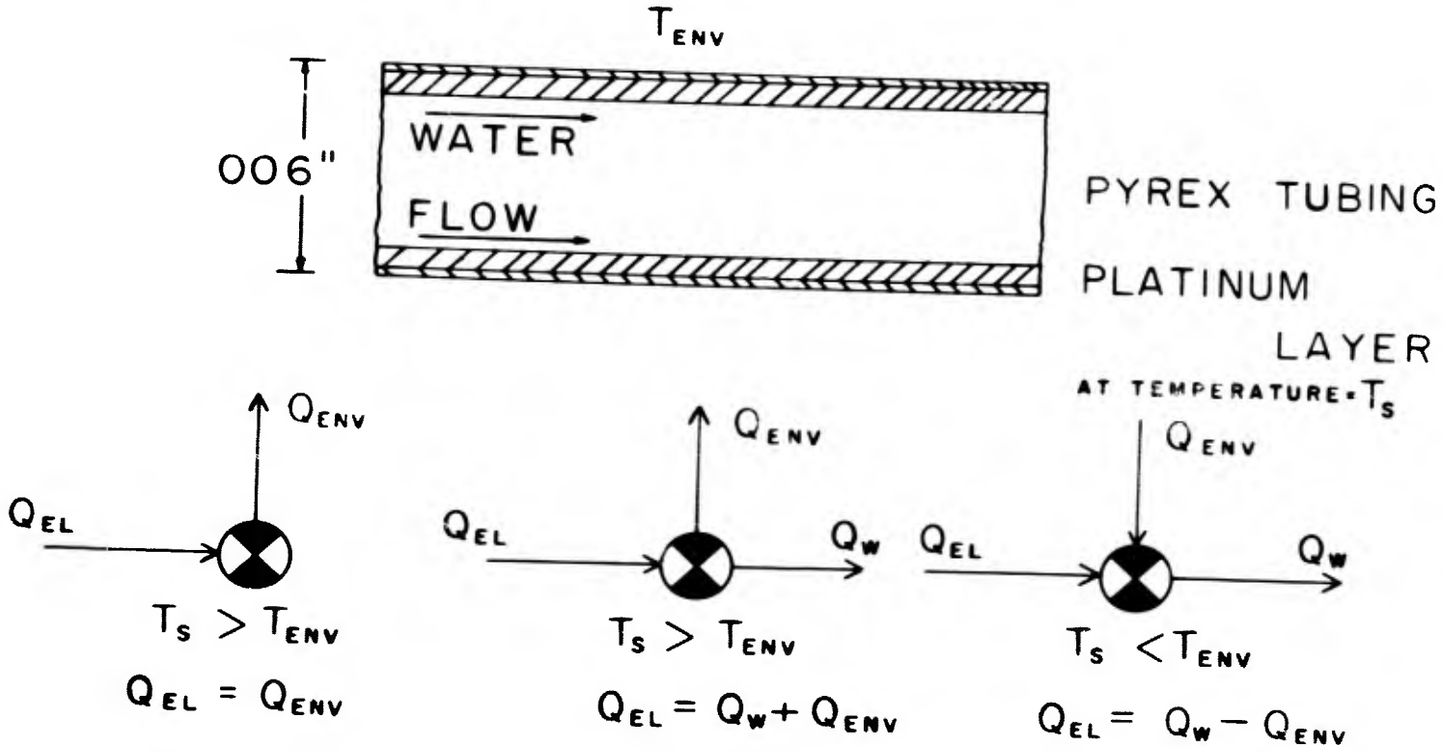

Fig.3 Flow chart of heat transfer for constant temperature operation

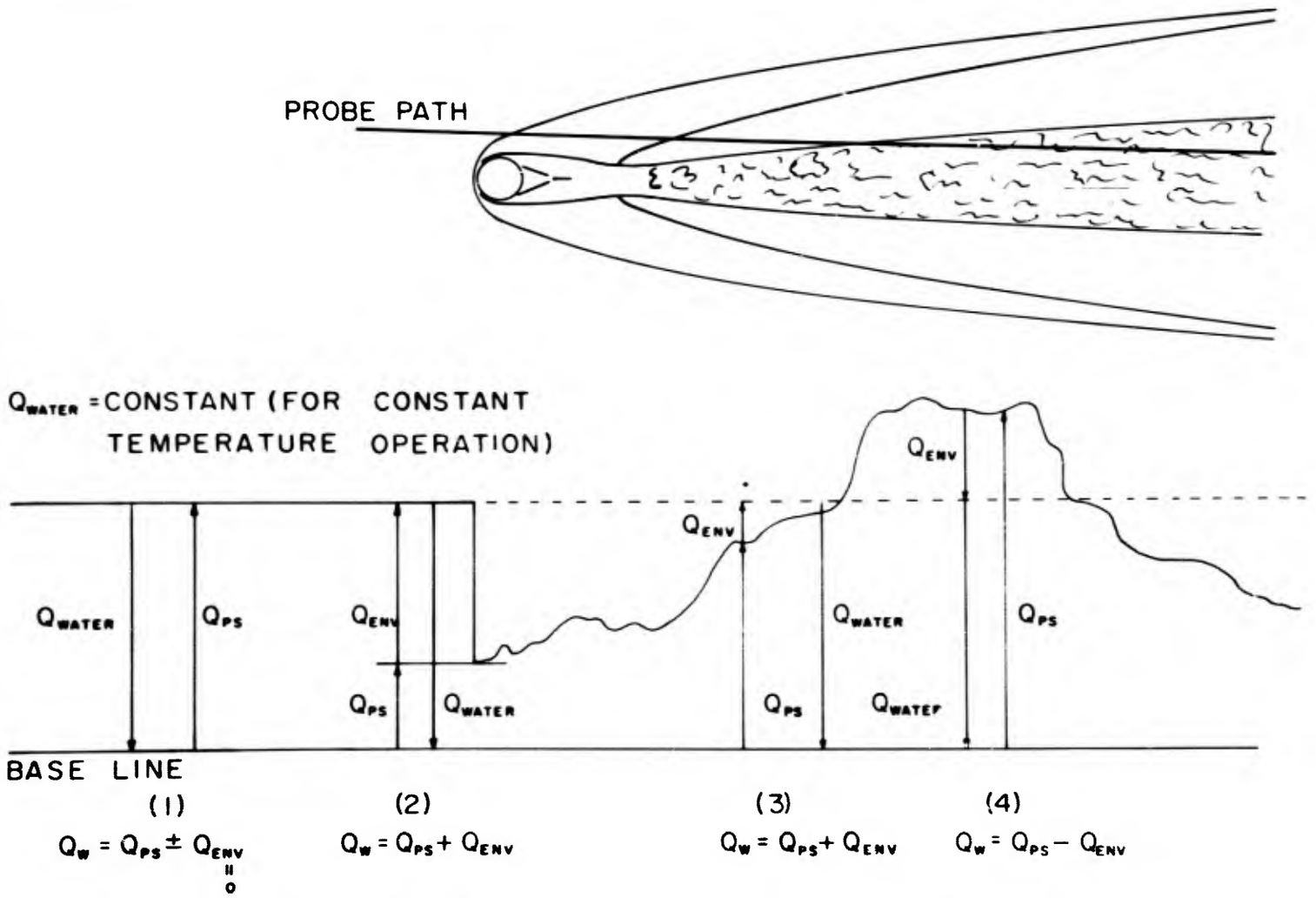

Fig. 4 Typical heat flux power balance in hypersonic wake application

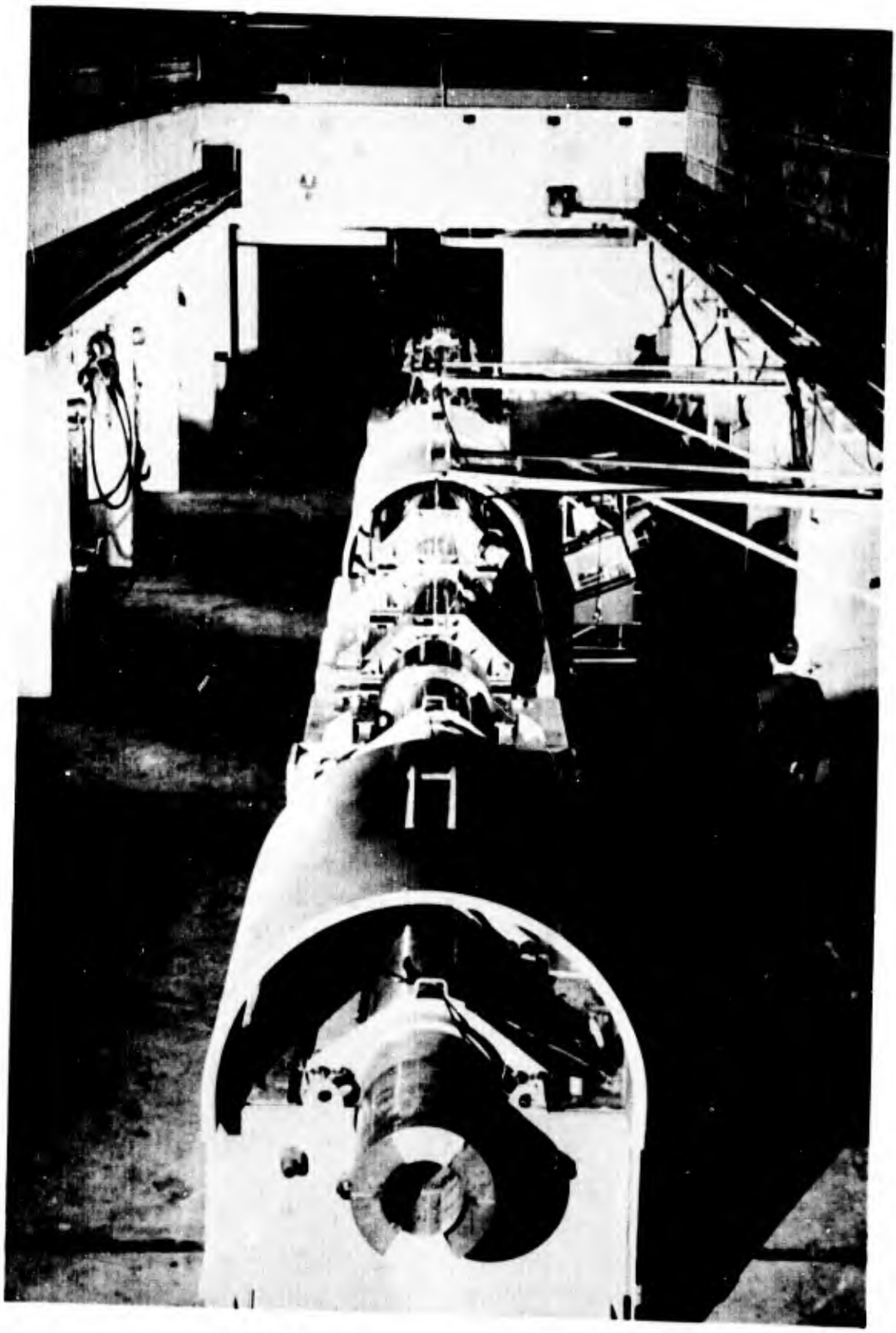

Fig.5 Hypersonic Range 5 facility

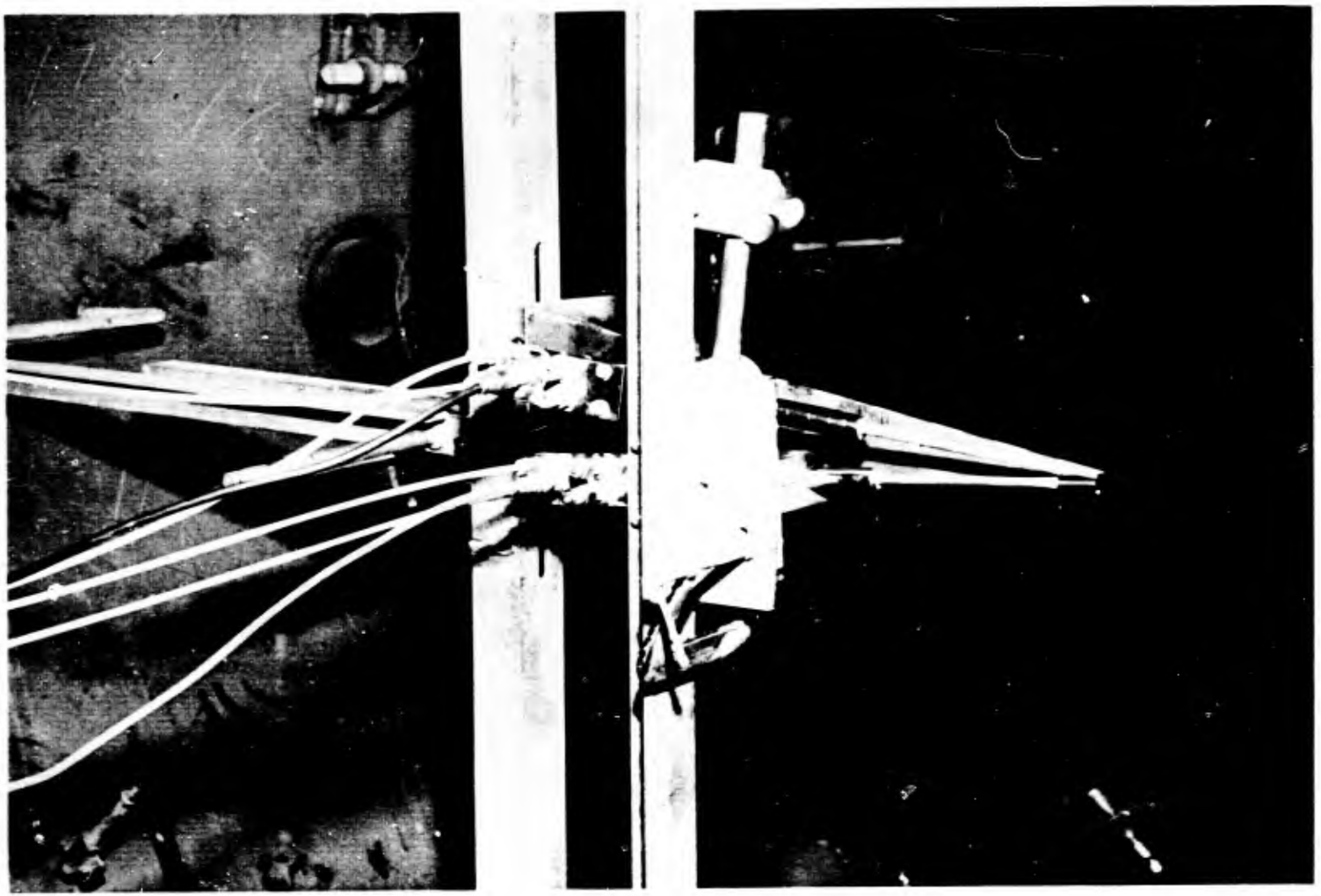

Fig.6 Downstream view of probe mount

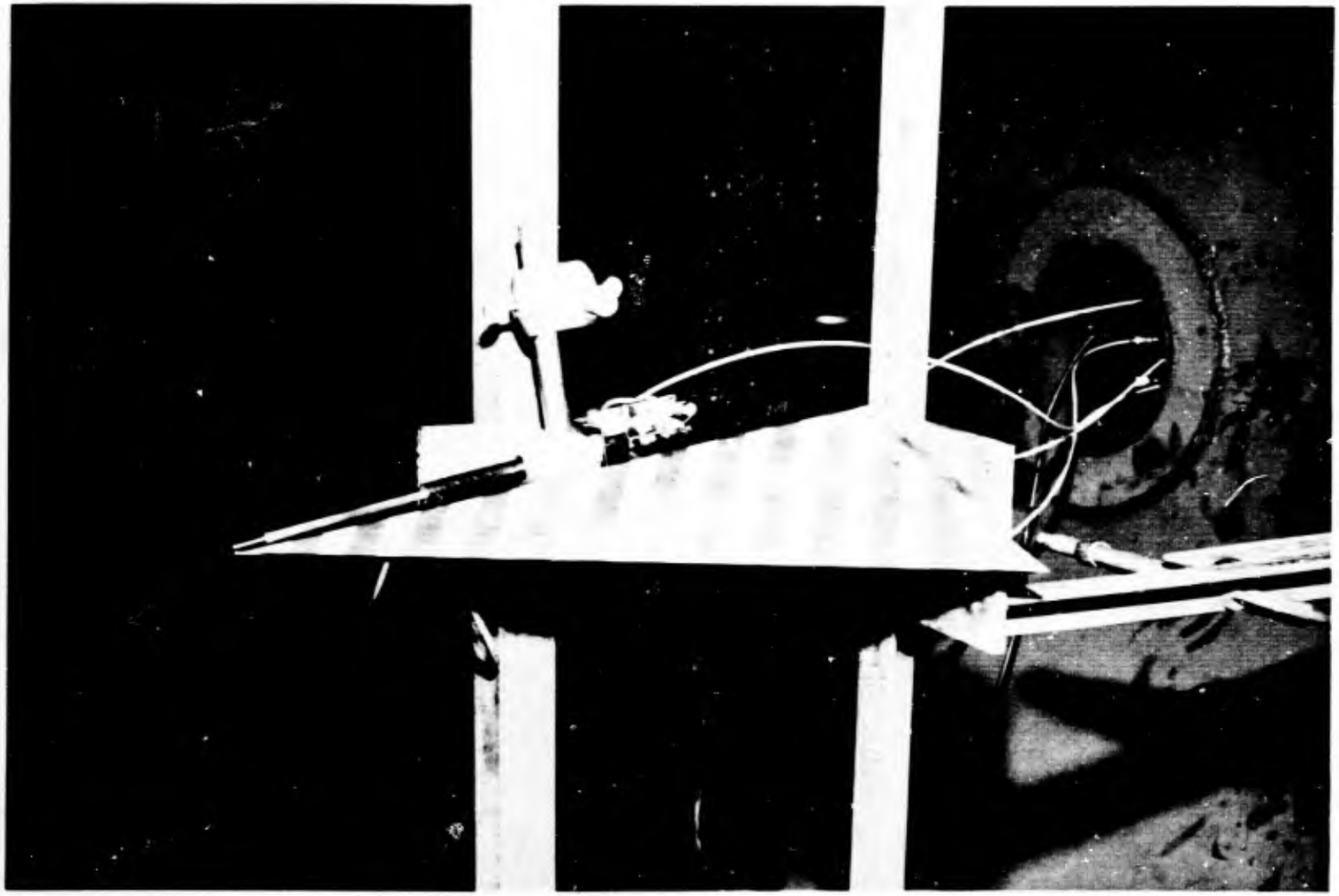

Fig.7 Upstream view of probe mount

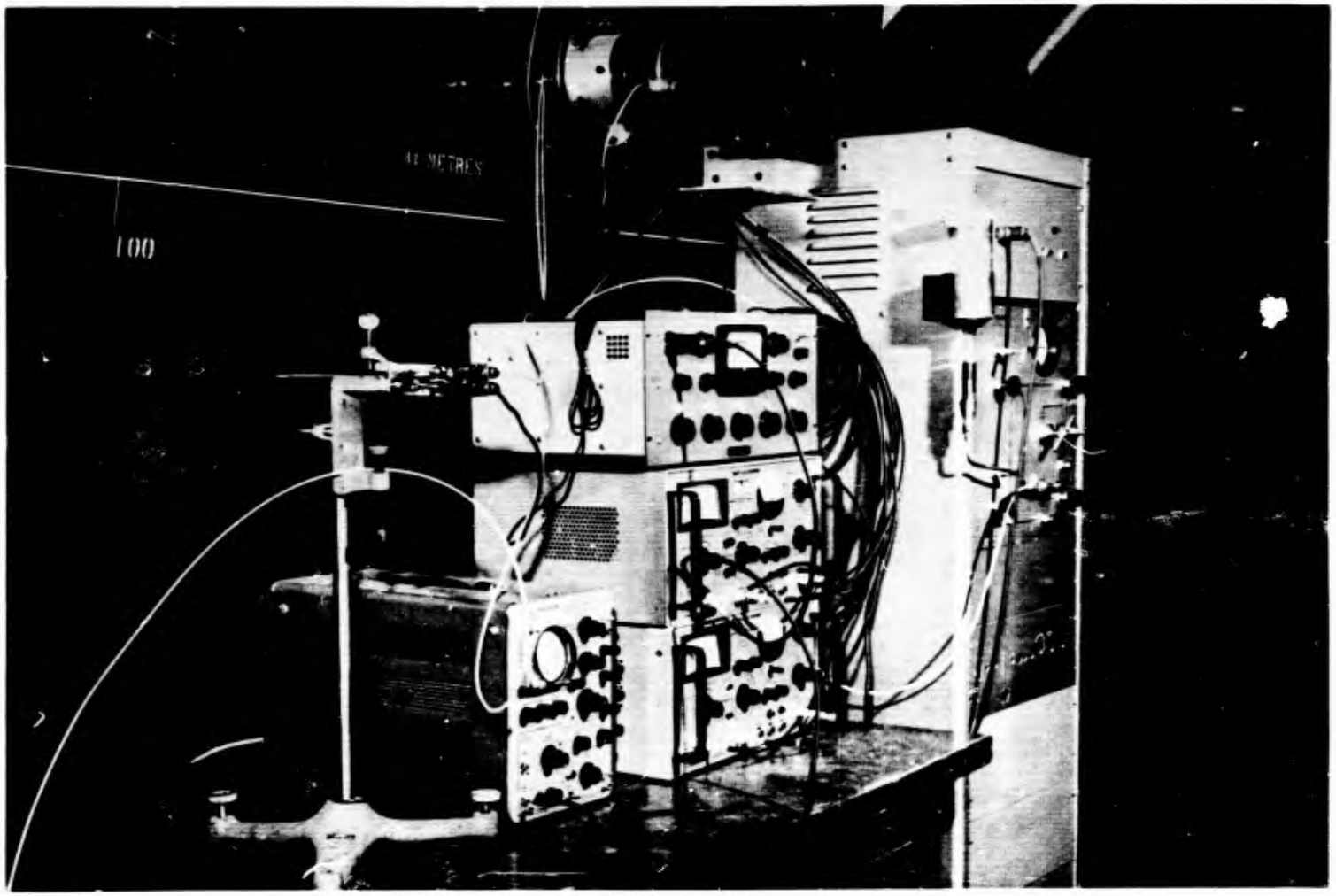

Fig.8 Heat flux system and coolant supply

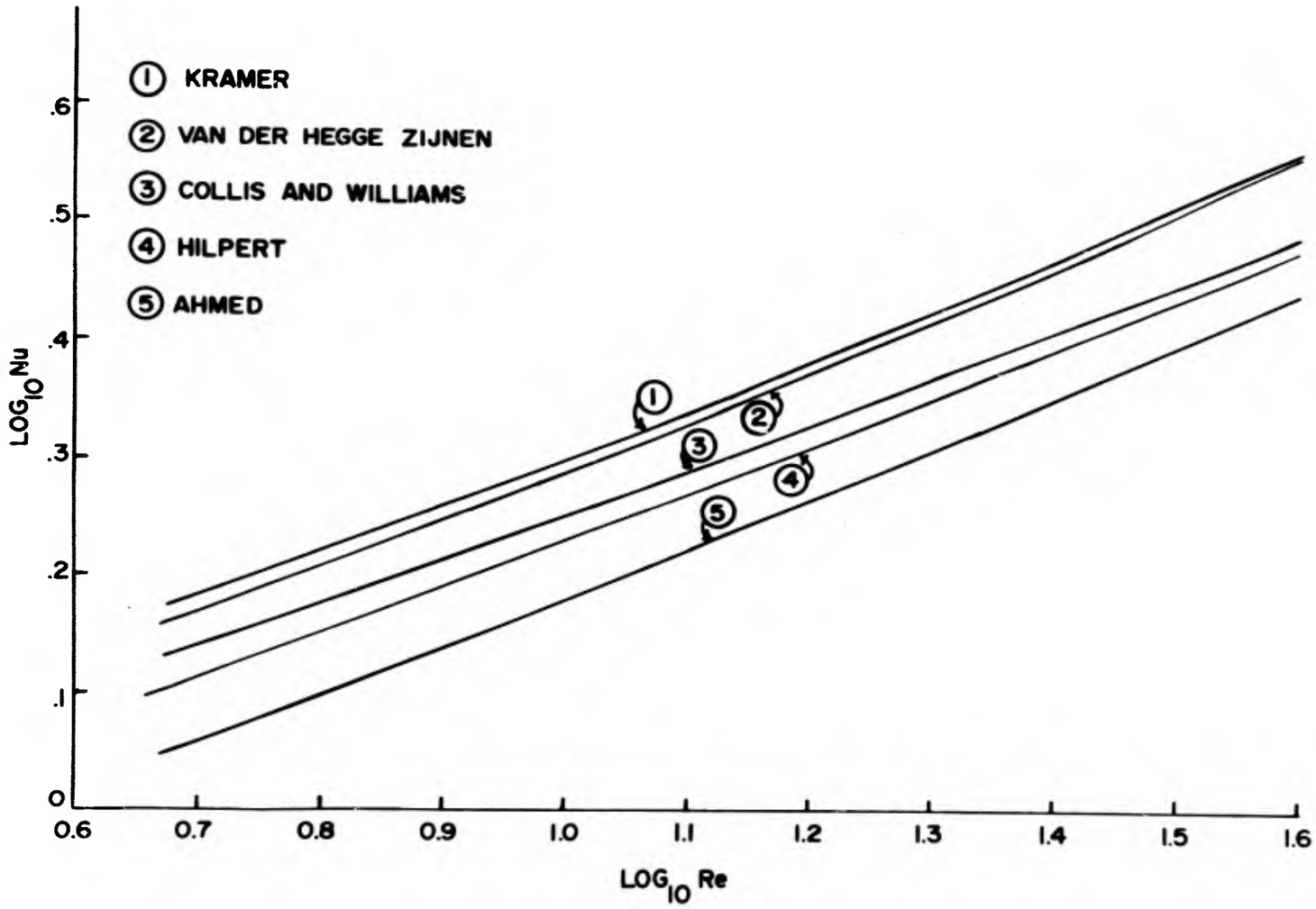

Fig.9 Comparison of various correlations

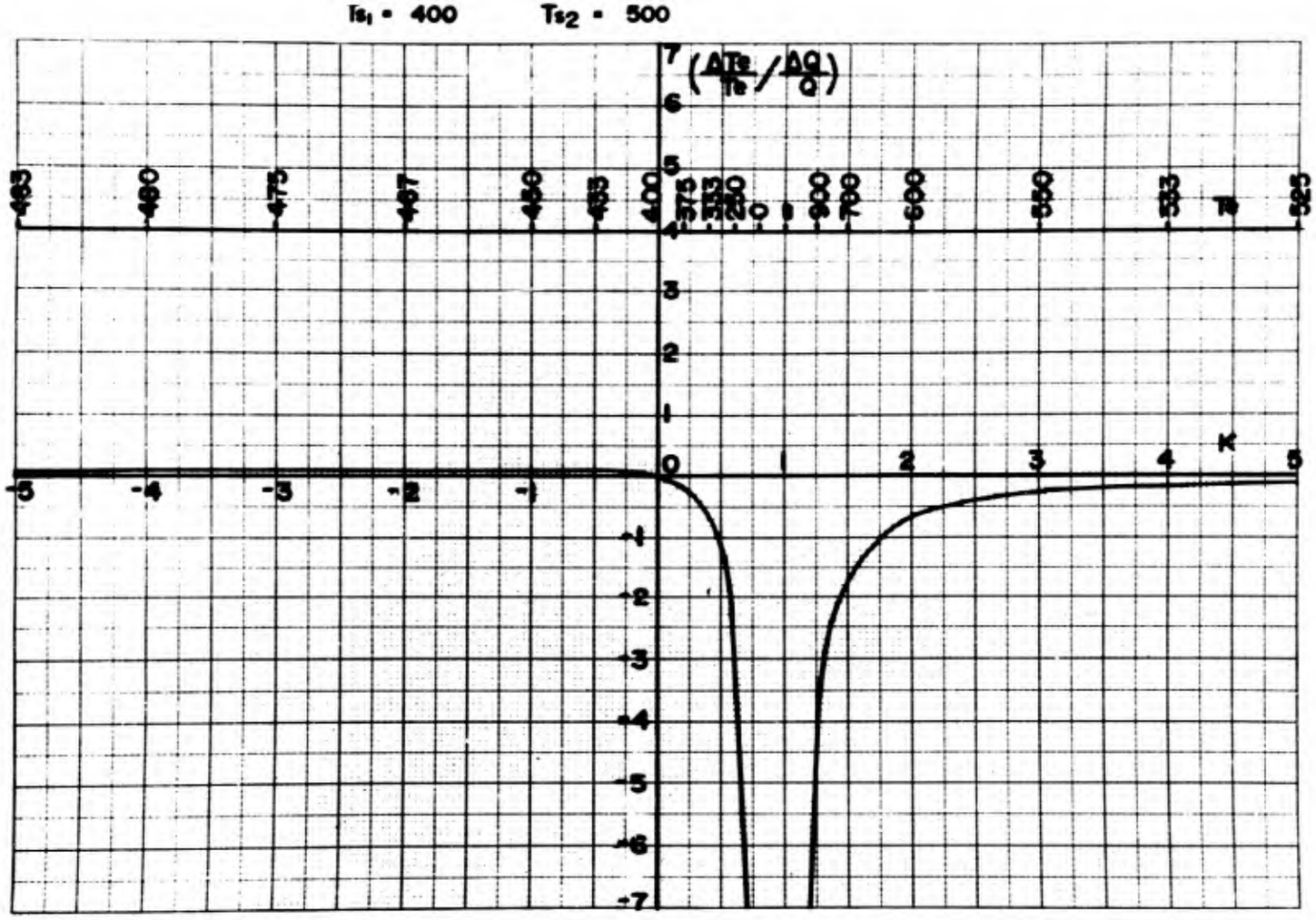

Fig. 10 Estimated maximum errors in wake temperature

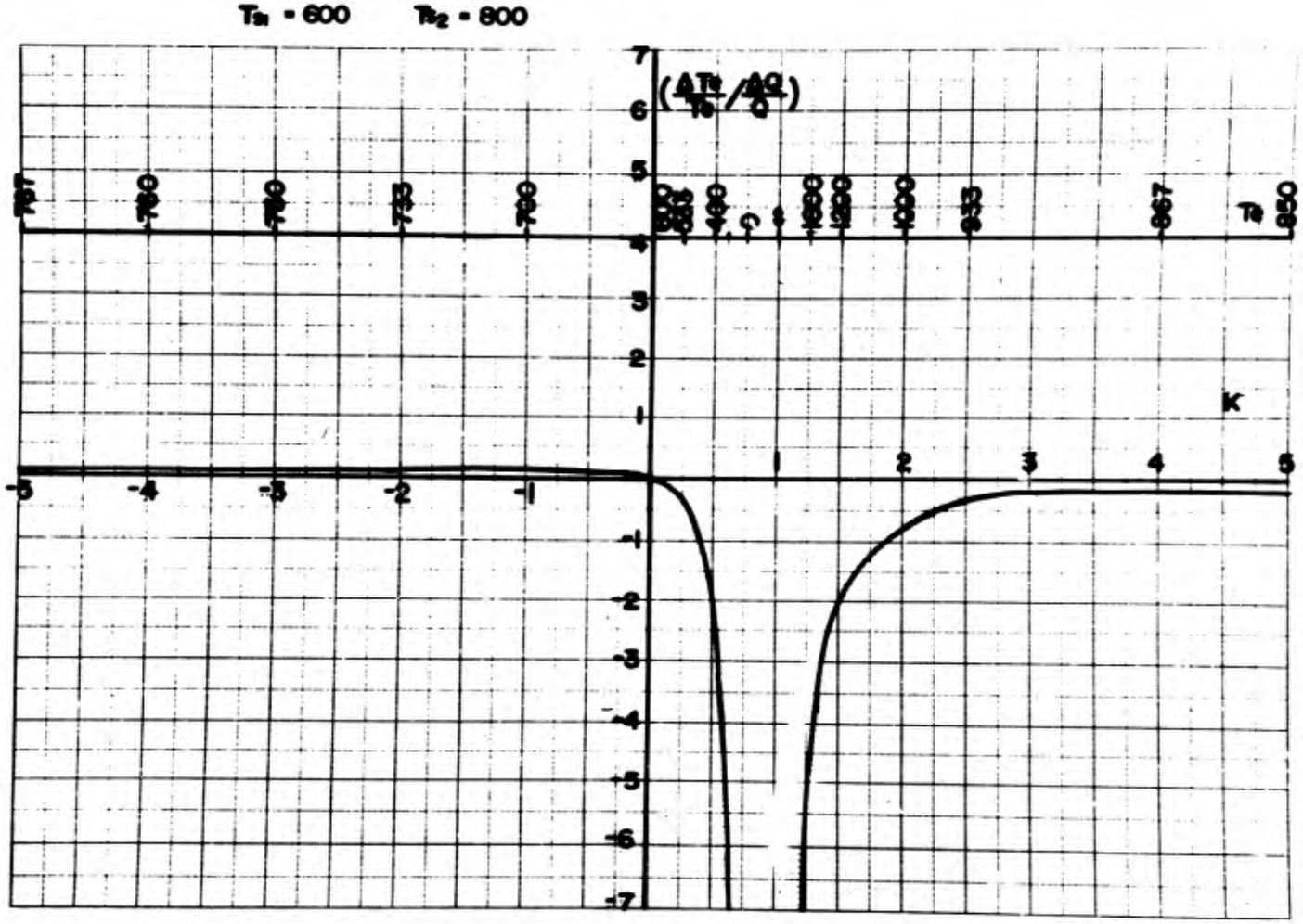

Fig. 11 Estimated maximum errors in wake temperature

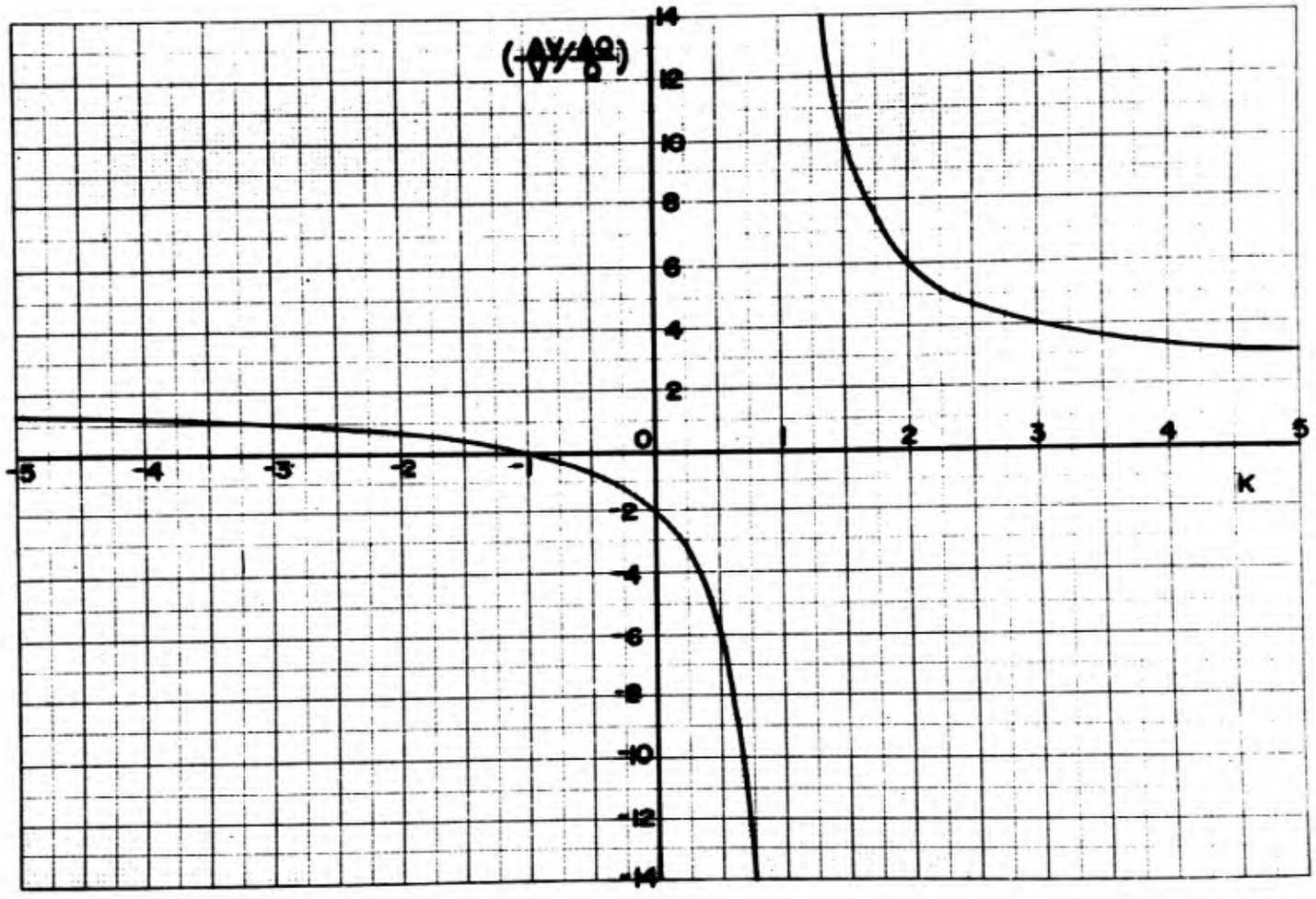

Fig. 12 Estimated maximum errors in wake velocity

SOME STATISTICAL PROPERTIES OF TURBULENT WAKES

by

J. Herrmann, W.G. Clay, R.E. Slattery
and R.E. Richardson

Lincoln Laboratory,*
Massachusetts Institute of Technology,
Lexington, Massachusetts 02173

* Operated with support from the U.S. Advanced Research Projects Agency

SUMMARY

Turbulent wakes of hypervelocity spheres launched from light gas guns at the Lincoln Laboratory Re-entry Simulating Range have been studied by analyzing densitometer tracings of schlieren photographs.

The correlation functions, spectral density, and variance of the turbulence of gas density in the wake of spheres of 3/16, 3/8 and 5/8 inch diameter, traveling at 20,000 fps, have been measured and will be compared with the author's previous work on 8000 fps spheres.

The statistical properties of the wakes are independent of pressure in the region of 10 to 80 torr. and are independent of the position behind the sphere out to about 9000 body diameters. The wakes appear to be statistically homogeneous and isotropic, consistent with earlier measurements at lower velocities. The rms density fluctuations of the wakes peak further behind the bodies than is the case at lower velocities, although the three-dimensional spectrum of the gas density falls off with the same power dependence.

Preliminary cross-correlation of the statistical properties of successive photographs of the same wake will be presented. By this technique one measures the ordered motion of the turbulence and its deceleration.

RESUME

On a étudié, en analysant les tracés densitométriques de photographies Schlieren, les sillages turbulents de sphères catapultées à de très grandes vitesses par des canons à gaz léger; les expériences ont eu lieu dans l'Installation de Simulation de Rentrée dans l'Atmosphère du Laboratoire Lincoln.

On a mesuré les fonctions de corrélation, la densité spectrale, et les variations de turbulence de la densité gazeuse dans le sillage de sphères de 3/16e, 3/8e et 5/8e de pouce de diamètre; les mesures obtenues ont été comparées avec les résultats des travaux précédents menés par l'auteur à l'aide de sphères évoluant à une vitesse de 8000 pieds par seconde.

Les propriétés statistiques du sillage sont indépendantes de la pression, lorsque celle-ci varie de 10 à 80 torr. ainsi que de la position du point étudié derrière la sphère, jusqu'à une distance correspondant à environ 9000 fois son diamètre. Les sillages s'avèrent être statistiquement homogènes et isotropes, et conformes aux mesures précédentes, effectuées à des vitesses inférieures. Les racines carrées de la moyenne des carrés des fluctuations de densité survenant dans les sillages culminent, derrière les corps étudiés, à des distances plus grandes que dans le cas de vitesses inférieures; toutefois le spectre tri-dimensionnel de densité gazeuse décroît dans le même ordre de dépendance, vis-à-vis de la puissance.

Les auteurs présenteront des corrélations transversales préliminaires des propriétés statistiques des photographies successives prises du même sillage. Grâce à cette technique, on mesure le mouvement ordonné de la turbulence et sa décélération.

BLANK PAGE

SOME STATISTICAL PROPERTIES OF TURBULENT WAKES

J. Herrmann, W. G. Clay, R. E. Slattery and R. E. Richardson
Lincoln Laboratory,* Massachusetts Institute of Technology
Lexington, Massachusetts 02173

Turbulent wakes of hypervelocity spheres launched from a light gas gun at the Lincoln Laboratory Re-entry Simulating Range have been studied by analyzing densitometer tracings of schlieren photographs.

The correlation functions, spectra, and variance of the turbulence of gas density in the wake of spheres of 0.48-, 0.96-, and 1.59-cm diameter, traveling at 6 km/sec, have been measured and will be compared with the authors' previous work on 2.5-km/sec spheres and with measurements using electrostatic probes.

The statistical properties of the wakes are independent of pressure in the region of 10 to 80 torr and are independent of the position behind the sphere out to about 3000 body diameters but change beyond that distance. The wakes appear to be statistically homogeneous and isotropic, consistent with earlier measurements at lower velocities. The rms density fluctuations of the wakes peak further behind the bodies than is the case at lower velocities, although the three-dimensional spectrum of the gas density falls off with the same power dependence.

Cross correlation of densitometer traces of successive photographs of the same wake are presented. By this technique wake velocity profiles and average wake velocity are measured.

I. INTRODUCTION

Turbulent wakes of hypervelocity spheres launched from a light gas gun at the Lincoln Laboratory Re-entry Simulating Range have been studied by analyzing densitometer tracings of schlieren photographs. Such analyses

*Operated with support from the U.S. Advanced Research Projects Agency

of densitometer tracings have previously been used to measure the statistical properties of the turbulent wake of spheres of 1-cm diameter at a velocity of 2.5 km/sec. In the present paper this work has been extended to higher velocities, longer wakes, and other projectile sizes. General techniques have also been developed so that statistically significant measurements of average wake velocity properties as well as the characteristics of the wake edge have been obtained.

These data (with the exception of certain probe results) are reduced from samples which are taken in submicrosecond times and constitute records of gas density gradient fluctuations. These records are between 50 and 190 correlation lengths long, depending on the size of the spheres used.

Section II of this paper is a short description of the equipment used in obtaining these data, followed by Sec. III in which the statistical properties of the gas density in turbulent wakes, the wake edge statistics, the wake velocity profiles, and the average wake velocity are presented. A short discussion on electrostatic probe data of electron fluctuation statistics completes this section, and in Sec. IV the results are summarized and some conclusions are discussed.

II. DESCRIPTION OF EQUIPMENT

All of the data presented in this paper have been taken at the larger ballistic range at the Lincoln Laboratory. This is a 150-cm diameter evacuatable tunnel serviced by a 20-mm light gas gun capable of firing spheres up to 1.6 cm in diameter at 6 km/sec.[1] Within the evacuated sections, six schlieren systems are permanently installed

and these systems have been used to accumulate the data presented herein.

Two of these schlieren systems are quite standard and differ in no essential way from the equipment previously described.[2] The other four, however, are contained in our so-called "four-spark" schlieren system. This is a set of four double-pass schlieren systems with independent sparks, cameras, and knife edges, which share a common main optical axis by means of a common main mirror of 30-cm diameter and 365-cm radius curvature. The cameras, sparks, and knife edges are arranged cart-wheel fashion in a plane perpendicular to the axis of the main mirror and share this axis by means of a carefully ground, front-surface-aluminized, right octagonal pyramid. A sketch of this equipment is shown in Fig. 1. The various spark sources are independently delayed from a common trigger so that successive schlieren photographs of the same wake may be taken at arbitrary intervals.[3]

When the moving projectile enters the field of view of the schlieren mirrors, its presence is detected and it triggers a shadowgraph system, orthogonal to the schlieren axis, which photographs the sphere. The trigger impulse also actuates delays which in turn fire the schlieren system sparks. These delay times are individually preset and also measured during each shot. In this way schlieren photographs can be taken at any desired position in the wake of the projectile. These measurements, combined with the shadowgraph picture of the projectile, determine the exact position in the wake of each of the six schlieren photographs.

The treatment of individual photographic plates to obtain significant statistical data on wakes has been described previously.[2] When the time intervals between

photographs of the same segment of wake are short enough so that significant decorrelation does not occur, the four pictures obtained from the four-spark system may be analyzed statistically to obtain the cross correlation between properties of the turbulent wakes in successive pictures. The cross-correlation functions, combined with a knowledge of the inter-picture timing, allow one to measure the average translational velocity of the wake in the laboratory frame of reference.

The spherical projectiles used in these wake studies were fabricated from copper-plated aluminum and are considered totally nonablating. They are fired from the gun while encased in sabots after carefully being checked for sphericity and cleanliness.

III. MEASUREMENTS

A. Statistical Properties of the Wake Turbulence

The authors' previous work[2] on 0.96-cm diameter spheres at velocities of 2.5 km/sec has been extended to the 5.6-km/sec regime, and data have also been obtained for spheres of 0.48-cm and 1.59-cm diameter. At the higher velocity the wakes are visible to schlieren systems for a longer time, due to the increased enthalpy content of the wakes, and schlieren photographs of wakes up to 50 000 diameters have been obtained (as compared to several thousand diameters for the earlier work). The limit on the z/d value (where z is the distance behind the sphere and d its diameter) at the present time is imposed by the growth of the wake into the mirror. Once the wake touches the mirror, the data are felt to be invalid and are no longer used. The distance from the trajectory to the mirror is 15 cm, and the largest z/d values are obtained for the smallest spheres.

The techniques of data reduction are identical to those described earlier.[2] A computer program is used to analyze the fluctuations in film contrast obtained from microdensitometer tracings taken parallel to the wake axis on a schlieren photograph. The output of the program is the correlation function and spectrum of the film contrast and a typical result is shown in Fig. 2. A very large number of these have been obtained.

As with the lower velocity cases, the results are consistent with the statistical isotropy and homogeneity of the turbulent wake. Since the wakes are homogeneous, all of the densitometer tracings are averaged to obtain a single result at any particular z/d.

In Fig. 2 the change in correlation function and spectrum is illustrated as a function of increasing distance behind the body. These results, for 0.48-cm diameter spheres at 40 torr, are typical of the results obtained for all sizes of spheres and all pressures studied. The increase in the correlation length is clearly visible from the changes of the correlation function. The spectra reveal a decrease in the higher wave number range as a function of time (or distance behind the body) with little or no change in the slope of the final falloff. This falloff, though unchanged in slope, does tend to translate towards lower wave numbers. The flattening of the spectra at the highest wave numbers is due to granularity of the developed film and represents a limit on the determination of the spectrum.

The normalized correlation functions, $R(\tau)$, are very well fitted by an expression of the form

$$R(\tau) = e^{-\tau/\tau_c} \quad ,$$

where τ_c is the correlation length. Thus from the definition of the integral scale of turbulence Λ,

$$\Lambda = \int_0^\infty R(\tau)\, d\tau \quad ,$$

it follows that the correlation length is equivalent to the integral scale; i.e., $\tau_c = \Lambda$.

In Fig. 3 the integral scale, or correlation length, is plotted against z/d for a variety of gas pressures and sphere sizes. At lower velocities it was noted that the integral scale was independent of gas pressure and of distance behind the body. This result is found to hold true for the higher velocity case only out to 3000 body diameters, after which the integral scale increases with increasing distance behind the body.

As demonstrated earlier,[2] the gas density fluctuations can be derived from the standard deviations of the film contrast, σ_c, as measured by the densitometer tracings. Some results for a variety of cases are shown in Fig. 4, and it may be noted that σ_c is proportional to $\Delta\rho/\rho$ where ρ is the gas density. These data reveal that the general behavior of the density fluctuations is similar to that which has been noted at lower velocities.[2,4] As z/d increases, the value of σ_c, or $\Delta\rho/\rho$, increases fairly rapidly until a maximum is reached and then it falls off quite slowly. The peak of the fluctuations for all values of upstream pressure are between 1000 and 2000 body diameters, which is further back in the wake than the 400 body diameter value found at 2.5-km/sec velocity. As in the earlier cases, the standard deviation of the film contrast is proportional to the pressure, and hence the relative density fluctuations would be expected to be pressure independent. For the data shown in Fig. 4 the peak value of the relative density fluctuations is 0.2, somewhat higher than at lower velocities.

The standard deviations scale as the square root of the body size, as might be expected from a random volume effect

where the length of the light path through the wake is directly proportional to the body size.

B. Wake Edge Statistics

The fluctuations of the wake surface as seen by their projection in schlieren photographs have been analyzed. For the sake of simplicity this projection shall be referred to as the wake edge. Data of this type have been reduced by several authors.[5,6]

These measurements have been made by tracing the wake edge onto a separate sheet of paper and digitizing the tracings by means of a Gerber plotter. The output of the Gerber plotter is an IBM punch card record of the fluctuations, and these records are reduced in a manner analogous to the densitometer tracings described in Sec. A.

The results of several such tracings are shown in Fig. 5. Here the correlation lengths (defined as the distances required for the correlation functions to reduce in value by 1/e) of the wake edge are plotted as a function of z/d. The points are quite scattered since only the two edges can be averaged on each plate; consequently one is forced to work with a short data sample.

The correlation length of the edge, in the early and middle portions of the wake, is much longer than the correlation length of the turbulence at the same distance behind the body. This is one more example of the negligible contributions of the surface as compared to the volume effects in schlieren photographs (see also Ref. 2, Sec. III-C).

C. Wake Velocity Profiles

The four-spark schlieren system, which was briefly described in Sec. I and sketched in Fig. 1, permits one to compare sequential photographs of the same portion of a

given wake taken at known time intervals. In this fashion information is obtained about the development of wake structures as a function of time; and, in particular, the average wake velocity profile may be found at any point in the turbulent wake.

The structure of the wake turbulence as seen by light passing through the wake decorrelates quite rapidly so that care must be exercised in taking and reducing data of this type. The time intervals required in the near wake are quite short (several microseconds); and since the wake moves very little in this time, careful spatial calibration of each plate is necessary in order that successive plates may be compared with accuracy. Because the wake decorrelates more slowly further behind the body, lengthened time intervals which one can use do not result in larger spatial motions since the wake is traveling more slowly. Absolute accuracy of 0.1 mm is required on the film, and such things as the differences in magnification between the cameras must be corrected as these differences result in errors which are cumulative in the determination of cross correlation.

For the purpose of measuring velocity profiles, a series of densitometer tracings, parallel to the wake axis, are made from individual schlieren plates. The resultant record of the photographic transmission through the plate is automatically punched onto IBM cards in a manner similar to the techniques used to determine wake statistic from individual plates. These outputs constitute sets of four random functions $f_{n,y}(z)$ (where n = 1, 2, 3, 4) for each shot. The parameter y numbers the series of densitometer tracings parallel to the wake axis. In order to obtain a profile, a series of individual passes at different y positions is made.

These records are used to compute (for a fixed value of y)

$$R_{mn}(t) = \frac{1}{Z - t} \int_o^{Z-t} f_m(z)\, f_n(z - t)\, dz \quad ,$$

where Z is the length of the record $f_n(z)$. For $m = n$, one gets the autocorrelation functions, and for $m \neq n$, the cross-correlation functions.

From the shift of the peak positions of these functions, a velocity can be derived. Let $C_1(z)$ represent the film contrast random function at time t and $C_2(z)$ the contrast at a time Δt seconds later. Then C_2 can be considered a translated and attenuated copy of C_1 with additional noise due to the random changes in the flow. Writing

$$C_2(z) = \alpha C_1(z - v\Delta t) + n(z) \quad ,$$

one may pick constants α and v which minimize the rms value of n. Thus we seek to minimize

$$\Phi(\alpha, v) = \int n^2(z)\, dz = \int [C_2(z) - \alpha C_1(z - v\Delta t)]^2\, dz \quad .$$

Then $\partial\Phi/\partial\alpha = 0$ implies that

$$\int [C_2(z) - \alpha C_1(z - v\Delta t)]\, C_1(z - v\Delta t)\, dz = 0$$

or

$$r_{12}(v\Delta t) - \alpha r_{11}(0) = 0$$

giving

$$\alpha = \frac{r_{12}(v\Delta t)}{r_{11}(0)} \quad ,$$

where r_{ij} are the correlation functions

$$r_{ij}(x) = \int C_i(z - x)\, C_j(z)\, dz \quad .$$

Then the function

$$\Phi = r_{22}(0) - 2\alpha r_{12}(v\Delta t) + \alpha^2 r_{11}(0) = r_{22}(0) - \frac{r_{12}^2(v\Delta t)}{r_{11}(0)}$$

is minimized by taking $v\Delta t$ at the maximum of the cross-correlation function r_{12}.

As derived here, v represents the velocity of the chosen piece of the wake averaged over the length Z and integrated through the wake. The quantity α is a measure of the decay of the "flow pattern."

The window width scanned by the Jarrell-Ash densitometer had to be taken much larger for the cross-correlation data than that used for the autocorrelation work described in Sec. II. For the velocity measurements the width was increased from 0.1 mm to 1.2 mm in order to reduce scatter in the results obtained by the cross correlation program. The scatter is a statistical one due to limited sample length. In the case of the wake statistics, this can be improved by averaging across the wake, as described earlier, a technique which cannot be applied to the cross-correlation data.

Figure 6 is an example of cross correlations obtained using these techniques. Here four pictures taken at three intervals give six cross correlations which are denoted by 12, 13, 14, 23, 24, and 34. The shift in the peak positions of the cross-correlation functions are interpreted as due to the average translation of the wake in the known time interval; from the translation and time the velocities are calculated. The decrease of its maximum from the value 1.0 is an indication of the decorrelation which occurred during the time between the light sparks.

In Fig. 7 the velocity profiles, obtained in this fashion, are plotted for a series of positions behind the body. The inside surface of the wake edge is sketched in to indicate the dimension of the wake at the particular stations. Despite fluctuations attributable to a number of sources (limited sample length, lack of precision in

spatial calibration, uncertainty in the peak of the cross-correlation function, etc.), the curves of velocity profile are strikingly flat.

Results of velocity profile measurements made at CARDE[7] by entirely different means seem to indicate a similar result. The authors wish to point out that the schlieren profiles could be explained by weaker gas density gradients in the center of the wake than near its edges, as well as by any serpentine formation in the wake tending to shift the wake axis about. However, in the absence of evidence to the contrary, we propose that the profiles indeed have this flat-topped shape.

D. Average Wake Velocity

Since the velocity profiles are flat, the velocities measured at any given position behind the body have been averaged to give an average velocity of the turbulent wake as a function of distance behind the body. The results are plotted in Fig. 8 as the ratio of the wake to the body velocity. They represent the average of a large number of cross correlations. Since simple incompressible theory would predict a $z^{-2/3}$ decay of velocity for a wake which grows as $z^{1/3}$, a line of slope $z^{-2/3}$ is included for comparison purposes. The experimental points follow the $z^{-2/3}$ decay quite closely.

E. Electrostatic Probes

The electrostatic probe equipment consists of a radial array of coaxial probes centered about the projectile trajectory. The probes are suitably biased and the data taken are records of probe current vs time as the wake grows out to and engulfs the probes. One measures probe currents in

order to gain information about electron density fluctuations in the wake. That the probe currents are proportional to electron density is borne out in part by comparing the average probe current behavior with microwave cavity measurements taken at the same time.[8]

The collecting electrode is a 0.12-mm diameter gold-plated cylinder exposed for 0.1 to 0.2 mm. It is supported in Teflon within a 0.5-mm diameter gold-plated hollow cylinder that serves as a current return path, collecting charges of opposite sign in order that the plasma remains neutral. Gold plating is used to facilitate cleaning of the probes before each shot and to minimize probe surface contact potential difference. The probes are placed radially in a plane perpendicular to the pellet path and are supported in a brass holder which carries transparent reticles that are photographed along with the passing pellet by spark photography in order to determine the exact trajectory of the pellet relative to the probes.

Currents collected by the probes are fed to bipolar "logarithmic" amplifiers whose outputs are displayed on oscilloscopes with various sweep rates and photographed. The amplifiers have approximately a logarithmic response between 2×10^{-5} amp (saturation level) and 5×10^{-9} amp with linear gain for smaller signals. Their gain is frequency-independent from 0 to 100 kHz, and a known correction can be applied so that they are useful to 300 kHz.

The data thus taken are from a fixed point in space and the time variations recorded result from the wake passing that point. Figure 9 is taken from such a record. Notice the general exponential decay with fluctuations superimposed. If the fluctuations are autocorrelated, a correlation time is obtained. The average velocity for the section of wake chosen can then be used to convert the

correlation time into a correlation length. For a few records this correlation length has been plotted vs z/d in Fig. 10. Note that these values are about the same as the schlieren results for the same portion of the wake.

IV. RESULTS AND CONCLUSIONS

The turbulent statistics of the gas density in the wakes of three sizes of spheres have been measured using schlieren techniques and have been found to be statistically isotropic and homogeneous. Out to 3000 body diameters the normalized correlation functions and spectra do not appear to vary as a function of gas density or position behind the body. Beyond 3000 body diameters the integral scale grows as the 1/2-power of distance behind the body. This is in excellent agreement with Schapker,[6] who indicates that the correlation length should grow as the 1/2-power of z but that the conditions for such growth should not be reached before $z/d \approx 10^3$.

The fluctuations of gas density, $\Delta\rho/\rho$, peak at a value of 0.2 in the region of z/d between 1000 and 2000 and then decay quite slowly. This too is similar to results obtained at lower velocities and differs from them only in that the maximum is further behind the body. Note in Fig. 9 that the fluctuations of the probe current are larger, with $\Delta I/I \approx 1$.

It is appropriate to comment that, due to the rapid deceleration of the wake in the observer frame, any point spatial measurement of a wake in a hypervelocity facility results in data smaples which are short. In fact, any given point in the wake only moves a total of about 50 body diameters from the time it is generated until it has come to a complete stop. In addition, the sample must be divided into still smaller intervals in order to reduce the

data. This can be contrasted with a photographic technique such as schlieren where a typical picture at any distance behind a body gives a sample which is many body diameters long.

The behavior of the gas density fluctuations and statistics tend to reinforce the picture of the turbulent wake as being composed of a "marble-cake-like" mixture of hot and cold gas. The changes in spectra in Fig. 2 could be described as resulting from the smaller sized eddies cooling by thermal conduction and disappearing. The shift of the falloff toward lower wave numbers leads to the conclusion that there is insufficient turbulent kinetic energy to regenerate these smaller eddies. Thus we conclude that there is no inertial range for the turbulent wakes we have studied. This leads to a fluid mechanical model in which a large part of the energy of the wake is contained in the hotter regions. Uberoi and Kovasznay described this earlier as "entropy spottiness."[9] The size of the electron density correlation length is consistent with this picture.

The velocity profiles at any given point in the wake are measured to be flat topped within the confines of the turbulent wake, and the average wake velocity decays about as expected from simple theory.

REFERENCES

1. R. E. Slattery, W. G. Clay and W. C. Worthington, Second International Congress on Instrumentation in Aerospace Simulation Facilities, Stanford University (August 1966).

2. W. G. Clay, J. Herrmann and R. E. Slattery, Phys. Fluids 8, 1792 (1965).

3. A. P. Ferdinand, Lincoln Laboratory, M.I.T. (to be published).

4. R. E. Slattery and W. G. Clay, American Rocket Society Preprint 2673-62 (13-18 November 1962).

5. S. Corrsin and A. L. Kistler, N.A.C.A. Report 1244 (1955).

6. R. L. Schapker, AIAA Journal 4, 1979 (1966).

7. Canadian Armament Research and Development Establishment, ARPA Re-entry Physics Research Program on Turbulent Wakes, CARDE Technical Note 1727/66 (August 1966).

8. W. M. Kornegay, Second International Congress on Instrumentation in Aerospace Simulation Facilities, Stanford University (August 1966).

9. M. S. Uberoi and L. S. G. Kovasznay, J. Appl. Phys. 26, 19 (1955).

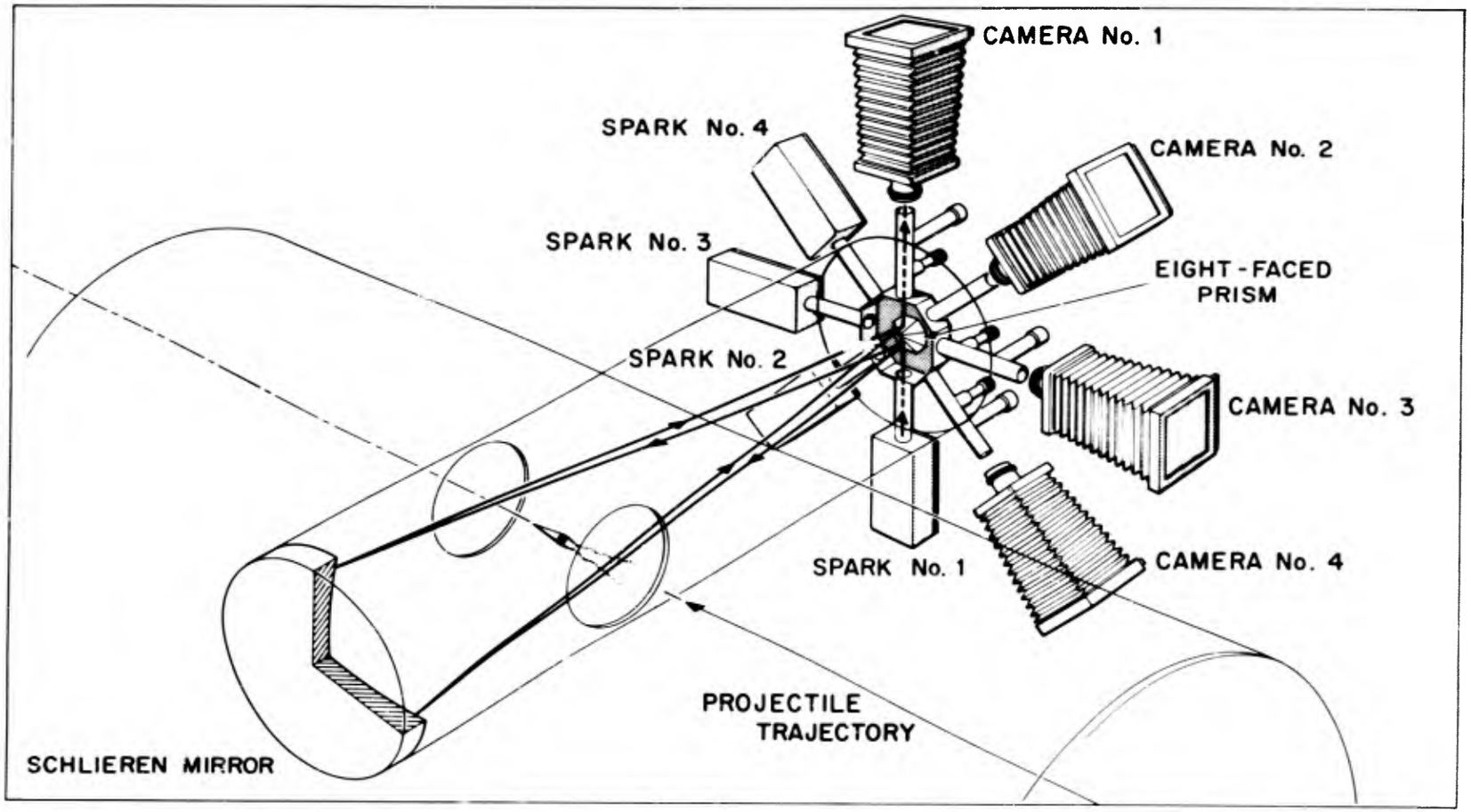

Fig. 1. Sketch of the four-spark schlieren system. Note the aluminized octagonal pyramid used to direct the light beams so that the four spark-camera pairs share the mirror.

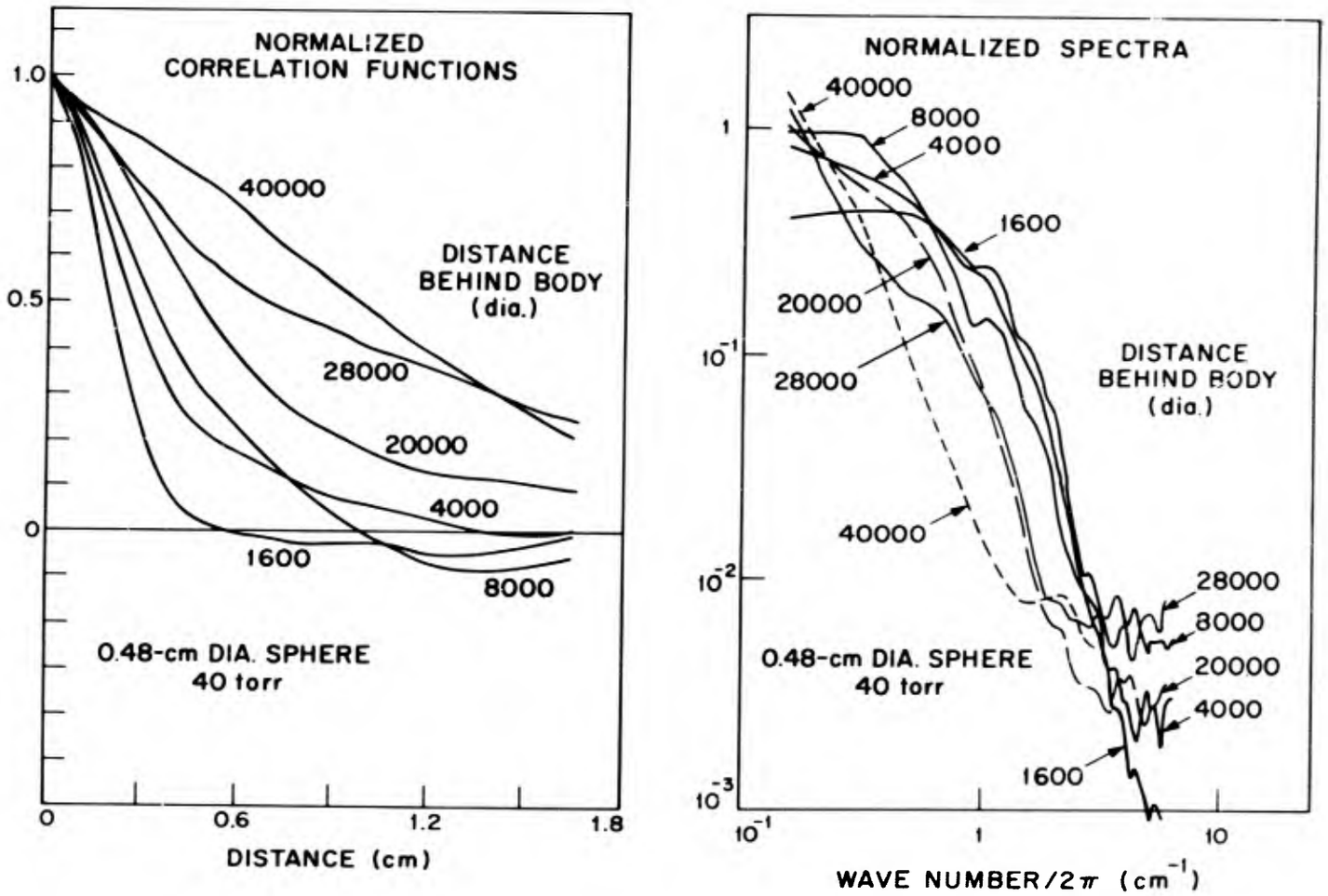

Fig. 2. The normalized correlation functions and spectra of the film contrast from schlieren photographs of a 0.48-cm diameter sphere at a pressure of 40 torr.

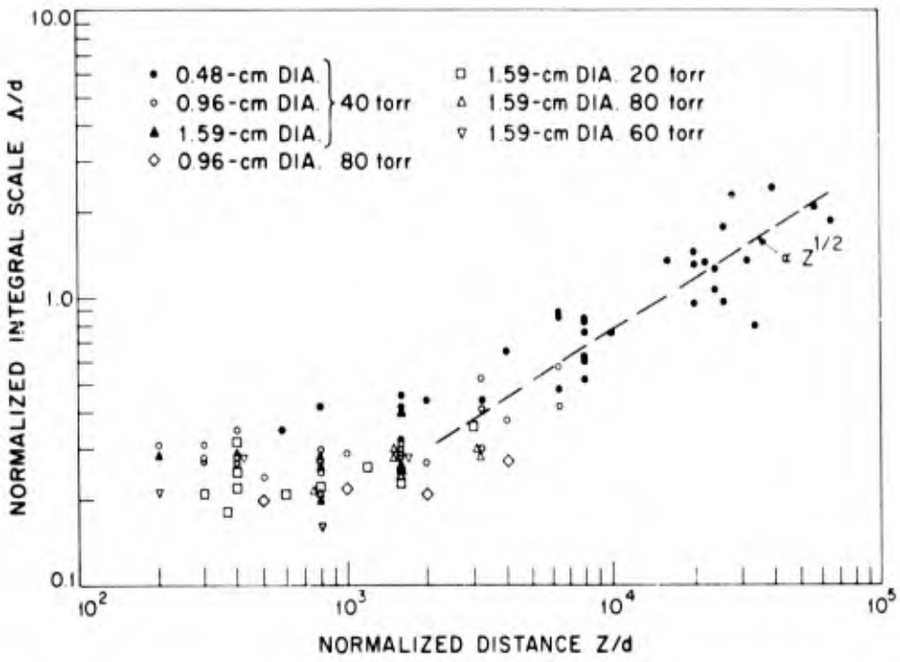

Fig. 3. The normalized integral scale, Λ/d, as a function of the normalized distance behind the sphere, z/d, for a variety of sphere diameters and pressures.

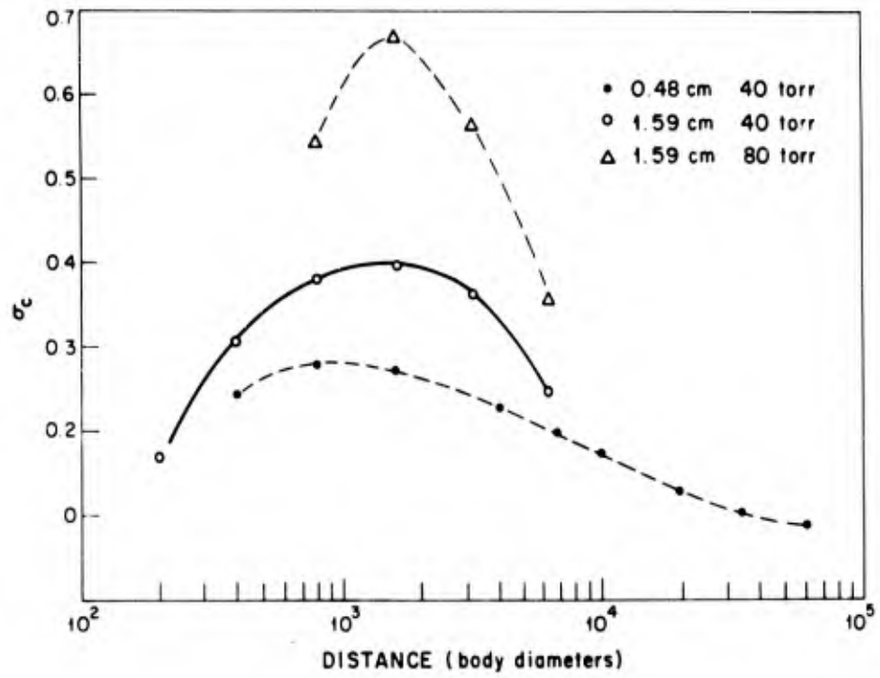

Fig. 4. Standard deviations of the film contrast as a function of distance behind the body.

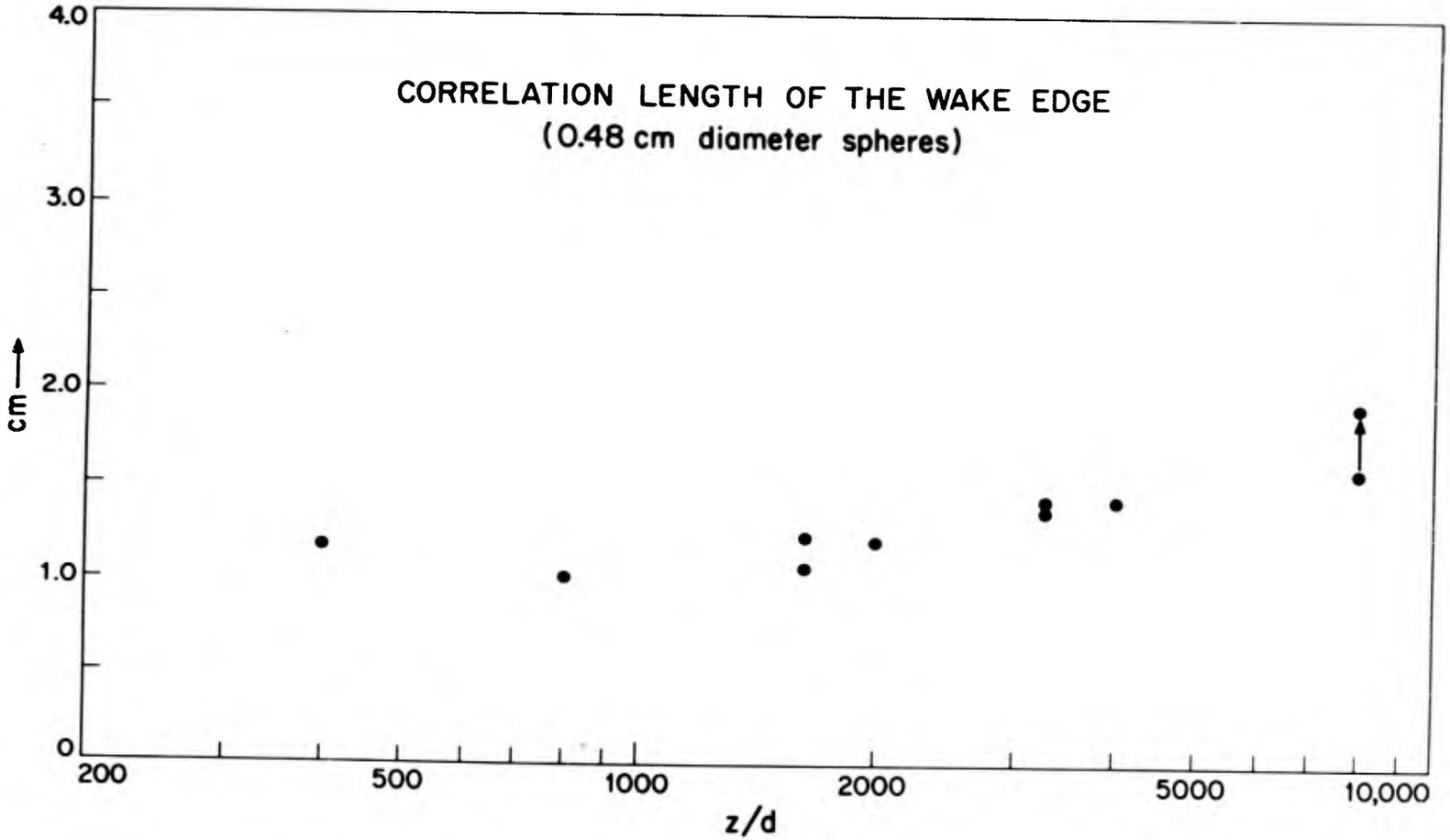

Fig. 5. The correlation length of the wake edge as taken from schlieren photographs for a 0.48-cm diameter sphere at 40 torr.

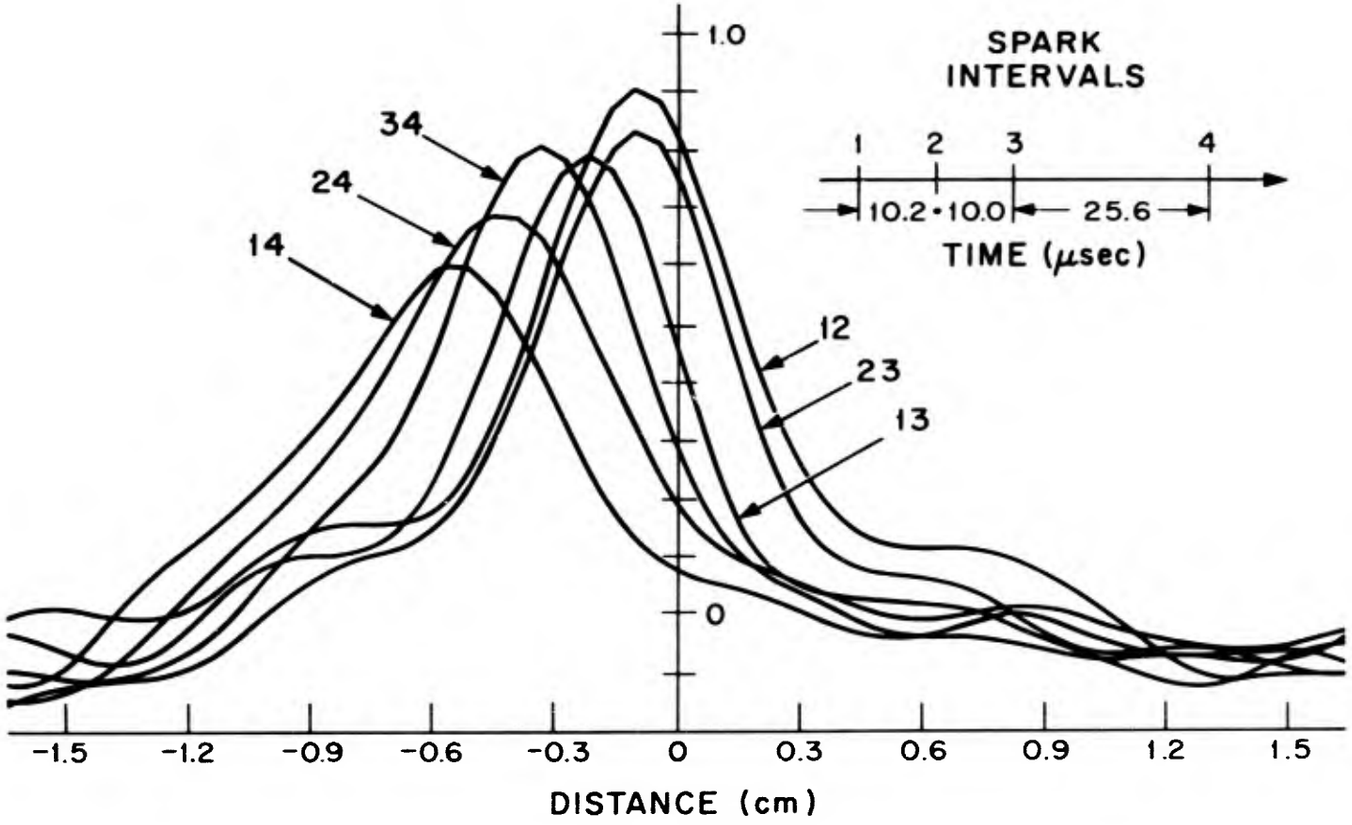

Fig. 6. The six cross-correlation functions for a particular shot (0.96-cm diameter sphere, 5.6 km/sec, 40 torr, 400 body diameters behind the sphere) with the inter-spark timing indicated. The numbers refer to the sequence of the pictures used in the cross correlation, and the positions of the peaks of the cross-correlation functions describe an average velocity of the wake.

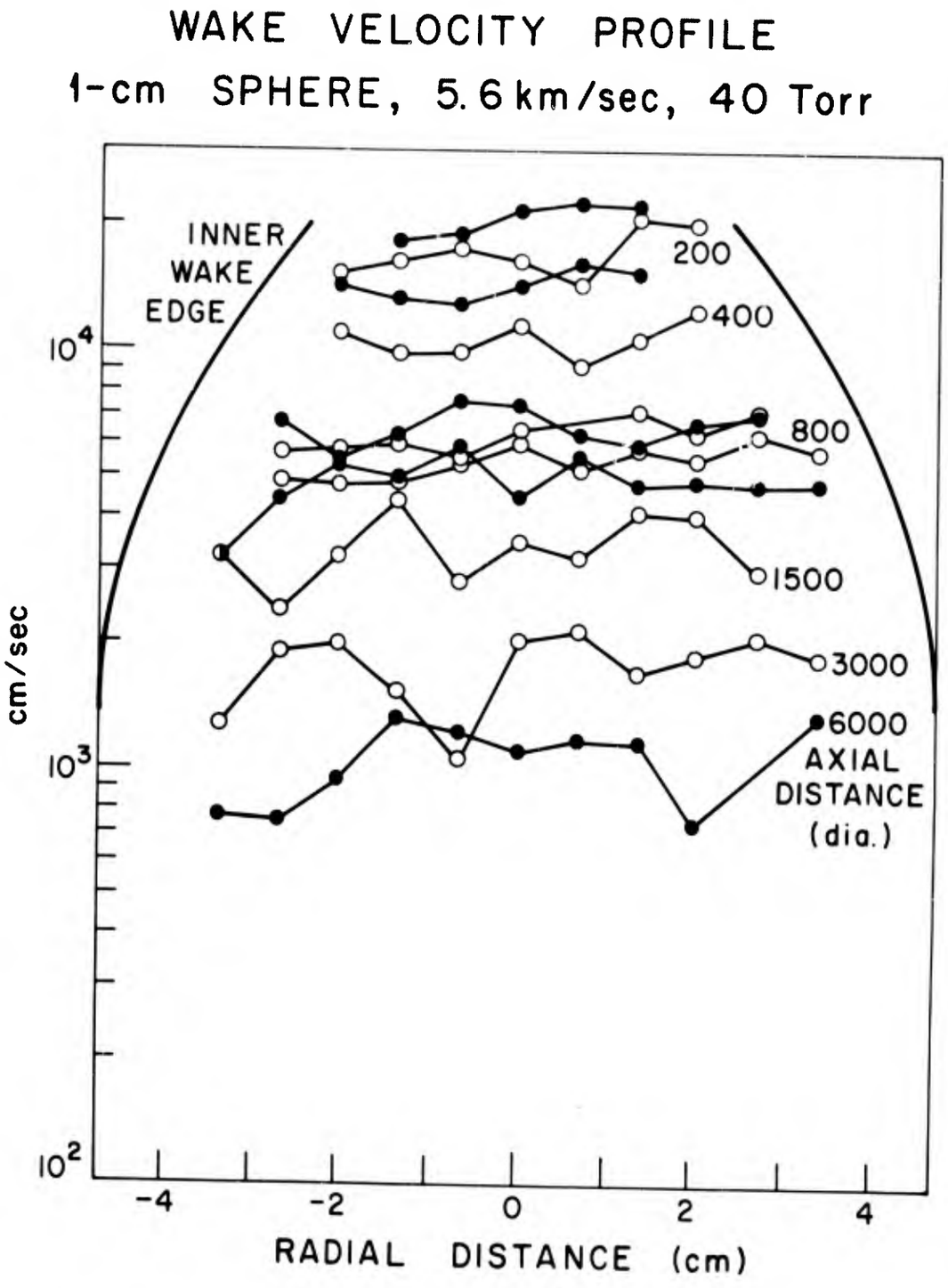

Fig. 7. The wake velocity profiles for spheres at different axial distances behind the body, as determined from the shifts of the peaks of the cross-correlation functions.

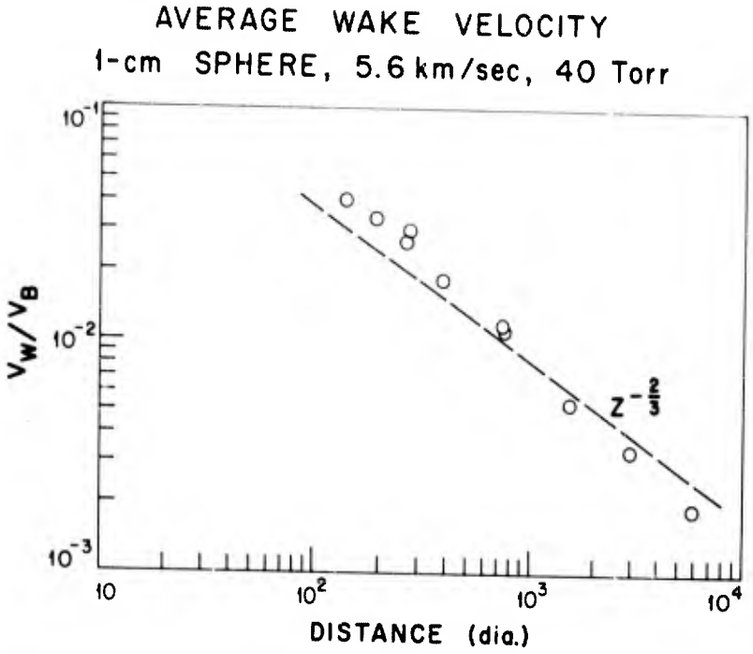

Fig. 8. The average wake velocity normalized to the body velocity as a function of the distance behind the body, determined with the four-spark schlieren system.

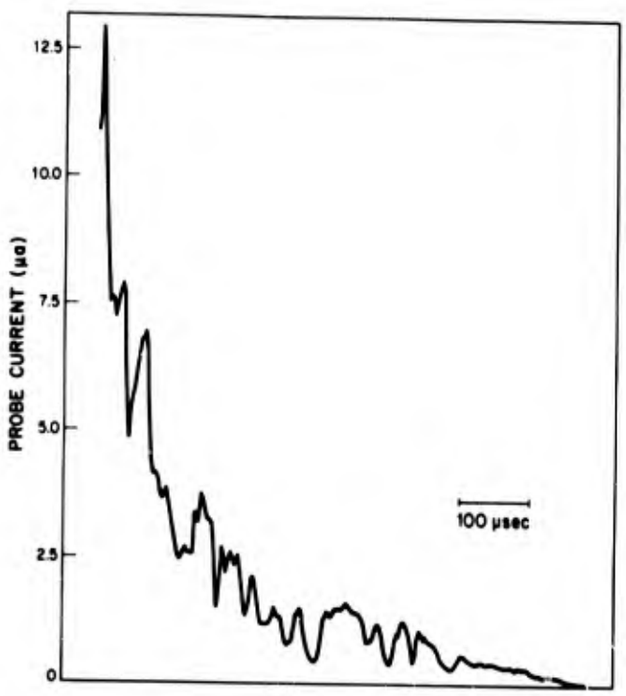

Fig. 9. The probe current as a function of time for a particular shot (0.96-cm sphere at 40 torr, velocity 5.6 km/sec).

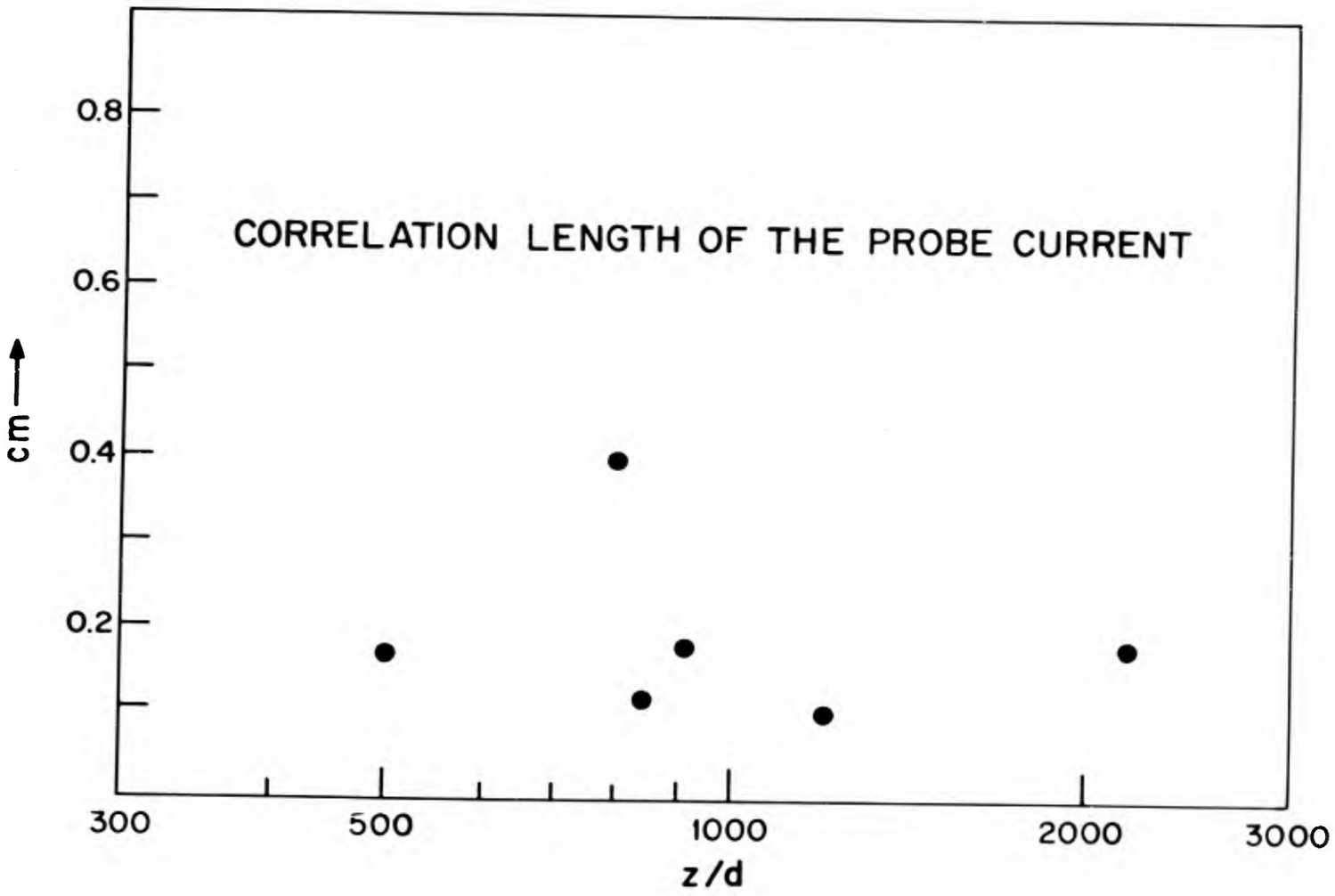

Fig. 10. The correlation length determined from segments of a probe current curve by means of the local mean velocity.

BLANK PAGE

PULSATIONS IN THE WAKES OF HYPERBALLISTIC SPHERES DURING ATMOSPHERIC RE-ENTRY

by

D.A. Spence*, R.L. Dommett**, and P.G. Smith***.

* Department of Engineering Science, Oxford University
(Formerly of Aerodynamics Department, Royal Aircraft Establishment, Farnborough, Hampshire.)

** Space Department, Royal Aircradt Establishment, Farnborough, Hants.

*** Royal Radar Establishment, Malvern, Worcestershire.
(Present address: British Embassy, Washington, D.C.)

SUMMARY

Two 17 inch diameter copper spheres were fired on the Woomera range as part of project Dazzle, and re-entered the atmosphere almost vertically at speeds of 16000 ft/sec. Head-on V.H.F. radar returns from the turbulent portions of the wakes showed marked periodicity in echoing cross-section, corresponding to the successive formation of peak echoing areas at a frequency of approximately 5 cycles/sec. in a region several thousand diameters behind the head. These peaks, corresponding it is thought to sharp maxima in the local electron density distribution, drifted backwards along the wake at ambient velocity, decaying rather slowly until overtaken by the final electron loss mechanism.

Their production frequency is two orders of magnitude lower than that corresponding to the Strouhal number for Vortex shedding from the sphere, and it is suggested that they are due either to a surging process in the near wake or to a periodic breakthrough of the turbulent portion of the far wake into the surrounding entropy layer.

RESUME

Dans le cadre du projet "Dazzle" on a procédé à la base de Woomera au lancement de deux sphères de cuivre, de 17 pouces de diamètre (environ 50 cm), qui effectuèrent leur retour dans l'atmosphère verticalement, à une vitesse de 16000 pieds par seconde. Dans les régions turbulentes de sillage, les données d'un radar à très haute fréquence, braqué vers l'avant, indiquèrent une périodicité marquée dans la section transversale de l'écho, correspondant à la formation successive de zones d'écho maximales d'une fréquence approximative de 5 cycles par seconde, dans une region située à plusieurs milliers de diamètres en arrière de la partie antérieure. Ces zones d'écho maximales, correspondant, pense-t-on à des maximas très marqués dans la répartition locale de densité des électrons, dérivaient vers l'arrière le long du sillage à la vitesse ambiante, pour s'atténuer assez lentement jusqu'à ce que survienne le mécanisme final de déperdition des électrons.

Leur fréquence de production est de deux ordres de grandeur plus faible que celle correspondant au nombre de Strouhal pour les tourbillons émanant de la sphère peut-être sont-elles dues soit à un processus de surintensité dans le sillage immédiat, soit à une irruption périodique de la portion turbulente des bords du sillage dans la couche entropique environnante.

PULSATIONS IN THE WAKES OF HYPERBALLISTIC SPHERES DURING ATMOSPHERIC RE-ENTRY

by

D.A. Spence*, R.L. Dommett **, and P.G. Smith***.

Two 17 inch diameter copper spheres were fired on the Woomera range as part of Project Dazzle, and re-entered the atmosphere almost vertically at speeds of 16000 feet/sec. The present paper is concerned with some fluid mechanical problems related mainly to unexpected flow pulsations and vortex motions observed in the firings. The turbulent portions of the wakes showed marked periodicity in echoing cross-section, corresponding to the successive formation of peaks at a frequency of approximately 5 cycles per second in a region several thousand diameters behind the head. These peaks, corresponding it is thought to sharp maxima in the local electron density distribution, drifted backwards along the wake at ambient velocity, decaying rather slowly until overtaken by the final electron loss mechanism.

---

* Department of Engineering Science, Oxford University
(formerly of Aerodynamics Department, Royal Aircraft Establishment, Farnborough, Hampshire.)

** Space Department, Royal Aircraft Establishment, Farnborough, Hants.

*** Royal Radar Establishment, Malvern, Worcestershire.
(Present address: British Embassy, Washington, D.C.)

Their production frequency is two orders of magnitude lower than that corresponding to the Strouhal number for vortex shedding from the sphere, and it is suggested that they are due either to a surging process in the near wake, or to a periodic breakthrough of turbulent portions of the far wake into the surrounding entropy layer, possibly associated with the dynamic motion of the head.

1. INTRODUCTION

Project Dazzle was an investigation of atmospheric re-entry phenomena based on a programme of firings of spheres and other re-entry heads at the Woomera range, with re-entry velocities close to 16,000 ft/sec., carried out under a joint UK/USA/Australia agreement. The bodies were designed by the Royal Aircraft Establishment, Farnborough, and launched by the British two stage Black Knight Vehicle. The electromagnetic scattering and optical radiation characteristics of the bodies and their wakes were monitored by ground based instruments provided by ARPA (USA) and Weapons Research Establishment, Salisbury, S. Australia, the radar data for far wakes being analysed by the Royal Radar Establishment, Malvern, and the optical data by W.R.E. Vehicle systems have been discussed elsewhere and therefore are not considered further in this paper. The background of re-entry physics and the interest in wakes is also well known so this part will also be ignored in this paper.

Spheres were included in the programme to meet the need for a simple shape which would provide a free-flight check, with minimum contamination, on more extensive tests of the flow field and wake aerodynamics that could be made in ground facilities such as wind tunnels and hypervelocity gun ranges.

The purest metal commercially available was copper of 99.95% purity which was therefore used, and there was no optical evidence of ablation during re-entry; moreover the rounds were recovered with no more than a few ounces loss of weight, all of which was attributable to impact damage. (Figure 1 is a photograph of the front half of the second sphere after recovery). The spheres discussed in this paper were both of 17 inch diameter, the re-entry velocities (at 250 K ft) being about 16,000 ft/sec.

Both rounds were spin-stablised during re-entry, at a rate of 2.6 revolutions per second. Calculations have been made of the dynamic oscillations of the head that would be expected under the influence of the rising drag force during re-entry, which provides a restoring moment to oppose the offest centre of gravity, taking account of the angular momentum of the spinning motion. The predictions for the two rounds are shown in Figure 2 in the form of a plot of the number of incidence peaks from 220 K feet downwards. (Below 30^{o} incidence, the effect of the oscillation is almost independent of its magnitude, since it is dominated by the spin rate, and is not highly sensitive to the assumed value of drag co-efficient).

2. RADAR DATA GATHERING EQUIPMENT

The radar was a pulsed, coherent system, permitting measurement of both amplitude and relative phase of the return signals. Two transmitters at 55 Mc/s and 153 Mc/s operated simultaneously into an 86 ft. steerable parabolic aerial. This was sited sufficiently close to the impact point to provide a near nose-on aspect angle to the target throughout re-entry, so permitting greater range resolution along the target wake. A flexible

transmitter pulse coding facility was provided, permitting the pulse code to be readily changed between trials as required.

"A" scope displays of individual pulse returns were recorded by high speed continuous motion cameras during re-entry, providing 30 seconds of recording on 35 mm film. A record during the complete trajectory was made on 5 Mc/s video tape as a back-up to this system, azimuth, elevation, range and time at the radar being recorded on paper print-outs.

A striking feature of the 55 Mc/s radar data from both sphere trials was the periodic variation in amplitude of the wake echoes which was observed at all altitudes. The effect is demonstrated in Figure 4 which plots the relative echoing area versus altitude for sections of the wake between 6K ft. and 9 K ft. behind the sphere. The general form of the radar echoes was practically identical on both shots. As described above, the spheres were spin-stabilised with the centre of gravity forward of centre by 0.6 and 2.25 inches respectively, so that the head dynamics were slightly different below 150 K ft., as shown in Figure 2. No significant change was shown in the period of echo modulation in Sphere 1 compared to Sphere 2 as a result of these changed dynamics.

3. INTERPRETATION OF RADAR ECHOES

3.1 Conditions for V. H. F. Radar Echoes

The conditions in which V. H. F. radar echoes will be obtained fall into two main types. Firstly, those in which the electron content of the wake is sufficiently large for the plasma frequency of the wake to be higher than the probing V. H. F. (overdense condition) and secondly, those in which the plasma frequency is less than the V. H. F. (underdense case). For 55 Mc/s the

critical electron density is 3.75×10^7 electrons/cc. whilst for 153 Mc/s the value is 2.9×10^8 electrons/cc.

In the overdense case scattering will occur at the surface of the plasma (ignoring the effects of skin depth) whilst in the underdense case the scattering will occur from the whole volume of the plasma. In the Dazzle programme the radar line of sight to the re-entry was such that only back-scatter would be observed and this involved additional criteria on the wake formation. The overdense wake will cause back-scatter at low aspect angles when the surface has roughness, the actual size and statistical distribution of this roughness for optimum effect varying with the particular radar frequency in use. In the underdense case the backscatter echoes only when inhomogeneities of electron distribution (and hence of dielectric constant) arise in the volume of the plasma. Such inhomogeneities are of course always present in a turbulent field. Again the amplitude of the backscatter at a given radar frequency is critically dependent on the amplitude and distribution statistics of the inhomogeneities.

Thus it follows that a full interpretation of the radar wake echoes must involve theories not only of the backscattering from a random distribution of electron density but also of the relation of this electron density distribution to the general fluid dynamics of turbulent wakes.

3.2. Far Wake Echoes

The theoretical radar scattering model of an underdense wake based on the original work of Booker and Gordon (Ref. 1) can be applied to this region but the model does not predict such long wakes if theoretical values of electron density are used as the starting point. Recent GASL calculations on the electron density in the wakes of cones and spheres appear to show reasonable agreement with

ballistic range data particularly over the first few thousand body diameters. Illustrated in Figure 3 are the GASL values for Sphere 1 (Refs. 2,3) compared with range data quoted by Kornegay (Ref. 4) for a copper sphere of 0.187 in. diameter at a velocity of 17.6 K ft/sec. and 18 K ft/sec. into pressure of 80 and 40 torr. Using binary scaling these pressures correspond to altitudes of 150 and 175 K ft. for Sphere 1. In the far wake binary scaling is of doubtful validity due to the presence of three-body reactions.

The crucial factor in the explanation of the long wakes observed in the Dazzle progremme is the postulation of a mechanism by which the free electron lifetime can be maintained for times much in excess of previous theoretical predictions. The data from Sphere 1 on the rate at which wake lengths decreased during re-entry is not totally inconsistent with dependence on the square of the ambient pressure (to be expected if three-body attachment was the dominant electron loss mechanism). But if one or two points are ignored, a better fit could be claimed against pressure to the first power.

The results can be taken to indicate that three-body attachment process does not in fact operate except possibly as a final clean-up mechanism. The reason the attachment process does not operate here is not known, but its explanation would probably require a more sophisticated model of temperature decay than at present exists. If the temperature is maintained above $700^{o}K$ attachment would be inhibited and therefore a process by which the wake temperature was maintained above this value into the far wake is required. The marked effect on wake electron density if attachment is prevented has been illustrated in the range work of Kornegay where he compared electron decay behind spheres fired into air and nitrogen (Ref. 4). The observed rates were several orders of magnitude faster in air, where electron-oxygen molecule attachment can occur, than in nitrogen.

4. OSCILLATION IN SPHERE WAKES

The most striking aerodynamic effect to emerge was the periodicities in amplitude of the echoing area of the wake. The modulations here referred to are distinct from those which are attributable to cyclic variations in drag coefficient as the result of varying body incidence. The period in the case of Sphere 1 appeared to be about 1/5 of a second, with a very slight tendency to decrease at lower altitudes. These frequencies are in rough agreement with those calculated for the dynamic oscillations caused by the sphere spinning with its c.g. offset.

A natural explanation when the echoing periodicity was first noted on Sphere 1 was a dynamic effect due to transverse body motion caused by the oscillations, the c.g. offset being 0.6 in. in this case. Some light on this might have been provided by Sphere 2, on which the c.g. was positioned 2.25 in. forward of centre, which would have increased the number of cycles by a factor rising with decreasing altitude (i.e. with increasing drag) from 1 to a value at 120 K ft. of approximately 2; unfortunately, however, the return from Sphere 2 was lost before any such change was observed. A snaking motion of the head could not in any case have greatly changed the effective echoing area of the wake under the conditions of the firing, since the aspect angle of the radar was very small at the relevant part of the trajectory.

The last consideration also seems to rule out the possibility of the pulsations being sideways translations in the paths due to vortex shedding of the type observed by Fay and Goldburg (Ref. 6). Such translations, moreover, if they occurred would do so at a frequency related to the Strouhal number U/d, which in the present case was approximately 10^4 cycles/sec., 1000 times too high.

Another possibility at first sight was that the periodicity was related to the large scale intermittency of turbulent "blobs" in sphere wakes described by Birkhoff, Eckerman and McKay (Ref. 7), which are attributed by these authors to the persistent effect of the long regions of laminar flow that are known to follow turbulent spots in the transition region. Examination of Figure 6 in the paper cited suggests, however, that the separation distance between "blobs" is typically of the order of 10-20 wake diameters. This would correspond on Sphere 1 to frequencies of the order of 200 cycles/sec., still much higher than that observed. (There remains in this context, however, the rather small possibility that what the radar is recording is an amplitude-modulated envelope of families of bursts of this type at different initiating frequencies).

The most obvious mechanism to initiate a periodic motion at a frequency comparable with that observed is the dynamic motion of the head. For the reasons already discussed, any resulting motion of the body as a whole would probably not be detectable, but the head motion would also result in variations in the separation line which could affect the wake downstream through its structure near the neck. We have to look for a mechanism involving the gross structure of the flow over a length scale of the order of 10^3 body diameters. Since regions of high electron density correspond to high temperatures, which in the case of sphere and blunt cone wakes are to be found not only in the turbulent core, but also in the inviscid entropy layer generated by the bow shock, it would be possible for the core to be re-heated at points spaced along its length if it were to move laterally far enough to bring it intermittently within the entropy layer. In other words a slow snaking motion of the trail relative to the enthalpy layer would provide an explanation of the hot spots which must be periodically spaced along the wake to produce the observed echoes. Since the turbulent core ultimately grows faster than the inviscid entropy layer, such "breakthroughs" must ultimately occur. The drift

velocities in the turbulent core are, however, higher than those in the surrounding entropy layer, so that a turbulent "blob" which has been heated in this way would not remain stationary relative to the points in the inviscid wake at which it was heated, but would advance relative to this point to show up as a hot spot in the centre of the wake.

Another possibility involving the flow structure would seem to be a mechanism of the type indicated in Figure 5 where the neck of the wake moves backwards and forwards relative to the body during a cycle, with corresponding variations in the electron density at the beginning of the far wake, which would then persist along its length at approximately the same frequency.

These possibilities are highly speculative, but in view of the repeatability of the phenomenon between the two sphere rounds fired, it would seem worth while to test them by firing in a ballistic range, with spheres possessing a range of dynamic characteristics.

5. REFERENCES

1. H.G. Booker, W.E. Gordon — A Theory of Radio Scattering in the Troposphere. Proc. Inst. Radio Eng. 38 401 (1950).

2. B. Kaplan, S.L. Zeiberg — Flow Field Calculations for a 17 inch Sphere. General Applied Science Labs., Tech. Memo 119 June 1965.

3. A. Rubel, S.L. Zeiberg — Some Effects of Turbulent Fluctuations on Ionisation Reaction Rates in Hypersonic Wakes. A.I.A.A. Conference on Aerothermochemistry of Turbulent Flows. San Diego December 1965. A.I.A.A. Paper 65 - 819.

4. W.M. Kornegay — Electron Density Decay in Wakes. A.I.A.A. Journal Vol.3, No.10, p.1819 October 1965.

5. L.N. Wilson — Body Shape Effects on Axisymmetric Wakes: Transition. A.I.A.A. Journal Vol.4, No.10, p.1741. October 1966.

6. J.A. Fay, A. Goldburg — Unsteady Hypersonic Wake behind Blunt Bodies. A.I.A.A. Journal Vol.1, p.2264 - 2272. October 1963.

7. G. Birkhoff, J. Eckerman, W. McKay — Transition and Turbulence in Hypersonic Wakes. Physics of Fluids Vol.9, No.3, p.446. March 1966.

Fig. 1 Front half of sphere 2 after recovery

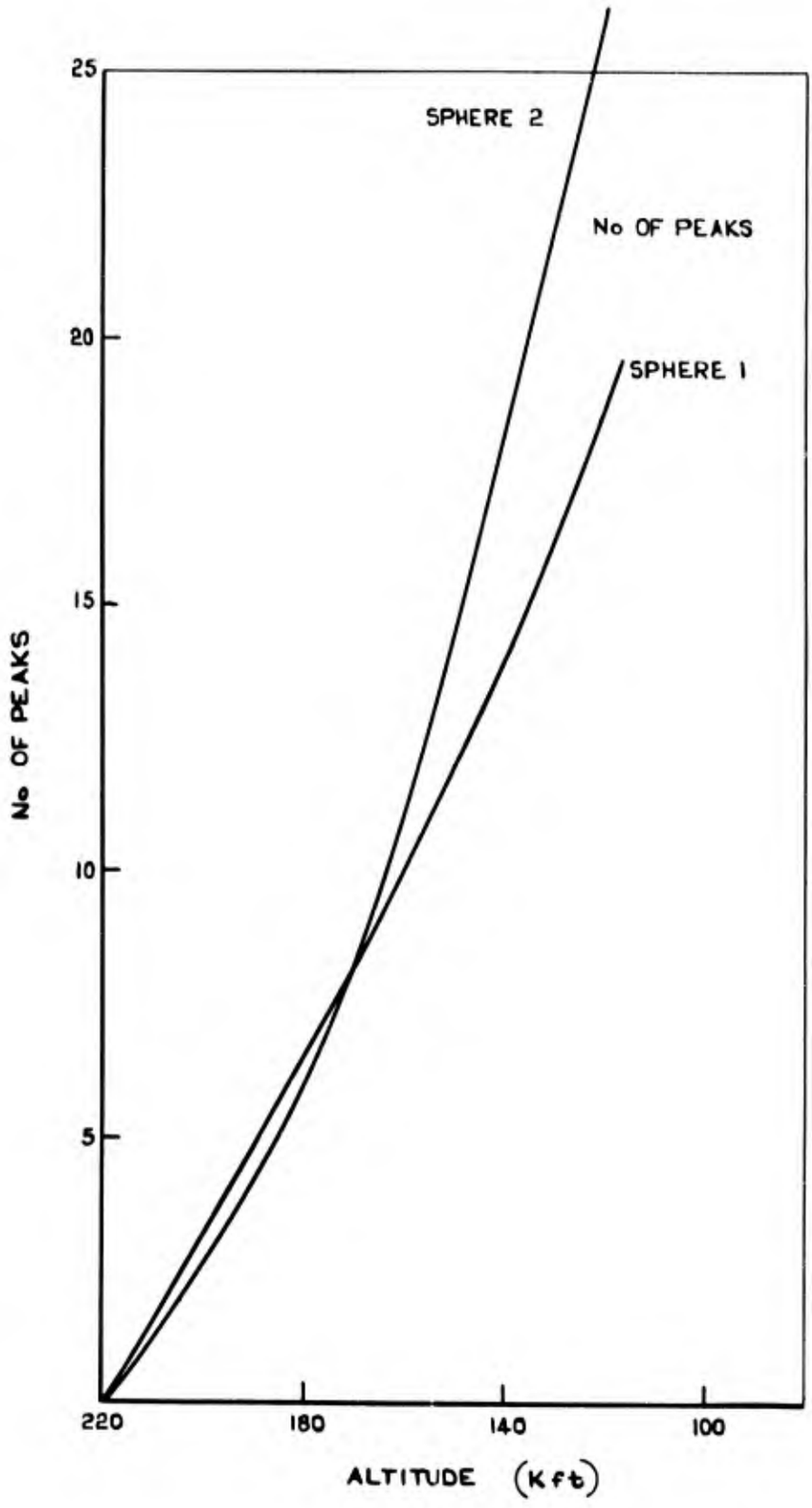

Fig. 2 Estimated number of incidence peaks from 220 Kft

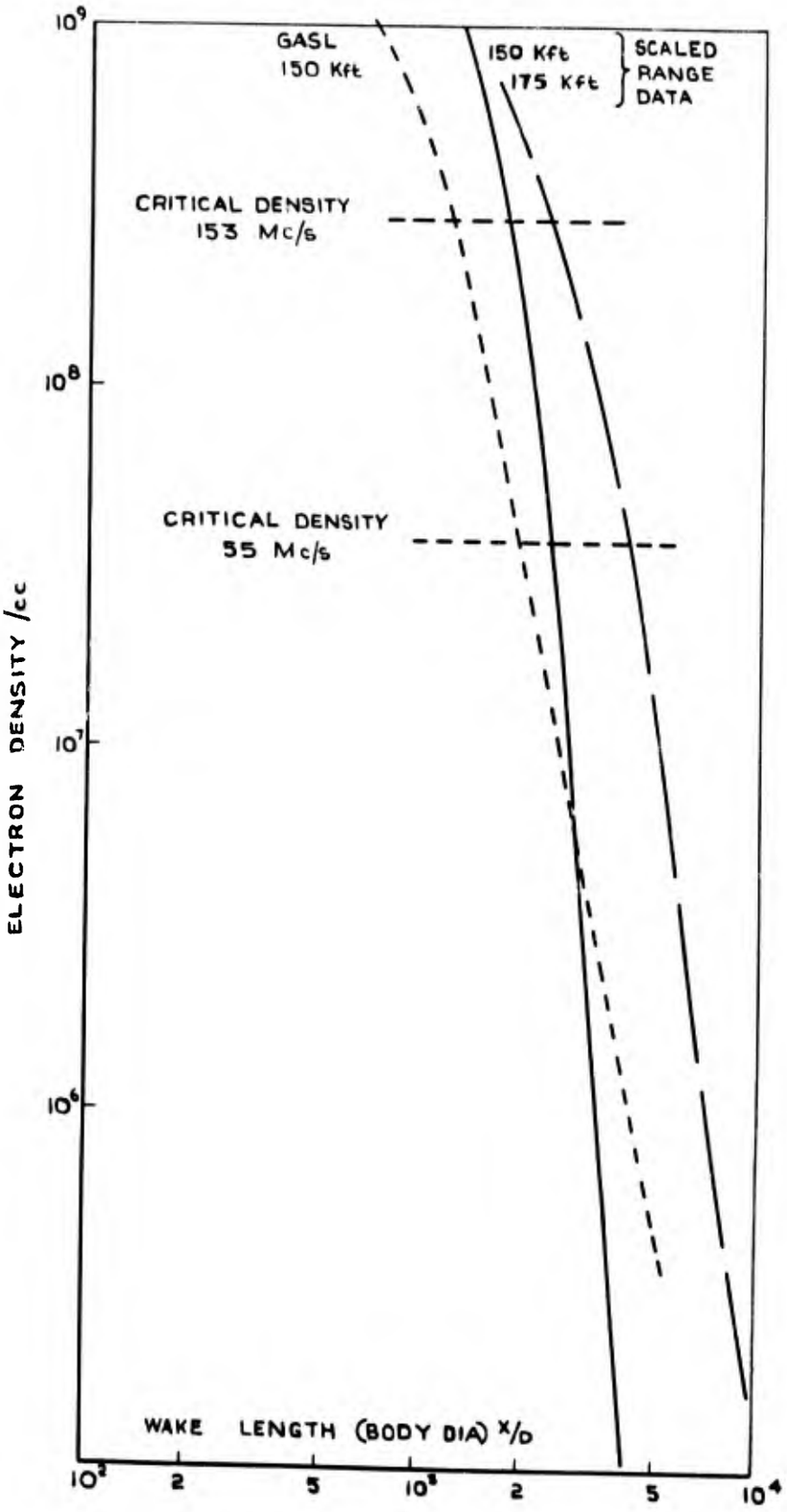

Fig.3 Electron density v wake length

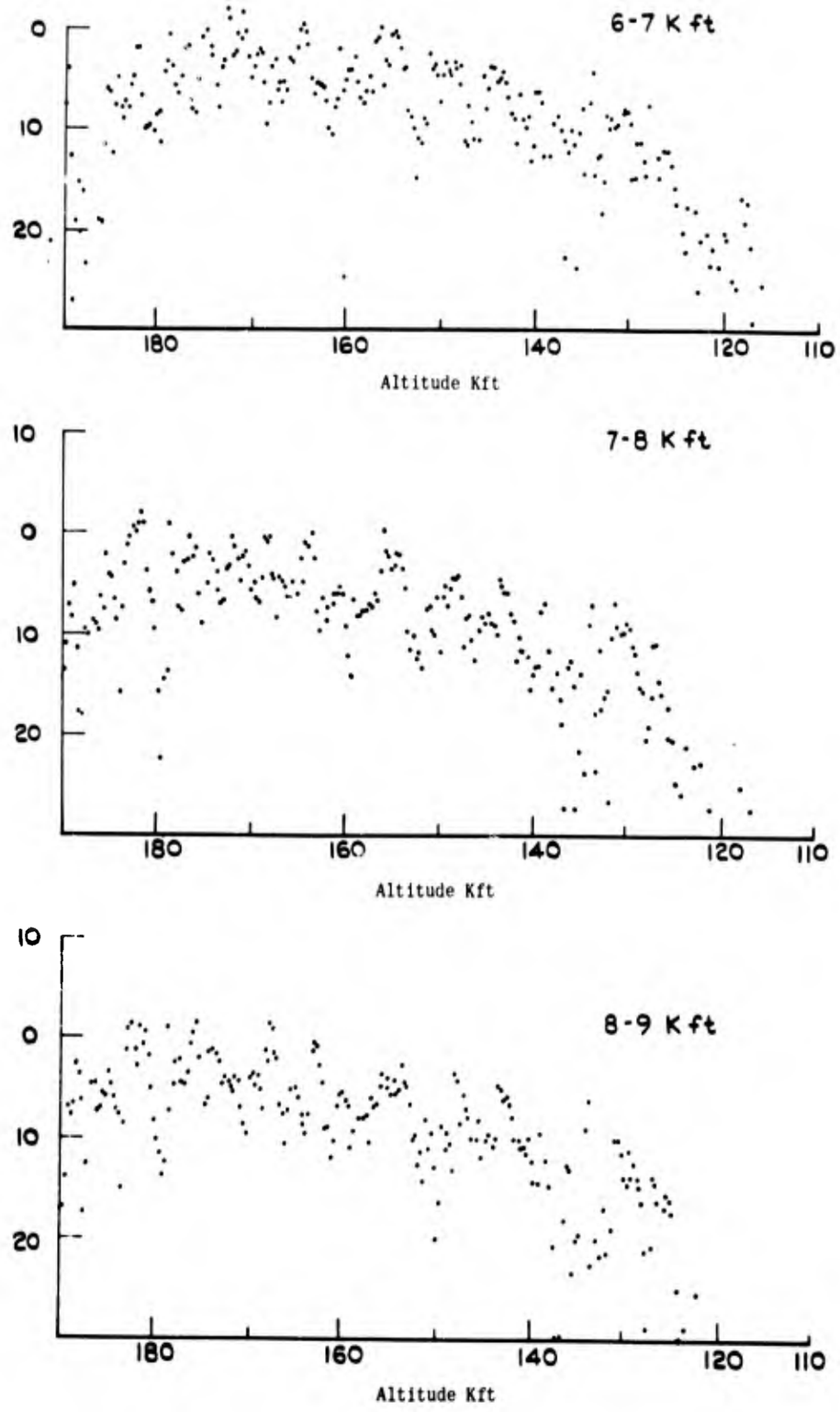

Fig. 4 Echoing area of the wake measured at different sections behind the sphere

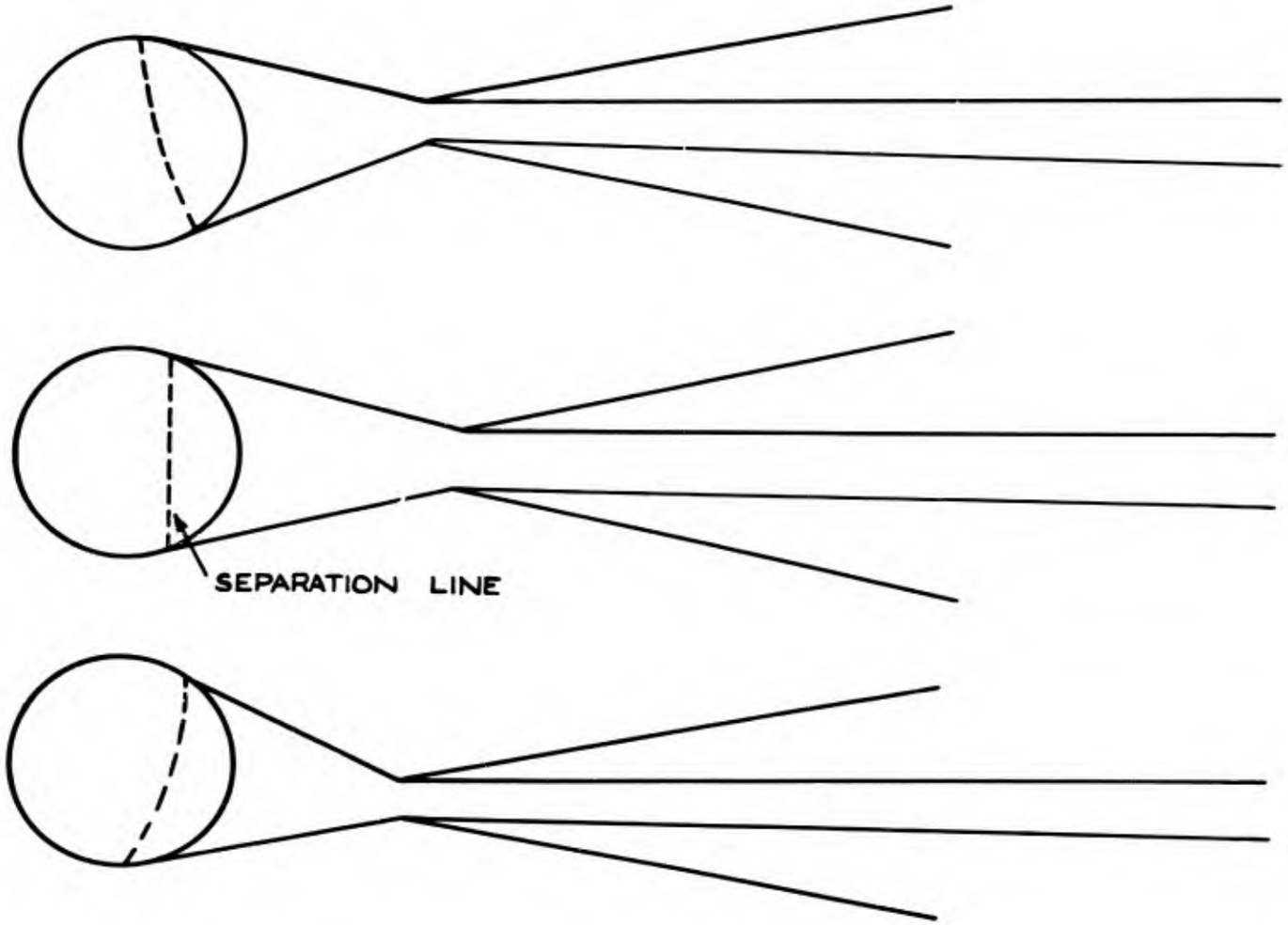

Fig.5 Possible cyclic variation of near wake structure due to variation of separation line in phase with body motion

BLANK PAGE

RADAR INVESTIGATION OF THE WAKES OF BLUNT AND SLENDER HYPERSONIC VELOCITY PROJECTILES IN THE BALLISTIC RANGE *

Authors: S. Zivanovic, Senior Research Engineer
P. E. Robillard, Research Engineer
R. I. Primich, Head, Microwave Physics Laboratory

Affiliation: Microwave Physics Laboratory
Aerospace Operations Department
AC Electronics Defense Research Laboratories
General Motors Corporation
6767 Hollister Avenue, Goleta, California

Telephone: (805) 968-1011

15 February 1967

* The work described in this paper has been supported by the Advanced Research Projects Agency under contract No. DA-01-021-AMC-11359(Z)

SUMMARY

This paper describes the study and experimental results of scattering of electromagnetic waves in the millimeter wavelength range from the wakes of hypersonic projectiles.

The four radars employed for the measurements are briefly described and their advantages and limitation are discussed.

The results obtained from wakes of both blunt and slender bodies are discussed in some detail. The wake radar cross-section, velocity, and location of the various transition phenomena can be obtained directly from the measured amplitude and the phase of the returned signal. In addition, various statistical properties of wake scattering, such as spatial correlation function, probability distribution function and spectra of wake fluctuation can be obtained.

RESUME

Les auteurs de cette communication décrivent l'étude de la diffusion d'ondes électromagnétiques de l'ordre de un millimètre de longueur d'onde, diffusion s'opérant à partir du sillage de projectiles hypersoniques. Ils exposent les résultats expérimentaux obtenus.

Après une brève description des quatre radars utilisés pour les mesures, les auteurs en exposent les avantages et les limitations.

Ils examinent ensuite de façon assez détaillée les résultats obtenus à partir de sillages de corps arrondis, d'une part, fuselés, d'autre part. La surface apparente radar du sillage, sa vitesse, et l'emplacement des divers phénomènes de transition peuvent être obtenus directement à partir de l'amplitude et de la phase du signal d'écho, telles qu'elles sont fournies par des mesures. On peut déterminer, en outre, certaines propriétés statistiques de la diffusion du sillage, telles que la fonction de corrélation spatiale, la fonction de répartition de probabilité, et les spectres de fluctuation du sillage.

1. INTRODUCTION

The study of electromagnetic wave interaction with the wakes of hypersonic projectiles launched in a ballistic range has many aspects. For example, the phase shift and the amplitude change of the transmitted wave can, after comparison with the incident wave, yield information on the electron density and the effective electron collision frequency.* These basic measurements can be performed either with a simple transmission probe[1] or with much more sensitive resonators[2] – the result is always in a form which involves an integral of electron density and therefore gives an average electron density. Or one can study the perturbation of an almost closed cavity[3] – the result will again be a volume average of electron density.

The reflection of an electromagnetic wave from a plasma depends, however, not only on the average magnitude of electron density but also on the spatial and temporal variation of electron density throughout the wake. So the study of reflection techniques provides an understanding of the wake structure as a complementary technique to the transmission method.

There is also an additional advantage in the use of reflection techniques. At present the only form of interaction of microwaves with the wake of a noncooperative reentering projectile is the reflection of radar beams from it. The study of the return is then a way to obtain information about the wake and, indirectly, about the vehicle. Duplicating the experiment on the ballistic range can thus provide help in understanding the field data.

Hence the radars described in this report were built to permit us to observe and understand the nature of radar reflection from the various

---

* Here "effective collision frequency" accounts for all mechanisms responsible for the conductivity of the plasma.

characteristic forms and parts of the wake, such as the laminar and turbulent portions of the wake, breakthrough of the viscous core, transition from laminar to turbulent flow, etc.

In the following sections the theory of reflections from underdense plasmas is briefly discussed and the radars and some experimental results are described in some detail.

2. SCATTERING FROM THE UNDERDENSE PLASMAS

Scattering from underdense plasmas has received very much attention compared with scattering from critically dense or overdense plasmas. One of the main reasons for this interest is that one can, with good accuracy,[4] use the first Born approximation to solve a class of problems which otherwise, in their general form, simply defy the exact solution. The technique for studying turbulent or fluctuating underdense plasmas was indicated by Booker and Gordon[5] in their early work* and used successfully by Fejer,[6] for example, and others[7] to explain scattering from the ionosphere. The scattered electric field E_s and the radar cross section σ, evaluated at very long distance from the plasma[6] are then proportional to the spatial Fourier transform of electron density n:

$$E_s = E_o \frac{q^2 \sin\gamma}{4\pi\epsilon_o Mc^2 R} e^{j(\omega_o t - kR)} \int_V n(\vec{r})\, e^{j(\vec{k}_i - \vec{k}_r)\cdot\vec{r}}\, d^3r \qquad (1)$$

---

* The so-called Booker-Gordon Theory which uses the spatial autocorrelation function of electron density to determine the cross section of plasma under observation cannot always be used for the study of reflections from the wakes. This is because the Booker-Gordon theory requires that the correlation function becomes negligible within a distance small compared to the scattering volume.

$$\sigma = \left(\frac{q^2 \sin\gamma}{4\pi \epsilon_o m \epsilon_o c^2} \right)^2 \left| \int_V n(\vec{r}) e^{j(k_i - k_r)\cdot r} d^3 r \right|^2 \qquad (2)$$

where E_o is the amplitude of the incident electric field, q is the charge of an electron, m is its mass, γ is the angle between the electric field of the incident wave and the direction of scattering, ω_o is the angular frequency of the incident wave, t is time, c is velocity of light in the free space, ϵ_o is the dielectric constant of the free space, $j \equiv \sqrt{-1}$, $\vec{k}_i$ is the wave vector of the incident wave, and V is the volume which contains the scattering plasma.

It is seen that the magnitude of the radar return depends on the single component in the spatial Fourier spectrum of electron density. Conversely, the measurement of the radar reflection from an underdense wake gives immediately the value of a point in the spatial Fourier spectrum of electron density with the wavelength equal to $\lambda_e = \lambda (2 \cos\alpha/2)^{-1}$ where α is the smaller angle between the incident and the reflected wave. Varying the incident frequency or the angle between the transmitter and the receiver, one can deduce the complete spectrum of electron density fluctuations and compare them with the theoretical predictions as well as the neutral density fluctuations.

Further, if the electron density changes in time, but the changes are slow enough that the condition

$$\frac{1}{n} \frac{\partial n(\vec{r}, t)}{\partial t} \ll \omega_o \qquad (3)$$

is satisfied, one can treat time as an independent parameter in the integration by replacing $n(r)$ with $n(r,t)$. The time variation will appear as the change in magnitude as well as in the phase of the receiver signal.

To understand the role of both amplitude and phase of the received signal, let us put Eq. (1) in a slightly different form. First, define the

constant A_o and the real numbers $A(t)$ and $\varphi(t)$, and vector $\vec{k}$ such that

$$A_o \equiv E_o \frac{q^2 \sin\gamma\, e^{-jkR}}{4\pi\epsilon_o mc^2 R} \tag{4}$$

$$A(t)e^{j\varphi(t)} \equiv \int_V n(\vec{r},t)\, e^{j\vec{k}\cdot\vec{r}}\, d^3r \tag{5}$$

$$\vec{k} \equiv \vec{k}_i - \vec{k}_r \tag{6}$$

With this, (1) becomes

$$E_s = A_o e^{j\left[\omega_o t + \varphi(t)\right]} A(t) \tag{7}$$

From (5)

$$A(t) = \int_V n(\vec{r},t)\, e^{j\vec{k}\cdot(r - l_k \varphi k^{-1} + \vec{\ell})}\, d^3r \tag{8}$$

where l_k is the unit vector in the $\vec{k}$ direction and $\vec{\ell}$ is any vector perpendicular to $\vec{k}$. Using the substitution

$$\vec{r}' = \vec{r} - l_k\, \varphi\, k^{-1} + \vec{\ell} \tag{9}$$

in (8) and substituting this result in (7) one has

$$E_s = A_o e^{j\left[\omega_o t + \varphi(t)\right]} \int_V n\left[\vec{r}' - l_k k^{-1}\varphi(t) + \vec{\ell}, t\right] e^{j\vec{k}\cdot\vec{r}'}\, d^3r' \tag{10}$$

The integration volume could have been extended in (1) (and

consequently in (8)) beyond the limits of the plasma, because n is zero outside of the plasma. So the volume in (10) is again the volume containing the entire plasma, but the whole integral is now a real number. The integration is performed in a fixed (with respect to the transmitter and the receiver) coordinate system in which the plasma moves with an apparent phase velocity $\vec{u}$ determined by

$$r' + l_k k^{-1} \varphi(t) + \vec{\ell} = \text{const} \tag{11}$$

or

$$u \equiv \frac{\partial}{\partial r} = -l_k k^{-1} \frac{d\varphi(t)}{dt} - \frac{d\vec{\ell}}{dt} = \vec{u}_k - \frac{d\vec{\ell}}{dt} \tag{12}$$

where

$$\vec{u}_k \equiv -l_k \frac{1}{k} \frac{d\varphi}{dt} \tag{13}$$

Hence this apparent velocity has the component u_k in the direction of $\vec{k}$, determined by the phase change of the received signal. Its component perpendicular to $\vec{k}$ remains undetermined.

In the case of frozen flow where plasma moves without rotation

$$n(\vec{r}, t) = n(\vec{r} - \int_0^t \vec{u}_f(t)\, dt) \tag{14}$$

where $\vec{u}_f(t)$ is the velocity of the frozen flow. Here one gets, following a similar procedure to that above,

$$E_s = A_o e^{j\left[\omega_o t + k^{-1} \int_0^t l_k \vec{u}_f(t)\, dt\right]} \int_v n(r)\, e^{j\vec{k} \cdot \vec{r}}\, d^3 r \tag{15}$$

i.e., only the phase of the returned signal changes and the amplitude remains constant. The velocity component of the plasma in the $\vec{k}$ direction can be easily obtained by differentiation, using (13).

It is important at this point to clarify what the phase velocity, as given by (13) means. In case of the frozen flow, this is the velocity of the fluid itself. However, at the other extreme, when creation and annihilation of electrons takes place one can observe phase velocity without any corresponding motion of the background fluid.

Hence the interpretation of the phase change from the decaying plasmas can be ambiguous if one wants to determine the fluid velocity from it, and care has to be exercised whenever large and rapid decays of electron density are present. The radar-observed velocity is, loosely speaking, only a velocity of a constant electron density contour, and this contour can either follow the fluid velocity or the move because of the plasma decay.

In the case of the narrow-beam radars which illuminate only a portion of the plasma volume, an additional restriction is imposed on the plasma if one wants to determine fluid velocity from the phase change. It is necessary that the fluctuations of electron density from one end of the scattering volume be uncorrelated in the fluctuations of electron density on the other side. This is because it is necessary to actively "track" or distinguish a particular eddy so one can determine its velocity.

The amplitude fluctuations, in the case of scattering from a turbulent or generally random medium, describe the fluctuations of a particular spatial Fourier component of electron density calculated over the scattering volume. In the case of a Gaussian process, these fluctuations are also Gaussian. There is, however, no evidence that the random fluctuations in wakes are Gaussian. In fact, some experimental results indicate that the process is not Gaussian. Nevertheless, the mean value (a time average) of the amplitude of the reflected signal is equal to the average value of the Fourier component of electron density, providing, of course, that all the mean quantities in the observed

volume remain the same during the averaging time. Study of the fluctuating quantities in this case can lead to an understanding of the type of random process which is responsible for the scattering fluctuations.

The mean components of received electric fields, if evaluated at various frequencies or various angles between transmitter and receiver, determine the spectral distribution of electron fluctuations. Present efforts in this area of fluid mechanics gives hope that this spectral distribution can, in turn, be theoretically predicted and hence it is an important connection between the fluid mechanical theory of fluctuations and radar scattering. They also can, together with the electron density measurements, be used to determine an experimental scattering model of the turbulent wake. This work is now in progress.

3. EXPERIMENTAL ARRANGEMENT

From the previous discussion, it appears that the scattering experiment, in order to yield maximum information, has to give independent information about the magnitude and the phase of the returned signal. Second, it has to have as many transmitter-receiver systems as practical in order to obtain more points on the spectral curve. These systems must illuminate the same volume of plasma (or as much as practical) so that meaningful comparisons can be made. Finally, it would be desirable to illuminate a volume of plasma located a fixed distance behind the body for sufficient time to obtain a good average of the received signal.

This last requirement is, of course, difficult to satisfy on the ballistic range, where any sort of tracking is extremely difficult to achieve. A compromise is achieved by having the radar beam wide enough that the plasma will stay long enough in the scattering volume, yet still narrow enough that the resolution is sufficiently good; this is discussed later in this section.

The light-gas gun on the AC Electronics-DRL Free-Flight Ballistics Range is capable of launching blunt and slender saboted models up to 25 mm in diameter for spheres and up to 12 mm in diameter for slender cones at velocities up to 7,000 m/sec into a controlled atmosphere. The free-flight chamber consists of a tube 60 cm in diameter, and about 20 m in length, and a 2.5m-diameter section about 15 m long at the end of the range which houses the radar system. (For details see Figure 1.)

The existing radar system consists of four radars operating at frequencies of 9, 17, 35, and 70 GHz. Each radar has a focused-lens antenna oriented at an angle of approximately 45^{o} with respect to the flight axis. All four radars are identical in principle, the difference being only in operating frequency. Hence, the operating principles that are described here apply to all of them.

Since the radars are operated inside a metal chamber, a relatively strong signal is reflected by the chamber walls, even if the walls are lined with a microwave absorber. This necessitates the use of doppler techniques, i.e., removing the carrier signal from the receiver and observing only the components due to the time-varying target.

A simple way to achieve this carrier removal was to mix the received signal with the original transmission – i.e., use the autodyne system. If the transmitted signal S_1 is

$$S_1 = A_o \cos \omega_o t \tag{16}$$

where A_o is a constant, and the received signal S_r is proportional to

$$S_r \approx A(t) \cos\left[\omega_o t + \varphi(t)\right] \tag{17}$$

where $A(t)$ and $\varphi(t)$ are, as before, the time-dependent amplitude and phase, then after mixing the signal would have the form

$$S_a = A_1 A(t) \cos \varphi(t) \tag{18}$$

where A_1 is a constant.

After amplification with an ac-coupled video amplifier, the carrier signal, which now appears as a dc voltage, is completely eliminated.

This principle was used in one of our early systems. Though it has the advantage of being simple to build and operate, it suffers from the shortcoming that the amplitude and phase changes appear as a product, and it is impossible to separate them if they are obtained in this form.

3.1 The Superheterodyne Radar

The use of the superheterodyne radar solves the problem of amplitude and phase separation by superimposing the phase component on a high-frequency carrier.

The choice of the intermediate frequency (IF) is dictated by the following requirements:

(1) It has to be much higher than any expected phase fluctuation rate;

(2) It has to have commercially available components; and

(3) It has to permit reduction in noise.

The IF of 30 MHz has been selected because it does meet all the above requirements.

The signal backscattered by the wake is given by expression (17). If this signal is mixed with a separate local oscillator signal $S_i = A_i \cos (\omega_o + \omega_i)t$ instead of the original transmission, one of the output components from the mixer will be proportional to $A(t) \cos\left[\omega_i t + \varphi(t)\right]$

where ω_i is the angular frequency difference between the local oscillator frequency and the transmitter frequency. If the IF is chosen to be much greater than the amplitude fluctuation rate, the amplitude of the IF carrier will be proportional to the amplitude of the received signal, undistorted by any phase modulation. Amplitude detection of the IF carrier gives the amplitude of the received signal directly.

The phase fluctuations of the received signal appear as a phase modulation of the IF carrier. The amplitude fluctuations can be eliminated from the IF carrier with limiters. Phase detection of the IF carrier, after limiting, provides the phase fluctuations of the received signal as a function of time undistorted by amplitude fluctuations.

4. DESIGN OF SUPERHETERODYNE RADARS

Four radars, operating at frequencies of 9, 17, 35, and 70 GHz have been designed and constructed. The choice of the operating wavelengths (33 cm, 1.7 cm, 0.86 cm, and 0.43 cm) was dictated by the expected size of turbulent eddies and by the desired spatial resolution. The size of the launched bodies varies from 2.5 mm to 2.5 cm in diameter. It would be desirable to have the resolution of about one body diameter for at least some frequencies. For maximum resolution, an f-number equal to one was used at the lowest frequency, and the rest of the radars were focused on the same volume. The size of the turbulent eddies is also of the order of the body diameter, so it was desirable to operate at a wavelength of around 1 cm, the exact number being dictated by the availability of the commercial equipment.

The design of all four radars is very similar and can be represented by the simple block diagram shown in Figure 2.

In this figure, the transmitter output frequency denoted as f_o is either 9, 17, 35, or 70 GHz. A CW source is used with power output in the order of 100 mW. The local oscillator frequency is set at

F_o+30 MHz, 30 MHz above the transmitter frequency. Since the phase of the received signal is of interest, the local oscillator output frequency has been phase-locked to the transmitter output frequency to maintain coherence at the mixer output.

The geometry of the antenna and the range assure that the signal backscattered from the moving target is higher in frequency than the transmitted frequency. If it is assumed that the received frequency is (f_o+f_d), the output frequency from the receiver mixer is 30 MHz-f_d. Typically, the information bandwidth will be from 28 MHz to within a few kilohertz below 30 MHz.

As a result of using a single antenna for transmission and reception (monostatic system) in conjunction with a CW transmitter source, the problem of transmitter signal leakage into the receiver is very severe. The ratio of transmitter power to receiver sensitivity is in the order of 120 dB and it is necessary to maintain a transmitter-to-receiver isolation of at least this magnitude for an operational period of time, in the order of thirty minutes. The problem of transmitter-to-receiver leakage is much more severe in the superheterodyne radar than the autodyne radar; in the autodyne radar the transmitter-to-receiver leakage appears at the receiver mixer as a dc current, and it is a trivial problem to separate 10 kHz from dc. In the superheterodyne radar, however, the leakage signal appears at the receiver mixer as 30 MHz and the information data may exist within a few kilohertz of 30 MHz. The problem of carrier separation is very difficult in this case.

To eliminate some of the transmitter-to-receiver leakage, the transmitter output signal is fed to the antenna through a four-port short-slot hybrid junction. Reflections from the antenna and the back wall of the range are partially suppressed by tuning the junction. Experience has shown that a maximum of 70 dB transmitter-to-receiver

isolation can be maintained on the free-flight range for the length of time required to fire the projectile and obtain data. Therefore, the transmitter leakage signal at the input of the receiver is approximately 50 dB above the receiver noise.

Hence, two frequencies are present at the output of the receiver mixer. One is the signal scattered from the moving target, which varies both in frequency and in amplitude, and this signal contains the desired information. The other is the constant-amplitude transmitter-leakage signal, approximately 50 dB above receiver noise.* This transmitter-leakage signal is of no significance and must be removed, since it will intermix with the desired scattered signal to produce unwanted signals at the receiver output.

The transmitter leakage signal is removed from the receiver output by a band-reject crystal notch filter centered at 30 MHz. The attenuation of the filter is greater than 50 dB at the rejection frequency of 30 MHz and has a bandwidth of ± 8.0 kHz at the 3.0dB attenuation level.

This filter is adequate to remove the leakage signal from the transmitter to the receiver. The bandwidth of the filter attenuates frequencies close to IF, and hence imposes the limit on the lowest velocity that can be observed. The influence of the filter is also much greater on the low-frequency radars: 8.0 kHz at 9.0 GHz represents a velocity of about 200 m/sec.

If the wake motion is slow enough for the doppler frequency to be within the filter rejection band, the radar output will, of course, be attenuated. However, it is possible that even if the doppler frequency is outside the bandwidth of the notch filter, fast transient signals would

---

* The level can vary slowly in time, but is constant during observation time; 50 dB is merely an orientation figure and can vary slightly depending on transmitter-receiver isolation.

have frequency components within the filter attenuation region. This type of phenomenon could result in severe distortion of the received signal.

The tuned hybrid junction in the transmitter is very sensitive to frequency and the transmitter-to-receiver isolation can only be maintained if both frequency stability of the transmitter source and mechanical stability of the entire radar system is maintained. The problem of mechanical stability can be improved by sturdy assembly of the radar components and the radar antenna; on the free-flight range, however, mechanical vibrations from vacuum pumps and other equipment always exist.

The transmitter frequency is controlled with a crystal frequency standard operating at 1.0 MHz. The output from the standard is frequency-multiplied to obtain the necessary reference signal for stabilization of the transmitter output frequency.

The frequency stabilization system, though very important to radar operation, is not described here since it is essentially the same system described elsewhere by Blore et al.[8]

The radar head consists of a number of standard waveguide components needed for signal level control and measurement and frequency measurements. These are mainly required to facilitate radar operation and therefore will not be described in this paper.

4.1 IF Radar Receiver

The radar receiver has been designed to record the amplitude and phase of all possible signals scattered by the wake. A block diagram of the receiver is shown in Figure 2. The signal is first amplified in a low-noise preamplifier. Following the preamplifier, the 30MHz leakage signal is removed by the crystal notch filter and then the received signal is divided into two channels.

In the first – the amplitude channel – the signal is amplified by

means of a logarithmic amplifier-detector.* The logarithmic amplifier is used mainly as a compression amplifier to provide greater dynamic range on the recording oscilloscopes. The logarithmic amplifier provides approximately 12 dB per cm of deflection on the CRT, or a total of 48 dB on a 4.0cm CRT. The best that can be recorded on a linear display is about 30 dB.

In the second channel – the phase channel – the amplitude fluctuations are removed from the IF carrier with a limiter amplifier. The IF carrier is then eliminated by mixing the signal with a 30MHz reference signal. The reference signal is derived from the same source as the reference signal used to phase-lock the transmitter to the local oscillator. Therefore, coherence is maintained throughout the receiver.

Following the mixer, the signal is amplified on the wideband video amplifier and recorded on an oscilloscope. The output of the phase channel is $A_c \sin\varphi(t)$, where A_c is a constant amplitude.

Because the bodies fired in the range are small, maximum resolution along the flight axis was desirable to permit measurement close to the body. Experience has shown that maximum resolution can be obtained with the focused-lens antennas. Focused-lens antenna systems have been used on the free-flight range on transverse microwave probe experiments, described in detail elsewhere.[1] It is shown that this maximum spatial resolution can be achieved when the diameter of the lens is equal to the distance of the lens to the focal regions, i.e., an f-number of 1:1 . With this geometry, the size of the beam in the focal region is approximately 1.5 wavelengths at the 3dB levels.

Since maximum spatial resolution was desirable on the oblique radar system, the 9GHz antenna was designed with an f-number of 1:1 . At 9 GHz ($\lambda \equiv 3.3$ cm), the expected resolution is five centimeters.

---

* A logarithmic amplifier-detector output is the logarithm of the amplitude of the IF carrier which is fed into the input.

The same spatial resolution obtained for the 9GHz antenna is obtained at the higher frequencies by increasing the ratio of the focal length to the lens diameter by the same ratio as the increase in frequency. For example, the 17GHz focused-lens antenna has a focal-length-to-diameter ratio of 2:1. Similarly, at 35 GHz and 70 GHz the focal length-to-diameter ratios are 4:1 and 8:1 respectively.

The lens f-number determines the gain and the resolution of the lens. For the selected f-number of 1:1 the lens diameter is equal to the distance to the flight axis. Because of limited space available, it is desirable to have a small lens diameter. However, it is also necessary to have the lens as far away as possible from the flight axis. These contradictory requirements resulted in the compromise selection of a lens diameter of 50 cm for the 9GHz radar.

An actual lens consists of two plane-convex lenses, with the plane surfaces firmly joined. The first lens has always an f-number of 1:1 and its purpose is to convert the spherical electromagnetic wave from the feedhorn to a plane wave. This plane wave is now focused by the second lens which has an f-number selected in the way described above, according to radar frequency.

Each lens is illuminated by an appropriate feedhorn. The feedhorn has been designed to reduce the sidelobes 20 dB below the main lobe. The feedhorn is oriented with the H-vector in the horizontal plane.

The beam patterns in the H-plane (horizontal plane) obtained at the four frequencies are shown in Figure 3. These patterns were obtained by probing in the focal region with an open-ended waveguide. The sidelobe level at the four frequencies ranges from 20 to 25 dB below the main lobe.

To assure adequate illumination of the wake in the direction perpendicular to the flight axis, the feedhorns were designed to produce a beamwidth in the E-plane (plane perpendicular to the flight axis) of at

least 10 cm. Since the projectile diameters are under 2.5 cm, this assures adequate illumination with some allowances for dispersion in flight trajectory.

It is desirable to keep the angle between each antenna beam and the flight axis at approximately 45 degrees. In the final design the angles are 45° for the 9GHz and 17GHz lenses and 53° for the 35GHz and 70GHz lenses. This slight deviation for the last two radars was dictated by practical considerations and available space.

A photograph of the 17GHz, 35GHz, and 70GHz antennas is shown in Figure 4, and the 9GHz antenna is shown in Figure 5.

The details of the radar operation and calibration are given in Reference 9.

5. EXPERIMENTAL RESULTS

The radar-scattering measurements on the AC-DRL free-flight ballistic range are performed on the wakes of various ablating and non-ablating models. The diameter of the models can vary from 2.5 mm to 25 mm for spheres and a variety of cones (up to 13mm-base diameter and 8° half angle at the nose) can be launched. Several other shapes have also been successfully launched. The speed at which the above projectiles can be stably launched is in excess of 7000 m/sec and the pressure of the gas into which they are launched can be varied from 0.1 to 760 torr. A variety of gases are used for the ambient atmosphere. Air is often used, but depending on the particular program, other gases — such as argon and nitrogen can be used. These other gases can also be mixed with air in various proportions.

The radar observation of the wakes of various models is carried out for every launching. The scattered signals are sometimes too weak for useful analysis and when one wants to observe the wake of a particular model, an appropriate choice of the ambient gas has to be made

in order to assure sufficient level. This choice of the ambient gas is discussed in the following section.

Various information about wake structure can be extracted from the radar returns – the amplitude decay as the function of the distance behind the body, statistics of the amplitude fluctuations, turbulent wake velocity and so on. But the most explicit observations are the transition phenomena in the wake. They are marked by sudden changes in radar backscatter and therefore easy to localize and compare with schlieren observations. In the remainder of this section the transition phenomena of the hypersonic wakes as seen by the doppler radar will be discussed in some detail.

5.1 Transition Phenomena

In case of scattering from underdense plasmas, as discussed in Section 2, the backscatter radar return is proportional to the spatial Fourier transform of electron density with the wavelength of $\lambda/2$. Any change of structure would, hence, correspond to the change in the radar cross section. If, as often is the case, a change of velocity accompanies the change of structure, then this change becomes easier to detect. This can be seen in Figure 6, in which the transition from laminar to turbulent flow occurs at about 160 μ sec (or 150 body diameters (BD)) behind the body. However, some transitions are difficult to detect only through an amplitude change. Also, in general, the transition process is distinctly different for blunt bodies such as spheres and for slender bodies. Hence, in the next sections the scattering from these two types of vehicles is discussed separately.

5.1.1 Spheres*

The transition distance in the sphere wake is a function of the body Reynolds number. At low Reynolds numbers (below the critical) the viscous wake cannot become turbulent. However, the whole inviscid wake can become turbulent but, due to its low viscosity, the transition occurs very far behind the body – at several thousand body diameters. This inviscid wake turbulence is seen on the backscatter radars as a sudden increase of the radar cross section at about the same distance from the body as the schlieren observation of the same phenomenon. Figure 7 shows the actual radar return from inviscid wake turbulence, and in Figure 8 the processed radar amplitude is given.

As the body Reynolds number increases beyond the critical Reynolds number, the transition point moves near the body and the viscous wake transition occurs within the first ten diameters from the body. Eventually the turbulent viscous wake grows faster than the inviscid wake, fills it completely, then breaks through the inviscid wake into the surrounding ambient gas. These transition distances as observed by schlieren as well as by radar are given in Figure 9.

Schlieren photographs cannot often penetrate the strong density gradients on the outside boundaries of the inviscid wake, so they generally show only the breakthrough point. Radars, operating at a sufficiently high frequency can, however, penetrate into the viscous core and shows clearly both viscous wake turbulence and the breakthrough of the inviscid wake into the cool air. In Figures 10 and 12, one can observe first the laminar wake, characterized by a slow phase change.

---

* The fluid mechanics description of sphere wakes transition is based on References 10 and 11. For more details the reader should consult these references.

The wake is overdense and fairly smooth for 17 GHz right behind the body and there is not much phase change. The amplitude drops until turbulence occurs because of the rapid electron density decay. The phase change is, from the onset of turbulence, proportional to the wake velocity. Then, around 500 μsec (or 200 BD) behind the body, a second large change in phase (or body velocity) occurs, corresponding to the viscous wake breakthrough. There are no drastic amplitude changes associated with the breakthrough in this round. However, in some rounds launched under identical conditions, an amplitude decrease of about 10 to 15 dB at 17 GHz was observed at the breakthrough point.

It is worth noting that the viscous wake transition from laminar to the turbulent flow occurs on the average at the distance given by Wilson,[11] but the individual transition distances fluctuate around this mean value. Hence the transition distance, as observed by radar, is a random variable (precise statistics have not been obtained due to the limited number of rounds launched under the same conditions). The radar resolution at 17 GHz is about 23 body diameters for the 15mm sphere and transition of the viscous wake has been observed practically from the body up to 20 body diameters.

The transition distance, as measured by radars, is also a function of radar frequency. This distance is often (but not always) shorter for higher frequencies. The turbulence starts with a small ripple which is comparable in size to the shorter wavelength so it is "seen" by the highest frequency radar first. As it grows in size, the others begin to "see" it.

To understand the amplitude results given in Figures 10 and 11, one must consult the electron density decay for this particular round.

In Figure 13* the integrated electron density across the wake is given as a function of distance behind the body. There is indication that in the laminar wake there is a very strong peak in the radial electron density profile corresponding with the viscous core. This highly ionized viscous core is underdense for 70 GHz, close to critical density for 35 GHz, partly overdense and partly underdense for 17 GHz, and completely overdense for the 9 GHz radar during the entire laminar wake, i.e., 0–20 BD. This is why one has very strong scattering for the 9 and 17 GHz radar, very sharp decay in cross section (with a slight increase after the transition point) at 35 GHz and very weak scattering at 70 GHz. After the turbulence sets in, this high peak in electron density slowly spreads so that the electron density is more uniform. The radar return is now due to the turbulent structure; the underdense analysis can be applied at 17, 35 and 70 GHz, almost immediately after the transition point. The electron density in the wake is probably still close to critically dense for the 9GHz radar for at least one or two hundred body diameters. Both transition points are hard to distinguish at that frequency.

5.1.2 Cones

The transition from laminar to turbulent flow can be easily observed in Figure 6. This is the return of the 17GHz radar from the wake of a slender cone, launched into an argon atmosphere. After the practically nonexistent return from the laminar part, the signal increases from the transition point on and then slowly decreases due to the electron density decay. The phase change gives the wake velocity, which is quite accurate up to about 500 body diameters. Measurements beyond that point are probably distorted by the notch filter (Section 4).

---

* Figure 13 and its interpretation is presented courtesy of Mr. R.A. Hayami, from his unpublished work.

The radar scattering from sharp, slender cones launched in the ballistic range are extremely difficult to observe in air at frequencies above 9 GHz due to the very sharp electron density decay, which is believed to be caused by the electron-oxygen attachment. The launchings in nitrogen and even in argon, while preserving the essential fluid-mechanics characteristics, do exhibit much slower electron density decays and also much higher initial levels of electron density. So nitrogen is an ideal substitute for air in the case when radar observables are too low to be distinguished from the receiver noise.

The transition from a laminar to a turbulent wake is generally observed in every cone launching in which sufficient signal is received so that it can be processed with confidence. Detailed analysis of the transition distance behind cones as a function of the range parameters will be the subject of a forthcoming paper.

CONCLUSIONS

It is seen that a side-looking radar can be a useful tool in gaining information on the structure and transition points in the wakes of hypersonic projectiles.

REFERENCES

1. R.I. Primich and R.A. Hayami, "Millimeter Wavelength Focused Probes and Focused Resonant Probes for Use in Studying Ionized Wakes Behind Hypersonic-Velocity Projectiles," GM DRL Report TR63-217C, Jul 1963

2. R.A. Hayami, D.H. Auston, K.J. Kelley, J.R. Faulkner, "Fabry-Perot Resonators at 5 Gc and 35 Gc for Wake Ionization Measurements in a Free-Flight Ballistics Range," GM DRL Report TR65-19B, May 1965

3. M. Labitt, Lincoln Laboratory, MIT Report TR307, 15 Apr 1963

4. S. Zivanovic, "A Numerical Investigation of the Validity of the Born Approximation for Determination of the Reflection Coefficient of Underdense Plasma Slab", GM contract technical note CTN4-08, Oct 1964

5. Booker and Gordon, "A Theory of Radio Scattering in the Troposphere," Proc of the IRE, Vol 38, No 4 Apr 1956, pp 401-12

6. F.A. Fejer: "Scattering of Radio Waves by an Ionized Gas in Thermal Equilibrium in the Presence of a Uniform Magnetic Field," Canadian J of Phys, Vol 38, p 716, 1961

7. T.P. Dougherty and D.T. Farley, "A Theory of Incoherent Scattering of Radio Waves by a Plasma," Proc Royal Soc, A, Vol 259, p 79-99, 1960

8. W.E. Blore, P.E. Robillard and R.I. Primich, "35- and 75-GHz Phase-Locked CW Balanced Bridge Model Measurement Radars," Microwave J, Vol III, No 9, Sep 1964

9. P.E. Robillard, "An Experimental Radar Facility to Study Backscattering from the Wakes of Hypersonic Velocity Projectiles," GM DRL Report TR66-01L, Jul 1966 (to be published in IEEE Trans on Aerospace and Electronic Systems)

10. L. Wilson, "The Far Wake Behavior of Hypersonic Spheres," GM DRL Report TR66-10, Jun 1966

11. L.W. Wilson, "Body Shape Effects on Axisymmetric Wakes: Transition," AIAA J, Vol 4, No 10, p 1741, 1966

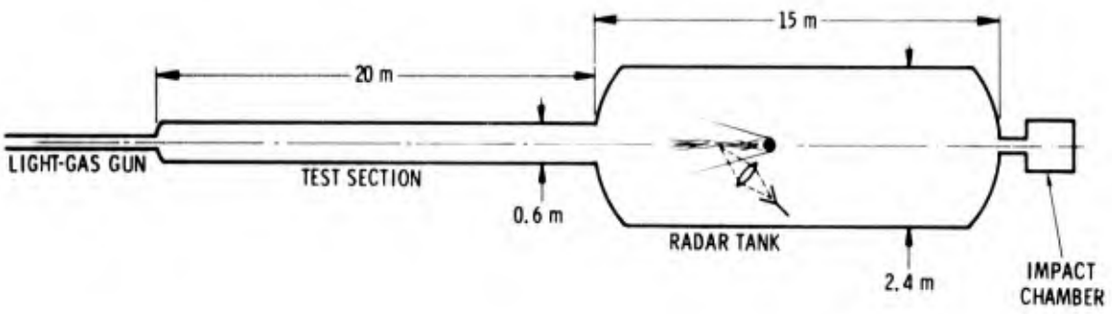

Fig. 1 Schematic of Free-Flight Range

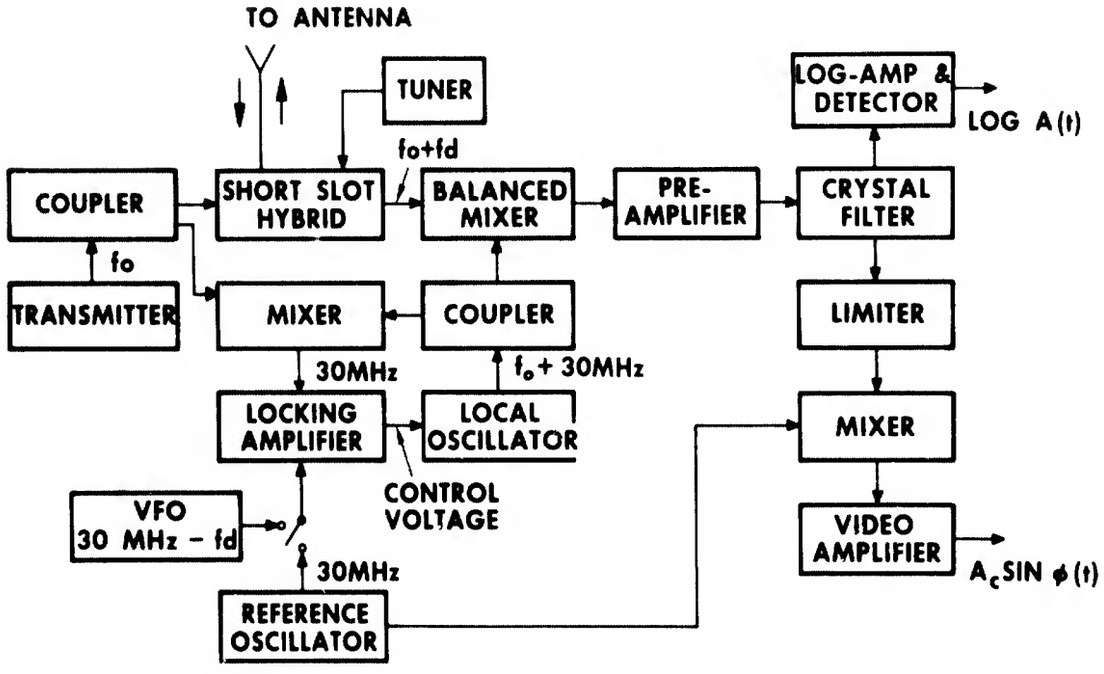

Fig. 2 Block Diagram of Superheterodyne Radar

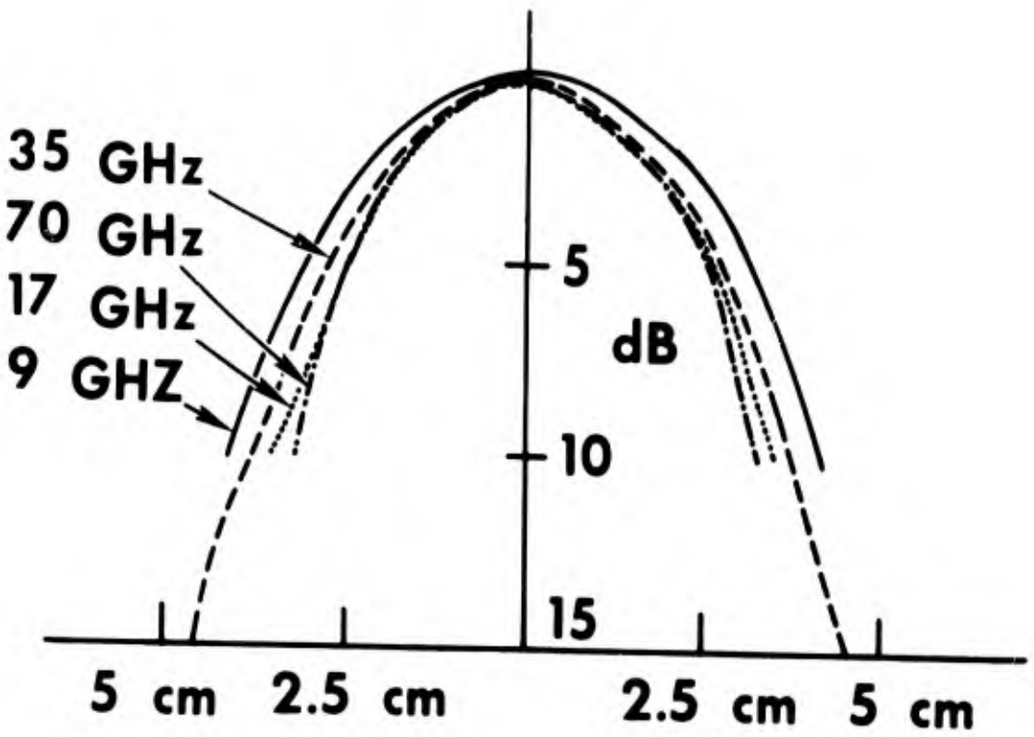

Fig. 3 Beamwidth (H Plane) of Multiple Antenna System

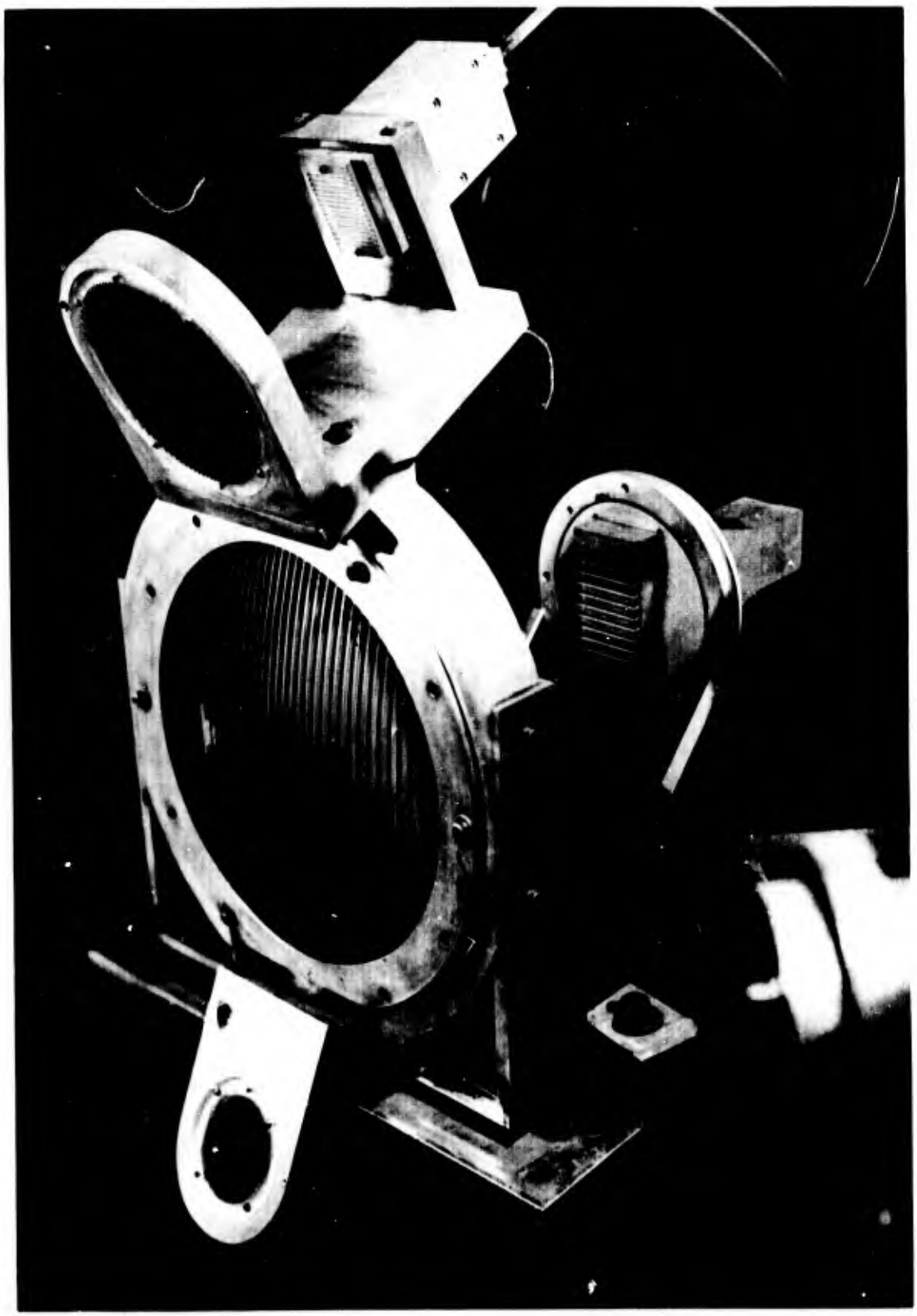

Fig. 4 Antenna for 17GHz, 35GHz, and 70GHz Radars

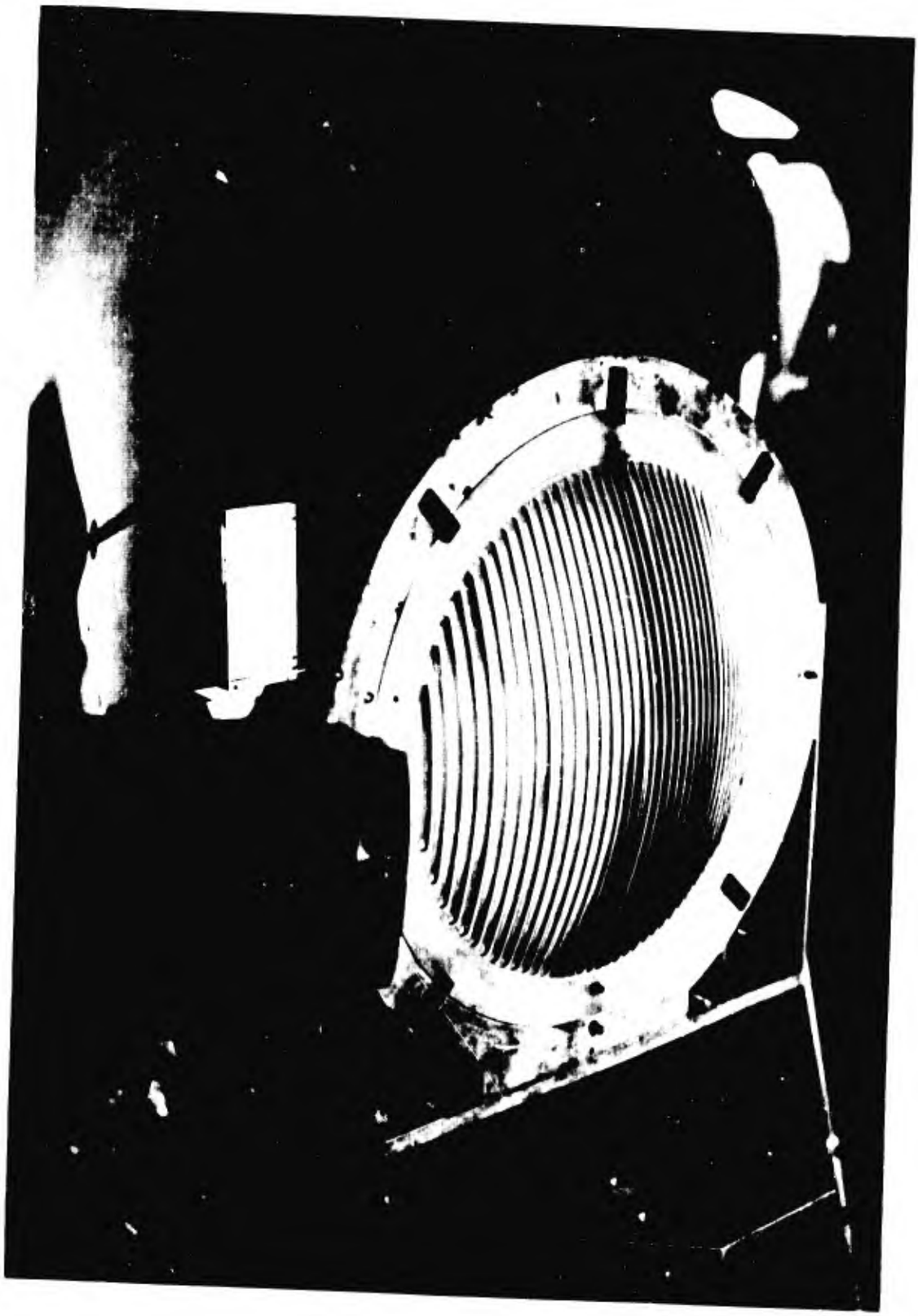

Fig. 5 9GHz Radar Antenna

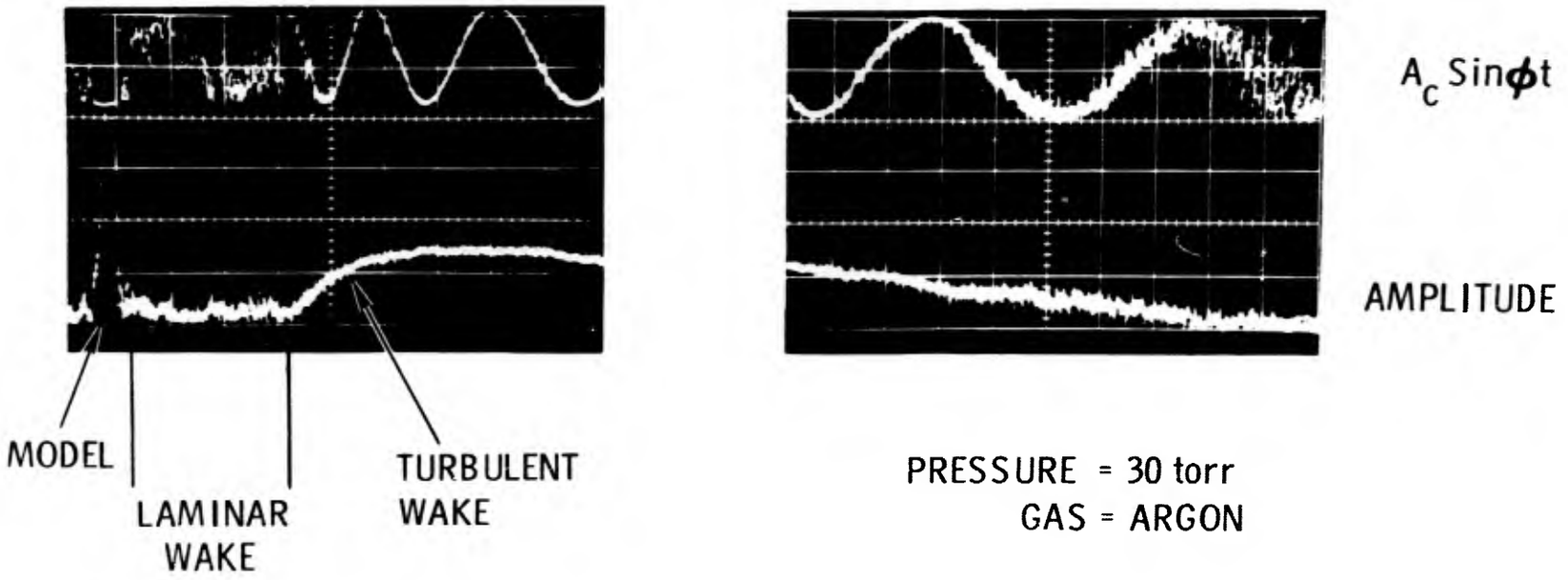

Fig. 6 Radar Scattering from Cone Wake in Argon at 30 torr

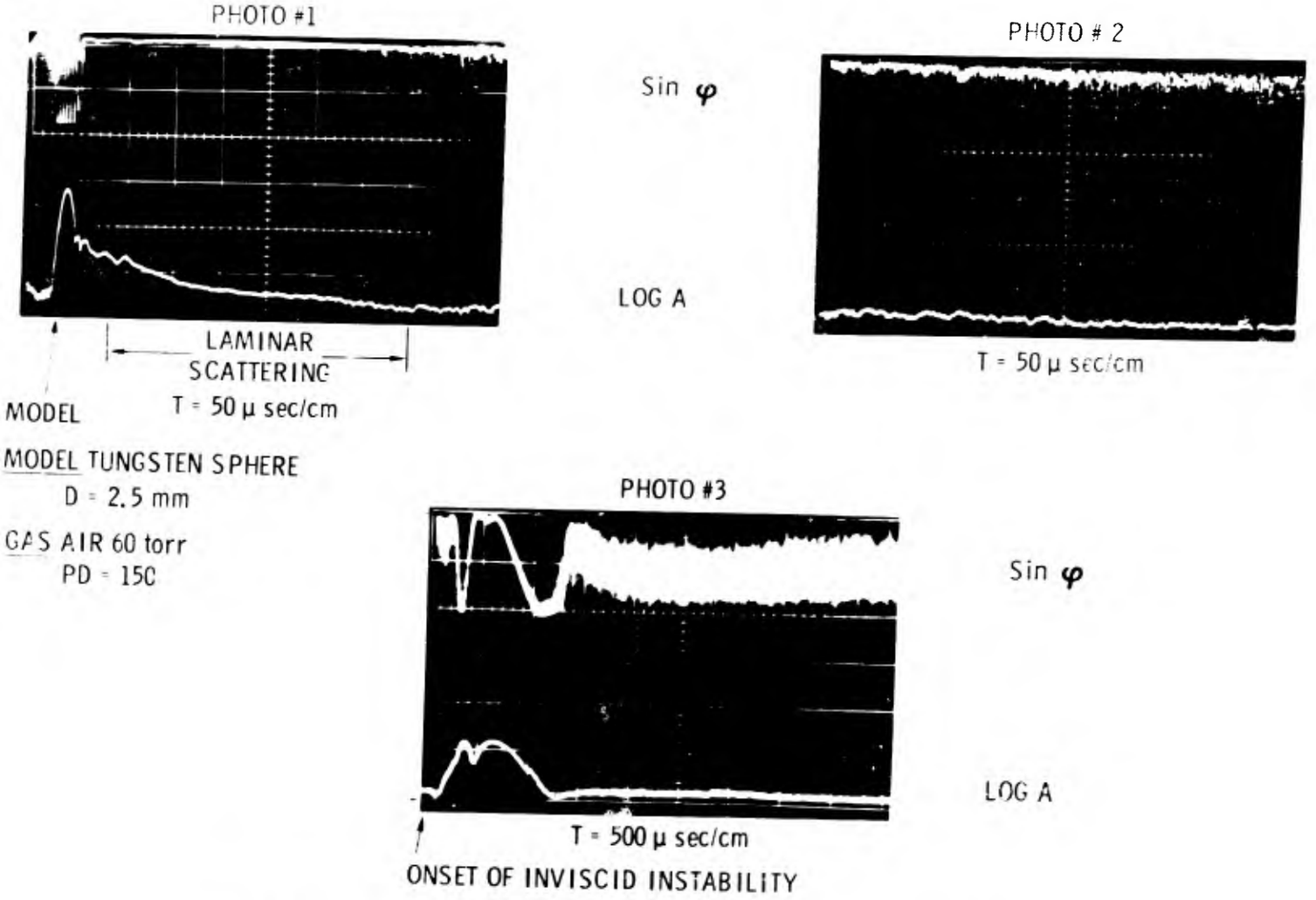

Fig. 7 Record of Inviscid Wake Turbulence, pD = 150

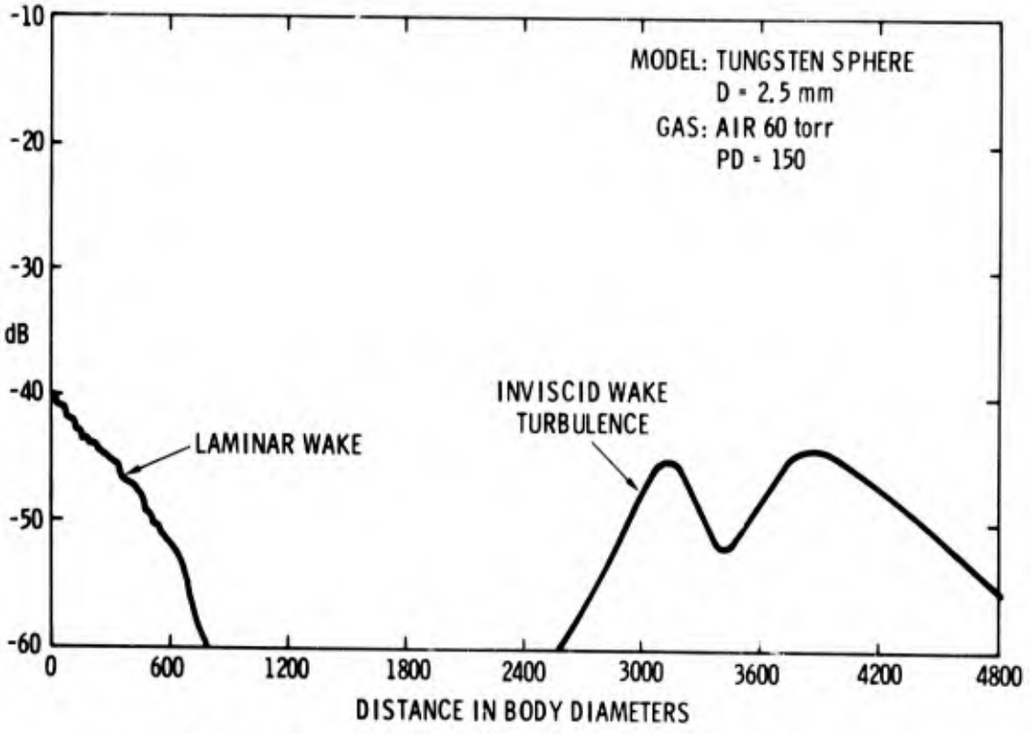

Fig. 8 Radar Detection of Inviscid Wake Turbulence

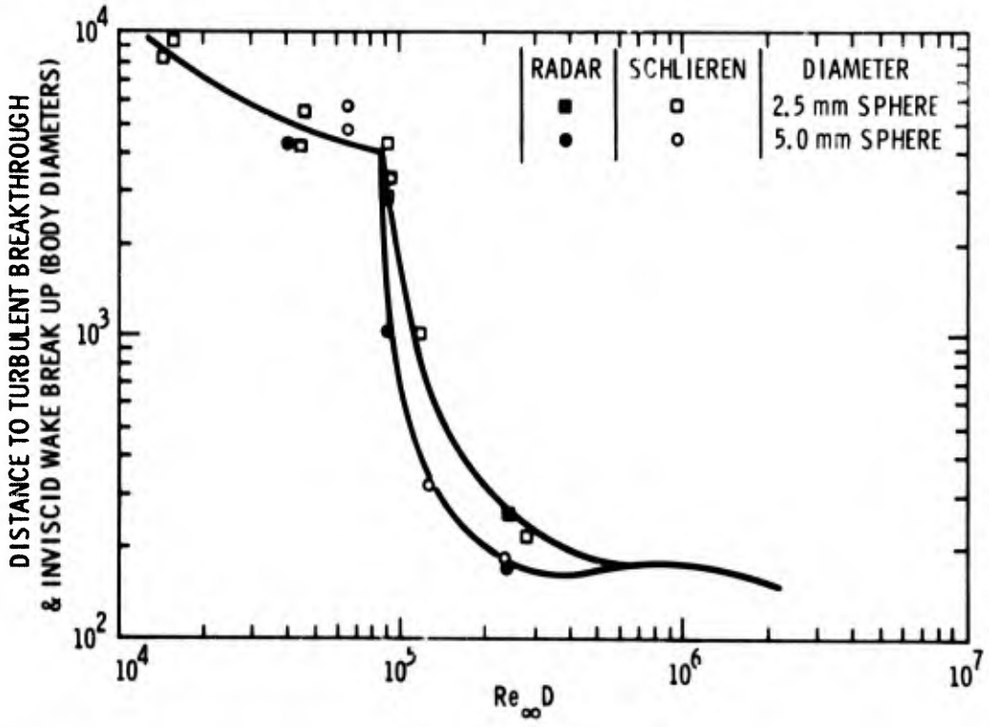

Fig. 9 Breakthrough Distance as Seen by Radar and Schlieren

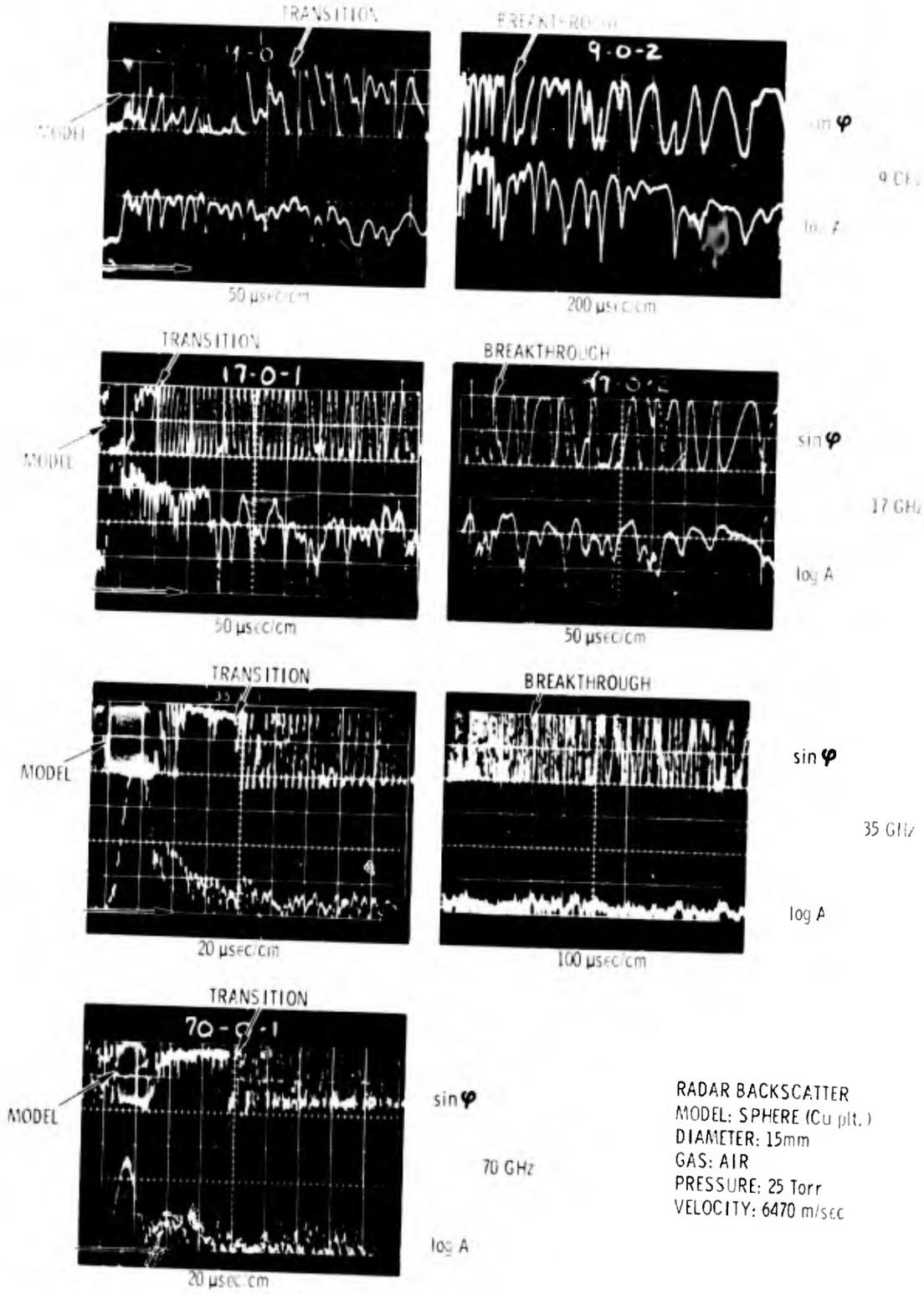

Fig. 10 Radar Backscatter Signal for Four Different Frequencies

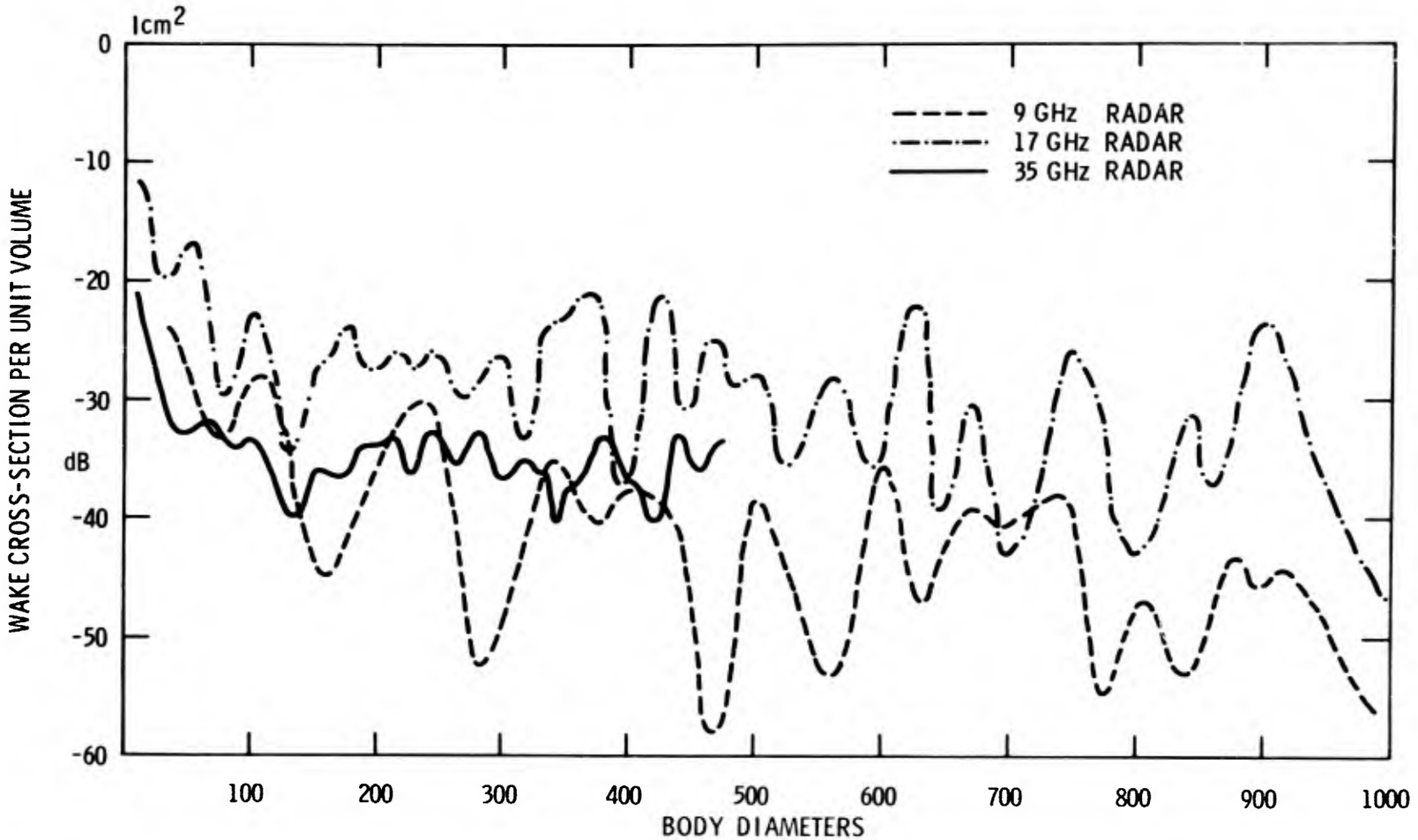

Fig. 11 Wake Cross Section per Unit Volume as the Function of Distance Behind the Body and Radar Frequencies

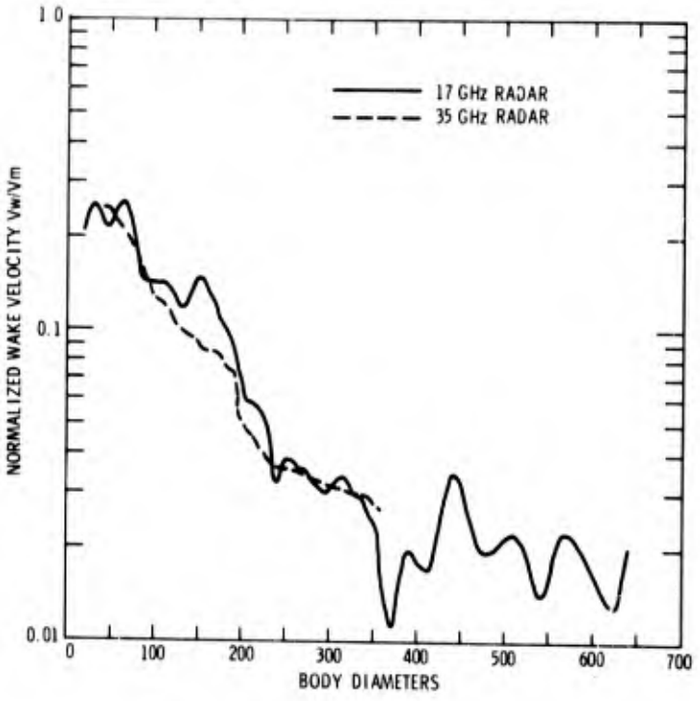

Fig. 12 Wake Velocity as Calculated Using (13) from the 17GHz and 35GHz Radar Returns

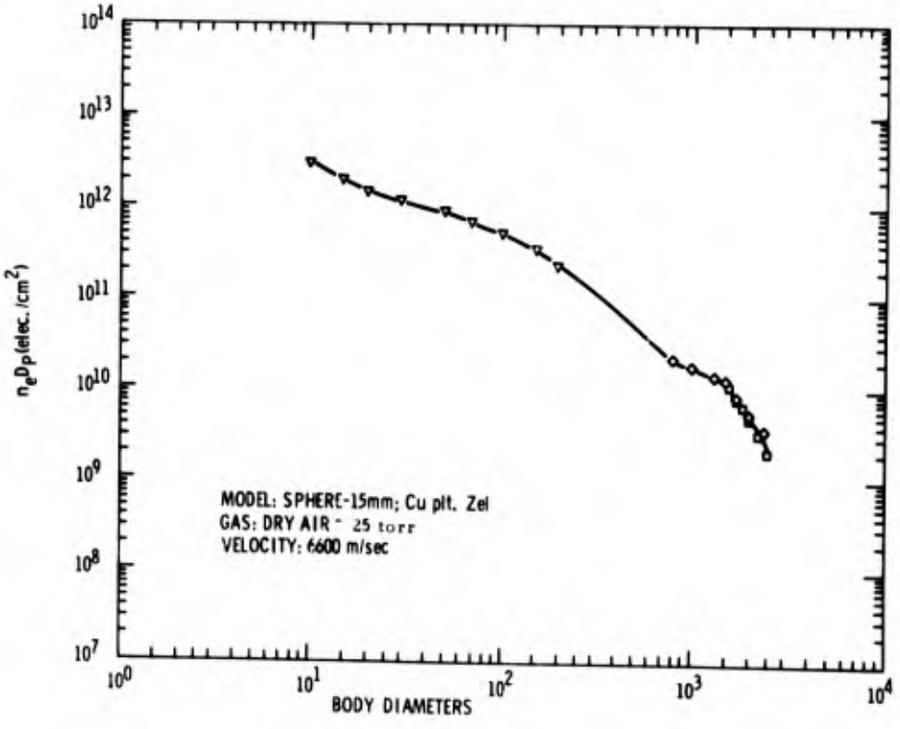

Fig. 13 Electron Density vs Distance

BLANK PAGE

"ELECTROSTATIC PROBE MEASUREMENTS IN THE TURBULENT WAKE OF HYPERSONIC SPHERES FIRED IN A BALLISTIC RANGE."

by

D. Heckman, A. Cantin and A. Kirkpatrick

This paper is generated under the CARDE-ARPA co-operative re-entry physics program of ARPA Order 133.

CANADIAN ARMAMENT RESEARCH AND DEVELOPMENT ESTABLISHMENT

VALCARTIER, P.Q., CANADA

February 1967

SUMMARY

Electrostatic probes have been used in the CARDE ballistic ranges to investigate the plasma characteristics of the turbulent core of the hypersonic wake. Cross correlations of the collected current signals obtained with arrays of electron or ion probes yield information relating tc the space correlation, convection velocity, and moving frame auto-correlation of the change density fluctuations in the wake cone. Also obtained are power spectra and autocorrelations from individual probe signals. Experimental data derived in the wake of 1.0 and 2.7 inch diameter non-ablating spheres at velocities exceeding 15,000 feet per second in air and at pressure between 1 and 100 mmHg. are presented. The results are discussed in the light of other experiments being conducted at CARDE.

RESUME

Dans les tunnels balistiques du CARDE, on a utilisé des sondes électrostatiques pour étudier les caractéristiques du plasma dans la partie centrale turbulente d'un sillage hypersonique. En procédant à des corrélations transversales des différents signaux du courant, recueillis à l'aide de séries de sondes ioniques ou électroniques, on obtient des données sur la corrélation spatiale, la vitesse de convection et l'auto-corrélation cinématographique des fluctuations des variations de densités dans le cône du sillage. On obtient également les spectres de forces et les auto-corrélations à partir des signaux des sondes individuelles. Les auteurs de l'exposé présentent les résultats expérimentaux obtenus dans les sillages de sphéres de 1,0 à 2,7 pouces de diamètres sans ablation à des vitesses supérieures à 15.000 pieds par secondes dans l'air, et pour des pressions variant de 1 à 100 mmHg. Ils étudient enfin ces résultats à la lumière d'autres expériences effectuées au CARDE.

LIST OF SYMBOLS

B.D.	Body Diameters
ΔI	Root Mean Square Electron Current
FRMS	Root Mean Square Value of F
$\bar{I}$	Mean Electron Current
KS	Wave Number (cm^{-1})
M	Number of Correlated Intervals
ν	Dynamic Viscosity (Ft/sec^2)
P	Range Pressure (mm)
P_1	Probe Number 1
PSD	Power Spectrum Density
R(x,τ) or R(x, TN)	Correlation Function
R(τ) or R(0,τ)	Autocorrelation
R(x,0)	Space Correlation
TN or τ	Time (microseconds)
τ'_m	Time Scale Moving Frame Autocorrelations (Microseconds)
$\tau_s = \Lambda / \bar{U}$	Space Scale (microseconds)
$\bar{U}$, U, V_w	Mean Wake Velocity (FPS)
U' or u'	Velocity Fluctuation (FPS)
V_∞	Projectile Velocity (FPS)
x	Distance between Probes (cm)
X/D	Axial Distance (B.D.)
Y/D	Transverse Distance (B.D.)

1. INTRODUCTION:

Electrostatic probes have been used in the ballistic range facilities at RARDE (10), MIT (8), and CARDE (7) during recent years in an effort to determine the characteristics of the plasma convected with the hypersonic turbulent wake. The usual technique employed is to mount an electrostatic probe in a ballistic range at some distance from the anticipated flight path of the projectile and to fire the projectile past the probe. The turbulent core of the wake following the projectile grows radially with increasing distance behind the projectile and at some point grows onto the probe. The pattern of the fluctuating electron density distribution in the wake core is reflected in the time history of the fluctuating current collected by the probe as the wake is swept past it.

A number of experimental limitations particular to the experimental technique arise because the observer in the ballistic range is required to make measurements of the statistical characteristics of the wake plasma within an observation time of the order of a few milliseconds. During the measurement the position of the fixed probe with respect to the moving projectile is continuously changing, and fairly large signal dynamic range and bandwidth are required to cope with the nonstationarity of the probe signal caused by the rapid decay of electron density with distance behind the projectile, the high frequency content of the signal, and the frequency shift caused by wake slowdown. The experimental situation becomes less difficult as the size of the projectile increases.

The CARDE Range 5 facility is capable of launching 2.7 inch diameter spheres at velocities in excess of 15,000 feet/second. For a sphere of

this size, 15,000 feet/second corresponds to a velocity of about 66 body diameters (B.D.) per millisecond. A probe located in the wake at a diatance of between 0.6 and 0.8 B.D. off the flight axis will experience essentially the full wake axial velocity at a distance of about 100 B.D. behind the projectile. At this point the axial velocity behind a 2.7 inch sphere is decreasing at the rate of about 15 - 20 percent per 60 body diameters which in the case of CARDE Range 5 is equivalent to 15 - 20 percent per millisecond. Thus by restricting analysis to consideration of signal segments of about 0.5 millisecond in length, the variation of wake velocity can be controlled to within 10 percent even in the very near wake. A signal segment length of 0.5 millisecond also seems appropriate from a consideration of the observed amplitude variation of signals from electrostatic probes in the near wake. Assuming a sampling frequency of about 300 kilocycles, we can expect to resolve the frequency content of 0.5 millisecond long signals into about 25 spectral bands each of width of about 6 kilocycles. In the near wake at an axial distance X/D of 100 B.D. and a radial distance Y/D of between 0.6 and 0.8 B.D., the frequency corresponding to an eddy of the body size (2.7 inches) would be 11 kilocycles; thus a sampling frequency of 300 kilocycles will permit the following of over one decade of turbulence decay from the body size even in the near wake.

(A sampling frequency of 300 kilocycles has been used in the above discussion because it has been the standard sampling frequency for CARDE probe measurements, but the present recording system could be pushed to give a sampling frequency of about a megacycle.)

2. INTERPRETATION OF ELECTROSTATIC PROBE SIGNALS IN THE PRESENT EXPERIMENT

The ambient conditions encountered by the electrostatic probes in the Range facilities include pressures varying between 7.6 and 76 mm., temperatures between 1000 and 2000 degrees Kelvin, and wake velocities varying from 3000 feet/second down to a few hundred feet per second. The maximum electron density seen by the probes probably does not exceed 10^{10} electrons per cubic centimeter. The hypersonic wake plasma in the range is thus both collision dominated and weakly ionized.

Most of the CARDE work has been done with positively biased probes. There are at least two reasons for collecting electron current. First of all electron collection permits greater sensitivity than ion collection, and secondly it is well known that ion current collection is affected when flow velocity begins to exceed a few hundred feet per second. (The advantages of working with ion collection include the fact that the saturated ion current region of the probe characteristic is well defined and essentially independent of probe voltage and also the fact that ion density deduced from ion probes agrees well with measurements of charged particle densities obtained with microwave techniques.)

The collecting electrodes of the CARDE probes are biased about 2 volts positive with respect to the grounded outer conductors and the stem of the array. This latter large metal surface should hold the plasma very close to ground potential. The fluctuating current collected by an electrostatic probe in a plasma may not only be determined by variations in electron density, but in addition may be influenced by fluctuations in electron

temperature, potential, and in the case of ion probes, by velocity fluctuations. Demetriades and Doughman (2) have carried out a careful analysis of electrostatic probe diagnostics of turbulent plasmas for the collisionless case. According to their analysis, when the probes are operated in the saturated electron current region, the sheath thickness is larger than the probe radius, and the probe is in free molecular flow, then the fluctuations of the probe current measure the fluctuations in electron density.

The collecting tip of an individual probe consists of a cylindrical wire of 0.27 mm. in diameter and between 1 and 2 mm. in length. Under the above-mentioned range conditions the mean free path for electron collisions is of the same order as the probe radius, and even at the lowest pressure and highest electron density the sheath thickness is as great or greater than the mean free path. This means that the collisionless theory of Langmuir as utilized by Demetriades and Doughman is not applicable under the above range conditions. However, for a probe operating at bias potentials large compared to the average electron temperature, one would expect the collected probe current fluctuations to be dominated by electron density variations since these expected to be greater than temperature fluctuations and since the probe current tends to follow a square root dependence on electron temperature. Guthart and his associates (5) at the Stanford Research Institute have carried out extensive measurements and comparisons of various plasma diagnostic techniques in low pressure turbulent flame plasmas. The turbulent flame is in chemical equilibrium and under these conditions the temperature modulation of the collected probe current is small compared to the modulation due to ion density. Of interest

for the present work was the fact that for measurements in which the ion mean free path was of the order of the probe radius and the sheath dimension, microwave measurements confirmed to within 20% the mean ion density values inferred from the electrostatic ion probe results using the simple collisionless Langmuir theory.

In a private communication, Guthart (6) has described some comparative measurements of ion collecting and electron collecting electrostatic probes, of geometry almost identical to the CARDE probes. In some of these measurements the charged particle mean free paths were about half the probe radius and corresponded to conditions in the near wake of projectile fired in the CARDE range at 76 mm. The electron density was varied over a range extending from 2×10^9 to 3×10^{11} electrons per cubic centimeter. The lower limit of electron density used in these experiments is of the same order as the maximum values of electron density indicated by collisionless theory and the electron probe measurements at CARDE, and considerably larger than the mean electron density present over most of the range of analyzed CARDE probe signals.

The plasma used at SRI was in thermal equilibrium, which means that temperature fluctuations would be small compared to charged particle density fluctuations. Fluctuations spectra were obtained with the ion electrostatic probe for the ion species. In the case of electron density, measurements of fluctuation spectra were made with a coaxial microwave probe excited by a cw microwave source whose input inpedence fluctuated with the electron density of the plasma in which the probe tip was immersed. The resolution of this probe was 5 mm., comparable to the resolution of the ion probe.

The conclusions of these experiments were twofold. The variation of probe current with electron density (measured by a microwave interferometer) was the same for electron and ion collection and the dependence of this current on electron density was approximately linear. Secondly, the normalized electron and ion fluctuation current spectra were in good agreement, indicating the electron current fluctuations on the positively biased electrostatic probe were linearly proportional to the ion current fluctuations detected with the ion collecting electrostatic probe.

The experiments of Guthart tend to confirm the validity of the use of electron collecting electrostatic probes to measure charge density fluctuations only at the higher limit of electron density encountered in the range. Nevertheless the results are encouraging, and lend support to the assumption that the fluctuating probe current will be proportional to the charged particle density variations in the wake even with the larger sheath dimensions encountered as the mean electron density decays from its maximum values with increasing axial distance behind the projectile.

3. THE ELECTROSTATIC PROBE ARRAY TECHNIQUE

Most of the work carried out in ranges in the past has concerned the use of single probes, and some assumptions concerning the wake velocity field were required before any attempt could be made to interpret the observed fluctuations in the probe signals (7, 10). Of course, in a turbulent wake flow, the applicability of such a procedure as using mean wake velocity to convert from a frequency scale to a space scale (i.e Taylors hypothesis) is a question to be investigated.

In June 1966, CARDE began testing the technique of using an array of electrostatic probes to measure the characteristics of wake plasmas (7). The CARDE array consisted of five identical coaxial probes with extended center collector wires (Figure 1), equidistantly spaced and mounted in a thin support to minimize flow disturbance. The array has normally been mounted in the range so that an imaginary line passing through the tips of the collector wires would be parallel to the projectile line of flight. As the wake following the projectile flows over the array it is seen in turn by the first probe, then the second, third, fourth, and finally the fifth. Depending on the spacing of the probes, one would thus expect the fluctuations observed on one probe to be correlated with the fluctuations seen on the neighboring probes. The overall spacing between the first and the last probes of the array in Figure 1 is 1.5 inches, slightly greater than half the body diameter of a 2.7 inch sphere.

Figure 2 shows an example of a set of signals recorded on Range 5 using the array. The signals are obviously very highly correlated. Such signals can be manipulated to produce a family of cross correlation curves, autocorrelations, autocorrelations in the moving frame, space correlations and also to measure wake velocity. The electrostatic probe array technique implemented at CARDE (7) for the study of the plasma characteristics of the turbulent wake will be recognized as the logical extension to the case of transient flowing plasmas of the one-stationary-and-one-movable-probe technique used to investigate steady turbulent flows such as encountered with jets (4,5).

4. RECORDING AND DATA REDUCTION

The fluctuating current signal collected by each of the individual probes is converted to voltage by a preamplifier unit located in the range, and then passed via a line driver unit to one of the sets of vertical deflection plates of a double beam oscilloscope located in a Recording Room, whence it is recorded on 35 mm. film using a Wollensak Fastax camera. (Film velocity in such a camera is about 2 inches per millisecond). Two channels may thus be recorded on each Fastax film. Since each camera will run at a slightly different speed, each pair of signals which it is desired to correlate are recorded on the same film, thus automatically synchronizing them. Normally, the output of the first probe (P_1) is recorded with the output of each of the other probes (P_1, P_3, P_4, and P_5). A flying spot scanner type of data reader (9) is used to read alternatively and essentially simultaneously each trace of a given pair of signals. Time marks occur on the signal every millisecond, and ensure that possible relative horizontal displacement of the two oscilloscope beams is accounted for.

Once read, the digitalized signals from each pair of probes are cross-correlated on a digital computer (3). This produces a set of spatio-temporal $R(x,\tau)$ correlations (Figure 3) for the various separation distances x between P_1 and the other probes (P_2, P_3, P_4 and P_5). The values of $R(x,0)$ for time delay τ equal to zero give an estimate of the space correlation function from which a space scale can be estimated. An envelope can be drawn over the cross correlation set (Figure 3) and the relationship between the separation distance x and the corresponding

delay τ at which the cross correlation curve is tangent to the envelope can be used to give the convection velocity of the turbulence pattern. The envelope of the cross correlation curves establishes the autocorrelation in the moving frame from which a time scale can be inferred. This time scale is a measure of the temporal change of the turbulence pattern with time. For example, if the turbulence pattern were frozen - Taylor's hypothesis would then apply - the envelope or autocorrelation curve in the moving frame would be a straight line parallel to the time delay axis and intercepting the $R(x, \tau)$ vertical axis at the value unity. Thus comparison of the space scale and the time scale provides information concerning the validity of the use of Taylor's hypothesis to transform time history autocorrelations and frequency spectra obtained with single probes into space correlations and wave number spectra (4).

Very briefly, the data reduction procedure is as follows: the various pairs of probe signals are digitalized and cross correlated. The various sets of cross correlation curves (normally one set for every 0.5 millisecond length of usable signal trace) are automatically plotted. The wake velocity history is derived from the sets of cross correlation curves and a rms fit of the velocity data points versus axial distance x/d behind the projectile is produced. This smoothed velocity history is introduced into the computer program (1) which autocorrelates and spectrally analyzes one of the probe signals (normally P_1) to produce both frequency and wave number power spectra. Normally one complete analysis is performed for every 0.5 millisecond segment of signal.

5. RESULTS AND DISCUSSION

The results to be described have been obtained from four 2.7 inch diameter aluminum sphere firings on Range 5. Conditions on these firings are listed in the following table:

Table 1

Range Conditions on Electrostatic Probe Firings

Round	Velocity	Pressure	Y/D
42	14,250 ft/sec	76 mm	0.83 B.D.
52	15,100	20	1.17
97	14,620	20	0.93
99	14,530	9.3	0.60

Unfortunately, in order to stay within the limits on the allowed length of this paper, only a minimum of discussion is possible.

5.1 CROSS CORRELATIONS

Figures 4 and 5 present typical sets of cross correlation curves obtained from electrostatic probe array signals. The equidistantly spaced marks on these curves give an indication of the degree of precision with which wake velocity is determined by the technique. In the examples given it will be seen that the temporal scale which measures the decay of the envelope (or moving frame autocorrelation) is considerably larger than the time scales which would describe the rate of decay of the autocorrelation of the individual probe signals.

5.2 WAKE VELOCITY

It has been previously pointed out (7) that the array first enters

the wake core at its edge, and thus sees a wake velocity which is smaller than the axial velocity, but that at larger axial distances, when the probes are deeply immersed in the wake, they tend to measure the full axial velocity.

Figure 6 summarizes the wake velocity data obtained on four rounds. No conclusions will be drawn from such a small number of firings. However it will be noted that the results for Rounds 42 and 97 appear to fall on a continuous curve, and that the velocities measured for Round 99 at 9 mm lie below those measured for Round 42 at 76 mm, even though Y/D was smaller for Round 99.

5.3 AUTOCORRELATION AND POWER SPECTRA

Figures 7 to 10 present examples of the standard autocorrelation and power spectral density analyses carried out on signals obtained with P_1. The data have been normalized to unity. Power spectra are corrected for preamplifier frequency response characteristics. Wave numbers have been calculated from smoothed velocity data obtained using linear rms fitting of original velocity data.

Figures 11 to 14 present the evolution of the one-dimensional wave number spectra with increasing axial distance behind the projectile. Here the various spectra from a round have received a common normalization to present a true picture of the relative intensity of the various spectra. While the fluctuation intensity decreases with distance behind the projectile, the relative shape of the spectra undergoes very little change. No detailed analysis of this data has yet been carried out.

5.4 CORRELATION FUNCTIONS AND TURBULENT SCALES

Figures 15 to 18 compare the various correlation functions. The space correlation $R(x,0)$ has been plotted against $\tau_s = x/\bar{V}_w$ where $\bar{V}_w$ is the smoothed wake velocity appropriate to mean axial distance behind the projectile.

It will be noted that in general the space correlation decreases less rapidly than the autocorrelation function. As noted by Fisher and Davies (4), in unfrozen turbulence, the distortion of the pattern as it is convected between two measuring positions, causes the autocorrelation function to have a value less than the space correlation.

If we take the distances (or corresponding times) at which the various correlation functions decrease to about 0.4 (approximately 1/e), then we can define a space scale Λ or an equivalent time scale $\tau_s = \Lambda/\bar{V}_w$ for the space correlation, and a time scale τ'_m for the autocorrelation in the moving frame. The ratio τ'_m/τ_s is a measure of the degree of frozenness of the turbulence. The greater the value of τ'_m/τ_s, the greater the degree of frozenness.

The ratio of $\bar{V}\tau'_m/\Lambda$ has been plotted in Figures 19 and 20. Comparing the data of Rounds 42, 52 and 99 over a similar range of axial distance behind the projectile, it will be seen that the trend of the data indicates the degree of frozenness is slightly larger in the case of the rounds which were nearest to the wake axis (smaller Y/D). Considering now the data of Round 97 which falls at considerably larger values of X/D compared to the other three rounds, we find a higher degree of frozenness than that present at smaller distances behind the body.

Returning to consideration of Figures 15 to 18 we note that the space correlation data for Rounds 42, 52 and 99 which pertain to the first 300 B.D. behind the projectile indicate a space scale of about half the body diameter. The data for Round 97 extending from 500 to 600 B.D. seem to indicate a turbulent space scale that is only 15 percent of the body diameter.

5.5 TURBULENT INTENSITY

Guthart (5) has shown that the turbulent intensity $u'/\bar{U}$, where u' is the rms value of the fluctuating velocity and $\bar{U}$ is the mean velocity, can be calculated from the data on turbulent scales using the formula

$$u'/\bar{U} \approx \left[1/3 \, (\bar{U} \tau_m'/\Lambda) \, (\bar{U} \Lambda/\nu)^{\frac{1}{2}} \right]^{-2/3}$$

where all symbols have been previously defined except ν, which represents the kinematic viscosity. The results are given in Figure 21.

5.6 RATIO OF RMS FLUCTUATING CURRENT TO MEAN PROBE CURRENT

Figure 22 presents the rms fluctuating probe current to mean probe current ratio obtained from the various analyses as a function of axial distance behind the projectile. Interpretation of this figure in terms of electron density is not possible without increased knowledge of the behavior of electrostatic probes in weakly ionized collision dominated plasmas.

6. CONCLUSION

The electrostatic probe array technique developed at CARDE for wake plasma diagnostics has been described, and typical results from four 2.7 inch diameter aluminum sphere firings in Range 5 have been presented. These include data on wake velocity, power spectra, correlation functions, tur-

bulent scales, the ratios of time scales and space scales, and estimates of turbulent intensity. The trends indicated by data from these rounds have been briefly discussed.

ACKNOWLEDGEMENTS

The authors wish to express their appreciation of the support received from all the members of Aerophysics Wing, and in particular, A. Emond, G. Boily, L. Tardif, G. Moisan, R. Gouge, K. Park, C. Desrochers and R. Bell. The authors are also grateful to Dr. A. Lemay and Mr. G.H. Tidy for the strong interest and support they have shown in this work.

REFERENCES

1. Cantin, A., Heckman, D., and Gouge, R., "An autocorrelation and power spectral density analysis computer program for random signals" CARDE TR 565/67 (to be published)

2. Demetriades, A., and Doughman, E.L., "Langmuir probe diagnosis of turbulent plasmas" AIAA Vol 4, pp 451-459, March, 1966.

3. Gouge, R., Cantin, A., and Heckman, D., "A cross correlation computer program for correlating pairs of random signals" Part 1, CARDE TN (to be published)

4. Fisher, M.J. and Davies, P.O.A.L., "Correlation measurements in a non-frozen pattern of turbulence" Journal of Fluid Mechanics, Vol. 18, pp 97-116, January, 1964.

5. Guthart, H., Weissman, D.E., and Morita, T., "Measurements of the charged particles of fluids, Vol 9, pp 1766-1772, September, 1966.

6. Guthart, H., "Electrostatic probe biased for electron collection as a measure of turbulent fluctuations" (private communication to A. Kirkpatrick)

7. Kirkpatrick, A., Cantin, A., and Heckman, D., "Progress in electrostatic probe measurements in a hypersonic turbulent wake" CARDE TN 1733/66, October, 1966.

8. Richardson, R.E., and Hermann, J., "Hypersonic wake structure observed with electrostatic probes" MIT Lincoln Laboratory Project Report PPP-59 (to be published)

9. Tardif, L., "A 35 mm film reader for digitalization of oscilloscope records" CARDE TN (to be published)

10. Tate, A., Fuller, P.W.W., and Wall, C.R.,"An investigation of the wakes of hypervelocity spheres using double Langmuir probes" Proceedings of the 2nd International Congress on Instrumentation in Aerospace Simulation Facilities, 29-31 August, 1966, at Stanford University.

Fig. 1 Electrostatic probe array

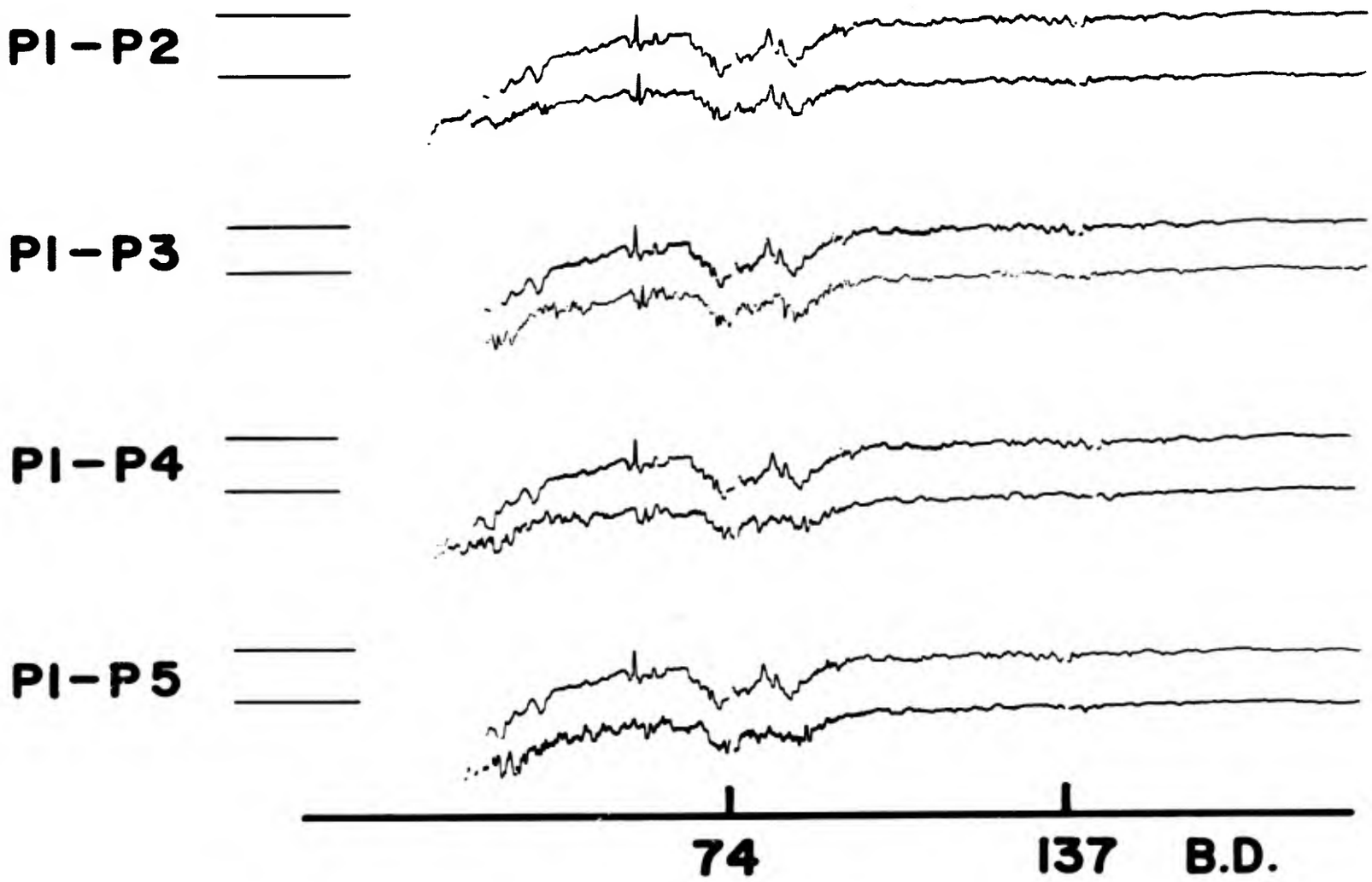

Fig. 2 Typical set of array signals

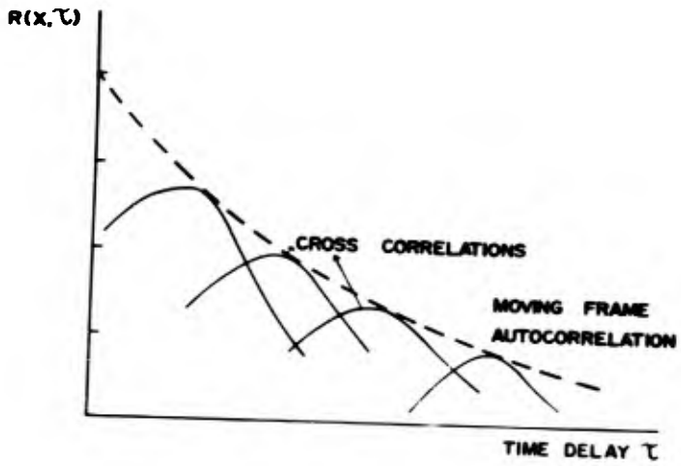

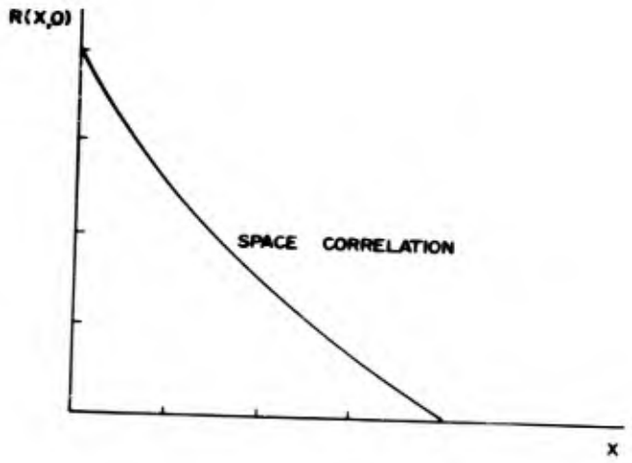

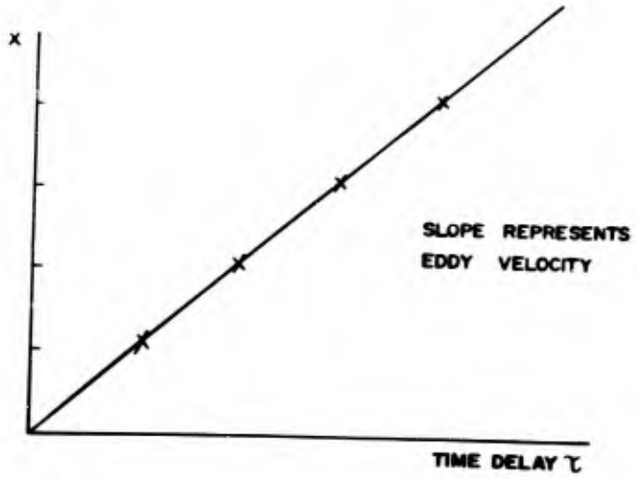

Fig.3 Correlations of array signals

WAKE VELOCITY DETERMINATION FROM CROSS CORRELATIONS OF

ELECTROSTATIC PROBE ARRAY SIGNALS

ROUND 42

RANGE 5

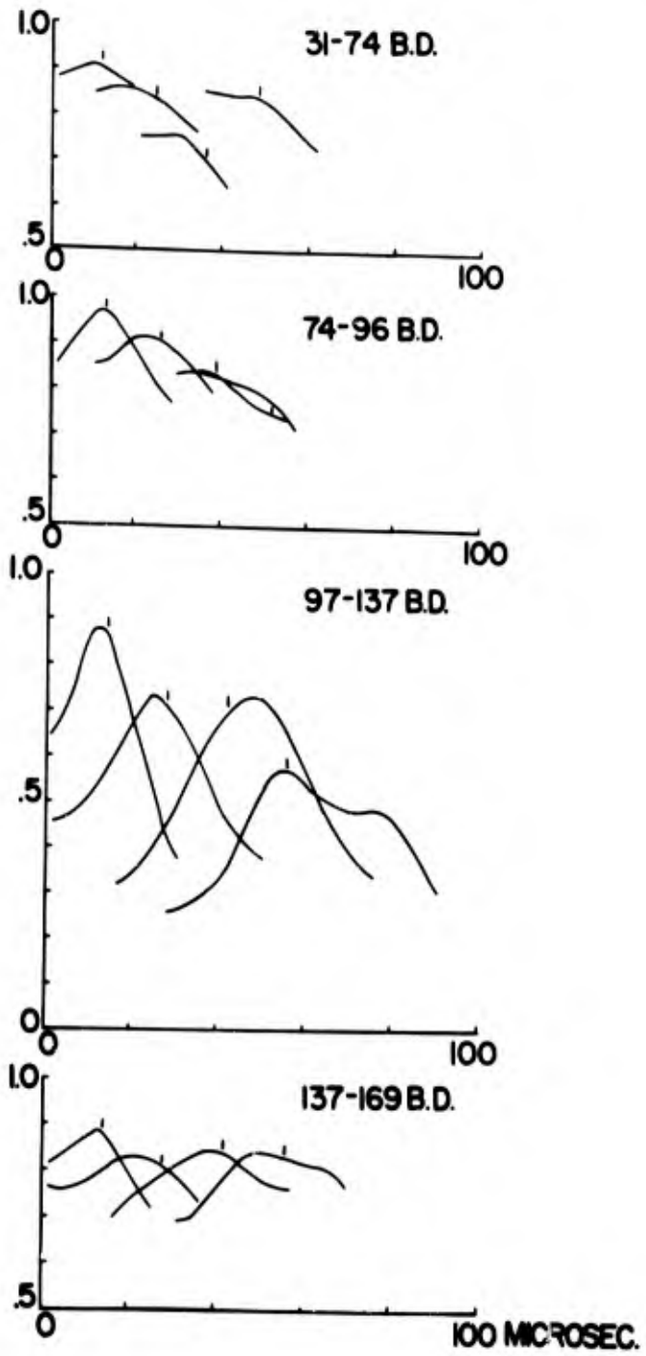

Fig. 4 Cross correlations of Round 42 signals

WAKE VELOCITY DETERMINATION FROM CROSS CORRELATIONS

OF ELECTROSTATIC PROBE ARRAY SIGNALS

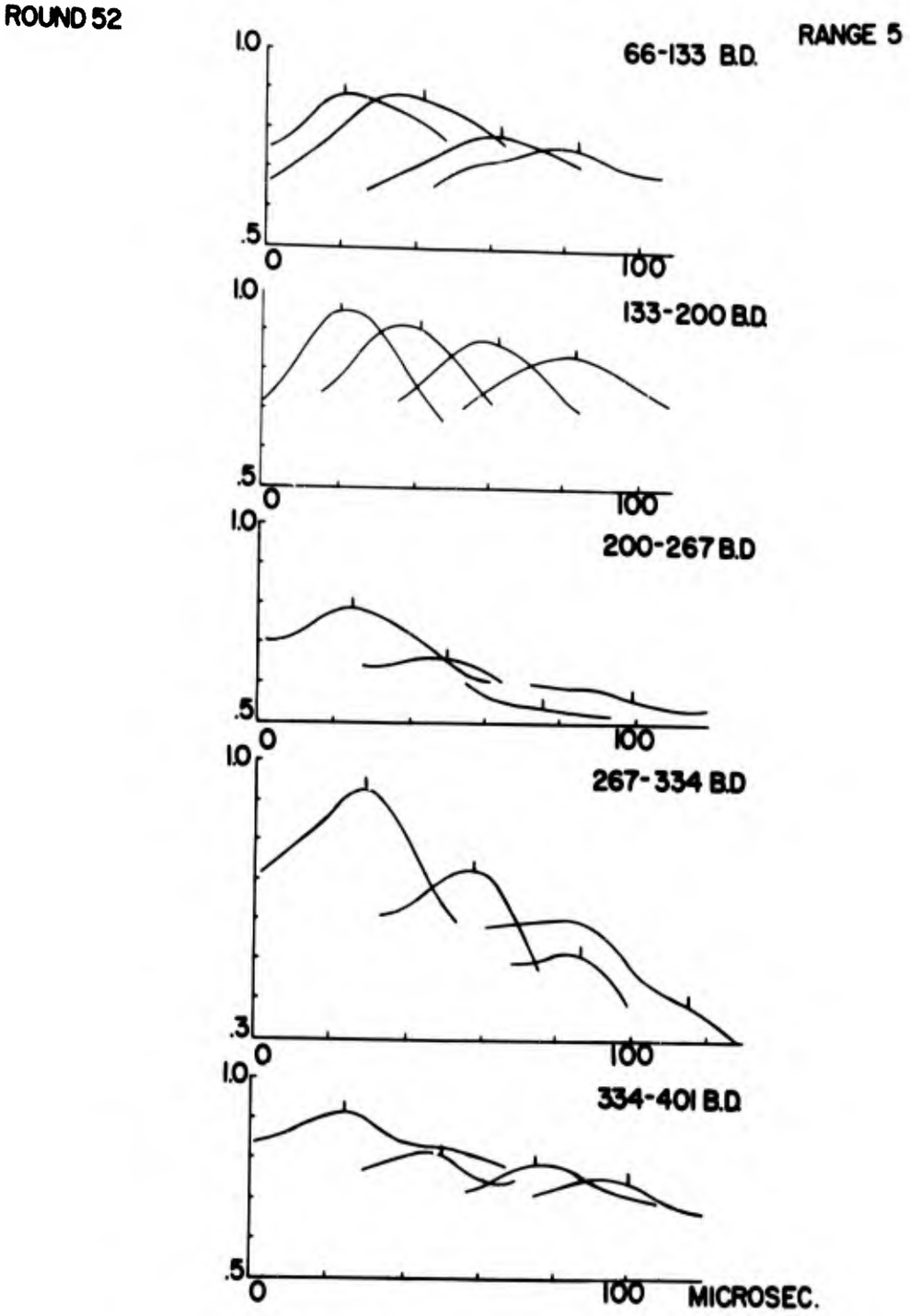

Fig.5 Cross correlations of Round 52 signals

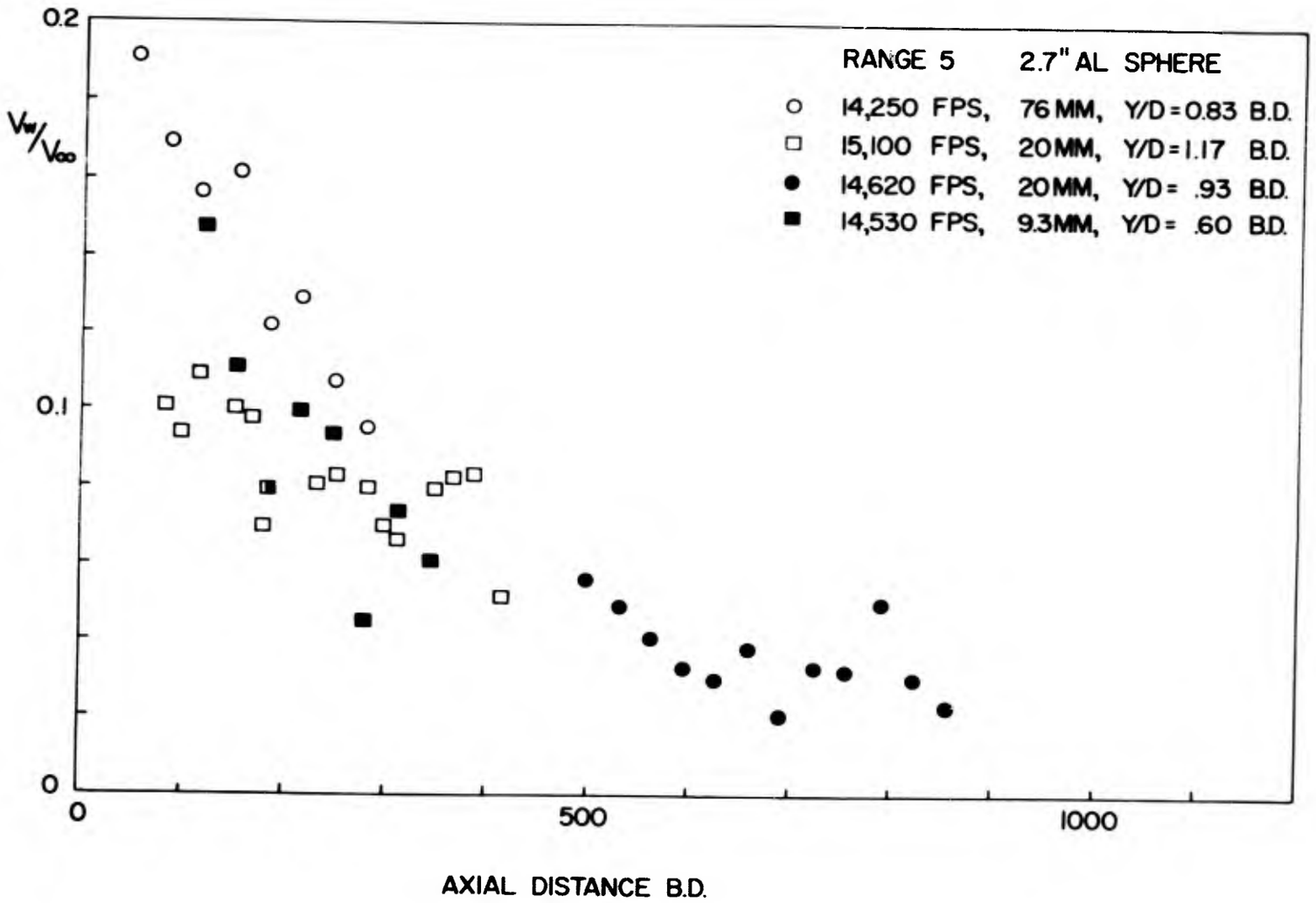

Fig. 6 V_w/V_∞ versus axial distance

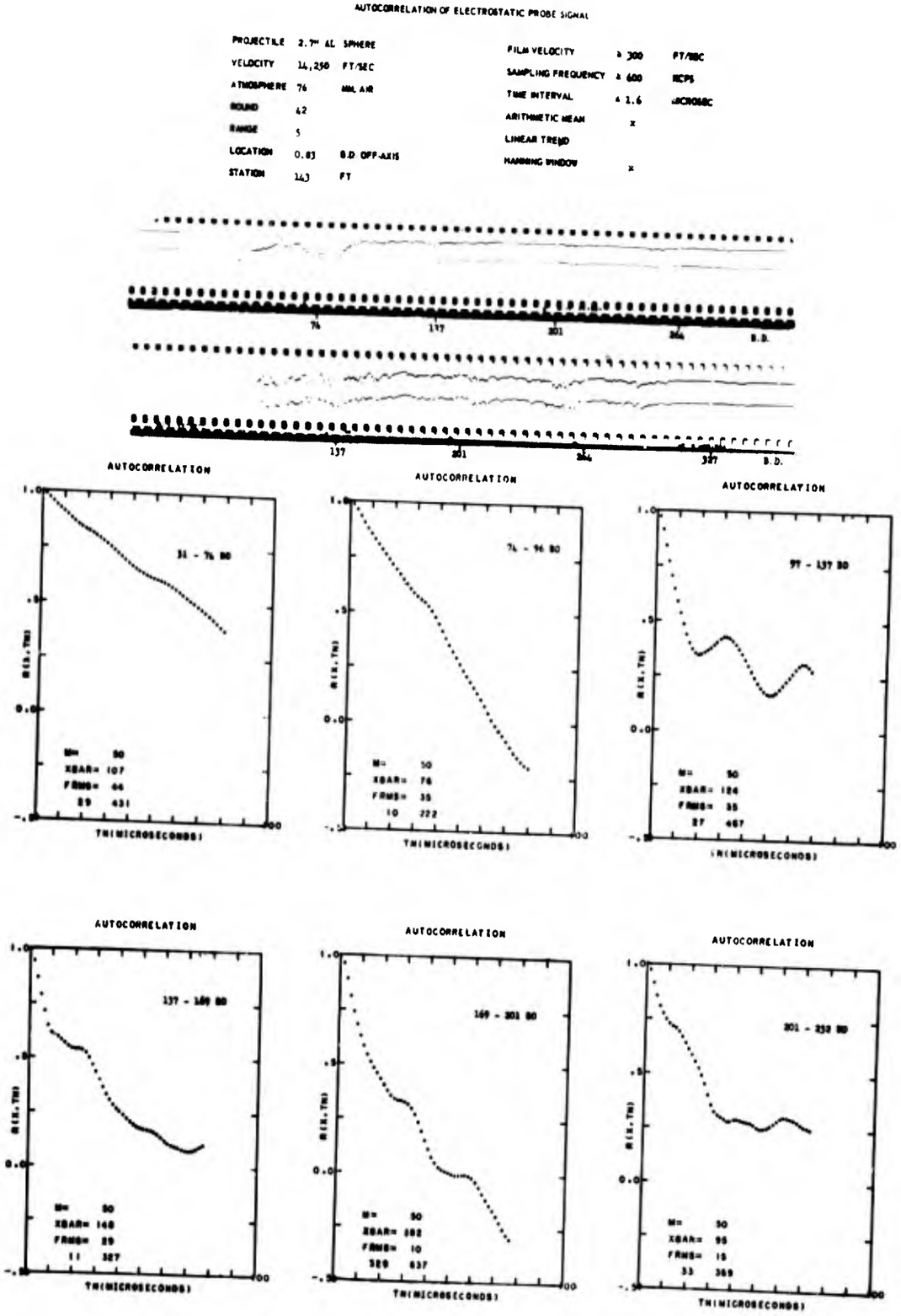

Fig. 7 Autocorrelations of Round 42 signals

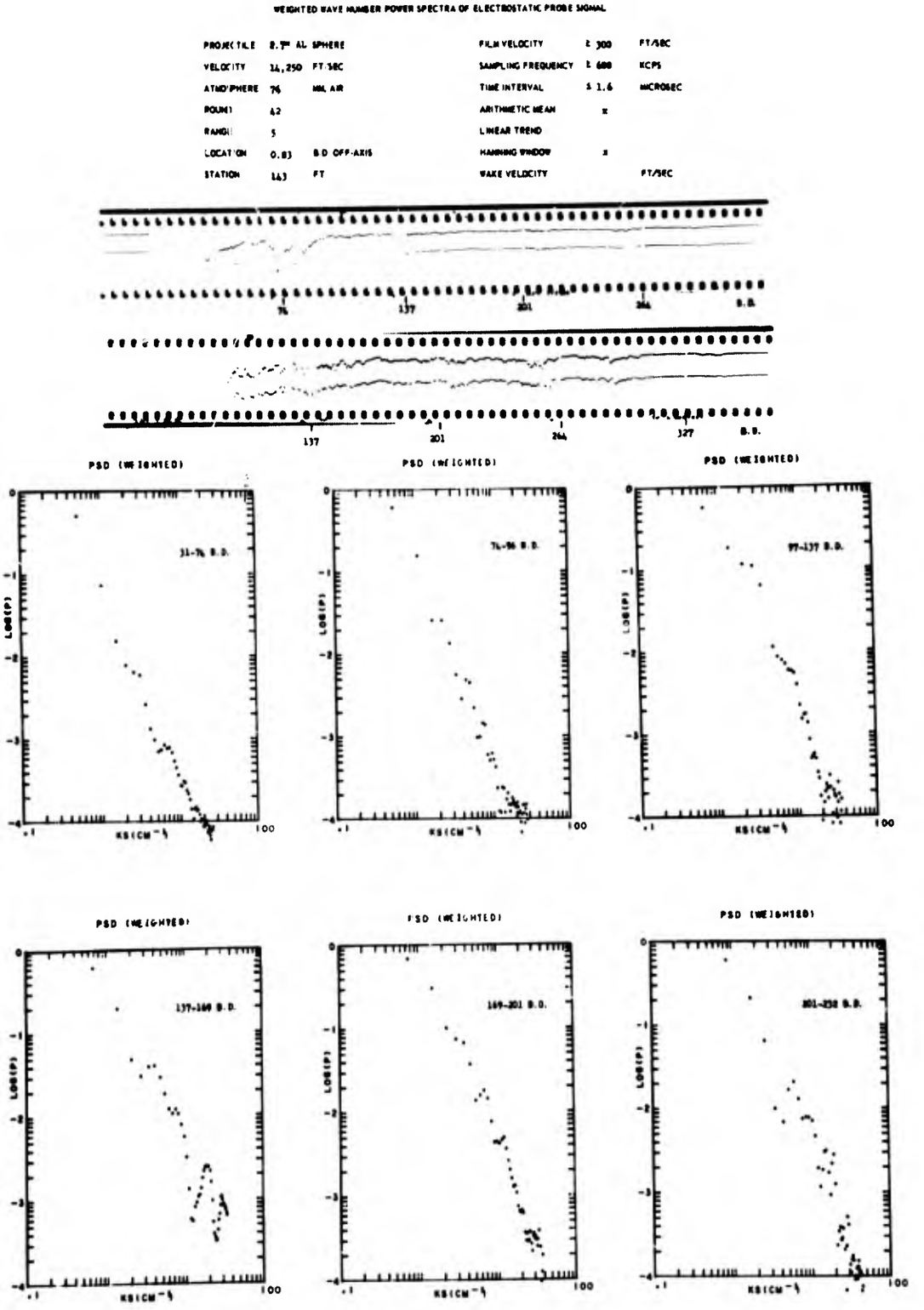

Fig.8 Weighted wave number power spectra of Round 42 signals

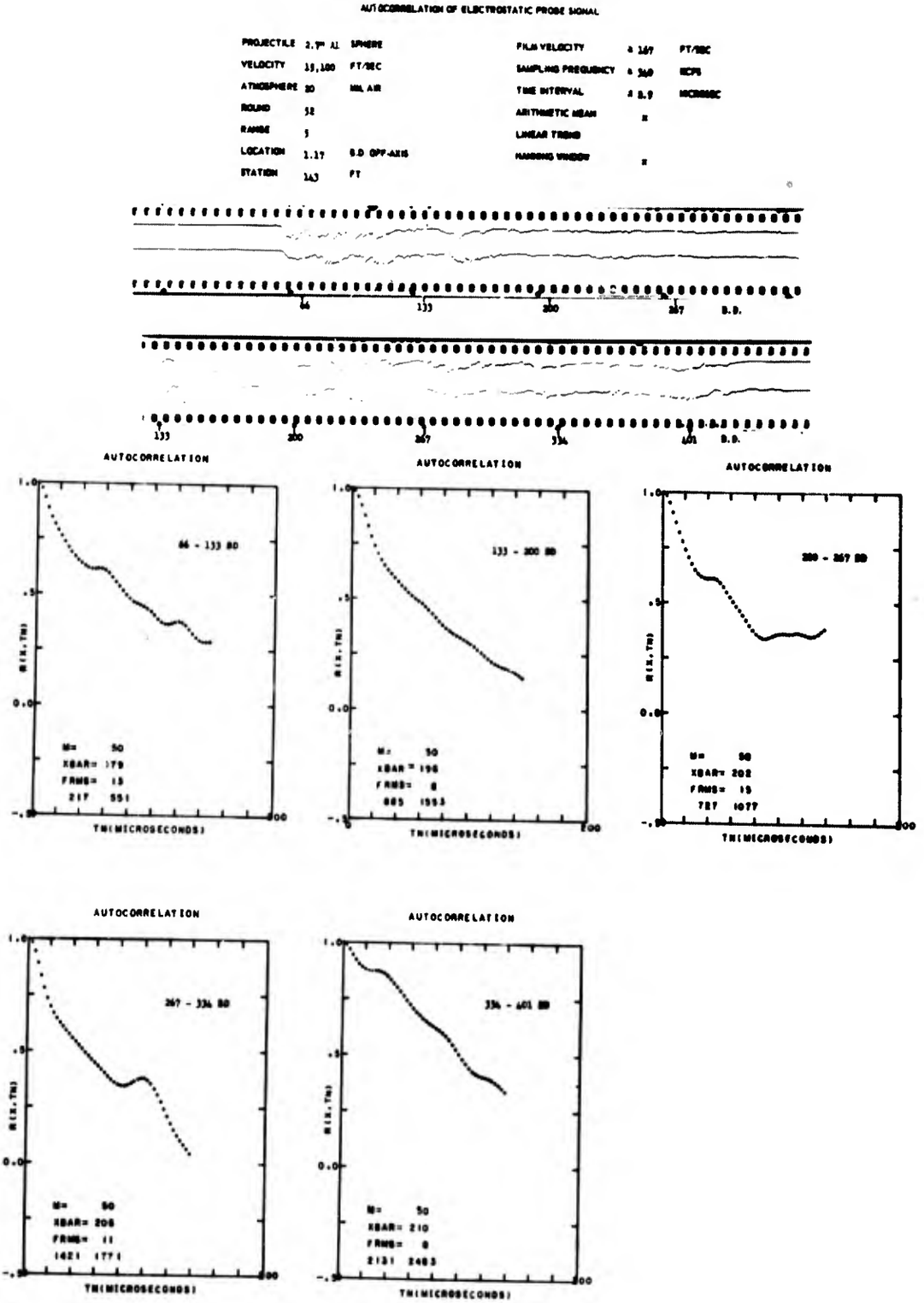

Fig. 9 Autocorrelations of Round 52 signals

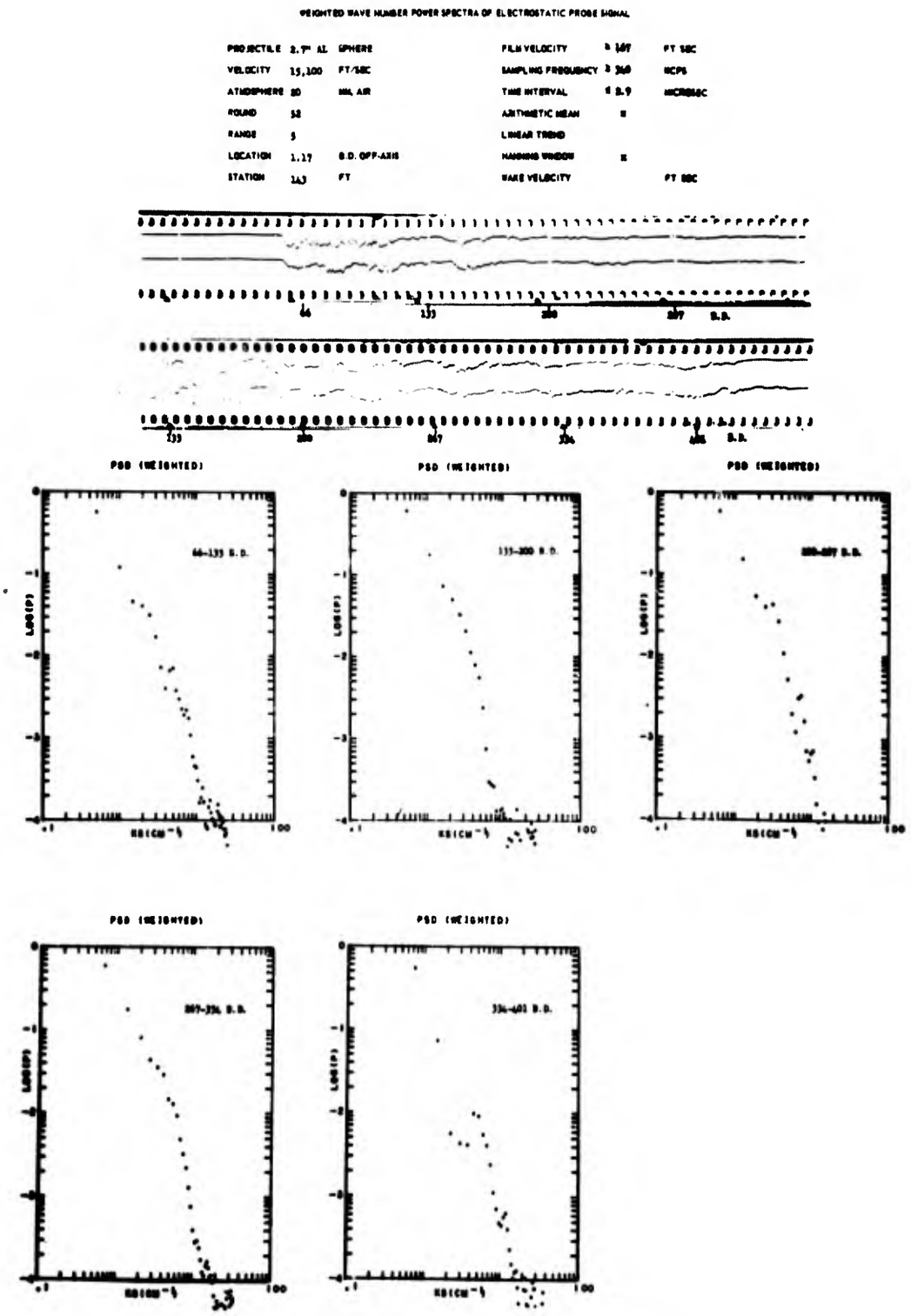

Fig. 10 Weighted wave number power spectra of Round 52 signals

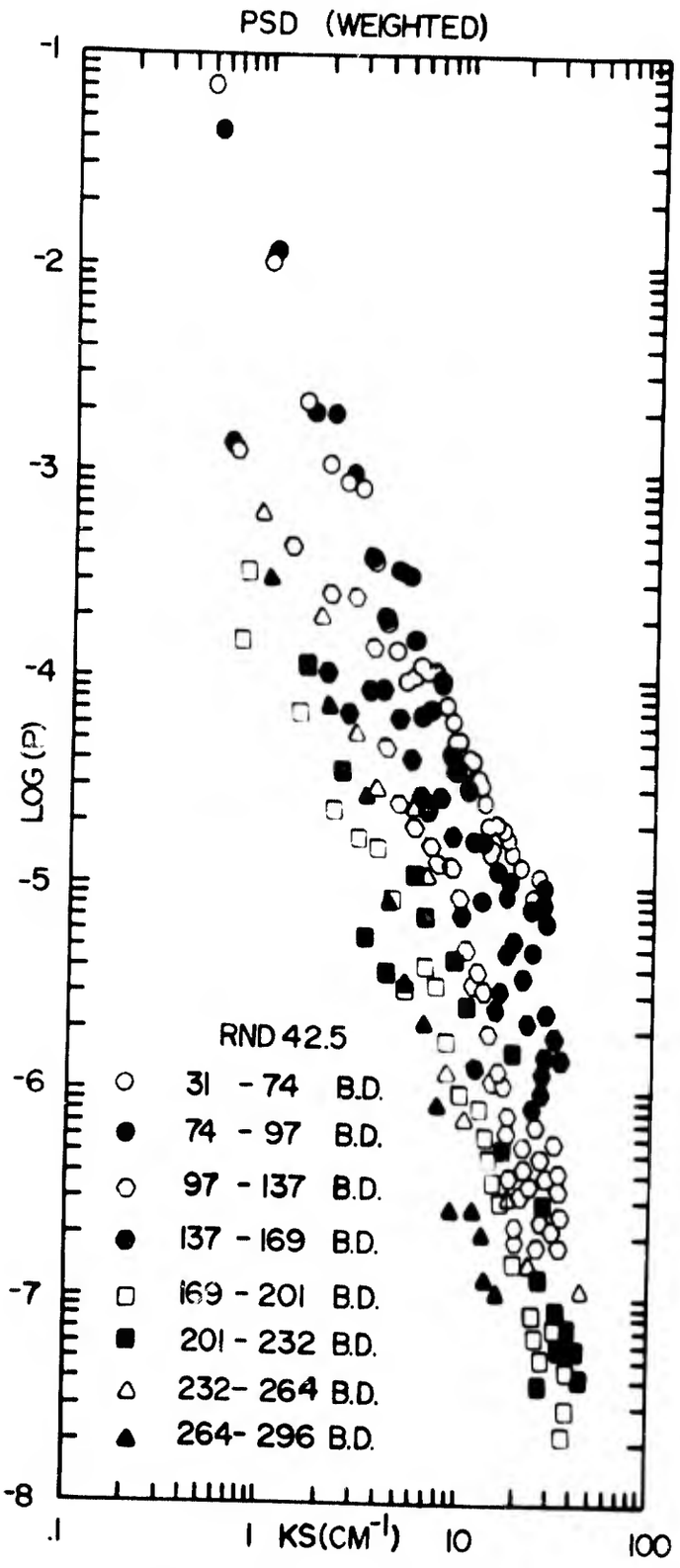

Fig. 11 Evolution of wave number spectra with axial distance, Rd 42

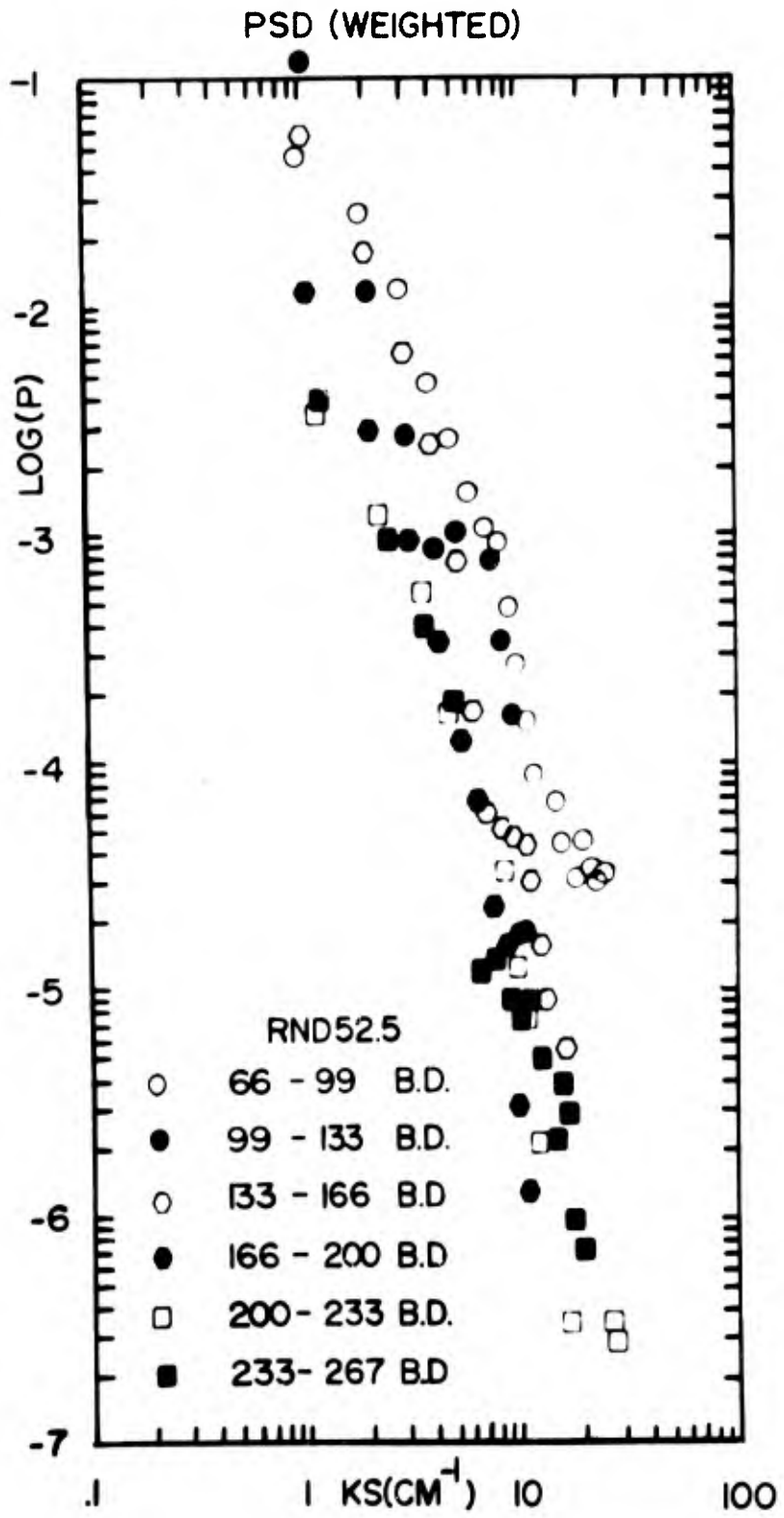

Fig. 12a Evolution of wave number spectra with axial distance, Rd 52

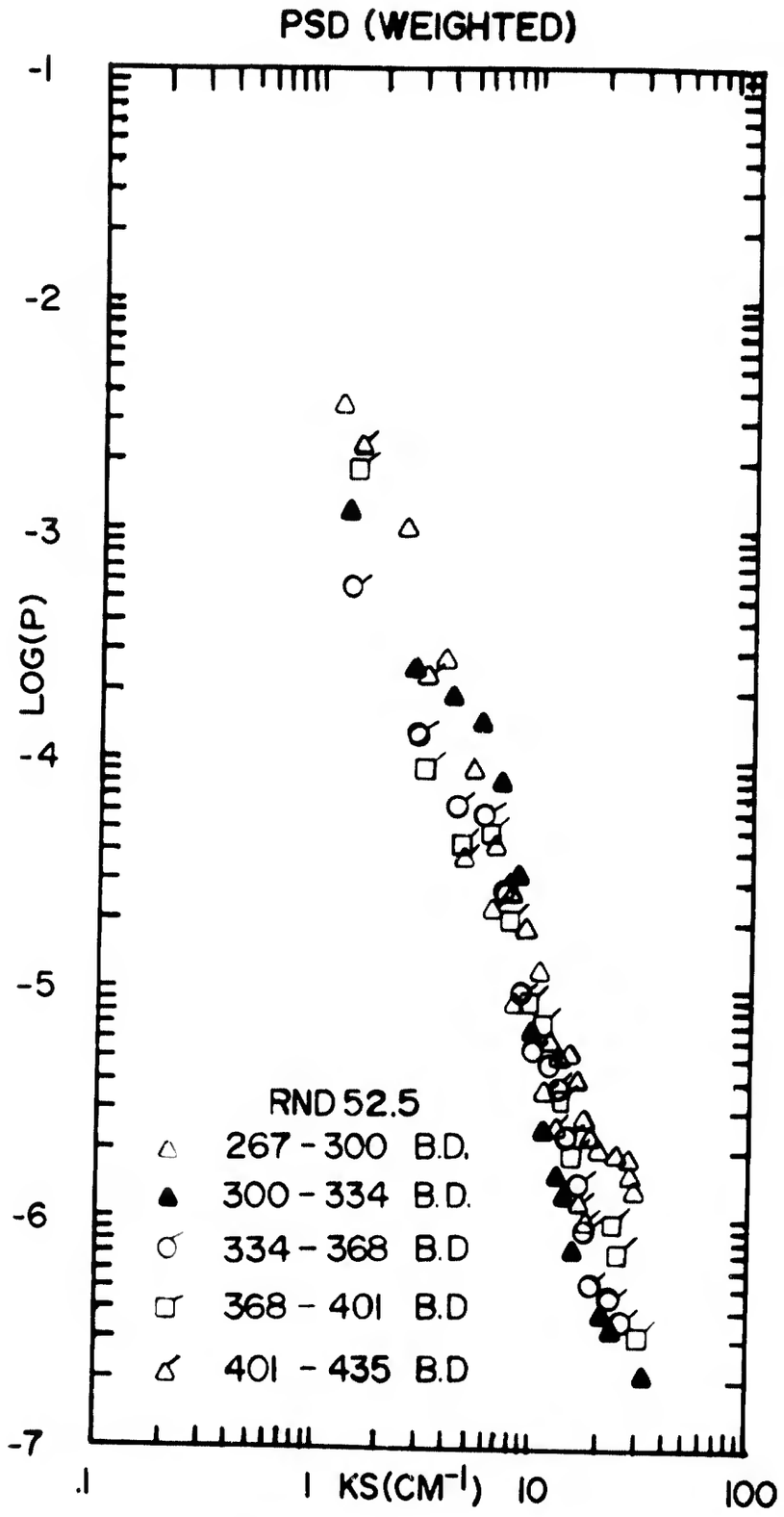

Fig. 12b Evolution of wave number spectra with axial distance, Rd 52

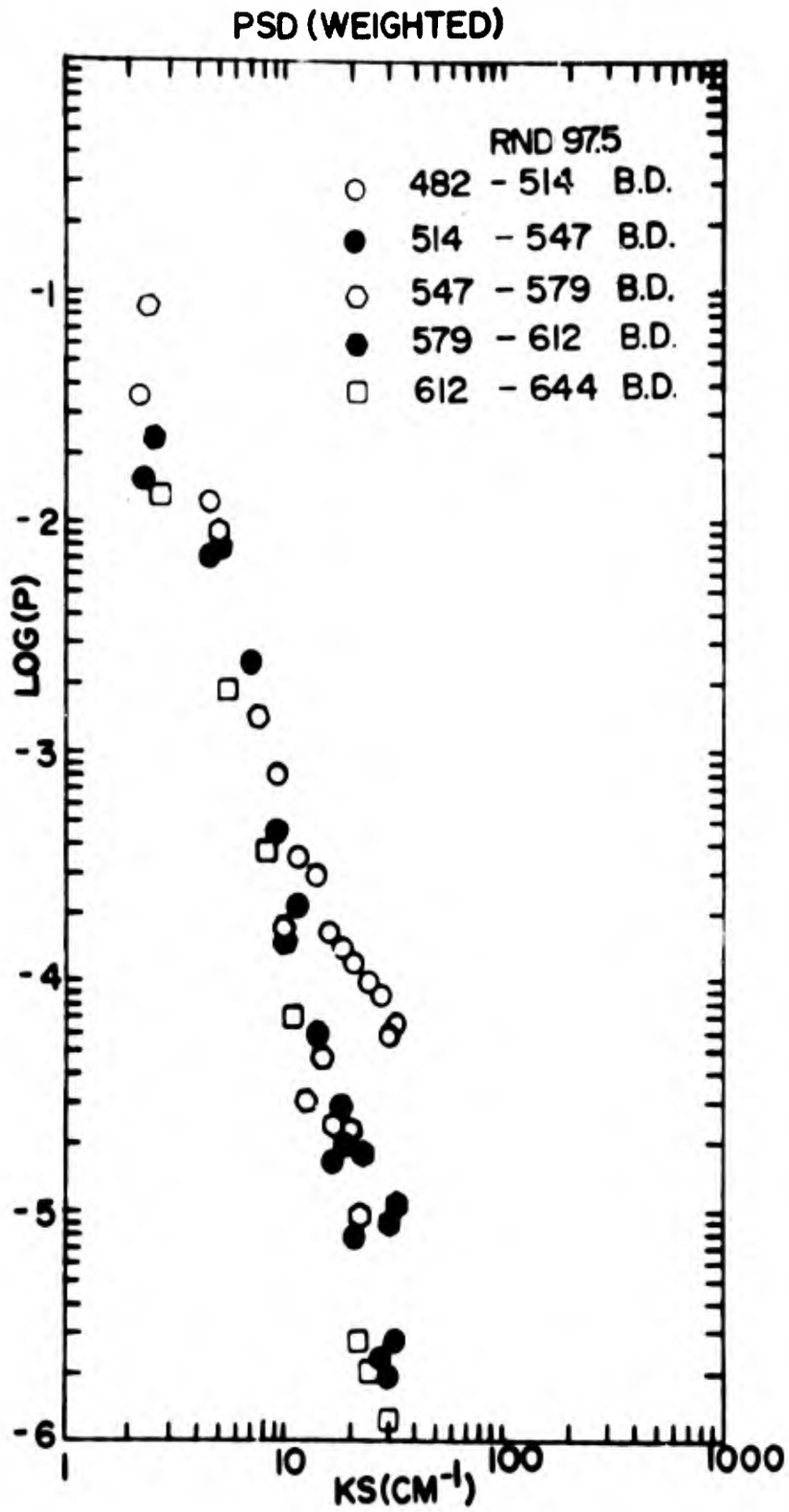

Fig. 13a Evolution of wave number spectra with axial distance, Rd 97

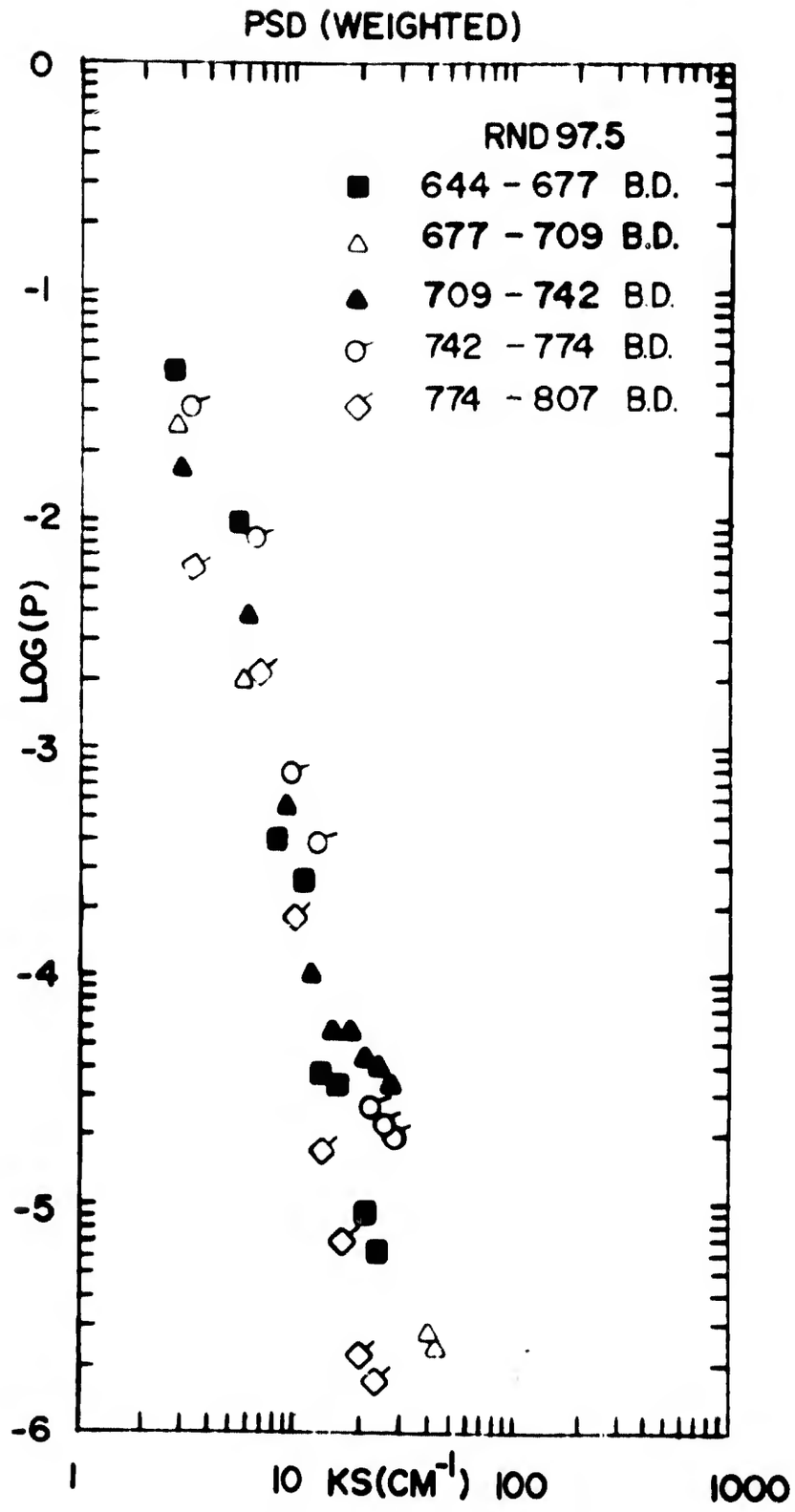

Fig. 13b Evolution of wave number spectra with axial distance, Rd 97

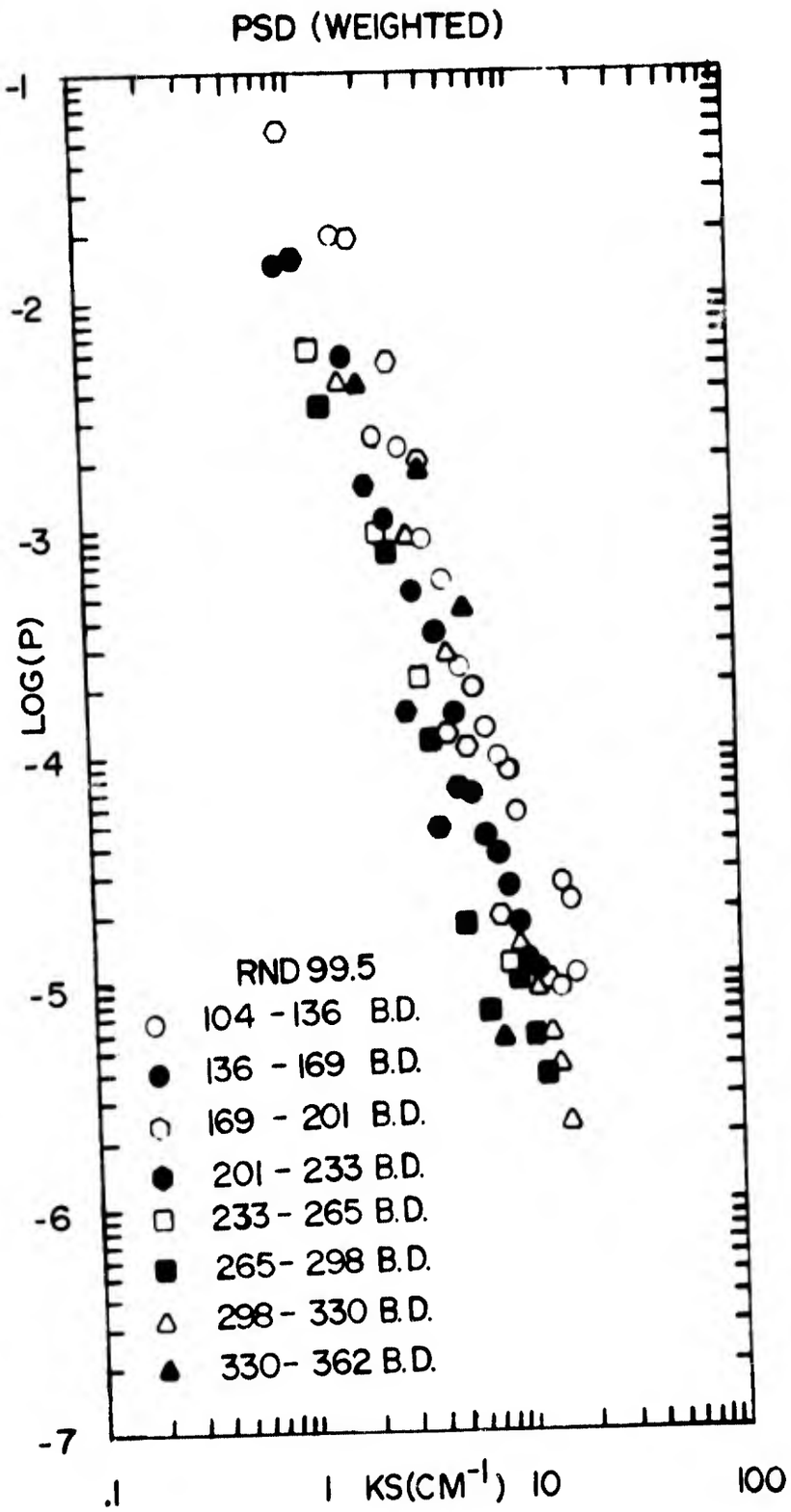

Fig. 14 Evolution of wave number spectra with axial distance, Rd 99

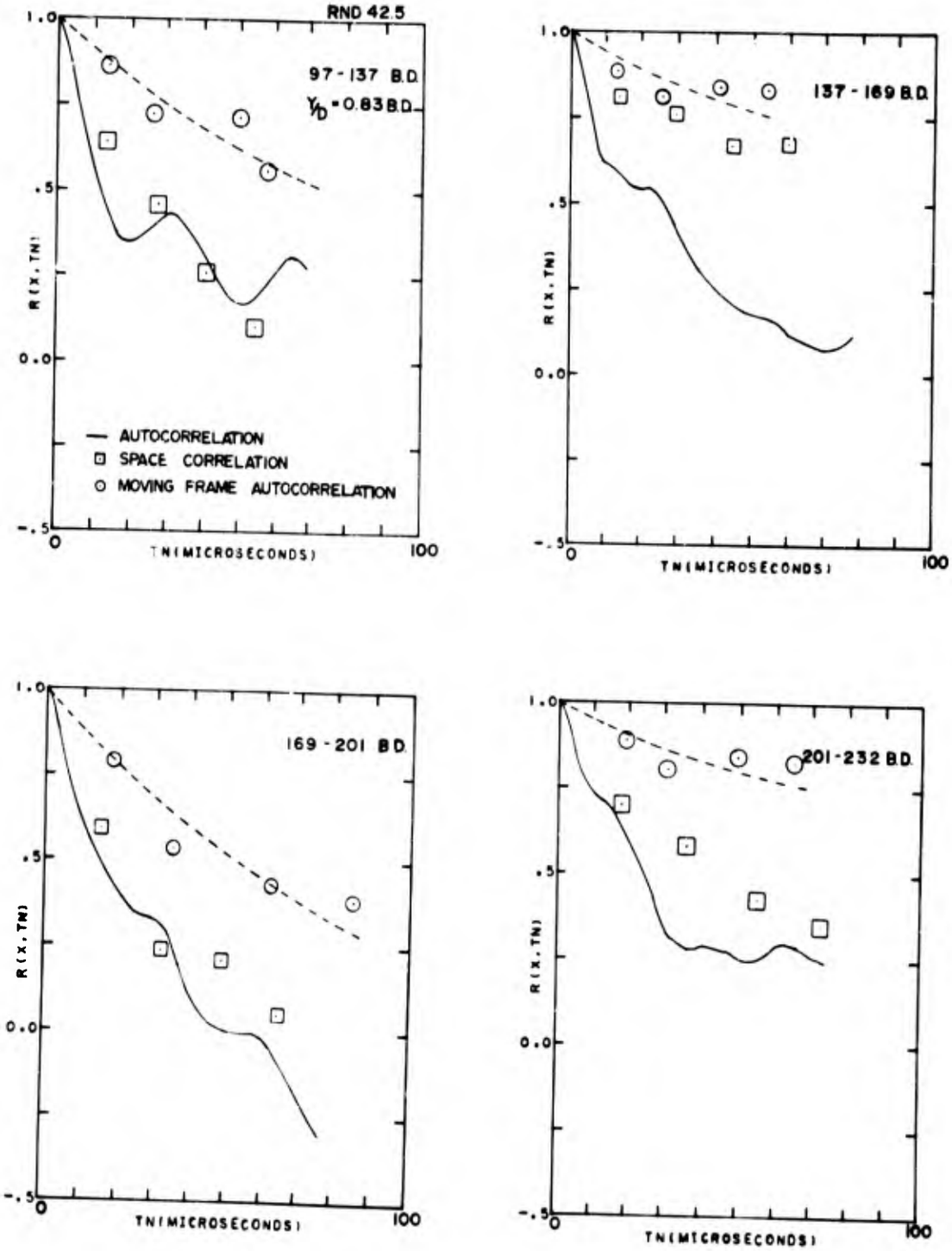

Fig. 15 Comparison of correlation functions, Rd 42

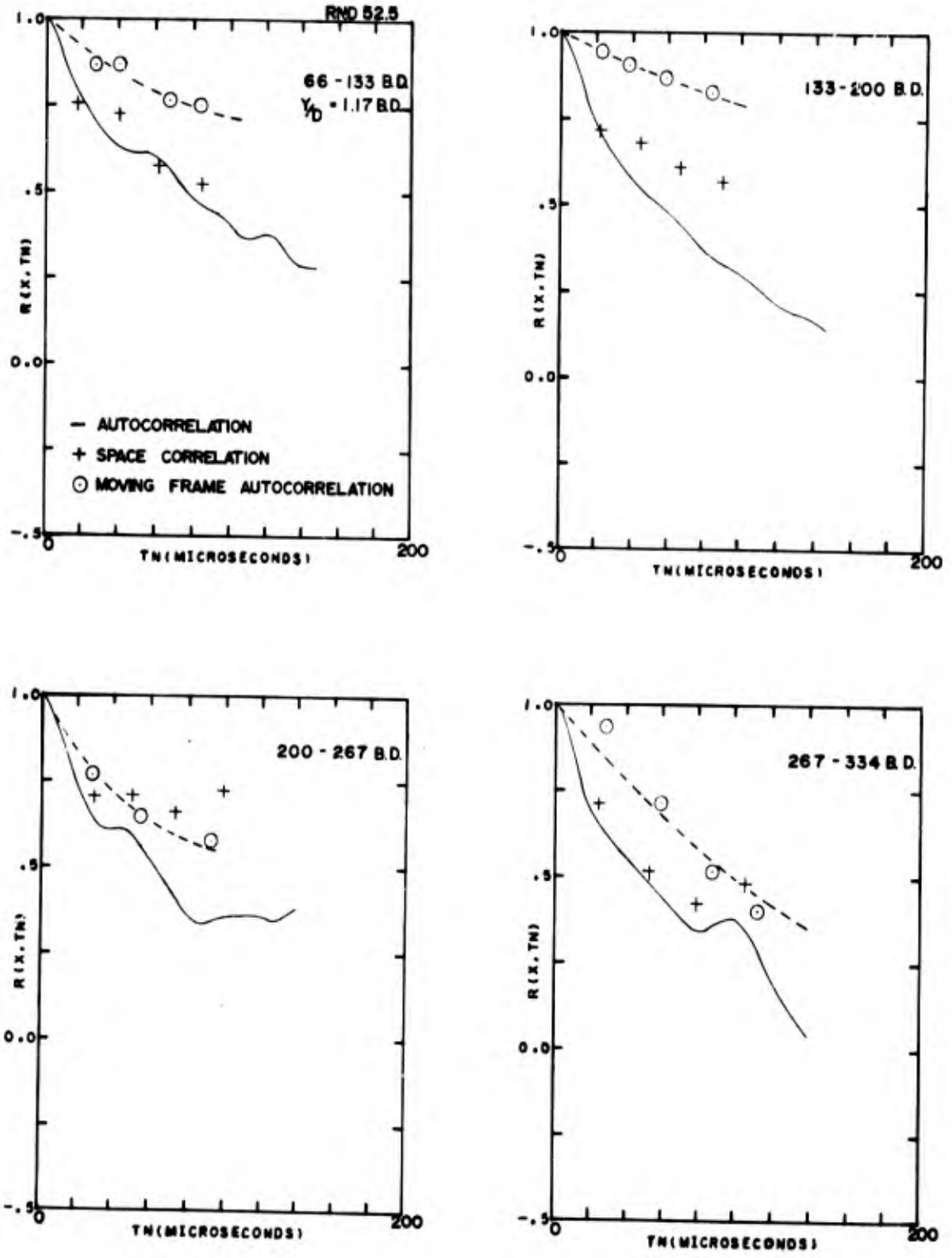

Fig. 16 Comparison of correlation functions, Rd 52

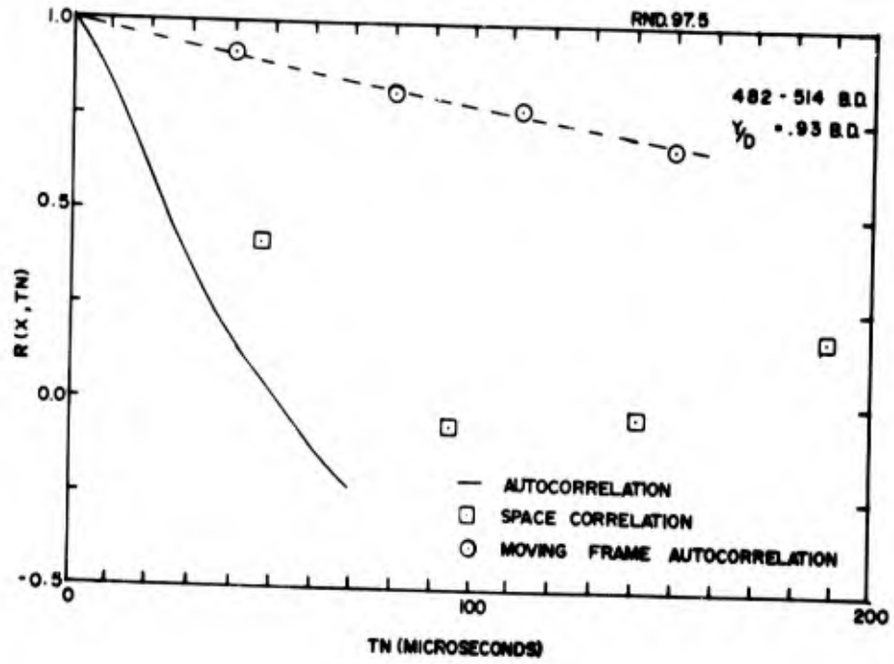

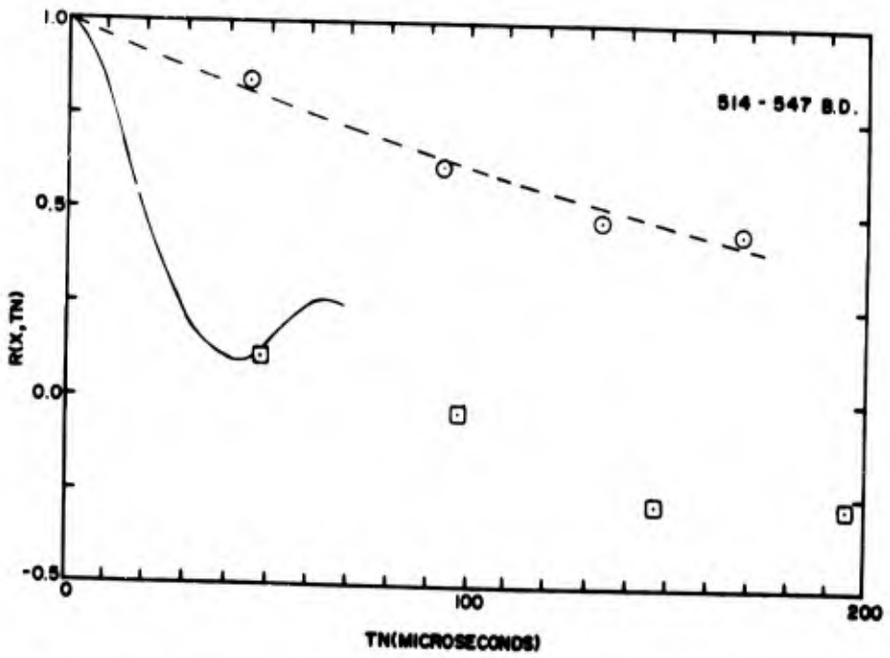

Fig. 17a Comparison of correlation functions, Rd 97

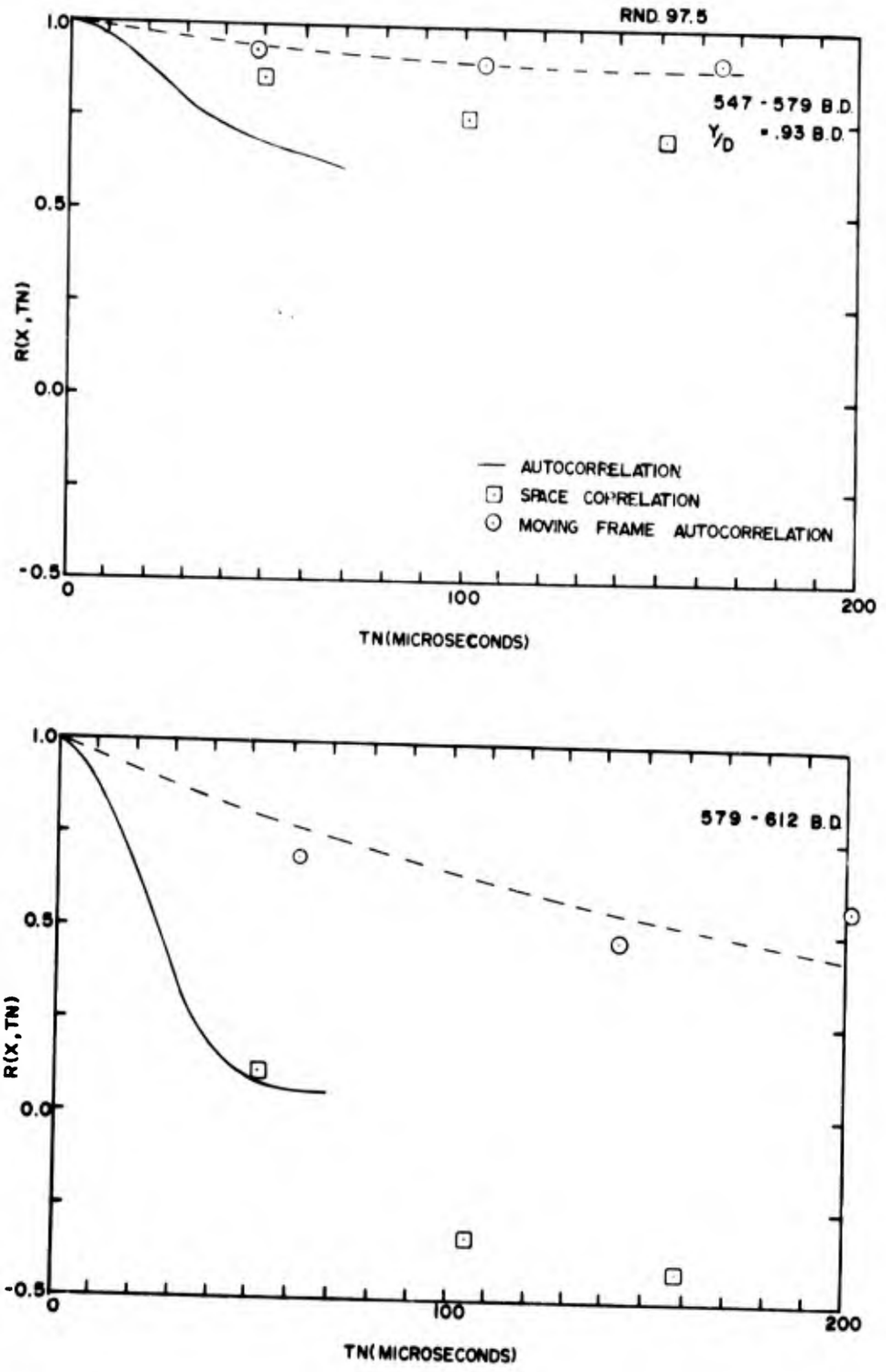

Fig. 17b Comparison of correlation functions, Rd 97

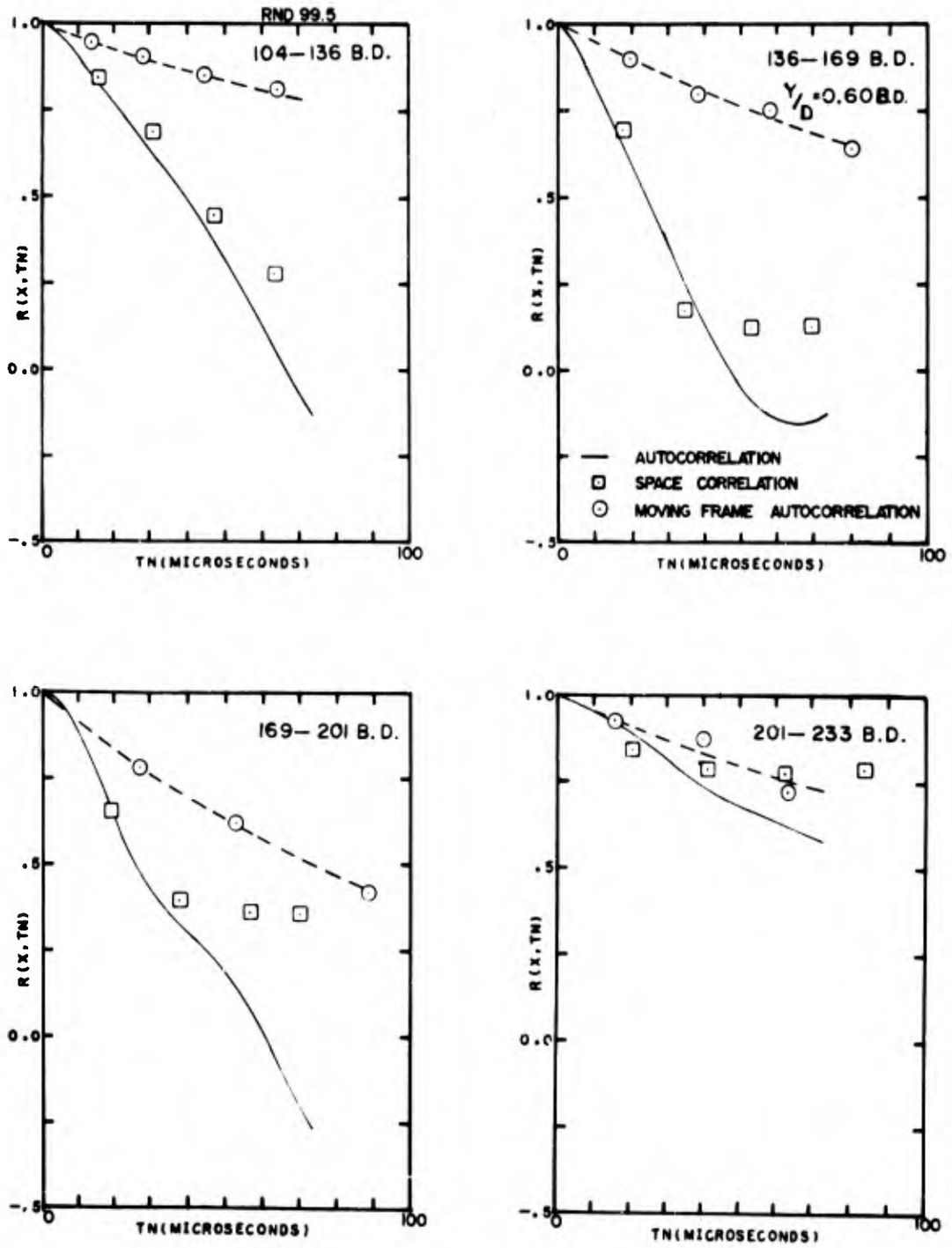

Fig. 18 Comparison of correlation functions, Rd 99

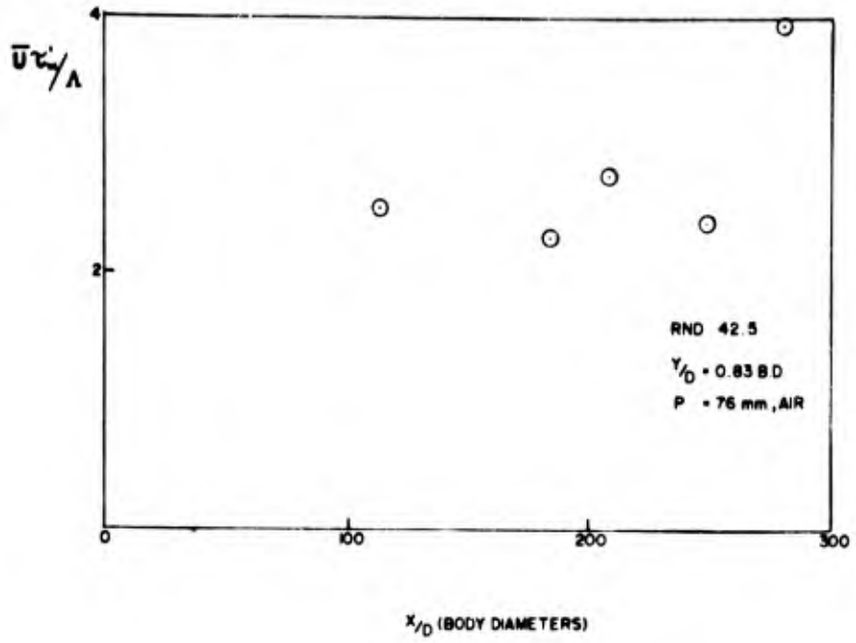

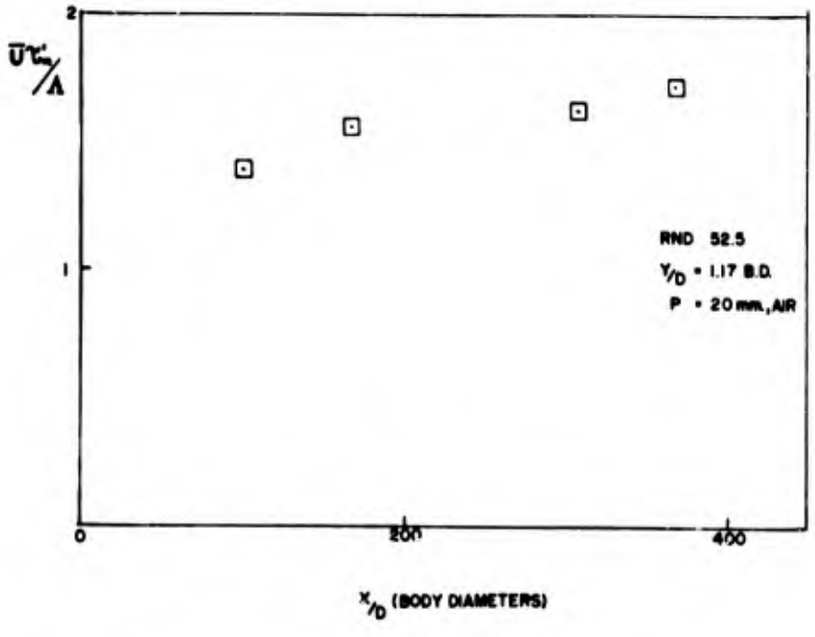

Fig. 19 Time scale to space scale ratio, Rd 42, 52

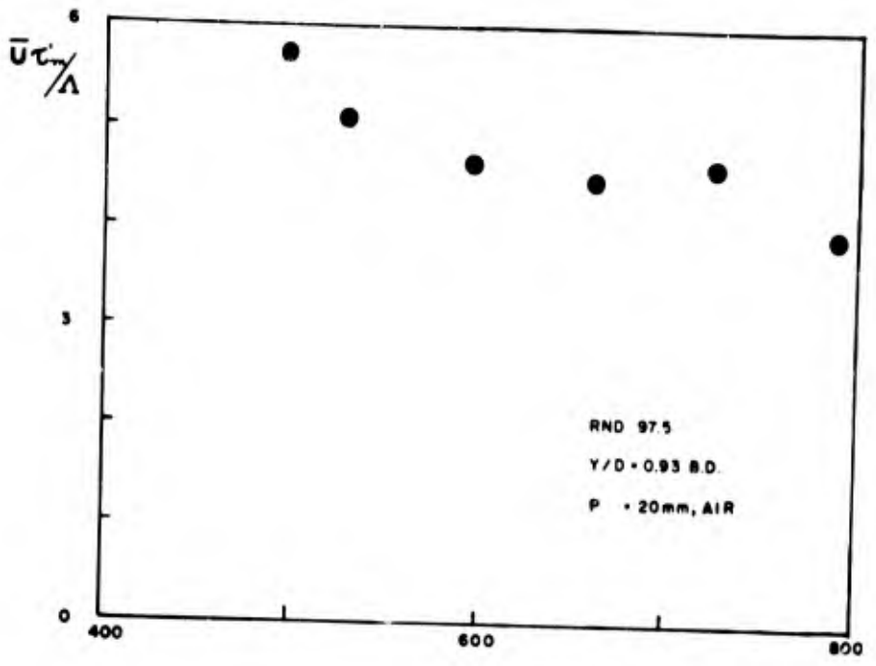

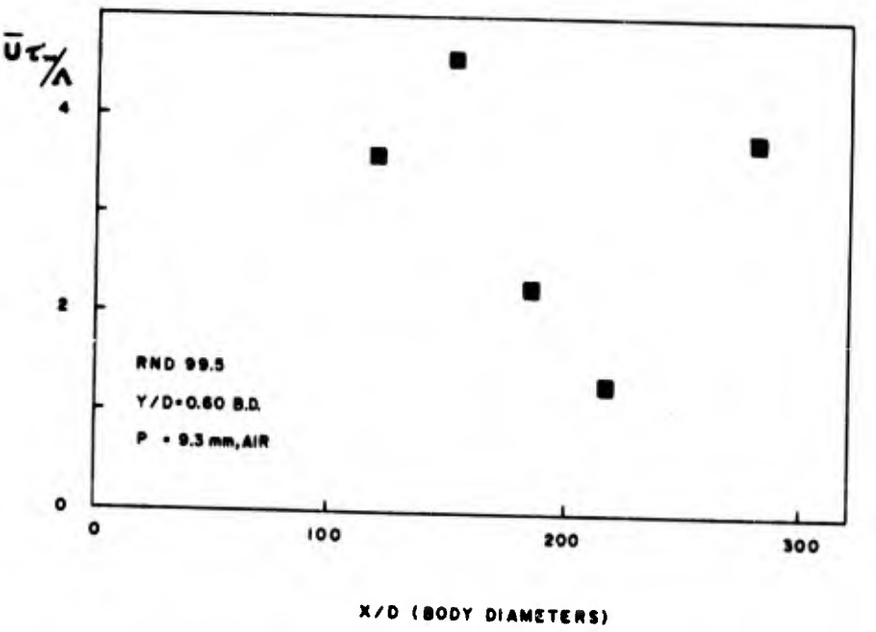

Fig. 20 Time scale to space scale ratio, Rd 97, 99

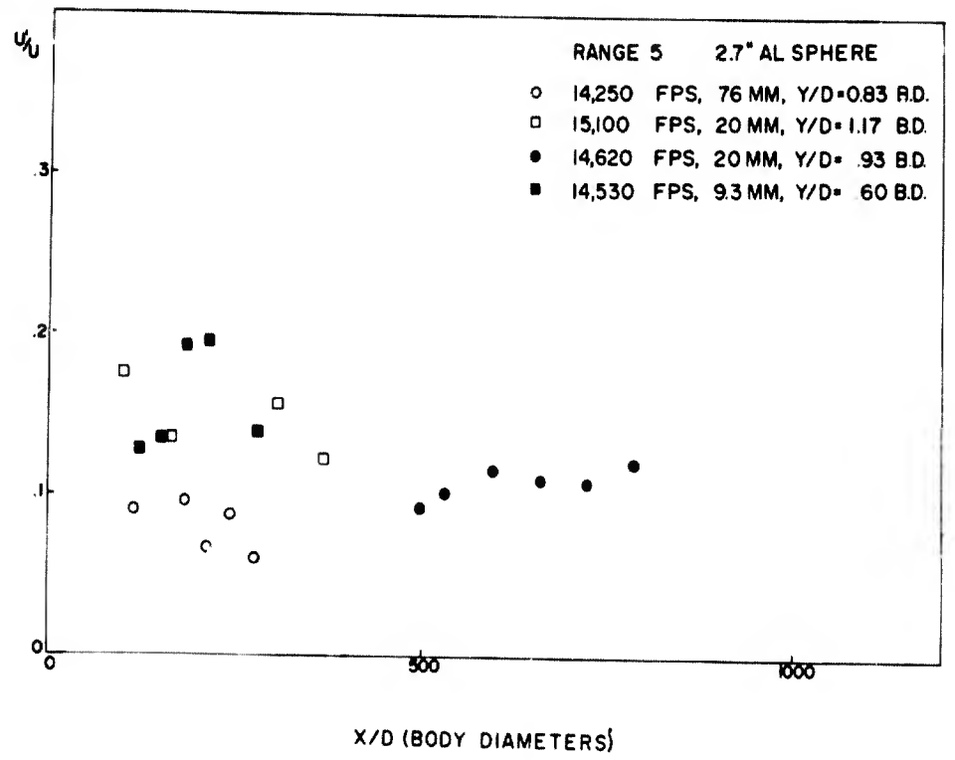

Fig. 21 Estimates of turbulent intensity versus axial distance

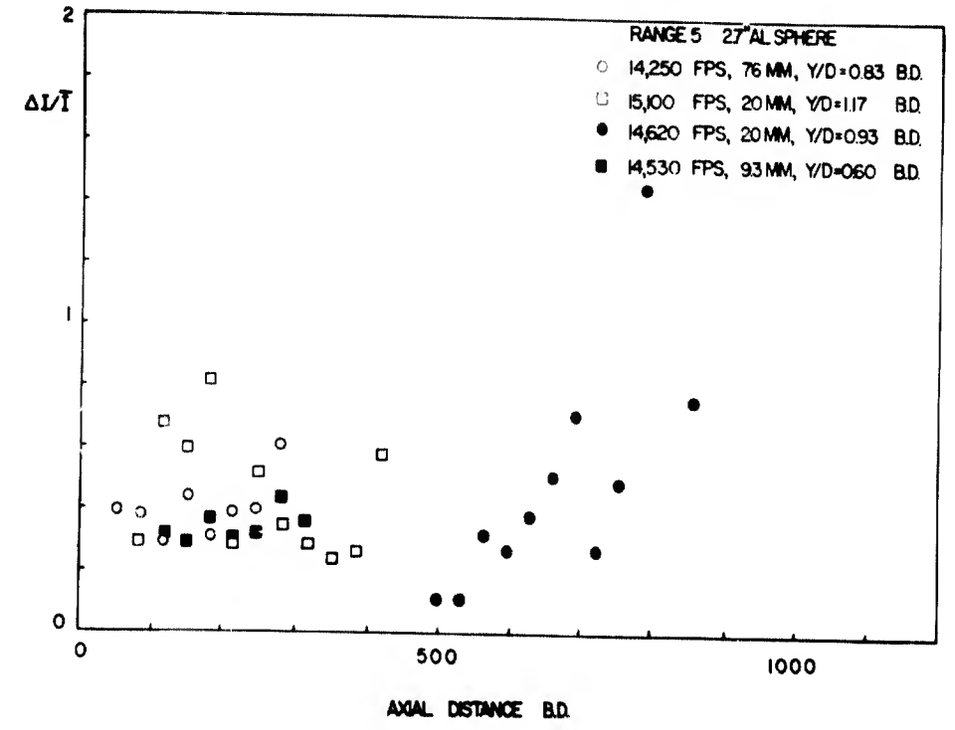

Fig. 22 RMS to mean probe current ratio versus axial distance, Rd 42, 52, 97, 99

ETUDES DE SILLAGES ELECTRONIQUES AU TUNNEL DE TIR HYPERBALISTIQUE

par

M. Laug

l'Institut Franco-Allemand de Recherches
de Saint-Louis (I. S. L.),
France

RESUME

Des projectiles généralement des sphères sont lancées dans le tunnel hyperbalistique de l'ISL à environ 6.000 m/s. Leurs sillages ionisés sont analysés par la méthode de la cavité résonnante (250 MHz) dont on enregistre l'impédance d'entrée sur abaque de Smith. On en déduit la fréquence des collisions entre électrons et particules neutres ainsi que le nombre total d'électrons présents à l'intérieur de la cavité.

A partir de ces résultats, on a tracé les courbes de densité électronique en fonction de la distance à condition de supposer la distribution radiale des électrons uniformes et d'attribuer au sillage un diamètre estimé théoriquement.

Des essais sont en cours en vue de mesurer le diamètre au lieu de le calculer, grâce à la mesure simultanée d'un troisième paramètre, qui est le déphasage d'une onde hyperfréquence. Un interférometre hyperfréquence à fréquence variable pourrait permettre de lever l'hypothèse d'une distribution radiale uniforme. L'instrumentation sera décrite.

SUMMARY

Projectiles, usually spheres, are fired at approximately 6,000 m/s in the ISL hyperballistic range. Their ionized wakes are analysed by the resounding cavity method (250 MHz), the input impedance of which is recorded on a Smith abacus. The frequency of collisions between electrons and neutral particles, and the total number of electrons inside the cavity are then derived.

From these data, the electron density curves as a function of distance have been drawn, assuming that the radial distribution of electrons is uniform and assigning to the wake a theoretically assessed diameter.

Tests are being conducted to measure the diameter, instead of computing it, by measuring simultaneously a third parameter which is the phase displacement of a hyperfrequency wave. A varying frequency hyperfrequency interferometer might allow the assumption of a uniform radial distribution to be discarded. The instrumentation will be described.

Etudes de sillages électroniques au tunnel de tir hyperbalistique

M. LAUG

1. Introduction: Le sillage électronique

Des projectiles sont lancés à grande vitesse (jusqu'à 6 000 m/s) par un canon à gaz léger dans un tunnel de tir contenant de l'air (ou plus précisément un mélange de 80% d'azote pur et 20% d'oxygène pur) à une pression de 1 à 50 mm Hg. On sait que de tels projectiles créent dans l'air une ionisation dont il subsiste des traces longtemps après leur passage. Pour disposer de quelques ordres de grandeur dès l'abord du problème, il est commode de comparer la formation du sillage au schéma suivant: l'air est comprimé, chauffé et ionisé par une onde de choc droite, se met rapidement en équilibre, puis se détend isentropiquement jusqu'à la pression ambiante p_∞. Soit T_f la température en fin de détente. Nous calculons la densité électronique n_{eq} et la fréquence de collision ν_{eq} à l'équilibre dans les conditions p_∞, T_f d'après la réf. (4). La table I donne n_{eq} et ν_{eq} pour une pression p_∞ = 10 mm Hg et une température T_∞ = 300°K devant le choc et pour deux vitesses de projectile: 5000 et 6000 m/s.

Or les densités électroniques mesurées près du projectile sont toujours très supérieures aux valeurs ainsi calculées: l'hypothèse de l'équilibre ne peut donc pas être retenue, au moins pour décrire le début du sillage. On peut alors se demander si l'équilibre peut être atteint en un temps inférieur à la durée des mesures (quelques millisecondes). Pour tenter de répondre à cette question, nous admettrons d'abord que la température reste voisine de 3000°K et que les électrons et ions en excès se recombinent suivant la réaction:

$$NO^+ + e \longrightarrow N + O,$$

réaction généralement considérée comme très prédominante (1), (2).

La vitesse α de cette réaction a été mesurée d'abord par LIN (3) et trouvée de la forme: $\alpha = 3 \cdot 10^{-3} T^{-3/2}$ cm^3/s. Elle est définie par: $\frac{d[e]}{dt} = -\alpha [NO^+] \cdot [e]$.

Le plasma étant supposé neutre: $[NO^+] = [e] = n$

$$\frac{dn}{dt} = -\alpha n^2 \qquad \text{ou} \qquad \frac{d\left(\frac{1}{n}\right)}{dt} = \alpha$$

Soit n_o la densité électronique à l'instant 0. On obtiendra la densité d'équilibre n_{eq} à l'instant t tel que:

$$\frac{1}{n_{eq}} - \frac{1}{n_o} = \alpha t$$

Si $n_o \gg n_{eq}$, $t = \frac{1}{\alpha n_{eq}} = \frac{10^3 T^{3/2}}{3 n_{eq}}$

l'hypothèse $n_o \gg n_{eq}$ n'est pas très restrictive puisque, pour $n_o = 2 n_{eq}$, on trouverait encore un temps moitié de celui qu'on vient de calculer. La fig. 1 représente t pour diverses valeurs de T et de p. On remarque que pour T = 3000°K et p = 10 mm Hg, l'équilibre est théoriquement atteint en 10 ms ($\alpha = 2 \cdot 10^{-8}$ cm^3/s, $n_{eq} = 5 \cdot 10^9$ cm^{-3}). Pendant un temps aussi long la température diminue, ce qui accroît encore le temps de mise en équilibre.

On peut donc s'attendre à ce que le sillage soit un plasma hors d'équilibre, non seulement près du projectile, mais en tout point. Le modèle le plus simple auquel on puisse alors comparer un sillage consiste en une détente isentropique pendant laquelle toutes les réactions chimiques sont en équilibre sauf l'ionisation qui est au contraire totalement figée. Celle-ci se calcule alors pour la formule:

$$n_{figé} = n_{choc} \times \frac{\rho_{sillage}}{\rho_{choc}},$$

où ρ désigne la masse spécifique. Les résultats sont donnés dans la table II, la valeur de n_{choc} étant toujours extraite de la réf. (4).

2. Dispositif expérimental

2.1 Cavité à diélectrique: Le projectile traverse une cavité cylindrique résonnant à la fréquence de 250 MHz sur le mode TM_{010}. On mesure l'impédance d'entrée de la cavité en parties réelle et imaginaire à l'aide d'un impédancemètre à quatre détecteurs, qui fournit un enregistrement XY sur abaque de SMITH (fig. 3). Cette instrumentation et la théorie de la perturbation de la cavité par un plasma ont déjà été décrites (5). Cependant deux modifications ont été apportées récemment:

1°) La cavité est un bloc de polyéthylène sur lequel on a plaqué des feuilles de cuivre, l'ensemble étant percé autour de l'axe (diamètre du trou = 55 mm, à comparer au diamètre de la cavité 600 mm et à sa longueur 120 mm). On a voulu résoudre ainsi les problèmes d'étanchéité et de rigidité, ainsi peut-être que les problèmes de diffusion d'électrons à l'intérieur de la cavité: ces avantages compensent notablement les risques d'accroître la perturbation de l'écoulement et les effets de capture d'électrons par la surface du polyéthylène.

2°) On s'arrange pour que l'abaque de SMITH ait son axe réel horizontal, et on enregistre en fonction du temps les signaux de sorties horizontale et verticale de l'oscilloscope XY (fig. 4). On dispose ainsi de deux mesures résolues dans le temps qu'on sait relier aux deux paramètres caractérisant le plasma.

Les paramètres mesurés de cette manière sont

$$\int \frac{n dV}{\nu^2 + \omega_0^2} \qquad \int \frac{n\nu dV}{\nu^2 + \omega_0^2}$$ où :

ω_o est la pulsation de résonance de la cavité: $\omega_o = 2\pi \cdot 250 \cdot 10^6 s^{-1}$,

ν est la fréquence de collision électrons - molécules,

n est la densité électronique.

Les intégrales sont étendues au volume (v) d'interaction entre le champ électrique et le plasma. Si on considère ν comme constant dans (v), on peut dire que la cavité mesure ν et $N = \int ndV$, nombre d'électrons dans le volume (v). La fig.2 montre les courbes N/C = cte et ν/ω_o = cte dans le diagramme de SMITH pour une cavité au couplage critique: ces courbes sont des arcs de cercle. Le même réseau d'arcs de cercles est utilisable pour un couplage quelconque, mais avec une graduation différente. (C est une constante sans dimension de la cavité.)

On considère souvent que la densité électronique n est elle-même constante dans (v), soit qu'on admette une telle représentation du sillage, soit qu'on lui attribue les mêmes propriétés électromagnétiques.

La cavité mesure alors nd^2 et ν, où d est le diamètre de plasma, c'est-à-dire le diamètre du sillage s'il est inférieur à celui du trou de la cavité, le diamètre du trou si celui-ci est entièrement rempli de plasma.

2.2 Interféromètre hyperfréquence: Un faisceau hyperfréquence (70 GHz) focalisé par une lentille est émis perpendiculairement à l'axe de tir. En présence du sillage, le faisceau est affaibli et déphasé. Pratiquement, dans les conditions expérimentales habituelles, la fréquence de collision ν est de quelques GHz si bien que le paramètre $\frac{\nu}{\omega}$, qui était voisin de l'unité pour une fréquence de 250 MHz (cavité), est très petit dans le cas d'un signal de 70 GHz. Il

s'ensuit que l'affaiblissement est très faible: expérimentalement, on a constaté qu'il ne pouvait pas être mis en évidence par détection directe.

L'interféromètre ne mesure donc qu'un paramètre: le déphasage φ , lequel est proportionnel à $\int n\,d\ell$ dans l'approximation de la lame de plasma, l'intégrale étant étendue à la distance d'interaction x du faisceau et du plasma. Si la distribution radiale est uniforme, on a une mesure du produit nx . Si les axes du faisceau et du sillage sont concourants, x n'est autre que le diamètre d du sillage. Si par suite de la dispersion du tube de lancement les axes sont distants de h, on a:

$$x = \sqrt{d^2 - 4h^2}.$$

L'analyse simple qui précède n'est valable qu'aux deux conditions suivantes:

1°) Le plasma est assez peu ionisé pour que les réflexions à la surface de séparation air - plasma soient négligeables. Dans ces conditions, l'expression de l'indice du plasma:

$$\mu = \sqrt{1 - \frac{ne^2}{4\pi^2 m \varepsilon_0 f^2}}$$

peut être développée au premier ordre. On obtient alors pour f = 70 GHz:

$$nd\ (cm^{-2}) = 8{,}3 \cdot 10^{12} \quad (rad),$$

le terme du 2ème ordre étant inférieur à la précision des mesures pour $n \leq 2 \cdot 10^{13}\ cm^{-3}$.

2°) Le diamètre d_f de la tache focale est très inférieur à celui du sillage. Celui-ci étant généralement estimé à 2,5 à 5,5 fois le diamètre du projectile d_p, on admettra que la condition peut s'écrire: $d_f \leq d_p$. Or d_f est de l'ordre de 2 longueurs d'onde (diamètre limitant

80 % de l'énergie émise par une lentille à faces hyperboliques), soit ici 8 mm. Les projectiles utilisés ont été:

- des sphères de 7 mm lancées par le canon de calibre 10: les résultats obtenus sont suspects;

- des sphères de 12,7 mm lancées par le canon de calibre 20 construit très récemment à l'ISL: les mesures n'ont pas encore fourni un nombre important de données, mais on discutera ci-après un résultat expérimental obtenu avec un tel projectile;

- des cylindres de 10 mm en polyéthylène lancés sans sabot par le canon de 10: les résultats doivent être valables, mais leur interprétation est compliquée par l'ablation et par l'incidence du projectile, variable d'un tir à l'autre.

3. Résultats expérimentaux

3.1 Cavité: La fig. 3 est un exemple d'enregistrement obtenu à l'aide de la cavité. Celle-ci a été surcouplée afin de rehausser le domaine des densités électroniques mesurables (6) (dans le cas étudié, elles sont multipliées par 2,5). On peut cependant comparer les fig. 3 et 2 compte tenu de la remarque faite au chapitre 2.1, et remarquer ainsi que la trace est voisine d'un arc de cercle à ν constant. On s'attend bien à un résultat de cette nature puisque la pression est constante ($p = p_\infty$) et que la température varie peu (en outre son influence sur ν est assez faible). De plus la valeur moyenne de ν au cours de la mesure (1,6 GHz) est remarquablement proche de la valeur théorique trouvée au chapitre 1.

La fig. 4 représente en fonction du temps les variations des amplitudes horizontale et verticale appliquées à l'oscilloscope XY (voir chapitre 2.1, 2°). On en déduit la fig. 6, courbe de nd^2 en

fonction du temps dans l'hypothèse d'un plasma homogène (ou plus généralement de $\frac{4N}{\pi L}$, où L est la longueur de la cavité).

3.2 Interféromètre: On a tracé sur la même fig. 6 la courbe de nd en fonction du temps, courbe déduite des mesures interférométriques (fig. 5). Sur ces dernières, on observe un affaiblissement nul (sauf pendant le passage du projectile), comme cela a déjà été dit.

4. Interprétation

4.1 Fréquence de collision: ν varie peu au voisinage de la valeur théorique trouvée au chapitre 1, où l'on avait supposé la détente isentropique et toutes les réactions en équilibre. Il est probable que la première hypothèse est fausse et que par conséquent la température T du gaz en fin de détente est plus élevée. On devrait donc obtenir une fréquence de collision inférieure à la valeur calculée plus haut à moins que la température électronique T_e ne soit supérieure à celle des neutres: on peut en effet admettre que ν est proportionnel à $\sqrt{T_e}/T$. Ainsi on aurait la même valeur de ν pour $T = T_e = 3\,000°K$ ou par exemple pour $T_e = 6\,000°K$ (température constante pendant la détente) et $T = 4\,200°K$.

Plus loin du projectile, on peut penser que les électrons se refroidissent plus vite que le gaz, de sorte que ν se maintient à une valeur à peu près constante, et cela jusqu'à ce que l'équilibre thermodynamique soit atteint. Ensuite, le gaz continuant à se refroidir, la fréquence de collision devrait augmenter comme $T^{-1/2}$. Bien que les mesures n'aient pas la précision voulue pour donner des résultats quantitatifs, nous avons observé une telle tendance à

l'accroissement de ν à partir d'une certaine distance, d'ailleurs peu reproductible.

4.2 Diamètre: Dans l'expérience choisie, l'interféromètre et la cavité ont répondu simultanément entre 0,25 et 0,5 ms. Ce chevauchement ne se produit malheureusement que dans des conditions assez précises de vitesse et de pression. Quand il se produit, les mesures simultanées avec les deux appareillages permettent de déduire le diamètre du sillage dans cet intervalle de temps. Dans l'exemple montré ici (fig. 6), le parallélisme des courbes de nd et de nd^2 montre que le diamètre est constant pendant cette période. Il est trouvé égal à 3 cm, soit 2,4 calibres.

4.3 Densité électronique: Nous avons alors supposé un diamètre de sillage constamment égal à 3 cm et déduit des courbes de nd et nd^2 la variation de n en fonction du temps (fig. 7).

Si on admet que le processus dominant est la recombinaison, on définit une vitesse α (comme au chapitre 1), dont la valeur expérimentale croît depuis $10^{-7} cm^3/s$ au début de la mesure (t = 10 µs) jusqu'à $2 \cdot 10^{-5} cm^3/s$ à la fin (t = 1 600 µs), au lieu de la valeur théorique $2 \cdot 10^{-8} cm^3/s$. Pour décrire le phénomène dans ses premiers instants, on peut admettre un coefficient de recombinaison corrigé de manière à tenir compte d'autres causes de pertes d'électrons: ESCHENROEDER et al.(1) ont suggéré un tel coefficient $\alpha = 1,5 \cdot 10^{-2} T^{-3/2}$ qui est en accord avec nos mesures.

Cependant l'écart croissant entre les valeurs théorique et expérimentale de α interdit de considérer la recombinaison dissociative comme prédominante à partir d'une certaine distance

derrière le projectile. ZEIBERG (7) et KORNEGAY (2) ont montré l'importance de l'attachement des électrons aux molécules O_2, qui devient plus rapide que la recombinaison à des températures inférieures à 700°K. Mais la décroissance de la densité électronique est importante avant que cette température soit atteinte: d'autres processus, comme la diffusion, jouent probablement un rôle important. Si le sillage proche (environ 40 à 50 calibres) peut être prédit à l'aide d'un modèle relativement simple (1), il n'en est pas de même du sillage lointain.

5. Conclusions et projets

Deux instrumentations sont employées simultanément à l'ISL pour étudier les sillages ionisés: L'interféromètre hyperfréquence est un moyen approprié à l'étude du sillage proche (jusqu'à 100 à 200 calibres) en raison de sa sensibilité aux densités électroniques élevées et de sa bonne résolution spatiale. La cavité résonnante, au contraire, permet l'analyse du sillage lointain: elle n'est pas sans inconvénient, mais on ne connaît guère de moyen concurrent pour les faibles densités électroniques. De plus, dans certaines conditions expérimentales, un recouvrement entre ces deux parties du sillage est possible: la zone commune est alors caractérisée par un plus grand nombre de paramètres expérimentaux. Ainsi on a pu fournir les valeurs de la densité électronique moyenne, de la fréquence de collision moyenne et du diamètre en fonction de la distance.

Mais les paramètres ne se réduisent au nombre de 3 (a fortiori de 2 ou 1) que dans les théories faisant appel à de nombreuses hypothèses. Pour appuyer par l'expérience des théories plus élaborées, il faudra mesurer des paramètres en nombre de plus en

plus élevé. C'est pourquoi nous avons commencé à introduire des sondes électrostatiques dont on espère déduire par exemple la température électronique: la mesure de la fréquence de collision, si elle pouvait être rendue plus précise, serait alors une mesure de la température du gaz. Nous envisageons d'autre part d'effectuer des mesures en hyperfréquence à plusieurs fréquences voisines et en un même lieu grâce à un interféromètre à fréquence très rapidement variable dans la gamme d'un carcinotron: il sera alors possible de définir la distribution radiale des électrons dans les zones où la fréquence de plasma ne sera pas trop éloignée de cette gamme. L'appareillage doit être mis en service prochainement. En fait il ne serait pas nécessaire d'employer toutes les techniques dans le même laboratoire s'il existait un modèle d'étude commun: malheureusement, dans l'état actuel des choses, il est presque impossible de comparer les résultats théoriques et expérimentaux des divers chercheurs, les techniques hyperfréquences ayant été utilisées avec des sphères de 15 mm (1), la cavité avec des sphères de 5 mm (2) ou des projectiles cylindro-sphériques de 20 mm (10), les sondes de Langmuir avec des sphères de 25,4 et 68 mm (9), le modèle théorique de LIN et HAYES (11) limité à des sphères lancées à 6 600 m/s, etc. Il nous paraît donc nécessaire de mesurer simultanément plusieurs grandeurs au cours de chaque essai, et c'est dans cette voie que nous sommes engagés.

Bibliographie

(1) A. ESCHENROEDER, R. HAYAMI, R. PRIMICH, T. CHEN
Ionization in the near wakes of spheres in hypersonic flight.
AIAA Paper No 66 - 55 (3rd Aerospace Sciences Meeting, N. Y. 24 Jan 66).

(2) W. M. KORNEGAY
Decay of electron density in the wakes of hypervelocity spheres.
Lincoln Lab. Tech. Rpt No 370, 23 Dec 64.

(3) S. C. LIN, R. A. NEAL, W. I. FYFE
Rate of ionization behind shock waves in air: I - Experimental results.
Ph. of Fluids 5, 12, Dec 62, p. 1633.

(4) M. P. BACHYNSKI, G. G. CLOUTIER
Communications in the presence of plasma media.
Symp. on manned lifting planetary entry (John Wiley and Sons, Inc., 1963) p. 206.

(5) M. LAUG, P. CLAVELIN
Sondage des plasmas par des mesures d'impédance.
IEEE Trans. on Aerospace, AS - 3 No 1, Feb 65, p. 30.

(6) M. LAUG
Mesure de l'ionisation derrière des projectiles à grande vitesse, à l'aide d'une cavité résonnante et d'un interféromètre hyperfréquence.
Note Tech. ISL, T 31/65, Oct 65.

(7) S. L. ZEIBERG
Oxygen electron attachment in hypersonic wakes.
AIAA Journal 2 No 6, June 64, p. 1151.

(8) J. HILSENRATH, M. KLEIN
Tables of thermodynamic properties of air in chemical equilibrium including second virial corrections from 1 500°K to 15000°K.
AEDC - TR - 65 - 58, March 65.

(9) A. KIRKPATRICK, A. CANTIN, D. HECKMAN, M. GRAVEL
Preliminary electron conductivity probe results at CARDE.
CARDE/T. N. 1719/66, May 66.

(10) E. L. MURPHY, S. EDELBERG, G. F. PIPPERT
Electromagnetic studies of ionized wakes.
Lincoln Lab. Tech. Rpt No 370, 20 April 62.

(11) S. C. LIN, J. E. HAYES
A quasi-one-dimensional model for chemically reacting turbulent wakes of hypersonic objects.
AIAA J. Vol. 2 No 7, July 64, p. 1214.

Table I - Ionisation à l'équilibre

V_∞ (m/s)	$\log \frac{p_{choc}}{p_{atm}}$	T_{choc} (°K)	T_f (°K)	n_{eq} (cm^{-3})	ν_{eq} (s^{-1})
5 000	0,53	5 900	2 800	$1,5 \cdot 10^{9}$	$1,6 \cdot 10^{9}$
6 000	0,70	6 900	3 300	$2,2 \cdot 10^{10}$	$1,5 \cdot 10^{9}$

Table II - Ionisation figée

V_∞ (m/s)	$\frac{\rho_{choc}}{\rho_0}$	T_{choc} (°K)	n_{choc} (cm^{-3})	$\frac{\rho_{sillage}}{\rho_0}$	$n_{figé}$ (cm^{-3})
5 000	0,13	5 900	$6 \cdot 10^{14}$	$1,1 \cdot 10^{-3}$	$5 \cdot 10^{12}$
6 000	0,15	6 900	$2 \cdot 10^{15}$	$8 \cdot 10^{-4}$	10^{13}

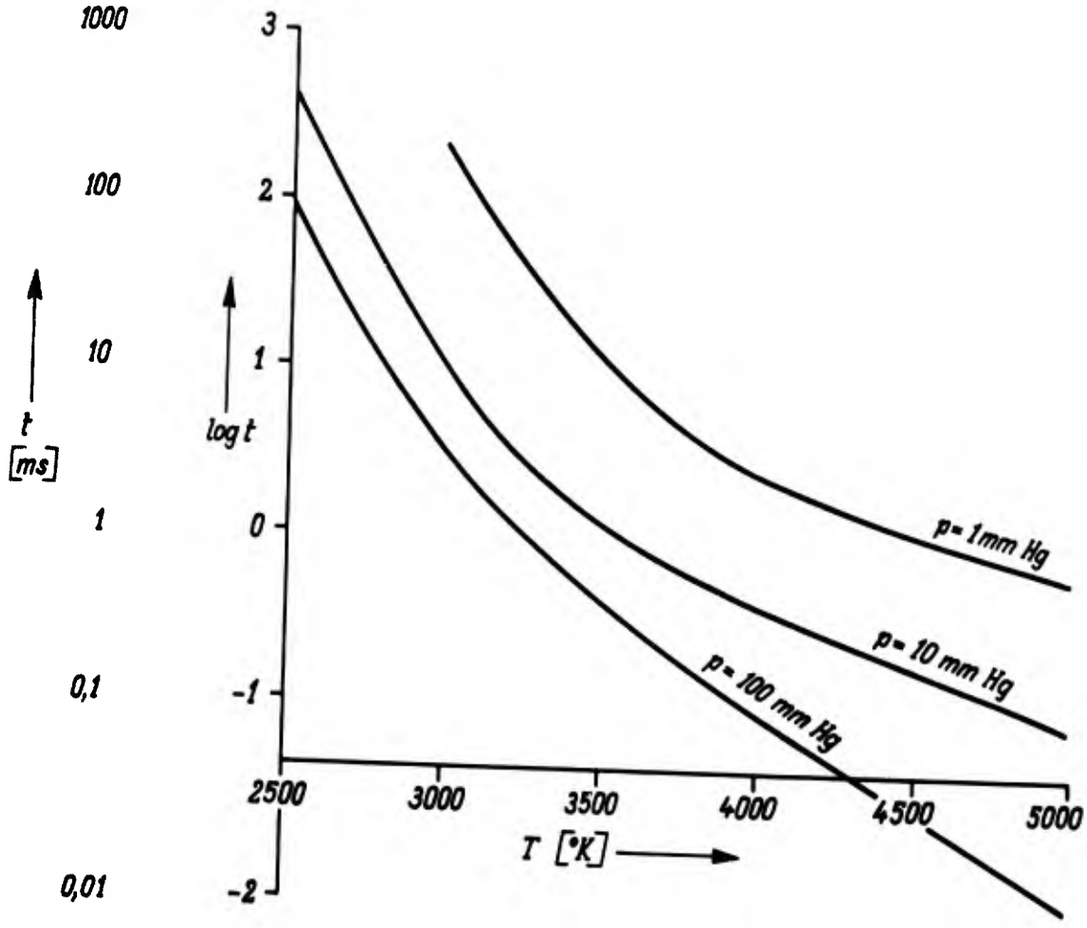

Fig. 1 Temps de mise en équilibre par recombinaison selon la réaction:
$NO^+ + e^- \rightarrow N + O$

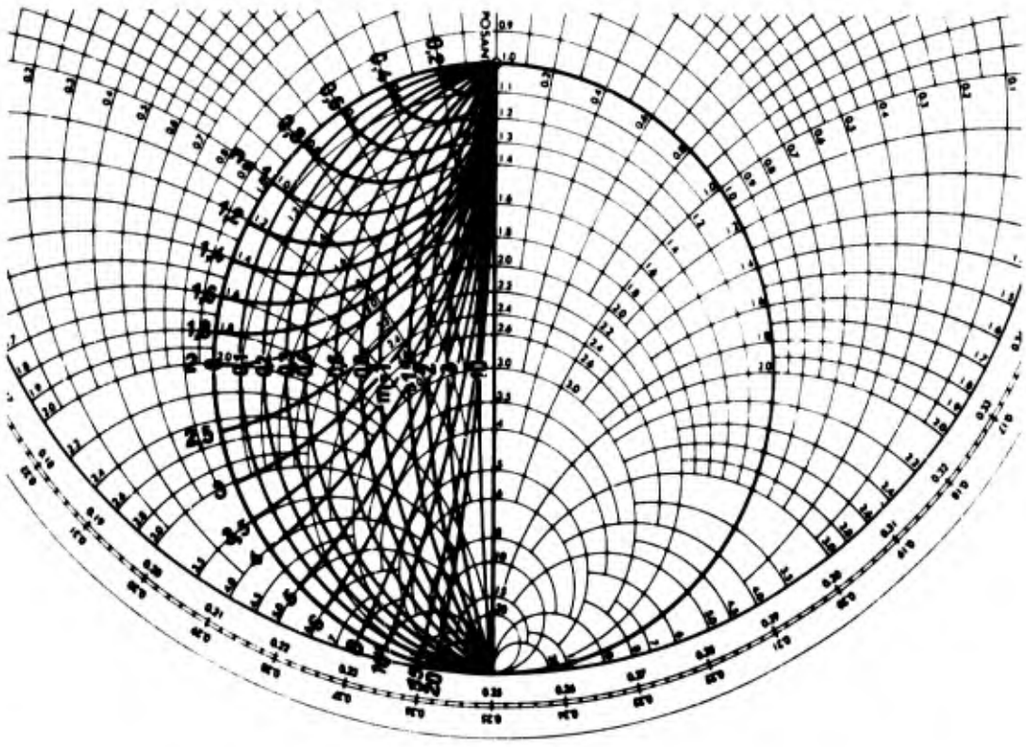

Fig. 2 Lieu des courbes $\frac{N}{C}$ = cte (n) et $\frac{\nu}{\omega_o}$ = cte (m) au couplage critique

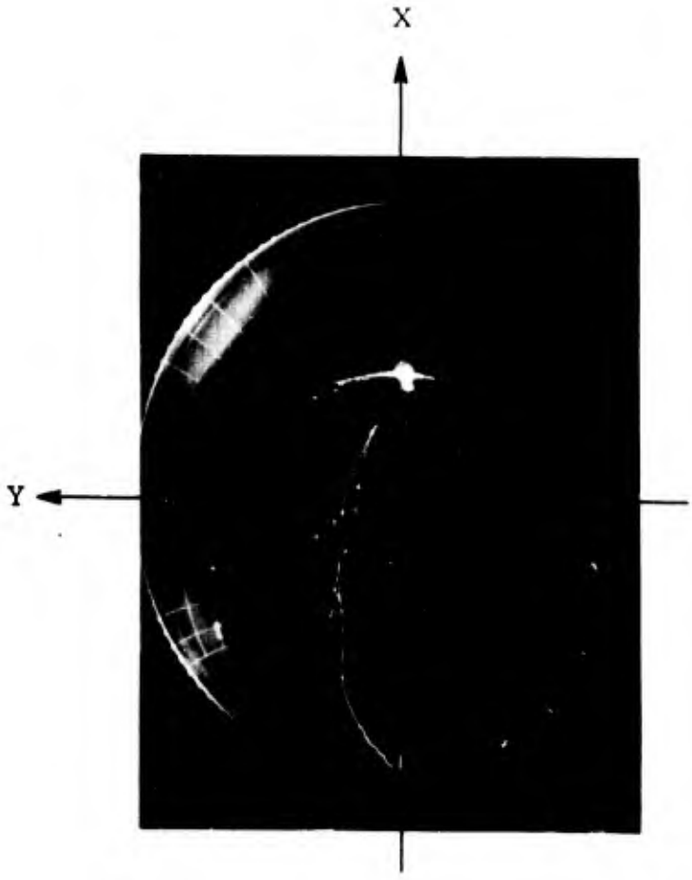

Fig. 3 Impédance de la cavité (en X Y). Période de marquage: 200 μs.

Conditions de l'essai: sphère alu $\emptyset$ 12, 7 mm
air 10 mm Hg
vitesse 4850 m/s.

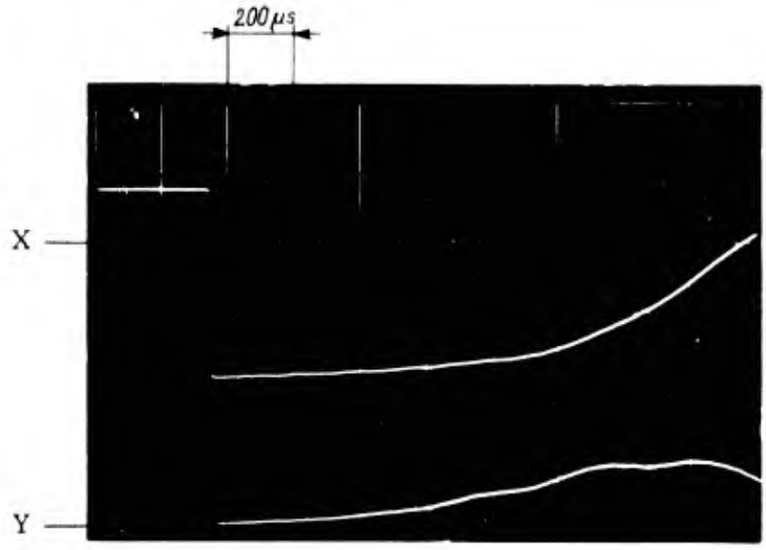

Fig. 4 Impédance de la cavité (avec résolution en temps)

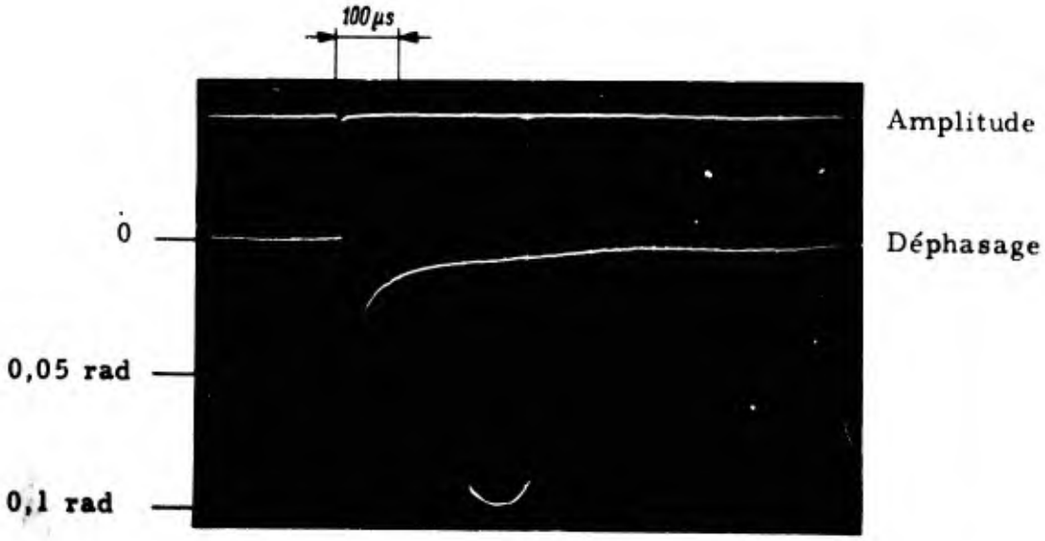

Fig. 5 Interférogramme 4 mm.

Conditions de l'essai: sphère alu ϕ 12, 7 mm
air 10 mm Hg
vitesse 4850 m/s.

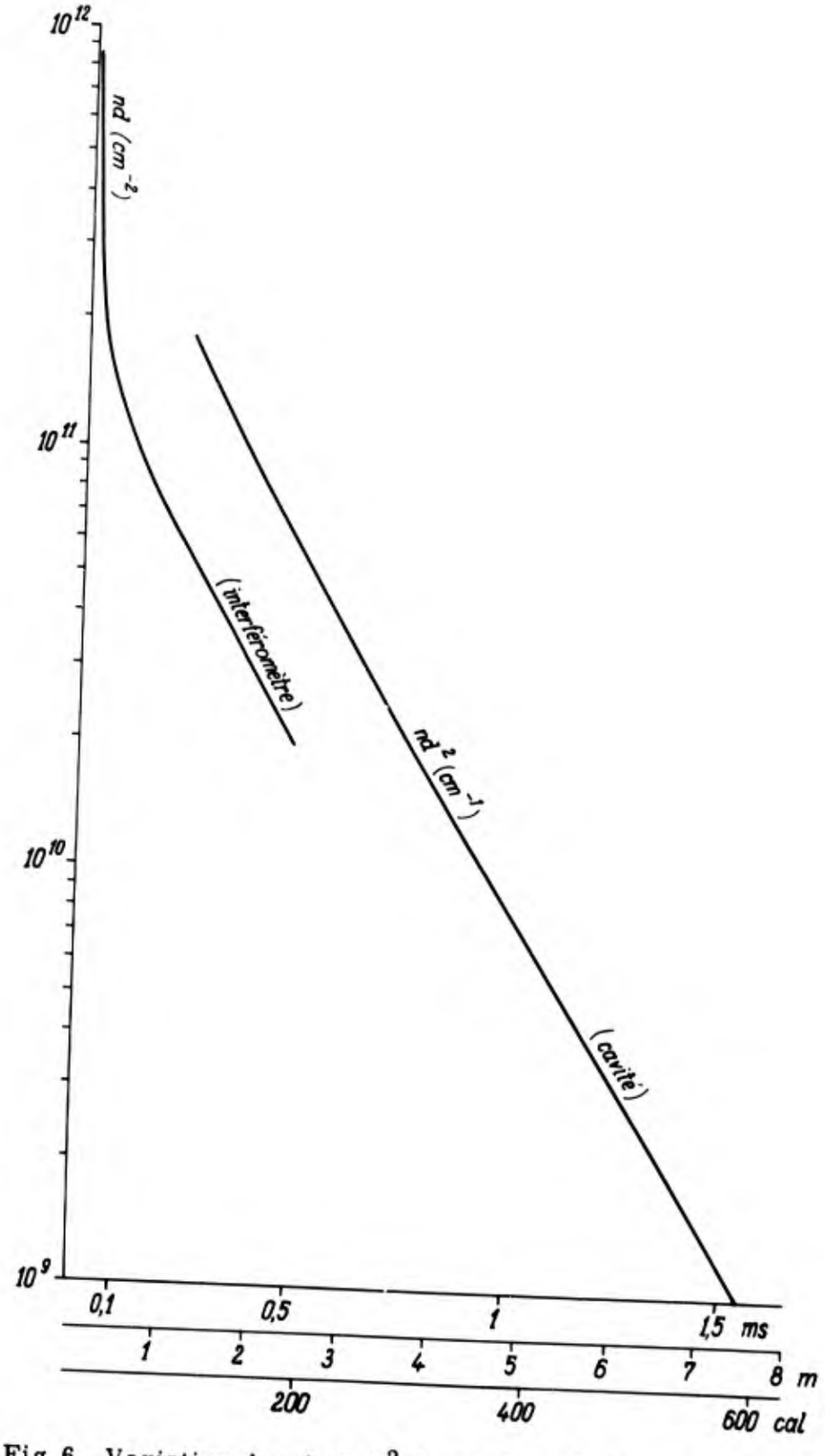

Fig. 6 Variation de nd et nd^2 (conditions de l'essai: v. Fig. 3)

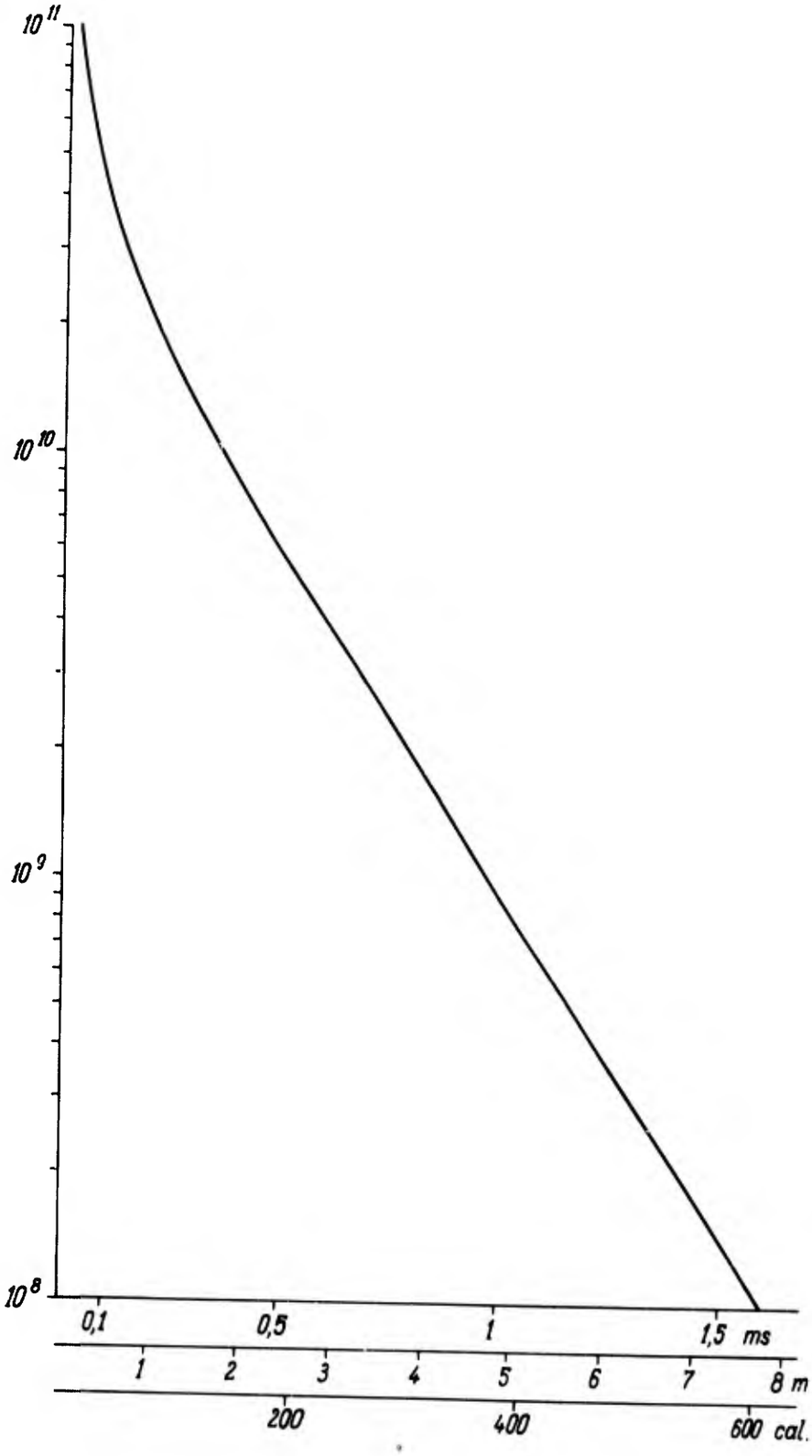

Fig. 7 Densité électronique

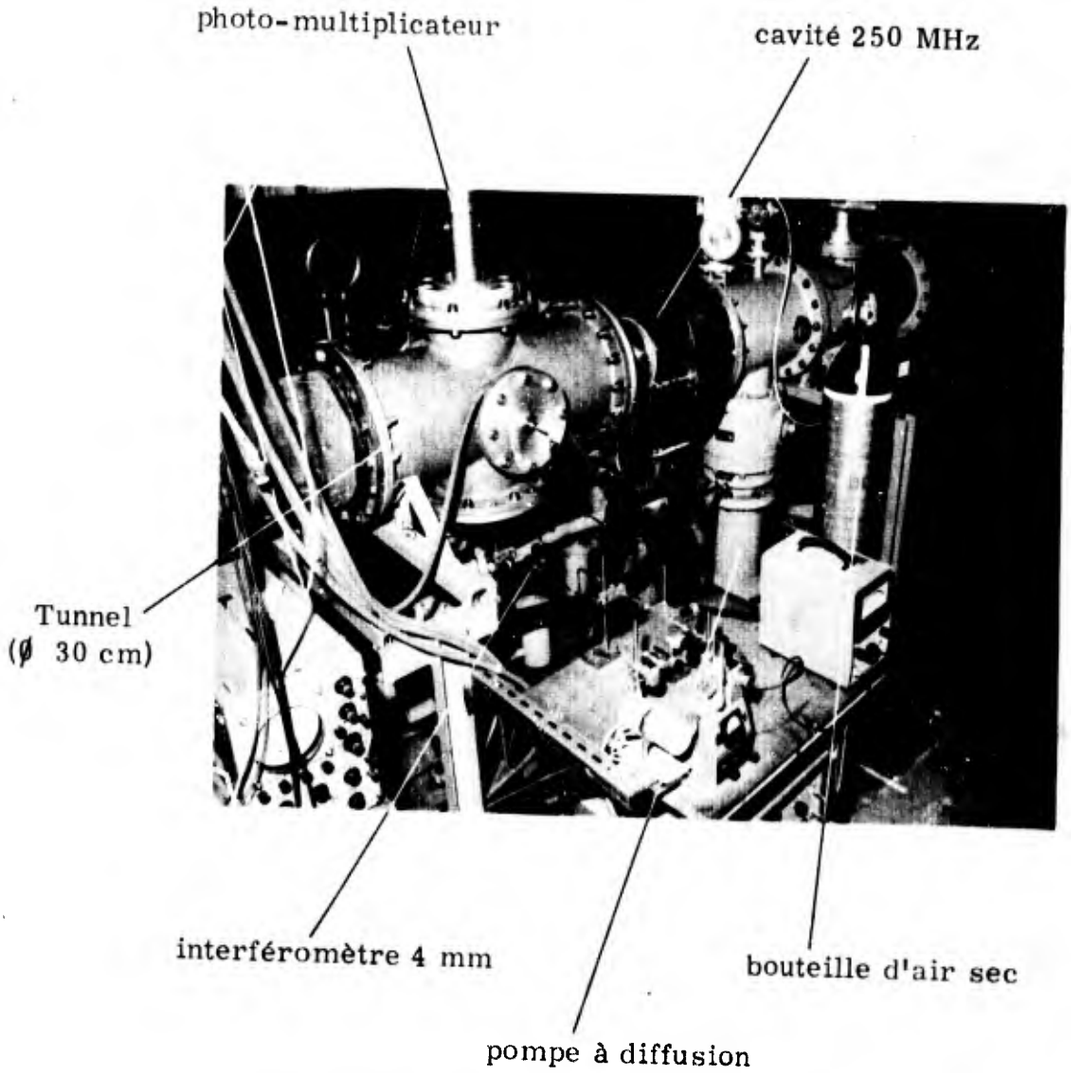

Fig. 8 Dispositif expérimental

BLANK PAGE

WAKE ELECTRON DENSITY MEASUREMENTS BEHIND HYPERSONIC SPHERES AND CONES*

Authors: R. A. Hayami, Experimental Physicist

R. I. Primich, Head, Reentry Physics Program

Affiliation: Aerospace Operations Department
AC Electronics-Defense Research Laboratories
General Motors Corporation
6767 Hollister Avenue
Goleta, California

Telephone: AC 805, 968-1011

February 1967

* The work described in this paper has been supported by the Advanced Research Projects Agency under contract No. DA-01-021-AMC-11359(Z)

SUMMARY

The experimental data is significant for a number of reasons. For spheres, the measured electron density level extends from the recompression zone immediately behind the sphere into the far wake and so includes all regions of the wake where different electron-removal mechanisms are believed to exist.

Different pressure régimes, in which various measured fluid dynamical effects are shown to have a profound influence on electron density decay, are also covered. Scalability of near-wake has been demonstrated previously and an example which shows binary scaling extending to the far wake is presented.

The wake electron density data behind cone models fired at velocities of 23,000 fps are believed to be unique. Data for firings of a 12.5^{o} half-angle cone with $\frac{1}{4}$ inch base diameter at different range pressures and ratios of N_2 - O_2 concentration will be presented.

RESUME

Les résultats expérimentaux sont significatifs pour un certain nombre de raisons. Dans le cas de sphères, la région où l'on procède à des mesures de densité électronique s'étend de la zone de recompression située immédiatement derrière la sphère jusqu'au sillage éloigné, et comprend donc toutes les zones du sillage où l'on pense qu'il existe différents mécanismes de soustraction d'électrons.

L'exposé couvre également différents régimes de pression auxquels divers effets, mesurés, de dynamique des fluides, se révèlent avoir, sur la diminution de densité électronique, une profonde influence. La discretisation du sillage proche a été démontré précédemment, et les auteurs présentent un exemple qui montre l'effet d'échelle binaire s'étendant jusqu'au sillage éloigné.

On estime que les données sur la densité électronique des sillages de maquettes en forme de cônes lancées à une vitesse de 23.000 pieds par seconde, sont uniques. Les auteurs présenteront des données sur les lancements de cônes de 12, 5° de demi-angle et d'$\frac{1}{4}$ de pouce de diamètre de base pour diverses pressions régnant à l'intérieur du tunnel de tir, et divers rapports de concentration de $N_2 - O_2$.

1. INTRODUCTION

Due to the complexity of the phenomena related to hypersonic reentry, controlled laboratory experiments are essential to the understanding of the processes taking place and thence to the formulation of correct analytical flow-field models.

While the wake electron density distribution is not accessible to direct measurement in the field, it is a particularly useful quantity to obtain in a laboratory measurement. This is not only because of its influence on the radar-scattering properties of the wake but also, due to its intimate coupling with the flow field and the resultant chemistry, the measured levels can be used both to set input conditions to the flow-field calculations and also to check the correctness of the analytical model by comparing the subsequent measured and calculated electron density decay in the wake.

The free-flight ballistics range provides the means to make wake electron measurements behind scaled models launched at reentry velocities under controlled conditions. By studying the effects of various parameters (such as model size, shape, material, velocity, and range gas pressure and composition) on wake electron density levels and by correlation with data from a large number of other diagnostics (such as schlieren pictures, spectrographs, radiometers and radar-scattering equipment), one can aim at understanding the processes which generate and remove electrons in the wake.

Both analytical and experimental efforts are being carried out in these studies at AC Electronics-Defense Research Laboratories (AC-DRL). This paper will emphasize the experimental aspects of the wake electron density studies being carried out here. This includes an outline of the instrumentation used to make the measurements, interpretation of the measured data in terms of the wake properties, and a few examples of results behind blunt and slender bodies. Also, some

comparison will be made of the experimental data with theoretical calculations.

The experimental data is significant for a number of reasons. For spheres, the measured electron density level extends from the recompression zone immediately behind the sphere into the far wake and so include all regions of the wake where different electron-removal mechanisms are believed to exist. Also covered are different pressure regimes in which various measured fluid-dynamical effects are shown to have a profound influence on electron density decay. Scalability of the near wake has been demonstrated previously[1] and an example which shows binary scaling extending to the far wake is presented here.

The wake electron density data behind cone models fired at velocities of 7,000 m/sec are believed to be unique. Data for firings of a 12.5° half-angle cone with 1/4-inch base diameter at different range pressures and gases will also be presented.

The main value of the experimental data is in the development of more accurate analytical flow-field models. The experimental data for wakes behind spheres has resulted in recent theoretical calculations, both for a laminar wake[2] and also for a turbulent wake[3] which show the effects of various mixing models on electron density decay. The much more rapid electron density decay rate observed in the wakes of slender cones at 75-torr air,[4] when compared with previous theories,[5, 6, 7] has stimulated the present experimental work and the development of new analytical flow-field models.[2, 8]

2. EXPERIMENTAL TECHNIQUES

2.1 Free-Flight Range

The free-flight ballistics range[9] in which these measurements are made uses an accelerating reservoir light-gas gun[10] to launch saboted models at hypersonic velocities.

In using the free-flight range for wake electron density measurements, certain precautions are necessary to insure the validity of the results obtained. Electron density levels are particularly sensitive to contamination in either vapor or suspended particulate form[11] in the range atmosphere, or due to products of spurious ablation from model failure.[12] To minimize contamination, gun gases and debris from sabot impact are prevented from entering the instrumented section of the flight range by a normally closed high-speed valve which opens for approximately one millisecond to permit passage of the model before closing again. At the completion of its flight, the model is trapped in a chamber where the impact debris is prevented from splash-back into the range by a valve which closes after the model enters the chamber.

Contamination of the model and sabot during fabrication is removed by special cleaning, and "white-glove" handling thereafter is standard practice.

The flight range is normally pumped down to about .050-torr pressure and refilled with bottled gas to the desired final firing pressure just prior to launch of the model. Rate of inflow of the gas is carefully controlled to minimize stirring of dust which can cause spurious results. After each firing the flight range is brought back to atmospheric pressure and "purged" by forced flow of air for about twenty minutes to remove most of the suspended particulate matter.

Due to the high stresses imposed on the model during launch, it is essential to determine whether model integrity is maintained during its flight. Slender cones are particularly difficult to launch at reentry velocities and model damage can occur during launch or due to excessive angle of attack during flight.

Direct visual indication of angle of attack and model integrity is given by photos from shadowgraphs located along the range, schlieren photos, and a flash X-ray photo taken at the end of the flight range.

Effects of spurious ablation on the observables during the model flight are monitored by duplicate radiometers and electron-density measuring instruments located at several locations along the range. A particularly useful diagnostic in determining the type and location of model failure has been the time-resolved spectrograph. This instrument and the time-integrated spectrograph have also been useful in monitoring range atmosphere contamination which typically shows up as sodium lines in the spectra.

2.2 Electron Density Measurement Techniques

Instrumentation requirements for wake-electron density measurements in the free-flight range are rather stringent. Sufficient time and spatial resolution are required to accurately measure the changes in electron density along the wake axis. The dynamic range of the instruments should cover from 10^{13} down to about 10^{7} e/cm.^{3} Spatial coverage should be such that data is obtained on all firings in which the flight trajectory is within, say, 2 cm of the range axis.

The ultimate utility of the studies lies in the scalability of the data to full-scale conditions. This means that measurements should be made over as wide a range as possible in model sizes to check any scaling relationships that are developed. Since it is desirable in many cases to study phenomena that extend to 10,000 body diameters and further behind the model, it is important that the measuring instrument does not perturb the flow field during the test period through the bow shock reflecting back onto the wake, or by the wake itself impinging on the instrument through wake growth with distance behind the model.

In the present facility, spheres ranging in size from 2.5 to 15mm and cones with base diameter of 6 mm are routinely fired at velocities of 22 – 23,000 fps. Since a turbulant wake grows roughly as $\left[C_D\, x/D\right]^{1/3}$, the wake diameter can be of the order of 15 cm and 33 cm at points of 1,000 and 10,000 body diameters downstream of the model respectively.

This gives an indication of the size of structure required to avoid perturbing the wake while making the electron density measurements. The problems will be even more severe in the new facility where spheres40 mm in diameter and cones with a base diameter of 20 mm are now being launched at velocities above 22,000 fps.

Free-space microwave transmission techniques were chosen as best fulfilling the overall requirements. The requirement for high spatial resolution, and also the measurement of high electron density levels (about 10^{13} e/cm^3), necessitates the use of high frequencies. However, since the change in the phase of a signal transmitted through an underdense plasma of a given diameter falls off linearly with increasing frequency, resonator techniques must also be used to extend the range of measurements to lower levels.

The following sections will discuss the operating principles of the two complementary techniques chosen to make the electron density measurements. These are, first the focused microwave beam, single-pass systems operating at 35 and 75 GHz for high spatial resolution and measurement of electron density levels in the range of 10^{11} to 10^{13} e/cm^3, and second, open resonators of the Fabry-Perot type, operating at 5 and 35 GHz, which extend the lower limits of electron density measurements to about 10^7 e/cm^3 while still preserving good spatial resolution along the wake axis.

Spatial resolution of the 35 and 70 GHz focused probes is 1.3 and 0.65 cm, respectively, and 2.5 and approximately 7.5 cm respectively for the 35 and 5GHz open-resonator systems.

2.3 Focused Microwave Probes

The difficulties of making meaningful interpretations of wake properties from the forward and backscattered signal of unfocused microwave energy from a wake with unspecified electron wake diameter and radial distribution has led to the development of the focused-beam

probes.[13, 14] This technique, which is now seeing quite widespread use[15] takes advantage of the fact that the microwave energy can be concentrated in the focal region through appropriate aperture illumination and lens contouring. As much as 90% of the energy can be enclosed within a beam size of 2.3λ.[16] This means that if the wake diameter is at least this size, very little error can result from waves passing around the wake and interfering with the part transmitted through the wake. Also, since essentially plane-wave conditions exist in the focal region[17] (within depth of field limits), the data interpretation is greatly simplified to that of plane-wave propagation through a slab geometry (not necessarily uniform distribution in the direction of signal propagation).

The output of the circuitry used gives the two quadrature components of the signal transmitted through the wake. These are $A(t)\sin\phi(t)$ and $A(t)\cos\phi(t)$, where $A(t)$ and $\phi(t)$ are the time-varying amplitude and phase change of the transmitted signal. This permits explicit derivation of $A(t)$ and $\phi(t)$ which can be used with a nonreflecting boundary approximation (NRBA) developed by Zivanovic[18] to determine the integrated electron density. This approximation is valid with only about 2% error at densities as high as $n/n_c=0.95$, which is well above density levels where the errors due to refractive deviation of the focused beam become serious. Of course, when $n/n_c \ll 1$ and $\nu_c/\omega \ll 1$, simpler approximations can be used as outlined previously.[11]

The use of the high frequencies of 35 and 70 GHz permit high spatial-resolution measurements along the wake axis and also permit measurements of electron densities as high as 10^{13} e/cm^3. The lower limit is determined by the minimum phase change that can be measured accurately, about one degree in these systems. For a wake one centimeter in diameter this works out to about 10^{11} e/cm^3 for these single-pass systems.

In focusing the beams to these small diameters the probability of

the wake missing the beam due to flight trajectory dispersion becomes serious. This is avoided by setting up a picket of beams as shown in Figure 1, each energized by its own feed system, with adjacent feeds cross-polarized to maintain high isolation between the beams.

Using the measured transmission coefficients obtained from each of the multiple focused beams with the nonreflecting boundary approximation and inversion of the Abel integral, Zivanovic and McLeod[19] have been able to obtain contour maps of electron density distribution in the near wakes of ablating spheres. A problem with this inversion technique is that relative errors in the measured inputs of the multiple beams of the order of 10%, which would be considered excellent for an integrated electron density measurement from one beam, can generate regions of apparent negative electron densities and other anomalies in a contour plot. Therefore, while the technique is fairly straight-forward in principle, the stringent requirements in accuracy of the signals in the various beams make it very difficult to obtain these contour maps in practice except for a relatively select set of conditions.

For routine data reduction, the traces recorded from the beam passing through the wake closest to its axis are processed with a digitized film reader, then through a computer program, to plot $\phi(t)$, $A(t)$, and the integrated electron density $\int_{-\infty}^{+\infty} n_e(r)dr$ (or more simply as $n_e D_p$ where n_e is the electron density averaged over an effective plasma diameter D_p).

2.4 Open-Resonator Technique

A major requirement for these reentry studies is the measurement of wake electron density behind slender nonablating cones fired into air at various pressures. The low initial levels and extremely rapid decay of electron density levels for many of the conditions of interest (in some cases several orders-of-magnitude decay within the resolution length of conventional closed resonators) prompted the development of

the open-resonator technique for wake measurements. This technique has the advantage of high spatial resolution together with good sensitivity. Its open structure (shown in Figure 2) also permits measurements extending to the far wake of spheres as large as 25 mm in diameter with little danger of the growing ionized wake touching the resonator structure. Since the resonator structure is kept far from the wake axis, the effects of the bowshock reflecting back from the structure onto the wake appear to be negligible. Thus this technique meets the requirements of the measurements behind nonablating slender cones and also permit tests of scaling relationships, since wakes behind a wide range in model sizes can be measured. Neither of these two important requirements can be adequately met by the closed-cavity technique, although for small blunt bodies they have provided much useful data.[20]

Various aspects of the microwave open resonators as applied to plasma diagnostics have been reported. This includes the sensitivity improvements possible when compared with nonresonant systems,[21] excitation and measurement of various modes in the resonator,[22] descriptions of operational systems used in transient plasma measurements,[23] analyses of the perturbation of the open resonators by dielectric media,[24] and studies of a quasi-optical imaging resonator with the highly desirable features of high resolution along the wake axis, multichannel measurement of the radial distribution of electron density, good sensitivity, and an open structure.[25]

The resonator systems used in the present measurements have metal reflectors with circular apertures and a spherical radius, with the reflector separation distance d_r set for non-confocal operation. The configuration is shown in Figure 2 with propagation of the signal transverse to the wake axis, which is into the plane of the paper.

A particularly attractive feature of these resonators is that the electric field distribution is very accurately predicted by theory.[22] For

the dominant TEMooq mode used, the field consists of standing waves with peaks at half-wavelength intervals along the longitudinal axis of the resonators between the reflectors, with the longitudinal mode number q referring to the number of peaks. The field transverse to the resonator axis (but along the flight axis) is Gaussian and its envelope to the 1/e power points are shown in Figure 2.

If an ionized wake (dielectric medium) is underdense enough that the electric field in the wake can be approximated (to the first order) by the field in the absence of the wake, then first-order perturbation has been found to apply with good validity . This assumes, of course, that the resonator has been designed so that the desired dominant mode is not degenerate with, nor close to, low-loss higher-order modes into which it can couple energy when perturbed. Loss of energy out of the resonator due to scattering of the wake is also assumed to be negligible. These factors have been analyzed in detail by Auston in Ref. 24.

Applying this first-order theory with the well defined electric field distribution in the resonator, one can readily derive the change in effective dielectric constant $\Delta\epsilon \approx n/n_c$ due to the presence of the wake if one knows or specifies the radial distribution of the electron density across the wake diameter. An effective electron wake diameter D_p must also be defined for a resonator system operating in a single dominant mode, as is the case for the system operating at 35 GHz.

2.5 Measurement of Electron Wake Diameter

It is evident from the above that measurements of the electron wake diameter is highly desirable. Some data on electron wake diameter behind spheres using a closed-cavity technique have been reported.[26] A new technique which shows considerable promise, particularly for measuring the electron wake diameter in the near wake of slender cone models, has just been developed.

Details of this technique are given in a forthcoming report.[27] In brief, two dominant longitudinal, adjacent moades, the TEMo, o, q and TEMo, o, q+1 modes, are excited by two separate sources. In the region near the center of the resonator, the null in the standing wave of the electric field of one mode is filled by the peaks of the other.

When a plasma cylinder is positioned in an accurately known location within the resonator, parallel to the Z-axis, the perturbation recorded by each mode is dependent only on the electric field distribution of that mode because of the frequency separation between the modes. Therefore, by measuring the perturbation recorded from each of the two modes, a measure of the wake diameter can be obtained. Using the value of D_p thus derived, one can reduce the possible errors in the derived quantity for electron density obtained for a single-mode system. In fact, one can then reduce the data in terms of volume, integrated, or line density of electrons.

The accuracy of the method depends on the plasma diameter (useful range about $0.02 < D_p/\lambda < 0.5$), location of the plasma axis relative to the standing waves of the electric field (ideally at $y_o = 0$; $x_o = n\lambda/4$, $n = 0, 1, 2, ---$), and the assumption of radial electron density distribution on the calculated value of D_p

Two of these dual longitudinal-mode resonators operating near 5 GHz are operational and results are currently being obtained with their use.

2.6 Recording Method

For both the single-mode system operating at 35 GHz and dual-mode system operating near 5 GHz, the time-varying amplitude and phase shifts in the signal transmitted through the resonator due to the passage of the ionized wake are recorded on Polaroid film from oscilloscope traces. The data is digitized, and then reduced by computer processing.

2.7 Error Estimates

Errors in the results are of three main types — those associated with the instrumentation, those due to interpretation of the data in terms of a derived quantity for electron density, and those related to the free-flight range.

The possible sources of errors in the focused-probe systems have been examined in some detail. These include imperfect beam collimation, refractive effects, multiple reflections, cross-coupling between beams, and errors due to the finite size of the beam relative to the wake diameter.

Of the above, the most serious possible source of error (providing the wake diameter is approximately equal to the beam diameter and the electron density is about one-tenth critical or less ($n/n_c \lesssim 10^{-1}$) are due to cross coupling between beams and multiple reflections. By cross polarizing adjacent beams, the cross-coupled signal has been reduced but is still high enough to cause possible errors of about 20%. Multiple reflections, particularly those set up due to imperfect matching between the transmitting and receiving horns, can cause errors of about 50%[28] unless care is taken to minimize the mismatch at the feed horns.

If one interprets the measured signal in terms of integrated electron density using Zivanovic's Nonreflecting Boundary Approximations, errors due to interpretation are negligible compared with the possible instrument errors. It is important to note that no assumption has been made of wake diameter or radial electron density distribution in deriving the integrated density.

For the open-resonator systems, the sources of error are more related to interpretation, with errors due to assumptions of radial electron distribution and wake diameter dominating. This assumes, of course, that correct resonator design has been used and that measurements are limited to electron densities such that within the dynamic range of the

resonator in terms of frequency perturbation there are no low-loss higher-order modes into which energy can be coupled. Through the use of mode charts as plotted by Auston[24] and appropriate choice of reflector aperture size, resonator design is quite straightforward.

Comparisons of Gaussian and uniform radial electron density distributions have shown differences of about 15% in the derived quantity. A larger error is possible in the assumption used for wake diameter, which is a necessary input to reduce the resonator data. As seen earlier, this error is largest when $D_p/\lambda < 1$ and measurement of the electron wake diameter by the dual-mode resonator will be particularly useful in minimizing this error. Prior to the use of the dual-mode resonator, errors of 50% were quite possible due to incorrect estimates of wake diameter. If the data is reduced in terms of integrated electron density $n_e D_p$, then errors due to incorrect assumption of wake diameter become negligible when $D_p/\lambda >> 1$.

The major sources of instrument errors in the resonator systems has been vibrations caused by strong bowshocks hitting the reflectors when they are not located far from the flight axis and drift in the resonant frequency of the device between the time of calibration and firing time. The resonator systems installed in the section of the range where the diameter is only two feet are particularly susceptible to vibration problems. Strong bowshocks, generated particularly by blunt bodies fired into high ambient range pressures, limit the useful recording time for these conditions. The newer resonator with a more massive structure and reflectors much farther from the flight axis permits measurements for 20 msec before bowshock problems become evident.

Overriding both the instrument and interpretation errors are the possible errors associated with the free-flight range. This includes the possible effects of model and range contamination and, for slender bodies, the effects of angle of attack and model ablation.

2.8 Range Contamination Effects

Through care in all the range procedures, contamination has been minimized to a degree that consistent results have been obtained on a routine basis.

In monitoring wake electron density levels for an experiment where a large number of spheres were fired at essentially identical conditions (15mm-diameter copper-plated spheres flown at about 6.5 km/sec into 25torr pressure) excellent reproducibility in data was observed. This is shown in Figure 3 where the crosshatched area shows the total spread in data, which is about a factor of two for 14 rounds. Some of this spread is accounted for by the scatter in flight velocity, which ranged from about 6.3 to 6.7 km/sec with most centered near 6.5 km/sec.

Several other rounds which showed evidence of range contamination, as evidenced by anomalous results in radar scattering and radiation data obtained for these rounds, show the type of scatter that can arise in the wake electron density results. Similar results on the effects of contamination have been found at MIT Lincoln Laboratory.[29]

2.9 Model Ablation Effects

For many of the conditions of interest, model ablation is not too serious a problem for the sphere firings when the standard 15mm-diameter copper-plated zelux sphere is used. Since the product of pressure times diameter, pD, is kept constant when binary scaling is used, the range pressure can become quite high for small-diameter models. For a 5mm-diameter copper-beryllium sphere, model ablation can arise at range pressures above 100 torr, depending on the length of the range. The 2.5mm-diameter spheres are made of solid tungsten to permit firings at 150 torr without ablation effects on the model.

Model ablation has been a much more difficult problem for cone firings at velocities near 7 km/sec. Wake electron density data is critically dependent on model integrity.[12] Following a large series of

tests, a nonablating configuration has been developed for our 6.35mm-base-diameter cones. This model, which was used to obtain the cone data to be presented, is shown in Figure 4. The use of tungsten for the tip material provided the greatest improvement in reducing observables due to ablation, as much as two orders of magnitude in the level of wake electron density when compared with a model with a copper tip. Rounding of the base edge and the use of titanium further reduced spurious ablation to the point that, for firings into air at pressures up to 150 torr and velocities near 6.7 km/sec, fairly consistent wake electron density data has been obtained. Slight amounts of ablation still occur, as evidenced by faint lines of tungsten and titanium seen in the spectra, and this may account for some of the scatter in the data.

2.10 Model Angle of Attack

The flight angle of attack of cone models introduces an additional variable. Since the angle of attack is not constant with distance along the flight axis, correlation of data with other observables becomes more difficult. Also, since excessive angle of attack can affect the flow field and onset of turbulence, one can expect some variability in the wake electron levels. The dependence of the wake electron density on the model's angle of attack has not been determined, so the data used here has been arbitrarily restricted to firings which showed an angle of attack less than half of the cone half-angle – that is, $\alpha_{max} < 6.25^{\circ}$ for the 12.5° half-angle cone models.

2.11 Overall Error Estimates

The combined possible errors of instrumentation and interpretation of both the focused probes and resonators is estimated to be of the order of 50%. Errors associated with the range can be much higher than this but, when proper care is taken, data for spheres should be accurate within a factor of 2. For cone models the data can have greater scatter

for the reasons mentioned and the data is estimated to be accurate within a factor of three in absolute leve. An interesting point to note in the slender-cone data is that, while there may be considerable scatter in the absolute level of the wake electron density data, the shape of the electron decay curves for a given condition are very similar.

2.12 Data Presentation

In the results shown, the data is plotted with the integrated electron density $n_e D_p$ $(e/cm^3)(cm)$ vs distance behind the leading edge of the model in normalized distance of body diameter in the case of spheres, and base diameters in the case of cone models. The quantity $n_e D_p$ was chosen for several reasons. First, where binary scaling is valid, the pertinent quantity to use in making scaled comparisons is the integrated electron density.[11] The velocity of the models for the two scale conditions must, of course, be the same to permit the comparison. Second, the data from the focused probe reduces directly to the integrated electron density from the measured phase shift without assumptions of radial density distribution or electron wake width. Third, for the data from the 35GHz Fabry-Perot resonator, the quantity $n_e D_p$ is the least sensitive to assumptions of wake diameter.[23] This was particularly important in minimizing possible error in the results prior to the use of the dual longitudinal mode resonators operating at 5GHz, which can provide wake diameter information for certain conditions but was not available at the time the present data was obtained.

Where the data covers a wide range in electron density, the results shown are based on composite curves obtained from several instruments. An example of how the data from the different electron-density measuring equipment complement each other for a given firing is shown in Figure 5.

3. WAKE MODELS

3.1 Sphere Wake Model

The wake model used to estimate the electron wake diameter is based on Wilson's schlieren observations.[31] For spheres, the effective electron wake diameter growth in the first 100 body diameters is not accurately known. Fortunately, the data in this region is measured by the focused probes where this wake width information is not necessary to reduce the data to integrated electron density. From data obtained to date, it is speculated that the effective electron wake diameter is closely related to the inviscid wake width[26] which is quite clearly defined by density gradients in the schlieren pictures. The inviscid wake diameter grows approximately as $(1-e^{-k\,x/D})$ to a limiting size of about 8 body diameters at a distance of less than 100 body diameters behind the sphere. This diameter is maintained until breakthrough of the inner viscous core through the inviscid wake boundaries occurs, or turbulence develops in the far wake due to inviscid wake boundaries occurs, or turbulence develops in the far wake due to inviscid wake instabilities of the firings where the Reynolds number is below a critical value. Beyond breakthrough or where full turbulence of the whole inviscid wake develops, the wake diameter seen on the schlieren photos grows assymptotically to about $\left[C_D\,(x/d_B)\right]^{1/3}$.

Since the electron density levels were generally quite high in the near wake ($x/D_B < 100$) measurements were usually made with the open resonators well beyond this distance. The electron wake diameter assumed for the deduction of the sphere data was the inviscid wake diameter until either breakthrough occurred or the whole inviscid wake became unstable. The turbulent wake width as defined by Wilson[31] has been used as the effective electron wake diameter for this part of the wake.

3.2 Cone Electron Wake Model

For slender, slightly blunted cones, where the wake observables are dominated by boundary layer effects as opposed to the effects of processing of the gases through the bowshock in the case of blunt bodies, it appears that the ionized species are confined to the viscous wake. A cool inviscid wake which grows rapidly to a limiting size of about four base diameters[32] surrounds this viscous core until either the whole inviscid wake becomes unstable in the far wake for low Reynolds number conditions or a turbulent viscous core breaks through the inviscid boundaries for the higher Reynolds number conditions. After breakthrough occurs or full turbulence is established, the wake growth again quickly approaches the $(C_D\, x/D)^{1/3}$ law.

The growth of the electron wake diameter for the low Reynolds condition where a long laminar run exists has not been establieshed. It is hoped that measurements now being carried out will resolve this question. For the cone wake data presented, the electron wake diameter was assumed constant in the short laminar run observed. Preliminary measurements with the dual mode open resonator have indicated an initial laminar electron wake width of about 0.8 base diameter. Growth of the wake diameter from onset of turbulence to the breakthrough point has been assumed to grow from the initial laminar wake width to the inviscid wake width of four base diameters roughly as $\left[C_D\,(x_o - x_i)/D\right]^n$ where the exponent n is computed to match the boundary conditions.

Once breakthrough occurs or far wake inviscid instabilities develop, the wake growth again approaches a variation like $(C_D\, x/D_B)^{1/3}$ The wake width as observed by Wilson has been used to reduce the data obtained from the open resonator systems.

4. RESULTS AND DISCUSSIONS – NONABLATING SPHERE

4.1 Near-Wake Ionization

Near-wake ionization data out to 100 to 200 body diameters has been presented previously,[11] but not published. For completeness, one example which has features that are unusual and appear to be explicable according to the present investigation will be repeated here.

For instance, in Figure 6 we see that electron density increases monotonically with pressure in the near wake, but beyond some point along the axis the trend is actually reversed. It will be seen in the next section that this can now be explained in terms of the development and rapid growth of the turbulence in the viscous wake close to the sphere at the higher pressures.

4.2 Scaling of Near-Wake Ionization

At low enough pressures the main ionizing and electron removal mechanisms are expected to be governed by two-body reaction processes and consequently wake ionization should scale in a binary manner. That is, if the product of ambient pressure and sphere diameter is held constant then the electron density integrated along a wake diameter at some fixed distance behind the body (measured in body diameters), should remain invariant.

A result where binary scaling is effective is shown in Figure 7. At a significantly higher pressure departures from binary scaling are noted (Figure 8). It is of interest to note that for the first case, Eschenroeder[2] has calculated that about 90% of the gas processes through the stagnation region achieves equilibrium there, indicating that the flow can pass through regions which are very nearly in chemical equilibrium and still exhibit ionization scaling. When equilibrium regions become very extensive, the susceptibility of near-wake ionization to binary scaling becomes invalid. Indications of this breakdown in scaling are

seen in the second case above where about 99% of the nose-cap is in equilibrium.

Figure 9 shows a recent result for copper spheres of 5 and 15mm diameter launched at 6.5 km/sec and pD - 375 torr-mm. For this firing condition, transition to turbulence occurs at about x/D - 10 and breakthrough at x/D-150. The good agreement in binary scaling up to 1000 body diameters where turbulence is well established might be explained by one or both of two possible reasons. The first is that homogeneous mixing does not take place at the turbulent front but develops gradually in a manner similar to the eddy diffusion model proposed by Wen, et al[8] for cone wakes; therefore, three-body attachment type reactions that depend on cooling of the wake with mixing and which would cause departure from binary scaling take much longer to become effective. This is seen more clearly in a later discussion. Another possibility is that some competing chemical reactions dominate over the attachment reactions to extend the region of binary scaling.

4.3 Effect of Fluid Dynamics on Wake Ionization

With the microwave instrumentation used to measure electron density, time variations in the output signal due to turbulent electron density fluctuations are too small to be detected, so that the presence of wake turbulence cannot be detected. Also, at high Mach numbers flow visualization techniques, for example schlieren photography, could not be used to detect turbulence in the near wake because of the screening effect of the hot inviscid wake. Thus, it was not clear how wake ionization decay was influenced by the onset and growth of turbulence.

More recently, however, Wilson, using schlieren observations of wake phenomena behind nonablating hypersonic spheres in air, has developed a comprehensive qualitative description of wake structure.[3] Comparison of ionization data with this model now shows quite clearly

how wake electron density decays are associated with individual fluid dynamical features.

Electron densities behind 5mm diameter copper spheres are shown in Figure 10, for three different pD values. Reference to Wilson's model will show that, for pD - 75 and 150 torr-mm, the inner wake does not go turbulent (since in each case the ambient Reynolds number is less than Lees critical value) but that the inviscid wake does go unstable and becomes turbulent at x/D of about 5000 and 2000. It is clear that the ionization decay now increases rapidly from the relatively slow laminar values, presumably due to sharply increased mixing rates of the inviscid wake with cold surrounding gas. At pd = 375 torr-mm the inner wake has gone turbulent close to the body and grows until it breaks through the inviscid layer at about x/D=150. It will be noted that the electron density decay increases rapidly beyond this point, again presumably due to mixing with cold air. It will be shown in the next section how these observations have been used to examine and improve the analytical model of wake ionization.

Another example of a laminar wake is shown in Figure 5 where a 2.5mm diameter copper sphere was fired at 10 torr. For this condition schlieren results showed that the inviscid wake became unstable at about 7000 body diameters. Since the inviscid wake is essentially constant in diameters beyond 100 body diameters behind the body to the point of inviscid instability, the decay rate seen in the plot of integrated electron density with distance appears to be due largely to dissociative recombination. Once the inviscid wake breaks up, we again see the very rapid decay of the wake electron density.

An example of a firing at very high Reynolds is shown in Figure 11. For this case a 15mm diameter copper-plated sphere was flown at 4 85 km/sec into 150-torr air. Transition to turbulence developed very close to the body and the effect of turbulent mixing on the decay rate up to the

point of breakthrough at 150 body diameters when compared with a laminar wake in this region can be seen. Beyond breakthrough we see a rapid change in the decay rate as cold air is mixed into the wake.

While breakthrough occurs at about the same distance behind the body (in body diameters) as for the pD - 375-torr-mm case, the rapid fall off in electron density occurs considerably earlier for the pD= 2250-torr-mm case. This might be expected because of the rapid mixing with cool surrounding gas which has a higher concentration of oxygen than for the lower pD case. The lower wake temperature resulting from the lower velocity firing also permits the attachment reactions to become effective earlier.

5. COMPARISON OF SPHERE DATA WITH THEORY

5.1 Near Wake ($x/D \lesssim 200$)

Electron density levels in the near wake of spheres calculated by Eschenroeder and Chen[33] using the inviscid random convection model in the quasi-one-dimensional approximation suggestion by Lin and Hayes[34] showed quite good agreement with the measured data.[34] The conditions covered a range in pressure-diameter product (pD) of 45 to 1500 torr-mm and flight velocities of 5.5 to 6.7 km/sec. Besides the usual neutral particle species the only reaction considered for electrons was $N + O \rightleftarrows NO^+ + e^-$.

While the integrated electron density appears to be fairly insensitive to the degree of mixing in the near wake for the lower pD values, at the very high pD values (pD = 1500, 2200) where transition occurs right near the sphere and turbulence develops very rapidly, a significant increase in the electron density decay rate prior to breakthrough. This can be seen by referring to Figures 6 and 11.

5.2 Extension to Far Wake (pD = 375 torr-mm)

In extending the calculations to the far wake the analytical model

employed for this case (5mm diameter copper sphere, 75 torr air, 6.25 km/sec) is similar to the quasi-one-dimensional treatment proposed by Lin and Hayes.[34]

The calculations by J. P. Appleton and C. C. Yang[35] shown in Figure 12 start immediately behind the bowshock wave and extend around the body into the far wake (greater than 1000 x/D) taking into account the chemical non-equilibrium character of the flow by a consideration of the major neutral and ionizing reactions associated with air chemistry. Instead of the patched Newtonian blast-wave constant pressure variation assumed for the near-wake calculations,[33] the stream-tube pressure distributions, which are an a priori requirement of the quasi-one-dimensional treatment, were obtained from inviscid solutions of the flow field around suitably chosen sphere-cone body combinations in which the assumption of complete chemical equilibrium was made.[37]

In each calculation the line integral of the electron density across the wake, this being the proper quantity for comparison with the microwave and cavity measurements reported here, was evaluated as a function of distance behind the body for the two extreme models of turbulent mixing proposed by Lin and Hayes, (i.e., inviscid random convection and homogeneous mixing). Both models gave results which were in close agreement with one another and with the experimental measurements in the near wake (approximately less than 100 x/D); a result which was to be expected provided the calculations used the correct chemical model, since the extent of the turbulent central core is only a relatively small proportion of the hot inviscid laminar wake in the near-wake region. However, as the calculations proceeded into the far wake (greater than 200 x/D) the agreement between the two mixing models became progressively worse. The inviscid random convection model, which does not allow any intimate turbulent mixing between the hot central wake and the cool ambient gas surrounding it, resulted in

electron densities which were too high in the far wake. On the other hand, the homogeneous mixing model gave electron densities which were too low in those calculations which used measured values for the growth of the turbulent front.[31] It was apparent that in this case the far-wake temperature fell too rapidly, thus resulting in excessively fast removal rates of the free electrons, first by dissociative recombination with the nitric oxide ion and subsequently by attachment to the oxygen molecule. However, further calculations carried out using the homogeneous mixing model with the assumption that the width in the turbulent wake region over which the flow was intimately mixed was approximately half the wake width as observed by schlieren photography,[31] gave good agreement with the experimental measurements over distances in excess of 1000 x/D. Clearly, such a technique is highly empirical, but must surely be justified by its relative simplicity and the results that it yields.

5.3 Long Laminar Wake (pD = 150 torr-mm)

While the quasi-one-dimensional model provides an excellent means of checking various analytical models, axisymmetric finite difference calculations can provide more detail of the wake flow field. Figure 13 shows the electron density curve calculated by Wen and Chen[2] compared with the experimental result. The separation between the two curves can be attributed to the velocity difference and when this is taken into account, the agreement is very good. For this firing condition the wake is laminar to about 2000 body diameters before instabilities occur and hence provides a good test of the kinetics used in the calculations.

6. RESULTS—CONE-WAKE IONIZATION

A few examples of the wake electron density measurements which have been obtained are summarized in Figure 14. All the results are

for cones with a 12.5° half angle, 6.35mm base diameter, nose-to-base radius ratio of 0.06, with tungsten tip and with copper-plated aluminum or plain titanium afterbody as detailed in Figure 4. The nominal velocity for the firings was 7.0 km/sec.

6.1 20-torr Air

The wake for the firing at 20-torr air was laminar, as seen by schlieren up to 100 body diameters.[32] The wake decay is very gradual following a fairly slow temperature change along the wake axis.[2] The dominant electron removal process for this case is the recombination of $NO^+ + e^- \rightleftarrows N + O$.

The laminar wake case is much simpler to calculate and the comparison of data for 20-torr air is shown in Figure 15 with the curve calculated by Wen and Chen[2] using their axisymmetric finite difference analysis. Only seven species (N_2, O_2, N, O, NO, NO^+, and e^-) are considered in their kinetic model. The agreement between the two curves is quite good, indicating that the wake model used is adequate in predicting the observed wake electron density levels for this condition. The slightly slower decay of the calculated curve beyond 50 body diameters is likely due to omission of attachment reactions.

6.2 75-torr Air

For this case the viscous wake shows first instabilities at about 30 body diameters; however, turbulence develops gradually with a fairly regular sinusoidal pattern up to about 50 body diameters before a fully turbulent flow is seen. Calculations by Wen[8] have shown that at 75 torr a laminar wake has an ionization decay rate very similar to that at 20 torr. Therefore, the marked change in slope between the 20-torr and 75-torr case in the near wake appears to be the result of turbulent mixing in the 75-torr wake. This point will be discussed further in the next section.

6.3 75-torr Nitrogen

The firing into nitrogen results in a much simpler chemical history in the wake while preserving essentially similar gross fluid mechanical features in wake such as transition distance to onset of turbulence and the development of turbulence. While a somewhat higher wake temperature might be expected for the nitrogen case due to the absence of O_2 dissociation, the major difference in the ionization decay rate between the 75-torr air and 75-torr nitrogen case is evidently due to oxygen and its various reaction species in removing the electrons in the air case by recombination and attachment reactions.

7. DISCUSSION OF CONE-WAKE IONIZATION

In the early results obtained for 75-torr air, the wake ionization decay rate seemed to correspond to a decay rate for electron attachment to molecular oxygen at 1000°K temperature using a reaction rate assumed by Lees.[37] Calculations by Wen have shown that with a laminar wake, the axis temperature would not decay sufficiently to permit this reaction to be effective.

The previously assumed model of the cone wake resulted in calculated electron density curves which showed poor agreement with theory.[5, 6, 7] The main difficulty appears to be the use of a constant value of the coefficient in the eddy viscosity coefficient. This results in an initial precipitous drop in electron density, and axis temperature, and in explosive growth in wake diameter which is much more rapid than actually observed.

The wake model proposed by Wen in which he uses a variable coefficient $K(x)$ appears to be more realistic in that it more closely represents observations in that turbulence grows gradually and the calculated wake growth and the electron density decay agree well with experimental data.

Figure 16 shows a comparison of experimental data with theoretical calculations which are described in detail elsewhere. In brief, three of the curves were computed with seven species (N_2, O_2, N, O, NO, NO^+, and e^-) and same initial conditions but different eddy diffusion models. With the laminar wake, the electron density decay is slow as might be expected. When a constant value of K is used in the eddy diffusion coefficient, the electron density drops precipitously at transition but eventually would level off to a decay rate similar to the laminar condition.

The proposed model which uses a variable coefficient $K(x)$ which varies from an initial value corresponding to an average value for the laminar diffusion coefficient at the point of instability to an assumed value $K_T = 0.02$, where full turbulence is assumed. In the first case, the distance for full turbulence to develop was assumed to be 100 body diameters. The decay curve falls between the laminar and "turbulent" case and shows reasonable agreement with the data.

When the assumed distance to turbulence is assumed to be 200 body diameters and additional species are included, the agreement between the calculated and experimental curves (case II) is excellent.

8. CONCLUDING REMARKS

The wake electron density measurements which have been presented for sphere and cone models have demonstrated the very close coupling between the electron density decay rate with gross fluid mechanical features of the wake such as laminar, unstable and turbulent regions, and effects of inviscid instability on breakthrough.

The better understanding of the wake resulting from these correlations has resulted in improved flow field models which more realistically reflect the measured data.

A few examples of the development of improved analytical models for both spheres and cones have been shown. The value of the relatively simple quasi-one-dimensional approach in testing various mixing models and chemistry on the wake electron density behind spheres with considerable economy in computer time has been shown. Wen and Chen have used the axisymmetric finite difference analysis which provides detailed descriptions of the wake flow field and has shown good agreement for the laminar wakes of spheres and slender cones. Wen has proposed an eddy diffusion model with variable coefficient to describe the transitional region between onset of instabilities and the development of full turbulence in the viscous wake of cones. This has resulted in greatly improved agreement between theory and data for both wake growth and electron density decay. Wen is currently extending this approach to the turbulent near-wake analysis of blunt bodies.

A growing body of data is being accumulated on the effects of various parameters on the wake electron density levels. Current programs include a more extensive study of electron removal mechanisms in the far wake of spheres for a wide range in sphere sizes (2.5 to 25mm diameter). The effects of cone geometry, size, material, range pressure and gas composition on electron density levels are also continuing. Close and continual feedback between the theoretical and experimental efforts are resulting in a better understanding of complex phenomena in the wake.

REFERENCES

1. A. Q. Eschenroeder and R. A. Hayami, "Scaling Experiments on Wake Ionization Behind Non-Ablating Hypersonic Spheres," GM Defense Research Laboratories, Report TR64-02L, Santa Barbara, Calif., Nov 1964

2. K. S. Wen and Tung Chen, "Preliminary Theoretical Results of Laminar Wake Ionization Behind Hypersonic Spheres and Cones," GM Defense Research Laboratories, Report TR66-22, June 1966

3. R. I. Primich, R. A. Hayami, J. P. Appleton, "Wake Ionization Behind Non-Ablating Hypersonic Spheres in Air," Unpublished Work, GM Defense Research Laboratories, Aug 1966

4. R. A. Hayami, D. H. Auston, K. J. Kelley, and J. R. Faulkner, "Fabry-Perot Resonators at 5 Gc and 35 Gc for Wake Ionization Measurements in a Free-Flight Ballistics Range," GM Defense Research Laboratories, Report TR65-19B, Santa Barbara, Calif., March 1965

5. J. Erdos, H. Lien, R. Weiss, and A. Pallone, "Theoretical Calculations and Comparison with Electron Density from Ballistic Ranges (U)," AMRAC Proc., Vol. XI, Pt. 1, Nov 1964, p. 111

6. S. L. Zeiberg and W. Daskin, "Comparison of Theoretical Predictions of Wake Electron Density with Ballistic Range(U)," AMRAC Proc., Vol. XI, Pt. 1, Nov 1964, p. 81

7. R. H. Edsall and W. T. Langan, "Theoretical Calculations and Comparison with Electron Density from Ballistic Ranges (U)," AMRAC Proc., Vol. XI, Pt. 1, Nov 1964, p. 101

8. K. S. Wen, Tung Chen, R. A. Hayami and R. I. Primich, "An Eddy Diffusion Model for Predicting Rapid Wake Ionization Decay Behind Hypersonic Cones," AIAA 5th Aerospace Sciences Meeting, New York, Jan 1967, Pre-print 67-21

9. "Aerospace Research Capabilities," GM Defense Research Laboratories, Report TR63-223, April 1963

10. A. C. Charters and J. S. Curtis, "How an Accelerated Reservoir Light-Gas Gun is Used in a Hypervelocity Free-Flight Range," GM Engineering Journal, Second Quarter, GMC, 1963

11. A. Q. Eschenroeder, R. A. Hayami, R. I. Primich and T. Chen, "Ionization in the Near Wakes of Spheres in Hypersonic Flight," AIAA Paper No. 66-55, Jan 1966

12. R. I. Primich, M. Steinberg, L. N. Wilson, R. A. Hayami, E. W. Evans, P. E. Robillard, and I. Liu, "Effect of Ablation Material and Nose Bluntness on Observables from a Slender Cone in a Free-Flight Range," GM Defense Research Laboratories Report TR64-60, Dec 1964

13. R. I. Primich and R. A. Hayami, "Millimeter Wavelength Focused Probes and Focused, Resonant Probes for Use in Studying Ionized Wakes Behind Hypersonic-Velocity Projectiles," Paper presented at Millimeter Wave Symposium, Orlando, Florida, January 1963; also, GM Defense Research Laboratories Report TR63-217C, July 1963

14. R. I. Primich, D. H. Auston, R. A. Hayami, J. D. McLeod and S. Zivanovic, "Two New Techniques for Determination of Transient Plasma Properties," Proc. of the Seventh International Conference on Phenomena in Ionized Gases, Beograd, 1966

15. P. L. Clemens, "The Von Karman Gas Dynamics Facility 1000-ft. Hypervelocity Range- Description, Capabilities and Early Test Results," AEDC TR-66-197, Nov 1966

16. R. I. Primich and F. H. Northover, "Use of Focused Antenna for Ionized Trail Measurements: Pt. I, Power Transfer Between Two Focused Antennas," IEEE Trans., AP-11, March 1963, p. 112

17. G. W. Farnell, Canadian Jour. Physics 35 (1957) p. 780

18. S. V. Zivanovic, H. M. Musal and R. I. Primich, "Determination of Plasma Layer Properties from the Measured Electromagnetic Transmission Coefficient," IEEE Trans., AP-12, Sept 1964, p. 618

19. S. Zivanovic and J. McLeod, "A Method for Determining Profiles of Radial Electron Density and Collision Frequency in the Wakes of Hypersonic Projectiles Using Transverse Microwave Probes," GM Defense Research Laboratories Report TR64-02M, Dec 1964

20. W. M. Kornegay, "Electron Density Decay in Wakes," AIAA Journal, Vol. 3, No. 10, Oct 1965, p. 1819

21. R. I. Primich and R. A. Hayami, "Application of the Focused Fabry-Perot Resonator to Plasma Diagnostics," IEEE Trans., Vol. MTT-12, Jan 1964, p. 33

22. D. H. Auston, R. I. Primich and R. A. Hayami, "Further Considerations of the Use of Fabry-Perot Resonators in Microwave Plasma Diagnostics," Proc. Quasi-Optics Symp., Polytechnic Press, Polytechnic Institute of Brooklyn, June 1964, p. 273

23. R. A. Hayami and K. J. Kelley, "The Measurement of Transient Ionization Levels Using Open Microwave Resonators," Proc. of 2nd International Congress on Instrumentation in Aerospace Simulation Facilities, Stanford University, Aug 1966; also, GM Defense Research Laboratories Report TR66-01K, July 1966

24. D. H. Auston, "A Perturbation Theory for Open Resonators, Part I, II, and III," GM Defense Research Laboratories Report TR66-55, Oct 1966

25. D. H. Auston, "A Quasi-Optic Imaging Resonator for Plasma Diagnostics," Proc. 2nd Int. Congress on Instrumentation in Aerospace Simulation Facilities, Stanford University, Aug 1966

26. W. G. Clay, M. Labitt, R. E. Slattery, "Measured Transition from Laminar to Turbulent Flow and Subsequent Growth of Turbulent Wakes," AIAA Journal, Vol. 3, No. 5, May 1965, p. 837

27. R. A. Hayami, K. J. Kelley, and R. I. Primich, "A 5 GHz Dual Longitudinal Mode Open Resonator for Hypersonic Wake Electron Density Measurements," GM Defense Research Laboratories (to be published)

28. K. E. Lonngren, "On the Interpretation of Multiple Reflections in Microwave Interferometers Used in Plasma Diagnostics," Japanese Journal of Applied Physics, Vol 5, No 3, Mar 1966, p 223

29. R. E. Slattery, W. G. Clay and W. C. Worthington, "Range Contamination and its Effects on Measurements," Proc. 2nd Int. Congress on Instrumentation in Aerospace Simulation Facilities, Stanford Univ. Aug 1966

30 M. Steinberg and I. Liu, Private Communication

31. L. N. Wilson, "The Far-Wake Behavior of Hypersonic Spheres," GM Defense Research Laboratories Report TR66-19, June 1966. Also, Preprint No 67-31 to the 5th AIAA Aerospace Sciences Meeting, New York, Jan 1967

32. L. N. Wilson, "Far Wake Behavior of Hypersonic Blunted Cones," GM Defense Research Laboratories Report TR66-80, Dec 1966

33. A. Q. Eschenroeder and T. Chen, "Ionization Behind a Sphere in Hypersonic Flight Part I. Near Wake Theory," AIAA Jour. Vol 4, No 12, Dec 1966, p 2149

34. S. C. Lin and J. E. Hayes, "A Quasi-One-Dimensional Treatment of Chemical Reactions in Turbulent Wakes of Hypersonic Objects," AIAA Journal 2, 1212-1222 (1964)

35. J. P. Appleton and C. C. Yang – Work to be published as AC-DRL Technical Report

36. R. A. Hayami and R. I. Primich, "Integrated Electron Density in the Near Wakes of Hypersonic Velocity Spheres," GM Defense Research Laboratories TR65-01F, May 1965

37. E. Lieberman, "Computer Programs and Analysis for Flow Fields About Bodies in Hypersonic Flight – Air in Chemical Equilibrium and Frozen Flow Chemistry," GASL TR-460, Sep 1964

38. L. Lees,. "Hypersonic Wakes and Trails," AIAA J., Vol. 2, 1964, pp 417-428

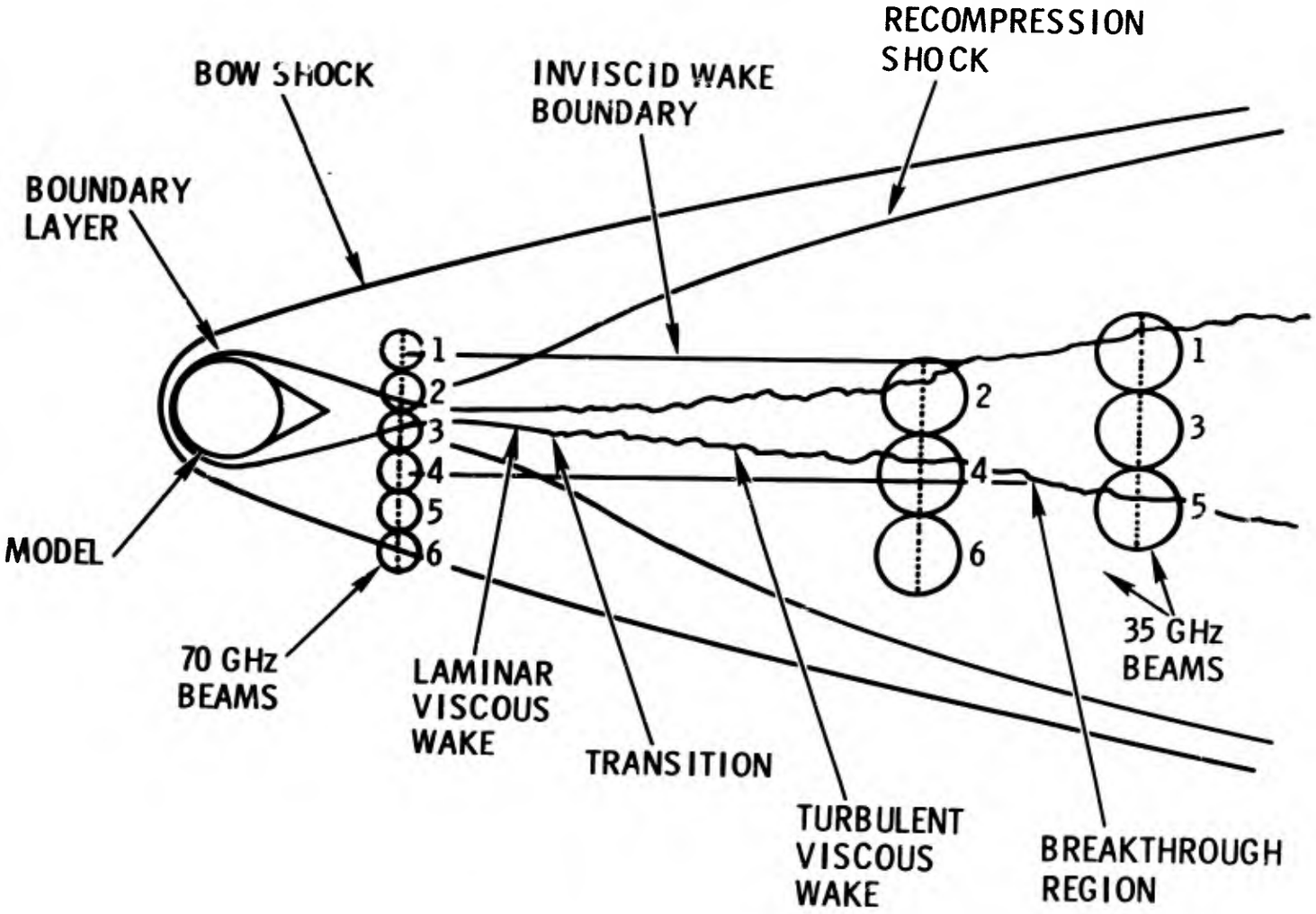

Figure 1 IDEALIZED LOCATION OF FOCUSED BEAMS IN A SPHERE WAKE

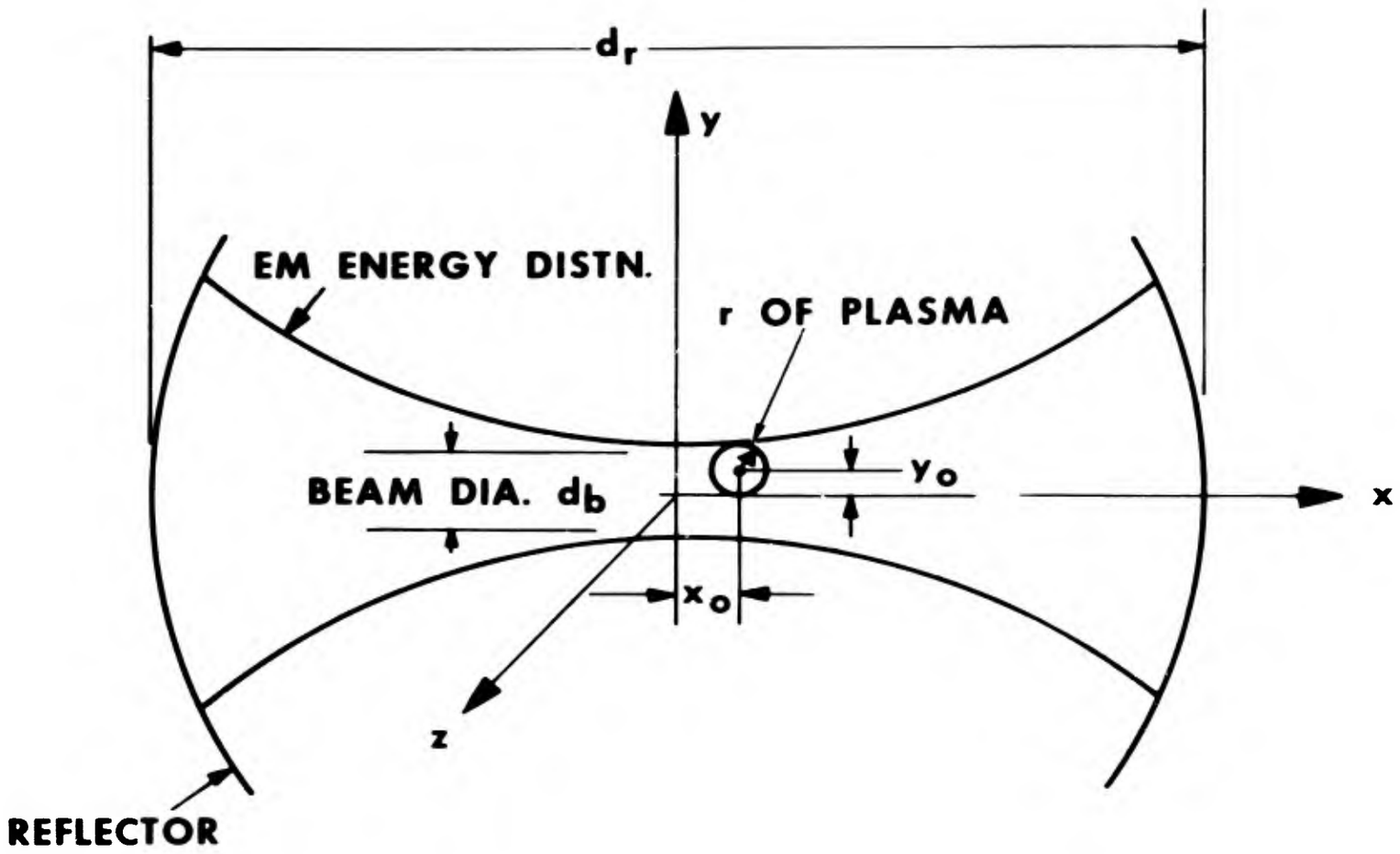

Figure 2 SCHEMATIC VIEW OF OPEN-RESONATOR GEOMETRY

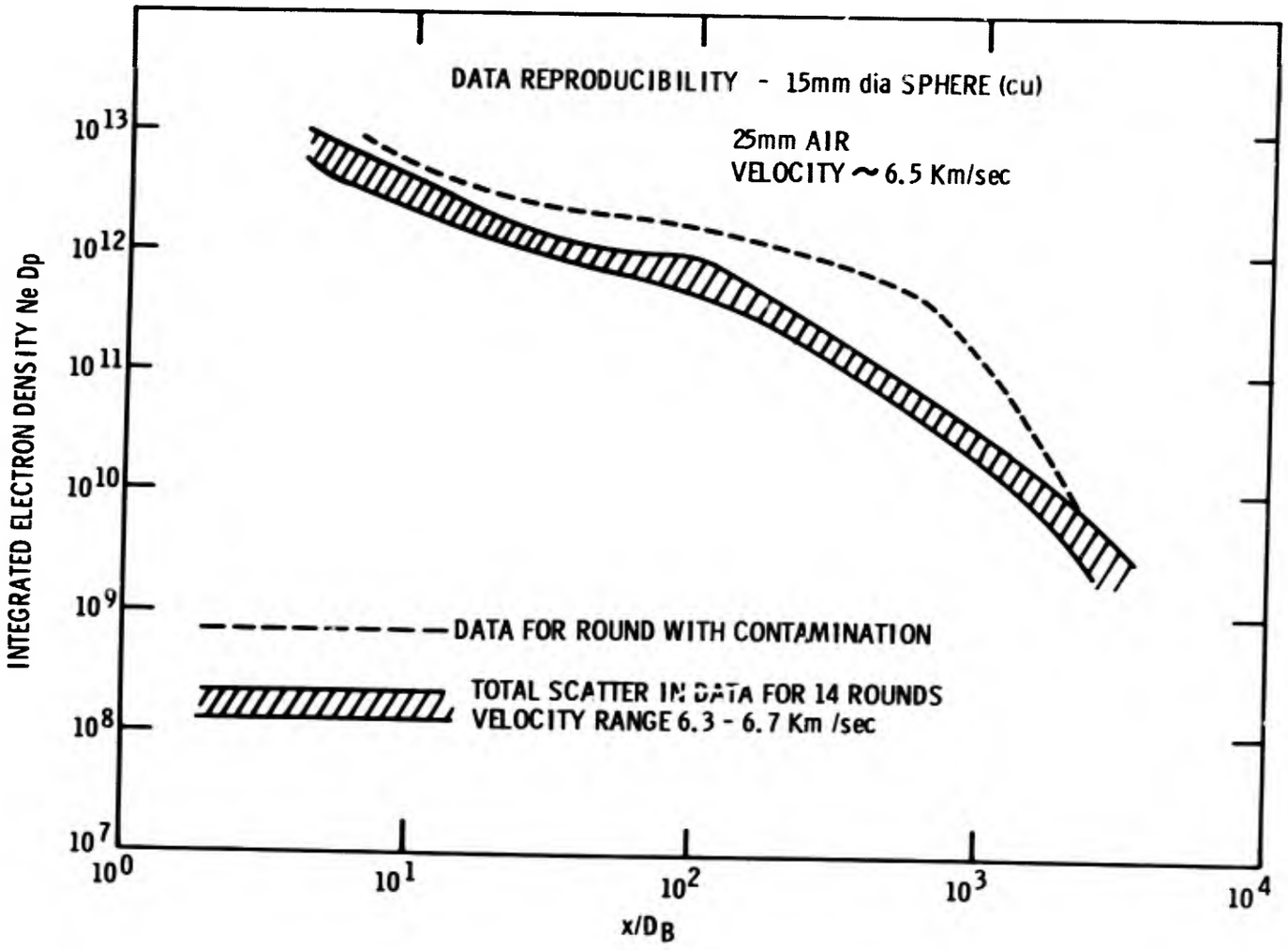

Figure 3 SPHERE WAKE IONIZATION DATA REPRODUCIBILITY

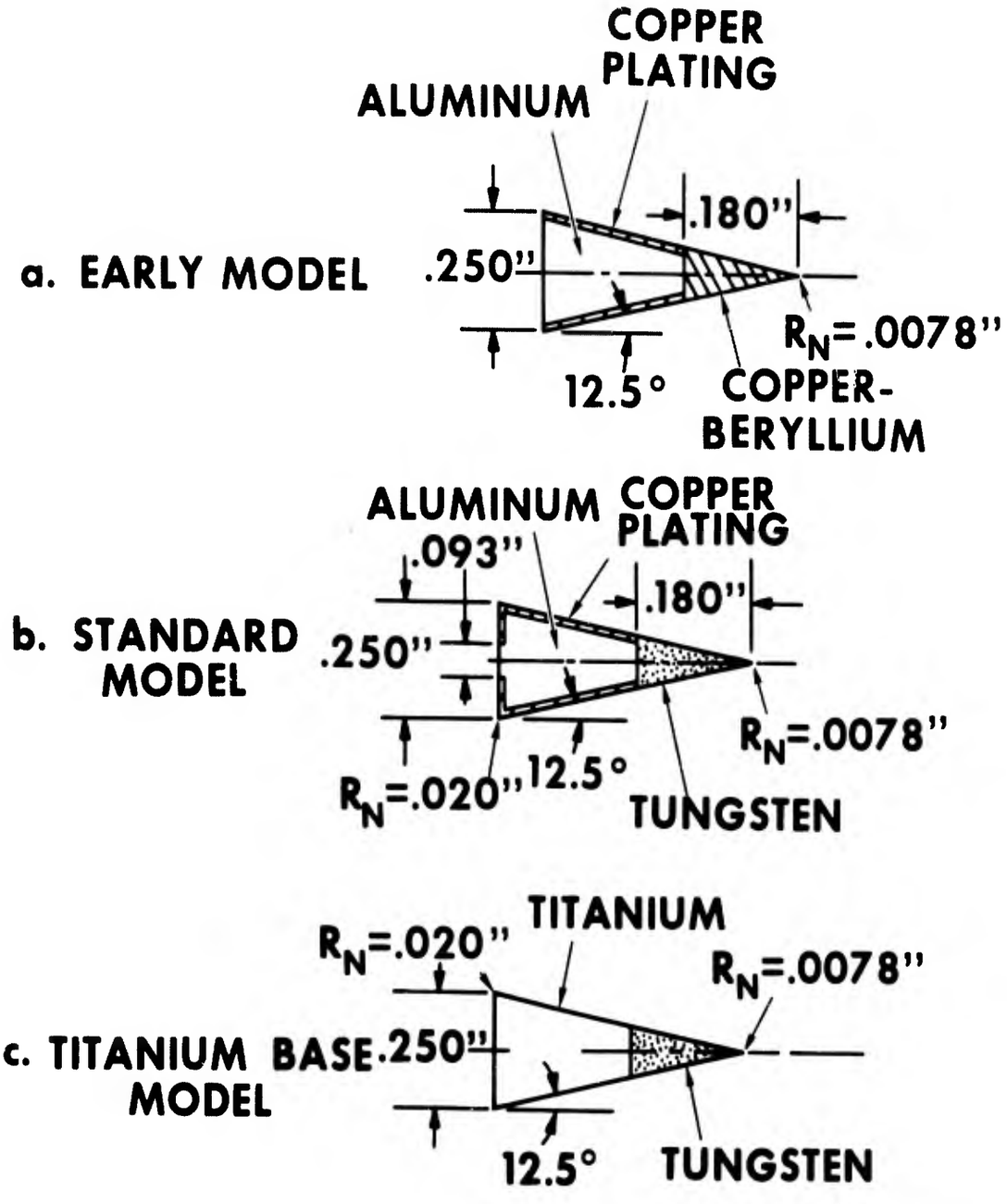

Figure 4 CONE MODEL CONFIGURATIONS

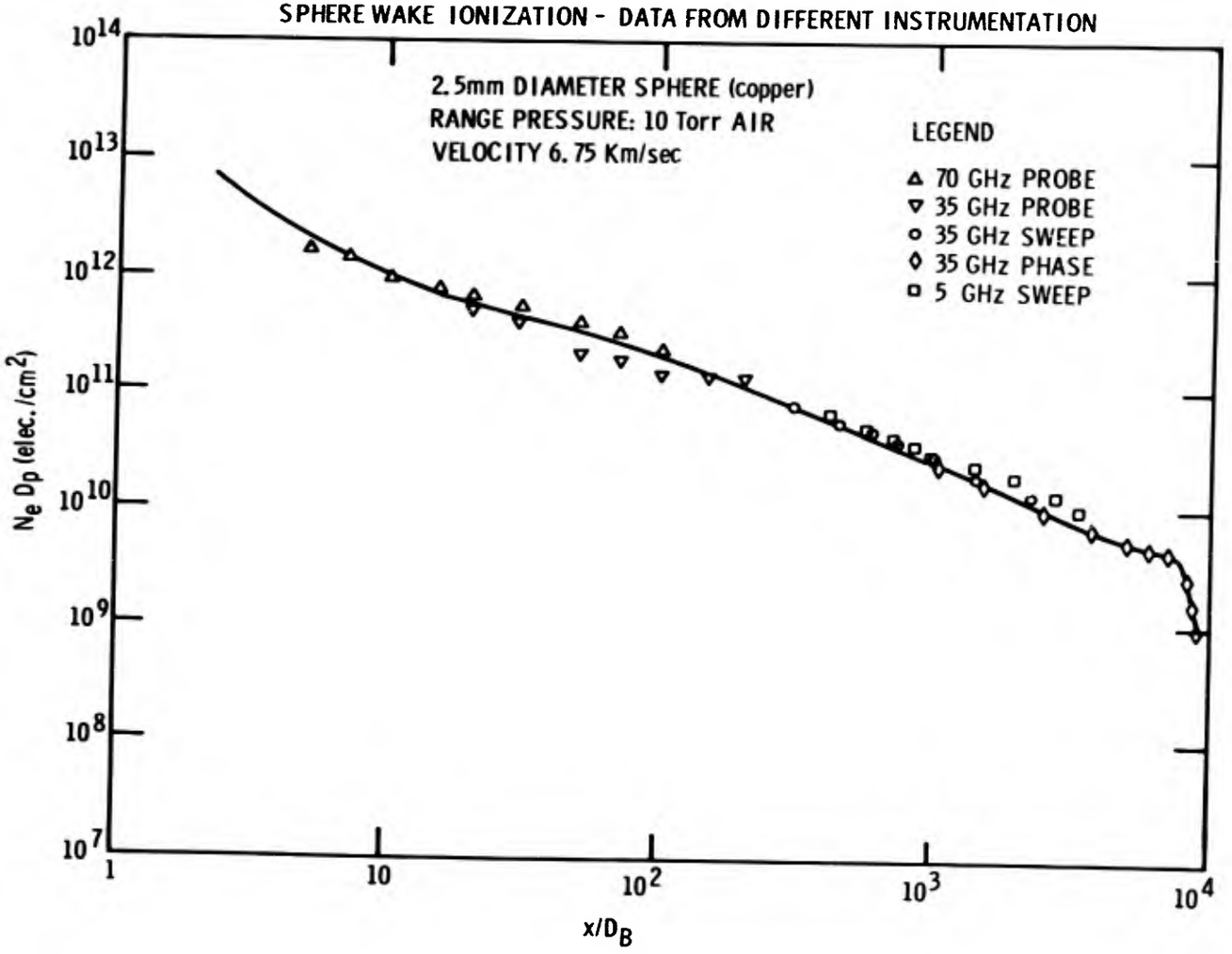

Figure 5 COMPOSITE DATA FROM SEVERAL INSTRUMENTS FOR A SINGLE FIRING

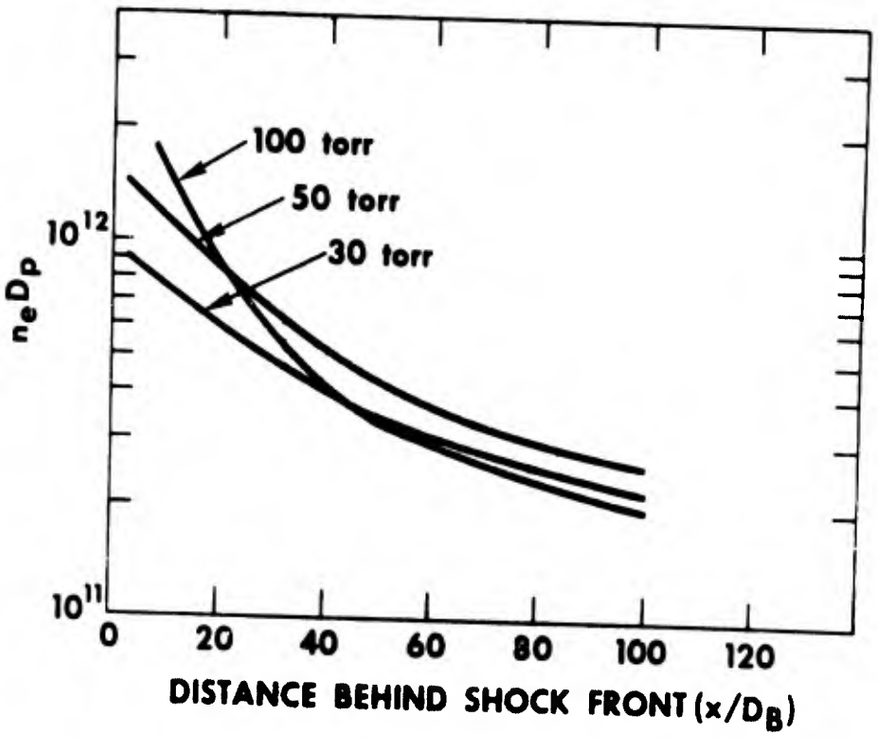

Figure 6 PRESSURE DEPENDENCE IN THE NEAR WAKES OF SPHERES

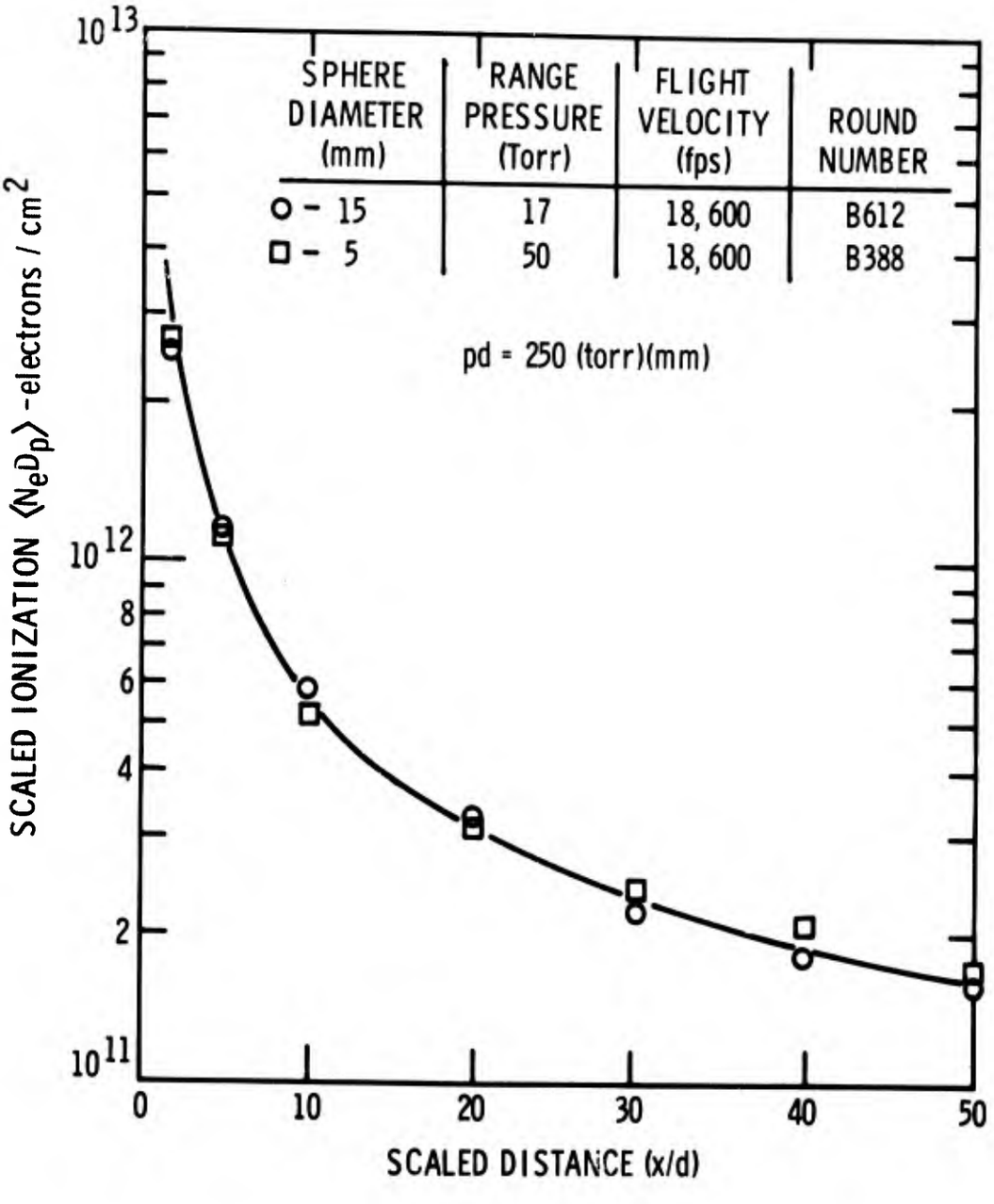

Figure 7 BINARY SCALING OF IONIZATION IN THE NEAR WAKE OF SPHERES, pD = 250 torr-mm

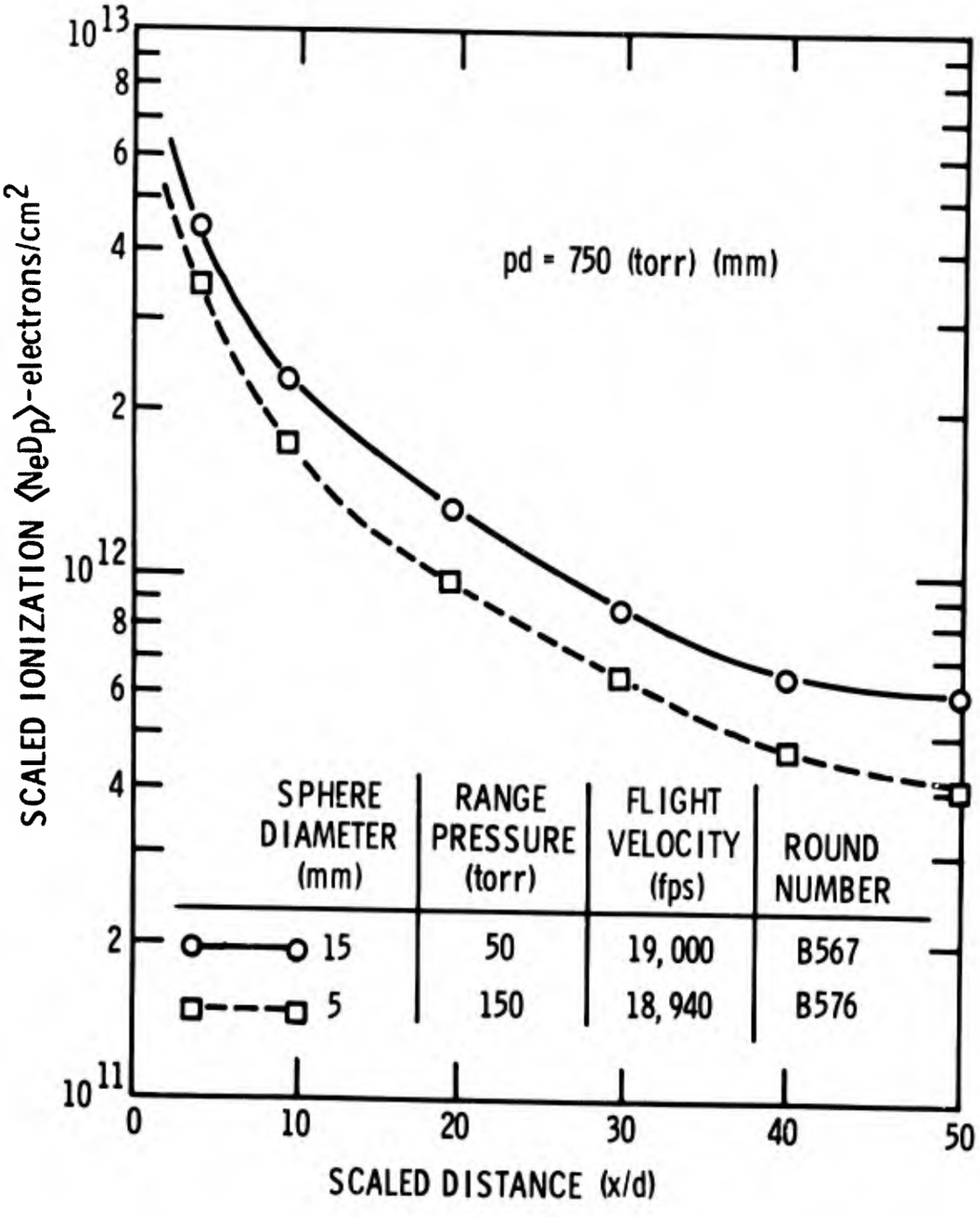

Figure 8 BREAKDOWN OF BINARY SCALING IN THE NEAR WAKE OF SPHERES, pD = 750 torr-mm

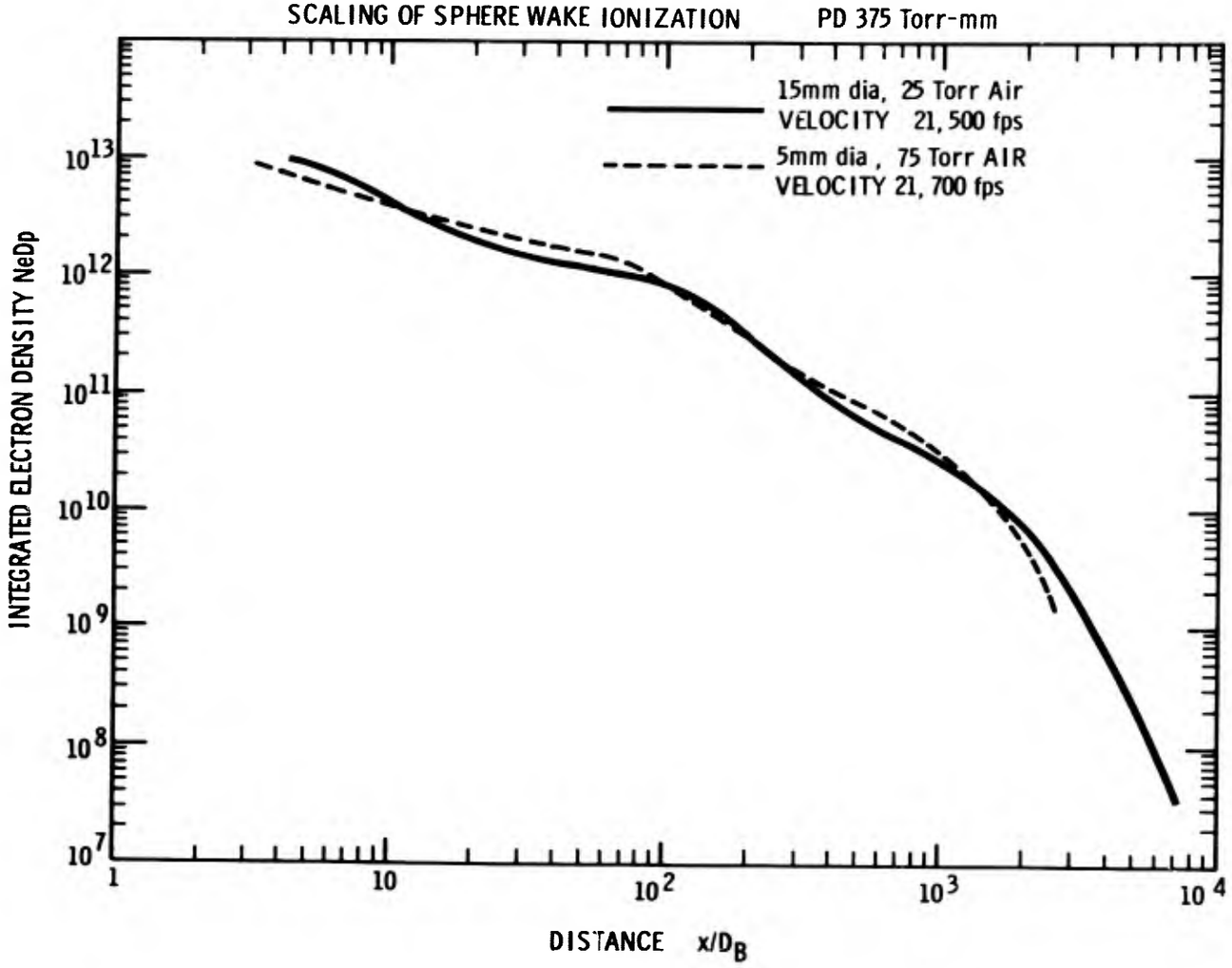

Figure 9 EXTENSION OF BINARY SCALING TO THE FAR WAKE, (pD = 375 torr-mm)

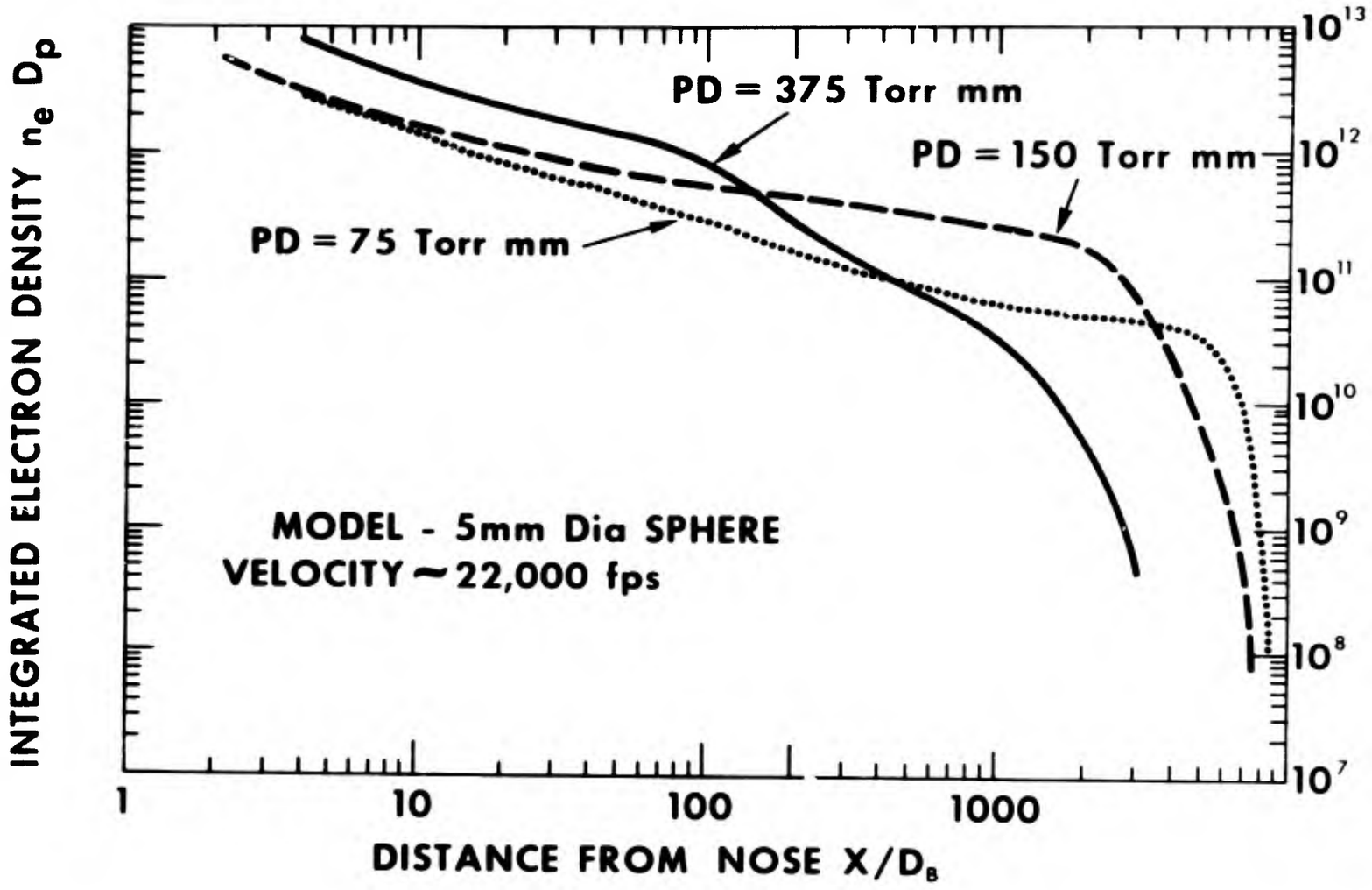

Figure 10 EFFECT OF FLUID DYNAMICS ON WAKE IONIZATION BEHIND SPHERES (PRESSURE DEPENDENCE)

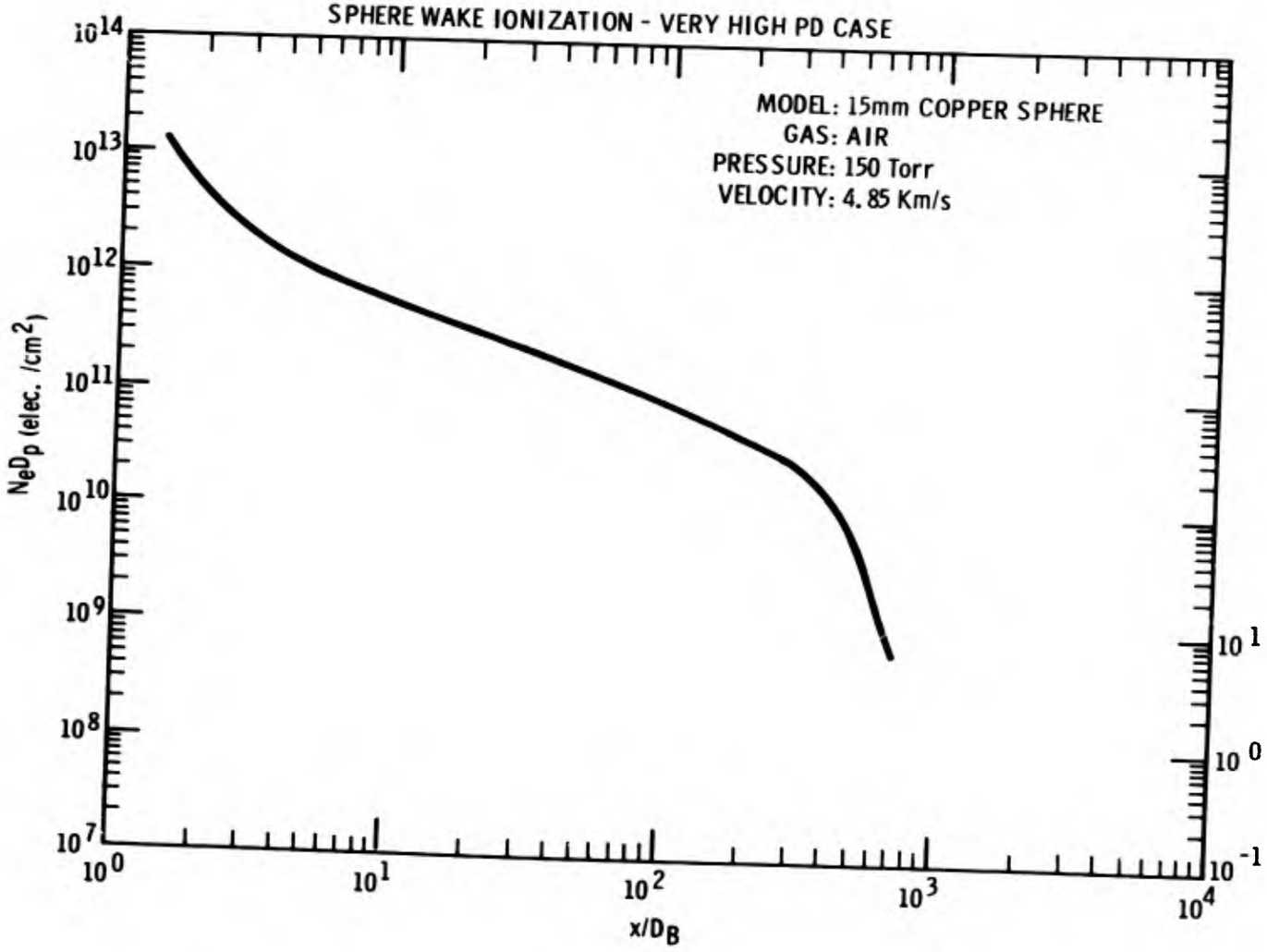

Figure 11 SPHERE WAKE IONIZATION, pD = 2250 torr-mm

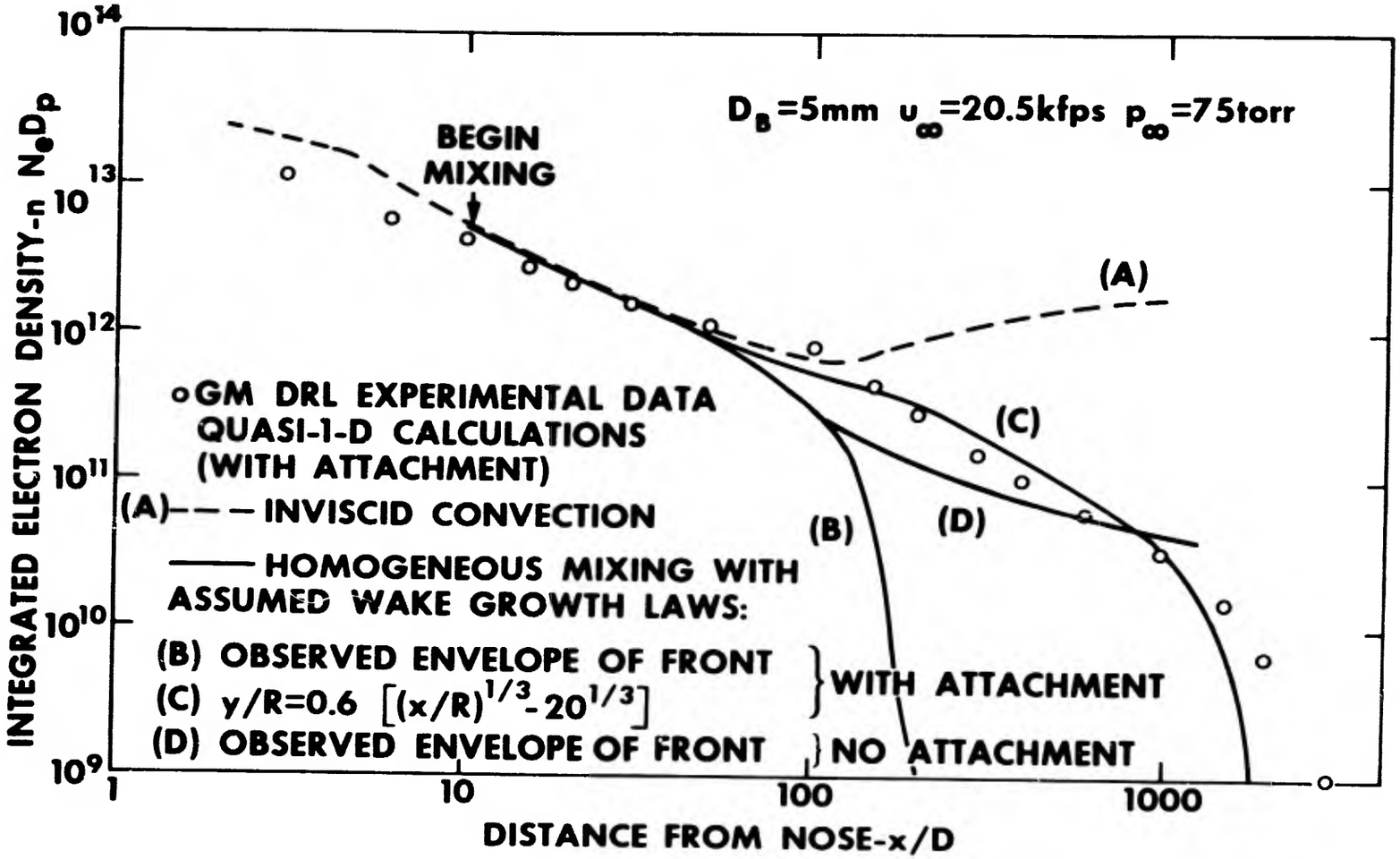

Figure 12 COMPARISON OF SPHERE WAKE IONIZATION DATA WITH CALCULATIONS, pD = 375 torr-mm

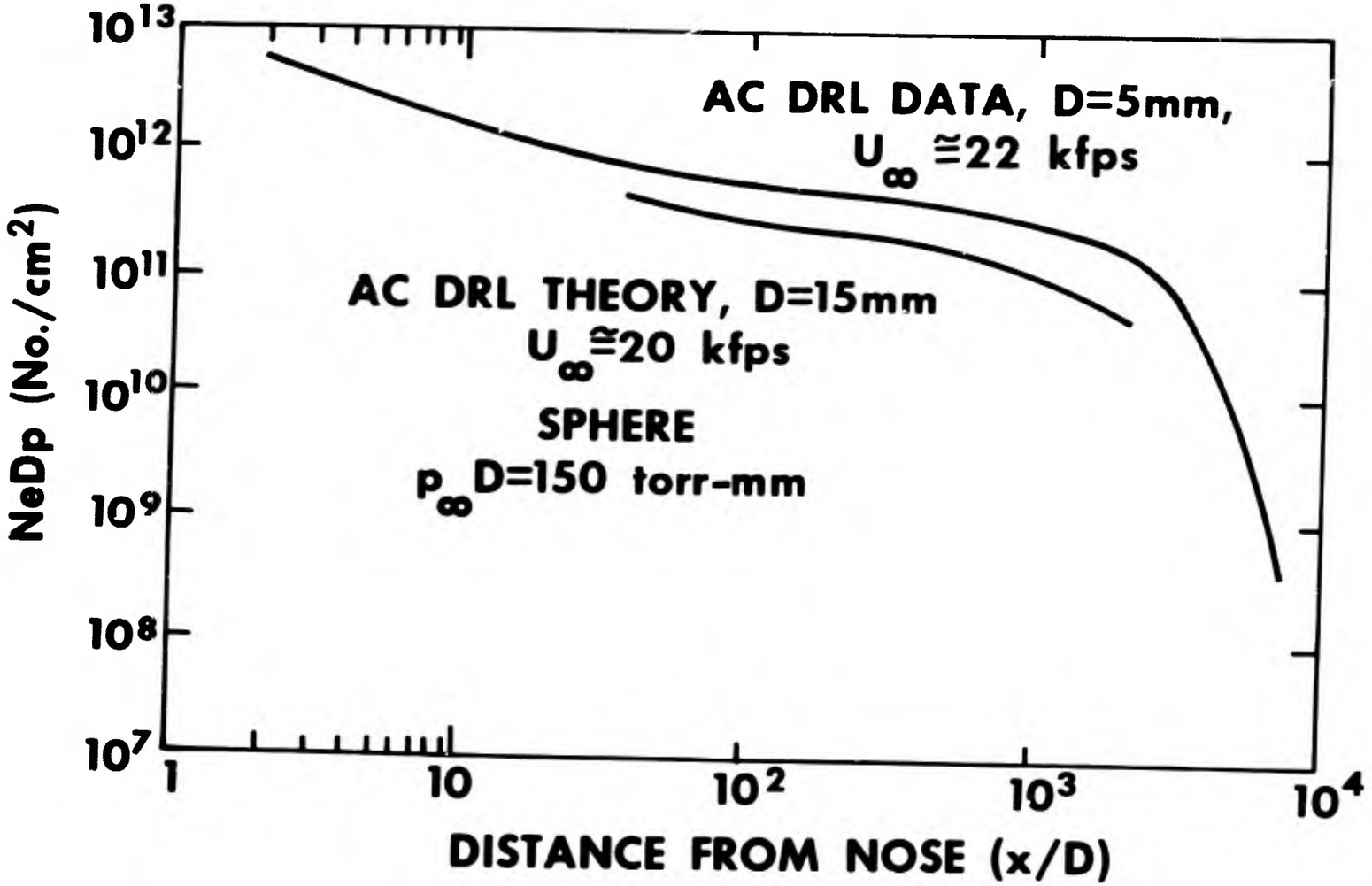

Figure 13 COMPARISON OF SPHERE WAKE IONIZATION DATA WITH CALCULATIONS, pD = 150 torr-mm

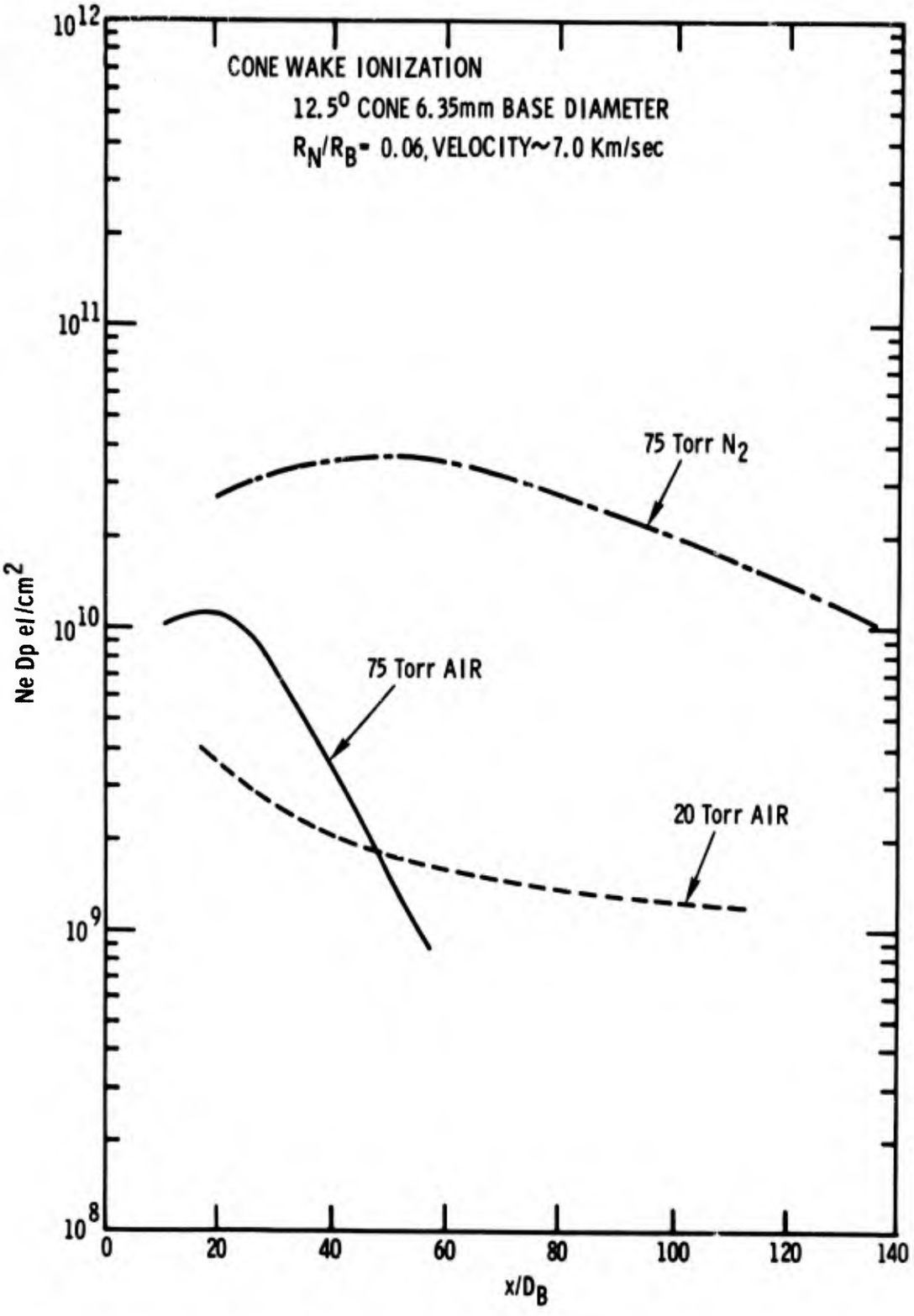

Figure 14 CONE WAKE IONIZATION

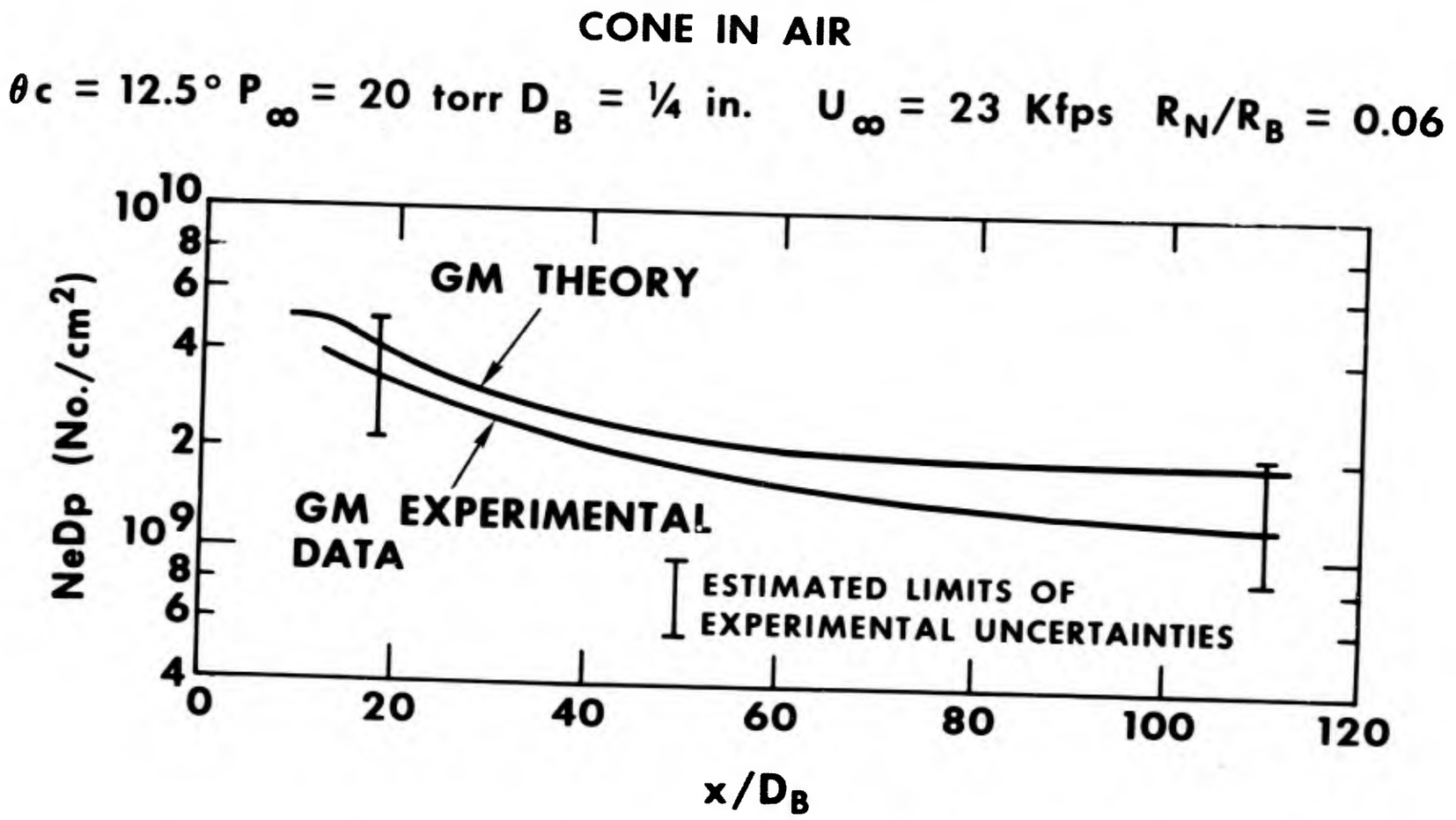

Figure 15 COMPARISON OF CONE WAKE DATA WITH CALCULATIONS, 20-torr Air

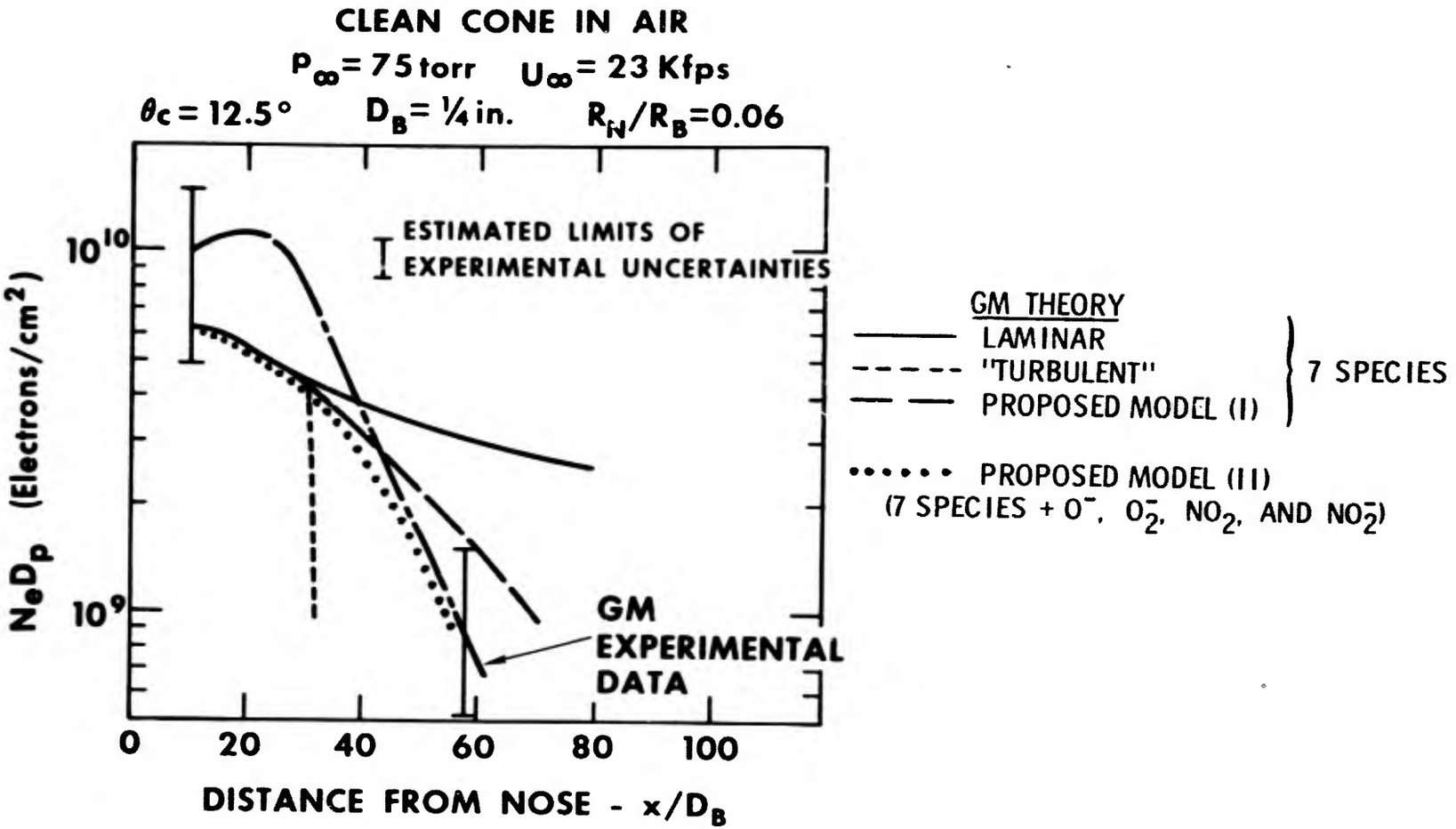

Figure 16 COMPARISON OF CONE WAKE DATA WITH CALCULATIONS, 75-torr Air

UTILISATION DES SOUFFLERIES A ARC BREF

POUR L'ETUDE DES SILLAGES IONISES

par

J. DOREY
et
D. COMPARD

OFFICE NATIONAL D'ETUDES ET DE RECHERCHES AEROSPATIALES
92 - CHATILLON FRANCE

RESUME

Les auteurs résument brièvement les études expérimentales et théoriques relatives à la gaine de plasma entourant des maquettes dans les souffleries à arc bref de l'ONERA: l'étude de la couche de choc à l'aide de sondes électrostatiques et de méthodes réflectométriques a permis de trouver un accord satisfaisant (pendant une grande partie de la rafale) entre les résultats expérimentaux et les déterminations théoriques relatives à un écoulement en déséquilibre chimique (ce qui justifie à postériori l'utilisation de ces souffleries pour de telles études). La détermination théorique des caractéristiques d'un sillage ionisé est encore trop incertaine pour qu'une confrontation avec l'expérience soit possible. Les auteurs décrivent donc ces expériences relatives aux sillages qui sont actuellement en cours de réalisation.

Les maquettes utilisées sont du type hémisphère-cône avec des diamètres de culot de 65 et 186 mm. Elles sont maintenues par des fils fins qui se rompent en début de rafale. Le déplacement de la maquette pendant la phase utile peut être court, et est dans tous les cas repéré.

Le diagnostic du sillage sera effectué par trois séries de peignes de sondes (triples-sondes électrostatiques); on obtiendra ainsi les caractéristiques locales du plasma, radialement et longitudinalement.

Enfin des tentatives d'ensencement de la couche de choc sont prévues afin de déterminer l'influence sur le gaz ionisé de l'injection de corps susceptibles d'augmenter eu de diminuer la densité électronique.

SUMMARY

The authors summarize briefly experimental and theoretical studies dealing with the plasma sheath surrounding models in the short arc wind tunnels of ONERA: the study of the impact layer by means of electrostatic probes and reflectometric methods has made it possible to reach a satisfactory agreement (during a great part of the gust) between the experimental results and the calculated determinations for a chemical non equilibrium flow (which justifies a posteriori the use of these tunnels for such studies). The theoretical determination of the characteristics of an ionized flow is still too uncertain to permit a comparison with experimentation. The authors therefore describe wake experimentation which is now in progress.

The models used are of the hemisphere-cone type with body-base diameters of 65 and 186 mm. They are held by thin wires which break at gust start. The displacement of the model during the useful phase may be short, and is in all cases recorded.

The wake diagnostic will be performed by three series of probe combs (electrostatic triple-probe); thus the local plasma characteristics will be obtained radially and lengthwise.

Finally it is planned to attempt to seed the impact layer in order to determine the effect on the ionized gas of an injection of substances capable of increasing or decreasing the electronic density.

LISTE DES SYMBOLES

V_1, V_2	Tensions définies au § 1.1.
J_i	Densité de courant ionique
n_e	Densité électronique en e par cm^3
q	Charge de l'électron
k	Constante de Boltzman
T	Température
m	Masse
F	Fonction de courant non dimensionnée (cf. Réf: (12)
V_s	Potentiel d'une électrode de sonde
V_p	Potentiel plasma
R	Rayon d'électrode de sonde
V_F	Potentiel flottant
I	Courant
S	Surface d'électrode
λ_D	Longueur de Debye
ϕ_s	Diamètre calotte sphérique
D_c	Diamètre culot
L	Longueur totale maquette
T_o	Température d'arrêt
p_o	Pression d'arrêt
M_∞	Nombre de Mach amont
T_{om}	Température d'arrêt moyenne d'un tir

Indices

e	Electron
i	ion
$\alpha, 1, 2, 3$	Electrode de triple-sonde

INTRODUCTION

Depuis quelques années, de nombreux laboratoires étudient les sillages ionisés. Les dispositifs expérimentaux sont principalement : le tunnel de tir hyperbalistique et le tunnel de choc.

Les études les plus nombreuses ont été conduites en tunnel de tir, car l'absence de support autorise des mesures non perturbées dans les sillages. Cependant les dimensions limitées des projectiles ne permettent pas d'études localisées des profils de densité et de température électroniques. La technique la plus fréquente consiste à utiliser un ou plusieurs interféromètres hyperfréquences qui ne donnent que des résultats intégrés d'une part sur le diamètre du faisceau, d'autre part le long du parcours des ondes dans le plasma ; ces techniques ne sont d'ailleurs utilisables que dans un domaine de densité électronique relativement élevé ($n_e > 10^{10}$ e/cm^3).

Il est possible de déduire des mesures radioélectriques des familles de courbes de densité électronique dans les sillages, mais ces profils sont si complexes qu'une déduction a priori paraît improbable.

D'autre part, un paramètre important du plasma est la température électronique. Cette grandeur intervient directement sur les vitesses de recombinaison électron-ion, les sections efficaces d'attachement électronique sur des gaz électronégatifs (O_2^-, F^- ....), sur la propagation d'ondes longitudinales électroniques et les conditions de couplage avec des ondes électromagnétiques, sur l'intensité de rayonnement de Bremsthralung.

La température électronique ne peut être déduite de mesures d'interférométrie hyperfréquence que par l'intermédiaire de la fréquence de collision électron-neutre qui fait intervenir d'autres grandeurs difficiles à mesurer (pression et température locales des particules neutres).

C'est pourquoi nous avons mis au point, à l'ONERA, des techniques de mesures localisées des grandeurs n_e et T_e . Ces mesures sont effectuées dans le sillage de maquettes larguées dans des écoulements en soufflerie à Arc bref.

.../...

On décrit dans cette note, les dispositifs expérimentaux et les premiers résultats obtenus.

Nous insistons particulièrement sur la technique des triples-sondes (1) car cette méthode, très commode d'emploi, est susceptible d'être utilisable dans de nombreuses configurations.

On décrit les dispositifs de largage et d'ensemencement en gaz électronégatif.

Après l'exposé des commentaires, on analyse dans la conclusion le programme expérimental et théorique déduit de cette première série de mesures

1. - METHODE DE MESURE UTILISEE POUR LA DETERMINATION DES CARACTERISTIQUES ELECTRIQUES DES SILLAGES

Dans l'étude de la caractérisation des plasmas animés de grande vitesse d'ensemble (type plasma de rentrée), la sonde électrostatique est un outil de diagnostic très employé. Elle permet, en effet, d'atteindre plus ou moins directement la température électronique et la densité des particules ionisées.

De nombreux auteurs ont fait après Langmuir, des études théoriques sur l'emploi des sondes électrostatiques (2). Dans la majorité des cas, les sondes étudiées sont supposées en régime moléculaire ; cependant elles ont été souvent utilisées à des pressions élevées (de l'ordre de la pression atmosphérique) et ont donné des résultats satisfaisants (Réf (3) par exemple), en particulier en ce qui concerne la température électronique (4).

Les méthodes de sondes simples, initialement utilisées pour des tubes à décharge, ont été également employées dans des écoulements de plasma; parmi les nombreuses applications les références (5) à (8) se rapportent plus particulièrement à des problèmes comparables à ceux rencontrés dans les sillages.

Cependant, dans les plasmas instationnaires et animés de vitesse moyenne, la sonde simple s'est avérée difficile à mettre en oeuvre; d'une part le courant de collection électronique peut perturber le plasma, d'autre part, l'apparition de potentiels induits dans les écoulements à grande vitesse risquent de fausser la mesure.

.../...

L'étude de ces plasmas a donc nécessité la mise en oeuvre de méthodes de sondes doubles (9) et (10) qui n'utilisent que le courant ionique et ne sont pas perturbées par les potentiels induits. Elles exigent cependant un balayage en tension. car comme dans le cas de la sonde simple, toute la caractéristique de sonde est nécessaire à la détermination des paramètres du plasma (Pour l'étude des sillages ionisés, une méthode de double sonde à potentiel fixe a cependant été utilisée par TATE (11) en parallèle avec une autre méthode de diagnostic).

La nécessité de balayer en tension pendant une durée où les caractéristiques du plasma peuvent varier et la difficulté d'exploiter les renseignements tension-courant obtenus, sont des inconvénients qui disparaissent en utilisant une triple-sonde (1). Dans l'étude présente, cette méthode est bien adaptée à la caractérisation des sillages, en particulier ceux rencontrés dans les soufflerie à arc.

1.1. - Principe de la triple-sonde

Après avoir rappelé le principe de la triple-sonde (1), nous exposerons brièvement les relations principales permettant de calculer les caractéristiques du plasma à partir de résultats de mesure.

On dispose de trois électrodes cylindriques de surfaces identiques dont les dimensions, dans les conditions des écoulements rencontrés en soufflerie à arc, permettent de vérifier les trois hypothèses suivantes:

- Régime moléculaire
- Epaisseur de gaine inférieure aux distances inter-sondes.
- Distribution maxwellienne pour les électrons.

Le schéma de principe est rappelé figure 1 ; le circuit de sonde 1 est un circuit à haute impédance de sorte que le courant circulant dans cette sonde est négligeable par rapport au courant I On mesure I et la tension V_1 entre sonde 1 et 2.

La tension V_2 étant imposée et la sonde 1 restant au potentiel flottant (fig. 2), on peut expliquer simplement le principe de la triple sonde en considérant que les trois électrodes ont la même caractéristique de sonde (cas idéal).
La méthode revient alors à déterminer trois points de cette caractéristique (fig. 3).

.../...

1.2. - Détermination de la température et de la densité électroniques

Le courant global circulant dans chaque circuit fait intervenir les densités de courants ioniques et électroniques. On utilise ici les résultats de la théorie de LAFRAMBOISE (12) qui se sont montrés très commodes d'emploi. Cette théorie a déjà donné de bons résultats dans des plasmas du type aérodynamique : Cf. Références (13) à (15) et plus récemment Réf. (16).

Pour ce qui nous intéresse ici, on retiendra que le courant de saturation ionique J_i a la forme:

$$J_i = n_e\, q \left(\frac{k T_e}{2\pi m_i}\right)^{1/2} F_\alpha \left(q\,\frac{V_{s\alpha} - V_p}{k T_e}, \frac{R}{\lambda_D}, \frac{T_i}{T_e}\right)$$

La fonction F_α apparaît comme une densité de courant non dimensionnée; elle est donnée par des abaques dont on donne un exemple figure 4 (exemple déduit de la référence (12)).

Ces résultats sont appliqués au schéma précédent de la triple sonde et donnent, en faisant le bilan des courants pour chaque circuit sonde

$$V_1 = \frac{kT_e}{q} \log \left[\frac{2 + \sqrt{\frac{m_e}{m_i}}\, \exp.q\,\frac{V_F - V_p}{kT_e} \left\{ \left(F_3 - F_2\right) - 2\left(F_1 - F_2\right) \right\}}{1 + \exp \frac{-q V_2}{k T_2}} \right] \qquad (1)$$

avec α = 1, 2, 3 relatif à chaque sonde.

$$V_F - V_p = \frac{kT_e}{2q} \log \left\{ \left[F_f \left(q\,\frac{V_F - V_p}{kT_e}, \frac{R}{\lambda_D}, \frac{T_i}{T_e} \right) \right]^2 . \frac{m_e}{m_i} \right\} \qquad (2)$$

où F_f est la fonction de courant relative au potentiel flottant.

D'autre part le potentiel V_2 est choisi de sorte que $V_2 >> V_1$ (ce qui est le cas en soufflerie arc pour les températures électroniques rencontrées dans ces expériences); le bilan des courants permet d'aboutir à l'expression:

$$n_e\,(e/cm^3) = 1{,}59.10^{-9}\left(\frac{M_i}{T_{e(eV)}}\right)^{1/2}\frac{I(\mu A)}{S(mm^2)}\left\{F_3\left[\frac{q(V_2+V_F+V_p)}{k\,T_e}, \frac{R}{\lambda_D}, \frac{T_e}{T_i}\right]\right\}^{-1} \quad (3)$$

Connaissant le gaz utilisé, les dimensions des sondes, les quantités n_e, T_e, V_e, les relations (1), (2), (3) permettent de déterminer un réseau de courbes paramétrées dont un exemple est donné figure 5.

Puisque V_1 et I sont des grandeurs mesurées et que λ_D est une fonction de T_e et n_e, on voit que deux itérations sont nécessaires pour remonter à T_e et n_e.

REMARQUES:

a - En pratique il suffit de connaître un ordre de grandeur de la longueur de Debye pour ramener la résolution à une seule itération.

b - On réalise des électrodes de dimensions identiques et placées dans un espace réduit pour que l'on puisse supposer les densités électroniques au voisinage des électrodes très peu différentes.

Des facteurs correctifs peuvent intervenir si on considère un cas moins idéal ; en particulier dans le domaine des expériences réalisées, l'erreur sur la température électronique peut atteindre 20%.

2. - DESCRIPTION DES EXPERIENCES ET DES DISPOSITIFS UTILISES

La soufflerie à arc "Arc 2 A" a été utilisée pour toutes ces études de sillage. On ne reviendra pas sur la description de cette installation qui a déjà été publiée (17), (18), (19). On insistera simplement sur le fait que les écoulements d'azote utilisés sont de durée relativement longue (100 ms) ce qui permet un diagnostic commode des plasmas aérodynamiques (20).

L'ensemble du dispositif d'étude du sillage est représenté schématiquement figure 6 : Les maquettes suspendues dans la veine sont larguées au début de l'écoulement; leur chute est visualisée et la mesure proprement dite est faite par trois peignes de triples-sondes fixes placés dans le prolongement de la veine.

2.1. - Maquettes

Deux maquettes hémisphère-clothoïde-cône ont été utilisées. La première (ϕ_s = 105 mm, Dc = 196 mm, L = 600 mm) a été choisie de façon à obtenir un modèle de dimensions maximales, acceptable dans la veine de la soufflerie. La seconde (ϕ_s = 35, Dc = 65, L = 200) pouvait permettre par sa taille, une étude dans la partie éloignée du sillage. Une troisième maquette dont les dimensions extérieures sont celles de la première a été munie d'un dispositif d'ensemencement (fig. 7) pour étudier l'influence de l'injection d'hexafluorure de soufre dans l'écoulement.

Le réservoir de gaz prolongé d'un col sonique permet d'éjecter le gaz par l'éventail d'ensemencement à débit constant (de l'ordre de 1 g/s). L'injection est faite à 45° autour de la calotte sphérique (fig. 7). L'ouverture d'une vanne qui déclenche l'ensemencement est effectuée à la cassure du fil de suspension (voir paragraphe suivant) avec un temps de réponse de quelques millisecondes.

2.2. - Largage

Les maquettes sont suspendues dans la veine par deux fils de nylon de 2/10 mm de diamètre. A la formation de l'onde de choc les fils se rompent et se détruisent presque totalement, les maquettes se trouvent ainsi en vol libre après un temps inférieur à 10 ms. Cette durée est courte par rapport à celle de l'écoulement (100 ms) et il reste un temps suffisant pour faire une mesure saine dans le sillage.

La chute des maquettes est cinématographiée à l'aide d'une caméra rapide ($\simeq$ 1000 images/s.). Ceci a rendu possible un relevé de trajectoires dont un exemple est donné fig. 8. On voit en particulier que le déplacement pendant la phase utilisable pour la mesure (50 ms environ) est faible, voir négligeable (maquette Dc=196) par rapport au diamètre du culot. La position des sondes se trouve ainsi pratiquement déterminée par leur position d'origine, et elle est connue à chaque instant.

.../...

Un exemple de visualisation est donné Figure 9 et Figure 10. Pendant toute la phase utile du tir l'incidence des deux types de maquette reste pratiquement nulle. Ceci a été vérifié sur la majorité des tirs. Certaines expériences ont dû cependant être rejetées, les conditions précédentes, pour des raisons aléatoires liées aux conditions initiales, n'étant pas satisfaites (trop grande incidence, fil restant dans l'écoulement....).

2.3. - Sondes de sillage

Trois peignes de quatre triples-sondes sont disposés dans le prolongement de la veine comme l'indiquent les figures 6 et 11; leur emplacement a été choisi afin de mesurer les caractéristiques électriques dans une zone intéressante du sillage proche (zone de recirculation et col...) tout en évitant d'être dans une région où le sillage pourrait être perturbé par des réflexions parasites (réflexion de l'onde de choc sur la couche limite).

Les peignes et leur support sont aérodynamiquement profilés (épaisseur maximale 4 mm) comme l'indiquent les figures 12 et 13. D'autre part, ils sont disposés à 120° les uns des autres ; dans ces conditions, les perturbations aérodynamiques d'un peigne sur l'autre sont réduites au minimum ;ceci a été vérifié pour deux tirs ayant des conditions génératrices comparables, la présence d'un peigne disposé de la façon précédente ne modifie pas de façon appréciable les caractéristiques électriques du plasma mesurées sur le second.

Les triples-sondes sont constituées d'électrodes de 10^{-1} et $5\ 10^{-2}$ mm de rayon espacées de 1 mm. Dans ces conditions, et compte tenu des caractéristiques d'utilisation de la soufflerie à arc, les conditions relatives à la triple-sonde décrites au paragraphe 1.1 sont satisfaites dans les sillages.

Les peignes utilisés sont enfichables (fig. 12) de sorte qu'ils peuvent être démontés pour le nettoyage des électrodes après chaque tir.

Enfin les mesures sont amenées par des connections noyées dans la masse du support aux dispositifs d'amplification, puis d'enregistrement, complètement isolés des masses de la soufflerie ; tous les circuits sonde sont rigoureusement indépendants. Dans ces conditions le dispositif utilisé était rendu pratiquement insensible aux couplages et aux parasites (arc intense...).

3. - RESULTATS ET COMMENTAIRES

3.1. - Mesures dans le jet libre

Des expériences préliminaires aux mesures propres aux sillages ont été effectuées sur l'écoulement en l'absence de maquette. La figure 14a représente pour un tir dont les conditions génératrices sont relativement élevées (4 800°K pour la température génératrice) l'évolution des courants collectés sur trois sondes. La densité électronique correspondante est représentée figure 14 b; elle reste toujours inférieure à 10^8 e/cm^3 . Cependant deux zones restent à éliminer l'une en début de tir et l'autre au désamorçage.

Les quinze à vingt premières millisecondes de l'écoulement correspondent à un taux maximum d'impuretés ou de parasites dont l'origine n'a pas été clairement mise en évidence.

Il faut remarquer que pendant la majeure partie de l'écoulement, celui-ci peut être considéré comme sain, puisque les densités électroniques équivalentes dans le jet libre sont de 10^2 à 10^5 fois plus faibles que celles à mesurer. Cette constatation expérimentale est à rapprocher de l'étude théorique effectuée en prenant a priori une densité électronique amont non nulle (voir référence 20) égale à 10^8, et en intégrant le système de cinétique chimique le long des lignes de courant (21). Cette étude montrait qu'une telle "préionisation" choisie a priori, ne modifiait pratiquement pas le profil des caractéristiques théoriques, de sorte que les diagnostics du plasma créé par l'onde de choc détachée gardaient leur sens.

3.2. - Mesures effectuées sur les sillages

Les résultats obtenus sont résumés par les figures 15 à 19. Les indices 1 à 4 correspondent à chaque sonde d'un peigne considéré, l'indice 1 étant relatif à la sonde située sur l'axe (cf: Fig. 11).

Sur l'exemple d'enregistrement fig. 15, on retrouve les différentes phases du tir définies dans le paragraphe précédent. Sur la partie correspondant à la phase utile du tir, la détermination des densité et température électroniques relative aux trois peignes est effectuée en fonction du temps (fig. 16). On peut ainsi déterminer la distribution spatiale de ces grandeurs, relative aux deux maquettes (fig. 17 - 18) à une époque déterminée.
On constate une excellente reproductibilité de la répartition d'un peigne au suivant. Le plasma est inhomogène et présente une structure tubulaire. La densité électronique est plus faible sur l'axe qu'à l'extérieur; cette particularité se conserve (voir § suivant) quand il y a ensemencement.

.../...

La carte de la figure 19 n'est pas définitive puisqu' obtenue à partir d'un nombre de points de mesure limité. Cependant ce schéma est très utile pour la définition des expériences ultérieures. Quoiqu'il en soit, il apparaît clairement que la structure électronique du sillage proche n'est pas aussi régulière qu'il ne semblait auparavant.

L'approximation couramment utilisée d'un sillage proche cylindrique à décroissance de densité électronique uniforme ne semble pas vérifiée, dans les conditions de ces expériences.

D'autre part, on constate que la température électronique peut être supérieure à la température d'arrêt des neutres; on peut rendre compte de ce phénomène en introduisant les termes inélastiques dans les équations hydrodynamiques macroscopiques du plasma (voir (22); Si l'on prend uniquement en considération des processus de recombinaison, l'augmentation de température obtenue par le calcul ne conduit pas aux ordres de grandeur observés dans ces expériences; il apparaît nécessaire d'introduire des chocs superélastiques résultant de collisions entre électrons et particules excitées (principalement les niveaux de vibration élevés des molécules neutres N_2). Cette étude est en cours de développement.

L'influence de l'échelle des maquettes peut être résumée ainsi:

Les valeurs maximales de T_e et de n_e pour des conditions génératrices identiques croissent avec les dimensions des maquettes, ce qui met en évidence l'influence des effets de cinétique sur les caractéristiques du plasma (20).

En ce qui concerne la répartition radiale et longitudinale, il n'a pas été possible d'obtenir des renseignements concernant l'influence de l'effet d'échelle; la résolution spatiale étant insuffisante pour l'échelle la plus petite.

3.3. - Essais d'ensemencement

L'affinité électronique de certains composés halogénés offre la possibilité d'agir sur la densité electronique. Des essais ont été effectués avec de l'hexafluorure de soufre (SF_6) qui avait donné dans d'autres expériences (23) des résultats plus satisfaisants que d'autres composés (CF_4, Fréon.....).L'hexafluorure est complètement dissocié à des températures supérieures à 3000°K et à des pressions partielles inférieures à une atmosphère.

.../...

Il se produit un processus d'attachement électronique selon une réaction du type trois corps:

$$F + e^- + M \underset{2}{\overset{1}{\rightleftharpoons}} F^- + M$$

La réaction dans le sens 1 est d'autant plus efficace que la température des électrons est plus basse et que la pression partielle de fluor est élevée. L'hexafluorure doit être préalablement dissocié à un taux élevé pour qu'une réduction notable de la densité électronique puisse être observée. C'est pour cette raison que l'injection a été faite dans la zone du nez de la maquette utilisée, comme cela a été décrit au paragraphe 2.1..

Les résultats représentés figure 20 sont relatifs à deux tirs dont les conditions génératrices sont comparables, pendant la majeure partie de l'écoulement ($T_{om} = 5.200\,°K$, $p_o \simeq 1\,at.$) - $(n_e)_{SF_6}$ représente la densité électronique mesurée pendant le tir où une injection d'hexafluorure a été effectuée. (Débit d'injection $\simeq 1g/sec$, , ce qui correspond à un pourcentage de 1 à 2% en poids, en supposant un mélange homogène dans la couche de choc).

On remarque que la réduction maximale de densité évolue successivement de la sonde 3 (20 a) à la sonde 2 (20 b) puis à la sonde 1 (20 c), quand on s'avance dans le sillage.

Ceci correspond à une des trajectoires optimales où l'injection, la dissociation puis l'attachement se sont effectués avec le meilleur rendement. D'autre part la réduction de densité paraît limitée à une zone du sillage interne qui va en se réduisant (fig. 20 c). Ces premiers essais d'ensemencement semblent montrer que l'injection de SF_6 réduit les densités électroniques d'une façon inhomogène et dans un rapport plus faible que prévu.

Si les effets mesurés restent faibles dans les conditions d'injection précédentes, des expériences comparables avec ensemencement dans la chambre à arc ont donné des résultats bien plus significatifs.
Ainsi l'évolution des courants mesurés sur trois sondes disposées dans la couche de choc d'une maquette hémisphère cylindre est caractéristique de l'influence de l'hexafluorure, comme le montre la figure 21.

La figure 22 montre que la réduction en densité électronique peut atteindre un rapport 100 quand on mélange 7% en poids d'hexafluorure. Ce rapport tombe à environ 10 avec 2,5%. Cette diminution se retrouve pratiquement dans toute la couche de choc; elle est plus forte (en valeur relative) pour les zones où la température du gaz est plus faible (sonde 3), ce qui est en accord avec les lois de variation de section efficace d'attachement.

CONCLUSION:

Ces premiers résultats obtenus sur les sillages ionisés de maquettes larguées en cours de tir sont très prometteurs. Ils mettent clairement en évidence la structure complexe du plasma dans le sillage proche et l'influence de réactions exothermiques pour les électrons. Ces études expérimentales permettent de vérifier l'importance relative des processus physico-chimiques mis en jeu dans les plasmas hypersoniques (en particulier, les collisions superélastiques pour les électrons).

D'autre part, les essais d'ensemencement montrent la différence notable observée lorsque l'injection est effectuée dans la chambre à arc ou au nez des maquettes; la méthode de largage utilisée permettra donc d'optimiser l'insémination des sillages sans introduire de perturbation par un dard. Enfin, les profils de densités électroniques obtenus permettront de prévoir les interactions entre ondes électromagnétiques et sillage ionisé.

Les études radioélectriques des sillages ionisés vont être effectuées dans les souffleries Arc 1 et 2 modifiées par l'adaptation de paroi en matériau diélectrique à faible perte.

Nous disposons ainsi d'un moyen d'étude expérimentale puissant où les différentes techniques de mesure pourront être utilisées simultanément.

(1) S.C. CHEN, T. SEKIGUCHI — Instantaneous direct display system of plasma parameters by means of triple probe. J. of Appl.Phys. Vol. 36, N°8, Aug. 65

(2) M. FITAIRE — Les sondes électrostatiques et leurs applications. Cours de la Fac. des Sc. (ORSAY) Lab. de Phys. des Plasmas.

(3) F. JOUBERT — Utilisation de sondes de Langmuir Dans un jet de plasma. Thèse de Doctorat - Fac. des Sc. (Lab. de Phys. des Plasmas)

(4) J.R. COZENS — Probes at high pressure. Un.of OXFORD - Dép. of. physics. 7 th int. conf.on Phenomena in ionized Gases - Beograd 1965.

(5) C.I. BRUNDIN, L. TALBOT — The application of Langmuir probe techniques to flowing ionized gases AGARD Rep. 478 - Sept. 1964

(6) WA.CLAYDEN — Langmuir probe and velocity measurements in ARDE plasmajet AGARDOGRAPH 68 - Ed. NELSON (1964)

(7) I. POLLIN — Stagnation point Langmuir probe in a shock tube; theory and measurements THE PHYS. OF. Fl. Vol. 17 n° 9 - Sept. 1964

(8) C.B. KRETSHMER, H.L. PETERSEN — Use of a Langmuir probes to study ion-electron recombinaison J. OF APPLIED PHYSICS Vol 34 n° 11 Nov. 1963

(9) E.O. JOHNSON, L. MALTER — A floating double probe method for measurements in gas discharges PHYS. REV. Vol. 80 n° 1 - Octobre 1950

(10) FF. CHEN — Double-probe method for unstable plasmas. The Rev. of sc. Instr. Vol. 35 n° 9 Sept. 1964

(11) A. TATE, P.W.W.FULLER, C.R. WALL — An investigation of the wakes of hype-velocity spheres using double Langmuir probes. Proceedings of the 2nd Int. Congress on Instrumentation in Aerospace facilities Aug. 1966 (Stanford - Un.)

(12) J.LAFRAMBOISE — Theory of spherical and cylindrical Langmuir probes in a collisionless, maxwellian plasma at rest. UTIAS Rep. n° 100 (Un.of Toronto) 1966

(13) A.A. SONIN — The behaviour of free molecule cylindrical Langmuir probes in supersonic flows and their application to the study of the blunt body stagnation layer. UTIAS Rep. N° 109 -(Un. of Toronto 1965)

(14) A.A. SONIN — The free molecule Langmuir probe and its use in flow field studies. AIAA paper 66-5

(15) K.A. GRAF — The determination of spatially non-uniform electron density distribution. UTIAS rep. n° 108 -(Un. of Toronto 1965)

(16) S.LEDERMAN, D.WILSON, E.DAWSON — The application of Langmuir type probe and microwave diagnostic technique to transient ionized flow. Proceedings of the 2 nd Int. cong. on instrumentation in aerospace facilities Aug. 1966 (Stanford - Un)

(17) J.P.CHEVALLIER, F. BOUNIOI — Problèmes d'interprétation des résultats de mesures dans une soufflerie à Arc. The high temperature aspects of hypersonic flow - AGARDograph 68 - Ed. W.C.NELSON (1964)

(18) J.P.CHEVALLIER — Problèmes expérimentaux particuliers aux souffleries à Arc. Colloque d'Aérodynamique Appliquée à l'AFITAE - Toulouse 8 - 9 novembre 1965.

(19) P. CARRIERE, J.P.CHEVALLIER — Recent progress in the ONERA wind-tunnels. To be presented at the 5th symp. on the hypervelocities techniques DENVER (col.) March 67

(20) J. DOREY, D. COMPARD — Experimental studies of plasma sheath surrounding models in hot-shot wind-tunnels, Proceedings of the 2 nd Int. Congress on Instrumentation in aerospace facilities Aug 1966 (Stanford Un.)

(21) D. COMPARD, M. FAUCHEUX — Détermination des densités de particules dissociées et ionisées dans un plasma d'azote hors d'équilibre - Rech. Aéro. n° 110 - 1966

(22) J. DOREY, C. VERET — Caractérisation des plasmas de rentrée. Communication présentée au 5ème Congrés I.C.A.S. - LONDRES - Sept. 1966

(23) R. EARL GOOD — Electron attachment to atomic fluorine in thermally ionized air NASA C.R. 516 - Jul. 1966

Cette étude a été réalisée avec la collaboration du groupe des Souffleries à Arc de l'ONERA, dirigé par M. J.P. CHEVALLIER, en particulier en ce qui concerne la réalisation des dispositifs de largage et d'ensemencement et la mise en oeuvre de la soufflerie.

La réalisation de l'électronique associée aux circuits de sondes et d'enregistrement a été effectuée par M. G. PINSON, cadre technique.

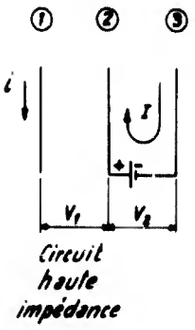

Triple sonde
Schéma de principe
fig. 1

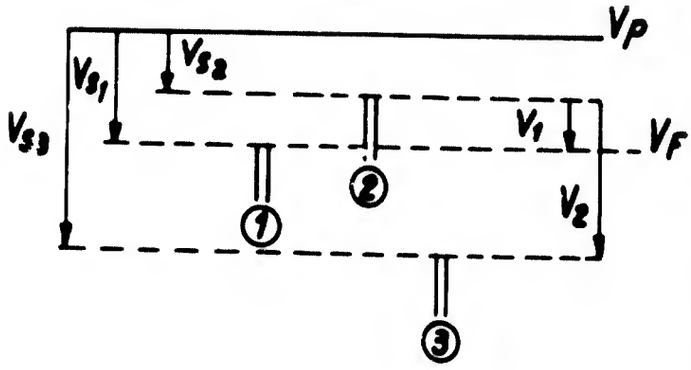

Triple sonde : répartition des potentiels

fig. 2

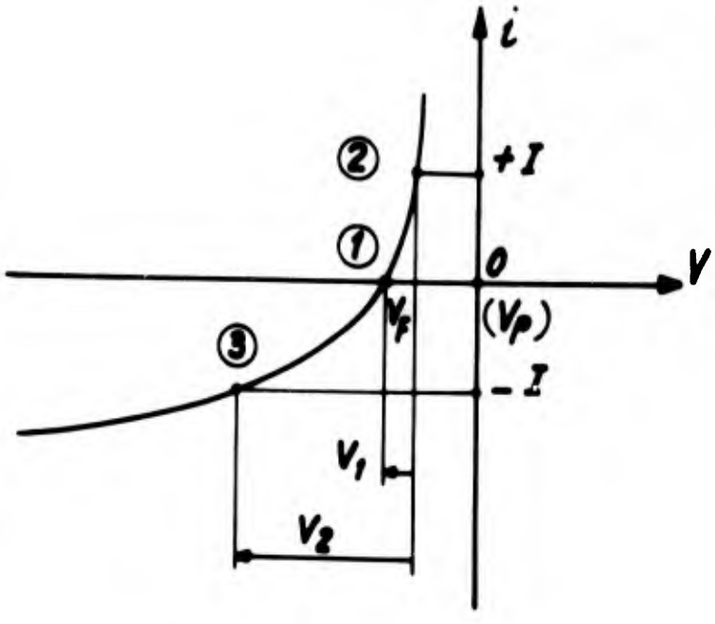

Représentation schématique
du principe de la triple sonde

fig. 3

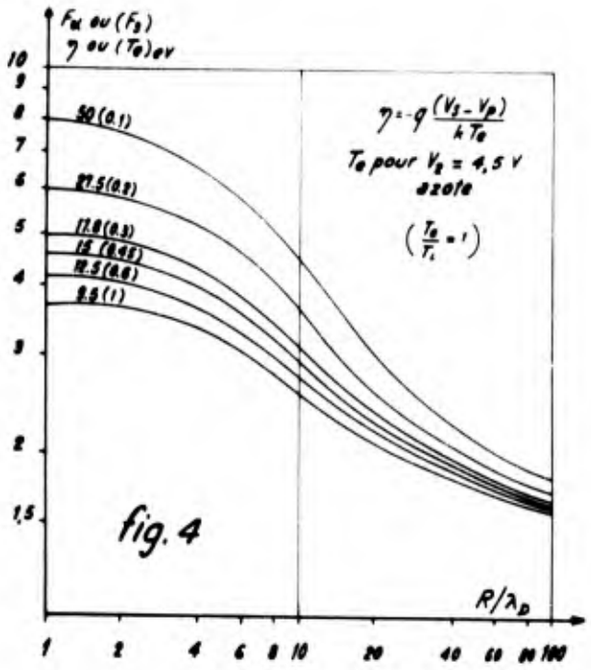

fig. 4

Fonction de courant non dimensionnée utilisée pour l'interprétation de résultats de triple sonde.

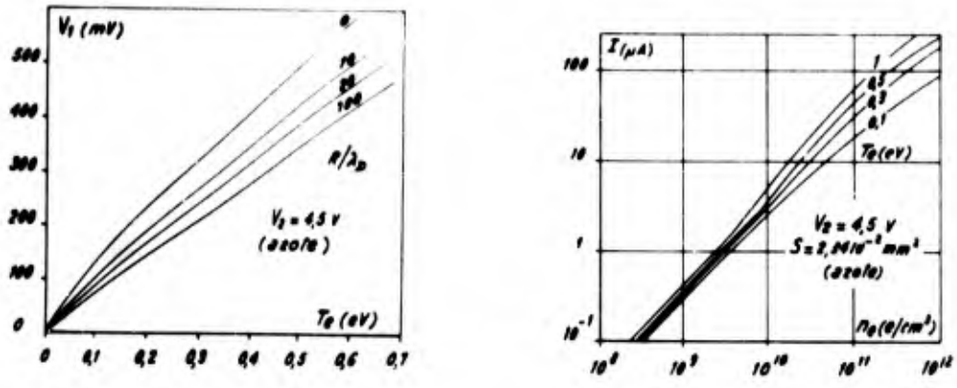

a) b)

Abaques donnant pour les conditions utilisées n_e et T_e (Triple_sonde)

fig. 5

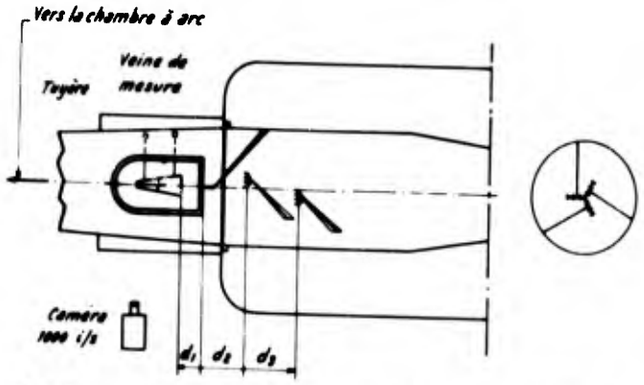

Schéma d'emsemble des expériences réalisées

fig. 6

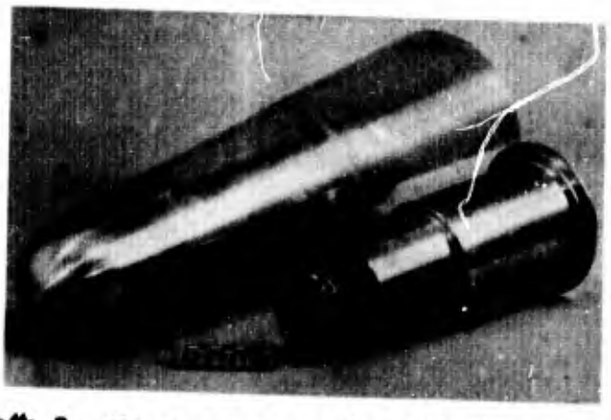

Maquette D_c = 196 mm avec son dispositif d'ensemencement

fig. 7

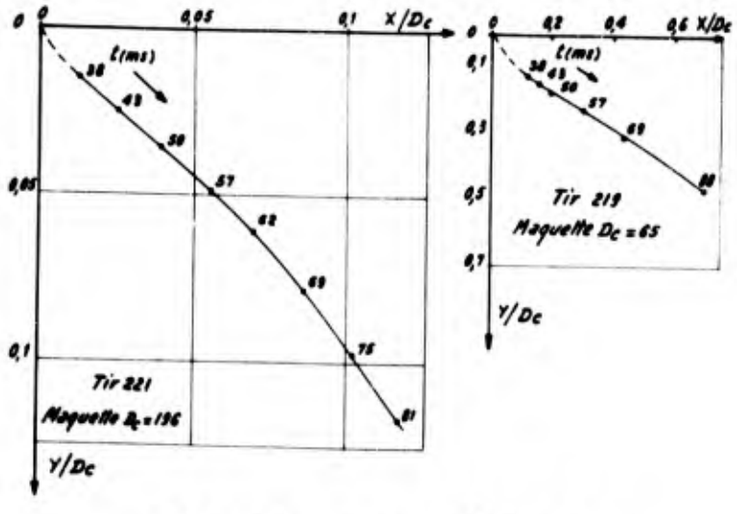

Trajectoires type après largage

fig. 8

Extrait de film

Chute maquette $D_c = 196$ mm

fig. 9

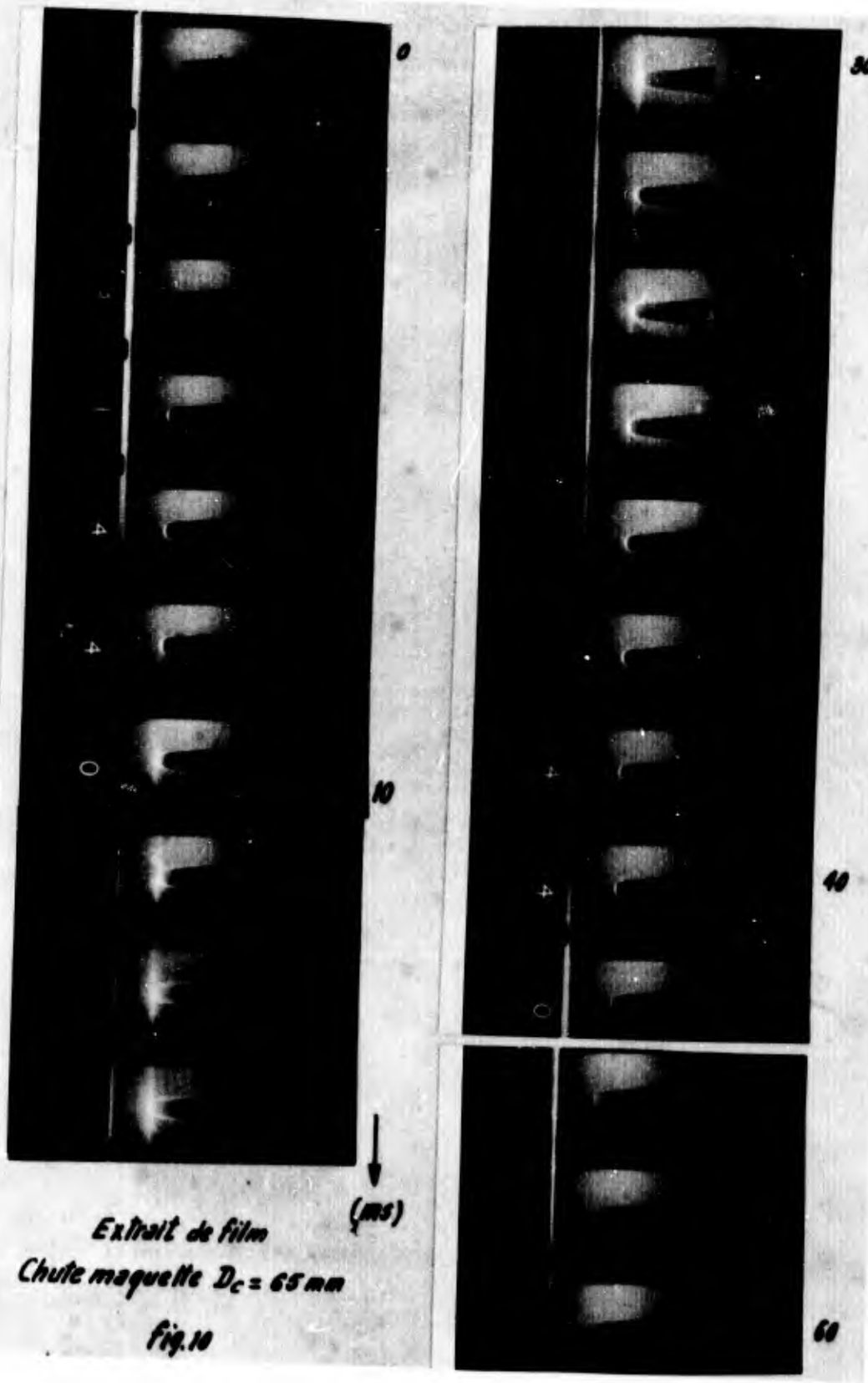

Extrait de film

Chute maquette $D_c = 65$ mm

fig. 10

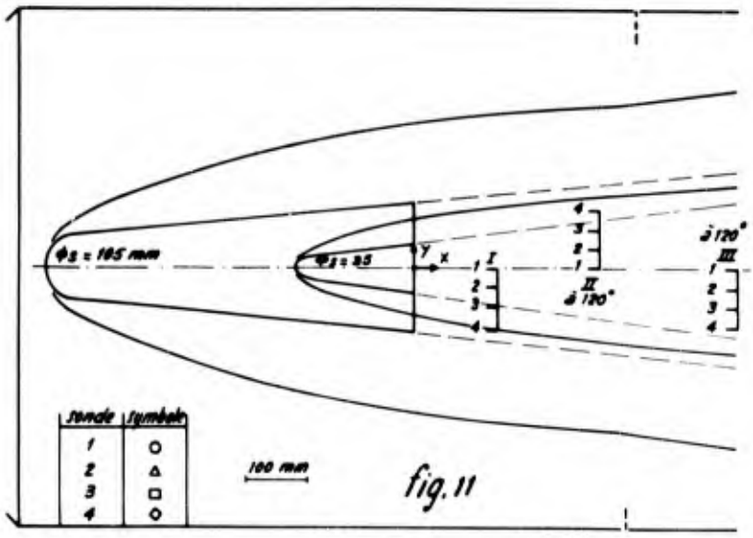

fig. 11

Position schématique des 3 peignes de sondes par rapport aux 2 maquettes utilisées

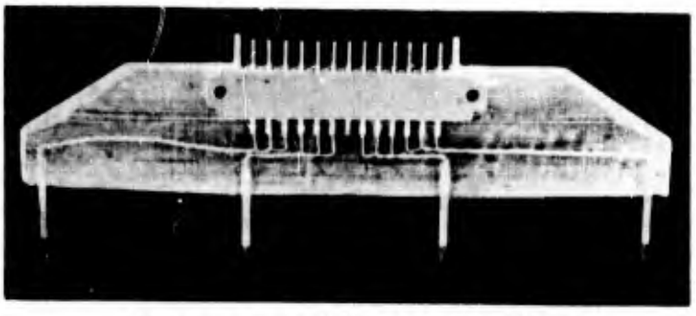

Peigne de 4 triples sondes (éch. 1)
fig. 12

Peigne et son support
fig. 13

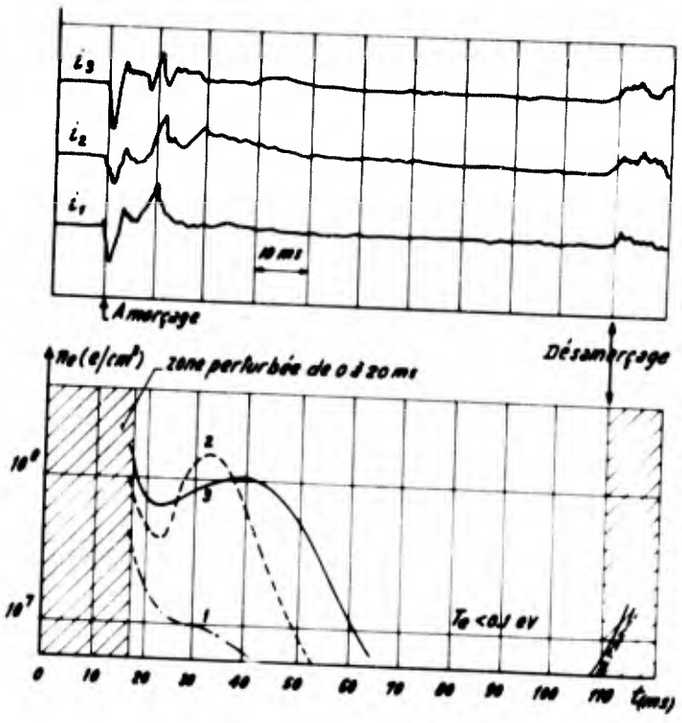

Mesure de la densité dans le jet libre

Tir 211 (T_{0max} = 4800°K, P_0 ≃ 0,1 at.) M_∞ = 16

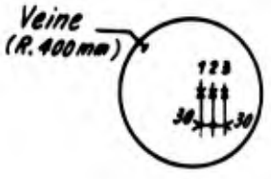

fig. 14

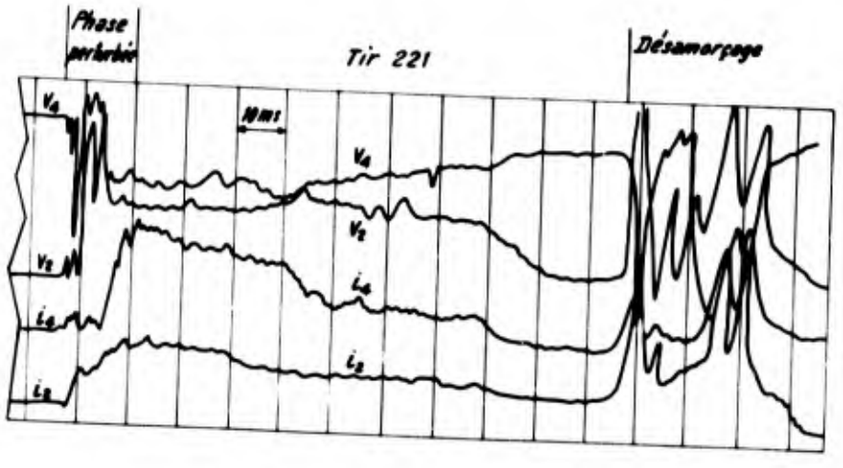

Exemple d'enregistrement, tension et courant sonde 2 et 4 (peigne II)

fig. 15

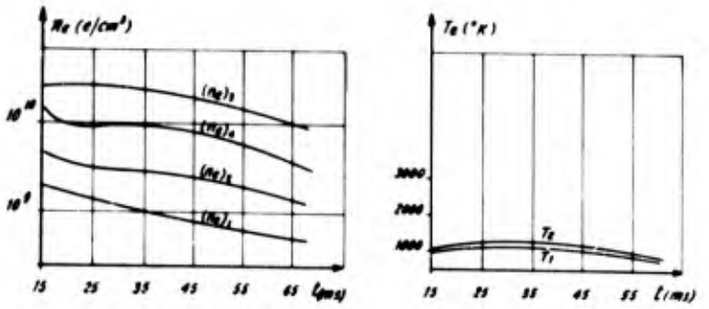

a) Peigne I ($\frac{X}{Dc} = 0,7$)

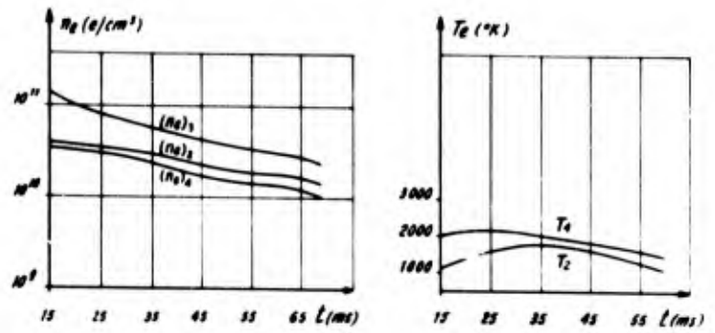

b) Peigne II ($\frac{X}{Dc} = 1,4$)

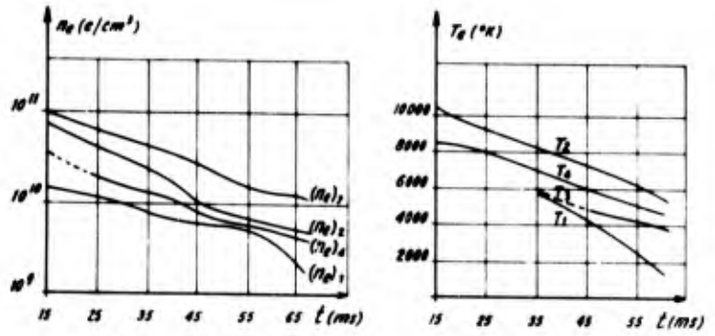

C) Peigne III ($\frac{X}{Dc} = 2,5$)

Evolution de la densité et de la température électroniques en fonction du temps
Peignes I. II. III – Maquette $D_c = 196$ mm
Tir 221 ($T_{om} = 5200$°K ; $p_o \simeq 0,1$ at., $M_\infty \simeq 16$)

fig. 16

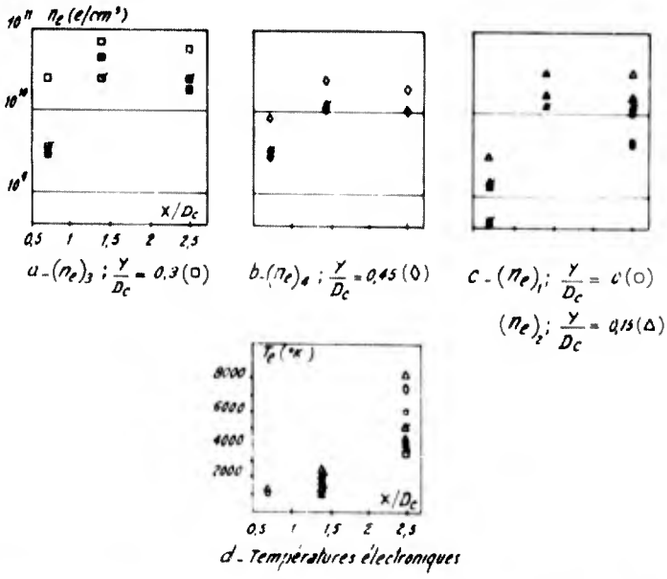

a - $(n_e)_3$; $\frac{Y}{D_c} = 0,3$ (□) b - $(n_e)_4$; $\frac{Y}{D_c} = 0,45$ (◊) c - $(n_e)_1$; $\frac{Y}{D_c} = 0$ (○)

$(n_e)_2$; $\frac{Y}{D_c} = 0,15$ (△)

d - Températures électroniques

Densité et température électroniques mesurées en 12 points du sillage proche à t = 30 ms – Maquette D_c = 196 mm

Tirs 221 (○), 222 (●), 225 (⊘) $\rho_0 \simeq 0,1$ at.

T_0 = 5200 °K, 5000 °K, 4900 °K $M_\infty \simeq 16$

fig. 17

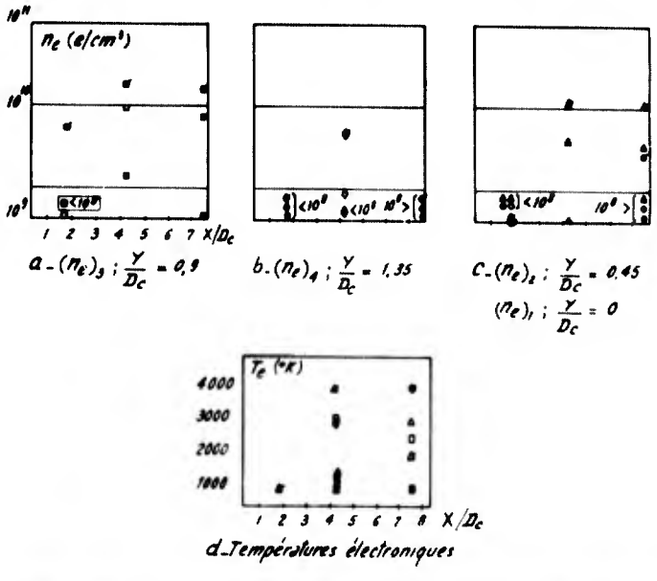

a - $(n_e)_3$; $\frac{Y}{D_c} = 0,9$ b - $(n_e)_4$; $\frac{Y}{D_c} = 1,35$ c - $(n_e)_2$; $\frac{Y}{D_c} = 0,45$

$(n_e)_1$; $\frac{Y}{D_c} = 0$

d - Températures électroniques

Densité et température électroniques mesurées en 12 points du sillage proche à t = 35 ms – Maquette D_c = 65 mm

Tirs 220 (⊘), 223 (●), 226 (○) $\rho_0 \simeq 0,1$ at.

T_0 = 5500 °K, 4600 °K, 4100 °K $M_\infty \simeq 16$

fig. 18

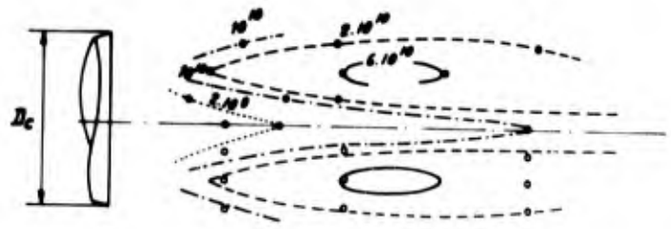

• point interpolé ou extrapolé
○ point expérimental

Carte des profils de densité électronique obtenue par interpolation entre les points expérimentaux
Tir 221. t = 30 ms _ D_c = 196 mm

fig. 19

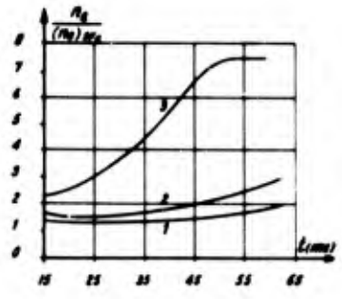

a) sondes 1,2,3 à $\frac{X}{D_c} = 0,7$

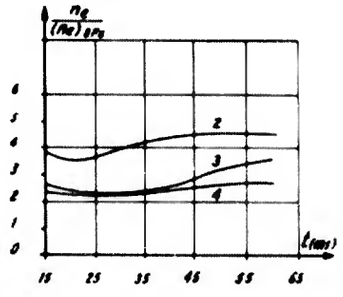

b) sondes 2,3,4 à $\frac{X}{D_c} = 1,4$

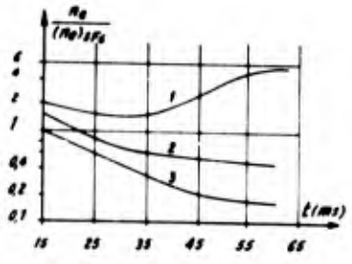

C) sondes 1,2,3 $\frac{X}{D_c} = 2,5$

Influence de l'injection SF_6 (45° au nez)
Maquette D_c = 196 mm

fig. 20

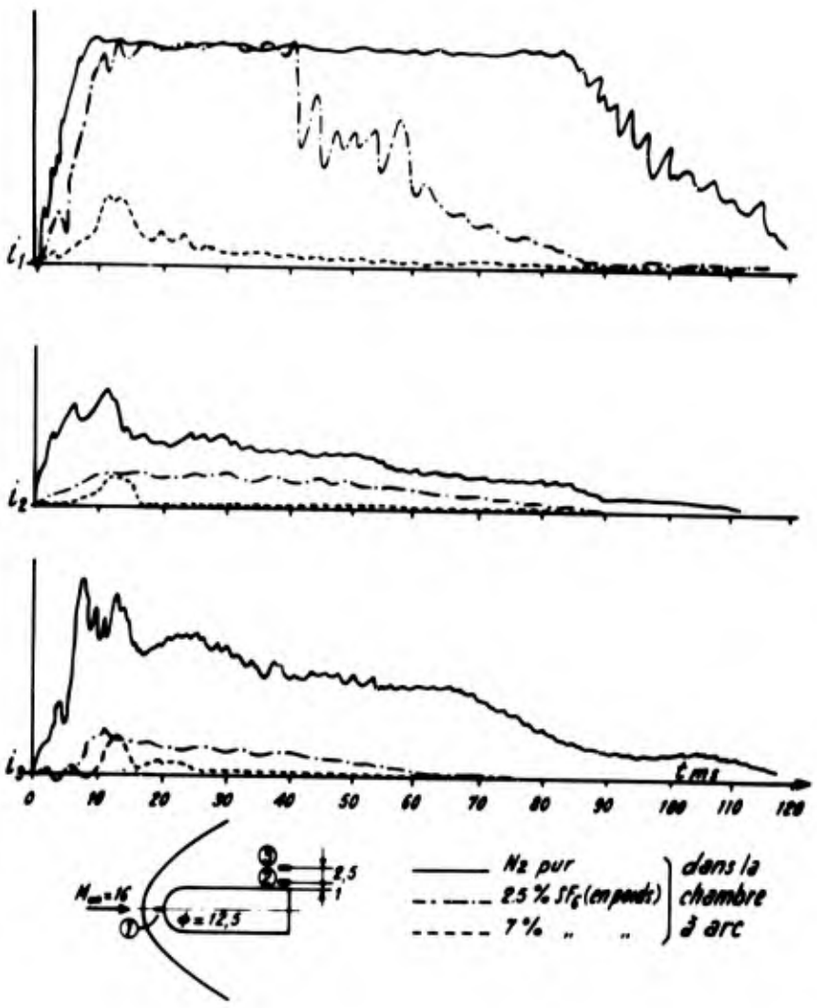

Enregistrement des courants collectés sur trois sondes avec et sans ensemencement au SF_6

fig. 21

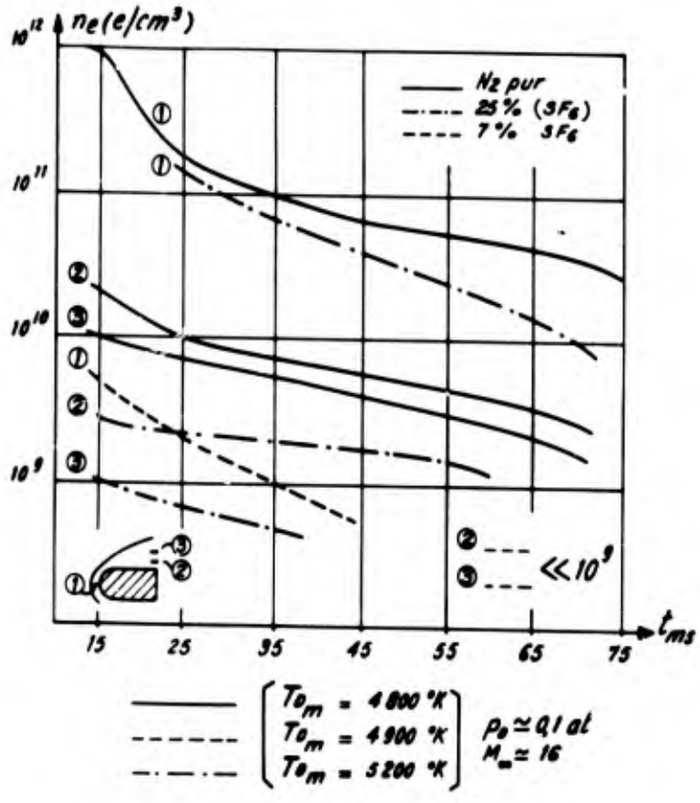

Densité électronique pour trois tirs
avec ou sans ensemencement (dans la chambre à arc)

fig. 22

MATERIAL EFFECTS OF LOW TEMPERATURE ABLATORS ON HYPERSONIC WAKE PROPERTIES OF SLENDER BODIES

BY

J. CRESSWELL
B. KAPLAN
R. PORTER
C. SARKOS

OF

GENERAL ELECTRIC COMPANY
PHILADELPHIA, PENNSYLVANIA

Summary

For slender ablating bodies in hypersonic flight, the aerothermochemical properties in the wake flow field depend strongly on the physical and chemical nature and delivery rate of the ablation products released from the body surface. For those ablation materials commonly called low-temperature ablators, the mass loss rate is relatively large and the associated wake property influences are correspondingly great. Representative materials in this category, frequently employed on practical re-entry bodies, are epoxy resins and Teflon. The former are hydrocarbons and the latter a fluorocarbon polymer. The thermal and chemical effects of the dissociation, oxidation and charged-particle reactions among the ablation species and the air species produce important effects on the aerothermochemical property distributions in the boundary layer and wake flow field, notably the electron density and temperature fields.

Reported and interpreted in this paper are the results of theoretical computations of flow field properties in the non-equilibrium boundary layer and wake of a slender conical body for both epoxy and Teflon ablation materials and for two altitudes. Finite - difference numerical solutions are employed to ascertain the importance of the various thermal and chemical effects, emphasizing the altitude - dependent influences exerted upon electron generation and disappearance since the radar scattering properties of wakes are of great interest currently. Besides the heat capacity and thermal effects of dissociation and oxidation reactions, some chemical processes peculiar to these

materials and of particular relevance to electron concentration are studied. These are hydrocarbon chemi-ionization and electron attachment to fluorine atoms. The significance of these processes in hypersonic flows has received relatively little theoretical analysis in the past.

The results reveal that the physical and chemical characteristics of low-temperature ablators create important effects upon the aerothermochemical properties of hypersonic boundary layer and wake flows. Furthermore, the relative significance of each causal mechanism is found to exhibit a notable sensitivity to the density level (i.e., altitude).

Resume

Considérons des corps fusiformes d'ablation en vol hypersonique; les propriétés thermochimiques du champ d'écoulement de leur sillage dépend dans une large mesure de la nature physico-chimique et du taux de dégagement des produits d'ablation émanant de leur surface. Pour ces matériaux d'ablation, appelés communément ablateurs à basses températures, le taux de perte de masse est relativement élevé et, parallèlement, les effets des propriétés du sillage sont importants. Parmi les matériaux représentatifs de cette catégorie, citons les résines époxy et le Teflon. Les premiers sont des hydrocarbures, le second un fluocarbure (polytetrafluoroéthylène). Les effets thermiques et chimiques de cette dissociation, de cette oxydation, et de cette réaction de particules chargées qui s'opérent parmi les substances produites par l'ablation et les éléments de l'air se font sentir avec force sur la répartition des propriétés aérothermochimiques dans la couche limite et le champ d'écoulement du sillage, et, en particulier, sur la densité en électrons et les champs thermiques.

Au cours de cette communication, les auteurs exposent et interprètent les résultats des calculs théoriques portant sur les propriétés du champ d'écoulement au sein de la couche limite et du sillage en état d'équilibre instable d'un corps conique fuselé, pour des matériaux d'ablation soit d'époxy, soit de teflon. Ils font appel à des solutions numériques aux différences finies pour vérifier l'importance des divers effets thermiques et chimiques, en soulignant les influences qui s'exercent sur la production et la disparition d'électrons. Ils étudient par ailleurs la capacité calorifique et les effets thermiques des réactions de dissociation et d'oxydation, et certains processus chimiques se rapportant particulièrement à la concentration en électrons: ionisation chimique des hydrocarbures et fixation d'électrons sur les atomes de fluor. On s'est relativement peu attaché, jusqu'ici, à analyser l'importance de ces processus dans les écoulements hypersoniques.

Notation

Symbol	Description	Units
C_j	Mass fraction of species j	----
f'	Dimensionless streamwise velocity, $\frac{u}{u_e}$	----
$\dot{m}$	Mass flux or flow rate	slugs/sec.
r_b	Local body radius	feet
u	Streamwise velocity	feet/sec.
u_e	Streamwise velocity at edge of boundary layer	feet/sec.
x	Physical coordinate along body surface	feet
y	Physical coordinate normal to body surface	feet
η	Transformed boundary layer coordinate: $\eta = \frac{r_b u_e}{(2\xi)^{\frac{1}{2}}} \int_o^y \rho \, dy$	----
μ	Fluid viscosity	$\frac{lb_f - sec}{ft^2}$
ξ	Transformed boundary layer coordinate: $\xi = \int_o^x \rho_e \mu_e u_e r_b^2 \, dx$	$\frac{slugs^2}{sec^2}$
ρ	Fluid density	$slugs/ft.^3$
$\hat{}$	Quantity evaluated at boundary layer peak temperature point	
w	Quantity evaluated at body surface	

BLANK PAGE

I. Introduction

During the hypersonic flight of an object through the atmosphere, the heated and ionized wake trail generated is observable from the ground by radar and optical detection systems. Also, the transmission of electromagnetic signals emitted or reflected from the object can be affected seriously by the electrical properties of the flow field about the body. The pertinent properties of these flows, in general including all of the properties describing the aerothermochemical state of the gas mixture, can be influenced significantly by products of ablation released through response of the surface material to aerodynamic heating, especially for slender bodies (References (1) and (2)). The extent of such ablation product effects depends, of course, on the physical and chemical nature of the ablated species, as well as on the quantity of such material added to the air stream.

For those ablation materials commonly called low-temperature ablators, the mass addition rate is large relative to that of other heat protection materials. Also, for some such ablators the released products exhibit chemical behavior of particular importance with respect to electron generation and disappearance, and so to the electromagnetic interaction problems mentioned above. Therefore, it is of interest to study the influences exerted by these materials on the aerothermochemical properties of the non-equilibrium chemically reacting boundary layer and wake flow fields for slender bodies.

Two low-temperature ablators, which can create interesting chemical effects in the flow field,are the epoxy resins and Teflon. The epoxy substances are hydrocarbons which, in the process of

degradation and oxidation (combustion) in the air stream, can supply free electrons to the flow by chemi-ionization (Reference (2)). Teflon, a fluorocarbon polymer, decomposes to yield a considerable concentration of fluorine atoms and molecules in the boundary layer. These can react with free electrons to form negative fluorine ions, thereby reducing the electron density in the field (Reference (2)).

Of course, for both materials the heat capacities and reaction energies (for example, cooling by dissociation and heating by oxidation) can produce appreciable modification to the gas temperature field, and so also to the rates of the several reactions which affect the electron concentration. In addition, the presence of trace quantities of impurities, especially alkali metals such as sodium, in the ablation material can produce enormous influences upon the electron concentration in the flow field for any ablation material. In many cases, such contributions can constitute the dominant source of electrons in the flow (Reference (1) and (2)).

Very little theoretical analysis has been performed of all these physical and chemical features in combination for the low-temperature ablation materials in realistic re-entry environments. Because the previously cited problems of electromagnetic interaction with re-entry flow fields are of great current interest, and since these particular ablation materials are representative of commonly employed heat shield materials, theoretical computations are reported here of the aerothermochemical property fields in the non-equilibrium boundary layer and wake of a slender body under hypersonic re-entry conditions

for both materials. In addition, computations for a nonablating vehicle are presented. Because several of the phenomena under study are sensitive to the density level, either through Reynolds number or chemical reaction rate dependences, computations have been performed for two altitudes in the atmosphere, differing in ambient density level by an order of magnitude. For the higher density condition, the epoxy case also is studied in the absence of alkali metal to examine chemi-ionization free of major competing ionization mechanisms.

II. Description of Analysis Methods

A. Flow Fields

The analysis of the non-equilibrium chemically reacting flow about and behind a slender conical body has been performed through the application of numerical solutions on an IBM 7094 digital computer. For the viscous flow regions, adaptations of the finite - difference formulations developed by Blottner (Reference (3)) for the boundary layer and Langan (Reference (1)) for the far wake have been utilized. These flow regions are the ones in which significant effects of ablation products are realized. Of course, the surrounding inviscid flow regions have been analyzed in order to provide the required boundary value data for the viscous flow problems. In addition, the near wake or base flow has been treated by an approximate semi-empirical analysis based on the experimental data of Muntz (Reference (4)). An important feature of the near wake analysis in the present application is the assumption of chemically frozen flow in this region. The methods for the inviscid flow and near wake analysis are described in References (1) and (2).

B. Chemical System

The reaction mechanisms and rate constants used are given in Tables 1-3. The system consists of 30 species and 48 reactions. A survey of the kinetics of the $H_2/CO/O_2$ system by Kaskan and Browne (Reference (5)) provided the basis for the kinetics of CO and H_2. Some of the reaction rate constants given in that report have since been up-dated by Browne and it is these revised values that are listed.

The mechanisms and rate constants for the oxidation of acetylene are the results of a recent investigation of low pressure flames and a tentative analysis of these data using a computer program which provides for diffusion and is capable of handling 30 species and 150 reactions (Reference (6)). Reaction rate constants for the oxidation of C_2F_4 are those suggested by Browne from a survey of the literature, as are those for the air and alkali metal systems (Reference (1) and (2)).

The approach taken to calculate electron production from acetylene is the result of a phenomonological analysis of data obtained with premixed acetylene flames burning at low pressures on flat, water cooled, porous metal burners (Reference (6)). The fraction of acetylene molecules that yielded ions were computed, taking into account diffusion of both ions and fuel, as well as ion recombination. The rate constant for ion recombination was determined in that region of the flame where ions are no longer produced but decay in a second order process. For computational purposes, acetylene is assumed to give H_3O^+ ions, the principal ion present in flames. It was observed that the ion yield, fraction of acetylene molecules oxidized to give ions, decreased with increasing ratio of fuel to oxygen in the feed gases and that this yield was proportional to the hydroxal radical concentration. The net rate of production of H_3O^+ ions, R_{H3O^+}, and of electrons, R_e, from acetylene is found to be given by:

$$R_{H_3O^+} = R_e = 1.81 \times 10^3 \, R_{C2H2} \, (OH) - 2.11 \times 10^{17} \, (H_3O^+) \, (e)$$

where $R_{C_2H_2}$ is the rate of disappearance of acetylene and where units are in gm-moles, cm^3, sec. This scheme could be readily extended to include other fuels if it were found that ion production from these is

also proportional to hydroxyl radical concentrations. Bulewicz and Padley (Reference (7)) have obtained relative ionization efficiencies for a large number of fuels which should prove useful for such calculations.

There are several approximations that might be expected to limit the accuracy of the present computations. Research programs currently underway at General Electric Company as well as elsewhere should, in the near future, alleviate some of the difficulties and put the results of the current investigation on a firmer footing. The ablation products from epoxy resins are approximated by acetylene, hydrogen, carbon monoxide and traces of N_2 and Na. To the extent that the chemistry of oxidation of the true products of ablation differ from those of the assumed products, discrepancies will arise. Of particular importance is this connection will be the slower or rate limiting steps of combustion. Fortunately, on a per carbon atom basis, all hydrocarbons give a rather similar yield of ions (Reference (7)). For example, the ratio of ions produced from acetylene to those produced from methane on a per carbon atom basis is about 3 or 4 to 1 with most other hydrocarbon fuels giving a yield somewhere between. The fraction of fuel molecules which yield ions on oxidation does not depend very strongly on temperature or on reaction conditions in lean systems. Similar yields have been observed in flames, shock tubes and flow tubes. In our own work with flames we were unable to detect any effect of temperature on ion production over a temperature range of 700°K. In view of the above and the higher burning velocity of acetylene in comparison with

many hydrocarbon fuels, it is believed that the present calculations will give electron concentrations from chemi-ionization that are somewhat on the high side. A possibly more serious source of error involves the neglect of particulate matter in the boundary layer and wake, which if present in substantial amounts might be expected to seriously alter electron concentrations by serving as either a source or sink for electrons. The chemistry of C_2F_4 oxidation is still speculative at this time. Nevertheless, the present calculations should give a reasonable description of the boundary layer and wake chemistry, although one which may not be correct in every detail.

III. Results and Discussion

A. Conditions Investigated

To meet the objectives of this study, seven body and wake flow fields have been calculated. These include two altitudes, 125 kft. and 175 kft.; and three basic chemical systems, Teflon - Sodium - Air, Hydrocarbon - Sodium - Air, and Sodium - Air. The seventh calculation is for the 125 kft. altitude and a Hydrocarbon - Air chemical system without sodium.

The flight conditions, body configuration and boundary layer edge conditions are listed in Table 4. The normalized injection rate applicable to all seven cases is shown in Figure (1) and the normalizing values are listed thereon. The injection rate for $x > 0.5$ feet was varied inversely as the square root of the wetted length, x. The blowing parameter is defined to be

$$B.\,P. = \frac{(\rho v)_w}{\rho_e u_e}\sqrt{Re_x}$$

It follows, for constant edge conditions, that the blowing parameter is constant for $x > 0.5$ feet. In addition to these considerations the reference injection rates were adjusted for the two altitudes so that the value of B. P. was nominally the same for all five large injection cases. (B. P. $\approx$ .6 for Teflon and Hydrocarbon calculations.) The ablation rates and the wall temperature are typical for low-temperature ablators. The sodium - air injection rate was calculated to give the same total sodium injection as the Teflon and Hydrocarbon cases; namely, 133 PPM.

B. Boundary Layer

Air - Sodium

The discussion and interpretation of results will be done by taking one chemical system (one surface material) at a time. Since the air - sodium system (nonablating body) is used as the reference case, and since these calculations were handled differently from the other five cases, the air - sodium system is discussed first.

The calculations pertaining to the boundary layer for the two sodium - air cases consist of finite - difference solutions to determine the overall boundary layer flow field and an approximate technique superimposed on these calculations for the purpose of determining the level and trends of the sodium ionization. Boundary layers for the other five cases, however, were entirely the results of finite - difference calculations. Returning to the two sodium - air cases, similarity techniques were used to calculate the fractional amount of sodium ionized at the peak temperature point and to calculate the mass flow of sodium ion in the boundary layer. Specifically, the technique for obtaining $\hat{C}_{Na^+}$, or equivalently $\frac{\hat{C}_{Na^+}}{\hat{C}_{Na^+} + \hat{C}_{Na}}$, is due to Lenard (Reference (8)). The actual values of peak temperature, $\hat{T}$, $\hat{C}_{Na}$, $\hat{C}_{O_2}$, $\hat{C}_O$,* $\hat{C}_m$, $\hat{M}$, etc. were taken from the existing finite - difference calculation. The mass flow of the sodium ion was assumed to be related to that of NO^+ by the peak values, i.e.

$$\dot{m}_{Na^+} = \frac{\hat{C}_{Na^+}}{\hat{C}_{NO^+}} \dot{m}_{NO^+}$$

The mass flow of NO^+ was determined from the existing calculations. The

*The ^ symbol refers to a quantity at the peak temperature point.

NO^+ profile should not be greatly affected by varying amounts of sodium since it (NO^+) is produced mainly in the immediate vicinity of the peak temperature and is largely diffusion controlled from there out. The mechanism for NO^+ production is

$$N + O \rightleftharpoons NO^+ + e^-$$

Near the peak temperature the forward rate prevails so that the mass fraction $\hat{C}_{NO^+}$ is little affected by the presence of additional electrons due to Na^+.

The gross features of the air - sodium calculations are a high value of peak temperature that stays relatively constant and close to the wall (Figures (3), (4) and (5)) and a high degree of sodium ionization at the peak temperature (Figures (6) and (7)). The peak temperatures are due almost entirely to viscous dissipation for both altitudes. At the lower altitude, there is a small decrease in temperature with wetted length attributable to the increased chemical activity at this altitude. Virtually all of this activity is manifested in the reactions

$$(1)\quad O_2 + M \rightleftharpoons 2O + M$$

$$(2)\quad N_2 + O_2 \rightleftharpoons 2NO$$

which are going to the right (endothermic).

The level of sodium ionization, as seen in the values of electron density at the peak temperature point, is relatively high for both the 125 kft. and the 175 kft. altitudes (Figures (8) and (9)). The several factors influencing the ionization level of sodium include temperature, density and distance downstream from the start of injection. The dominant reaction producing both sodium ions and electrons is the direct ionization reaction (N_O. 20)

$$Na + M \rightleftharpoons Na^+ + e^- + M$$

Two other reactions of lesser importance are Numbers (18) and (19);

$$Na + O_2 \rightleftharpoons Na^+ + O_2^-$$

$$Na + O \rightleftharpoons Na^+ + O^-$$

The more important of these two is the first (No. (18)) because of the large amount of molecular oxygen available in a sharp-cone boundary layer.

Hydrocarbon Boundary Layers

An outstanding feature of the hydrocarbon boundary layers is the dramatic drop in temperature due to the wall injection (Figures (4) and (5)). As expected, the sodium-dominated electron density follows the peak temperature trends (Figures (6) and (7)) to reach the lowest values of electron density exhibited by the six sodium cases. Only the hydrocarbon boundary layer without sodium showed a lower level of electrons over the five foot length (Figure (6)). This latter case differs from the other 125 kft. hydrocarbon boundary layer only in the sodium injected. Therefore, they will be discussed concurrently.

Hydrocarbon Boundary Layer at 175 Kft.

The initial drop in temperature from the pure air initial condition occurs as the boundary layer adjusts to the blowing at the wall. The temperature drop is due primarily to decreased viscous dissipation ($\frac{\partial u}{\partial \eta}$ decreases) and to an increase in average specific heat.

The velocity profile (Figure (2)) indicates that the velocity gradients are smaller for the blowing case. This in turn leads to less viscous heating and therefore, lower temperatures. The average specific heat from the wall to somewhat past the peak temperature point is larger than the pure air case due to the presence of large amounts of acetylene

($C_p \approx 2.4\ C_{pair}$) and molecular hydrogen ($C_p \approx 14\ C_{pair}$). The net effect on the specific heat is about a 50% increase over the pure air value near the peak temperature.

Except for ion production, there is no important chemistry going on because the boundary layer pressure is too low. Mass fractions of the dominant injected species are nearly constant at the peak temperature points (Figure (10)) and the boundary layer mass flux of acetylene, CO, and molecular hydrogen are virtually identical to their injected values (Figures (11) and (12)).

Ion production is dominated by the direct ionization mechanism (No. (20))

$$Na + M \rightleftharpoons Na^+ + e^- + M$$

which is quite temperature sensitive. For this reason, virtually all of the sodium ions are produced in the vicinity of the peak temperature point and are diffusion controlled elsewhere. A manifestation of this fact is seen by comparing sodium mass fraction at peak temperature to the mass flux of sodium (Figures (13) and (14)) and noting similarities in their respective trends.

$$\dot{m}_{Na^+} = 2\pi r_b u_e \int_0^{\delta} C_{Na^+} \rho f^1 dy$$

$$= 2\pi (2\xi)^{\frac{1}{2}} \int_0^{N_e} C_{Na^+} f^1 d\eta$$

$$\approx 2\pi (2\xi)^{\frac{1}{2}} \hat{C}_{Na^+}(X) \int_0^{\eta_e} \frac{C_{Na^+}}{\hat{C}_{Na^+}} f^1 d\eta$$

$$\dot{m}_{Na^+} = (\text{Const})(X^{3/2})(\hat{C}_{Na^+}(X))$$

$$\frac{\dot{m}_{Na^+}(X_1)}{\dot{m}_{Na^+}(X_2)} \approx \left(\frac{X_1}{X_2}\right)^{3/2} \frac{\hat{C}_{Na^+}(X_1)}{\hat{C}_{Na^+}(X_2)}$$

The above relation will hold generally when profiles are similar and $\hat{C}_{Na^+}$ (species) are functions of X (or ζ) only.

The major effect of large blowing in this case is the reduced level of sodium ions, attributable to the reduced temperature. A secondary effect of blowing, which is also a materials effect, is that the element mass fraction at the peak point is lower than for the air and Teflon cases. Simply stated, there is less total sodium available to be ionized at the peak temperature point.

The reaction second in importance to direct ionization is

$$Na^+ + O_2 \rightleftharpoons Na^+ + O_2^-$$

This reaction is affected by blowing in the same way as the direct ionization. Also, while it is of some importance at the 175 kft. altitude, it will be seen to be of less importance at the lower altitude (125 kft.) because burning depletes the available O_2 supply near the peak temperature point.

Hydrocarbon Boundary Layer 125 Kft.

The initial drop in peak temperature is qualitatively the same as for the 175 kft. case. Unlike the higher altitude hydrocarbon boundary layer, however, the peak temperature starts to rise at the two-foot station (X = 2.0 feet)(Figure (4)). Consistently, the boundary layer mass flow of acetylene drops and that of carbon monoxide rises from their respective injected values (Figures (17) and (19)).

Once the gross flow properties adjust to large mass injection ($X \approx 0.7$ feet), there is a region of approximately constant peak temperature until $X \approx 2.0$ feet and then the (peak) temperature starts to rise due to hydrocarbon burning. The delay experienced in attaining a significant temperature rise ($0.7' < X < 2.0'$) is due to the time required for the necessary intermediate radicals (C_2H, CH_2, CH, etc.) to build up (Figures (15), (16), (17) and (18)) so that the overall combustion chain can go fast enough to cause an increase in temperature. The dominant exothermic reactions are numbers (36), (38), (39), (41), (42) and (43). At this point ($X \approx 2.0$ feet), all of the intermediate species are chemically controlled. Acetylene, carbon monoxide and molecular hydrogen are controlled by the fluid mechanics of the boundary layer (wall injection and diffusion).

Downstream ($X \approx 5$ feet), diffusion is expected to exert more influence. For example, the value of C_2H at the peak temperature point is decreasing (Figure (16)). This is due to reaction (36) slowing down and leveling off because of decreasing C_2H_2 and increasing CO (Figure (15)). Both the C_2H_2 deficiency and the CO excess are due to diffusion (or normal convective) limitations. Another sign of diffusion limiting is the relation between molecular and atomic oxygen. From two to five feet molecular oxygen went down by a factor of ten (Figure (15)) while atomic oxygen went up only by a factor of three and appears to be steadying out. Most of the reactions are, in fact, leveling off either because the level of the reactants is decreasing or the product level is increasing, or both. A "steady-state" is still not reached by the end of the body.

When sodium is present, its ion is dominant and controls the electron production (Figures (13) and (14)). The H_3O^+ ion plays a poor second to Na^+. However, when sodium is removed, not only does H_3O^+ become the controlling ion but it rises above the level it attains in the presence of sodium by a factor of twenty in mass fraction (Figures (20) and (21)) and a factor of fifty in total mass flux (Figures (22) and (23)).

Again, the controlling reaction for the production of Na^+ is the direct ionization reaction.

$$Na + M \rightleftharpoons Na^+ + e^- + M$$

Reaction (18)

$$Na + O_2 \rightleftharpoons Na^+ + O_2^-$$

is of some importance for $X < 2.0'$, but declines rapidly as the mass fraction of O_2 drops (Figure (15)). Reaction (19) never assumes a prominent role in ion production.

Virtually all of the H_3O^+ ions are produced in the region of the peak temperature point, in accord with the empirical reaction scheme which relates this chemi-ionization process to the acetylene consumption.

The large amount of electrons produced by sodium suppresses the net production of H_3O^+ by neutralization. Without sodium-generated electrons, there is more H_3O^+ and the resulting electron level is quite significant by the and of the body ($Ne^- \approx 2 \times 10^{10}$ electrons/cm^3, Figures (6) and (21)). Thus, it appears that a significant level of electron population may be reached at this altitude even without metallic contamination.

As in the 175 kft. case, the major effect of blowing is manifested (in the sodium case) by reduced ionization due to a reduced temperature

(Figure (20). A secondary blowing effect, also due to the thermodynamic properties and to combustion taking place somewhat beyond the peak temperature point, is that the total sodium mass fraction at the peak temperature point is reduced to a value of $\frac{C_{Na}}{C_{Na_{wall}}} \approx 0.4$ (compared with 0.5 and 0.6 for Teflon and air, respectively). The peak temperature point has moved out from the wall while the fluid mechanically dominated element mass fraction profile has been relatively unaffected by the material properties and combustion processes.

Teflon Boundary Layer

The peak temperature drop for both altitudes is due primarily to the heavy blowing condition at the wall and the associated decrease in velocity gradients (Figures (2), (3), (4) and (5)). The drop for Teflon is less severe than for the hydrocarbon case mainly because of the difference in specific heats. Those for the Teflon species are generally comparable to pure-air species while the hydrocarbon specific heats tend to be much higher.

At the higher altitude, the temperature is virtually constant while at the 125 kft. altitude there is an appreciable temperature decline $\left(\frac{dT}{dx} < 0\right)$. Consistently, there are no important thermal effects due to chemistry near the peak temperature point at the high altitude while, for the low altitude case, two endothermic reactions are causing temperature to drop. These two reactions are

$$(27)\quad CF_2 + O_2 \rightarrow 2F + O + CO$$

$$(29)\quad F_2CO + M \rightarrow 2F + CO + M$$

Reactic (27) is the more effective because it is going at a faster rate. This is mainly due to a higher rate constant (ten times greater).

At both altitudes, C_2F_4 is quickly dissociated into CF_2. At 175 kft., the mass flux of CF_2 is nearly equal to the injected mass flux (Figures (25) and (26)) implying that there is no other chemistry going on at a comparable level. Consistently, the peak temperature is virtually constant since the breakup of C_2F_4 occurs near the wall and has little direct effect on the peak temperature. At 125 kft., there is far more difference between the mass flux of CF_2 and the injected mass flux (of C_2F_4) (Figures (28) and (29)). These observations together with the trends of the peak temperature provide a gross estimate of the level of chemistry going on in the boundary layer.

At the high altitude, the ion chemistry is dominated by sodium (Figure (30) and (31)). Sodium ions are produced for the most part in the vicinity of the peak temperature point. The mass fraction of sodium ion produced depends on the temperature (fractional ionization = $\frac{\hat{C}_{Na^+}}{\hat{C}_{Na}}$ being quite temperature dependent) and on the element mass fraction of sodium ($\hat{C}^{Na}$) at that point. The temperature level is determined mostly by the fluid mechanics in this case. The element mass fraction, which is approximately proportional to the velocity defect, i.e.,

$$\frac{\hat{C}^{Na}}{C^{Na}_{wall}} \approx \left(1 - \frac{\hat{u}}{u_e}\right)$$

has a value of 0.5 at the peak temperature point - compared to values of $\sim$0.6 for air and $\sim$0.4 for hydrocarbon.

The ions for the 125 kft. case are also sodium dominated, but here fluorine attachment has become relatively more important (Figures (32) and (33)). Attachment occurs predominately near the wall while ionization is controlled farther out at the peak temperature point. The major attachment processes are

$$F_2 + e^- \rightleftharpoons F^- + F$$

$$F + e^- + M \rightleftharpoons F^- + M$$

both of which have maxima near the wall. The relative importance of F^- and Na^+ may be seen by comparing mass flows (Figure (33)) or mass fractions at the peak temperature (Figure (32)). Both figures show that the F^- is rising more rapidly than the Na^+. This is due to a decreasing peak temperature which inhibits the production of Na^+.

Massive wall injection, as such, has had less effect on sodium ionization for the Teflon cases than for the hydrocarbon boundary layers. This is primarily because the temperatures do not drop as much for the Teflon as for the hydrocarbon species, because of the heat capacity differences.

C. Wake

The discussion of the wake results is confined primarily to the axis of symmetry, realizing that the off axis behavior may be significantly different. For example, the decay of some particular species concentration on the axis may be controlled by chemistry, but the concentration curvature off the axis may change substantially and cause the diffusion to predominate there. Therefore, the axis aerothermochemical behavior

in the following discussion is not necessarily indicative of the behavior across the entire viscous wake cross section.

Temperature

The temperature decay along the wake axis is shown in Figures (34) and (35) for the Teflon, hydrocarbon and air cases. Chemical reactions occurring in the laminar wake at 125 kft. have a significant effect on the temperature. In the hydrocarbon case, the combustion of C_2H_2 raises the temperature; while in the Teflon case, the rapid rate of the endothermic reaction $CF_2 + O_2 \rightarrow CO + 2F + O$ (Reaction (27)) lowers the temperature. Dissociation of C_2F_4 (Reaction (25)) is also endothermic and is quite rapid in the initial portion of the wake, but because of its rapid depletion, its effect on the axis temperature is small compared with Reaction (27). Upon transition to turbulent flow at an axial distance of 25 ft. from the wake neck, the assumed sudden commencement of rapid turbulent mixing causes a steep decrease in temperature. However, because of the rapid combustion of C_2H_2 occurring off the axis, the hydrocarbon case develops an off-axis temperature peak (Figure (36)) which helps to raise the axis temperature above the air value after transition. The relative temperature levels in the turbulent wake will have an effect on the rate of electron attachment for the different cases. At 175 kft., the temperature distribution in the laminar wake is controlled primarily by conduction which is more important at this altitude than at 125 kft. The dominant reactions affecting the temperature distribution are the same as for 125 kft.; however, their rates are not as fast. The combustion of C_2H_2 in the laminar wake for the hydrocarbon case raises the temperature above the

Teflon and air values. After transition, the relative temperature levels are the same as at 125 kft., i.e., the hydrocarbon case has the highest temperature, the Teflon case has the lowest, and the air case lies in between.

Electron Density

Shown in Figures (37) and (38) is the electron density decay along the wake axis for each of the seven cases considered. At 175 kft., the decay rates are fairly similar and the electron level is essentially determined by its initial value. The hydrocarbon case has a much lower initial electron density than either the air or Teflon cases because of its lower temperature in the boundary layer; consequently, the sodium ionization is reduced. In the laminar portion of the wake, the decay is controlled by diffusion and is not influenced significantly by the differences in temperature between the three cases. After transition, the electron decay is controlled by turbulent diffusion with molecular oxygen attachment (Reaction (24)) becoming more important with increasing distance from the neck. By about 1,000 feet these two effects are nearly equal in value and by 3,000 feet O_2 attachment is depleting electrons several times faster than turbulent diffusion. Atomic oxygen attachment (Reaction (23)) and fluorine atom radiation (Reaction (33)) are the most rapid electron removal reactions in the initial laminar wake; however, their effect on the electron decay is decidedly less than that of diffusion. For the hydrocarbon case, there is no significant chemi-ionization to alter the electron level.

The effect of the different heat shield materials on the electron density becomes more pronounced at 125 K. This is to be expected since

the higher density causes the chemical reactions associated with the degradation products from the different heat shield materials to proceed at faster rates, and the diffusion rate will be smaller than at 175 K. The chemistry in the hydrocarbon case raises the electrons above the level of the air case, while in the Teflon case it brings them increasingly farther below the air values. The Teflon curve decays more rapidly than the hydrocarbon curve because of rapid electron attachment to molecular and atomic oxygen (the molecular attachment is the more important of the two). These reactions proceed more rapidly in the Teflon case because of a higher mixture density, lower temperature, different degree of proximity to equilibrium, and higher availability of O_2 and O. (In the hydrocarbon case, much of the O and O_2 is used during combustion.)

Another interesting comparison at 125 kft. is between the two hydrocarbon cases. For the case with sodium, O_2 attachment (Reaction (24)) becomes important about 100 ft. from the wake neck and contributes significantly to the electron decay beyond this location. However, for the case without sodium, this reaction is not as important, the reason being that it is nearly in equilibrium because of the rapidity of the reverse rate ($O_2^- + M \rightarrow O_2 + e^- + M$). For the case with sodium, the reverse rate is not as rapid because of the depletion of O_2^- by Reaction (18) ($Na^+ + O_2^- \rightarrow Na + O_2$). Thus the speed at which O_2 attaches electrons is influenced by the mechanisms for O_2^- removal (whether they be chemical or diffusive). The relatively large amount of electrons for the case without sodium were generated by chemi-ionization and not from Reaction (7) ($N + O \rightarrow NO^+ + e^-$). This allows for the possibility of

significant electron population in the wakes behind "clean" heat shields.

Species

Figure (39) shows charged species concentrations (proportional to mole fraction) for the comparison mentioned above. In both cases, the electron decay follows the dominant positive ion until O_2 attachment becomes important. The levels of the other charged species do not affect the electron concentration.

The variation of charged species concentration along the wake axis is shown in Figures (40) and (41) for the hydrocarbon (with sodium) and Teflon cases. Both altitudes have rapid chemical reactions occurring far into the turbulent wake. The species whose axis mass fractions increase after transition develop off-axis peaks in the laminar regime which diffuse toward the axis because of the large turbulent diffusivity. The most notable of such species is O_2^-, whose off-axis peak results from rapid electron attachment. Again, the several other ions shown are observed to be insignificant in determining the wake axis electron level. Although F^- has the largest negative ion concentration, it does not control the electron decay in the wake. Its concentration increases in the laminar regime because of attachment (Reactions (31), (32) and (33)) and diffuses away after transition. Since these reactions are attaching electrons at a rate which is far from equilibrium, their effectiveness would not be influenced by some F^- removal reaction, e.g., $F^- + Na^+ \rightarrow F + Na$.

For completeness, Figures (42) and (43) show the variation of the neutral degradation products along the wake axis for the hydrocarbon case at 175K and 125K. Also included is the variation of O_2 and O.

The behavior of O_2 and O at 175 kft. indicates that the combustion of C_2H_2 is not very pronounced; however, their rapid decrease in the laminar position at 125 kft. shows that the combustion is proceeding much more rapidly at this altitude. Generally speaking, the concentration of the intermediate species seems to be most affected by the combustion process as compared with the major degradation neutrals which tend to be controlled by diffusion.

Shown in Figures (44) and (45) is the variation of the Teflon neutrals along the wake axis at 175 kft. and 125 kft. The initial rapid decay of C_2F_4 is caused by Reactions (25) and (26) which proceed very rapidly near the wake axis, causing an off-axis peak to develop. The initial minimum occurs where the diffusion of C_2F_4 towards the axis is balanced by its depletion by chemical reaction. Diffusion controls the decay downstream from this point with Reaction (26) becoming slightly important in the turbulent regime. All of the other species are controlled by diffusion and Reaction (27) ($CF_2 + O_2 \rightarrow CO + 2F + O$), except for CO_2 which is controlled by diffusion and Reactions (16) and (17), and F_2CO which is entirely diffusion controlled.

IV. Conclusions

Given below is a summary of the major conclusions derived from the present theoretical study of the effects of the physical and chemical properties of low-temperature ablators on the aerothermochemical properties of hypersonic boundary layer and wake flows.

(1) The flow field temperature is cooled appreciably by decreased viscous dissipation due to boundary layer blowing, the heat capacity of ablation species and the endothermicity of the reactions through which ablation products are degraded.

(2) For hydrocarbon materials such as epoxy, combustion of the ablation products can create a significant temperature rise.

(3) These effects on temperature are reflected directly in the ionization of sodium, a common impurity in heat materials.

(4) During hydrocarbon combustion, the chemi-ionization process can yield important concentrations of electrons.

(5) For Teflon bodies, the relative importance of fluorine attachment of electrons increases rapidly with increasing density level, although the present quantitative results (based upon speculative reaction rate information) indicate little absolute significance of this process.

(6) Regardless of the ablation product composition (for those studied, at least), the process which controls electron decay in the far turbulent wake is the attachment to molecular oxygen. The rate of this process, however, is

influenced by the ablation material effects through the temperature and other indirect paths.

(7) In general, the material effects of low-temperature ablators can be very important in determining the flow properties, and the physical and chemical mechanisms through which these effects are realized can exhibit appreciable sensitivity to the imposed density level (altitude).

V. Recommendations for Future Study

Several influential phenomena associated with low-temperature ablators have been found in the present study. Some of these have been examined here on the basis of uncertain data or methods. Therefore, the questionable features to which the important effects are related are summarized here for the purpose of stimulating interest in their continued study by the scientific community.

The present boundary layer analysis utilizes conventional boundary layer theory. For the large mass addition rates associated with low-temperature ablators, the boundary layer can be sufficiently thick that a higher order boundary layer theory, including all the thermochemical and kinetic features of the present work, is required.

The detailed ablation mechanisms require further investigation in order to specify better the chemical composition of the ablated material. Since numerous gas phase chemical processes have been shown to exert significant influences, accurate knowledge of the relative proportions of ablation species is essential.

The gas phase chemical kinetics can be questioned, as has been pointed out. In particular, the scheme describing the reactions among Teflon ablation products and air requires considerable refinement, perhaps also in combination with alkali metals. (For example, can an important fraction of the alkali metal be consumed through formation of its fluoride?)

For hydrocarbon/air systems, a few questions remain to be answered. The detailed mechanism of chemi-ionization is not yet understood, even though the empirical method of the present analysis should constitute a

reasonable estimate of its overall rate. Similar techniques are required for hydrocarbons other than acetylene, since many other hydrocarbons can be released during ablation. The problem of particulate matter (soot) is potentially important for the low-temperature ablators since their high ablation rates give rise to boundary layer gas mixtures which can be very "fuel rich".

VI. References

1. Langan, W., Cresswell, J. and Browne, W.: "Effects of Ablation Products on Ionization in Hypersonic Wakes," AIAA Journal, Volume 3, pp. 2211-8, (December, 1965). See also AIAA Preprint No. 65-54 (January, 1965), or General Electric Technical Information Series Report 65SD208, (January, 1965).

2. Friel, P., Langan, W., Cresswell, J. and Browne, W.: "The Effects of Heat Shield Materials on the Wake Observables of Slender Bodies," Anti-Missile Research Advisory Council Proceedings, Volume XII, (November, 1965) (Secret).

3. Blottner, F.: "Non-Equilibrium Laminar Boundary Layer Flow of Ionized Air," AIAA Journal, Volume 2, pp. 1921-8, (November, 1964).

4. Muntz, E. and Softley, E.: "A Study of Laminar Near Wakes," AIAA Journal, Volume 4, pp. 961-8, (June, 1966). See also General Electric Technical Information Series Report R65SD6 (March, 1965).

5. Kaskan, W. and Browne, W.: "Kinetics of the $H_2/CO/O_2$ System," General Electric Technical Information Series Report R64SD37, (July, 1964).

6. Porter, R., Clark, A., Kaskan, W., and Browne, W.: "A Study of Hydrocarbon Flames," Eleventh Symposium (International) on Combustion, pp. 000, (1967).

7. Bulewicz, E. and Padley, P.: "A Cyclotron Resonance Study of Ionization in Low Pressure Flames," Ninth Symposium (International) on Combustion, pg. 638, Academic Press, New York, (1962).

8. Lenard, M.: "Ionization of Cesium and Sodium Contaminated Air in the Hypersonic Slender Body Boundary Layer," General Electric Technical Information Series Report R64SD22, (August, 1964).

The authors gratefully acknowledge the contributions of several employees of the General Electric Company. Mr. W. Browne recommended the bulk of the chemical reactions and rates, and entered into helpful discussions of the results. Mr. B. Morton, Miss L. Bickel and Mrs. E. Dienna performed computer programming and calculations to generate the numerical results. Miss K. Murphy meticulously prepared the manuscript.

Table 1

Chemical Reactions

1.	$O_2 + M_1$	$\rightleftharpoons 2O + M_1$
2.	$N_2 + M_2$	$\rightleftharpoons 2N + M_2$
3.	$NO + M_3$	$\rightleftharpoons N + O + M_3$
4.	$NO + O$	$\rightleftharpoons O_2 + N$
5.	$N_2 + O$	$\rightleftharpoons NO + N$
6.	$N_2 + O_2$	$\rightleftharpoons 2NO$
7.	$N + O$	$\rightleftharpoons NO^+ + e^-$
8.	$OH + H_2$	$\rightleftharpoons H_2O + H$
9.	$H + O_2$	$\rightleftharpoons OH + O$
10.	$O + H_2$	$\rightleftharpoons OH + H$
11.	$2OH$	$\rightleftharpoons H_2O + O$
12.	$2H + M_4$	$\rightleftharpoons H_2 + M_4$
13.	$H + OH + M_5$	$\rightleftharpoons H_2O + M_5$
14.	$H + O + M_6$	$\rightleftharpoons OH + M_6$
15.	$OH + CO$	$\rightleftharpoons CO_2 + H$
16.	$CO + O + M_7$	$\rightleftharpoons CO_2 + M_7$
17.	$CO + O$	$\rightarrow CO_2 + h\nu$

Table 1

Chemical Reactions (Continued)

18. $Na + O_2 \rightleftharpoons Na^+ + O_2^-$

19. $Na + O \rightleftharpoons Na^+ + O^-$

20. $Na + M_9 \rightleftharpoons Na^+ + e^- + M_9$

21. $Na + e^- \rightleftharpoons Na^+ + e^- + e^-$

22. $Na^+ + e^- \rightarrow Na + h\nu$

23. $O + e^- + M_8 \rightleftharpoons O^- + M_8$

24. $O_2 + e^- + M_8 \rightleftharpoons O_2^- + M_8$

25. $C_2F_4 + M_9 \rightarrow 2CF_2 + M_9$

26. $C_2F_4 + O \rightarrow F_2CO + CF_2$

27. $CF_2 + O_2 \rightarrow CO + 2F + O$

28. $CF_4 + M_9 \rightarrow CF_2 + 2F + M_9$

29. $F_2CO + M_9 \rightarrow CO + 2F + M_9$

30. $F_2 + M_9 \rightleftharpoons 2F + M_9$

31. $F_2 + e^- \rightleftharpoons F + F^-$

32. $F^- + M_9 \rightleftharpoons F + e^- + M_9$

33. $F + e^- \rightarrow F^- + h\nu$

34. $C_2H_2 + H \rightleftharpoons C_2H + H_2$

Table 1

Chemical Reactions (Continued)

35. $C_2H_2 + OH \rightleftharpoons C_2H + H_2O$

36. $C_2H_2 + O \rightleftharpoons CH_2 + CO$

37. $C_2H + OH \rightleftharpoons CH + HCO$

38. $C_2H + O \rightleftharpoons CH + CO$

39. $C_2H + O_2 \rightleftharpoons HCO + CO$

40. $CH_2 + O \rightleftharpoons HCO + H$

41. $CH_2 + OH \rightleftharpoons HCO + H_2$

42. $CH + OH \rightleftharpoons CO + H_2$

43. $CH + O \rightleftharpoons CO + H$

44. $HCO + H \rightleftharpoons CO + H_2$

45. $HCO + OH \rightleftharpoons CO + H_2O$

46. $HCO + O \rightleftharpoons CO + OH$

47. $HCO + M_9 \rightleftharpoons CO + H + M_9$

48. Chemi-ionization process (See text)

Table 2

Reaction Rates

Notes: $k = aT^b \exp(-E/RT)$ Units are gm-moles, sec., cm^3, cal, ^oK

Reaction	Forward Rate			Reverse Rate		
	a	b	E	a	b	E
1	2.5×10^{16}	-0.5	117,945	8.9×10^{14}	-0.44	0
2	2.0×10^{21}	-1.5	225,014	1.91×10^{20}	-1.57	0
3	5.5×10^{20}	-1.5	150,002	1.67×10^{20}	-1.52	0
4	3.2×10^{9}	1.0	39,100	2.67×10^{10}	0.92	7,042.5
5	6.8×10^{13}	0	75,011.5	2.13×10^{13}	-0.04	0
6	6.69×10^{24}	-2.54	128,454	2.4×10^{23}	-2.5	85,500
7	6.4×10^{9}	0.5	64,356.5	7×10^{18}	-0.9	0
8	5.0×10^{12}	0	4,600	1.85×10^{13}	0.01	19,387
9	5.0×10^{14}	0	16,750	4.17×10^{12}	0.27	97.5
10	4.0×10^{13}	0	10,200	1.29×10^{13}	0.03	8252.5
11	7.6×10^{12}	0	1,000	8.65×10^{13}	-0.02	17,734.5
12	2×10^{18}	-1.0	0	1.43×10^{18}	-0.82	103,240
13	2.3×10^{21}	-1.5	0	6.06×10^{21}	-1.31	118,027
14	3×10^{14}	0	0	6.96×10^{13}	0.21	101,292.5
15	1.5×10^{11}	0	200	1.41×10^{16}	-0.8	24,642.3
16	5×10^{15}	0	3,500	1.09×10^{20}	-0.58	129,235
17	2×10^{6}	0	3,200	0	0	0
18	1.07×10^{17}	0.07	107,521	2×10^{17}	0	0
19	1.46×10^{19}	-0.7	83,842	2×10^{19}	-0.6	0
20	1.62×10^{12}	1.46	117,621	3×10^{20}	- 0	0
21	2.16×10^{31}	-3.04	117,621	4×10^{39}	-4.5	0
22	1.2×10^{14}	-0.75	0	0	0	0
23	2×10^{19}	-0.5	0	1.48×10^{11}	1.05	33,779

Table 2

Reaction Rates (Continued)

Reaction	Forward Rate			Reverse Rate		
	a	b	E	a	b	E
24	2×10^{18}	-0.5	0	1.87×10^{10}	0.9	10,100
25	7.82×10^{15}	0.5	55,690	0	0	0
26	6.0×10^{11}	0	0	0	0	0
27	2.92×10^{10}	0.5	13,280	0	0	0
28	9.24×10^{14}	0.5	95,648	0	0	0
29	4.29×10^{11}	0.5	55,575	0	0	0
30	7.9×10^{12}	0.2	36,714	3.29×10^{12}	0	0
31	3.3×10^{15}	0	0	3.0×10^{7}	1.4	42,807
32	3.0×10^{11}	0.7	79,521	1.36×10^{19}	-0.9	0
33	2.0×10^{9}	0	0	0	0	0
34	2×10^{14}	0	19,000	1.92×10^{11}	0.58	8250
35	5×10^{12}	0	6,000	1.78×10^{10}	0.60	10,037
36	5×10^{12}	0	2,500	2.73×10^{8}	1.1	48,004.5
37	1.6×10^{14}	-.08	28,627.5	3.0×10^{13}	0	9,000
38	2.0×10^{13}	0	0	3.7×10^{11}	0.5	61,274.5
39	1.0×10^{13}	0	10,000	2.47×10^{11}	1.08	154,402
40	3.0×10^{13}	0	0	6.25×10^{14}	-.28	102,352.5
41	3.0×10^{13}	0	0	1.95×10^{15}	-.31	104,300
42	3.0×10^{13}	0	0	3.4×10^{15}	-.01	178,102
43	3.0×10^{13}	0	0	1.1×10^{15}	.02	176,154.5
44	3.0×10^{13}	0	0	1.8×10^{13}	.29	78,822
45	3.0×10^{13}	0	0	6.5×10^{13}	.30	93,609
46	3.0×10^{13}	0	0	4.1×10^{13}	.11	76,874.5
47	5.0×10^{13}	0	24,418	5.83×10^{12}	.32	0
48	(See Text)			(See Text)		

Table 3

Third Body Efficiencies

(Multiplicative factors for reaction rates involving non-reacting collision partners, M_i)

i	O_2	N_2	N	O	CO	CO_2	H	H_2	OH	H_2O	C_2H_2	CH	CH_2	C_2H	HCO	NO	CF_4	C_2F_4	CF_2	F_2	F	F_2CO
1	5	2	2	25	2	5	5	2	2	5	5	2	5	5	5	2	5	5	5	2	1	5
2	2	5	3	5	2	5	2	2	2	5	5	2	5	5	5	2	5	5	5	2	1	5
3	2	2	5	5	2	5	5	2	2	5	5	2	5	5	5	2	5	5	5	2	1	5
4	2	2	5	5	2	5	10	2.5	2	7.5	5	2	5	5	5	2	5	5	5	2	1	5
5	2	2	2	2	2	5	2	2	2	8	5	2	5	5	5	2	5	5	5	2	1	5
6	2	2	2	5	2	5	5	2	2	5	5	2	5	5	5	2	5	5	5	2	1	5
7	2	2	2	2	2	5	2	2	2	5	5	2	5	5	5	2	5	5	5	2	1	5
8	25	1	0	0	0	0	0	0	0	0	5	2	5	5	5	0	5	5	5	2	1	5
9	2	2	1	1	2	5	1	2	2	5	5	2	5	5	5	2	5	5	5	2	1	5

Table 4

Conditions Investigated

Flight Velocity = 22,400 fps.

Body Configuration: 7^{o} half angle cone

5.0' slant length

15" base diameter

Angle of Attack = 0

	Boundary Layer Conditions					Ablation Product Composition (Mass Fractions)					
Case No.	Altitude (kft.)	P edge (lbf/ft^2)	T edge (^{o}R)	T (^{o}R)	Mass Addition Rate at x=0.1' (slugs/ft^2sec)	Na	C_2F_4	CO	H_2	N_2	C_2H_2
1	175	11.13	1218	1800	3.2^{-8}	1	0	0	0	0	0
2	125	85.17	1173	1800	9.15^{-8}	1	0	0	0	0	0
3	175	11.13	1218	1800	2.4^{-4}	1.33^{-4}	0	2.2^{-1}	4^{-2}	4^{-2}	6.9987^{-1}
4	125	85.17	1173	1800	6.87^{-4}	1.33^{-4}	0	2.2^{-1}	4^{-2}	4^{-2}	6.9987^{-1}
5	125	85.17	1173	1800	6.87^{-4}	0	0	2.2^{-1}	4^{-2}	4^{-2}	7^{-1}
6	175	11.13	1218	1800	2.4^{-4}	1.33^{-4}	9.9987^{-1}	0	0	0	0
7	125	85.17	1173	1800	6.87^{-4}	1.33^{-4}	9.9987^{-1}	0	0	0	0

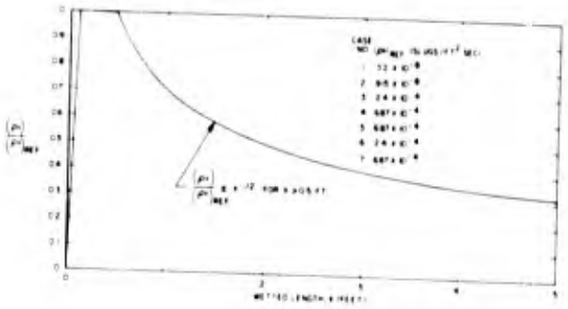

Figure 1. Normalized Injection Rate

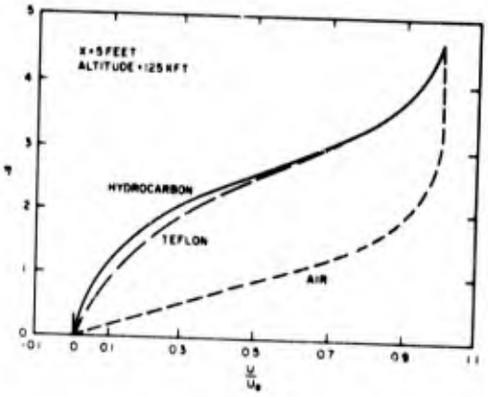

Figure 2. Boundary Layer Velocity Profiles

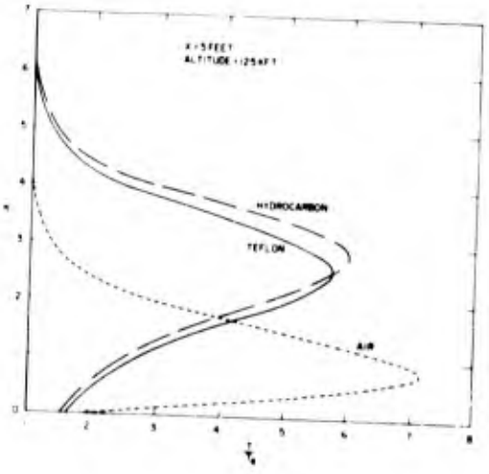

Figure 3. Boundary Layer Temperature Profiles

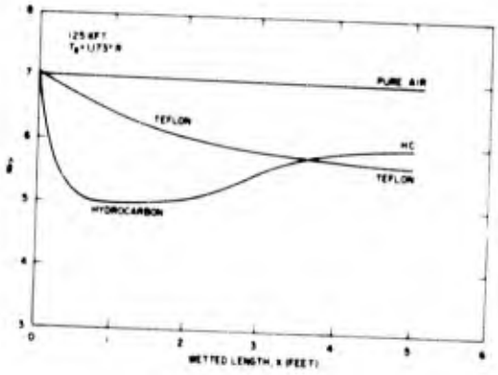

Figure 4. Boundary Layer Peak Temperature Trends

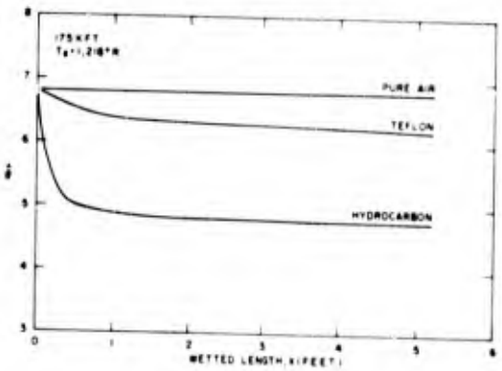

Figure 5. Boundary Layer Peak Temperature Trends

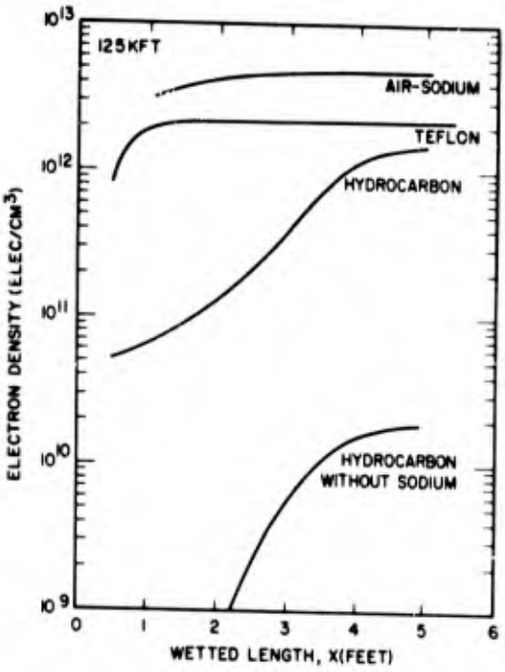

Figure 6. Boundary Layer Electron Density at Peak Temperature Point

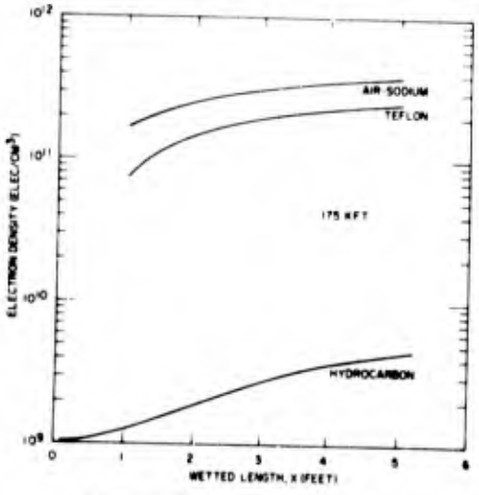

Figure 7. Boundary Layer Electron Density at Peak Temperature Point

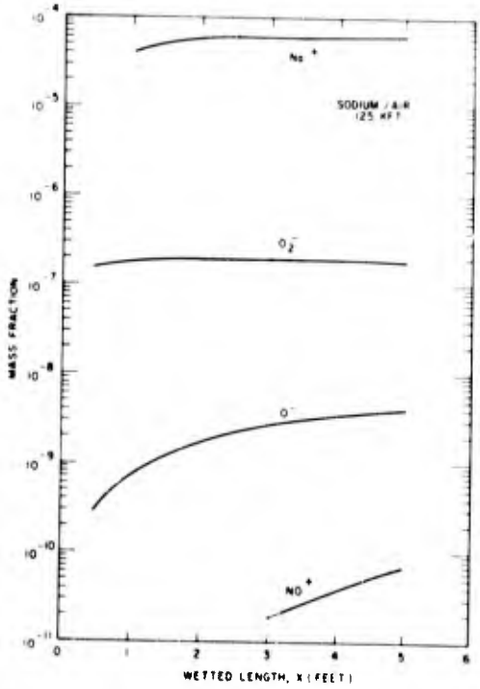

Figure 8. Boundary Layer Ion Mass Fractions at Peak Temperature Point

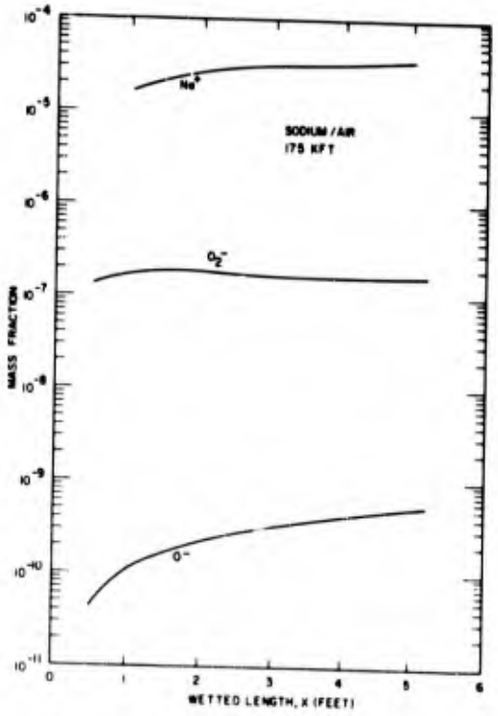

Figure 9. Boundary Layer Ion Mass Fractions at Peak Temperature Point

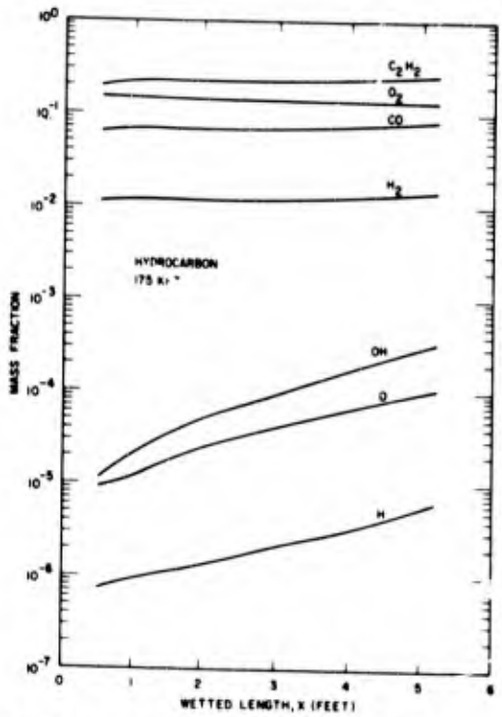

Figure 10. Boundary Layer Neutral Mass Fractions at Peak Temperature Point

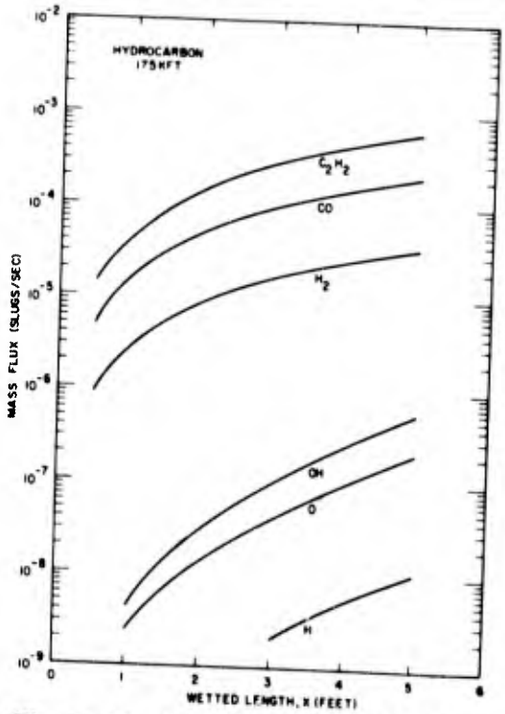

Figure 11. Boundary Layer Mass Flux of Neutral Species

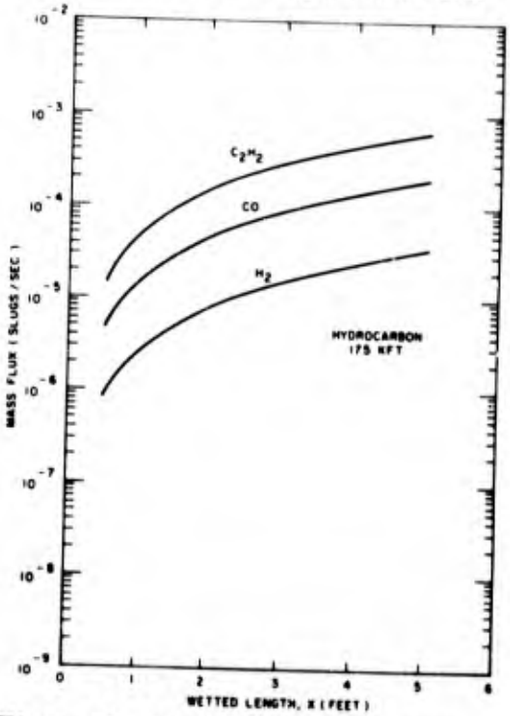

Figure 12. Boundary Layer Injected Mass Flux

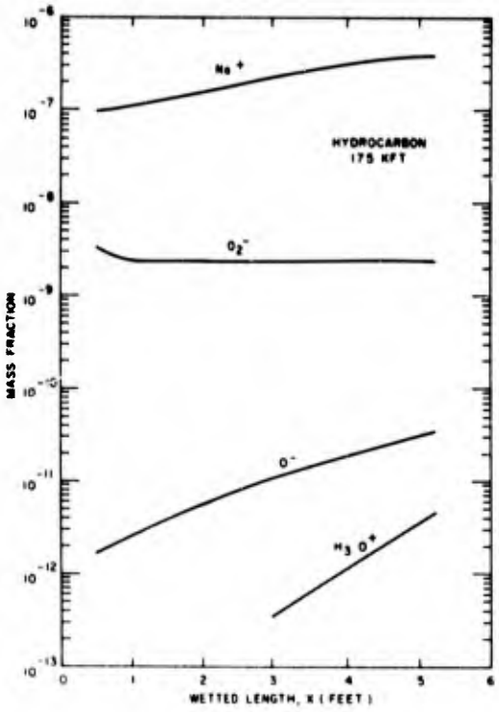

Figure 13. Boundary Layer Ion Mass Fraction at Peak Temperature Point

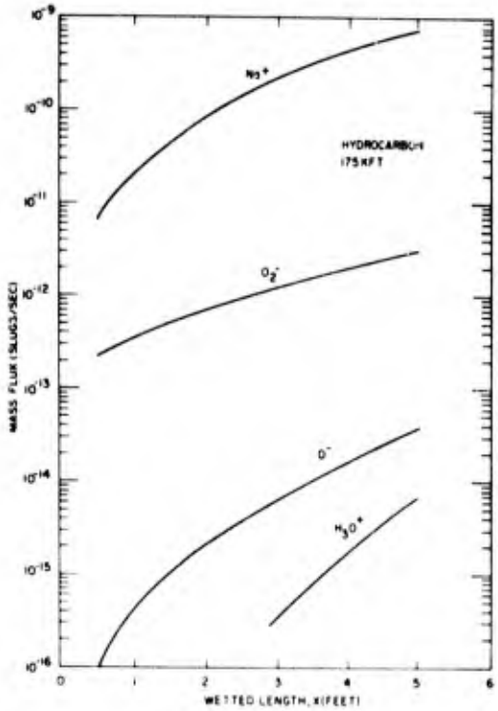

Figure 14. Boundary Layer Ion Mass Flux

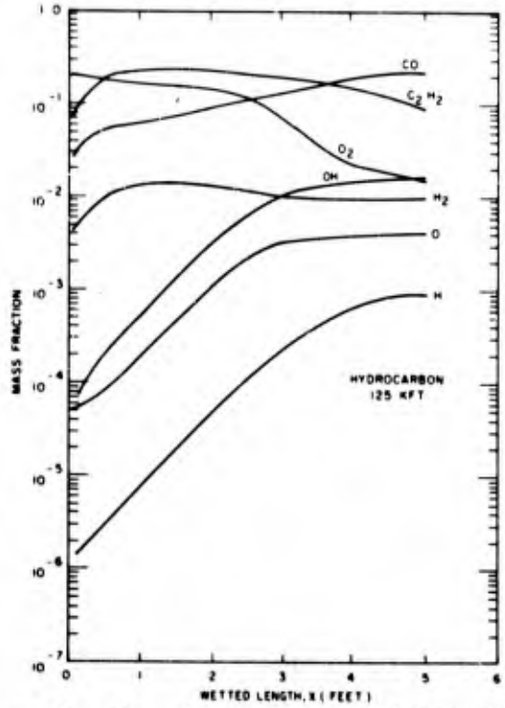

Figure 15. Boundary Layer Neutral Mass Fractions

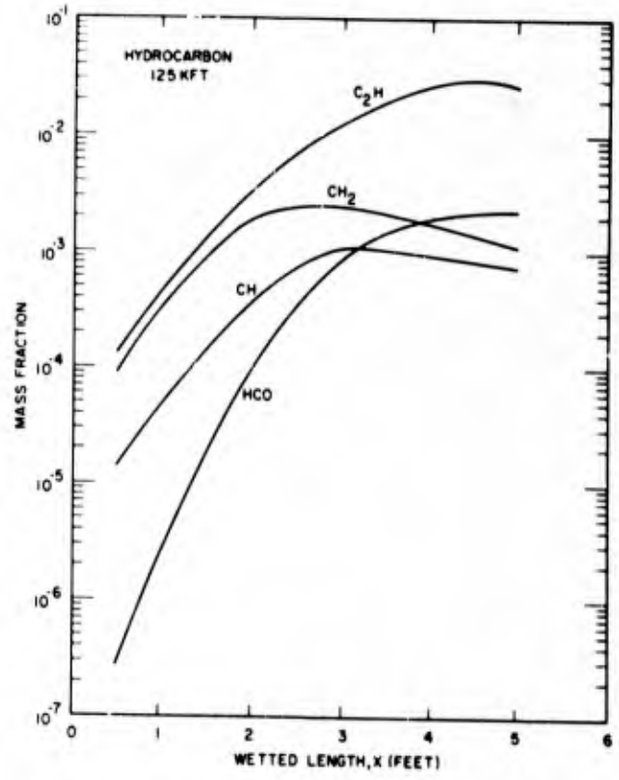

Figure 16. Boundary Layer Neutral Mass Fractions at Peak Temperature Point

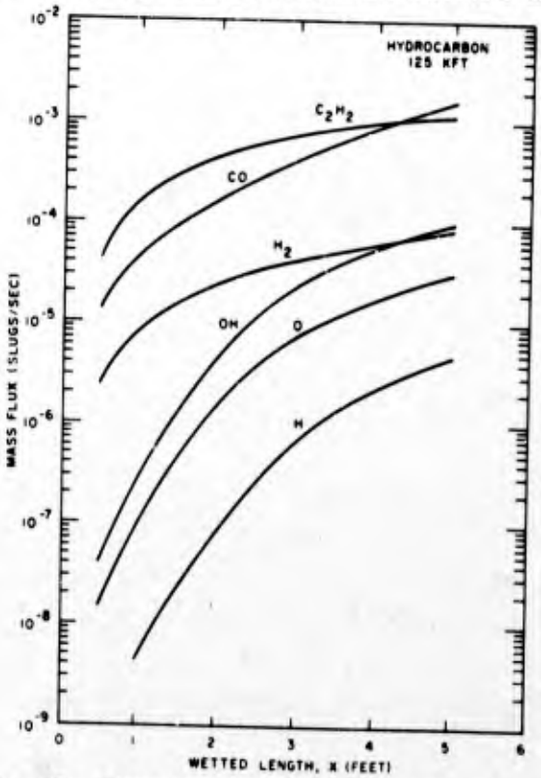

Figure 17. Boundary Layer Mass Flux of Neutral Species

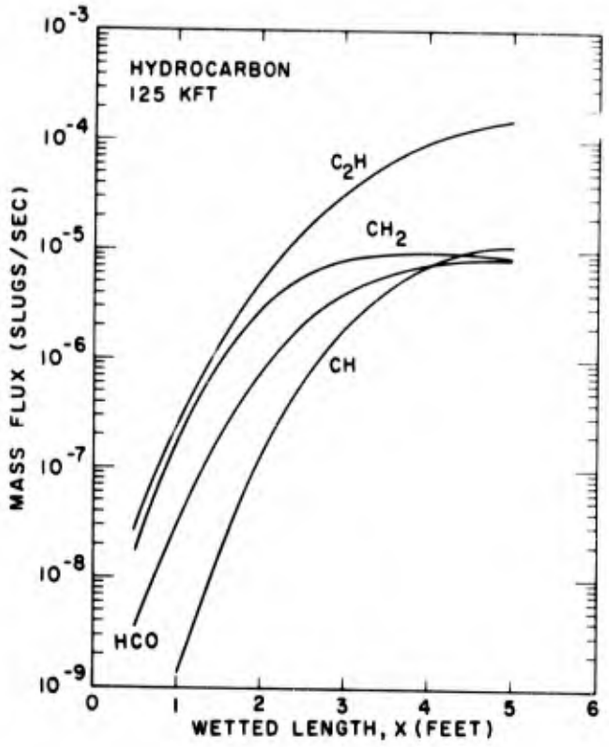

Figure 18. Boundary Layer Mass Flux of Neutral Species

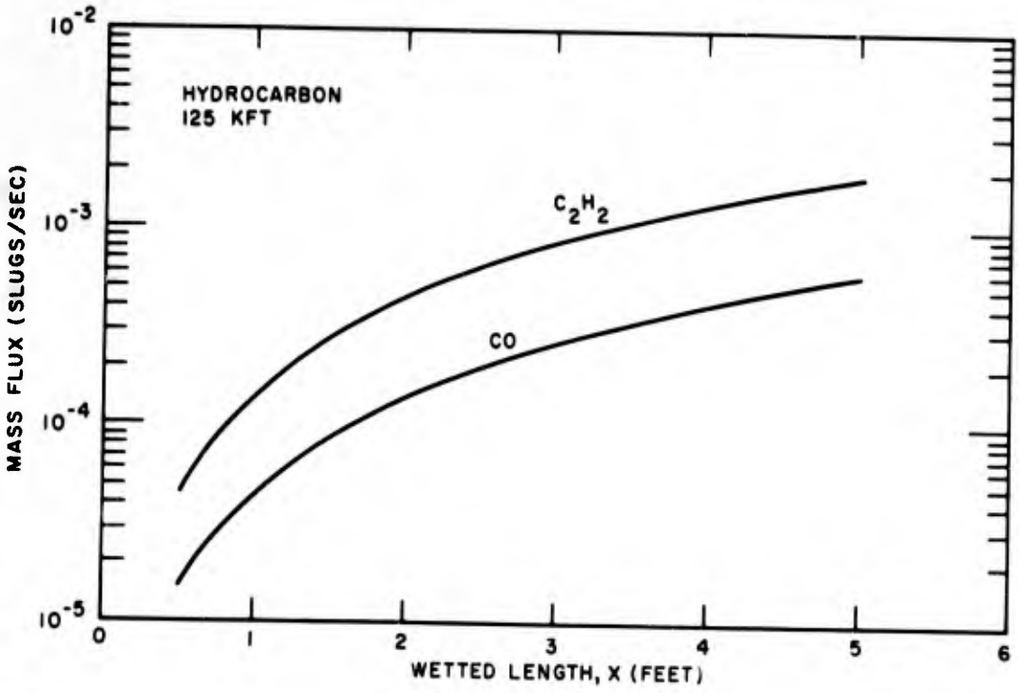

Figure 19. Boundary Layer Injected Mass Flux

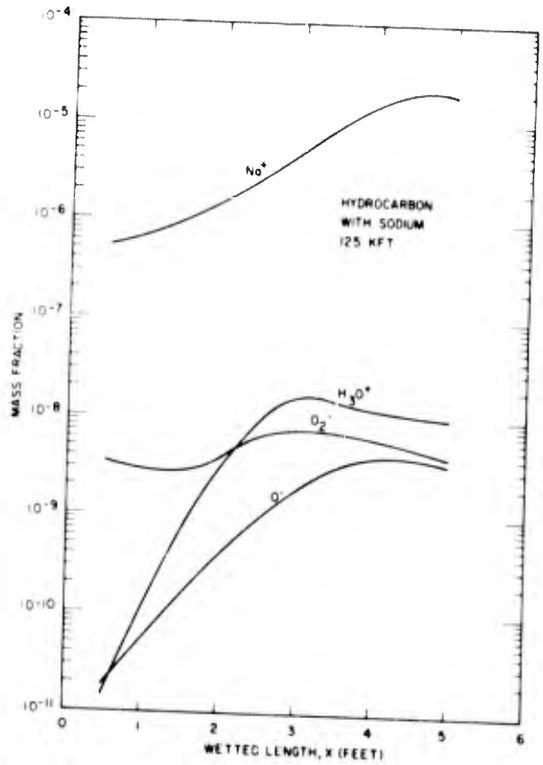

Figure 20. Boundary Layer Ion Mass Fractions at Peak Temperature Point

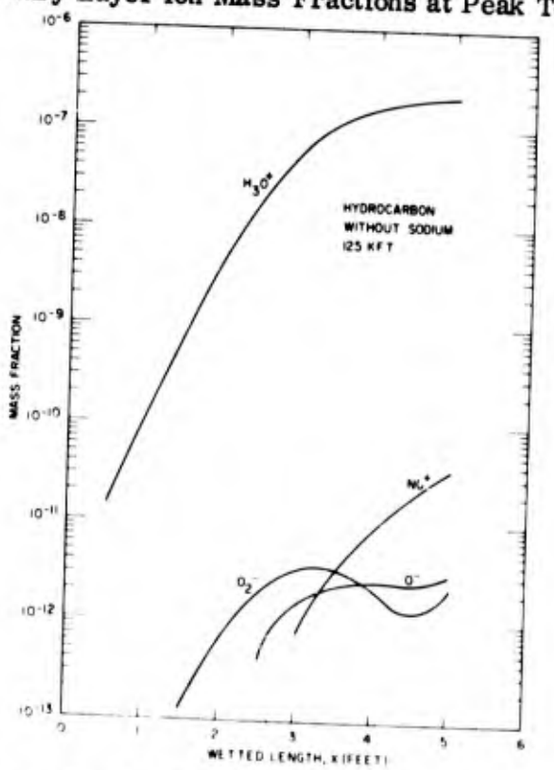

Figure 21. Boundary Layer Ion Mass Fraction at Peak Temperature Point

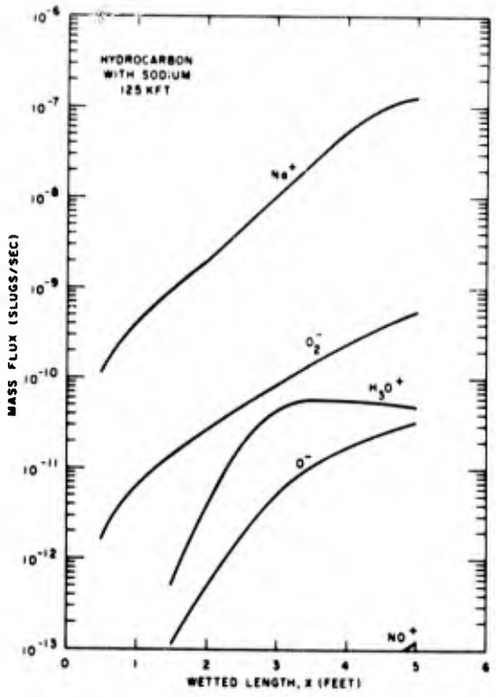

Figure 22. Boundary Layer Ion Mass Flux

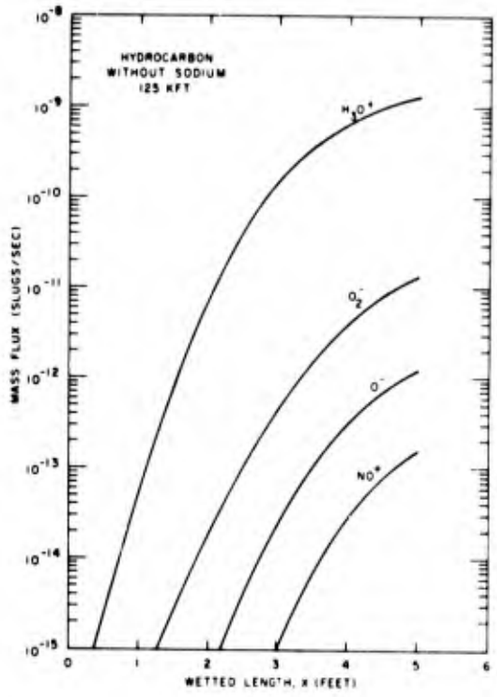

Figure 23. Boundary Layer Ion Mass Flux

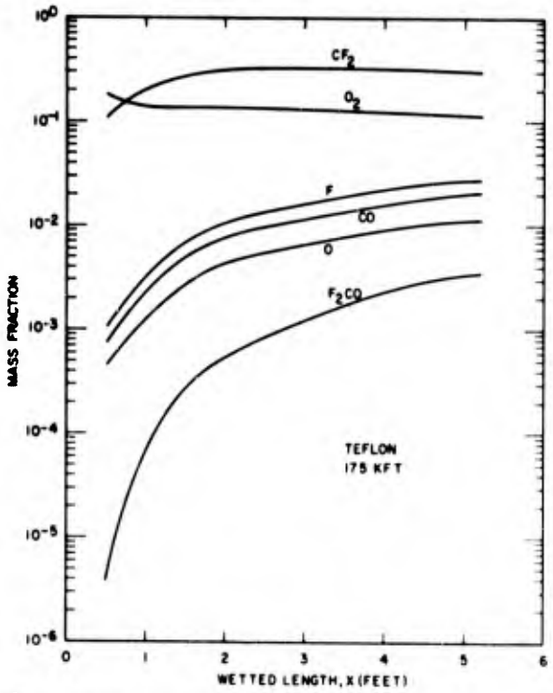

Figure 24. Boundary Layer Neutral Mass Fractions at Peak Temperature Point

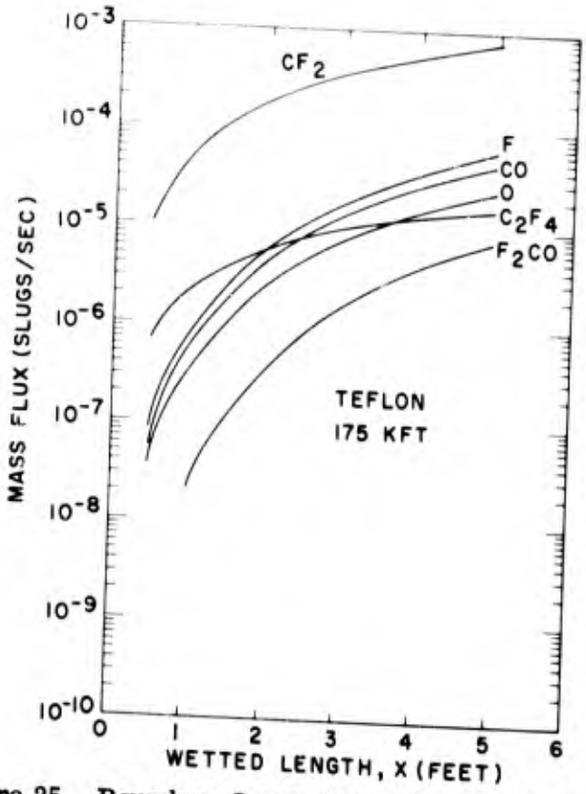

Figure 25. Boundary Layer Mass Flux of Neutral Species

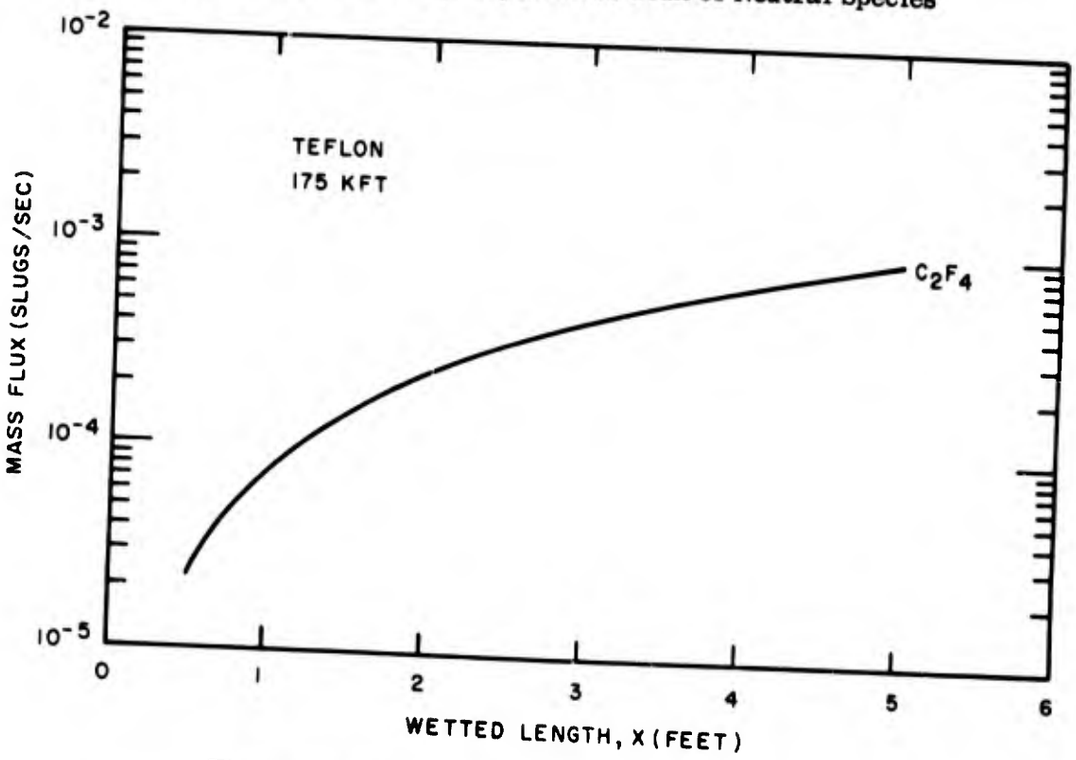

Figure 26. Boundary Layer Injected Mass Flux

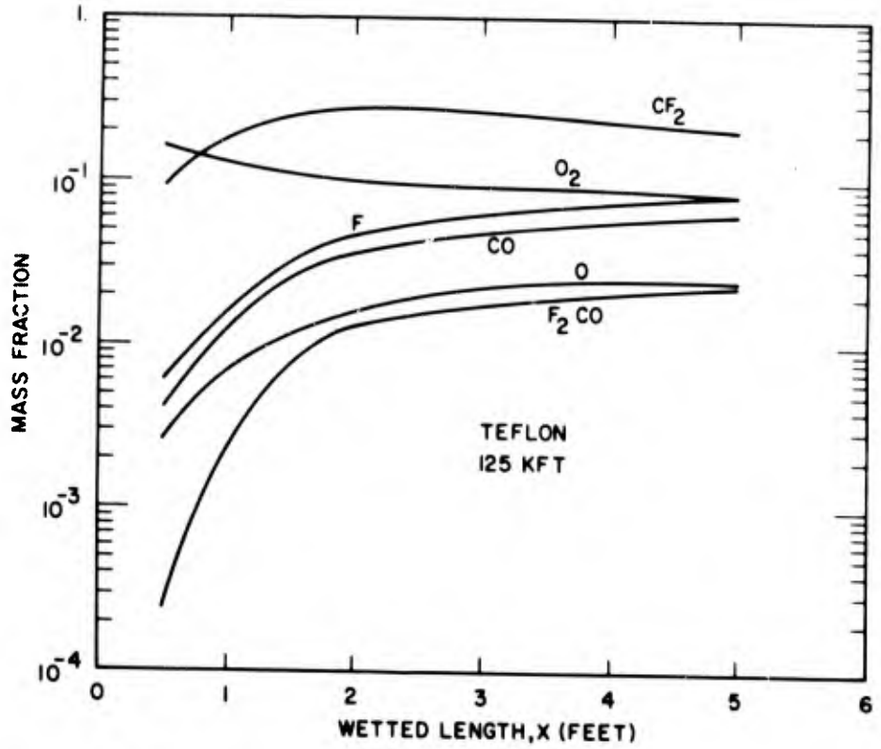

Figure 27. Boundary Layer Neutral Mass Fractions at Peak Temperature Point

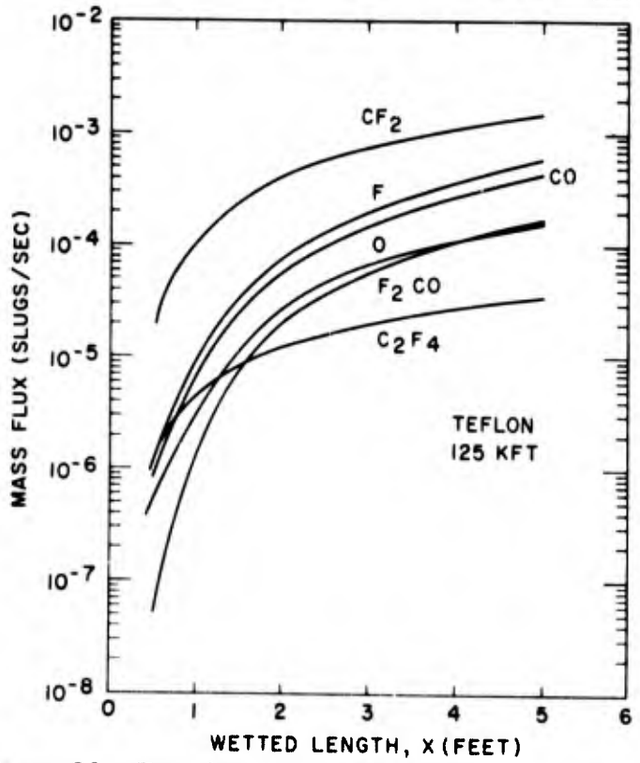

Figure 28. Boundary Layer Mass Flux of Neutral Species

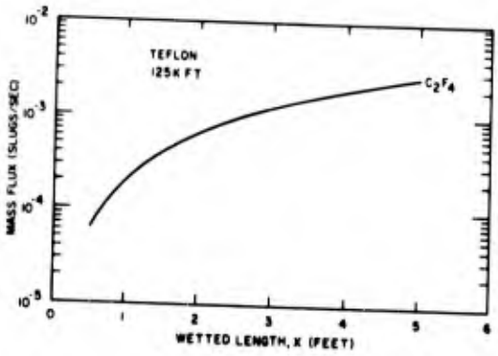

Figure 29. Boundary Layer Injected Mass Flux

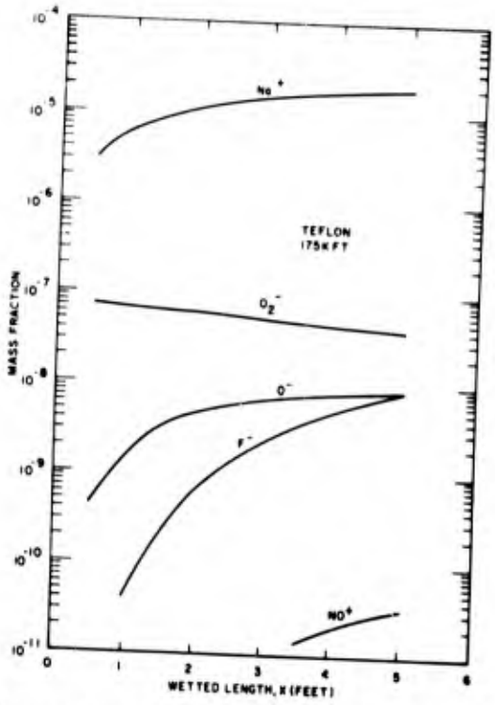

Figure 30. Boundary Layer Ion Mass Fraction at Peak Temperature Point

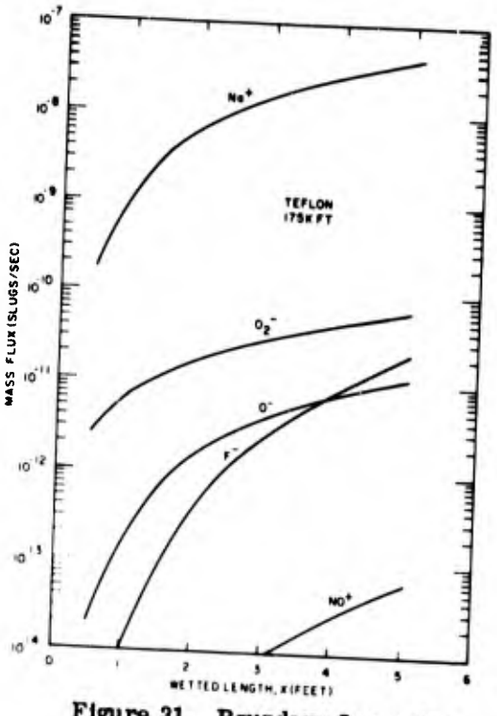

Figure 31. Boundary Layer Ion Mass Flux

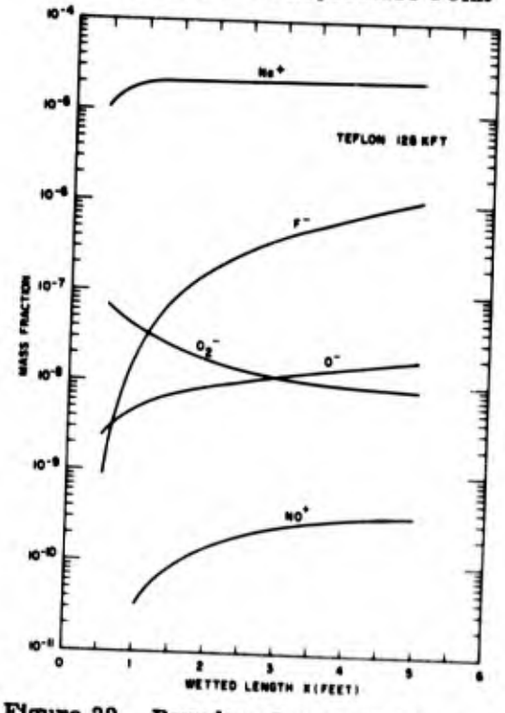

Figure 32. Boundary Layer Ion Mass Fractions at Peak Temperature Point

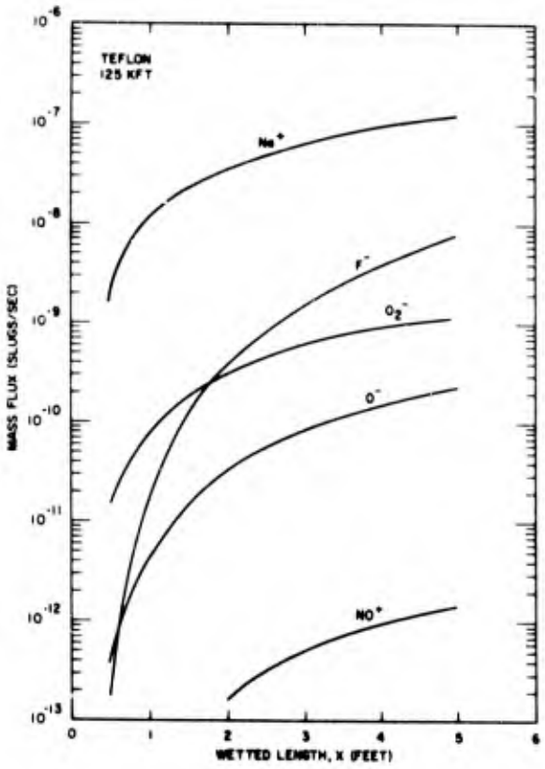

Figure 33. Boundary Layer Ion Mass Flux

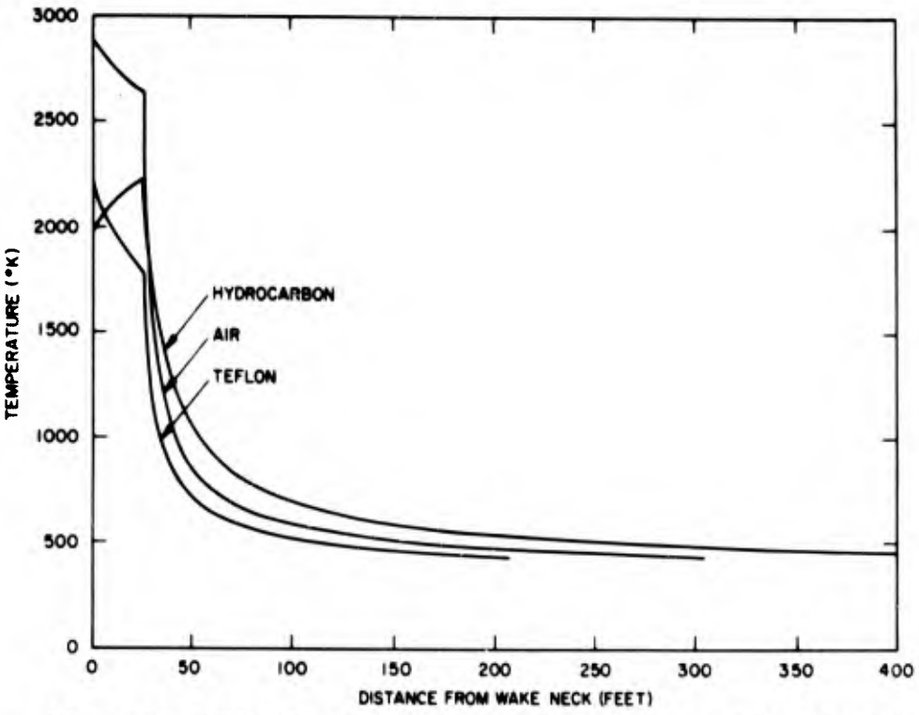

Figure 34. Wake Centerline Temperature Distribution at 125 KFT

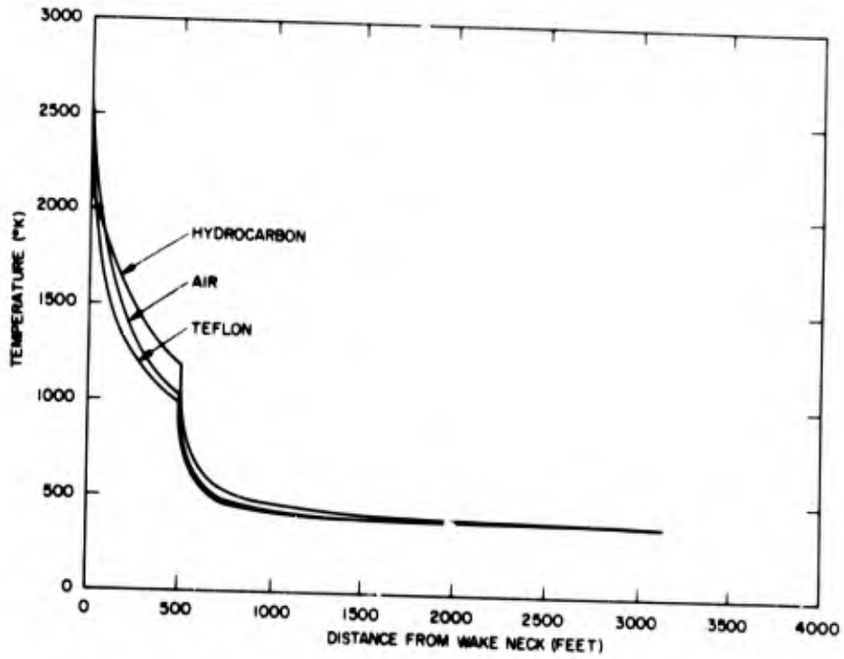

Figure 35. Wake Centerline Temperature Distribution at 175 K

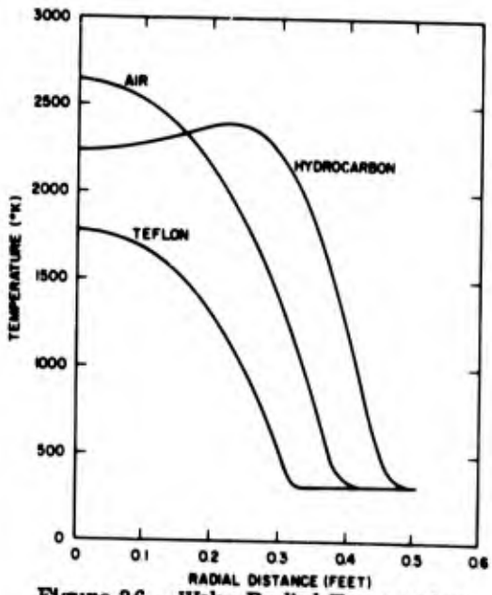

Figure 36. Wake Radial Temperature Profiles at Transition at 125 K

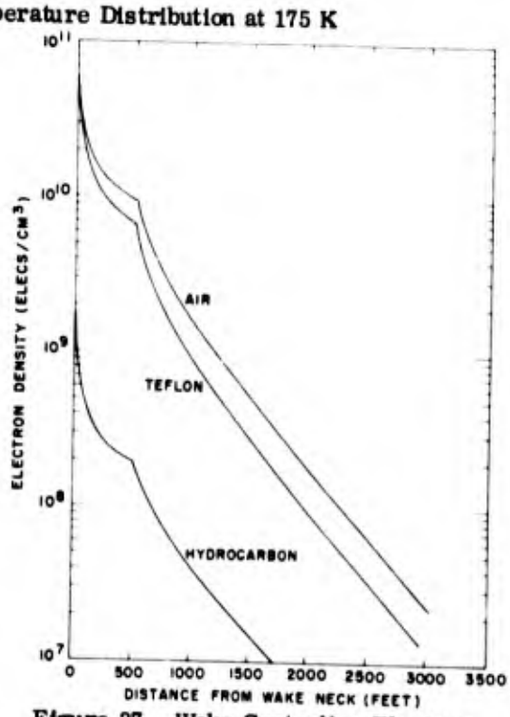

Figure 37. Wake Centerline Electron Density Distribution at 175 K

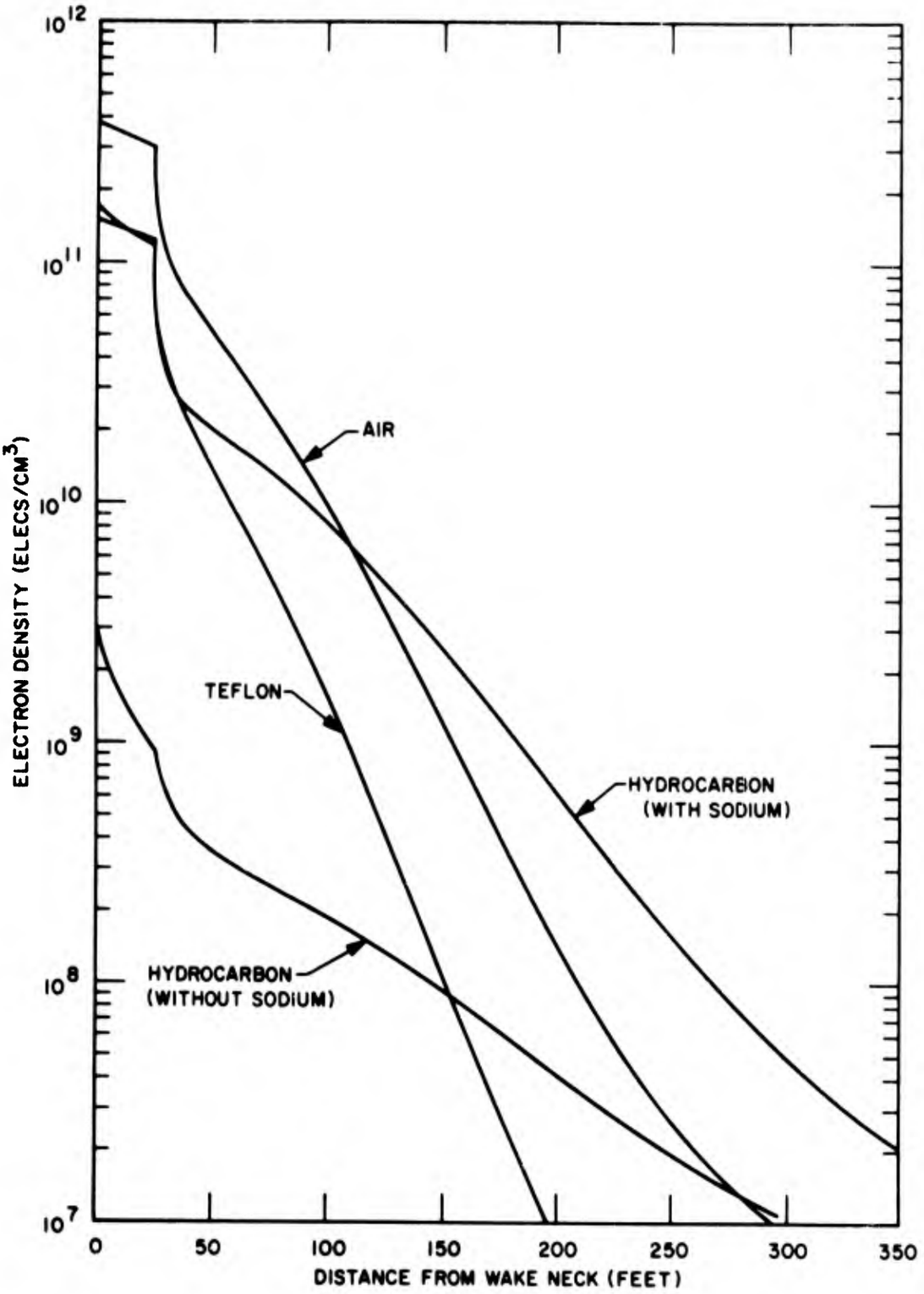

Figure 38. Wake Centerline Electron Density Distribution at 125 K

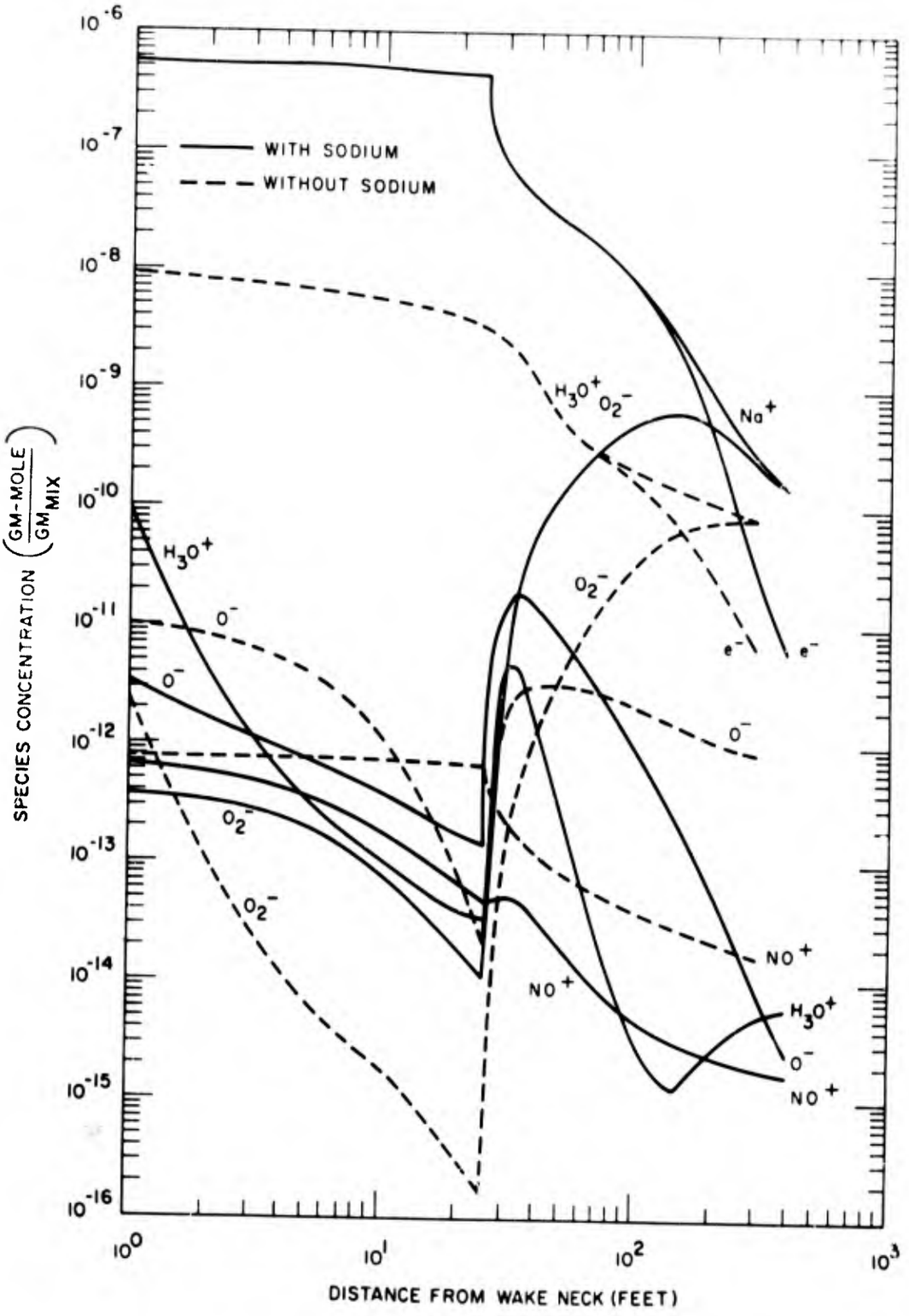

Figure 39. Wake Axis Species Concentrations for Hydrocarbon Cases at 125 K

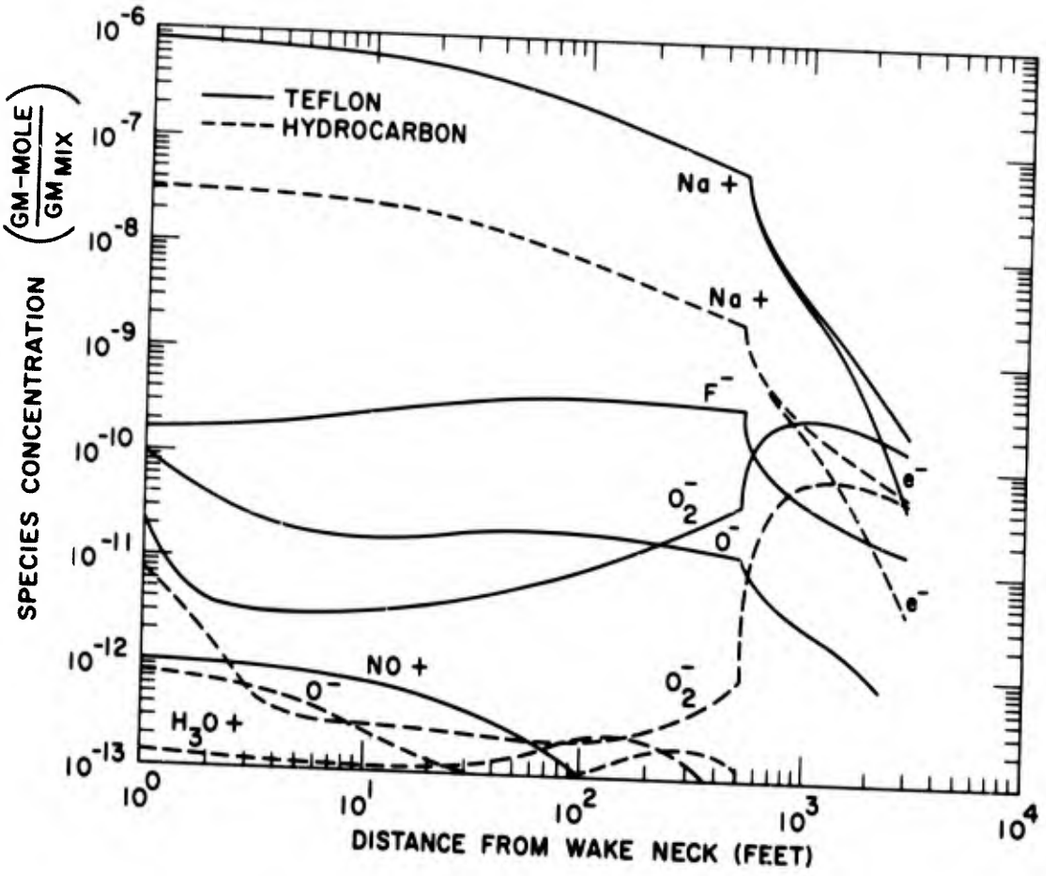

Figure 40. Wake Axis Species Concentrations at 175 K

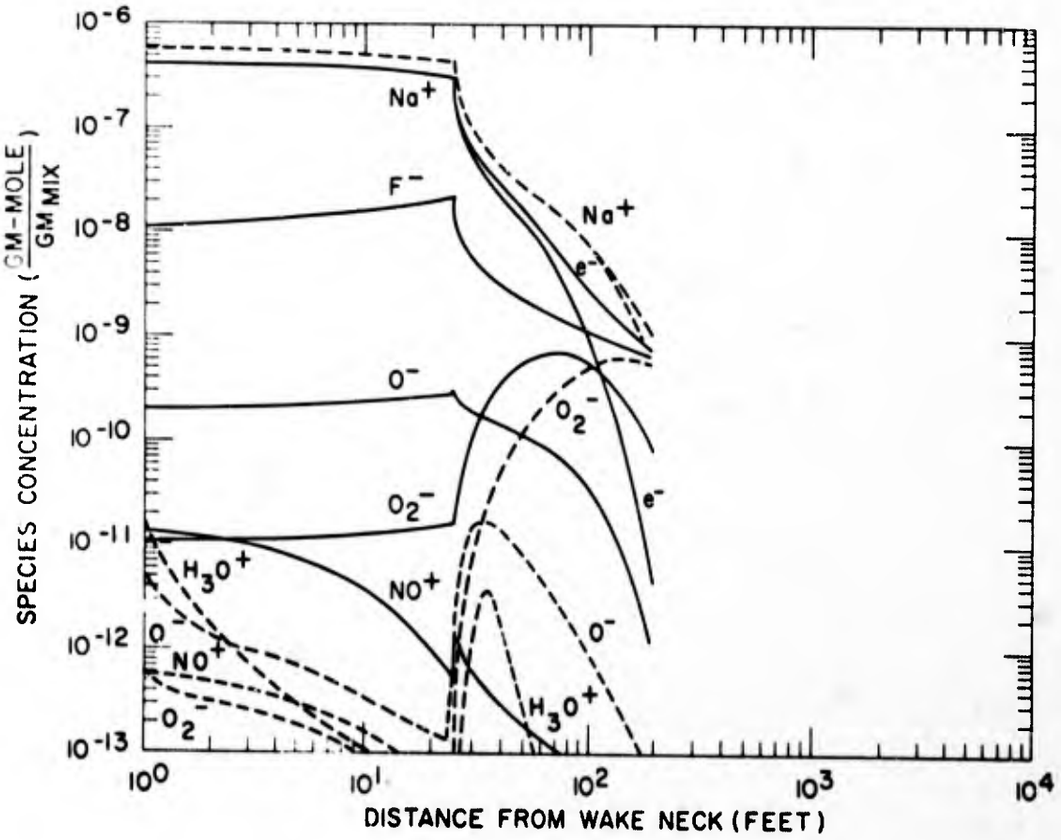

Figure 41. Wake Axis Species Concentrations at 125 K

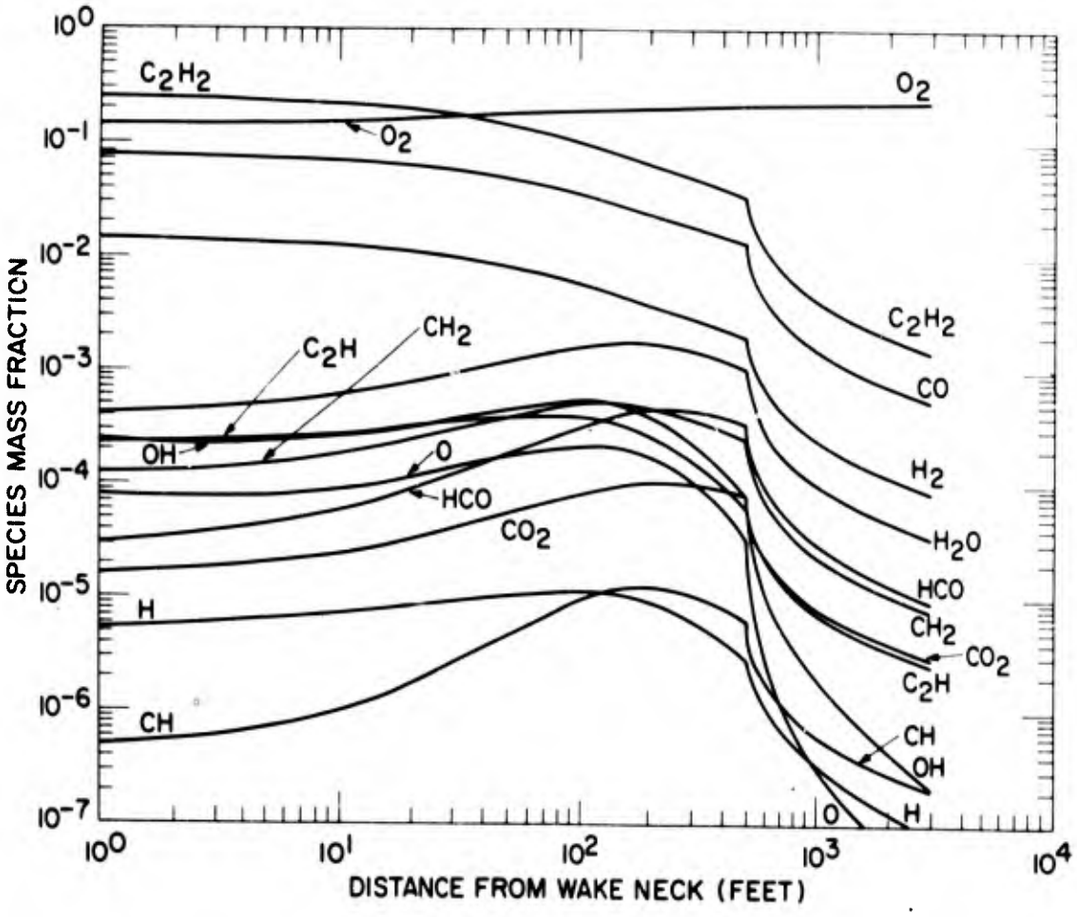

Figure 42. Wake Axis Species Mass Fractions at 175 K for Hydrocarbon Case

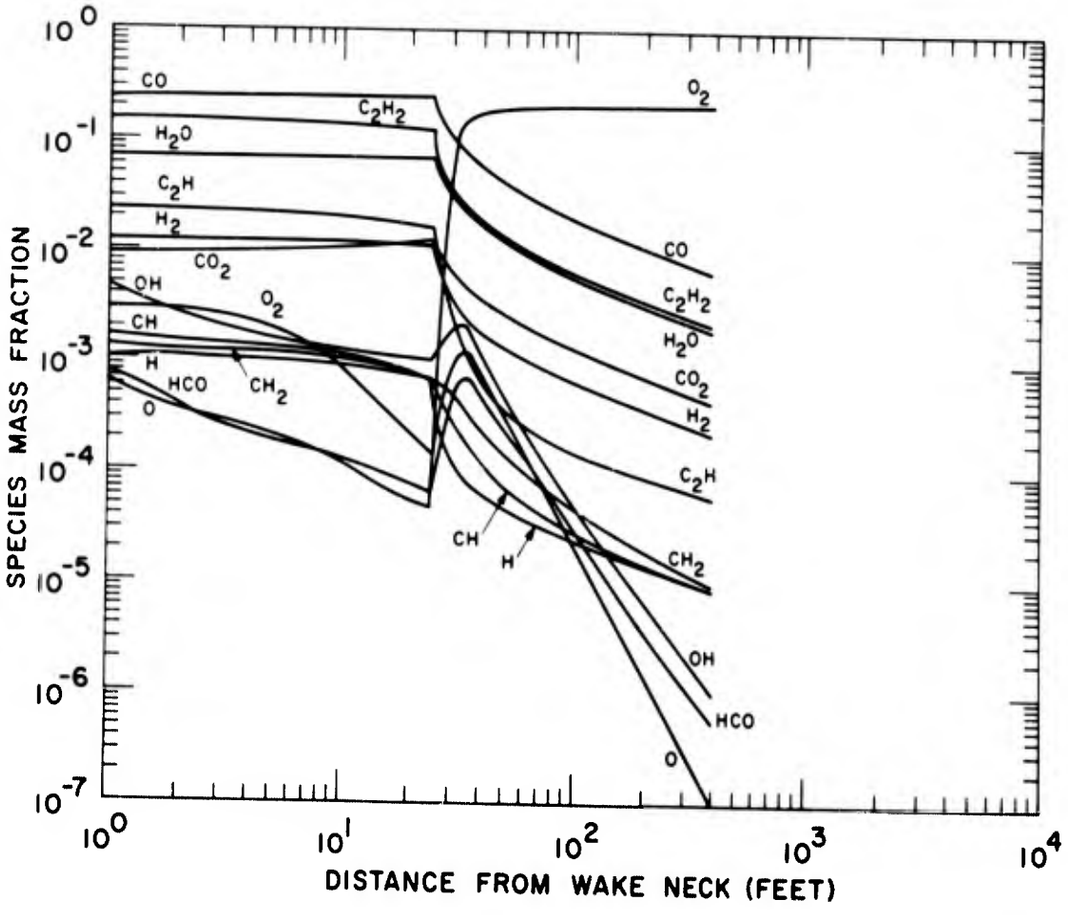

Figure 43. Wake Axis Species Mass Fractions at 125 K for Hydrocarbon Case (With Sodium)

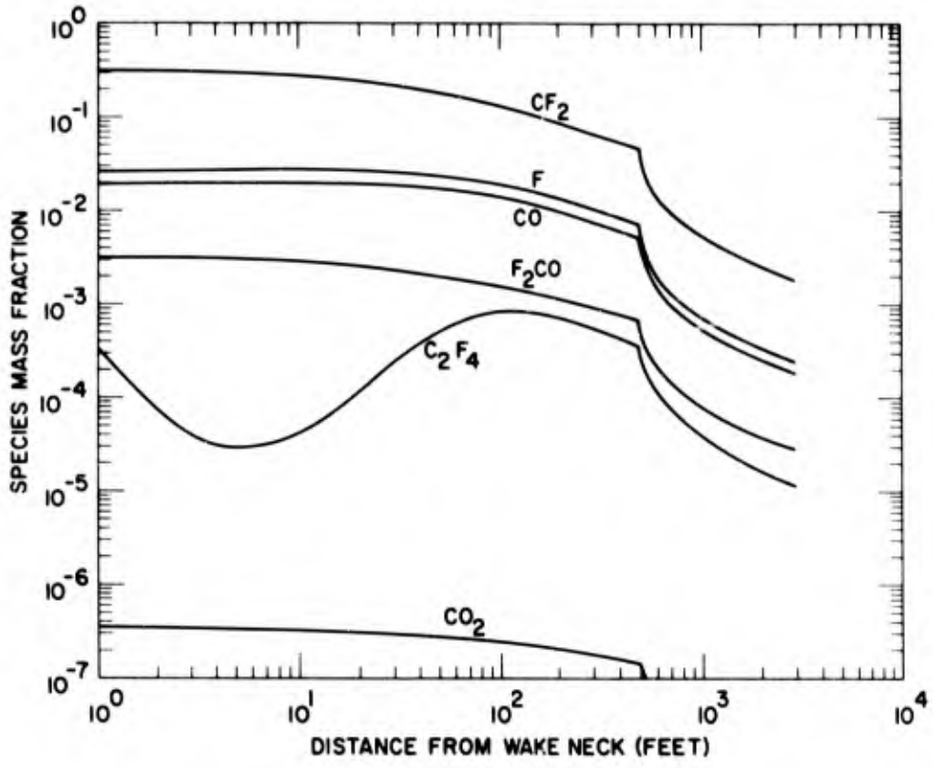

Figure 44. Wake Axis Species Mass Fractions at 175 K for Teflon Case

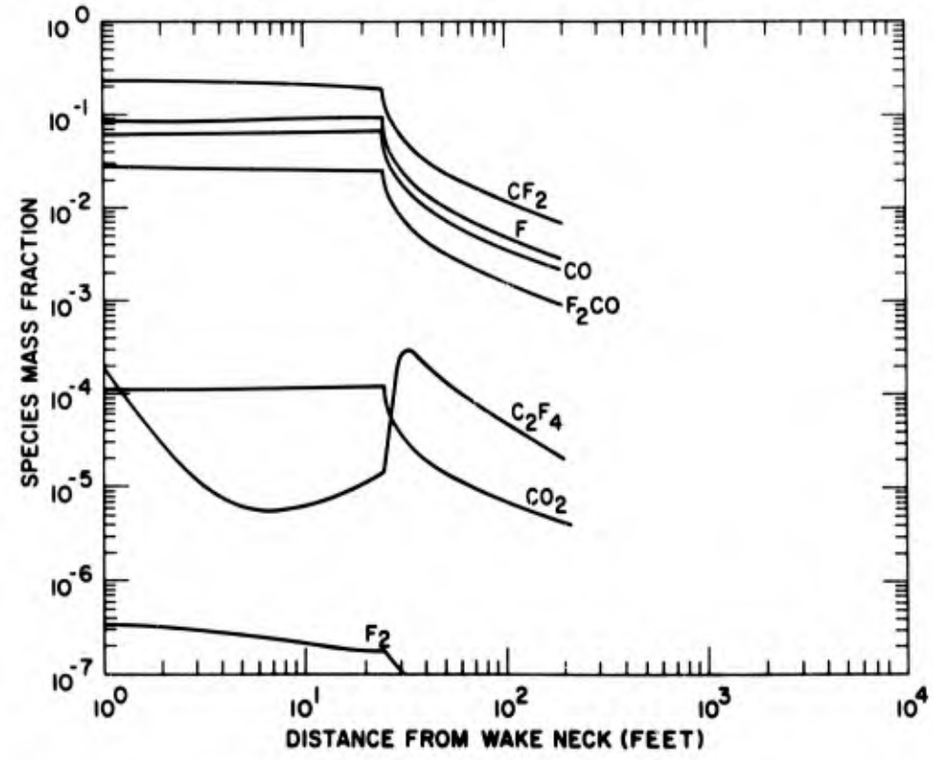

Figure 45. Wake Axis Species Mass Fractions at 125 K for Teflon Case

MEASURED AND PREDICTED ABLATION-PRODUCT RADIATION IN THE NEAR WAKE

by

Jack D. Stephenson

Ames Research Center, NASA
Moffett Field, Calif.

SUMMARY

The present study is an effort to predict and measure emission from the near wake of models fired in a ballistic range. The experiments were conducted in the Ames Prototype Hypervelocity Free-Flight Facility, a ballistic range with a counter-current shock-heated airstream, in which spherically blunted models, 1.3 cm in diameter, were fired through air or nitrogen at speeds of approx. 7.5 km per sec. The radiation from the near wake was resolved spectrally in the wavelength interval from 0.3 μ to 0.64 μ with two photographic prism spectrographs and spatially with a set of bandpass radiometers, which cover a spectral range from 0.2 μ to 1.2 μ. The radiometer bandwidths vary from about 250 Å in the ultraviolet to 900 Å and 500 Å, respectively in the visible infrared. During the tests the models attain essentially steady-state ablation before reaching the station where the radiation measurements are made.

To calculate the wake radiation, the gas properties and composition in the region being studied must first be obtained. For the calculations presented here it is assumed that the viscous wake comprises that region which appears as a luminous trail behind ablating models in image-converter photographs taken from the side, and as a dark absorbing area on shadowgraphs. The local gas properties at the edge of the viscous wakes are obtained from a digital computer solution for inviscid flow around blunt bodies; the apparent edge of the viscous wake is treated as a solid boundary. The mass fractions of air and ablation products in the wake are determined by taking the total mass flow of air within the forebody boundary layer and the total mass flux of ablation products as calculated from the computed cold wall convective heating rate and the effective heat of ablation of the model material. Since the experiments have been performed at free-stream Reynolds numbers greater than 100,000, the air and ablation products are considered to be thoroughly mixed upon reaching the brightest part of the wake, generally just aft of the trailing shock wave. Within the viscous wake, the species distribution is computed for various assumed temperatures, by use of a thermochemical equilibrium program developed by the Lewis Research Center. Continuity and energy conservation relations applied to the viscous flow are then solved to obtain the average wake temperature. Using this temperature and the corresponding concentrations of major radiating species given by the equilibrium chemistry program, the wake radia ion is estimated. For this estimate, the method of Williams and Treanor is used to calculate the emission from CN and C_2 band systems. Also Mie scattering theory, as calculated by Stull and Plass and Main and Bauer, is used to estimate the emission from particulate carbon.

Most of the data discussed in the paper were obtained with polyethylene as the ablation material, because its thermodynamic and chemical properties are well known.

RESUME

Au cours des travaux qu'il nous présente ici, l'auteur s'est efforcé de prédire et de mesurer les radiations émises par le sillage proche de maquettes lancées dans un tunnel balistique. Les expériences furent conduites dans l'installation prototype à très grande vitesse pour essais en vol libre du Centre d'Ames; dans ce tunnel de tir comportant un contre-courant chauffé par choc, on a procédé au lancement, à travers l'air ou l'azote, et à des vitesses d'environ 7 km. 5 par seconde, de maquettes à extrémités sphérique, de 1 cm, 3 de diamètre. Les radiations émises par le sillage proche furent décomposées spectralement dans un intervalle de longueur d'onde allant de 0,3 à 0,64 microns, à l'aide de deux spectro-graphes photographiques à prisme, et spatialement à l'aide d'une série de radiomètres à bande passante couvrant un domaine spectral s'étendant de 0,2 à 1,2 microns. Les largeurs de bande passante des radiomètres varient d'environ 250 Å pour l'ultra-violet à 900 Å et 500 Å, respectivement, pour le visible et l'infra-rouge. Au cours des essais, les maquettes arrivent à un stade d'ablation essentiellement stable avant d'atteindre la station où sont effectuées les mesures de radiation.

Avant de calculer les radiations émises par le sillage, on doit connaître les propriétés et la composition des gaz dans la région étudiée. Dans le cas des calculs présentés ici, on suppose que le sillage visqueux comprend la région qui apparaît sous forme de traînée lumineuse derrière les maquettes à ablation sur les photographies à conversion d'image prises de côté, et sous forme de zone absorbant l'obscurité sur les images radio-graphiques. On obtient les propriétés locales des gaz à la périphérie des sillages visqueux à partir d'une solution d'ordinateur numérique pour écoulements non visqueux autour de corps arrondis; le bord apparent du sillage visqueux est traité comme une frontière solide. On détermine les fractions de masse d'air et de produits d'ablation présents dans le sillage en prenant le débit-masse total de l'air à l'intérieur de la couche limite en avant du corps et le débit-flux total des produits d'ablation valeurs obtenues par calcul à partir du taux d'échauffement par convection de la paroi froide (taux d'échauffement fourni par ordinateur), et de la chaleur effective dégagée par l'ablation du matériau constituant la maquette. Les expériences ayant été effectuées à des nombre de Reynolds en écoulement libre supérieurs à 100.000, on considère que l'air et les produits de l'ablation sont parfaitement mélangés lorsqu'ils atteignent la partie la plus brillante du sillage, située généralement immédiatement à l'arrière de l'onde de choc de fuite. Pour différentes températures supposées, on calcule la répartition des diverses substances présentes à l'intérieur du sillage visqueux, à l'aide d'une méthode d'équilibre thermochimique mise au point par le Centre de Recherche Lewis. On résout ensuite les rapports de continuité et de conservation de l'énergie appliqués à l'écoulement visqueux pour obtenir la température moyenne du sillage. Sur la base de cette température et des concentrations correspondantes des principales substances rayonnantes, concentrations fournies par la méthode d'équilibre chimique mentionnée plus haut, on évalue le rayonnement du sillage. Au cours de cette évaluation, on fait appel à la méthode de Williams et Treanor pour calculer les radiations émanant des systèmes à bande de CN et C_2. On a également recours à la théorie sur la diffusion de Mie, telle qu'elle est calculée par Stull et Plass, et par Main et Bauer, pour évaluer l'émission du carbone particulaire.

La plupart des résultats exposés au cours de cette communication ont été obtenus en utilisant comme matériau d'ablation le polyéthylène dont les propriétés thermodynamiques et chimiques sont bien connues.

MEASURED AND PREDICTED ABLATION-PRODUCT RADIATION IN THE NEAR WAKE

By Jack D. Stephenson*

Ames Research Center, NASA

Moffett Field, Calif.

1. INTRODUCTION

A need for information on the details of flow in the near wake of ablating blunt bodies has been recognized by various investigators who have developed methods of analyzing wake flows. It is pointed out (1) that even though the far wake may be the region of primary interest (because of its importance to the understanding of radar echoes produced by bodies entering the atmosphere), theory for calculating far-wake characteristics can be considerably improved if its starting conditions in the near wake are known. Information on the near wake is also important in the study of radiative heating of rearward-facing surfaces of hypersonic bodies. When some heat-shield materials ablate, it has been observed that there can be intense thermal emission from the wake (2).

During recent years, ballistic-range experiments have been an important source of data on radiative heating from air and ablation products in shock layers (3,4). It was observed that these and similar experiments (5-8) can also furnish useful wake-flow data, because the wakes of models made of most plastic materials are

luminous. Thus, they can be photographed (6,8,9), and radiometers can be employed to record such features of the luminosity as its longitudinal and temporal variations as well as absolute spectral intensity. Information of this type can be analyzed to reveal various wake characteristics. Ref. 7 describes the use of streak photographs of luminosity to determine the flow velocity in the near wake, and the analysis of radiometer data to detect the existence of laminar, turbulent, or transitional structure in wakes. The investigation described here was undertaken to study the use of radiometer measurements of wake-radiation spectral intensity as a method for determining gas properties in the near wake.

A general theoretical treatment of blunt-body wakes is mathematically very complex (10,11), even when ablation and chemical reactions can be excluded. An objective of the study reported here was to ascertain whether wake properties and the corresponding radiation, as predicted by a theory based on rather extreme simplifications of the problem, might show any correlation with detailed radiation measurements. A major simplification is the assumption that, under the conditions of the experiments, the viscous flow is isolated from the external inviscid flow with respect to chemical interaction, heat transfer, or mass exchange everywhere except on the forebody.

The primary purpose of this paper, then, is to test such a simplified model of the flow. As one test of this model, calculated temperatures are compared with temperatures derived from

measurements of molecular radiation from CN. Where a significant difference between predictions and experiment is observed, it is expected that the experimental results presented will be of value in guiding the development of improved analytic techniques.

2. APPARATUS, TECHNIQUES, AND INSTRUMENTATION

Experiments that are described herein were conducted in the Hypervelocity Free Flight Radiation Facility, at Ames Research Center, shown in Fig. 1. This is a ballistic range in which models are fired through an instrumented test section 5.5 m in length, past four stations with shadowgraph optics in vertical and horizontal planes and one station where radiation is measured with an array of 16 radiometers. The facility can be operated with a countercurrent hypersonic air flow in the test section, supplied by a reflected-wave shock tube and hypersonic nozzle. The experiments discussed here were all conducted without flow in the test section.

The radiometers are Bausch & Lomb 1/4-m monochromators (66 Å/mm reciprocal dispersion) equipped with photomultipliers and electronic-amplifier packages. The instrument rise time is 50 nsec. During the present test program, the monochromator entrance slits were maintained at a width of 1 mm and the exit slits were set at widths varying from 1 to 9 mm. Examples of the response characteristics of some of the radiometers with these slit settings are illustrated in Fig. 2, and a complete listing of the channels by center wavelength and half-response bandwidth is given in table 1. One

additional radiometer was assembled by combining a photomultiplier and spectral filters, rather than a monochromator, centered at a wavelength of 0.75 μ; its band pass at half-peak sensitivity was 0.030 μ. The radiometers viewed a segment along the axis of the wake, the length of which varied slightly with the location of the radiometer relative to the test section. These lengths, designated as the field of view, are also listed in table 1. The method of calibrating the radiometers was generally similar to that described in Refs. 3 and 4.

Photographic spectra were obtained with two prism spectrographs. The plates were exposed during the time interval from the appearance of the model in the field of view until an explosive-driven shutter was closed 50 μsec later. One of the spectrographs, a Huet model UV 24 (f3.5 aperture), recorded spectra in the range from 0.29 to 0.48 μ, and the other, a Huet model CI (f0.7 aperture), covered the spectral range from 0.36 to 0.65 μ. The resolving power was degraded to some degree because of the need to operate these instruments with rather wide slit openings, up to 200 μ, in order to obtain adequate exposure.

The geometry and the spatial distribution of luminosity in wakes were obtained with two image-converter cameras. Depending on the model flight velocity and ambient density, shutter speeds were varied from 10 to 200 nsec.

The models used in the tests were short spherically blunted cylinders having a nose radius of 0.92 cm and a diameter of 1.3 cm (see Fig. 3). All of the models considered here were made of high-density polyethylene.

3. GAS COMPOSITION AND RADIATION CALCULATIONS

In this section, calculations are described which were used to estimate the gas composition and temperature and radiative properties of the region in the viscous flow behind the trailing shock wave. In this region, the diameter of the luminous flow is a minimum, and, in general, the wake is the brightest. First, a solution for the inviscid flow around the body is obtained; next, the equilibrium species concentrations and gas properties in the viscous wake neck are computed; then, the spectral intensities of the species that are judged to be dominant are calculated.

3.1 Inviscid Flow Around Body

The inviscid flow surrounding and behind the body is obtained from theory in order to define the pressure, flow velocity, and enthalpy at the edge of the viscous regions. The body shape of the model used in the present study was well suited to the application of a computer solution programmed at Ames for the flow around a blunt hypersonic body (12,13). (The fact that the sonic line on the body occurs naturally ahead of the forward corner greatly facilitates the use of the programmed solution.) The program utilizes real, equilibrium gas properties. The inviscid flow field is bounded by the body shape until the flow separates from the body

at the base, at which point it is assumed that the streamline denoting the inner boundary of the inviscid flow shown in Fig. 4 coincides with the edge of the luminous viscous wake. The geometry of the luminous regions, photographed with an image-converter camera during tests at two free-stream densities, is shown in Fig. 5. It is apparent that there is a significant difference in the two wakes as a result of the change from the low stream density and corresponding low Reynolds number to a higher Reynolds number. At low Reynolds number, the wake is laminar for many body diameters and the separated boundary layer persists as a bright annulus. At the higher Reynolds number, turbulence is observed in the recompression zone at the termination of the converging flow from the model base, resulting in a more uniform distribution of luminosity. The analysis presented here is limited to conditions under which the latter type of wake flow prevails.

Results of the inviscid-flow calculation are used in the following analysis primarily for estimating the pressure at the viscous-inviscid interface at the edge of the region of maximum luminosity. It is assumed that the pressure is constant across the inner wake, so that this calculation furnishes one of the properties of the gas mixture comprising the viscous wake.

3.2 Viscous Wake Neck

The method used to solve for the temperature and concentrations of chemical species in the (recompression) neck region of the wake is based on the assumptions that the mass flow in the viscous wake

is equal to the mass flow in the body boundary layer, and that essentially all the boundary layer is generated on the spherical surface of the body. The rate of mass injection into the boundary layer was calculated from the known effective heat of ablation of polyethylene (14) and the computed cold-wall convective heating rate (15). The total mass flow in a boundary layer with mass injection is obtained, for example, by the method given in Ref. 16, and so the mass flow of air is readily determined as the difference of the total and the ablation-product flow rates. Ref. 17 discusses another method that was found to be especially useful for estimating the mass flow in the boundary layer.

Before a mean wake velocity can be estimated, it is necessary to know the density and composition of the mixture of chemical species that exist in the wake. For this calculation, the materials comprising the forebody boundary layer are assumed to become thoroughly mixed by the time they reach the neck region. As has been mentioned, this is not a plausible assumption if the Reynolds number is low and the wake remains laminar. For the conditions considered here, however (a free-stream density of 0.07 atm and Reynolds numbers in excess of 10^5), the observed turbulence indicates complete mixing is a realistic possibility. The experimental results indicate that variations of some properties within the wake cannot be neglected. Observed effects of the nonuniform wake will be discussed later.

The equilibrium concentration of chemical species at any location can be calculated if the temperature, pressure, and mass ratios

of the original species are known at that location. This calculation has been made for the wake neck, assuming that the original constituents are those comprising the boundary layer on the body and that the pressure is equal to that from the inviscid solution. At selected temperatures, the distribution of species was calculated by use of a computer-programmed thermoequilibrium chemistry solution developed at Lewis Research Center (18). This solution handles up to 15 chemical elements and a total of 90 reaction products including condensed species. The mole fractions of various species plotted as functions of temperature, for polyethylene models in flight in air and in a nitrogen environment are shown in Fig. 6. A velocity of 6.7 km/sec and an ambient pressure of 60 torr are assumed, for which the wake pressure was computed to be 1.50 standard atmospheres. Fig. 6 shows that there is large concentration of carbon in the condensed phase when temperatures are low, and that the CN concentration increases rapidly with temperature in the range from 3100° to 3700° K.

Expressing the conservation of mass in the viscous flow from the boundary layer to the wake furnishes the relation

$$V_w = \frac{\dot{M}_w}{\rho_w A_w} \tag{1}$$

in which $\dot{M}_w$ is the total mass flow, A_w is the area of the viscous wake based on the diameter of the luminosity, and ρ_w is the wake density from the equilibrium chemistry solution.

Another relation is obtained from conservation of energy. Assuming that no heat is exchanged between the viscous flow and the

surroundings, after the formation of the boundary layer on the forebody, the total enthalpy is calculated as the sum of the free-stream stagnation enthalpy times the mass fraction of air in the viscous flow and the enthalpy (based on the heat of formation from elements in their reference states) of the unheated ablation material times the mass fraction of the ablation products. Thus it is assumed that all the heat transferred from the boundary layer to the body appears in the products of ablation. This is the case when the ablation has attained a steady state. Heat exchange between the body and the boundary layer resulting from departure from steady-state conditions has been neglected. At any assumed wake temperature, with the static enthalpy h from the equilibrium chemistry solution, and total enthalpy, H, defined above, the velocity in the wake is given by the equation

$$V_w = \sqrt{2B(H - h)} \qquad (2)$$

where B is a constant converting enthalpy to units of velocity squared. Eqs. (1) and (2) are solved simultaneously for wake velocity and temperature. For conditions corresponding to tests of polyethylene models at a flight velocity of 6.7 km/sec in air and in nitrogen environments at a pressure of 60 torr, the following temperatures are obtained: air, 3172° K; nitrogen, 3125° K. Table 2 lists the calculated mole fractions of the species from the equilibrium solution at these temperatures.

3.3 Calculated Radiative Spectral Intensity

The theory developed by Williams and Treanor (19), as applied by Woodward (20), which presents data in terms of radiation intensity per molecule for six molecular species, was used to estimate radiation from the predicted concentrations of CN, C_2, and N_2. The spectral intensity of CN(violet) was obtained from a computer-programmed solution in use at Ames which takes into account the P and R electronic-vibrational-rotational branch structure of the transition. The equations on which this program is based are outlined in Ref. 21. Results of the calculations for CN(violet), CN(red), and C_2(Swan) systems are shown in Fig. 7 for a model velocity of 6.7 km/sec and a nitrogen environment, for which the calculated temperature is 3125° K. Fig. 7 shows that the maximum C_2(Swan) intensity is considerably below the prominent sequences of both the red and the violet CN bands. Radiation from molecular nitrogen N_2 (first positive) is computed to be negligibly small. In Fig. 7, the radiation intensity is in units of watts per micron-steradian per square centimeter. The radiating area has been computed on the assumption that the emission of the radiating wake volume is distributed uniformly over the projected area, as viewed from the side, of the luminous core. Self-absorption was not considered in obtaining these results. It is seen by comparison to the black-body curve that for the $\Delta v = 0$ band sequence of CN(violet), self-absorption cannot properly be neglected.

The output signal of any specific radiometer that would result from the calculated molecular radiation can be evaluated with the equation

$$W_m = \frac{1}{\Delta\lambda} \int_{\lambda_1}^{\lambda_2} sR_\lambda W_\lambda \, d\lambda \qquad (3)$$

where W_m is the indicated mean intensity over the interval $\Delta\lambda$ to which the radiometer is responsive; R_λ is the normalized response of the photomultiplier-monochromator combination; and s is the component of the transfer function determined by the radiometer slits. In Fig. 2 sR_λ is shown for each monochromator.

At the temperatures that have been estimated in the wake, the equilibrium-chemistry solution indicates that a significant fraction of the carbon from ablated polyethylene exists as soot. The radiation from solid particles cannot be calculated uniquely from only the temperature and the mass concentration, because the emissivity per unit mass of an aggregation of very small particles can depend upon particle size. This effect is shown in Ref. 22, which presents solutions of the Mie theory for carbon, and Ref. 23 (based on the same theory), which extends considerably the applicable ranges of wavelengths and particle sizes. Absorption coefficients from Ref. 23 were used to calculate the radiation from the soot particles assuming several particle sizes.

4. EXPERIMENTAL RESULTS

4.1 Spectrograph Data

Densitometer traces of photographic spectra obtained during the flight of polyethylene models flying at 7.4 km/sec at a pressure

of 60 torr are shown in Fig. 8. Because the shock layer on the model forebody is in view for only a few microseconds, this region does not contribute appreciably to the spectra shown. The spectra do not, of course, represent only the wake at its brightest station, but are the integration of the possibly varying spectral-intensity distributions extending up to 30 diameters behind the model. There is evidence, however, (2) that the wake spectra may not vary greatly with distance, so that integrated spectra can furnish a good indication of the spectral quality in the region of interest here. In the wavelength range from 2900 Å to 4800 Å, upper spectrum, the CN(violet) band sequencies at 3590 Å ($\Delta v = 1$), 3883 Å ($\Delta v = 0$), and 4216 Å ($\Delta v = -1$) are prominent, and a band probably due to NH at 3360 Å is evident. In the spectrum covering wavelengths from 3600 Å to 6500 Å, CN(violet) bands are again in evidence at 3883 Å and 4216 Å. Strong bands are also apparent at wavelengths near 4740 Å, 5200 Å, 5600 Å, and 6200 Å that are identified as the C_2(Swan) system. A background continuum is also evident in the red portion of the visible spectrum.

4.2 Radiometer Data

Data obtained with the set of 15 radiometers were analyzed to give the absolute intensity of the wake radiance in the brightest part of the wake. Results are shown in Fig. 9 for tests conducted in air and in nitrogen at a free-stream pressure of 60 torr. The data from each radiometer are plotted as a function of the model flight velocity. The ordinates are in the same units as those

defined for the intensities calculated from theory (Fig. 7). With the aid of these graphs, which permitted some minor smoothing of the data, the measured radiation is plotted as a function of wavelength in Fig. 10 for velocities of 6.9 and 6.74 km/sec, respectively, for air and nitrogen. The data are shown as a series of rectangular bars, the widths of which represent the wavelength intervals of half-peak sensitivity of the radiometers.

The data show that at equivalent velocities, the wake radiation measured in the tests conducted in nitrogen was significantly greater than that measured in air. Also, the spectral distributions tend to be similar for the two different atmospheres, with minor exceptions. The spectral radiometer data can be interpreted as an underlying continuum upon which is laid enhanced intensities in discrete spectral regions. For example, the radiometer set to observe the CN(violet) band sequence for $\Delta v = 0$, 0.380 to 0.388 μ, indicates the highest intensities in the violet portion of the spectrum, both in the air and the nitrogen tests. As will be developed in more detail later, the variation in the measurements of adjacent radiometers (in the visible and infrared) are attributed in part, at least, to the bandheads of CN(red) and C_2(Swan). The C_2(Swan) system is particularly to be expected because it was observed in the spectrogram (Fig. 8). In addition, the identification of CN(violet), both in the spectrogram (Fig. 8) and in the radiometer data (Fig. 10), implies that some evidence of CN(red) should be found in the radiometer data. The strong bandheads of CN(red) should appear at 0.695, 0.790, and 0.92 μ.

4.3 Absorption Measurements

A series of tests was conducted to measure absorption characteristics of the soot particles in the wake. The absorption was estimated from shadowgraphs obtained at selected wavelengths, determined by the transmission of optical interference filters inserted into the shadowgraph system. The ratio of light transmitted through the center of the wake (I_c) to that transmitted through the flow field outside the absorbing viscous region (I_o) is used to obtain an absorptivity, α, which is related to the wake thickness (i.e., D_w) and the number density N of carbon particles by the formula

$$1 - \alpha = I_c/I_o = \exp(-N\sigma_s D_w) \qquad (3)$$

in which N is a function of the mass density of solid carbon and particle size, and σ_s is the particle optical cross section given by the Mie theory as a function of particle size and wavelength. The particles are assumed to be of constant size and are spherical: Only a few spectrally resolved shadowgraphs of good quality were obtained with accurate step wedge calibrations of the photographic emulsion. The best measurement was obtained at a wavelength of 0.57 μ, where the indicated absorptivity was 0.137, corresponding to a particle radius of 0.55 μ. Other measurements in the wavelength range from 0.4 to 0.57 μ indicated particle sizes from 0.38 to 0.55 μ. No effect of wavelength was discernible, but to show conclusively that there was no such effect would require additional data to assess more accurately the effects of scatter in the data.

5. THEORY AND EXPERIMENTS COMPARED

The most prominent feature of the radiometer data (Fig. 10), that is, the strong CN(violet) intensity at a wavelength of 0.39 μ,

is emphasized by comparing the data with the Planck black-body function for the calculated wake temperature, shown in Fig. 11 for conditions corresponding to tests in a nitrogen environment. Even with the relatively broad bandwidth of 400 Å, the radiometer set to measure this band sequence indicates an average intensity about twice that of the black body. This result implies immediately that the CN gas temperature is considerably higher than the computed wake neck temperature of 3125° K. A detailed discussion of this temperature discrepancy is presented later. In order to quote quantitatively the observed contributions of the various CN bands, it is necessary to consider the effect of the background radiation. Regions in the data that can be expected to be relatively free of the major molecular structure lead to the conclusion that the background at the longer wavelengths is primarily a continuum from soot particles.

5.1 Continuum Radiation

It will be shown in the next section that temperatures calculated from the intensity of CN radiation are substantially greater than 3700° K, for which there is essentially no solid phase carbon present at equilibrium. Examination of shadowgraphs in which absorption is attributable to soot in the wake indicates that the distribution of the bulk of the absorbing material across the wake differs from the luminosity distribution. The diameter of the absorbing wake is slightly smaller than the radiating wake, and the greatest absorption is near the axis, decreasing toward the edges. It is concluded from this that the radiating CN is concentrated toward the periphery of the viscous core and exists at a temperature

considerably higher than that of the inner wake. Thus the method of computing the mean wake temperature described earlier is considered to be applicable to the estimation of soot temperature only.

If the size of soot particles is known, the theory of Ref. 22 can be used to calculate the radiation from a given concentration of condensed carbon at a known temperature. As mentioned earlier, an effective particle radius of 0.38 to 0.55 μ is indicated by the absorption measurements. For this range of sizes, the emissivity of the aggregation is relatively insensitive to wavelength variation. An analysis of the effects of soot radiation from boundary layers of ablating blunt bodies (24) indicates that the particles in boundary layers are of a size similar to those estimated here from absorption measurements in wakes. These apparent sizes are substantially larger than particle sizes that have been quoted for soot particles collected from diffusion flames and measured with an electron microscope. As mentioned in Ref. 24, the process by which the carbon particles are formed and enter the flow is possibly so different from the formation of soot in flames that large differences in the average particle sizes are not necessarily unexpected.

The computed continuum radiation based on the absorption coefficients given in Ref. 23 is shown in Fig. 11 for a series of particle sizes and a temperature of 3125° K. At this temperature, the calculated radiation from soot particles having a constant radius between 0.3 and 0.4 μ is in general agreement with the

measured continuum, as indicated by the data (at wavelengths above 0.6 μ) in the intervals that exclude CN and C_2 bands. The effects of varying the temperature of the soot between 3000° and 3600° K were calculated for particle sizes of 0.3 and 0.4 μ and are illustrated in Fig. 12. The soot concentrations, as before, are from equilibrium calculations, Fig. 6. Temperature variations in the range from 3000° to 3400° K resulted in only relatively small variation in radiation intensity at wavelengths greater than 0.7 μ.

5.2 Radiation From CN

Assuming that the background spectral intensity is primarily a continuum from soot with little molecular structure other than from CN affecting the radiometer data in the wavelength intervals where the radiometers cover the various CN band sequences, the data, shown again in Fig. 13, obtained from tests in a nitrogen atmosphere indicate effects of two sequences of the CN(red) system, one with a bandhead at 7895 Å and one with a head at 9172 Å, as well as the CN(violet) sequence at 3883 Å. There is also evidence of molecular structure in the radiometer measurement centered at 7100 Å, covering the CN(red) $\Delta v = 3$ band. This measurement is too large to be accounted for by CN alone and undoubtedly includes contributions by other molecules (C_2 is a likely contributor). The results of applying Eq. (3) to the calculations in five wavelength intervals where radiometer measurements were made, covering portions of the two CN(red) bands and three CN(violet) bands, are shown in Fig. 13. In table 3 the results of these calculations are compared with

the measured averaged power (with continuum removed) in the same intervals. It is evident that the experimental values are significantly greater than the predictions, and that the ratio of the power from the CN(red) sequence for $\Delta v = 2$ to the power from the sequence for $\Delta v = 1$ is also larger in the experimental data. The higher intensities as well as the larger ratios would occur if the gas temperature is higher than assumed; hence these results, too, indicate that the temperatures in the wake are substantially greater than those obtained from the calculations.

The theory presented is not adequate for predicting the absolute intensity of the CN gas radiation because of the variation of temperature and an accompanying variation of the species concentration across the wake. However, the experimental results can be utilized to estimate the temperature of the CN gas producing the intense molecular radiation. For this estimate, Eq. (3) is used to compute the intensities of two of the CN(red) band sequences. These intensities divided by the intensity of CN(violet), $\Delta v = 0$, (also obtained from Eq. (3)) are plotted in Fig. 14 as functions of temperature for the following four wavelength intervals, designated by the center wavelengths of the intervals to which the radiometers responded: 0.79, 0.825, 0.92, and 0.93 μ. For each of these intervals, the ratios of the measured CN intensities, shown in table 4, were used with Fig. 14 to obtain the temperatures shown in Fig. 15 and listed in table 4. The temperatures range from 5200° to 6170° K. Fig. 15 also shows the temperatures calculated for the viscous and inviscid

wake flow. At the velocities where experimental data are shown, inviscid wake temperatures were calculated to be between 6300° and 6600° K.

Some qualitative information on the temperature of the CN in the wake is supplied by the Huet CI spectrograph data. The CN(violet), $\Delta v = -1$ band sequence, reproduced in Fig. 16, shows the relative intensities of the stronger vibrational transitions. The figure also shows relative strengths of these transitions calculated for temperatures of 3000°, 4000°, 5000°, and 6000° K from Ref. 20. The wavelength at which the intensity is a maximum suggests that the temperature is near 5000° K. The spectrum shown here was obtained in an air environment with a model velocity (7.5 km/sec) somewhat higher than that at which the radiometer measurements were made, but the predicted temperature in the viscous wake (3600° K) is still relatively low compared with that indicated by the spectrum.

6. CONCLUDING REMARKS

Spectral intensities of the radiation from the wakes of small ablating polyethylene models in flight at speeds between 6 and 7 km/sec in air and in nitrogen environments have been measured at wavelengths ranging from 0.27 to 1.04 μ. Several of the major sources of radiation were identified, and from the tests conducted in nitrogen, CN radiation intensities were analyzed to show gas temperatures in the brightest part of the wake. The temperatures thus obtained were significantly greater than the average viscous

wake temperatures calculated, assuming flow in chemical equilibrium and no mixing of the viscous and inviscid flows. From this, it is concluded that most of the gas radiation is from a region at the outer edges of the viscous core, where ablation products mix with the higher temperature inviscid flow. It is interesting that this distribution of the radiation is shown visually by the image converter photograph of a laminar wake (Fig. 5(a)).

When models were fired into a nitrogen atmosphere, the presence of solid carbon particles in the wake was indicated by absorption, and by radiation that was apparently continuum. If a particle size deduced from the absorption experiments is used to calculate radiation from the soot, and the mass density of the solid phase carbon is calculated for equilibrium chemistry, comparison of the radiation with measurements indicates that the temperature of the inner carbon-bearing part of the wake agrees with that predicted by the theory presented. The carbon particles were found to have a radius of the order of 0.4 μ.

7. REFERENCES

1. Lees, Lester; and Hromas, Leslie: "Turbulent Diffusion in a Wake of a Blunt-Nosed Body at Hypersonic Speeds." J. Aerosp. Sci., vol. 29, no. 8, 1962, pp. 976-993.

2. Stephenson, J. D.: "Measurement of Optical Radiation From the Wake of Ablating Blunt Bodies in Flight at Speeds Up to 10 Km Per Second." NASA TN D-2760, 1965.

3. Page, William A.; and Arnold, James O.: "Shock-Layer Radiation of Blunt Bodies at Reentry Velocities." NASA TR-R-193, 1964.

4. Craig, Roger A.; and Davy, William C.: "Thermal Radiation From Ablation Products Injected Into a Hypersonic Shock Layer." NASA TN D-1978, 1963.

5. Steinberg, M.; Maiden, C. J.; Leak, W. R.; and Hansen, C. F.: "Preliminary Studies of the Effects of Ablation Contaminants on Radiation." TR62-209H, General Motors Corp. Aerospace Operations Dept., Dec. 1962.

6. Lemay, A.: "Radiation Measurements From the Plasma Sheath Surrounding Hypersonic Projectiles." TM 693/62, CARDE (Canadian Armament Research and Development Establishment), Mar. 1962.

7. Hidalgo, Henry; Taylor, R. L.; and Keck, J. C.: "Transition in the Viscous Wakes of Blunt Bodies Flying at Hypersonic Speeds." J. Aerosp. Sci., vol. 29, no. 11, 1962, pp. 1306-1331.

8. Washburn, W. K.; Goldburg, A.; and Melcher, B. W.: "Hypersonic Cone Wake Velocities Obtained From Streak Pictures." AIAA Journal, vol. 2, no. 8, 1964, pp. 1465-1467.

9. Taylor, R. L.; Melcher, B. W.; and Washburn, W. K.: "Studies of the Luminous Hypersonic Wake." AIAA Journal, vol. 2, no. 10, 1964, pp. 1731-1738.

10. Lees, Lester: "Hypersonic Wakes and Trails." AIAA Journal, vol. 2, no. 3, 1964, pp. 417-428.

11. Lin, S. C.; and Hayes, J. E.: "A Quasi-One-Dimensional Treatment of Chemical Reactions in Turbulent Wakes of Hypersonic Objects." AIAA Journal, vol. 2, no. 7, 1964, pp. 1214-1222.

12. Inouye, Mamoru: "Blunt Body Solutions for Spheres and Ellipsoids in Equilibrium Gas Mixtures." NASA TN D-2780, 1965.

13. Inouye, Mamoru; Rakich, John V.; and Lomax, Howard: "A Description of Numerical Methods and Computer Programs for Two-Dimensional and Axisymmetric Supersonic Flow Over Blunt-Nosed and Flared Bodies." NASA TN D-2970, 1965.

14. Savin, R. C.; Gloria, H. R.; and Dahms, R. G.: "The Determination of Ablative Properties of Materials in Free-Flight Ranges." NASA TN D-1330, 1962.

15. Georgiev, Steven; Hidalgo, Henry; and Adams, Mac C.: "On Ablating Heat Shields for Satellite Recovery." Res. Rep. 65, Avco-Everett Res. Lab., 1959.

16. Howe, John T.; and Sheaffer, Yvonne S.: "Mass Addition in the Stagnation Region for Velocity Up to 50,000 Feet Per Second." NASA TR R-207, 1964.

17. Chapman, Gary T.: "Total Boundary-Layer Mass Flow With Mass Transfer at the Wall." AIAA Journal, vol. 4, no. 9, 1966, pp. 1688-1689.

18. Zeleznik, Frank, J.; and Gordon, Sanford: "A General IBM 704 or 7090 Computer Program for Computation of Chemical Equilibrium Compositions, Rocket Performance, and Chapman-Jouguet Detonations." NASA TN D-1454, 1962.

19. Williams, M. J.; and Treanor, C. E.: "A Method for Calculating Diatomic Spectra Using a Digital Computer." Rep. QM-1626-A-5, Cornell Aero. Lab., May 1962.

20. Woodward, Henry T.: "Predictions of Shock-Layer Radiation From Molecular Band Systems in Proposed Planetary Atmospheres." NASA TN D-3850, 1967.

21. McKenzie, Robert L.; and Arnold, James O.: "Experimental and Theoretical Investigations of the Chemical Kinetics and Non-equilibrium CN Radiation Behind Shock Waves in CO_2-N_2 Mixtures." AIAA Thermophysics Specialist Conference, New Orleans, Louisiana, April 17-19, 1967.

22. Stull, V. R.; and Plass, G. N.: "Emissivity of Dispersed Carbon Particles." J. Opt. Soc. Am., vol. 50, no. 2, 1960, pp. 121-129.

23. Main, Roger P.; and Bauer, Ernest: "Opacities of Carbon-Air Mixtures at Temperatures From 3000-10,000° K." J. Quant. Spectr. Radiative Transfer, vol. 6, no. 1, 1966, pp. 1-30.

24. Page, William A.: "A Survey of Thermal Radiation Studies of Ablating Bodies in the Ballistic Range." NASA TN D-3741, 1967.

8. ACKNOWLEDGEMENT

The author wishes to acknowledge with gratitude the work of Messrs. Ellis E. Whiting, James O. Arnold, and Gilbert C. Lyle, who programmed a solution for integrated rotational-vibrational line intensities of CN(violet) combined with radiometer responses that was employed in analysis of the data.

TABLE 1.- RADIOMETER CHARACTERISTICS

Center wavelength λ_c, μ	Bandwidth for 1/2-peak sensitivity, $\Delta\lambda_H$, Å	Bandwidth total (2% sensitivity), $\Delta\lambda_T$, Å	Field of view, cm	Radiometer component for spectral resolution
0.275	595	658	1.79	Monochromator
.35	397	454	1.60	↓
.39	388	454	1.67	
.39	125	192	1.67	
.43	394	444	1.60	
.485	395	460	1.67	
.50	595	660	1.67	
.55	590	645	1.60	
.55	390	446	1.60	
.55	64	125	1.67	
.59	269	336	1.55	
.60	600	667	1.55	
.65	390	447	1.55	
.71	600	657	1.60	
.71	388	445	1.79	
.79	388	444	1.67	
.825	388	444	1.67	
.85	598	666	1.79	
.88	600	667	1.79	
.88	400	467	1.79	
.92	394	451	1.67	
.93	600	665	1.79	
.93	594	652	1.67	
1.00	594	652	1.67	
1.04	600	658	1.60	
.75	297	920	1.49	Spectral filters

TABLE 2.- CALCULATED MOLE FRACTIONS OF CHEMICAL SPECIES IN WAKE AT EQUILIBRIUM, p_∞ = 60 TORR

Environment	Air	Nitrogen
Flight velocity, km/sec	6.7	6.7
Computed temperature, ^{o}K	3172	3125
Species mole fractions		
H_2	0.286	0.274
N_2	.219	.279
CO	.144	.000
H	.105	.084
HCN	.081	.081
C_2H_2	.033	.027
CN	.012	.0104
C_2	9×10^{-5}	5.7×10^{-5}
C(solid)	.113	.238

Other species mole fractions were less than 0.1%

TABLE 3.- CALCULATED CN RADIATION COMPARED WITH MEASUREMENTS; CALCULATED TEMPERATURE, 3125° K

Transitions	Radiometer center wavelength, λ_c, μ	W_m calculated Eq. (3), $W/\mu\text{-sr-cm}^2$	W_m experimental $W/\mu\text{-sr-cm}^2$	
			Total	Continuum removed
CN(v), $\Delta v = +1$	0.35	0.051	5.1	4.9
CN(v), 0	.39	.84	20.9	20.0
CN(v), -1	.43	.083	8.2	6.8
CN(R), +2	.79	1.54	13.3	2.4
CN(R), +1	.93	3.97	15.2	3.6

TABLE 4.- EXPERIMENTAL DETERMINATION OF CN TEMPERATURE

Test round	V_∞, km/sec	λ_c, μ	W_m, total	W_m, continuum	$W_{m_{CN}}$	$\frac{W_{m_{red}}}{W_{m_{violet}}}$	Temperature, ^oK
A	6.70	0.39	21.1	0.9	20.2	---	---
		.79	13.0	10.9	2.1	0.104	5420
		.93	15.0	11.8	3.2	.158	5760
B	6.74	.39	20.9	.9	20.0	---	---
		.79	13.3	10.9	2.4	.120	5200
		.93	15.2	11.6	3.6	.180	5550
C	6.96	.39	84.0	1.0	83.0	---	---
		.825	17.6	12.2	5.4	.0651	5740
		.92	19.0	12.6	6.4	.0771	5430
D	7.04	.39	27.0	1.0	26.0	---	---
		.79	14.4	12.2	2.2	.0846	5770
		.93	16.4	13.2	3.2	.123	6170

NOTATION

A_w	wake cross-section area, cm^2
B_λ	Planck black-body radiation function, $W/\mu\text{-sr-cm}^2$
D_w	wake diameter, cm
h	static enthalpy, cal/gm
H	total enthalpy, cal/gm
I_c	intensity of transmitted light, erg/cm^2
I_o	intensity of incident light, erg/cm^2
I_p	radiation intensity per particle, $W/\mu\text{-}4\pi\text{-sr}$
$\dot{M}_w$	mass flow rate, gm/sec
N	soot particle number density, cm^{-3}
p_w	pressure in the wake, atm
p_∞	free-stream pressure, torr
R	carbon particle radius, μ
R_λ	normalized response of radiometers
s	normalized effect of radiometer slits
T_w	temperature in the wake, ^oK
V_w	velocity of viscous wake flow relative to body, km/sec
V_∞	velocity of model, km/sec
W_m	mean radiation intensity for specified wavelength interval, $W/\mu\text{-sr-cm}^2$
W_λ	radiation intensity, $W/\mu\text{-sr-cm}^2$
λ	wavelength, μ
σ	particle cross section, cm^2

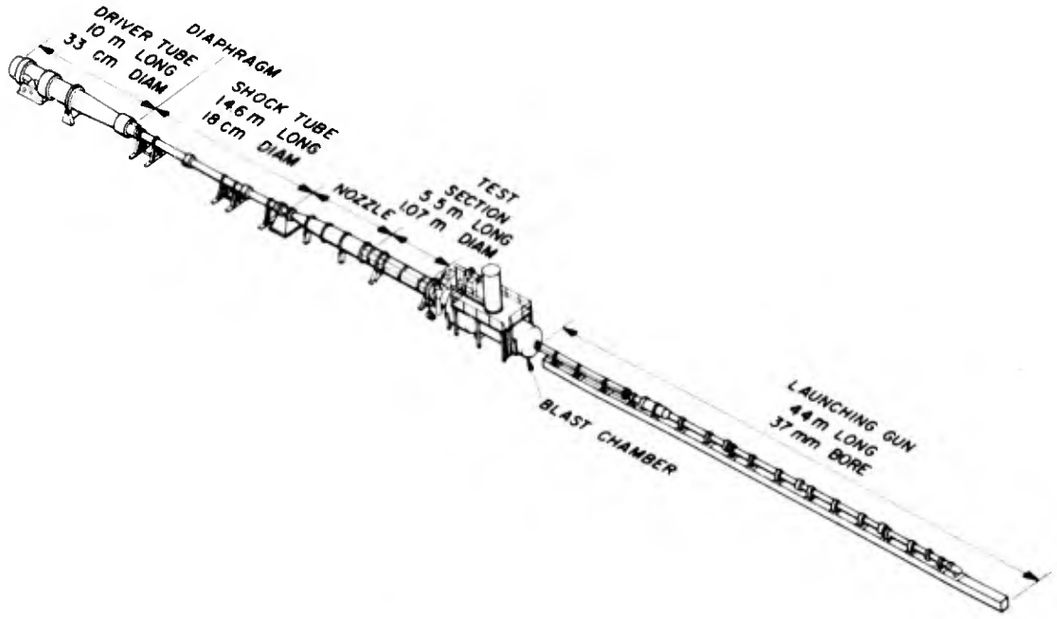

Fig. 1 The Ames Hypervelocity Free-Flight Radiation Facility

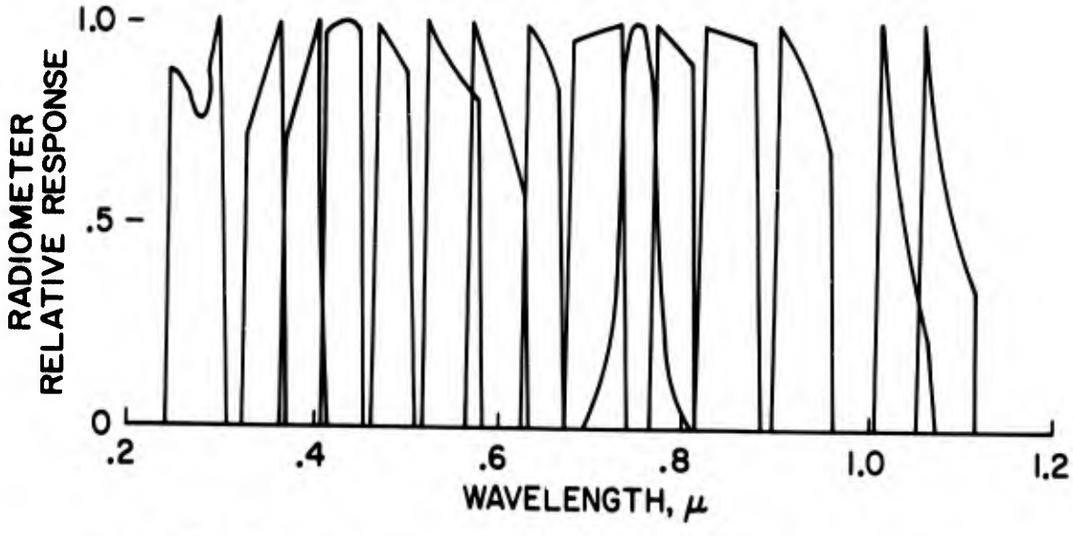

Fig. 2 Radiometer responses as functions of wavelength

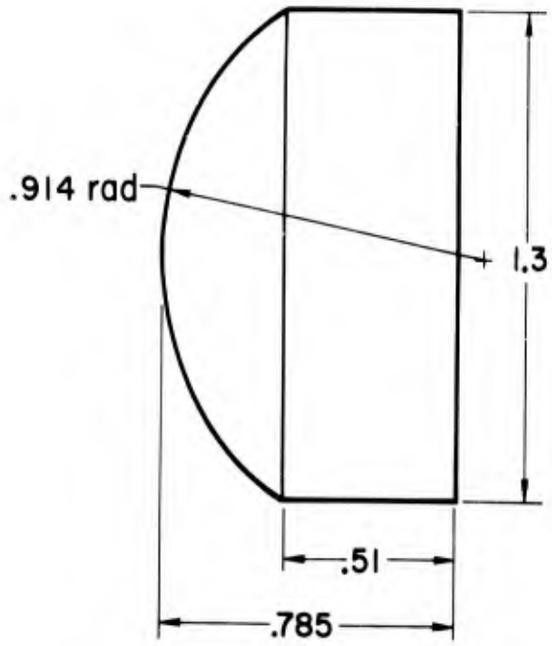

Fig. 3 Model geometry

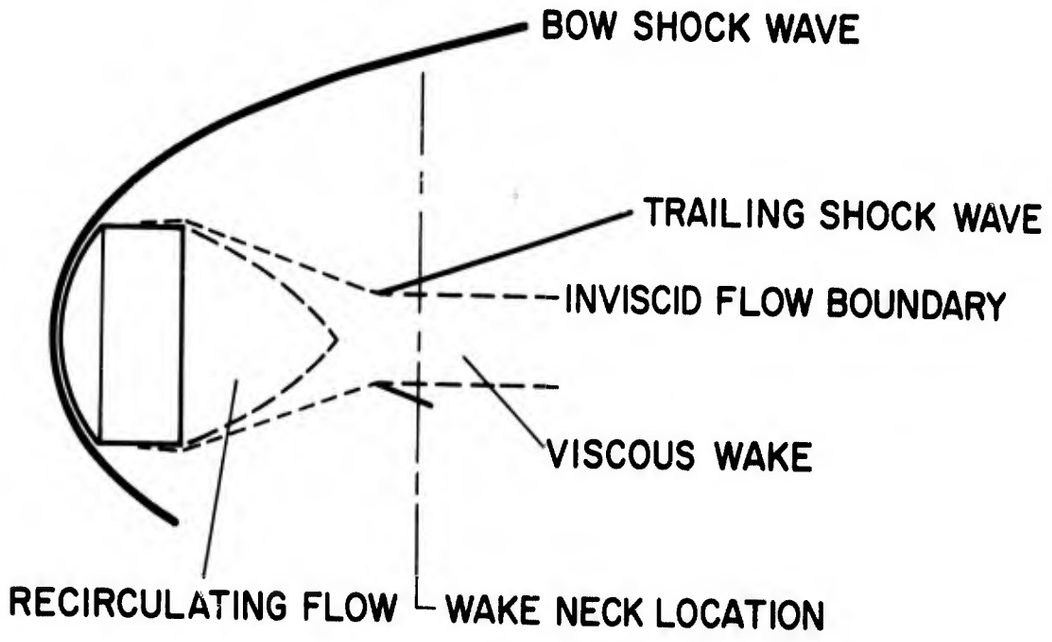

Fig. 4 Sketch of the flow-field geometry used in the calculations

LAMINAR WAKE; p_∞, 5 torr; V_∞, 7.4 km/sec; Re_∞, 21,500

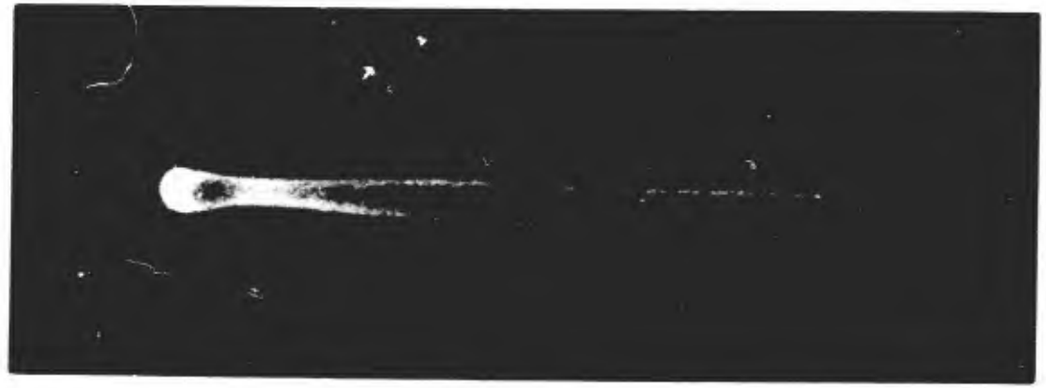

TURBULENT WAKE; p_∞, 60 torr; V_∞, 7.5 km/sec; Re_∞, 480,000

Fig. 5 Image-converter camera photographs of luminous flow in shock layer and wake

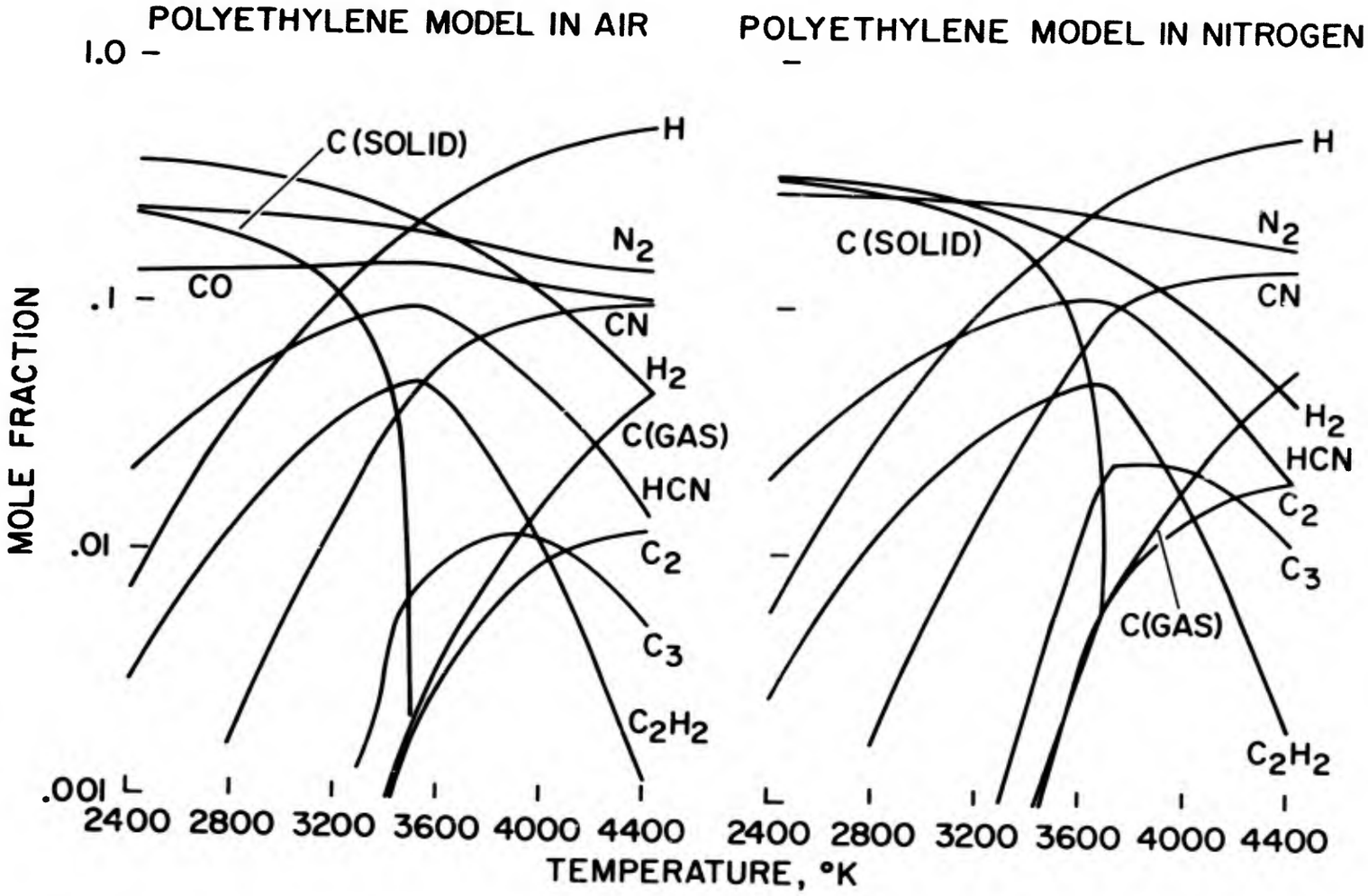

Fig.6 Species mole fractions as functions of temperature from equilibrium chemistry program; V_∞ = 6.7 km/sec; p_∞ = 60 torr, p_w = 1.5 atm

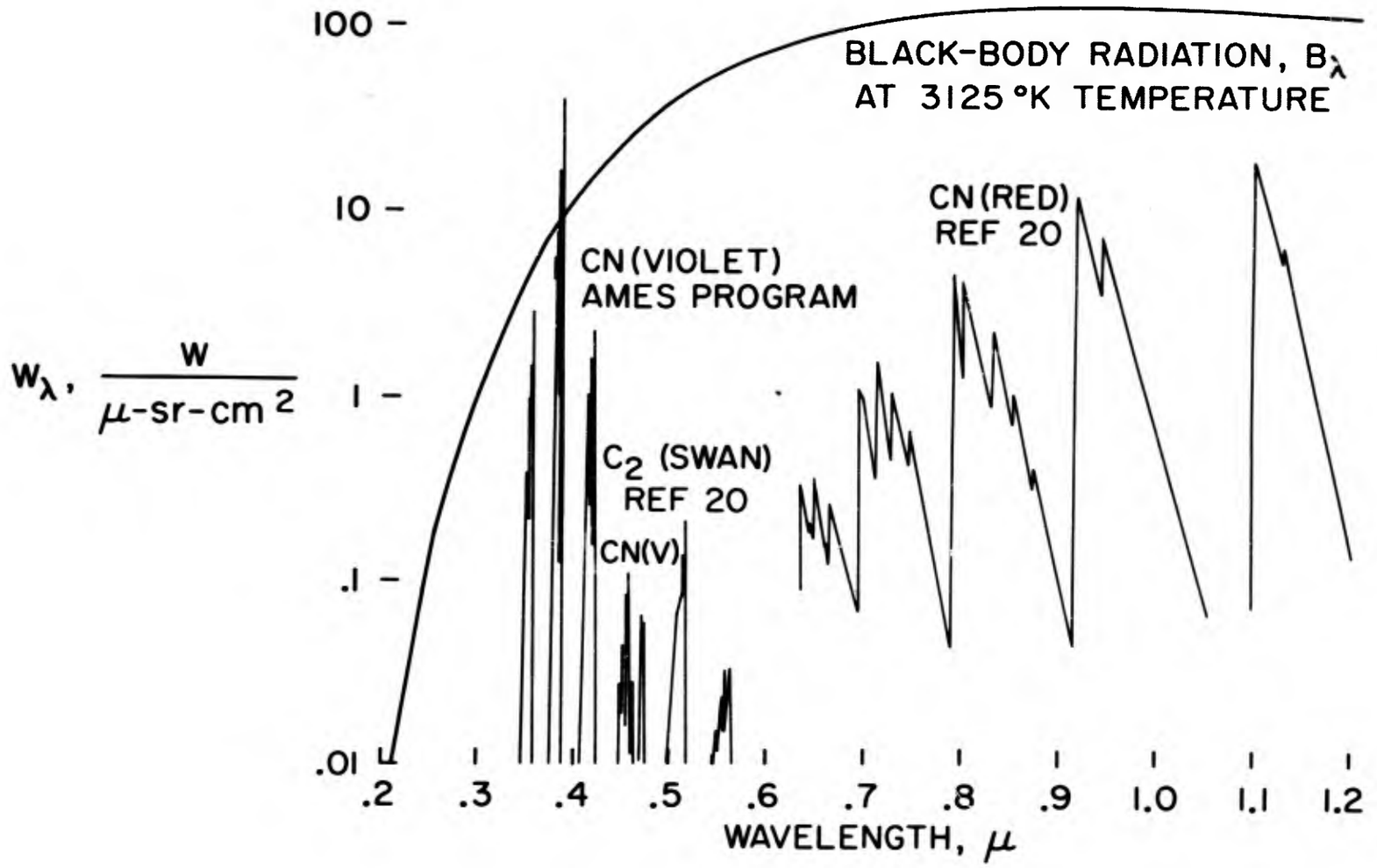

Fig. 7 Calculated molecular radiation for a polyethylene model in nitrogen; V_∞ = 6.7 km/sec; p_∞ = 60 torr; T_w = 3125° K

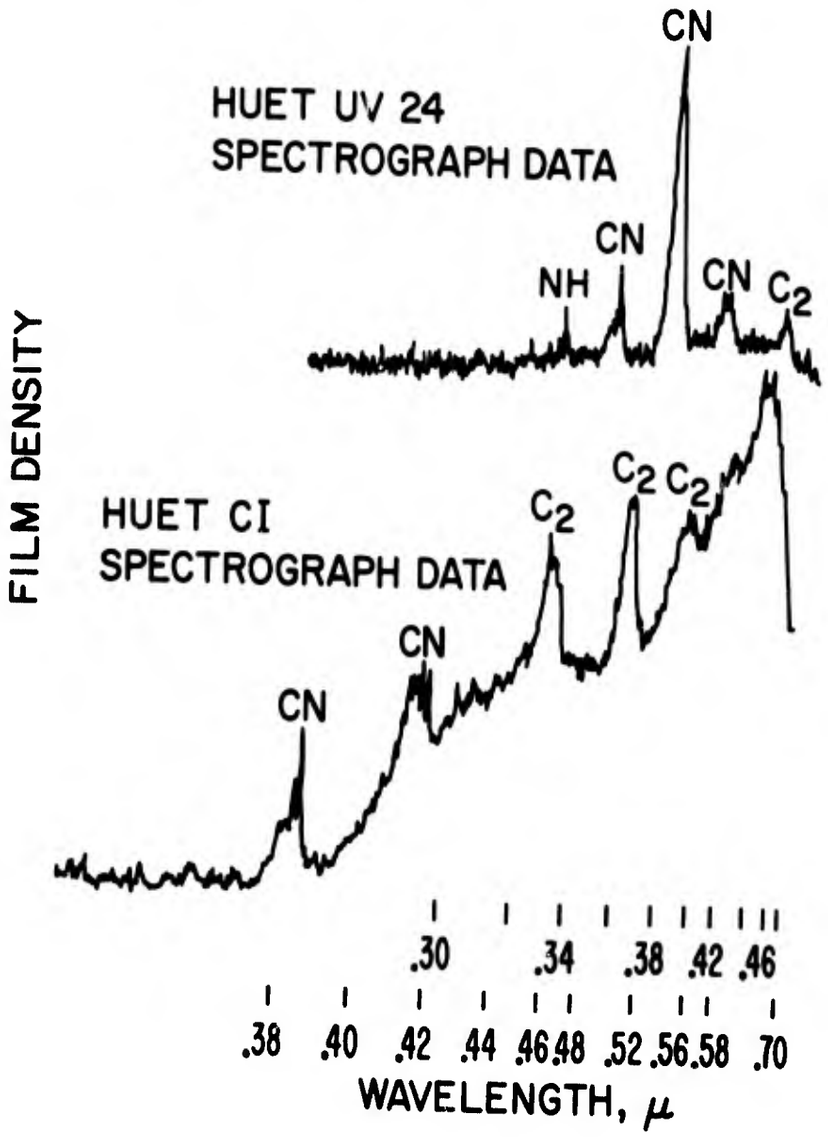

Fig.8 Densitometer records of photographic spectra; polyethylene model in air

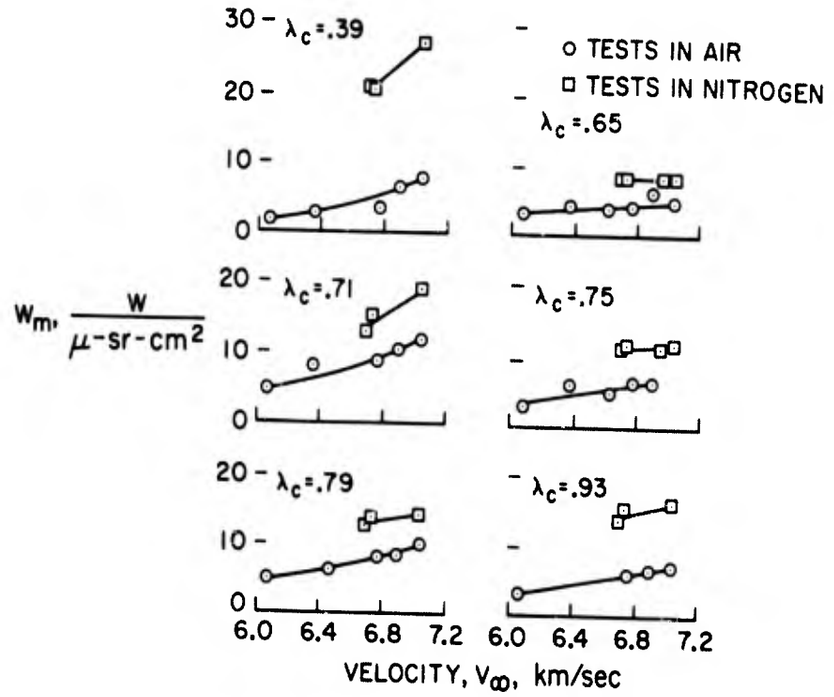

Fig. 9 Radiometer measurements as functions of model velocity

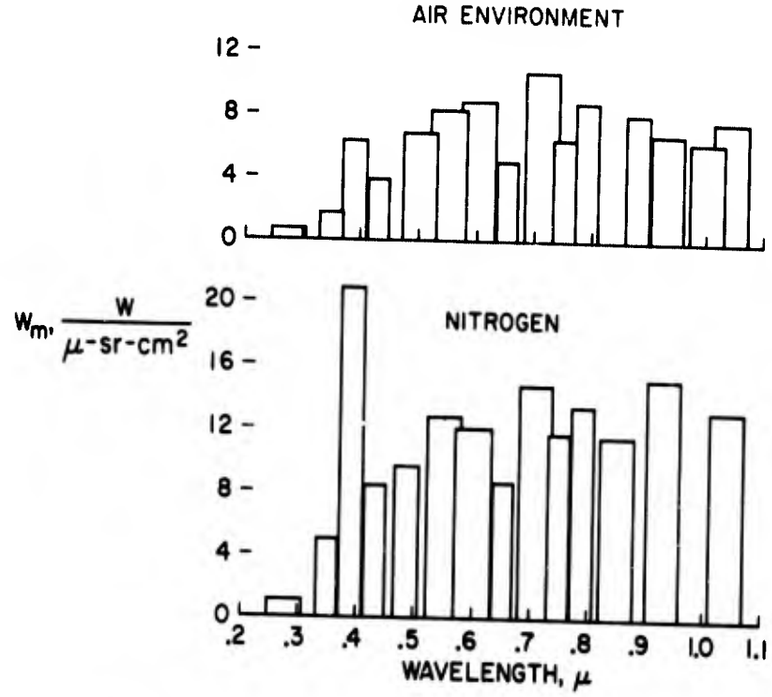

Fig. 10 Radiometer measurements as functions of wavelength

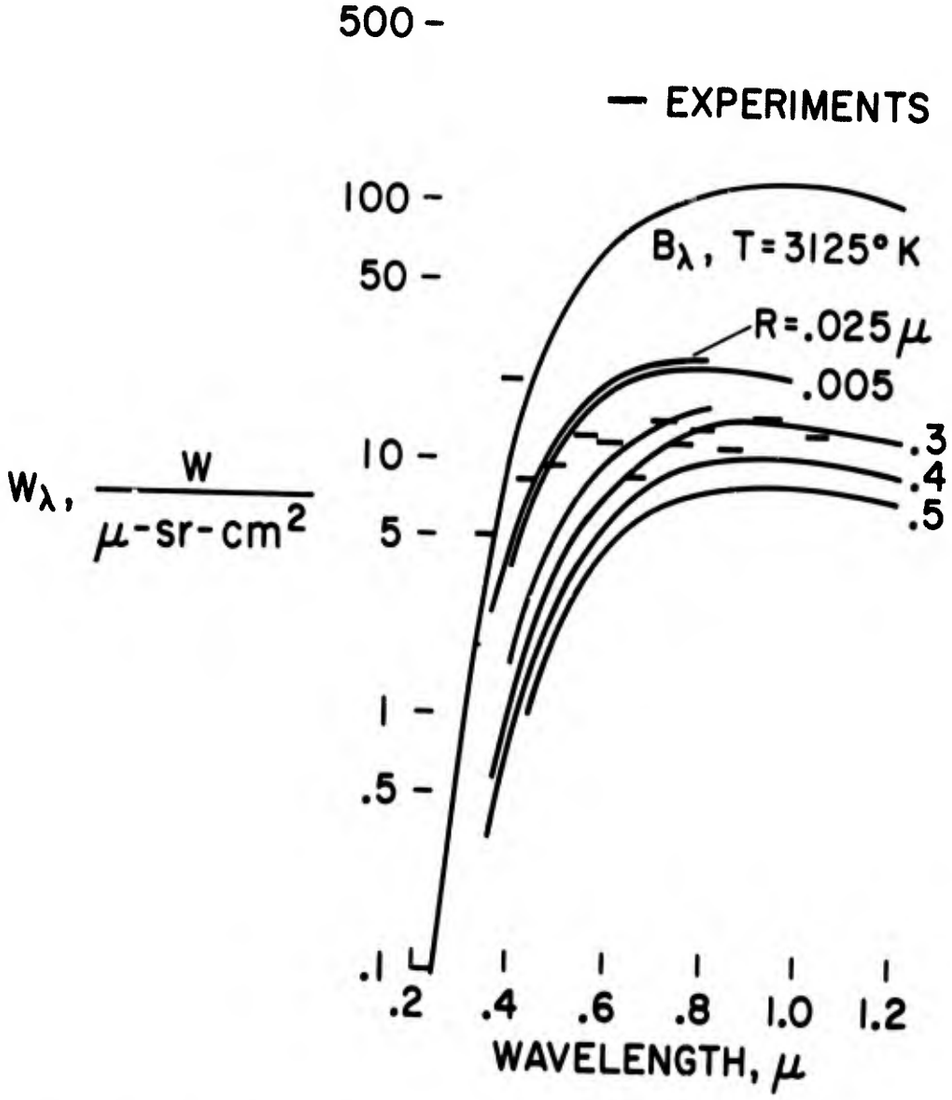

Fig. 11 Calculated radiation from soot particles compared with radiometer measurements; nitrogen environment

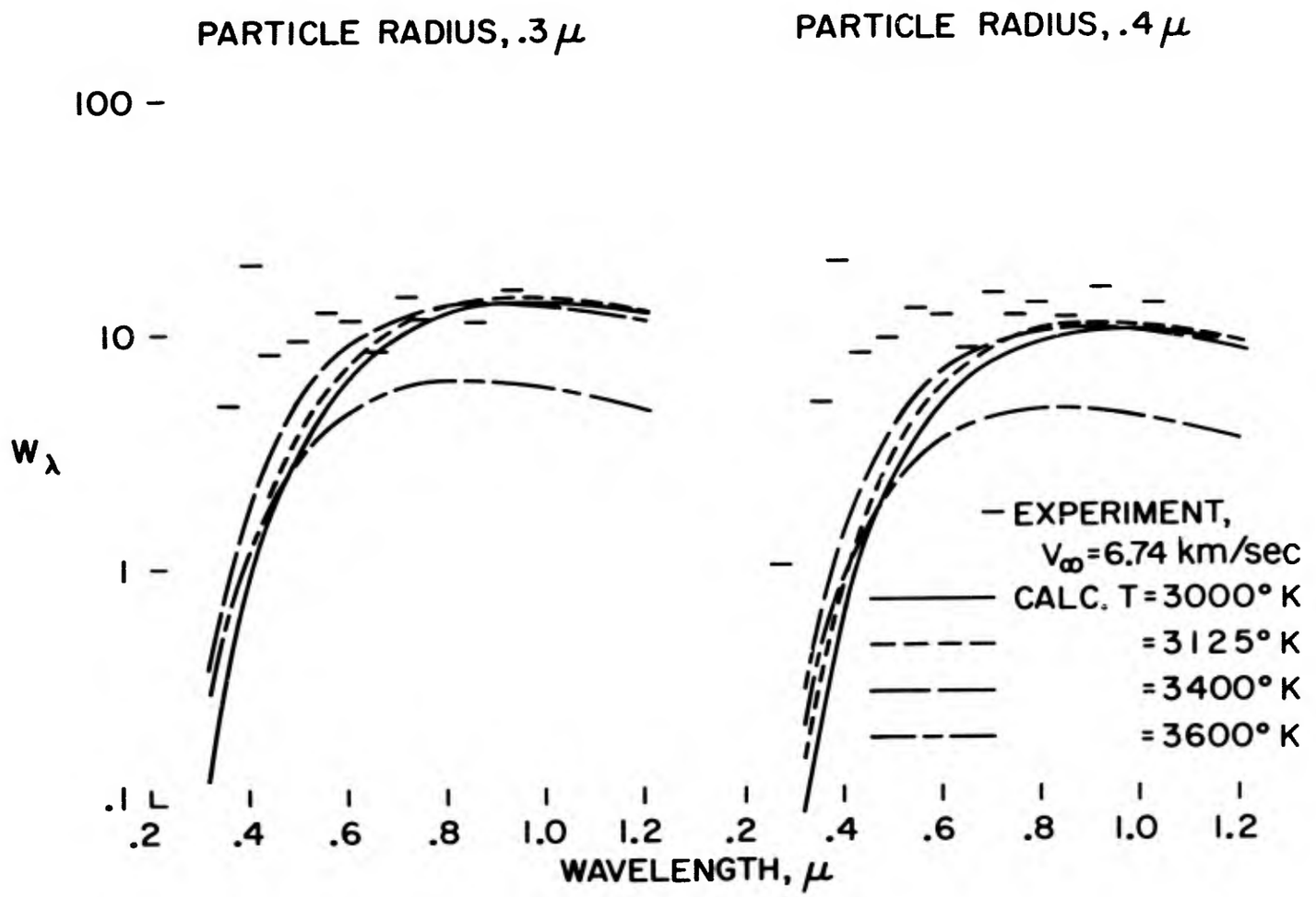

Fig. 12 Calculated radiation from soot in the wake compared with measurements; nitrogen environment

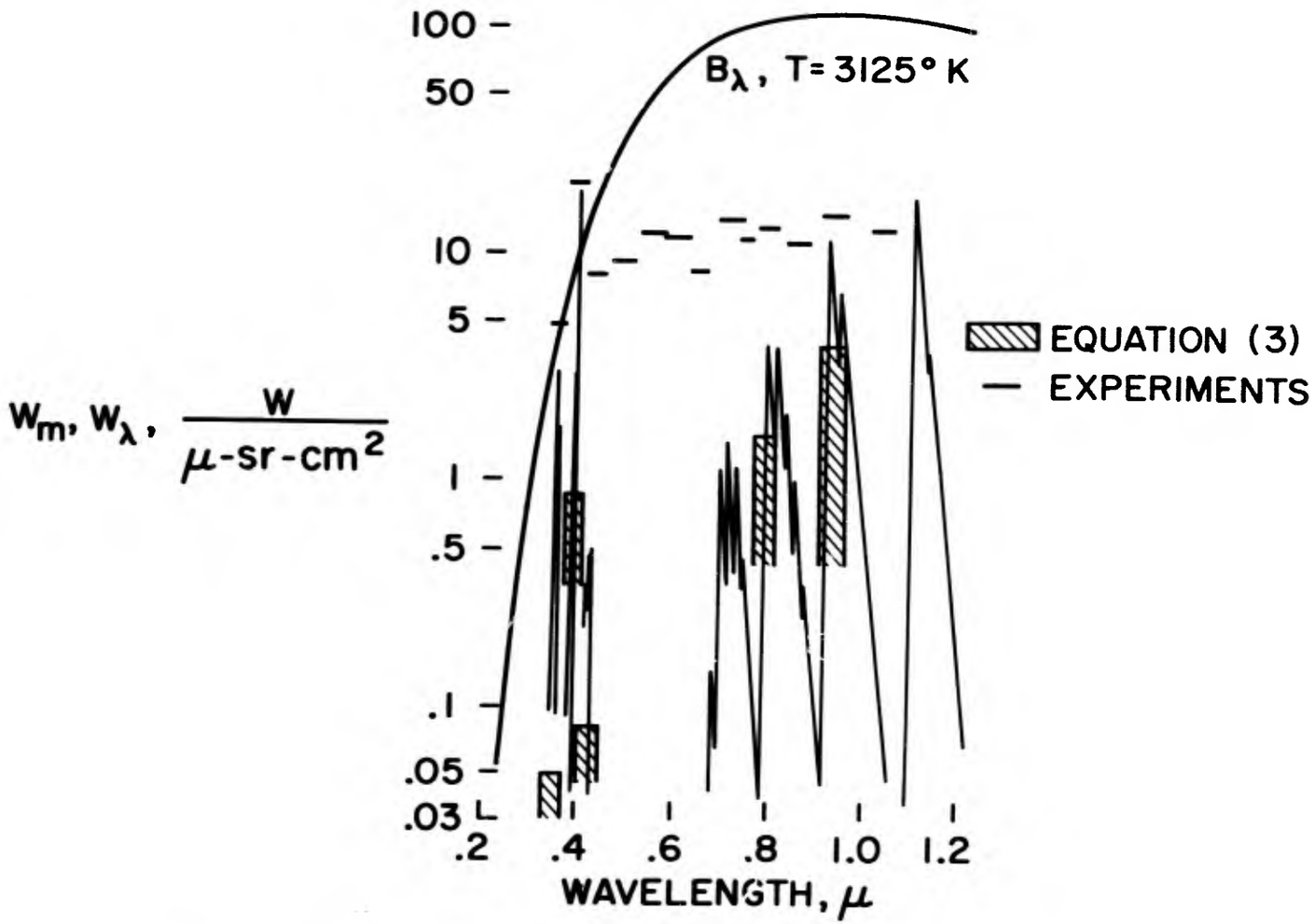

Fig. 13 Comparison of the measured wake radiation with calculated radiation from CN(violet) and CN(red); nitrogen environment

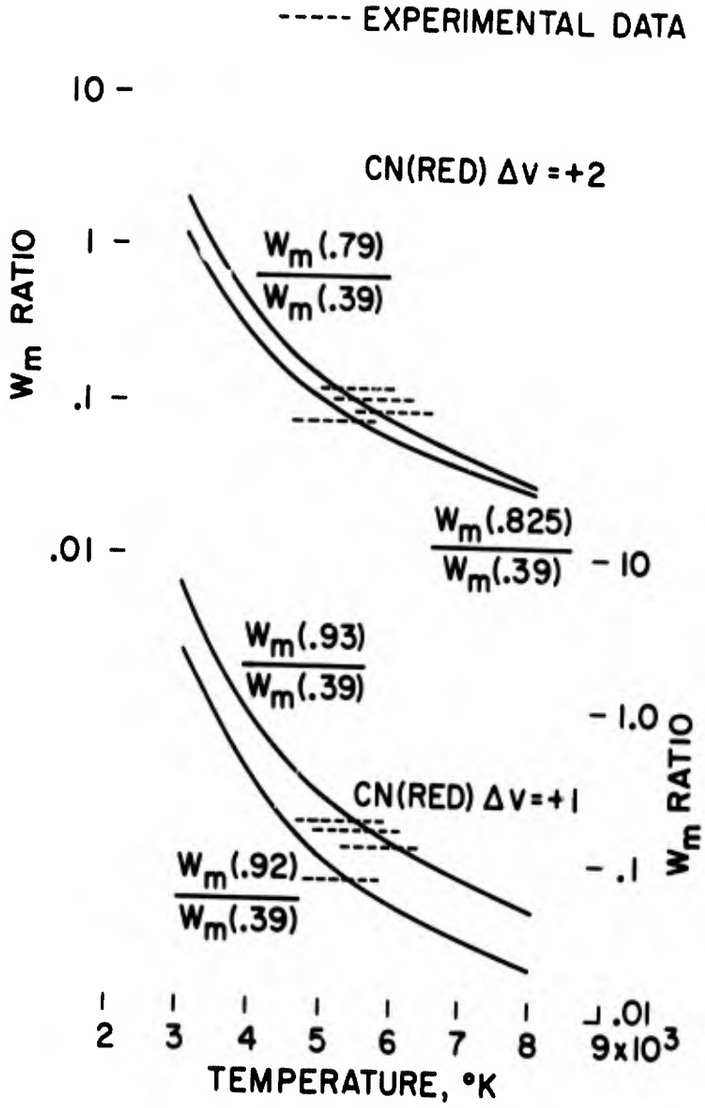

Fig. 14 Calculated ratios of intensities of various band sequence of CN(red) and CN(violet) as functions of temperature

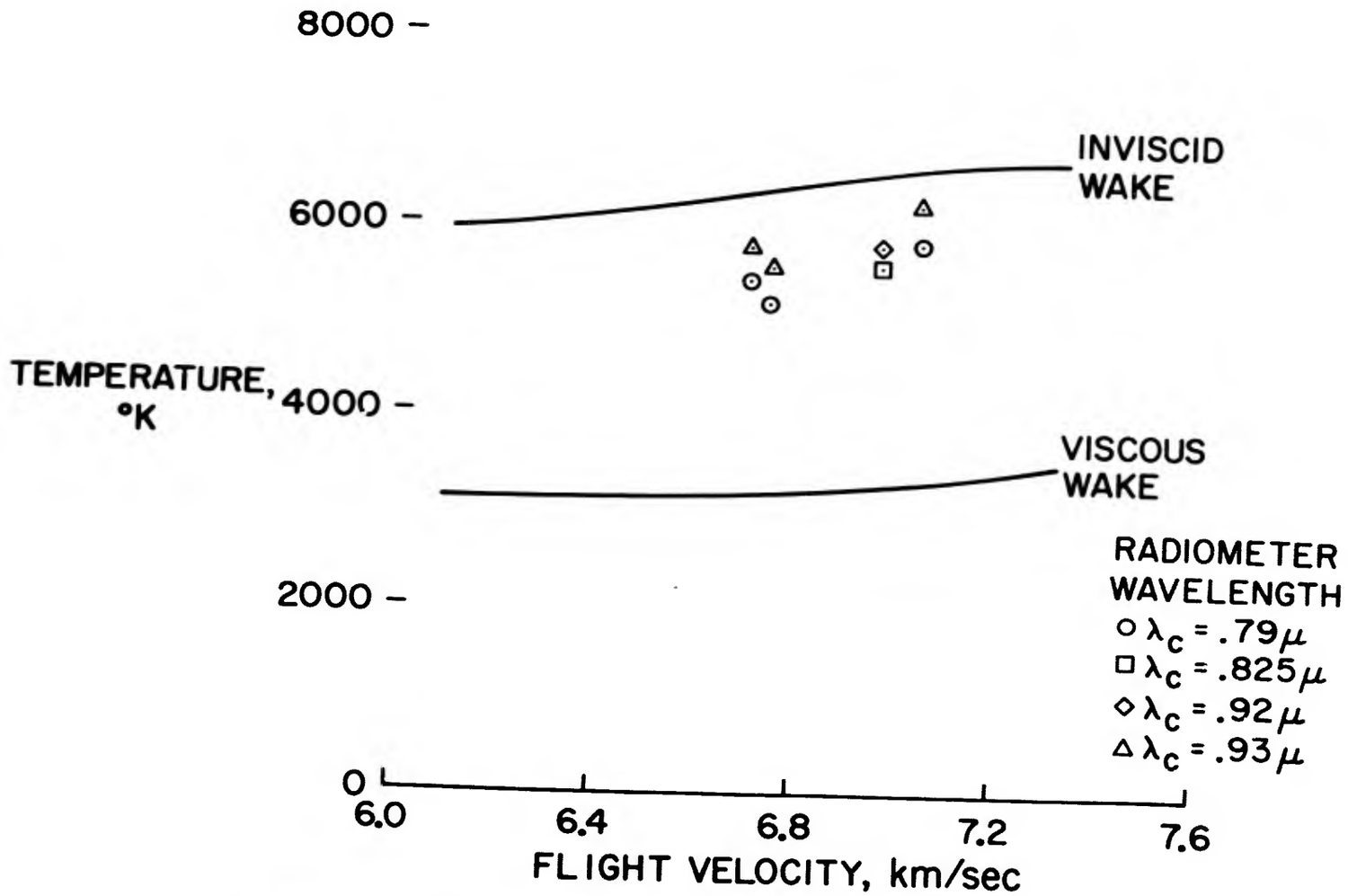

Fig. 15 Wake temperatures as functions of model velocity; inviscid and viscous wakes; nitrogen atmosphere

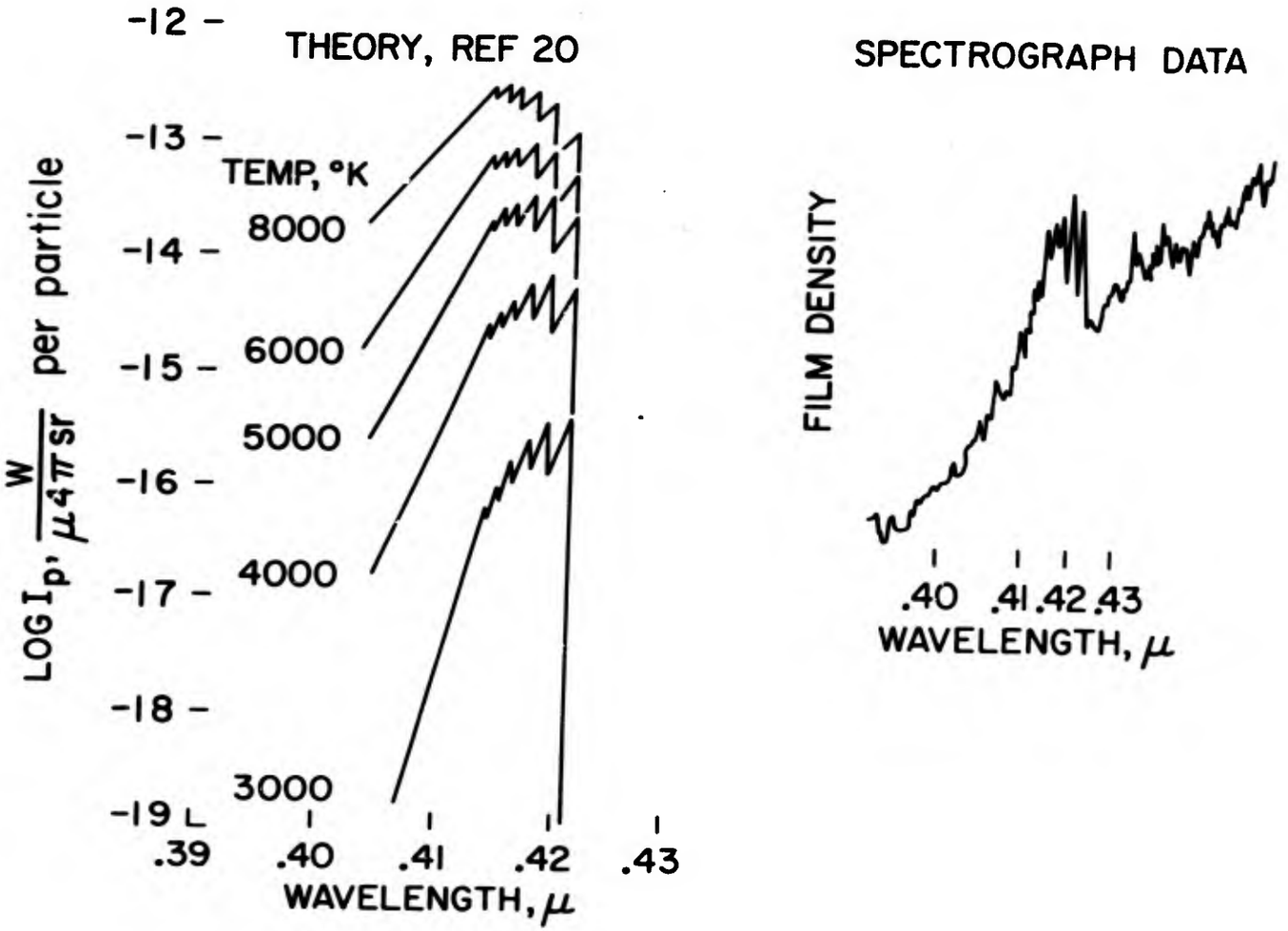

Fig. 16 Structure of the $\Delta v = -1$ band sequence of CN(violet) from (20) compared with spectrograph film density record

BALLISTICS RANGE MEASUREMENTS OF WAKE ELECTRON DENSITY AND SPECTRAL EMISSION

C. J. INFOSINO, R. R. GASTROCK
and R. A. LEVERANCE

U. S. Naval Ordnance Laboratory
White Oak, Silver Spring,
Maryland, USA

SUMMARY

Experiments in ballistic ranges have been made, to determine the electron density and the spectral emission from the wake of projectiles subjected to re-entry flight conditions. These projectiles have been flown at velocities from 12,000 to 19,000 feet/sec. at simulated altitudes of 50,000 to 125,000 feet. Models range in size from .25 to 1.25-inch base diameters and include spheres, cones and hemispheres-cylinder shapes. In addition to varying the flight condition, and the model size and shape, the model material is also varied. Materials include stainless steel, copper, aluminium, titanium, nylon phenolic, teflon and many others.

Wake electron density is determined as a function of distance behind the projectiles through the use of 5 and 25 kmc focused microwave interferometers. Since there is a 40-foot separation between interferometers, angle of attack effects for bodies of revolution can be isolated.

The spectral emission in the visible and near infrared region is also determined as a function of the distance behind the projectile. Spectral resolution is achieved through the use of prism and grating dispersion elements as well as the use of filters.

Since it is not possible to preheat models, the surface temperature of the model at a given point in the range is determined by the aerodynamic heating during its rather short trajectory. This factor is troublesome when it is desired to compare material effects since the ablation processes may be quite different. Nine spectrophotometers located along the range tube yield the radiation intensity from the model as a function of distance along the range. With certain simplifying assumptions these data can be converted to give the ablation rate history of the projectile.

The capabilities of each of the various diagnostic techniques will be illustrated through a brief presentation of recent representative results. The main portion of the paper will be concerned with the presentation of wake electron densities, spectral emission and ablation rate data for various materials.

RESUME

Il a été procédé à des expériences en tunnels balistiques afin de déterminer la densité en électrons et l'émission spectrale de sillages de projectiles placés dans des conditions de rentrée dans l'atmosphère. Ces projectiles ont été soumis à des vitesses variant de 12.000 à 19.000 pieds par seconde, à des altitudes simulées allant de 50.000 à 125.000 pieds. Les maquettes dont les diamètres de base varient de 0.25 à 1.25 pouces comprennent des sphères, des cônes et des cylindres hémisphériques. Outre les conditions de vol et les dimensions et formes des maquettes, on a fait varier les matériaux composant ces dernières: acier inoxydable, cuivre, aluminium titane, nylon phénolique, teflon, etc.

On détermine la densité electronique du sillage en fonction de la distance du point étudié par rapport à l'arrière du projectile, grâce à des interféromètres à micro-ondes de 5 et 25 kmc. Ces interféromètres étant séparés par une distance de 40 pieds, on peut isoler les effets de l'angle d'attaque pour des corps de révolution.

L'émission spectrale dans la région visible et proche de l'infrarouge est également déterminée en fonction de la distance à l'arrière du projectile. C'est à l'aide de prismes et d'éléments de dispersion en réseau, ainsi que de filtres, que l'on obtient une décomposition spectrale.

Les maquettes ne peuvant être chauffées préalablement, on détermine leur température superficielle en un point donné du tunnel sur la base de leur échauffement aérodynamique au cours de leur assez brève trajectoire. Ce facteur est gênant lorsqu'on désire comparer les effets des matériaux utilisés, car les processus d'ablation peuvent différer totalement. Neuf spectrophomètres situés le long du tunnel balistique indiquent l'intensité des radiations émises par la maquette en fonction de la distance. En faisant appel à certaines hypothèses simplificatrices, on peut convertir ces données pour obtenir les taux d'ablation du projectile le long de sa trajectoire.

Les auteurs illustreront les possibilités offertes par les diverses techniques diagnostiqueesen présentant sous forme condensée certains résultats représentatifs obtenus récemment. La majeure partie de la communication sera consacrée à l'étude des densités électroniques, des émissions spectrales et des taux d'ablation pour divers matériaux.

NOTATION

ω - angular frequency of transmitter

ω_p - angular plasma frequency

ν - collision frequency

n_e - electron density (cm^{-3})

n_c - critical electron density (cm^{-3})

$\Delta\varphi$ - phase shift (radians)

ℓ - wake width

$\bar{n}_e\ell$ or NEL - integrated electron density across wake width

$$\text{i.e., } \bar{n}_e\ell = \int_0^{\ell} n_e(x)\, dx$$

K - constant

T - transmission coefficient

GHz - 10^9 cycles per second

BALLISTICS RANGE MEASUREMENTS OF WAKE ELECTRON DENSITY AND SPECTRAL EMISSION

C. J. Infosino, R. R. Gastrock
and R. A. Leverance

1. Introduction

The ionized flow field around and behind hypervelocity vehicles as they re-enter the earth's atmosphere has received considerable attention for many years. A thorough understanding of the formation and structure of this ionized flow and its interaction with electromagnetic radiation has proved difficult to achieve even in the simplest cases. Complex mathematical treatments and solutions have been carried out but to date solid experimental verification is lacking either in whole or in part. The chemical species present and their rates of reaction, the turbulent scale, the mean electron density, and the wake temperature are just a few of the properties which must be determined experimentally.

To this end, controlled laboratory experiments on models can be performed in a ballistics range. By simulating as many of the full-scale flight conditions as possible, the electromagnetic properties of the wake can be studied using an assortment of conventional plasma diagnostic tools. In particular, in the ranges at the Naval Ordnance Laboratory (NOL) the mean electron density and the spectral emission in the wake behind hypervelocity models can be measured. This

paper will discuss the range instrumentation at NOL and show some of the results obtained to date.

2. Range Facilities

2.1 1000-foot Hyperballistics Range

The largest range at NOL is 1000 feet long, 10 feet in diameter, and can be evacuated down to 3×10^{-4} atmospheres. Using a two-stage light-gas gun, models varying in size from .25-to 1.25-inch base diameter have been launched in this range up to velocities of 20,000 ft/sec. Twenty-seven spark shadowgraph stations located within the range provide accurate velocity and trajectory information. In addition, two microwave interferometers, a Doppler radar, 12 luminosity stations, and an optical spectrograph are presently being used in this range.

2.2 Aerophysics Range

The Aerophysics Range is 50 feet long, 5 inches in diameter, and can be evacuated to 1×10^{-4} atmospheres. While velocities up to 25,000 ft/sec can be attained in this range, the maximum projectile size is 1/2 inch. This facility is primarily used to study optical phenomena of the flow field around and behind hypervelocity projectiles. In addition, it is used as a pilot facility to develop new instrumentation and techniques for later use in the larger ranges.

3. Optical and Microwave Instrumentation in the 1000-foot Hyperballistics Range

3.1 Optical Radiometers

Over the first 600 feet, the 1000-foot Hyperballistics Range is equipped with a series of luminosity stations. Each station consists of a phototube and slit arrangement as shown schematically in figure 1. The phototubes presently in use are sensitive to radiation in the band 3,800 to 10,000 Å (i.e., S_1 cathodes).

These radiometers were placed in the range to investigate the transient behavior of the ablation rate of plastic models launched in the range.(1) When the model enters the pressurized range environment after very rapid acceleration in the launching gun, there will necessarily be some finite time period before its skin temperature and material ablation rate reach a state consistent with the aerodynamic flight conditions.

Since the data obtained from the microwave interferometers and other instrumentation are used to compare the effect on the wake of different ablative materials, it is important that the state of ablation for each model be the same at the point in the range where these data are collected. If this were not the case, then it would not be possible to compare one material against another.

Since the radiation intensity is directly proportional to the amount of radiating species present for an optically thin medium, the output of the luminosity stations is proportional to the mass of ablation products present for a given material and consequently proportional to the mass ablation

rate of the material released from the model's surface. Thus by recording the change in optical luminosity as a function of the flight path length, the transient behavior of the model's ablation rate can be determined.

Data obtained for two such ablative plastic models, teflon and a reinforced phenolic material, are shown in figures 2 and 3, respectively. The results for teflon show that a "steady state" condition with respect to ablation was reached prior to station one. The decrease in intensity is due to the decrease in velocity as the model proceeds down the range. In the case of the phenolic material, it is clear that a flight path length of several hundred feet is necessary before a steady-state ablation process is approached.

3.2 Microwave Interferometers

A schematic of the basic components of the focused beam microwave interferometer is shown in figure 4. Each focusing lens is 30 inches in diameter and has a focal length of 30 inches. The lens system, by careful design, focuses the microwave energy such that the distance between half power points at the focus is about 1.5λ.

Just prior to a missile launching in the range, the interferometer is balanced so that the portion of the electromagnetic energy passing through the range (unknown path) and that passing through the reference path arrive in phase at the crystal detectors. After the missile is launched, the wake (or plasma) passing through the focused beam upsets

this balance, producing a phase shift proportional to the average electron density across the section of the wake in the beam.

Assuming for the moment that the collision frequency of the plasma is small compared to the microwave operating frequency, i.e., $\nu/\omega << 1$, the resulting phase shift can be written

$$\Delta\phi = \int_0^{\ell} \left[1 - \left(1 - \omega_p^2/\omega^2 \right)^{1/2} \right] 2\pi/\lambda \, dx \qquad (1)$$

where $\omega_p^2 = n_e e^2/\epsilon_0 m$.

Substituting $\omega_p^2/\omega^2 = n_e/n_c$ and assuming that $n_e << n_c$ to first order in n_e/n_c we have,

$$\Delta\phi \simeq \int_0^{\ell} \pi/\lambda n_c \; n_e(x) \, dx$$

$$= K \int_0^{\ell} n_e(x) \, dx$$

$$\equiv K \bar{n}_e \ell$$

where $\bar{n}_e$ is some average electron density across the wake. Note that the measured phase shift does not give the electron density directly but is an integrated electron density across the wake width. The interferometer results must consequently be expressed as some average or integrated electron density (designated by $\bar{n}_e \ell$) until the distribution function for electrons across the wake is known.

Any change in the transmitted amplitude is simultaneously recorded with the phase shift. Thus, if the transmission

coefficient deviates significantly from unity, the simplified analysis given above can no longer be used. In this case both $\bar{n}_e \ell$ and ν/ω are computed from more exact equations based on the two measured quantities $\Delta\phi$ and T.

For transmission through the plasma, the underdense condition $\left| \frac{(\omega_p/\omega)^2}{1 - j\nu/\omega} \right| << 1$ must be maintained. This obviously places an upper limit on the range of electron densities that can be measured. In particular, it can be shown that negligible error is incurred when the associated plasma frequency is $\leq 1/3$ the microwave operating frequency. We have then

$$n_e \text{ (max)} = \begin{cases} 8.5 \times 10^{11} \text{ electrons/cm}^3 \text{ for 25 GHz} \\ 3.45 \times 10^{10} \text{ electrons/cm}^3 \text{ for 5 GHz} \end{cases}$$

The lower limit is determined by the smallest phase shift that can be measured. For the instrumentation being discussed, this corresponds to approximately one degree. Assuming a uniform distribution of electrons across the wake, values for the minimum electron density, at 5 and 25 GHz and for several values of the wake width, are shown in Table I.

Table I

n_e (minimum) for 1° phase shift

Wake Width	1"	3"	6"	9"
25 GHz	2.04×10^{10}	6.8×10^{9}	3.3×10^{9}	2.3×10^{8}
5 GHz	4.09×10^{9}	1.36×10^{9}	6.8×10^{8}	4.5×10^{7}

Past test results using the interferometer have shown the effect of different model configurations and flight conditions on the electron density levels and decay rates in the wake. Blunt and slender configurations, made up of heat sink or ablative materials, and launched at different velocities into different range pressures, have all been shown to have considerably different wake signatures.

Figure 5 is a sample of some recent data obtained in a program where the objective was to investigate how the wake electron density is affected by changes in the model velocity. Heat sink (copper) spheres, 0.75 inch in diameter, were used in these tests. The results indicate that the integrated electron density (NEL) is exponentially dependent on the velocity at least in the region from 14,000 to 19,000 ft/sec at a range pressure of 37 Torr. The data points tend to be more scattered in the far wake because the phase angles measured here are approaching the noise level of the interferometer. To complete this study, data will be obtained at several different pressures as well as for cone configurations.

To investigate the effect of material ablation on the electron density, spheres of different materials were launched in the range, all at very close to the same flight conditions (16,500 ft/sec and 26 Torr). Figure 6 shows the results for just a few of these materials, namely: lexan, teflon, and linen phenolic. As a reference level, the electron density signature for a heat sink body (stainless steel) is also shown

on the graph. These experimental results represent only a small portion of the body of data necessary to evaluate the effect of ablators on the wake electron density. If slender cone models are used or the flight conditions are changed appreciably, the behavior or effect of each of these materials may be quite different.

3.3 Experimental Doppler Radar

An oblique Doppler radar, operating at 25 GHz, is also being used in the range to monitor the reflected signal from the missile and its wake. Figure 7a is an abbreviated schematic of this system.

The antenna (25 db gain) is mounted at a 45-degree angle with respect to the range axis so that the moving target reflects the incident signal back to this antenna at a slightly different frequency (Doppler effect). This provides a convenient method of separating the desired target signal from the high background return produced by the wall reflections in the tank. The return signal is mixed in a crystal detector with a small portion of the power from the transmitter and the resultant beat or Doppler frequency recorded directly on an oscilloscope. The amplitude of this signal is directly proportional to the unknown signal reflected from the wake. Figure 7b shows a sample of the type of data obtained with this system. The model used in this illustration was a 1 1/4-inch diameter stainless steel sphere.

4. Optical Instrumentation in the Aerophysics Range

4.1 Rotating-Mirror Camera

When the velocity of a model can be predicted, the rotating-mirror camera, figure 8, provides an excellent means of obtaining sharp exposures of the shock wave and gas flow near the model. The camera shown in figure 8 was designed to use a 70-mm film strip on an 18-inch radius semicircle and a 4-sided mirror driven by an air turbine capable of 3000 rps. This rotational speed is adequate to "pan" or freeze the motion of a 30,000 ft/sec projectile. The image that is recorded is 1 1/2 times the object size.

Typical photographs taken with the rotating-mirror camera are shown in figures 9 and 10. Figure 9 illustrates with sharp definition the shock detachment in the case of a 0.5-inch sphere moving at 8,020 ft/sec. Figure 10 brings out the flow field at the base of a 0.75-inch hollow cylindrical slug at 6,000 ft/sec.

One important feature of the camera is its ability to integrate the light from the spark source and/or the model, thereby permitting the use of lower speed, fine grain, clear base films, or permitting narrow-band light filtering to eliminate chromatic aberration problems when using large, simple lenses.

This integrating feature was used recently to photograph and study the increase in radiation when a reflected shock wave passed through the wake of a highly luminous

ablating model. Figure 11, taken with the camera, clearly shows the reflected bow shock crossing the wake behind a 3/8-inch projectile. This can be correlated with the sudden increase in wake radiation as indicated by the photodetector signal shown in the same figure. The bow shock was reflected from two large plates placed in the range, one positioned 3/4 inch above range center, the other 3/4 inch below. Figure 12 shows this same effect, but in this case the model flight path was closer to the bottom reflecting plate. Consequently, the reflected shock from each plate is observed to cross the wake core separately, i.e., at different points in the wake.

4.2 Mach-Zehnder Interferometer

A Mach-Zehnder interferometer has been used in the range for gas density measurements. Figure 13a illustrates a typical photograph of a 1/2-inch sphere launched at 6,000 ft/sec into a pressure of 78 Torr when the interferometer plates are adjusted for multiple fringes. Here, variations in the local gas density are determined by the shift of the fringes relative to the unperturbed interference pattern. Figure 13b, on the other hand, for the same model and conditions, illustrates a single fringe setting. Here zones of equal path length are connected by light or dark fringes which can be interpreted in a manner similar to topographical maps. This single fringe interferogram, however, is seldom used to obtain quantitative data. Color photographs of the

interferograms can also be taken and have proved to be quite useful, particularly in turbulent wake studies.

4.3 Radiation Detectors

To study air radiation intensities, the range is equipped with several single detector units similar to those installed in the 1000-foot Hyperballistics Range (fig. 1). A better, but more complicated, arrangment for observing the radiation is shown in figure 14. This system, utilizing four to seven phototubes and a grating spectrometer unit, can measure narrow-band radiation and spans the region from the ultraviolet to the near infrared.

Figure 15 illustrates radiation data obtained from several materials, using the above detection system. The seven photo-tube channels, each with a 20 Å bandwidth, were spaced 500 Å apart so that the spectral region 2900 to 5900 Å could be covered. The model spheres used in this program were all launched at 18,000 ft/sec into a range pressure of 8 Torr.

While only the peak signals (radiation from the stagnation region) are plotted in the bar graph of figure 15, the complete record from each photodetector shows the radiation emitted by the wake, as well as that from the stagnation region. In analyzing these records, three different radiation profiles or signatures could readily be distinguished. The first, illustrated in figure 16, is characterized by low wake radiation compared to the stagnation or peak radiation. All of the materials exhibiting a similar characteristic output signal

and the associated wavelength channels on which such a signal was recorded are listed together under this curve and referred to as Group I materials. The second, illustrated in figure 17, is characterized by medium level wake radiation compared to the peak radiation. Only nylon, polyethylene, and linen phenolic at 5900 Å (labeled Group II materials) were observed to have this type of profile. The third, illustrated in figure 18, is characterized by very strong and extensive wake radiation compared to the stagnation region radiation. Again, only three materials (nylon, polyethylene, and linen phenolic) exhibit this behavior but in this group similar profiles were recorded on four of the wavelength channels (3900 Å, 4400 Å, 4900 Å, and 5400 Å).

5. Future Plans

The range facilities and capabilities mentioned in this paper are undergoing considerable modification. The present 1.5-inch bore, light-gas gun in the 1000-foot Hyperballistics Range will be replaced by a more advanced design gun capable of operation with either a 2-inch or a 4-inch barrel. This will enable larger projectiles to be launched (up to 3 1/2 inches) at higher velocities (up to 25,000 ft/sec). Conversely, by reducing the velocity, some of the more fragile types of model configurations can be launched, since the inertial forces will be lower than those presently

encountered (≈200,000 g). High quality laser and spark shadowgraph stations are also being installed.

The 25Gc interferometer will be converted to a multi-beam system so that measurements can be taken through several transverse paths across the wake. This will provide information concerning the radial distribution of the wake electron density.

In addition, a high-speed mass spectrometer, a focused beam radar and a closed UHF resonant cavity are under development for use in this range.

The Aerophysics Range will be relocated in a new building this year. This will provide additional space so that more test sections and instrumentation, microwave as well as optical, can be added.

REFERENCE

(1) Plummer, M. J., "Transient Behavior of the Ablation Rate of Plastic Models in a Ballistics Range," Proceedings of 7th Navy Aeroballistics Symposium (BOWACA), Jun 1966

ACKNOWLEDGEMENT

The authors wish to express their appreciation for the assistance and encouragement given to them in their work by Mr. L. L. Hill

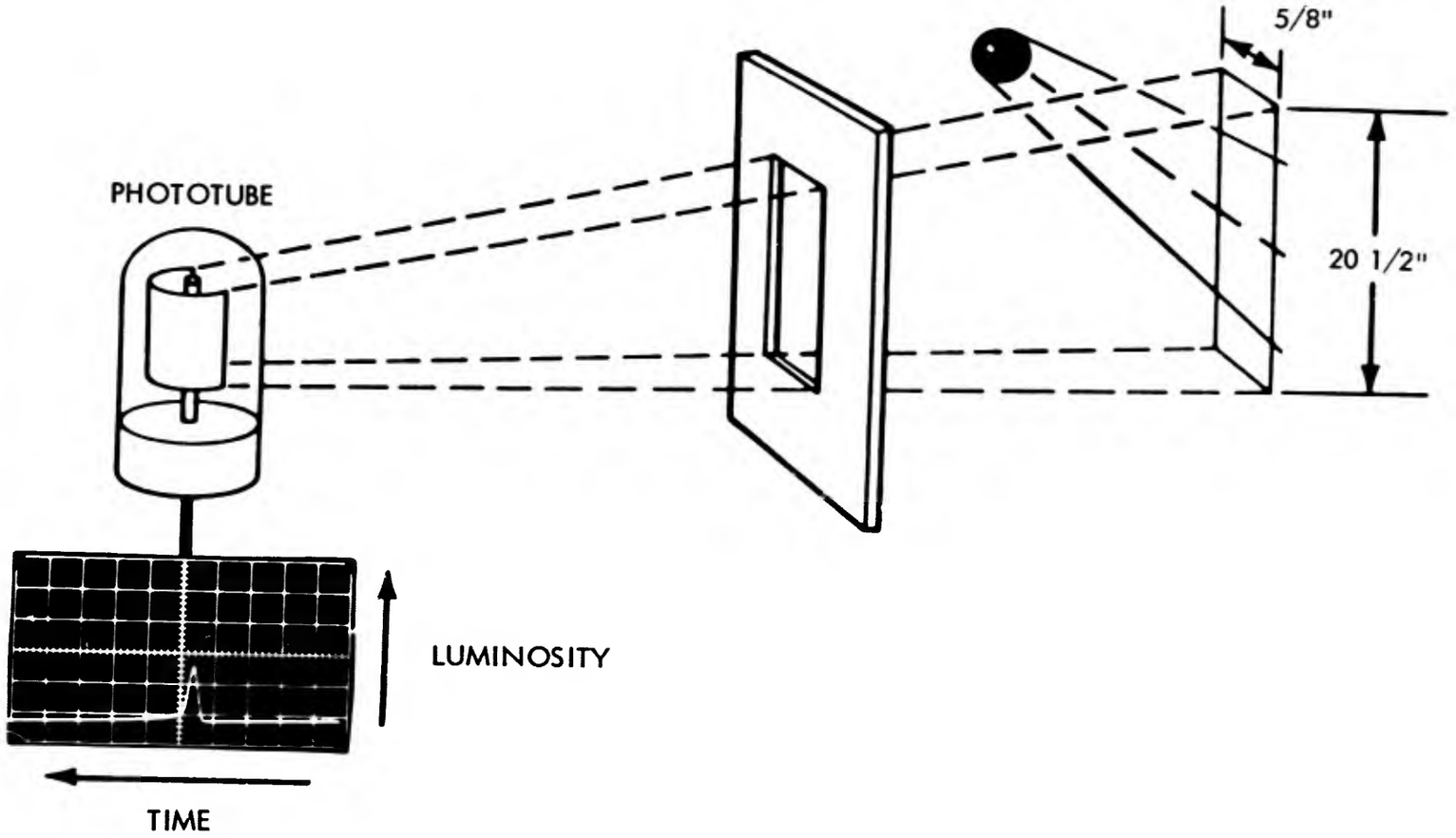

FIG. 1 SCHEMATIC OF LUMINOSITY DETECTOR

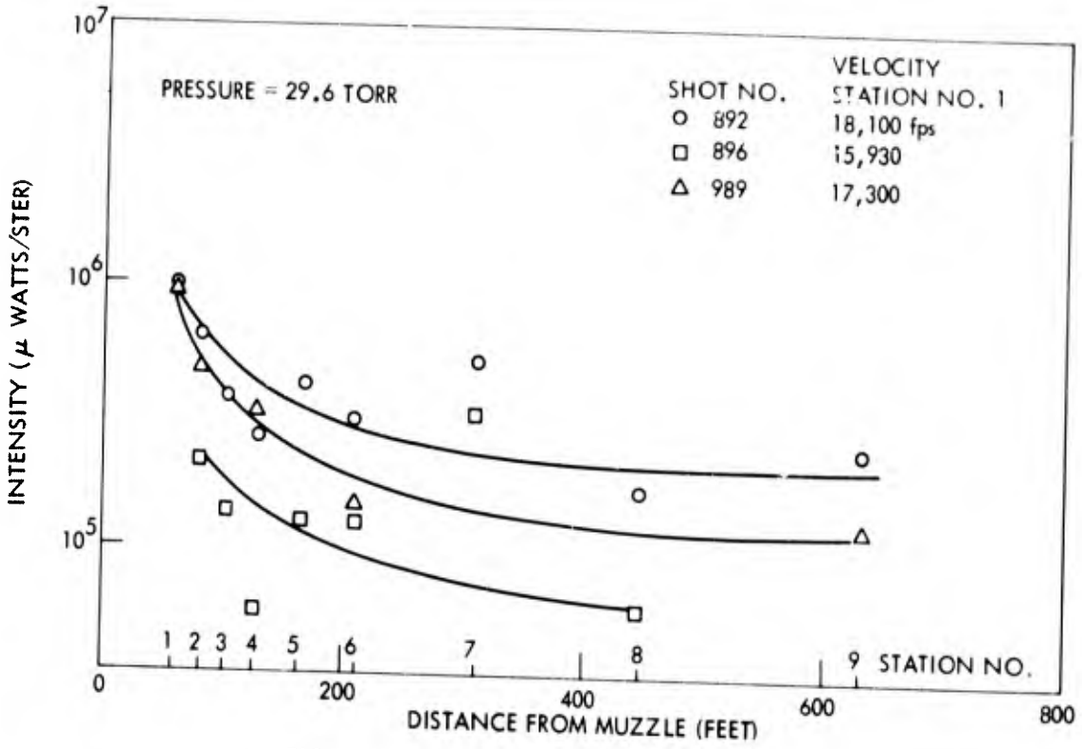

FIG. 2 LUMINOSITY HISTORY OF TEFLON SPHERES

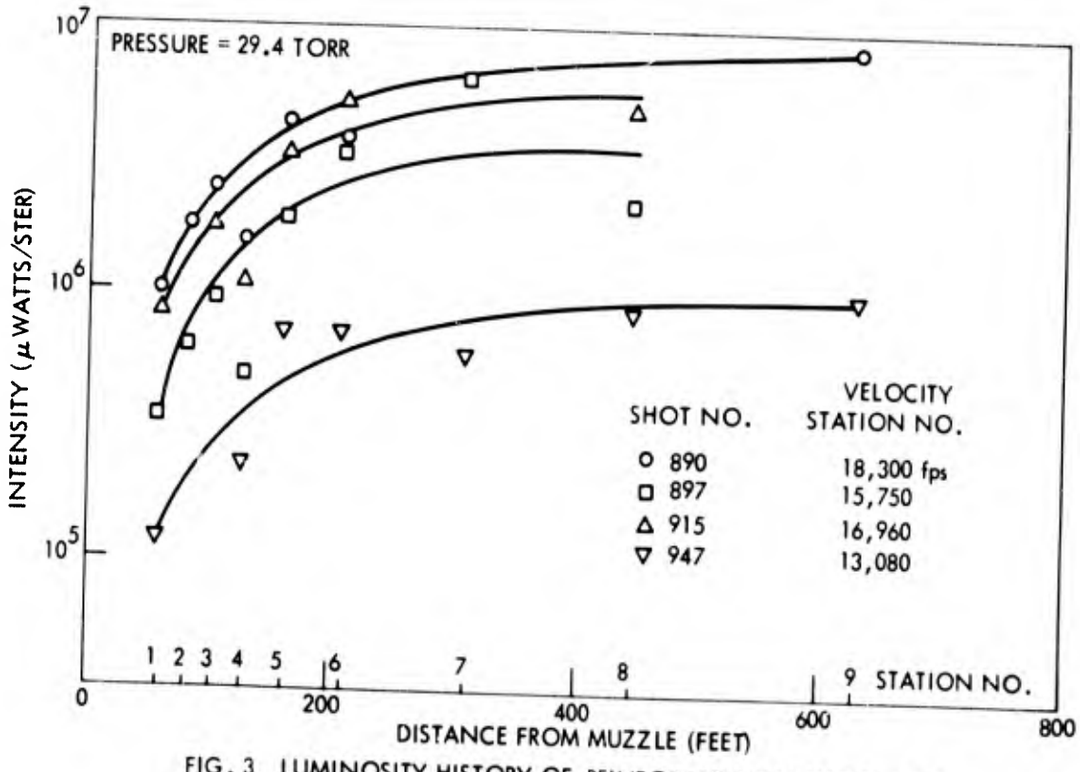

FIG. 3 LUMINOSITY HISTORY OF REINFORCED PHENOLIC SPHERES

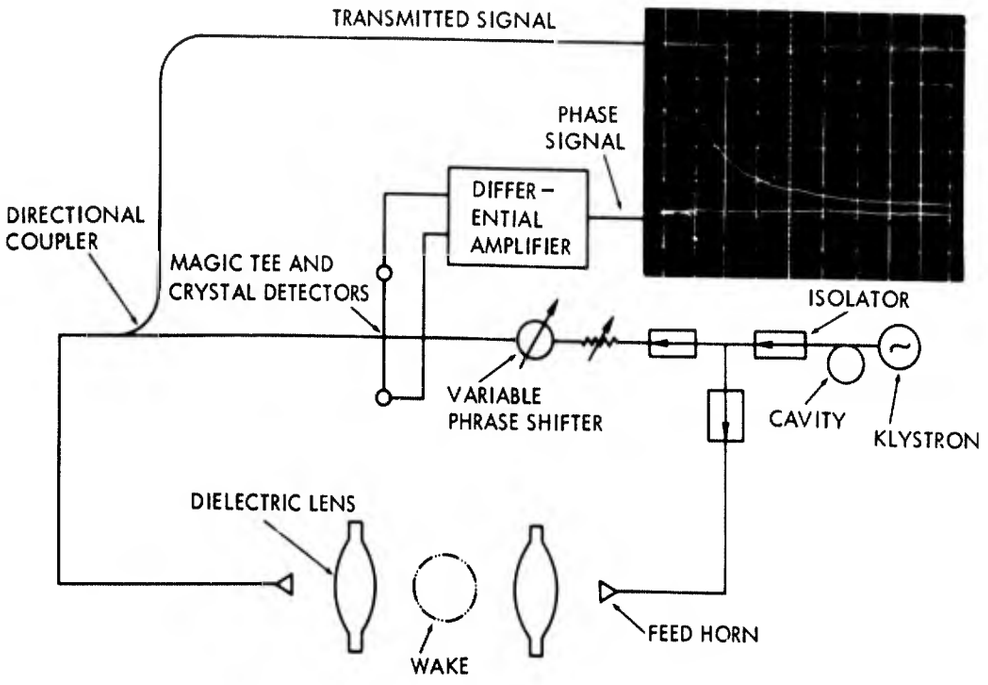

FIG. 4 SCHEMATIC OF MICROWAVE INTERFEROMETER

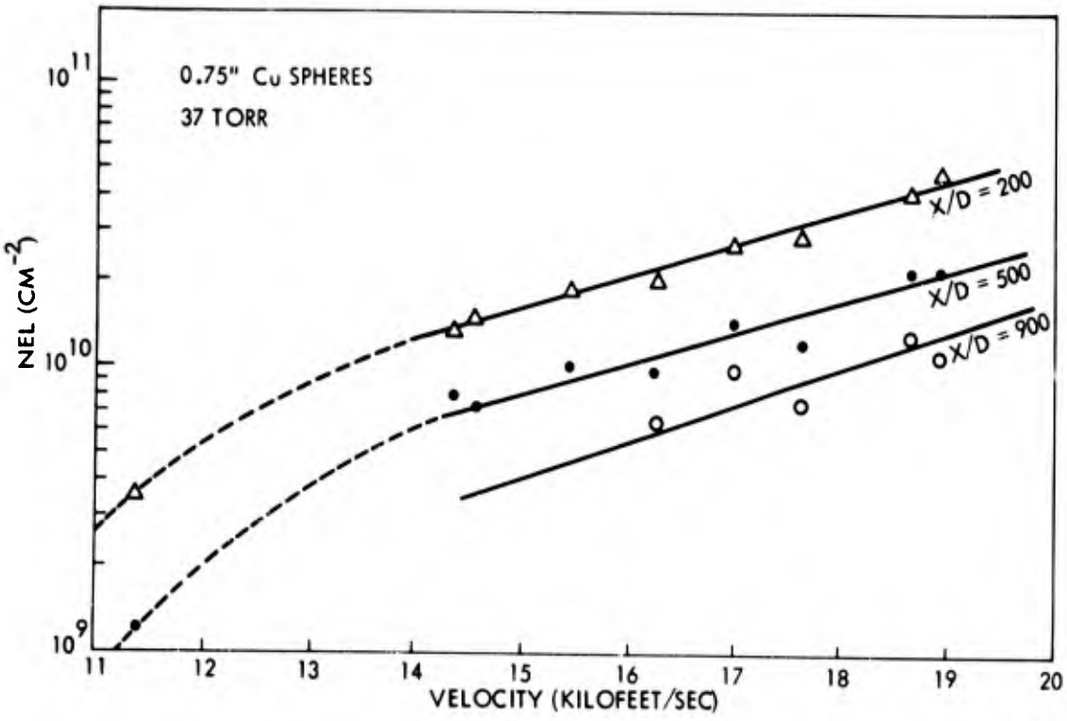

FIG. 5 NEL VS VELOCITY

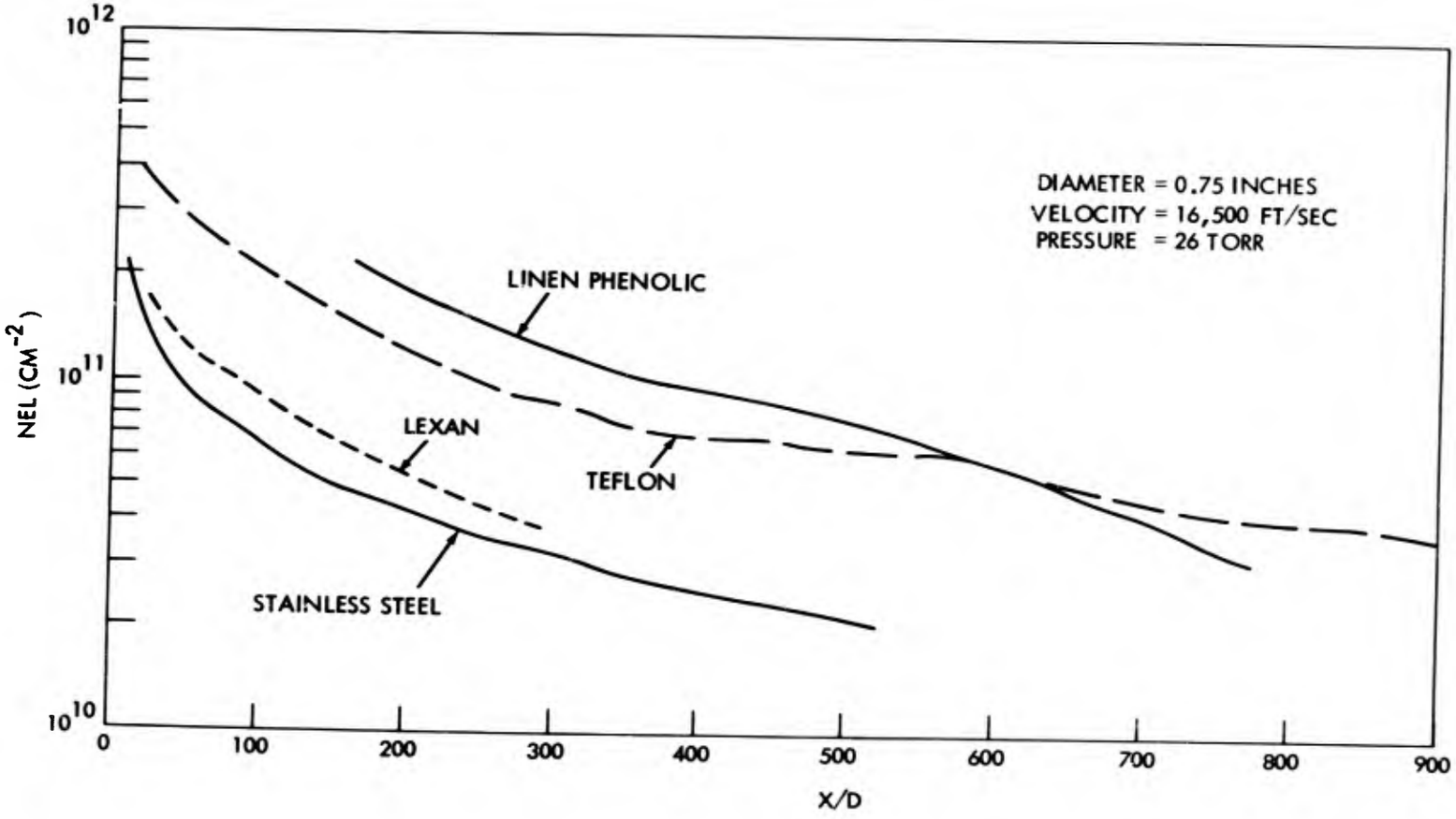

FIG. 6 NEL VS X/D FOR VARIOUS ABLATION MATERIALS

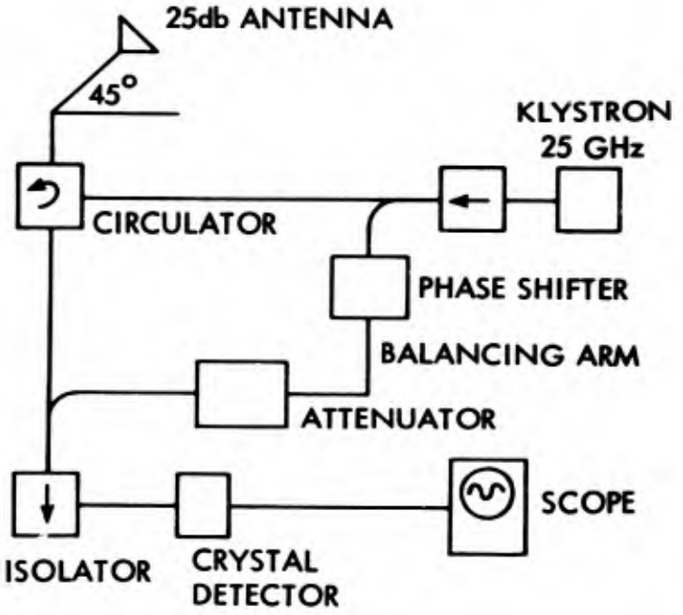

FIG. 7a SCHEMATIC OF RADAR

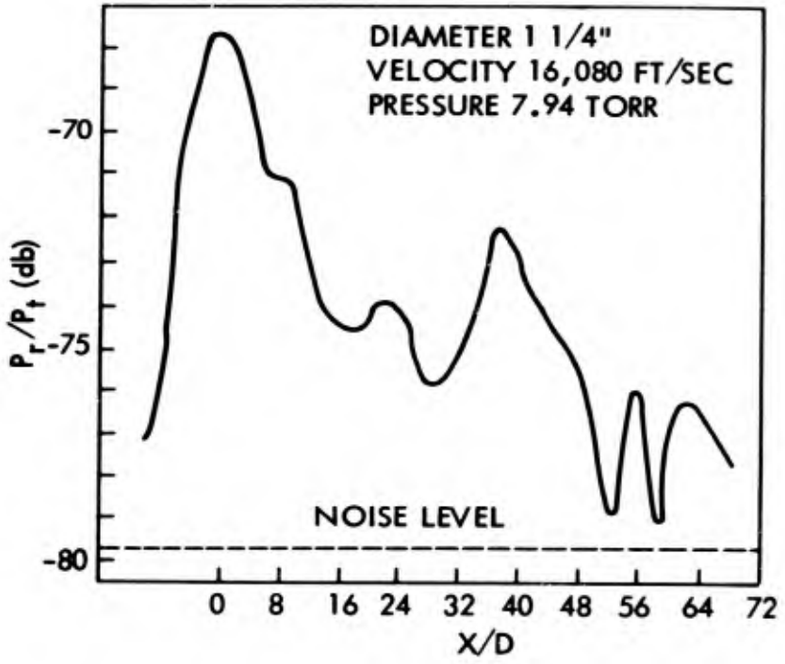

FIG. 7b TYPICAL RADAR RETURN

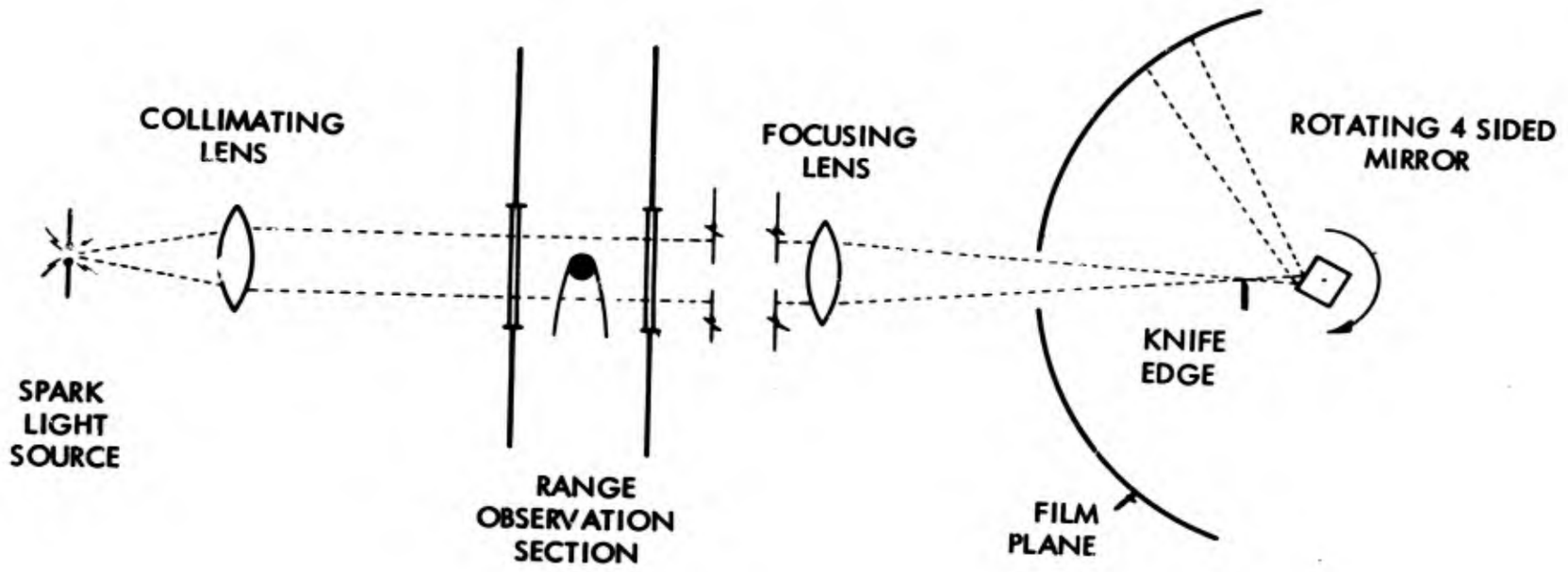

FIG. 8 SCHEMATIC OF ROTATING MIRROR CAMERA
AND SCHLIEREN OPTICAL SYSTEM

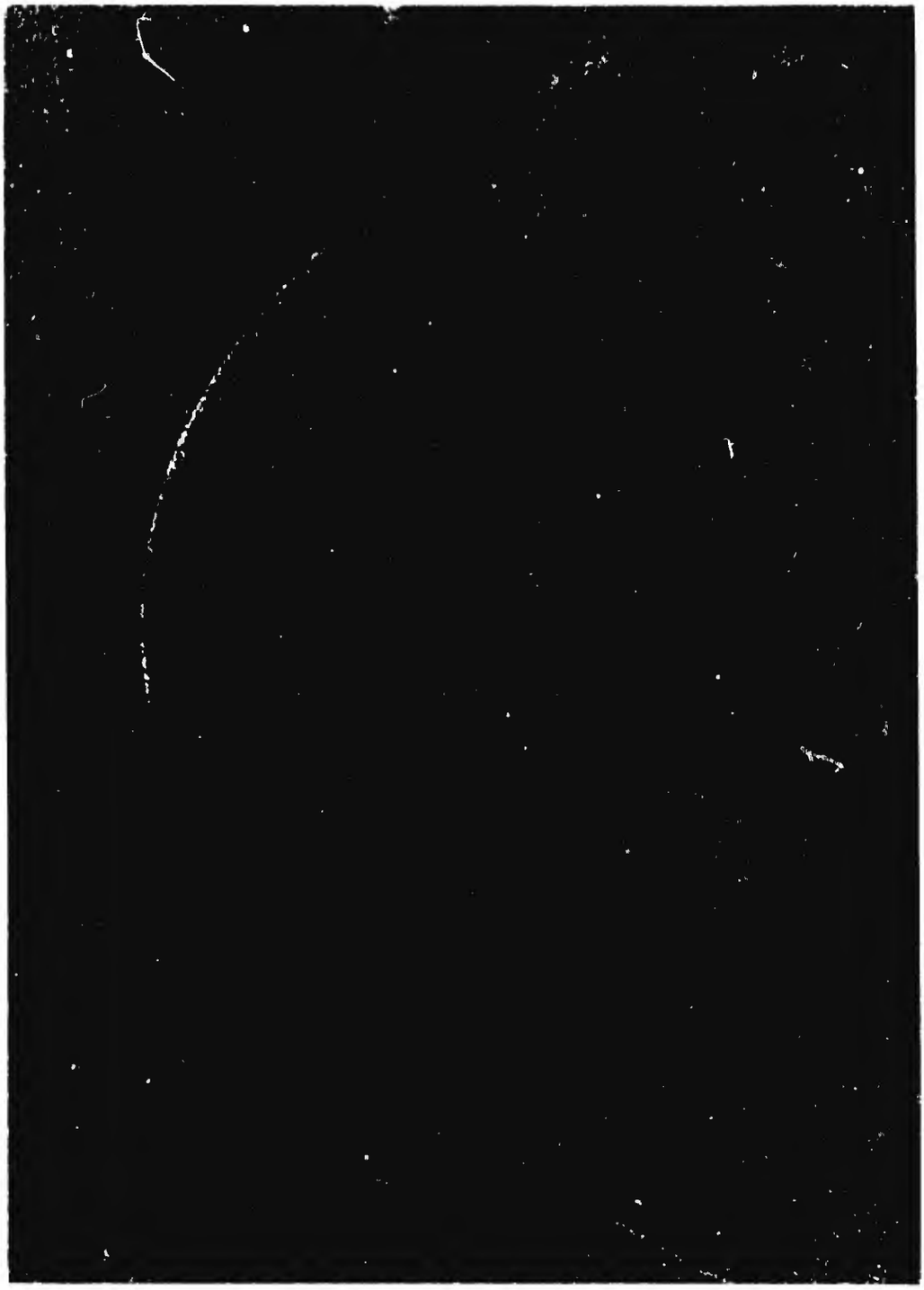

FIG. 9 NYLON SPHERE IN AIR. DIAMETER = 1/2",
VELOCITY = 8,020 ft/sec, PRESSURE = 10mm Hg.

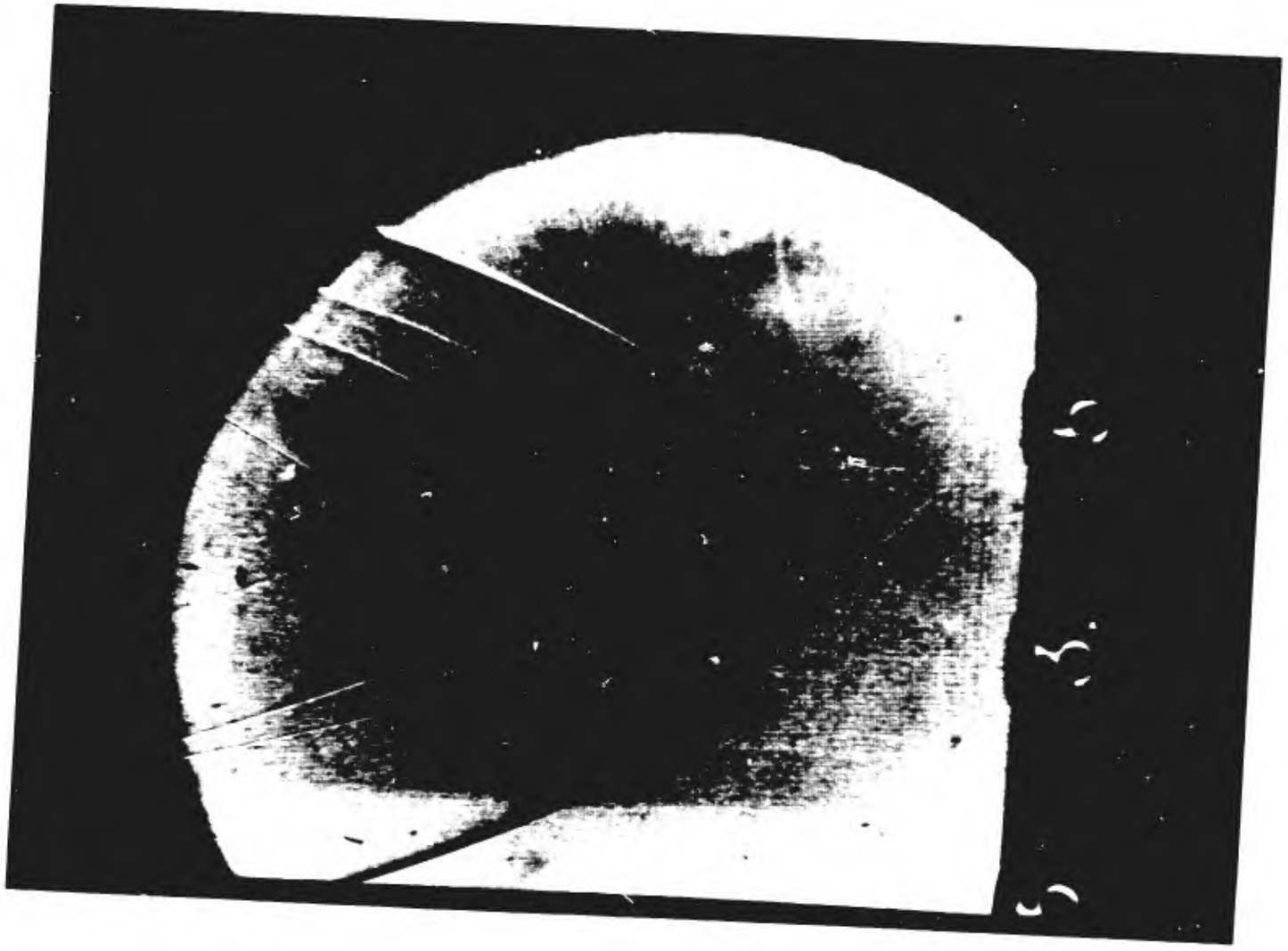

FIG. 10 PHOTOGRAPH OF FLOW BEHIND A SLUG

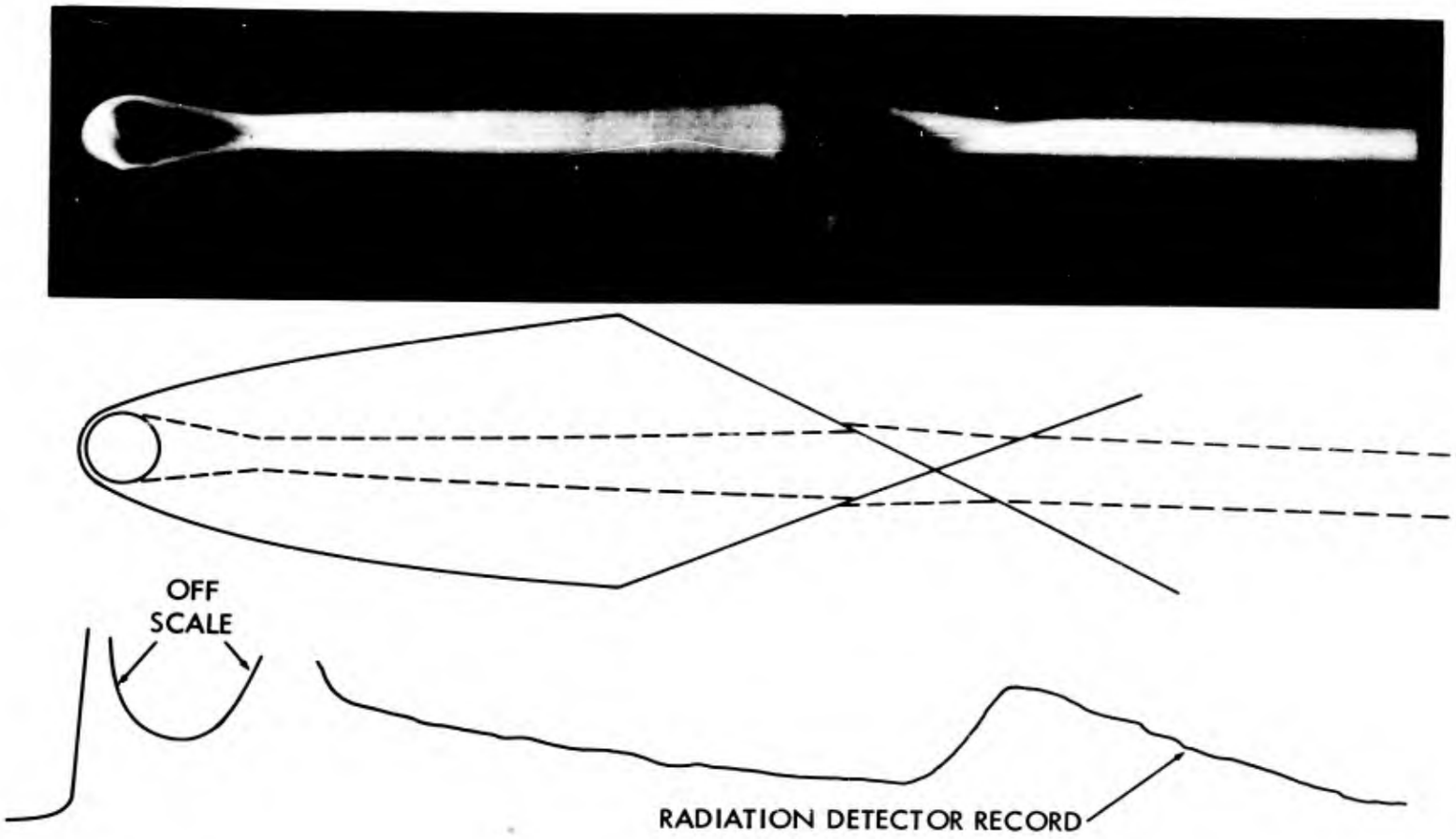

FIG. 11 INTERACTION OF SHOCKWAVE WITH WAKE

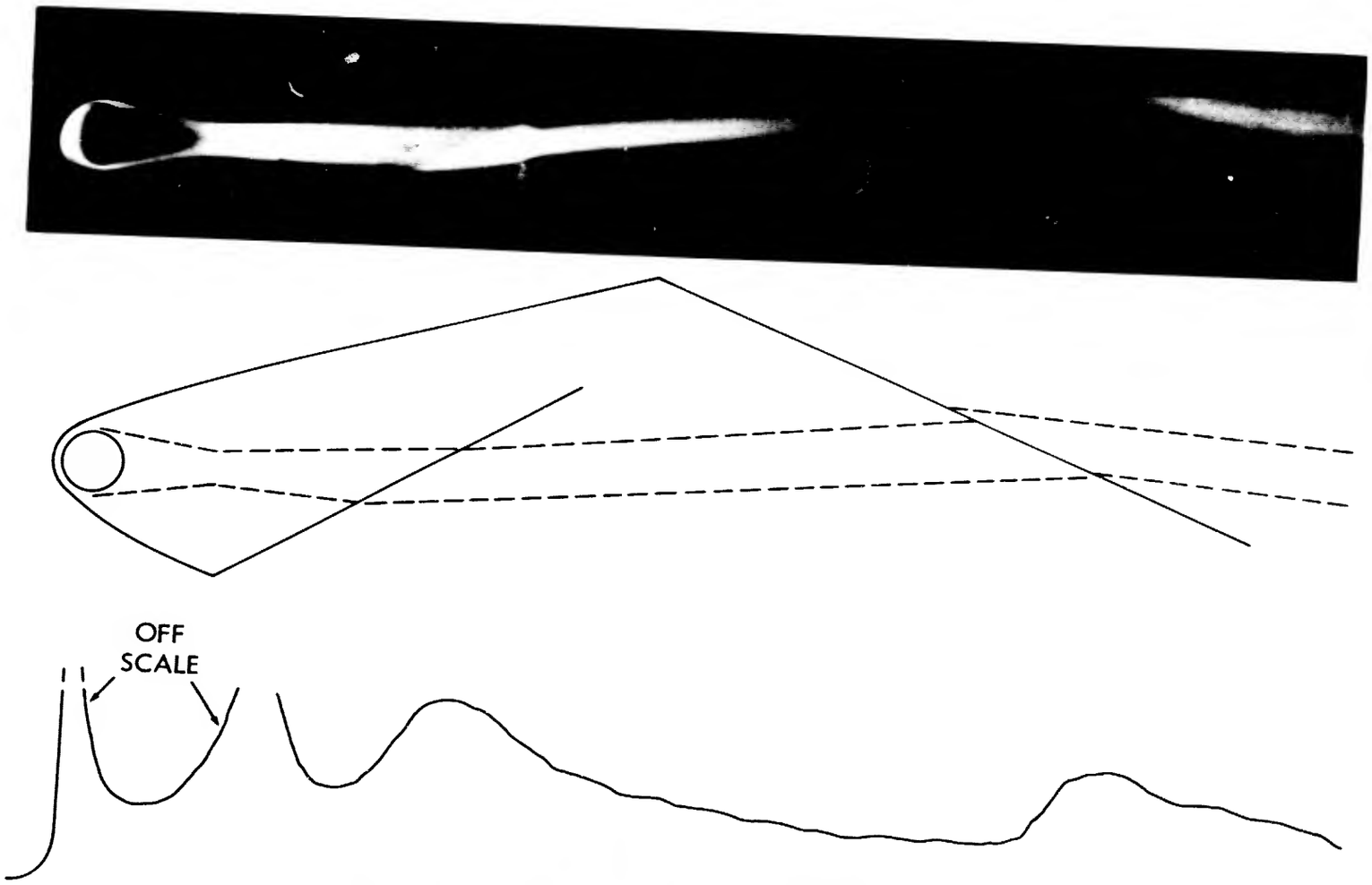

FIG. 12 INTERACTION OF SHOCKWAVE WITH WAKE

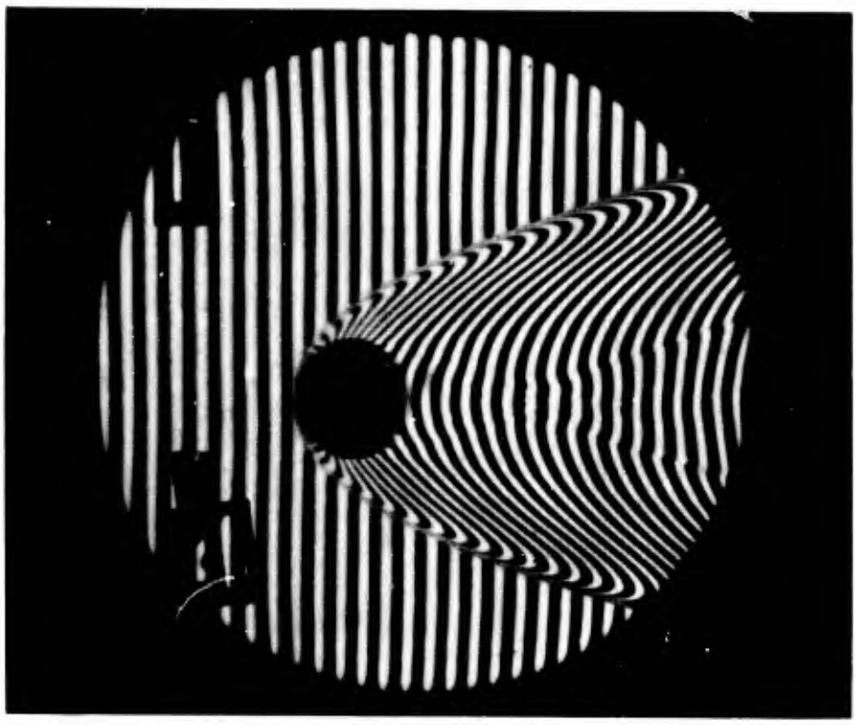

FIG. 13a MULTIPLE FRINGE MACH ZEHNDER INTERFEROGRAM

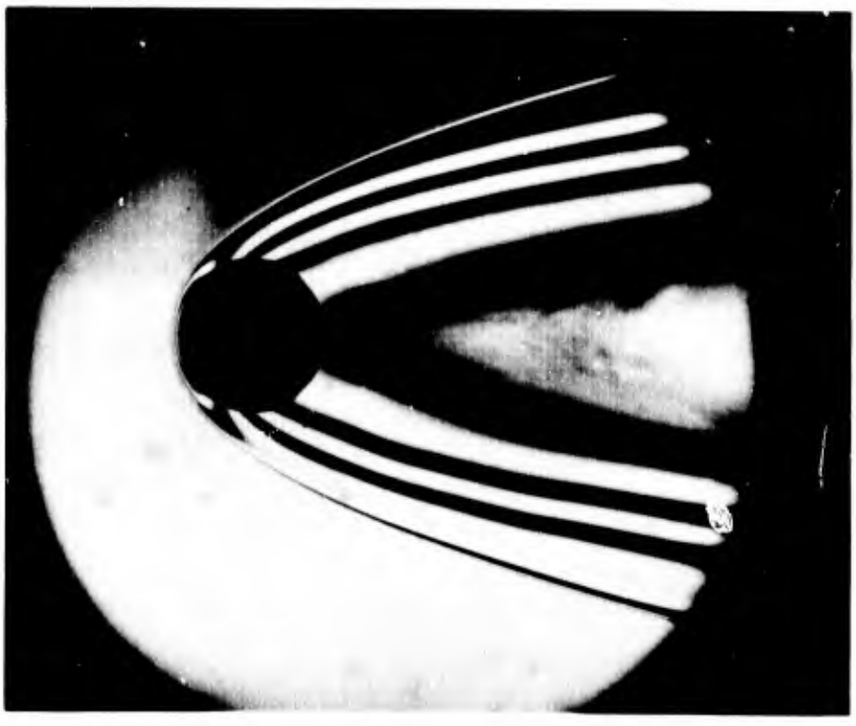

FIG. 13b SINGLE FRINGE MACH ZEHNDER INTERFEROGRAM

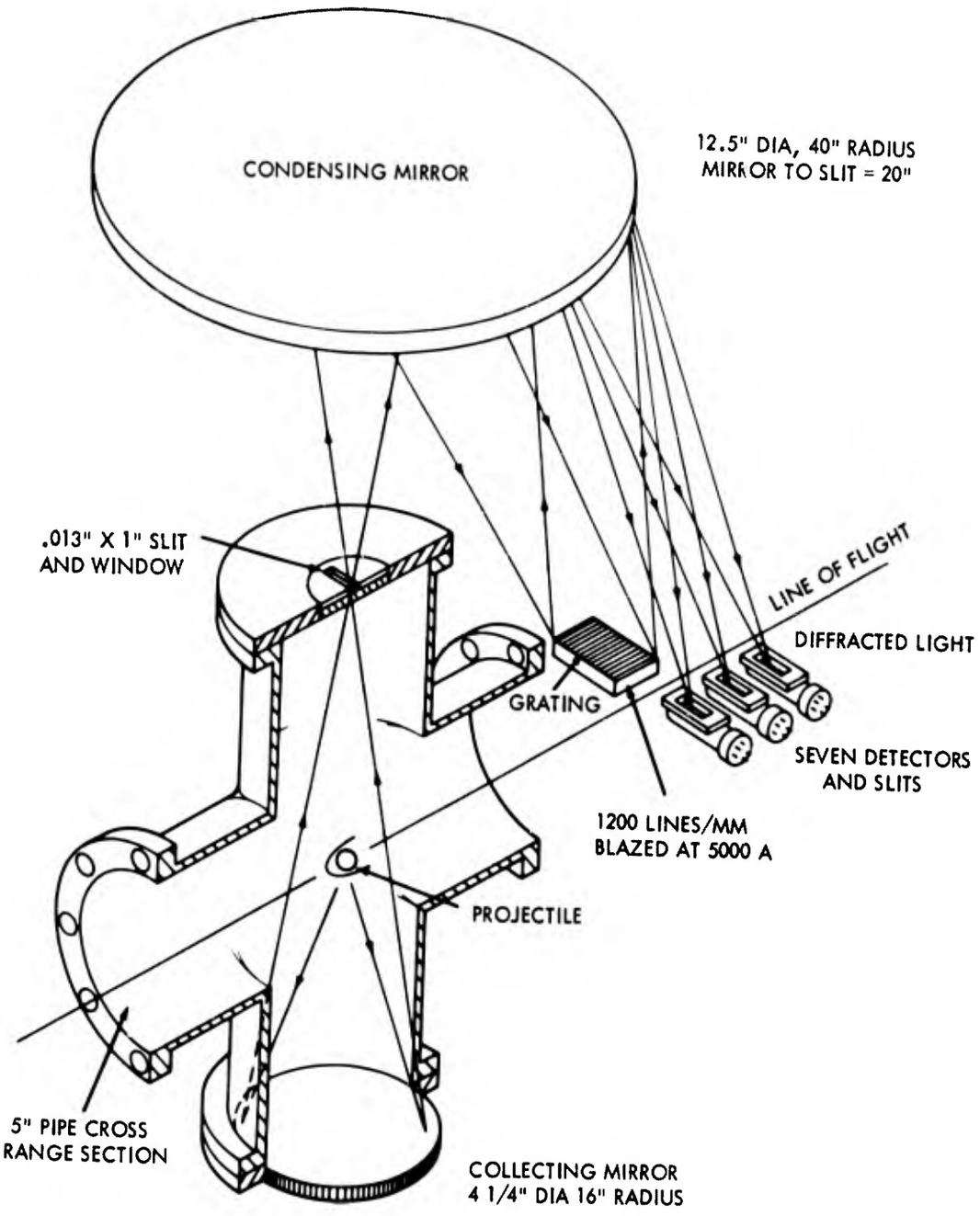

FIG. 14 RADIATION DETECTOR SYSTEM

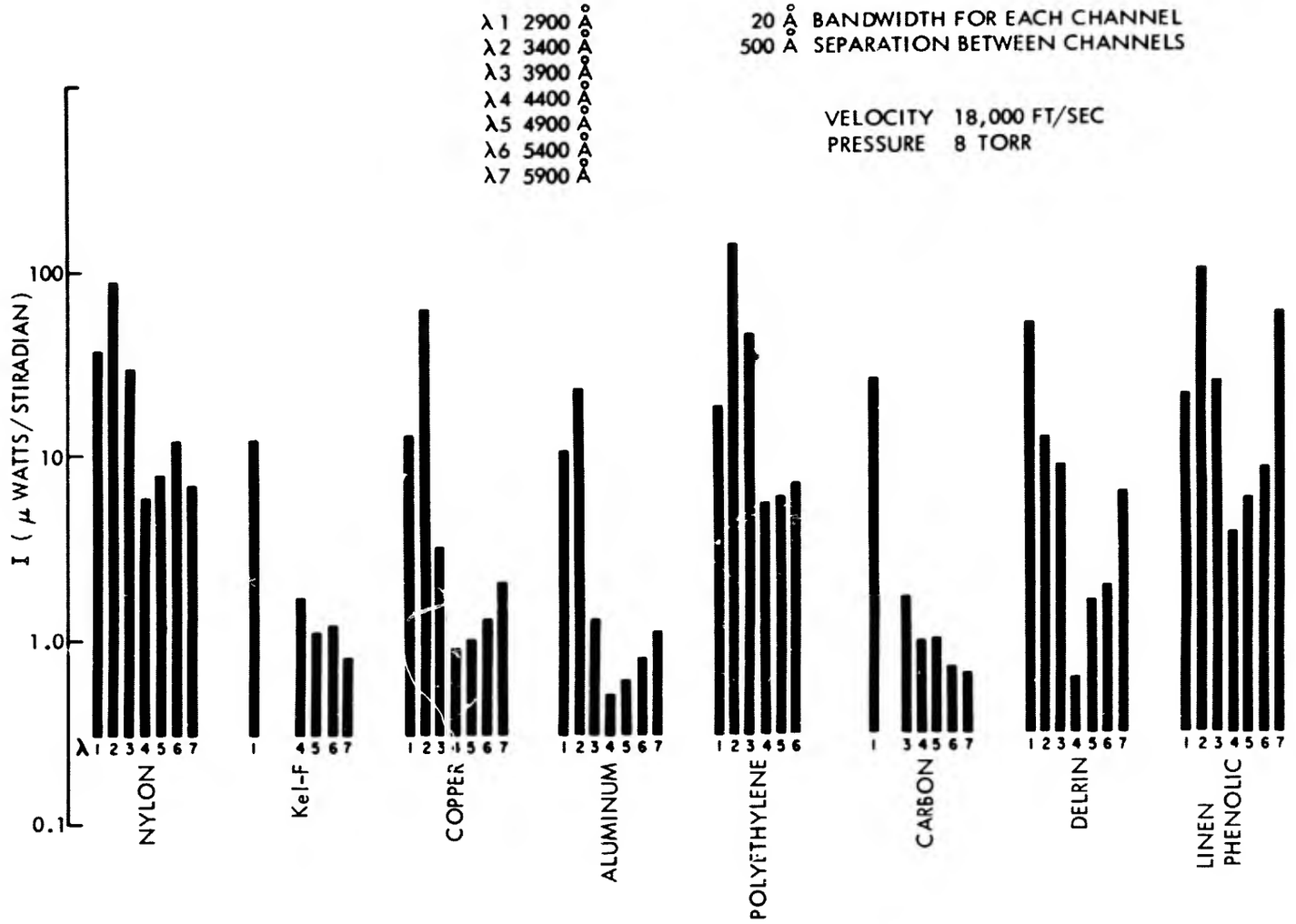

FIG. 15 PEAK RADIATION AMPLITUDE FOR DIFFERENT PROJECTILE MATERIALS

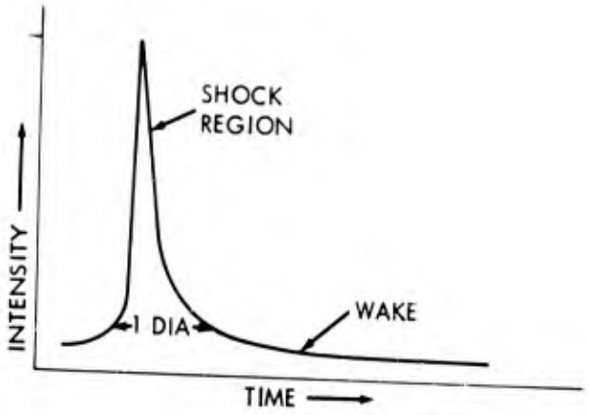

GROUP I

KEL-F	2900 Å	NYLON	AT
DELRIN	3400 Å	POLYETHYLENE	2900 Å
COPPER	3900 Å	LINEN PHENOLIC	3400 Å
ALUMINUM	4400 Å		
CARBON	4900 Å		
	5400 Å		
	5900 Å		

FIG. 16 RADIATION SIGNAL FOR GROUP I MATERIALS

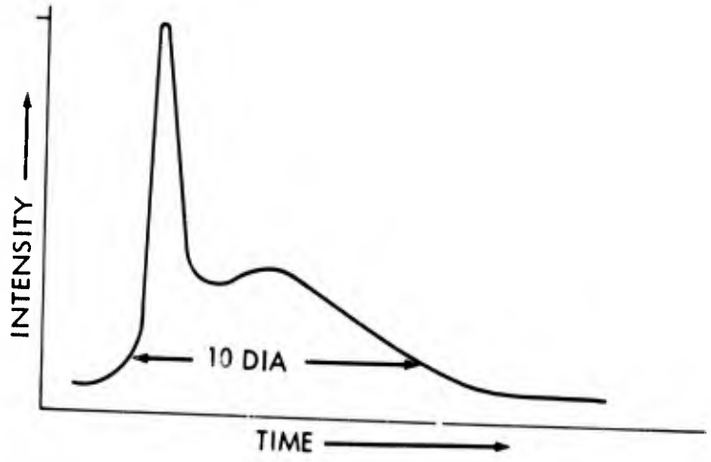

GROUP II

POLYETHYLENE	AT
LINEN PHENOLIC	5900 Å
NYLON	

FIG. 17 RADIATION SIGNAL FOR GROUP II MATERIALS

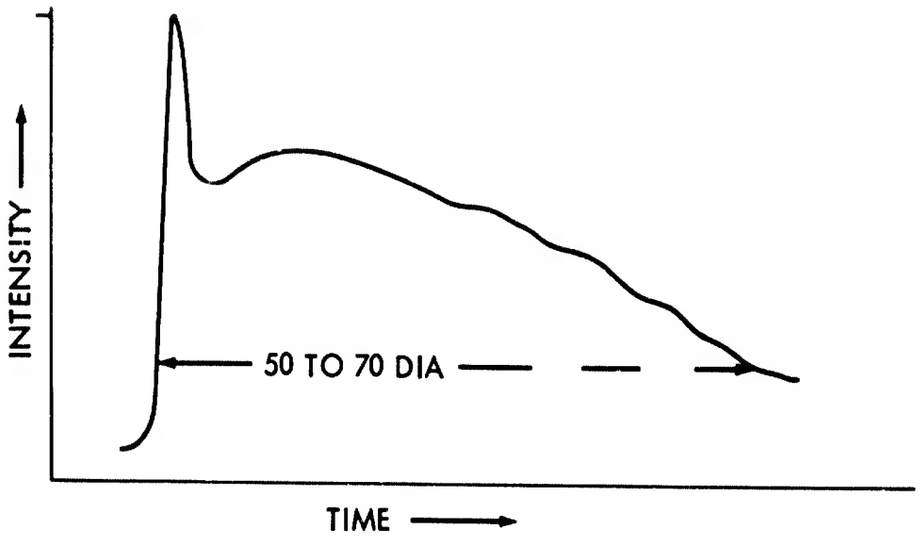

GROUP III

	AT
NYLON	3900 Å
POLYETHYLENE	4400 Å
LINEN PHENOLIC	4900 Å
	5400 Å

FIG. 18 RADIATION SIGNAL FOR GROUP III MATERIALS

BOUNDARY-LAYER PHENOMENA OBSERVED ON THE ABLATED SURFACES OF CONES RECOVERED AFTER FLIGHTS AT SPEEDS UP TO 7 KM/SEC

by

Thomas N. Canning,* Max E. Wilkins,** and
Michael E. Tauber**

Ames Research Center, NASA
Moffett Field, Calif.

---

*Chief, Hypersonic Free-Flight Branch

**Research Scientist

SUMMARY

Ballistic range tests were conducted to determine the extent of laminar flow which may be attainable on ablating cones. The experiments consisted of free flights of 1 cm diameter 30° half-angle plastic cones in air at velocities up to 7 km/sec and maximum local Reynolds numbers from 3 to 12 million. The ballistic range was long enough to allow the models to decelerate aerodynamically to low speeds and to be recovered intact. Microscopic examination of the surfaces of recovered models showed several interesting patterns depending on the type of boundary-layer flow experienced. Four distinct orderly patterns have been observed:

1. Wavelets which cover the entire conical surface regardless of the type of boundary-layer flow. The frequency of the wavelets is believed to be a function of the shearing stress shortly before the melt layer solidified and the thickness of the molten layer and, therefore, of the launch velocity.

2. Wedge-shaped patterns alined with apexes upstream which are thought to be produced by transverse spread of turbulence initiated by small surface imperfections.

3. In some cases, well-defined hyperbolic-shaped curves occurring downstream of the apexes of "turbulence wedges" indicating ordered vorticity in the region of laminar to turbulent transition.

4. Cross-hatch patterns which seem to be associated with fully developed turbulent flow. Two types have been observed. In one, at low magnification the patterns are diamond-shaped, but at high magnification they look like elongated hexagons. The arrangement of the hexagons is similar to a composition shingled roof or to fish scales. In the other, at low magnification the pattern again appears diamond-shaped but at high magnification they form a gradually undulating cross-hatched pattern.

In addition to the surface features observed, the mass ablated was measured and compared to predictions for fully-laminar and fully turbulent boundary layer flow. At local Reynolds numbers below 5 million, fully laminar flow seems to predominate. Tip recession from ablation was also measured and found to agree reasonably well with theory. These and various other surface features will be described and related to the model-material properties and to the flight environment.

RESUME

On a procédé à des essais en tunnel balistique afin de déterminer le degré d'écoulement laminaire susceptible d'être atteint sur des cônes à ablation. Ces essais consistaient à faire évoluer, en vol libre et dans l'air, des cônes de plastique de 1 cm de diamètre et de 30° de demi-angle, à des vitesses atteignant 7 km à la seconde et à des nombre de Reynolds locaux maxima variant de 3 à 12 Millions. Le tunnel balistique était suffisamment long pour permettre aux maquettes de retrouver, par décélération aérodynamique, de faibles vitesses, et d'être récupérées intactes. Un examen microscopique de la surface des maquettes récupérées a révélé plusieurs configurations intéressantes suivant le type d'écoulement de couche limite rencontré au cours des expériences. On a pu observer quatre configurations régulières distinctes:

1. De petites ondes couvrant la totalité de la surface conique, indépendamment du type d'écoulement de la couche limite. On estime que la fréquence de ces ondes est fonction de l'effort de cisaillement subi peu de temps avant que la couche en fusion ne se solidifie ainsi que de l'épaisseur de la couche fondue et, par conséquent, de la vitesse de lancement.

2. Des motifs en forme de coins alignés sommet vers l'amont; on pense que ces motifs sont produits par un étalement transversal de la turbulence créée par de petites imperfections de la surface.

3. Dans certains cas, des courbes bien définies, en forme d'hyperboles, se produisant en aval des sommets des "coins de turbulence" dont il est fait mention ci-dessus, et indiquant la présence d'un régime tourbillonnaire ordonné dans la région de transition entre écoulement laminaire et écoulement turbulent.

4. Des contre-hachures qui semblent accompagner l'écoulement turbulent au plein de son développement. On peut en observer deux catégories. Dans l'une, les motifs, faiblement grossis, revêtent la forme de losanges, mais ressemblent sous fort grossissement à des hexagones allongés. La disposition des hexagones rappelle un toit de bardeaux ou des écailles de poissons. Dans l'autre catégorie, sous faible grossissement, les motifs ressemblent encore à des losanges, mais observés sous fort grossissement, ils forment une configuration de contre-hachures qui ondule graduellement.

Outre ces observations de la surface, on a procédé à des mesures de la masse éliminée par ablation, et on a comparé les résultats de ces mesures aux prédictions portant sur les écoulements de couche limite purement laminaires et purement turbulentes. Pour des nombres de Reynolds locaux inférieurs à 5 millions, la forme d'écoulement purement laminaire semble prédominer. On a également mesuré la régression présentée par l'extrêmité à la suite de l'ablation; il s'est avéré qu'elle concordait assez bien avec la théorie. Les auteurs de l'exposé décriront les caractéristiques de la surface dont il est question ci-dessus ainsi que diverses autres et les rapporteront aux propriétés des matériaux composant les maquettes, et au milieu ambiant où se déroulèrent les vols.

NOTATION

k	constant in Eq. (2)
m	mass of body
m_o	mass of body at launch
r_b	body base radius
$\dot{r}_n$	rate at which nose radius of curvature is changed by ablation
V	flight velocity
V_o	launch velocity
x_n	tip recession
$\dot{x}_n$	rate of tip recession at the nose as a result of ablation
α	transpiration effectiveness parameter
$\bar{\rho}$	air density in stream normalized by sea-level density
θ_c	cone half-angle
ζ	energy required to ablate unit mass

BOUNDARY-LAYER PHENOMENA OBSERVED ON THE ABLATED SURFACES OF CONES RECOVERED AFTER FLIGHTS AT SPEEDS UP TO 7 KM/SEC

By Thomas N. Canning,* Max E. Wilkins,** and
Michael E. Tauber**
Ames Research Center, NASA
Moffett Field, Calif.

1. INTRODUCTION

The initial purpose of the present study was to determine the extent of laminar flow attainable on ablating cones by recovering gun-launched plastic models after hypervelocity flight and determining the mass removed by ablation. In the course of pursuing this objective, it became apparent that if the microscopic surface details could be preserved intact as the model is recovered, a great deal of additional information on the nature of the boundary-layer flow could be obtained.

Careful microscopic study of the models recovered after these tests has revealed a wealth of interesting features eroded into the surfaces. The regularity of many of these features of transitional and turbulent boundary layers evoked much speculation on the existence of orderly processes in both. The description of these features, their possible

---

*Chief, Hypersonic Free-Flight Branch

**Research Scientist

relation to phenomena observed by earlier investigators, and speculation on the detailed mechanisms responsible are the principal subjects of this paper. Preliminary results of the initial study (1-2) are summarized in part herein, and then the surface features are discussed.

2. EXPERIMENTAL PROCEDURE

Models were launched in free flight in air at 1, 1.5, or 2 atm static pressure. The plastic models were 30° half-angle cones with base diameters of 1 cm. A typical calculated variation of model velocity and heating rate, and also a spark shadowgraph taken at 2.6 km/sec are shown in Fig. 1. After the cones were recovered, their surfaces were examined minutely with a metallurgical microscope. The depth of the surface patterns was measured by three methods (all described in (3)): (a) by focusing on high and low points and measuring the vertical movement of the microscope tube; (b) by surface interferometry; and (c) by wire-shadow techniques. The plan form of the features was measured from photomicrographs or directly with the microscope.

The cones were made of either of two plastics: Delrin (an acetal) and Lexan (a polycarbonate). The first essentially sublimes at high heating rates; whereas the second forms a very thin liquid layer in addition to vaporizing, even at the extremely high heating rates encountered.

3. ANALYSIS

The extent of laminar and turbulent boundary-layer flow during the period of ablation was determined by two methods: measuring the mass loss resulting from ablation, and studying the surface patterns found on

recovered models. The ablation of the tip of the cone was also calculated and compared to measurements on recovered models. With the exception of a few new points, the data shown are the same as in (2). However, the preliminary results shown in (2) have since been refined.

3.1 Mass ablated

To relate the mass-loss measurements to the surface features of the recovered cones, it is very important to know at what stage of the flight the features were formed. The most deeply etched features formed doubtless resulted from ablation during the high speed portion of the flights, when both the Reynolds number and the heating rate are maximum.

3.1.1 Comparison with theory

The mass loss resulting from ablation of the models was compared to theoretical mass losses computed for the limiting cases of fully laminar and fully turbulent heating; the boundary-layer flow was assumed to be either laminar or turbulent during the entire period of ablation except at the tip (in the vicinity of the stagnation point) where it was always assumed to be laminar. The comparison between the mass losses determined from weighing the models and from theory (see (2) for details) is shown in Fig. 2. The data are seen to lie between limits provided by the theory for all laminar and all turbulent boundary layers. The four points marked with solid black flags are for models into which craters, about 0.1 mm deep and 0.07 to 0.09 mm in diameter, were impressed to serve as boundary-layer disturbance sources. (The protruding rim formed around each crater during the impressing was removed before the models were launched.) Both the number and location of these craters were

varied, but in most cases they were situated 0.25 cm from the tip and spaced 30° apart. The data points marked with white flags represent cones that, upon recovery, showed signs of irregular erosion at the tip; in many cases there were indications that the boundary layer was tripped at, or immediately aft of, the tip. It is believed that the tips of these cones were damaged by lateral accelerations experienced during launching. These data points are included since they indicate the mass losses to be expected with predominantly turbulent boundary layers.

Although suspected earlier, it was found, after these data were published (1,2), that most of the models showed definite signs of imprinting during launch from the four-finger sabot which completely encapsulated the model. This occurred usually toward the base of the model, and these imprints frequently tripped the boundary layer. In fact, on the great majority of models it is now possible to identify the location of the roughness element responsible for tripping the boundary layer. If the areas downstream of sabot imprints and deliberately made craters are excluded from consideration, the success in attaining predominantly, and even completely, laminar flow at Reynolds numbers up to 8 million is high.

3.1.2 Variation of mass loss with extent of turbulence

The fraction of the area on each model showing evidence of turbulence was estimated from photomicrographs or by direct viewing with the metallurgical microscope. A plot, showing the mass loss as a function of the amount of surface area covered by turbulence, is shown in Fig. 3 for a launch velocity of about 6.1 km/sec. (The data shown were adjusted

to a common velocity from the actual values which ranged from 5.35 to 6.5 km/sec.) The correlation between the mass loss and the percent of the surface covered by turbulence is generally good and supports the hypothesis that the turbulence occurred during the high speed part of the flight when most of the mass loss occurs. The mass-loss data for Lexan show similar trends.

3.2 Tip ablation

The equations for nose recession given in (2) have since been modified. This change was made following the recent discovery that the value used for the constant, k, (Eq. (2), below) had been in error. Use of the correct value indicates that a nose ablation model consisting of a hyperboloid asymptotic to the cone is an improvement over the spherical section. The nose recession rate is related to the change in nose radius of curvature by the relation

$$\dot{x}_n = \dot{r}_n / \tan^2 \theta_c \tag{1}$$

This simple mathematical model leads to a closed-form solution, although rather lengthy, for the tip recession at the end of ablation. At launch velocities greater than about 4 km/sec, the equation for the tip recession can be greatly simplified if the wall and free-stream static enthalpies are neglected; and it becomes

$$\frac{x_n}{r_b} = k\left(\frac{1}{\bar{\rho} r_b \sin^8 \theta_c}\right)^{1/3}\left[\frac{\cos^2 \theta_c}{\alpha} \ln\left(1 + \frac{\alpha}{\zeta} V_o^2\right)\right]^{2/3} \tag{2}$$

where $k = 1.25 \times 10^{-3}$ meter $^{1/3}$ and the base radius r_b is in meters. The comparison between theory and experiment is shown in Fig. 4. The agreement with the data is good.

4. OBSERVED FEATURES

Thus far the connection between the measured mass loss and the extent of turbulent flow has been made. Exhaustive microscopic study, in addition to that required for assessing the turbulent area, of the many models recovered during this exploratory study has revealed many surface features produced by laminar, transitional, and turbulent flows. These suggest that a high degree of order exists in turbulent and transitional flows produced by isolated three-dimensional roughness elements. Many of the features appear as a result of particular properties of the model materials themselves as influenced by local imperfections therein, for example, viscosity of the melt layer and nonhomogeneities. It is necessary when observing and discussing these features to keep in mind that each surface is the end of a history which starts during final preparation of the model, before it is loaded into the gun, and ends at its recovery. Some of the smallest surface features must, of necessity, have been formed immediately prior to the cessation of ablation; others, more deeply engraved, must have been formed early in the flight when ablation rates were high. In all cases ablation commences after less than a meter of flight. Since the bodies decelerate very rapidly at first, the time available for ablation at the high-speed high Reynolds number conditions is short (see Fig. 1). As long as the adiabatic-wall temperature remains slightly above the melting point of the plastic the surface layer will remain fluid. For both materials this temperature is reached at about Mach 2, when the boundary-layer-edge Mach number is about 1. The residual features, therefore, are a sort of "geological overlay," and considerable uncertainty surrounds their interpretation.

The only features found in the continuously laminar regions were ring waves on the noses of Lexan models (Fig. 5), like those found on tektites (4) and a multitude of similar, although smaller, wavelets formed in the molten surface on the conical portions of the Lexan bodies (Fig. 6). In contrast to the wavelets on the Lexan models, the Delrin surfaces show a pebbled appearance not unlike that of Scotch grain leather as may be seen in Fig. 7. This fine structure is believed to represent the individual powder grains from which the Delrin bar-stock was made. The individual bumps are typically 25 microns across and about 3/4 micron high. No further discussion of these features is included.

Figure 6, in addition to showing the minute surface waves in Lexan, also displays a series of interesting patterns immediately downstream of a visible imperfection in the surface. Such patterns were observed quite frequently and could be induced by the aforementioned indentations or craters. Visible features include arrays of streamwise grooves, originating inside a triangular region, with apex at the surface imperfection. These patterns were eroded appreciably deeper than the surrounding surface, and are interpreted as evidence of so-called "turbulent wedges" in the transition process.

In areas thought to have completely turbulent boundary layers during the high-speed part of the flight, the same kind of longitudinal grooving is apparent as in the transitional flow. In addition, a completely different set of orderly grooves and lines, running obliquely in both directions around the cones was sometimes identified (hereafter referred to as groove- and line-type crosshatching (Fig. 8)).

These features, the conditions under which they are produced, their analogs in other studies where available, and possible boundary-layer mechanisms to produce them are discussed at length below.

4.1 Roughness-induced transitional flow

The turbulent wedge patterns produced by controlled model indentations are usually barely visible to the naked eye, but with a metallurgical microscope reveal great detail. Typical wedges in both Lexan and Delrin are shown in Fig. 9. The forward parts of these wedges appear to subtend a half-angle of about 5°; farther downstream this envelope ıcreases to about 10°. The ablation within these areas greatly exceeds that outside as attested by the mass-loss results described earlier.

Additional features which can better be seen in Fig. 6 are, in spatial order of their appearance behind the roughness element, a pair of grooves trailing downstream, a second pair of grooves just outboard of the first pair, and a sequence of new grooves each outboard as before. Then, on some Lexan models, and sometimes faintly suggested in photographs of the Delrin bodies, there is a low ridge (hyperbolic in shape) which crosses the wedge-shaped area containing the multitude of grooves. This ridge lies obliquely transverse to the flow and appears eventually to cross the leading edge of the wedge from which the grooves emanate.

One model was purposely impressed with craters so as to produce several overlapping wedges and hyperbolic-front ridges. It was found that the ridges turned more transverse to the stream as they approached one another and met in a smooth curve.

The line-type crosshatching believed to be characteristic of turbulent boundary-layer regions is seen occasionally within individual turbulence wedges on Lexan bodies. This crosshatching appears to be similar to that observed on large areas but the pattern size increases rapidly with increasing distance from the roughness element. The angle of obliquity of the lines varies as well as a result of the "fanning out" of the pattern. No analogous observations are known to the authors and no hypotheses are advanced regarding its formation.

4.1.1 Relation to other observations

Turbulent wedges originating at point disturbances in laminar boundary layers are well-known phenomena (see, e.g., (5-7)). The lateral growth rate of the forward part of the wedges eroded into the recovered models matches rather well that of continuous turbulent flow downstream of single elements of roughness in subsonic flow as reported in (7). In both cases the lateral-growth half-angle is about 5°. The lateral growth of the rearward portions of the wedges is about 10°, matching that observed for intermittent turbulent flow (7). No consistent differentiation between the inner and outer regions has been noted in the present study.

The details of erosion within the wedge have essentially no counterpart in earlier results except that (8) reports that the wakes of single projections from surfaces persist downstream for over a hundred boundary-layer thicknesses. The authors know of no published description of the other details noted, that is, the successive longitudinal grooves or hyperbolic front.

4.1.2 Interpretation

The succeeding discussion of possible mechanisms for the formation of the observed erosion within the wedges is, necessarily, predominantly conjecture; it is included only to suggest possible mechanisms for the sudden transition from laminar to turbulent flow at the wedge leading edges.

The successive creation of longitudinal grooves at the leading edge of the forward part of a given wedge appears to result from periodic induction of vortices outboard of the existing vortices. No single surface feature suggests a wave front or vortex along the leading edge of this region; the grooves simply appear to start. This apparent start may represent coalescence of vorticity in the approaching boundary layer.

No mechanism is postulated with confidence to explain the increase, from 5° to 10°, of the lateral induction rate. It is tempting to guess that the hyperbolic-front ridge records the location late in the flight of a strong, transverse, single-vortex filament in the boundary layer capable of producing a sharply local reduction in shear. In fact, the ridge is suggestive of a separation line in oil-film flow-visualization tests.* Such a vortex might easily produce sharply defined transition from laminar to turbulent flow in the boundary layer, thus establishing the wedge leading edge.

It is believed that the hyperbolic-front feature probably is formed very late in the flight, while the wedge is certainly formed at high

*Each hyperbolic-front ridge is formed because of disturbances from a single roughness element. No ridge of this nature has been found in the absence of such an element.

speeds. A similar ridge may actually exist at the wedge leading edge during high-speed flight and be erased or moved progressively as the model decelerates. No direct connection has been established to exist between them. The lateral propagation angle of the wedge approaches the boundary-layer-edge Mach angle at the highest test speeds (it is always relatively slower at lower speeds); consequently, no conclusion can be drawn about the level within the boundary layer at which disturbances propagate.

These observations show that a high degree of order exists in what is usually considered to be chaos. If such is the case, a revision of accepted physical models for turbulent flow may be in order.

4.2 Turbulent-flow areas

Two classes of surface markings observed in regions of turbulent boundary layers are streamwise grooves persisting from transition regions, and crosshatch patterns believed to indicate systems of diagonal vortices or waves lying deep in the boundary layer. The streamwise grooves, previously discussed, may persist over the entire surface from their origin in the region of influence of a roughness element. These longitudinal features vary in distinctness from the sharply defined grooves emanating from obvious surface imperfections to undulations so subtle that microscope illumination must be adjusted carefully to reveal their presence. The nonhomogeneities in the flow which produce these grooves, however small, with perhaps the stabilizing influence of the grooves themselves, persist downstream for many hundreds of boundary-layer thicknesses.

Another feature which may be seen to cover substantial areas, sometimes more than 90 percent, of the recovered body's surface consists of extremely regular oblique markings which divide the surface into diamond- or hexagonal-shaped areas (Fig. 8). This figure consists of six photomicrographs of surfaces of two recovered Lexan cones after flight through air at 2 atm static pressure. Those in the upper group show one area of the high-speed model at three magnifications. The same magnifications are used on the low-speed model. This class of marking must be further subdivided into what is here called "groove crosshatching" and "line crosshatching" in order to distinguish their very different appearances. The grooved type consists of periodically spaced, shallow grooves running obliquely, symmetrically in both directions, which intersect at regular intervals. The relief of this feature can be much deeper than that of the line type described below. The depth of the deepest of these grooves was found to approach 10 percent of the total surface recession. The grooves are therefore believed to form early in the flight when the heating is most severe.

The line crosshatching has been seen only on Lexan models. The lines are actually edges of relatively flat surfaces, each of which resembles a hexagonal roof tile. Each element slopes gradually up in the flow direction and ends abruptly in a step.

Under similar ambient conditions, and once on the same recovered model, the groove-type patterns were observed to be about twice as long as the others. This contrast is illustrated in Fig. 8. The dimensional properties of both appear to vary from place to place on a given model and do not appear to follow any rigid systematic pattern. The wavelength

of groove crosshatching was about three to four times the turbulent boundary-layer thickness calculated for a nonablating surface at the highest speed and decreased more rapidly than the boundary-layer thickness with increasing ambient pressure.

The obliquity of the markings, the angle measured from the cone generator, differs for the two types of crosshatching. The groove-type angles range from 23° to 28°. The line type generally ranges from 28° to 37° with two observations over 41° and one under 24°. No systematic behavior with varying ambient pressure or initial speed could be found.

4.2.1 Relation to other observations

Two other fluid-flow environments have produced features nearly identical to, or suggestive of, the crosshatch patterns described above: wind tunnels and shallow water flowing over sand. The first wind-tunnel test to come to the authors' attention was an ablation experiment, as yet unpublished, on a Teflon-covered cone. The test was conducted at NASA Marshall Space Flight Center for the Douglas Aircraft Company. The test facility was the 164 HT Burner Facility; the grooves etched in the model closely resembled those in the present groove-crosshatching areas.

The other wind-tunnel observation was made by Nagamatsu (9), who used a spark schlieren system to observe the structure of a thick turbulent boundary layer on a large sharp cone in a hypersonic shock tunnel. He found a "waffle-like appearance due to the turbulent eddies" in his pictures. Studies of good photographic enlargements show the length of these patterns to be about four times the local boundary-layer thickness.

Most of the crosshatch patterns in shallow-water flow over sandy

bottoms have been evident on the sand after wave recession from beaches; occasionally these patterns have been observed to cover areas as great as 300 square meters.

Two photographs of patterns, taken just after wave recession from the beach, are presented in Fig. 10. The coloration results from differential deposition of fine black flakes and coarse light sand. The darkest parts of the large pattern were recessed well below (perhaps 2 or 3 grain diameters) the adjoining light areas.

A further casual observation of steady water flow in a stream about 1 meter deep also exhibited crosshatching from time to time. The sandy bottom was not visible because of sand entrained in the water, but regular diamond patterns of peaked surface waves formed. The maximum wavelength observed was about 1.5 meters; the waves grew steadily in height to about 20 cm at which point they broke, and then quickly subsided. This cycle was repeated over the course of a few minutes.

4.2.2 Interpretation

It is felt that the two orderly patterns both longitudinal and oblique, eroded into many of the recovered models, may be clues to unexpected, orderly phenomena in turbulent boundary layers. The persistence of the streamwise grooves, over the length of the cone, representing a several-million increase in Reynolds number, suggests that each groove resulted from a stable longitudinal vortex in the boundary layer. The uniformity of this sheet of discrete vortices suggests vortices of preferred size and strength; it is intuitively plausible that the compliance of the surface to the local variations in heating

may stabilize the positions of the vortices.

Even more surprising than the longitudinal grooves was the discovery of the groove and line crosshatching. Their geometric similarities argue that they result from the same boundary-layer-flow processes even though they differ in detail.

It is tempting to draw a hasty connection between the "waffle" pattern observed by Nagamatsu and the present patterns. It is not known, however, whether the filaments shown by his schlieren are vortex cores or simply regions of different density, nor is it known whether these filaments lie along the stream direction or are oblique to it. That the wavelength in both cases appears to be about three or four times the boundary-layer thickness suggests a connection.

The appearance of similar patterns in shallow-water flows suggests that the free surface may play a role similar to that of the boundary-layer edge in forming the patterns observed there. If a test facility can be found in which these phenomena can be readily created in steady flow, it may be possible to study the flow itself as opposed to the ablation patterns. The uncertainty of the time of formation of each feature argues for this experimental approach.

5. CONCLUDING REMARKS

The technique of recovering ablating ballistic range models in undamaged condition has proven to be a powerful research tool for boundary-layer transition studies. By combining the measurements of mass loss and microscopic study of surface features, information can be gained under conditions not afforded by other types of laboratory investigation.

From a study of the data collected so far, it appears possible to maintain laminar flow to local Reynolds numbers of 6 to 8 million on 30° half-angle cones, with edge Mach numbers in the neighborhood of 4.5. A study of the surfaces of the recovered models suggests that a high degree of order (as opposed to essentially random phenomena) must exist in the transitional and turbulent boundary layer.

REFERENCES

1. Wilkins, M. E.: "Evidence of Surface Waves and Spreading of Turbulence on Ablating Models." AIAA Journal, vol. 3, 1965, pp. 1963-1966.

2. Wilkins, M. E.; and Tauber, M. E.: "Boundary-Layer Transition on Ablating Cones at Speeds Up to 7 Km/Sec." AIAA Journal, vol. 4, 1966, pp. 1344-1348.

3. Wilkins, M. E.; and Darsow, John F.: "Finishing and Inspection of Model Surfaces for Boundary-Layer-Transition Tests." NASA Memo 1-19-59A, 1959.

4. Chapman, D. R.; Larson, H. K.; and Anderson, L. E.: "Aerodynamic Evidence Pertaining to the Entry of Tektites Into the Earth's Atmosphere." NASA TR R-134, 1962.

5. Korgegi, R. H.: "Transition Studies and Skin-Friction Measurements on an Insulated Flat Plate at a Mach Number of 5.8." IAS Journal, vol. 23, 1956, pp. 97-107.

6. James, C. S.: "Observations of Turbulent-Burst Geometry and Growth in Supersonic Flow." NACA TN 4235, 1958.

7. Schubauer, G. B.; and Klebanoff, P. S.: "Contributions on the Mechanics of Boundary-Layer Transition." NACA Rep. 1289, 1956.

8. Spangler, J. G.; and Wells, C. S., Jr.: "Effect of Spiral Longitudinal Vortices on Turbulent Boundary Layer Skin Friction." NASA CR-145, 1964.

9. Nagamatsu, H. T.; and Sheer, R. E., Jr.: "Boundary-Layer Transition on a 10° Cone in Hypersonic Flows." AIAA Journal, vol. 3, 1965, pp. 2054-2061.

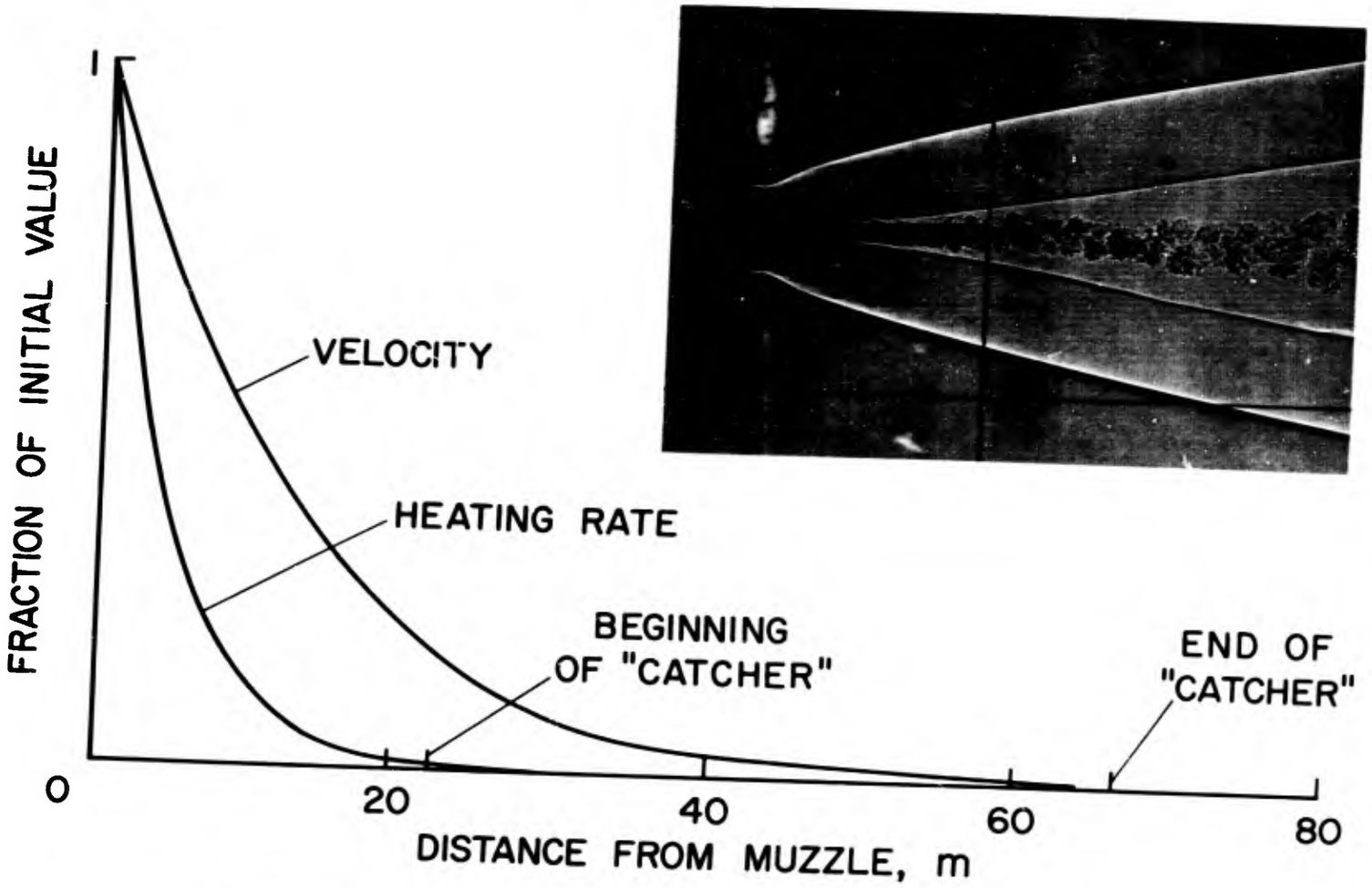

Fig. 1 Qualitative variation of velocity and heating rate along flight path

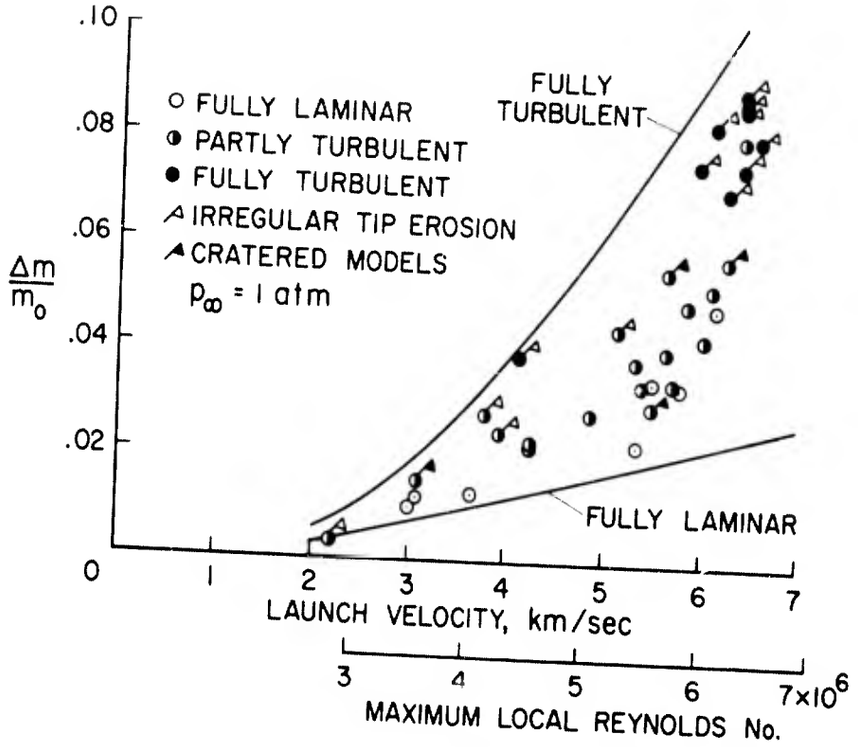

Fig. 2 Comparison of theoretical and measured mass loss for Delrin

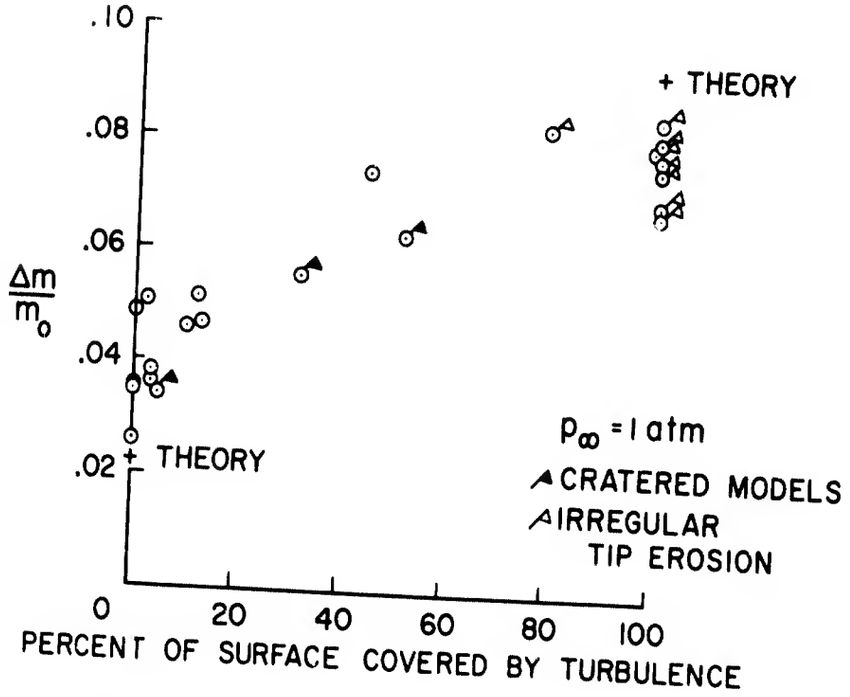

Fig. 3 Variation of mass loss with area covered by turbulence for launch velocity ≈ 6.1 km/sec (Delrin)

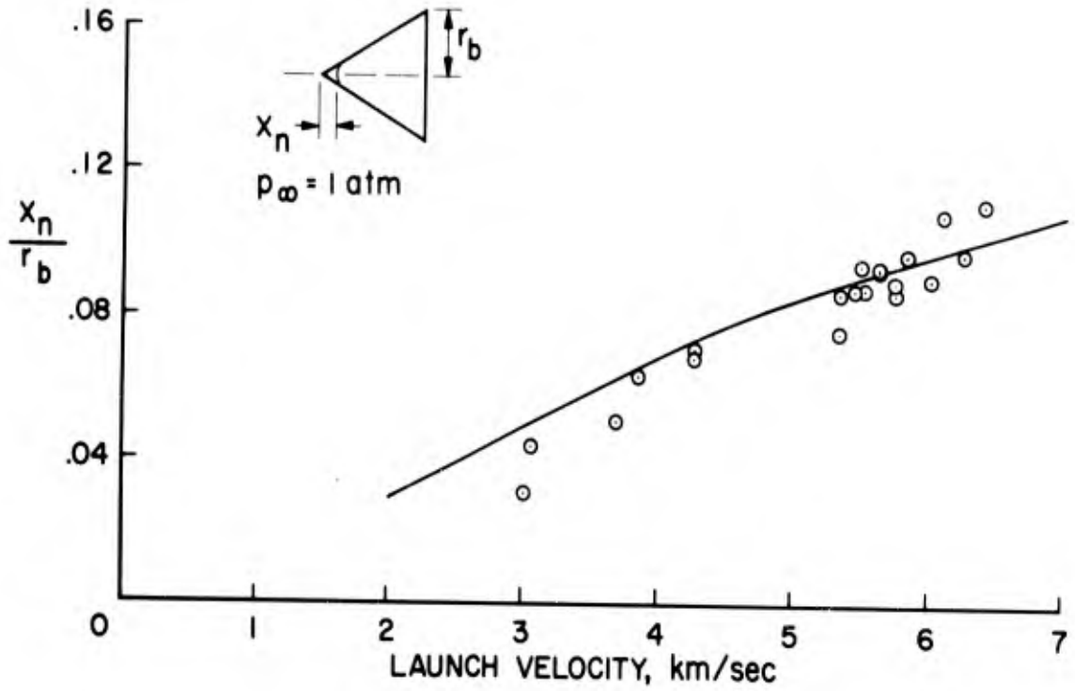

Fig. 4 Comparison of nose ablation theory and experiment for Delrin

Fig. 5 Nose tip details on Lexan

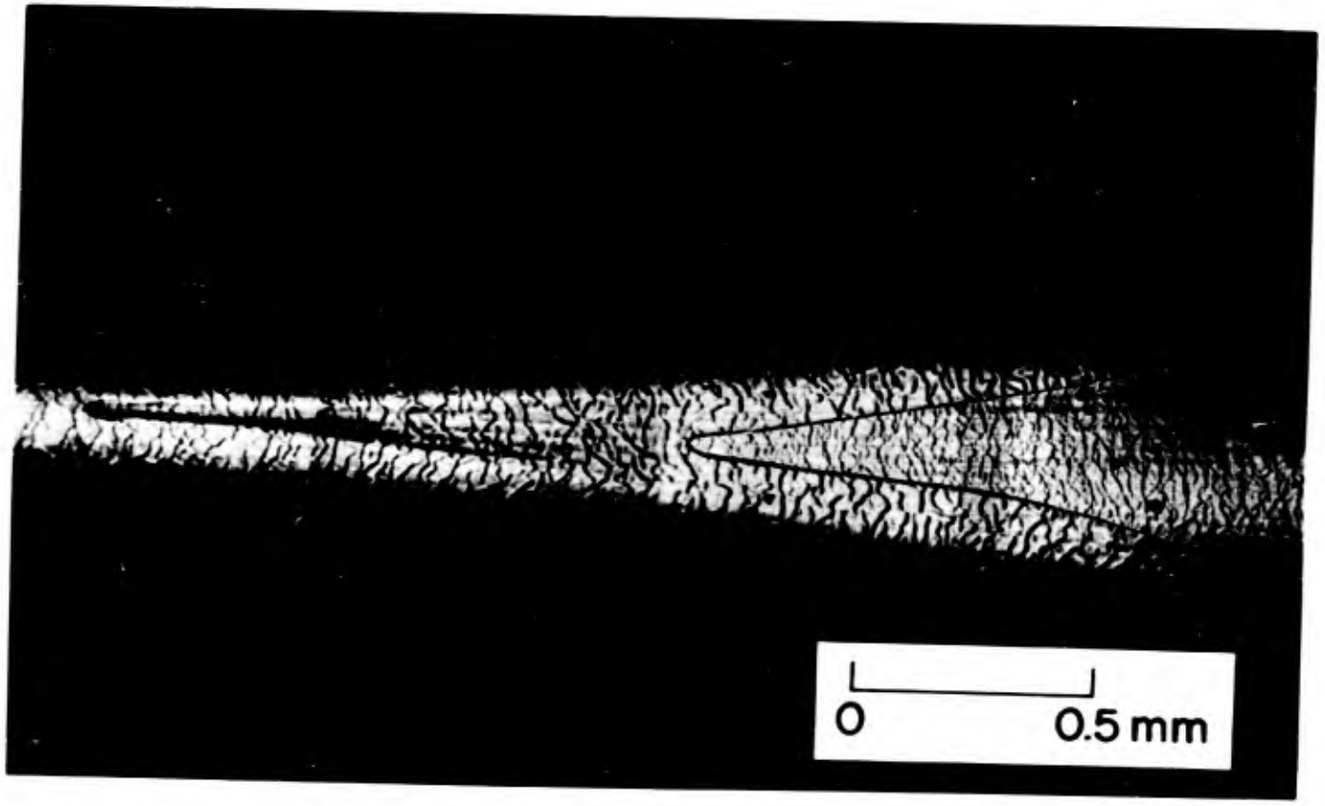

Fig.6 Various surface features on Lexan

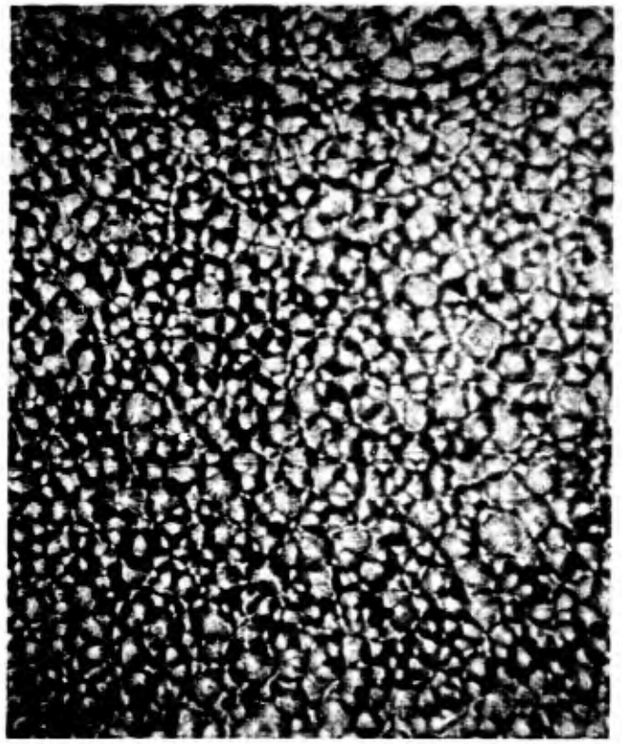

0 0.05mm

0 0.25mm

Fig.7 Fine surface details on a recovered Delrin model

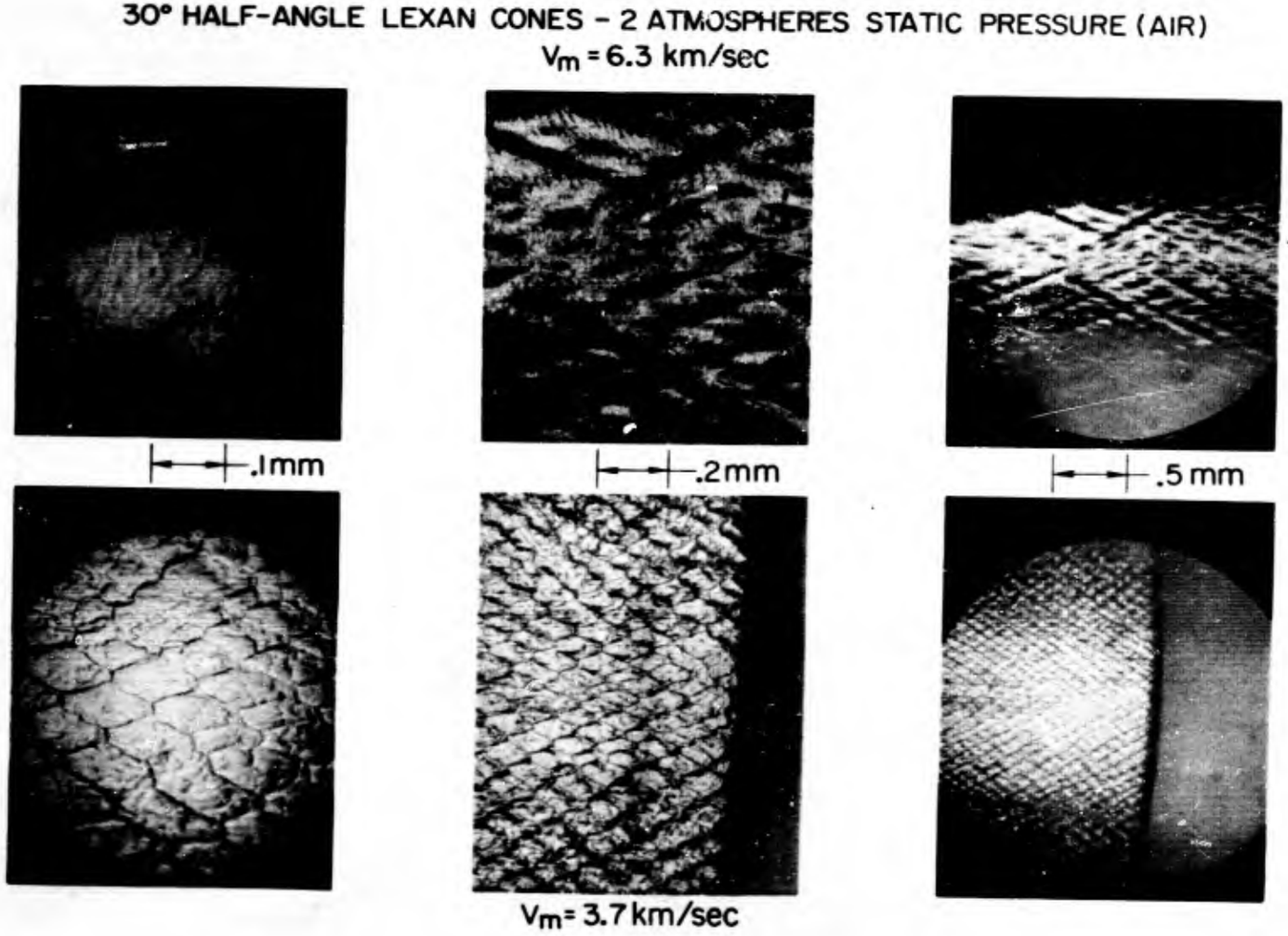

Fig.8 Two cross-hatched patterns at different magnifications

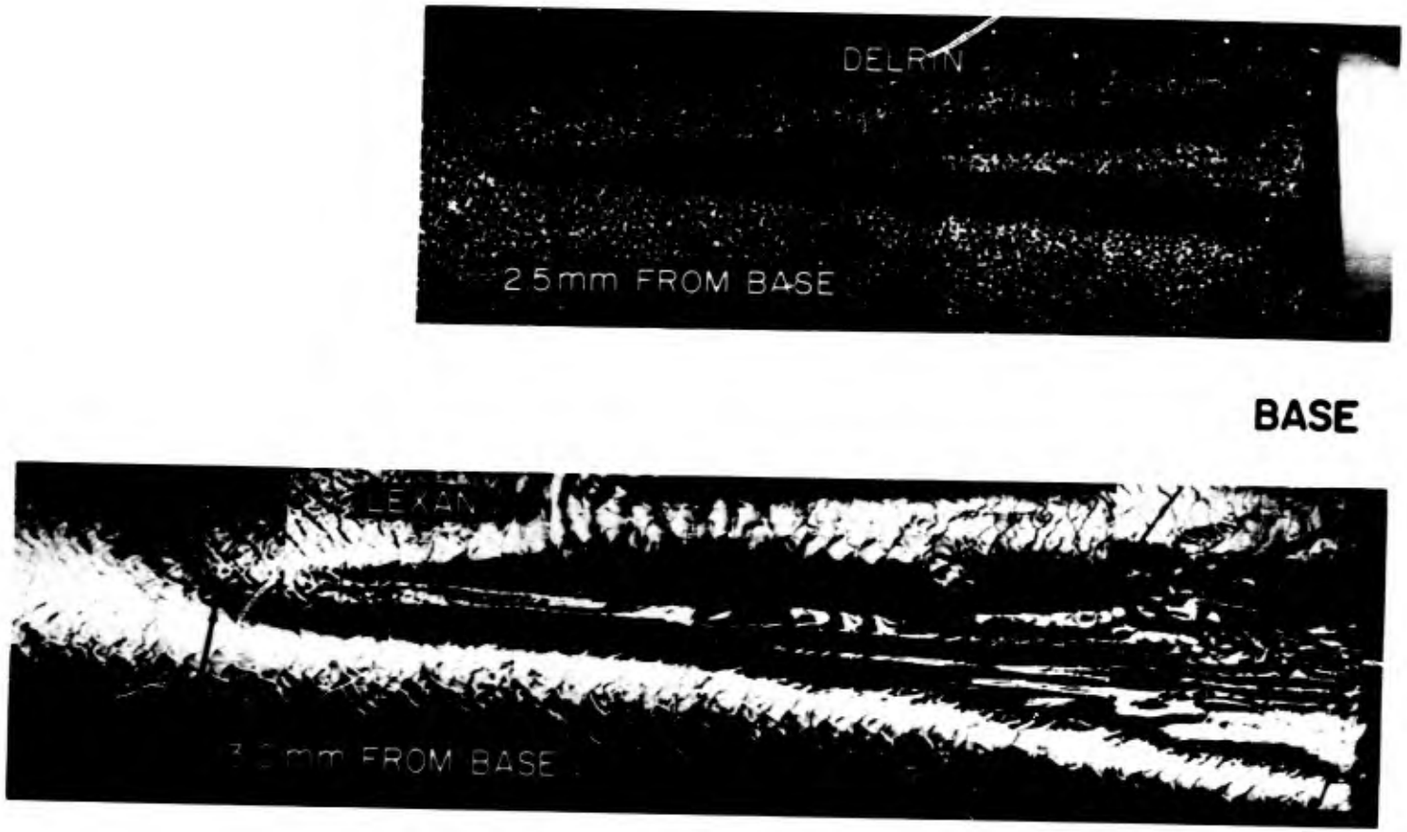

Fig. 9 Examples of turbulence wedges

Fig. 10 Sand patterns

APPENDIX

LIST OF SPEAKERS AND QUESTIONERS
DISCUSSIONS ON PAPERS AFTER THEIR PRESENTATION

LIST OF SPEAKERS AND QUESTIONERS

A. B. Bauer	Philco-Ford Corp.	USA
S. M. Bogdonoff	Princeton University, New Jersey	USA
A. G. Boyer	General Electric Co., Valley Forge, Pa.	USA
F. Browand	Massachusetts Institute of Technology, Cambridge, Mass.	USA
T. Canning	NASA-Ames Research Center, California	USA
A. Cantin	CARDE, Valcartier, P.Q.	Canada
R. L. Chapkis	TRW Systems, Redondo Beach, California	USA
D. G. Compard	ONERA, 92 - Chatillon	France
R. J. Cresci	Brooklyn Polytechnic Institute, New York	USA
J. Cresswell	General Electric Co.	USA
J. Delerey	ONERA, 92 - Chatillon	France
C. F. Dewey	Colorado University, Boulder	USA
J. G. G. Dionne	CARDE, Valcartier, P.Q.	Canada
D. Ellington	CARDE, Valcartier, P.Q.	Canada
A. Eschenroeder	AC Electronics Defense Research Laboratories, Santa Barbara	USA
J. Fox	TRW Systems, Redondo Beach, California	USA
M. Giddens	Aerospace Corp., San Bernardino	USA
B. H. Goethert	University of Tennessee Space Institute	USA
F. Hama	Jet Propulsion Laboratory, California	USA
R. A. Hayami	AC Electronics Defense Research Laboratories, Santa Barbara	USA
J. H. Hermann	Massachusetts Institute of Technology, Lincoln Laboratory, Lexington, Mass.	USA
W. G. Hill, Jr	Grumman ACFT	USA
M. Holden	Cornell Aeronautical Laboratory	USA
C. F. Infosino	Naval Ordnance Laboratory, Maryland	USA
L. S. G. Kovasznay	Johns Hopkins University	USA
H. H. Kurzweg	NASA, Washington	USA
H. K. Larson	NASA-Ames Research Center, California	USA
M. Laug	Institut Franco-Allemand des Recherches St. Louis	France
L. Lees	California Institute of Technology	USA
R. Legendre	ONERA, 92 - Chatillon	France
A. Lemay	CARDE, Valcartier, P.Q.	Canada
W. Merzkirch	Ernst-Mach-Institut, Freiburg i. Br.	Germany
E. P. Muntz	General Electric Co., Valley Forge, Pa.	USA
E. M. Murman	Princeton University, New Jersey	USA
J. T. Ohrenberger	TRW Systems, Redondo Beach	USA

M. Scala	General Electric Co.	USA
R. Sedney	RIAS Martin Co.	USA
R. E. Slattery	Massachusetts Institute of Technology, Lincoln Laboratory, Lexington, Mass.	USA
E. J. Softley	General Electric Co., Space Sciences Laboratory, Valley Forge, Pa.	USA
E. A. Sutton	AVCO-Everett Research Laboratory, Massachusetts	USA
K. M. Thomas	General Electric Co., Space Sciences Laboratory, Valley Forge, Pa.	USA
M. Viviand	Laboratoire d'Aerothermique, Centre National de la Recherche Scientifique, 92 - Meudon	France
R. White	University of Illinois	USA
R. E. Wilson	Naval Ordnance Laboratory, Maryland	USA
M. Wyborny	DVL-Institut für Angewandte Gasdynamik, Porz-Wahn	Germany
S. Zivanovic	AC Electronics Defense Research Laboratories, Santa Barbara	USA

Discussion of the Paper
FLUID MECHANICS OF WAKES
presented by
Lester Lees, USA

H.K.Larson

(i) With regard to your statement that turbulent flow on the body results in an all-turbulent wake, there is considerable evidence in the literature that sufficiently rapid expansion of a turbulent boundary layer will result in laminar flow downstream for both separated and attached flows. Therefore at higher Mach numbers your statement may not be correct.

(ii) With regard to your correlation of the spreading parameter, sigma, we have recently found a discrepancy between measurements at Ames and some by Gray at ARO, Inc., Tullahoma, Tennessee. The cause of this is believed to be the large difference in the ratio of the length of measurement relative to the initial boundary-layer thickness. Our sigma was based on the old, conventional definition. We have not compared the two sets of measurements using the momentum-thickness definition of sigma.

L.Lees

(i) I agree with Mr Larson's observation. However, I have the impression that once a fully developed turbulent boundary layer is established on a body there is a minor sub-layer that remains turbulent soon after expansion around the base.

(ii) Since the eddy viscosity is reduced greatly at high Mach numbers (for isoenergetic mixing) it takes a considerable distance to establish a fully developed turbulent half-jet. Many of the published results suffer from this defect. In addition one must be certain to have the spreading rate, $d\theta/dx$, of the momentum thickness if one tries to correlate data from many different sources.

D.Ellington

How important are the pressure fluctuations compared with the fluctuations in entropy and vorticity in a compressible hypersonic turbulent wake?

L.Lees

There are numerous experts in the audience who are much better qualified to answer this question. However, in the wakes behind blunt bodies it is my impression that the turbulent structure is not very much different from what it is at low speeds. If that is the case then the pressure fluctuations would not be important in most of the wake. Of course, near the body one observes the small "shock waves" produced by turbulent eddies. For slender bodies, on the other hand, the relative Mach number across the wake, $\Delta u/a_0$, is supersonic for a fairly long distance, and it is quite possible that pressure fluctuations are significant in this zone.

L. S. G. Kovasznay

(i) Is there a theoretical treatment of the instability of the outer wake driven by the turbulent fluctuations of the inner wake?

(ii) A recent publication by O.M. Phillips (Journal of Fluid Mechanics) suggests turbulent viscosity $E \simeq \overline{v}^2\theta$, where $\overline{v}^2$ is the mean square velocity of fluctuations normal to the streamline and θ is the Lagrangian time scale.

L. Lees

The theoretical treatment of the instability of the outer, vortical wake follows "classical" lines, in that the eigensolutions and characteristic frequencies are found without reference to any impressed disturbance. It would be very interesting to follow up Dr Kovasznay's suggestion to study the effect of input spectrum, especially from the inner wake as a trigger.

Discussion of the Paper
KINETIC PROCESSES IN HYPERSONIC WAKES
presented by
Alan Eschenroeder, USA

E. A. Sutton

The reaction $N_2 + O_2 \rightarrow 2NO$ has been included in a number of non-equilibrium chemical reaction programs. Recently it was found by Camac and Feinberg that earlier interpretations of the disappearance of the reactants in terms of the formation of NO are erroneous. They show that the rate which was studied is the one for the process

$$N_2 + O_2 \rightarrow N_2O + O \ .$$

The inclusion of the nitric oxide producing branch in flow field calculations will lead to an erroneously high production of NO in the near flow field - which, as I shall show in a moment, is of great importance in the prediction of the electron concentration in the far wake.

Now, as Dr Eschenroeder has mentioned, I would like to make some comments about the chemistry of electrons in the far wake.

We have a fluid mechanical model that is like the one Dr Eschenroeder described, so I would like to talk about the chemistry and particularly I would like to confine my remarks to the far wake.

In the Figure A* is shown a comparison of the calculated electron line density and the line density as measured by Kornegay in the Lincoln Laboratory ballistic range.

There is an almost indecent fit between the calculations and the data. I would like to explain why this is so. The electron and ion chemistry of these pure air wakes is also of importance for the electron concentrations in the ionosphere. For this reason there has been a large effort among geophysicists to measure the predominant reactions of the ionosphere. Recently a large number of the rate constants for the ion-molecule reactions have become available. In particular the work of Fehsenfeld, Ferguson, and Schmeltekopf must be mentioned as they have recently measured so many of the rates needed for the wake chemistry problem. This work, plus the work by many others on the chemistry of the neutral constituents, allows the statement to be made that the chemistry controlling the electron levels in pure air wakes is known. That is, in the sense that all the important rate constants have been measured, both neutral and ionic.

Let us talk about the important reactions which play roles in the electron chemistry. Dr Eschenroeder has shown how the electron concentration of the near- and mid-wake regions is determined predominantly by the dissociative neutralization of N^{0+}. In the far wake the neutralisation becomes much slower than other processes which effectively reduce the level of free electrons. Once the atomic oxygen concentration

---

* Printed at the end of this Discussion

is reduced, the electrons no longer become detached as quickly as before. Its main electron-determining chemistry then becomes a complicated series of negative ion reactions involving attachment, ion exchange, and associative detachment. The main reactions of this chemical system are shown in Figure B. The numbers following the reactions show the net rate of the particular reaction compared to the neutralisation process. The electrons can be seen to cycle about two orders of magnitude more rapidly than they neutralise.

The neutral species which play an important role in the wake are seen to be O, O_2, O_3, NO, and NO_2. The most important of these is the atomic oxygen. It is the large concentration of atomic oxygen in the early parts of the wake which allows the electrons to stay mainly detached, thus allowing the dissociative neutralisation to dominate the electron depletion in this region.

Due to recombination and turbulent dilution, eventually the atomic oxygen is reduced to the point where a significant fraction of the negative species are ions. Finally, the exchange processes which lead to the formation of NO_2 and NO_3 remove the electrons from the cycle permanently.

One of the main features of this system is the dominance of exothermic reactions. Although many endothermic reactions are included in the program, none were found to be as important as the exothermic reactions. The lack of endothermic reactions with their strong dependences on temperature through the Boltzmann factor leaves the present chemical model far less sensitive to the proper calculation of the wake temperature than if endothermic reactions were important.

In Figure C, the role played by atomic oxygen is illustrated by calculations where associative detachment is left out, leading to the rapid decrease through attachment. Also the effects of varying oxygen concentration and a model containing only neutralisation are shown.

In Figure D the initial fluxes of nitric oxide have been varied to show how the final electron decay is strongly affected by the NO and its product, NO_2.

Summarising one can make the following points:

The ion chemistry is so rapid compared to the rates of neutral species that, while the electron level relative to the negative ion concentrations is determined by the ion reaction rates, the rate of change of the electron concentration follows the more slowly varying neutral species.

Secondly, the reaction rates used in this work were all taken from measurements at the lower temperatures one finds in wakes. Many of the present reviews of chemical reaction rates mix measurements from low and high temperatures, which often leads to large errors when rates are extrapolated too far.

R. Legendre

When the experimental results are compared with the theoretical ones, both are supposed to correspond to axisymmetric flows. Whatever the stability of the model, there is certainly a slight incidence, making no change in the near wake, but, when

the results are studied for x/D greater than 100, I imagine that the mixing by the vortices is significant, even for small incidences, and increases the cooling of the gases.

A. Eschenroeder

It is correct that slight incidence does occur in launching slender cones. This alters the ionisation history throughout the wake to some extent. The influence of incidence has been found to be less than the experimental scatter and uncertainty (approximately ±50%) for incidence angles smaller than one half the cone half-angle. Incidence angle is monitored in all flights and the data presented here is believed to be representative of zero incidence within the limits of experimental uncertainty.

D. Ellington

(i) The $N_2 + O_2 \rightleftharpoons 2\,NO$ reaction was not included in the reaction kinetics. What would be the effect of this reaction on electron density concentrations?

(ii) Have any comparisons been made with Lees and Hromas theory?

A. Eschenroeder

(i) In the blunt body shock layer it is relatively important. We have included it to verify this conclusion. Camac and Feinberg have found that the products of the reverse reaction (for which the rate is often quoted) are $N_2O + O$. As Dr Sutton has just pointed out, the electron concentration behind slender bodies is highly sensitive to NO production; therefore in these cases we might expect the 2 NO reaction to be significant.

(ii) Dr Menkes of IDA has recently conducted a wake flow field comparison for various methods. For identical initial conditions, rate constants, and transport coefficients the finite-difference approach, which is cited here, and the integral methods (e.g. Lees and Hromas) agree rather well for axis values of temperature and electron density.

C. F. Dewey, Jr

(i) Can your predictions in the near wake be successfully scaled to conditions where rate constants in the near wake are important?

A. Eschenroeder

(i) As long as we consider the near wake as that part controlled by the dissociative recombination reaction, it will obey binary similitude; i.e. that similitude preserving both the flight velocity and product of ambient density, with length as constants. The sub-scale experiment is a more severe test of scaliny because tertiary

processes become important relatively earlier in the wake. We should realise however, that the near wake is an extremely limited region in terms of field observations. Therefore, it appears necessary to develop a theoretical model for a complete description where direct scaliny may not be valid.

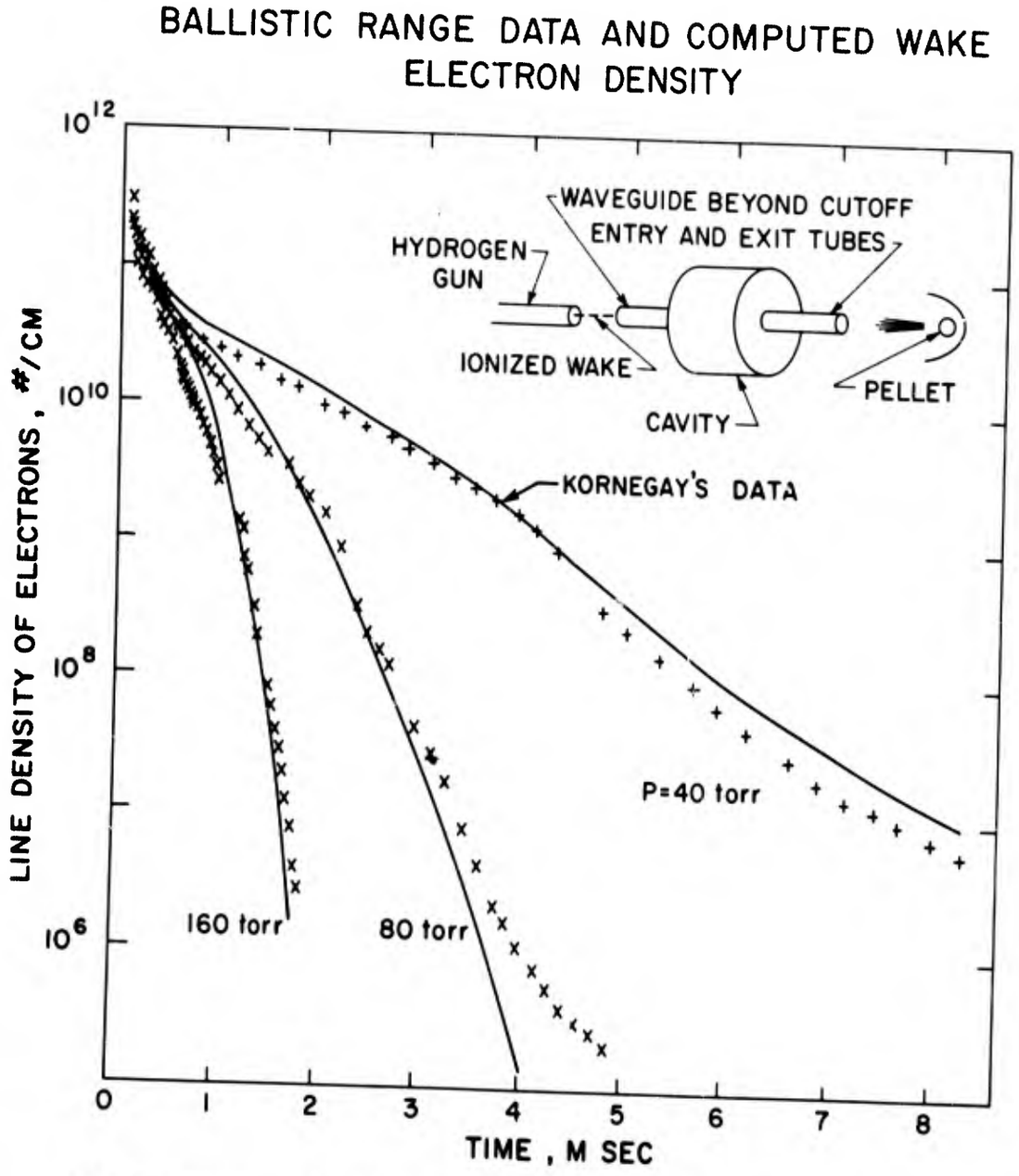

Fig. A Comparison of the calculated and measured electron line densities

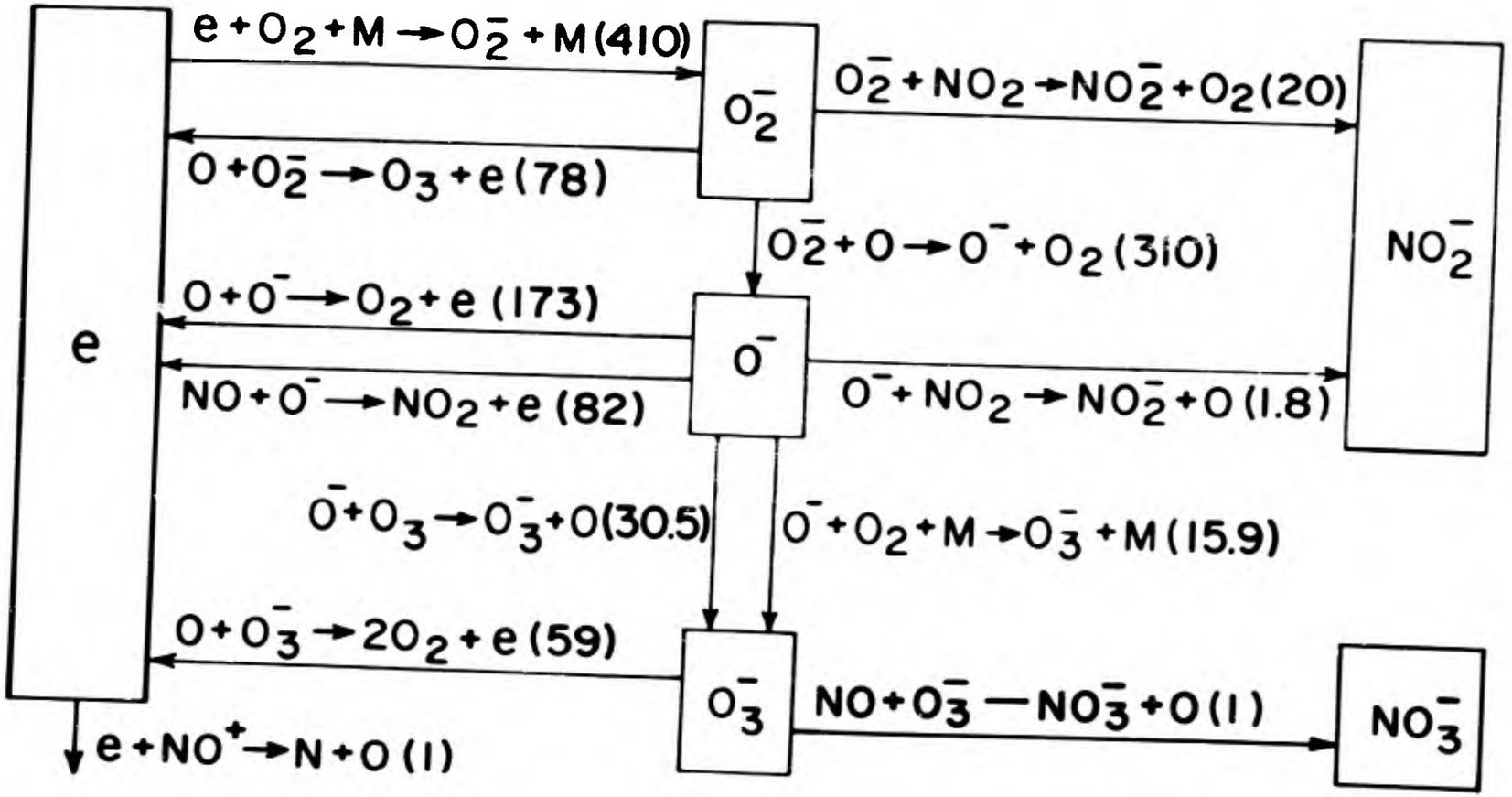

Fig. B The relative rates of the major negative charge reactions for the 40 torr case 4.5 milliseconds after the body has passed. It can be seen that the attachment and detachment reactions between e, O_2^-, and O^- are more than two orders of magnitude faster than neutralisation. In this part of the wake the principal electron loss process involves exchange to form NO_2^-

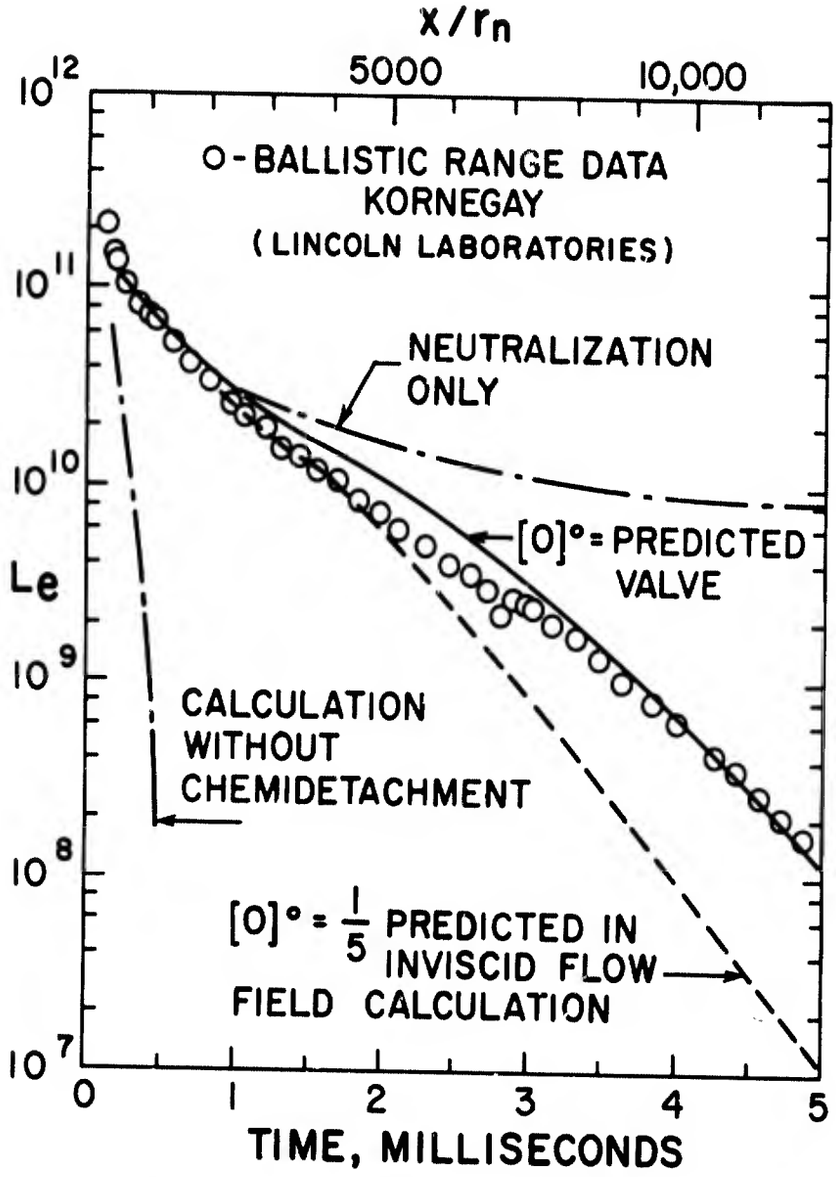

Fig.C Sample calculations for the 40 torr case showing the result of partial models based on neutralisation only, neutralisation and attachment only, and less atomic oxygen than calculated from the near-flow-field program. The rapid decay due to attachment when the chemi-detachment reactions are left out is clearly shown

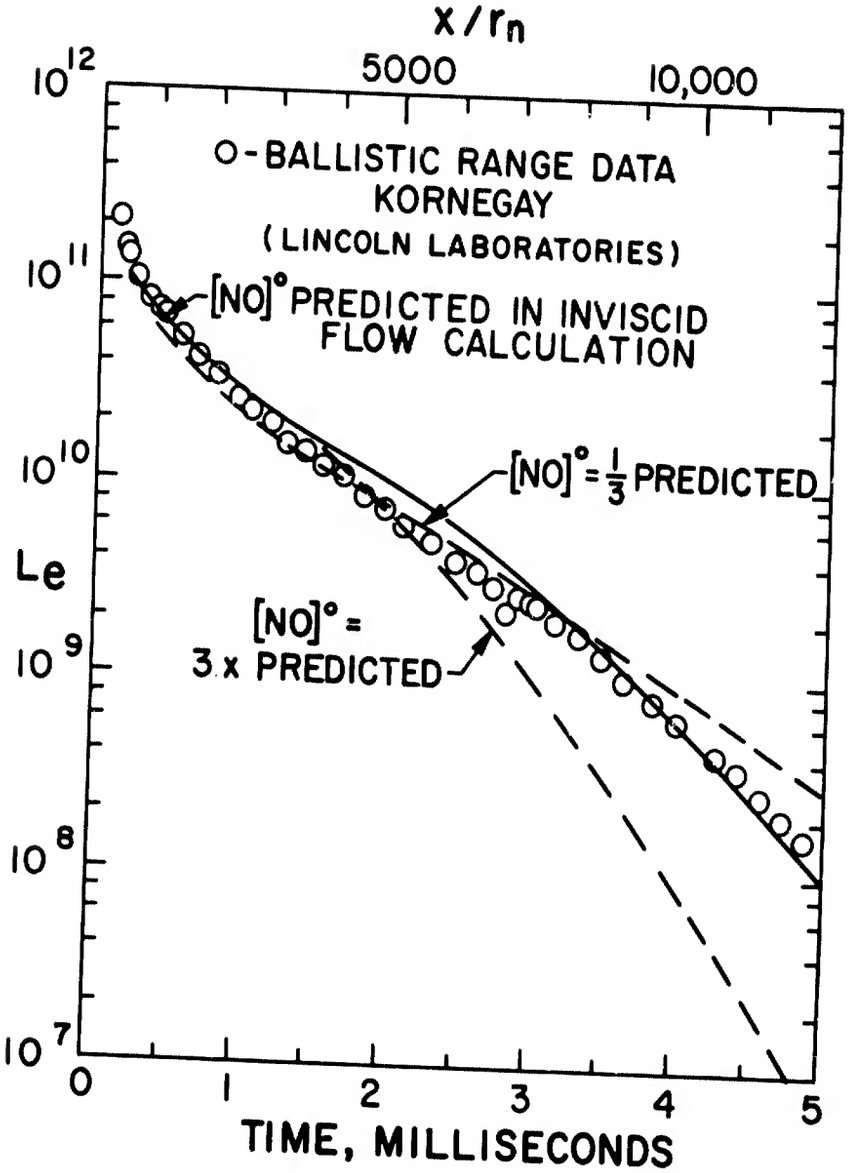

Fig. D Sample calculations showing how the final wake electron decay depends on the initial NO concentration in the wake. The amount of NO_2 in the far wake is directly proportional to the initial NO concentration

Discussion of the Paper
DIAGNOSTIC STUDIES OF LAMINAR HYPERSONIC CONE WAKES
presented by
E.M.Murman (Speaker), C.W.Peterson and S.M.Bogdonoff, USA

T.N.Canning

The change from frozen adiabatic wall conditions to cold-wall conditions should change the wake-core details only in that a very thin region of slightly higher density may be formed.

E.M.Murman

This is the sort of change in the fine structure of the wake that one would expect to uncover in the cold-wall case. If a temperature maximum exists off the wake axis, then the density profile will reflect this as a local minimum. Such detailed differences are not expected to alter the overall structure of the wake as found for the adiabatic bodies.

L.Lees

I am impressed with similarities between the axi-symmetric and two-dimensional flows; the viscous wake edge, if defined as the boundary where total temperature equals free-stream total temperature, lies outside the trail of the body base and, downstream of the wake shock, is nearly parallel to the wake axis; the chief difference between this study and Ball's work at $M = 6$ is the difference in local Mach number. The trailing Mach ray of the expansion fan will be pointing toward the axis in this case, which accounts for the differences in static pressure, laterally.

E.M.Murman

The Mach number effects are definitely quite important, and are evidenced in the lateral and axial pressure distributions. The structure and strength of the trailing shock appear to be different in this experiment from that of Batt. This may be due either to the Mach number difference or to the change from two-dimensional to axi-symmetric flow.

E.P.Muntz

(i) Could you sketch the static pressure profile used in the calculations? The point is that I would like to emphasise the static pressure overshoot that has been observed in other facilities by previous investigators for cone wakes; perhaps some comparison is in order.

(ii) It would be of interest to compare your results with other cone wake measurements at similar Mach numbers, which are available for both cold and hot walls.

(i) The static pressure profile in the sketch is obtained from measurements with conventional static pressure probes. The determination of the axial static pressure distribution is not yet completed. Several probes are being used to isolate and correct for any viscous interaction effects on the instrument. However, the general profile appears to be as shown

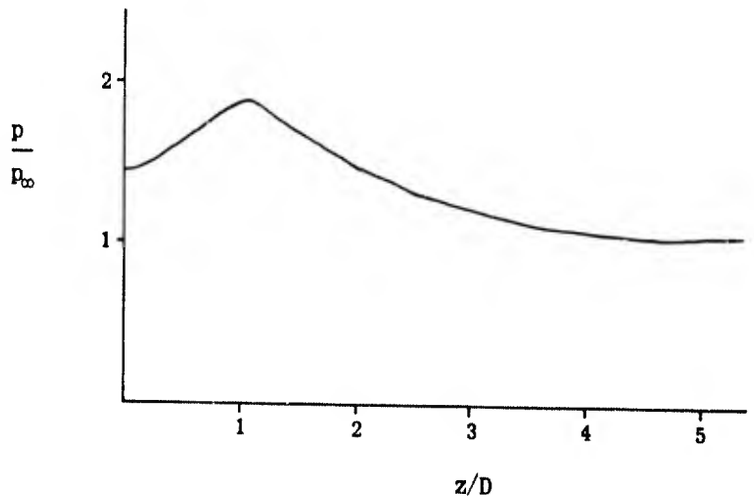

(ii) Several sets of data are available in the literature covering the same régime of Mach number and Reynolds number. Comparisons with data from General Electric show qualitative agreement with the density profiles and static pressure distributions.

Discussion of the Paper
WAKE MEASUREMENTS BEHIND A CONE SUSPENDED MAGNETICALLY IN A MACH NUMBER 4.3 STREAM
presented by
M.Finston, F.Browand (Speaker) and D.McLaughlin, USA

E.J.Softley

(i) Why is observed real stagnation point as far back as 4 base diameters? Observation by Lees for low M_∞ (blunt wedges) and for cones at higher M_∞ identifies the rear stagnation point at $X/D_n = 0.75$!

(ii) What is the basis for the statement that the measurement probe does not interfere with the flow? Our observations (at General Electric) suggest that an extremely small probe can interfere with the flow field, moving the rear stagnation point back!

F.Browand

(i) The rear stagnation point was placed about 3½ diameters downstream of the base, but this is admittedly only a rough estimate. Increasing M_∞, decreasing wall temperature, or the onset of turbulence would all have the effect of moving the rear stagnation point closer to the body.

(ii) We have no guidance that the probes we have used affect the flow, although with larger probes asymmetries and wake movement are noticed. Schlieren observation of the wake region, with no probes present, gives a similar estimate of the recirculation régime length.

S.M.Bogdonoff

I am concerned with the author's use of pitot pressure surveys alone to draw conclusions about the location of the stagnation point and details of the velocity defects downstream of a cone. We have found it almost impossible to do this without other measurements by other techniques and perhaps these difficulties may be the reason for some of the discussion.

F.Browand

I agree with Professor Bogdonoff. But I still feel that the rear stagnation point can be roughly located, in this fashion, to be about 3 to 3½ base diameters downstream. We have some supporting evidence from schlieren observations also.

T. N. Canning

The bifurcation represents the discharge of the trailing vortex "horseshoe" due to lift, even at the smallest angle of attack mentioned. Therefore I fail to share the surprise of the earlier conversation at the appearance of the two lobes at 0.4° angle of attack.

F. Browand

Yes, it should not be surprising. What is surprising is the magnitude of these effects.

Discussion of the Paper
ANALYSE EXPERIMENTALE DU PROCHE SILLAGE D'UN CORPS ELANCE, LIBRE DE TOUT SUPPORT LATERAL
presented by
M. Sirieix and Jean Delery (Speaker), France

L. S. G. Kovasznay

Please define the quantity N.

J. Delery

N is the equivalent frequency of the harmonic oscillation tangent to the auto-correlation curve of the turbulent signal. This frequency is a representation of the characteristic scale of the turbulence, λ.

J. T. Ohrenberger

With regard to using the method of rotational characteristics to calculate the expansion of the boundary layer into the near wake, my experience has been that the pressure field can indeed be predicted to good accuracy (as determined by comparison with experiment). However, in my case the reason was that the pressure boundary conditions on the characteristics were forced at the onset of the calculation to agree with the experimental data. Contrary to this, the streamline pattern, i.e. flow inclination distribution, was found to be in substantial disagreement with that inferred from experimental data (taken by R. G. Bail at CIT and discussed by Professor Lees earlier in the paper "Fluid Mechanics of Wakes"). The reason was traced to the use of a centered expansion originating at the sonic line in the boundary layer at the base station, together with the assumption that the streamlines were parallel to the body surface at this station. We now know that there is an upstream influence of the base pressure on the boundary layer structure and hence that the expansion process begins upstream of the corner. Recalculating the flow by characteristics assuming a non-centered expansion again gave good agreement of pressure with flow inclination. The point to be made here is that the good agreement of pressure between experiment and theory shown by Sirieix and Delery is not necessarily an indication that the characteristics method is accurately predicting the flow field.

J. Delery

In our calculations we disregarded the subsonic portion of the boundary layer, and the influence of the expansion must certainly be felt upstream of the base through this subsonic portion. However, when the boundary layer is turbulent and the outside Mach number high, the subsonic portion is extremely thin, and the displacement of the expansion in the upstream direction must be very small.

Discussion of the Paper
NEAR WAKE OF A SLENDER CONE IN HYPERSONIC WAKE
presented by
E.M.Schmidt and R.J.Cresci (Speaker), USA

C.F.Dewey

(i) If one makes any "reasonable" interpretation of your pressure variation across the base, the predicted recirculation velocities at angle of attack are enormously greater than one would expect from simple extensions of data at zero angle of attack. Would you please comment.

(ii) If these large velocities exist, why wouldn't hot-wire measurements or other standard techniques be useful in verifying the order of magnitude of this recirculation velocity?

R.J.Cresci

(i) A possible explanation of the large velocities that appear to occur in this region is that they are caused by the large scale vortices that occur in the base (recirculation) region. If the bifurcated recirculation region exists (as proposed by Finston, et al.), then the flow in the plane of symmetry would lie between these recirculation regions and therefore could attain a very high velocity.

(ii) Standard techniques such as hot wires, or even pitot probes extending from the base, could be used to determine these velocities accurately; however, we have not performed these measurements as yet.

E.M.Murman

Are the reported static-pressure-probe results measured data or data corrected for viscous interaction on the probe? Has an estimate of such corrections been made?

R.J.Cresci

The data reported are the actual measured data. An estimate of the correction has been made for most downstream stations (largest Mach numbers) and was found to be less than 8%. Since this is within the accuracy of measurements for static pressures, no correction was made.

H.K.Larson

Measurements showing laminar flow at the $\phi = 0^{\circ}$ and 90° stations do not necessarily determine that the flow is laminar inbetween. Recent tests on a 15° Cone at 15° incidence showed the most forward transition location to be at about the 45° position -

in fact the distance to transition from the cone apex was about twice as large at $\phi = 90^{o}$, compared with the 45^{o} position.

R.J.Cresci

Unfortunately, in the present tests no transition data were obtained at intermediate peripheral locations around the cone surface, so there may be some transitional flow even in the low Reynolds number tests ($Re_{\infty D} = 0.15 \times 10^{6}$). Additional tests will be performed to verify or repudiate this point before the final PIB report on this test program is issued.

Discussion of the Paper
REYNOLDS NUMBER EFFECTS IN THE NEAR WAKE BEHIND A WEDGE AT SUPERSONIC AND HYPERSONIC SPEEDS
presented by
W.Merzkirch, Germany

F.Hama

The analysis presented in this paper is based on an earlier inviscid rotational theory by Weiss and Weinbaum. However, recent experimental investigation by Hama (JPL TR 32-1033, December 1966 and AIAA Preprint 67-29, January 1967) indicates that the viscous separation phenomena must play important roles in the formation of lip shock. It is also recognised, as discussed already by Dr Ohrenberger, that the upstream effect of the expansion is also an important factor. The results obtained without taking these additional features into account are highly suspect.

W.Merzkirch

The present model cannot predict an upstream influence since it is based on a centered corner expansion. As indicated in an earlier paper (Merzkirch: DGRR/WGLR annual meeting, October 1966) the secondary wave system in connection with a non-centered expansion will change the flow geometry and is able to explain the upstream influence. In the present paper, however, a centered expansion was used, since the main purpose was not to investigate the lip shock but the wave reflection conditions in the free shear layer. I admit that a non-centered expansion - or the upstream influence - will slightly change the criterion for the lip shock formation. But the principle itself will not change as long as the model of the secondary wave system is used.

E.J.Softley

Concerning the existence of a lip shock, the model should recognise the extent of upstream influence - at least 3 boundary layer thicknesses - and this may modify the flow (and wave) geometry.

W.Merzkirch

No comment.

R.White

The conclusion that the lip shock will not form at hypersonic Mach numbers must be questioned, since tests with an approach Mach number of 7 performed at the Aeronautical Research Institute of SWGSON clearly show such a shock.

W. Merzkirch

The upstream influence of the corner expansion might be of influence on the lip shock formation. The helium flow tests referred to in this paper were performed with a highly sensitive optical system and gave (even at high Reynolds numbers) no indication of the existence of a lip shock.

Discussion of the Paper
WAKES OF CYLINDERS AND WEDGES IN RAREFIED GAS FLOW
by
E. Brun, France, presented by M. Viviand, France

W. G. Hill, Jr

Did you attempt to determine the effects of end conditions on your overall base flows? I noted that one end of your model extended through the edge of the jet, while the other end was within the jet. It has been shown many times that edge effects can greatly affect separated regions on the whole, even though the flow appears two-dimensional. Did you try end-plates or varying span?

M. Viviand

We did not study the effects of the end conditions of the wedge. It should be noted that, in the study of the wakes and of the pressure measurements, the model extends throughout the jet, including the portion issuing from the boundary layer of the nozzle. It is only for the visualisation that one end of the wedge (that on which the adjustment is made) is located at the edge of the isentropic core.

We did not try end-plates.

L. S. G. Kovasznay

(i) Did you measure and plot the recovery temperature (equilibrium temperature)?

(ii) If you did measure the recovery temperature, did you not try to solve for the flow conditions by using a third piece of information, such as pitot pressure?

M. Viviand

(i) Yes, Figure 12 shows the curves of equal temperature of the wire friction in the base flow area.

(ii) The measured pitot pressure is not equal to the theoretical pitot pressure, due to viscosity effects. The divergence, which represents a low percentage in the free flow, can be much higher in the near wake and it is very difficult to estimate it. We are at present developing local density measurements by means of an electron gun, which will enable us to determine the local parameters of the flow.

E. M. Murman

In Figure 16 a line has been drawn and identified as the edge of the boundary layer on the wedge surface. Can this boundary be interpreted as something other than

a boundary-layer edge? Could it be an outer boundary of an expansion process emanating from the rear corner and felt far upstream? Could it be another rotational region which is different from the viscous boundary layer? The dark region in the glow discharge picture of Figure 17 does not seem to coincide with the line constructed in Figure 16.

M. Viviand

This line is the location of the point of break of slope of the pitot pressure profiles, which point characterises the boundary layer edge. On the photograph (Fig. 17) the transition from the dark region to the light region is continuous and it is difficult to determine the boundary layer edge accurately. However, determining this edge with the pitot tube is an accurate process.

Discussion of the Paper
AN EXPERIMENTAL INVESTIGATION OF BASE MASS INJECTION ON THE LAMINAR WAKE BEHIND A 6-DEGREE HALF-ANGLE WEDGE AT M = 4.0

presented by

R.L.Chapkis (Speaker), Jay Fox, L.Hromas and Lester Lees, USA

K.M. Thomas

The results of Dr Chapkis and his co-authors, complement the earlier work of Professor Zolkoz of NYV, wherein it was shown rather conclusively that small amounts of mass injected into a hypersonic wake through a porous surface, covering virtually the entire base region, could indeed "detach" the recirculation region from the base region. In contrast to this, some preliminary injection results obtained at the General Electric Space Sciences Laboratory show that, for the case of relatively massive injection rates (an injection rate equal to the boundary layer mass flow rate at the base of the body), the recirculation region, as we normally think of it, is still preserved. The major difference between these experiments and those just reported is the method of injection, which consists of injecting helium into the wake through a series of 24 sonic orifices of 0.145 in. diameter located at the periphery of the base (Y/R = 0.86). These experiments were performed for a sharp 10^{o} half-angle cone in an $M_{\infty} = 12$ shock-tunnel-generated flow. Our results are based on concentration measurements made with the electron beam. In addition, some embarrasingly simple injection experiments were performed by Dr R.H.Johnson of the General Electric Research and Development Center on the water table. I should like to emphasise that the water table is by no means a simulation of a hypersonic environment. It is, however, useful in illustrating gross effects, and in this context I can think of no more gross effect than the detachment of the recirculation region. Suffice it to say that the water table results confirmed our interpretation of the shock tunnel experiments (i.e. preservation of the recirculation region) and also showed that injection of relatively small amounts of mass from the entire base can indeed detach the recirculation region and form the so-called bubble that Dr Chapkis mentioned. The point of all this is that, in addition to the rate of mass injection, the method of injection is a vitally important parameter in determining the effects of mass injection on the near wake.

R.L. Chapkis

No comment.

B.H. Goethert

The experiments of Dr Chapkis were conducted at a constant mass injection rate. It appears to me that the test results will greatly depend upon the mass injection rate, and that the reported case might be a quite special one; that is, the case when the viscous wake is expanded by the injection so that the rear stagnation point disappears and the static pressure is nearly constant throughout the wake. My question is whether the injection rate used was determined through experiments with ranging rates or was selected more or less coincidentally as the special value.

Also, all injection tests were conducted for very small differences between total pressure of the injected gas and the base static pressure. I agree that the total pressure of the injection gas is another important parameter. Do you have any data for the configuration where the gas is injected in the base through one or more small jets with big velocities?

R. L. Chapkis

The injection mass flow rate used for the present tests was chosen primarily on the basis of Hertzog's results for the circular cylinder. It appeared from his results that an injection rate of about 3% would be large enough to affect the wake significantly, and this was the rate chosen for this first series of tests.

A new series of tests is now underway, using the same wind tunnel model but emphasising turbulent wakes. In these tests the effect of changing the injection rate is being investigated. In addition, both helium and nitrogen are being used as injectants. Since, for the same mass flow rate, the Mach number of the nitrogen is higher than for the helium, the results of this test should help to determine the importance of injectant Mach numbers. At present we have no data for the wedge in which the gas is injected through small jets rather than through a porous base.

C. F. Dewey

With injection your shear layer is nearly straight and one would expect the static pressure to be nearly constant across the inner wake cone. This suggests a nearly ideal flow, for which mixing calculations could be performed. Have you done this calculation?

R. L. Chapkis

One nice feature of the wake structure with injection is its relative simplicity. The wake with injection should be easier to analyse theoretically than the no-injection case. Your suggestion of performing mixing calculations is a good one; however, these have not yet been carried out.

A. B. Bauer

The fluid injection phenomena presented by Dr Chapkis are similar to the measurements made recently at Philco-Ford for the use of injection behind a cone at Mach 3. The fact that the injection both pushed the recompression shock outward from the center line and also weakened the shock is in agreement with our observations. However, the two-dimensional nature of the work by R. L. Chapkis et al. contrasts with the three-dimensional nature of our cone flow in that the two-dimensional shock location and strength showed a greater sensitivity to the injection.

Discussion of the Paper
RADIAL AND AXIAL VELOCITY PROFILES OF HYPERSONIC AND SUPERSONIC WAKES MEASURED BY THE SEQUENTIAL SPARK METHOD

presented by

C. Lahaye, E. G. Leger and A. Lemay (Speaker), Canada

B. H. Goethert

The authors' very impressive measuring method used the assumption that the path of each arc in the sequence of arcs is attached to the same gas particles and thus allows an evaluation of the absolute local speeds. I wonder what information exists about the accuracy of this basic assumption. To what extent does the arc always follow the path determined by the gas particles? For what reason does the spark take short-cuts in curved arc paths, and to what extent do magnetohydrodynamic forces influence the arc path? I expect that at regions of large local arc curvature the deviation might be significant.

A. Lemay

It is difficult to assess at this time the accuracy of the basic assumption. We have been working, up to now, under experimental conditions minimising the errors. For instance, when a sharp velocity gradient exists, and if the time interval between the sparks is rather long, creation of the new spark path can occur and thus lead to a large error. This has been overcome by selecting appropriate short time intervals which lead to a reasonable spark displacement in the region under measurement, where each successive spark follows the displaced ionised path of the previous spark.

The sparks also have a tendency to take the shortest path around a sharp curvature. The error that could be thus generated has been minimised by making measurements at somewhat higher densities. Under these conditions the spark is very well defined as a fine ionised filament and the error does not appear to be significant.

H. H. Kurzweg

Did you observe any ablative material in the wake? In other words did you use materials other than aluminium for your spheres?

A. Lemay

Only aluminium spheres have been used up to now in these measurements. The supersonic spheres do not ablate, but with hypersonic spheres ablation has been evidenced by other methods.

S. M. Bogdonoff

Is there any information concerning the effects of the waves reflected from the electrodes on the wake development?

A. Lemay

The reflected bow and recompression shocks off the electrodes should not affect the wake development, since the electrodes present a very thin area along the axis of flight. Moreover weak shocks are also generated by the sparks themselves. These shocks vary slightly above Mach 1, under the conditions prevailing in the range outside the wake, and appear to have no influence on the wake.

R. E. Slattery

In reply to Professor Bogdonoff's remarks: a large number of schlieren motion pictures taken at Lincoln Laboratory fail to indicate any effects of weak reflected shocks on either the structure or velocity of the wake. Rather, the variation in density of the turbulent wake tends to break up and refract the shock.

Discussion of the Paper
AN EXPERIMENTAL STUDY OF THE PRESSURE AND HEAT TRANSFER ON THE BASE OF 9° CONES IN HYPERSONIC FLOWS

presented by

E.J.Softley (Speaker) and B.C.Graber, USA

M.Holden

I would like comment on the time to establish a steady separated flow. At Cornell Aeronautical Laboratory we have made a very careful study of the time to establish a steady separated flow over a flat-plate wedge compression surface in the régime of high Mach number and low Reynolds number ($M = 20$, $Re = 10^5 ft^{-1}$) in our various shock tunnels. We find that, whereas the attached boundary layers are established at 500 μS, up to 2 mS are required to establish a steady separated region over our models. The character of the heat transfer and pressure records in the separated flow differed markedly from those in the attached boundary layer in our work, whereas I noticed that the records you presented show no significant time-dependent features. Some measurements made in the Shock Tunnels at CAL, in the separated base flow downstream of an axisymmetric step, also exhibited the same basic character and time-dependence as the measurements over the compression surface just quoted.

E.J.Softley

When the flow formation time is rapid (in a small conical nozzle) the observed wake formation times are of order 1.5 milliseconds (for a 2 in. base-diameter model). In the large constant nozzle, the free stream itself takes some 2-3 milliseconds, with the density and pressure (etc.) rising smoothly to the trial quantities. Under these conditions the data indicate that the base flow formation for a 5 in. base-diameter model does not need any additional time but takes place during the period of free-stream flow formation.

R.Sedney

How do you determine whether the state of the boundary layer or the shear layer is laminar or transitional?

E.J.Softley

We don't, directly! We are applying knowledge of boundary-layer transition as determined on a cone in the same General Electric SSL shock tunnel (in an alternate programme). This information is complete enough and indicates that, for a sharp cone at the highest Reynolds number, at least 2.5 ft of laminar run is expected before transition begins. The model used here for base measurements is 1.4 ft long. Shell nose bluntness delays transition further; hence, for all cases considered in the paper, the boundary layer would be expected to be laminar.

Discussion of the Paper
HYPERSONIC INVESTIGATION ON THE LOCAL AND AVERAGE HEAT TRANSFER IN CAVITIES AND AFTER STEPS OF BODIES OF REVOLUTION

presented by

W. Wyborny (Speaker), H.P. Kabelitz and H.J. Schepers, Germany

J. Dewey

As a general comment, one must be very careful about interpreting the heat transfer distributions at the reattachment on the body surface behind the cavity; the heat transfer in previous investigations at similar lock Mach numbers has shown very large peaks, within one or two boundary-layer thicknesses of reattachment. Such peaks don't appear in your data, and I wonder if you could compare your local heat transfer solution with the local boundary-layer thickness at reattachment?

W. Wyborny

Surely, one can do; we will do it in the future. We can make measurements in a hypersonic tunnel, where we are able to change the total temperature and the wall temperature of the separation point, and so have different boundary-layer thickness.

S. M. Bogdonoff

The blunt geometry chosen and the location of the cavity so close to the nose assumes that the local Mach number is probably no more than 2 or 3. So the tests are not hypersonic. In addition, the cavity will be in a region of variable pressure in the axial direction. This makes it somewhat difficult to compare the results with the theory, which assumes uniform external flows.

W. Wyborny

Thank you for your remark: you are right, the local Mach number on the separation point is surely "supersonic" in our case, but we have defined our investigations as "hypersonic" from the free-stream Mach number. For a better comparison of the measured data with the theoretical, we have in mind to make pressure distribution measurements and then calculations.

R. White

With the external approach, Mach number is hypersonic and the local Mach number is only supersonic, due to the proximity of the nose. For supersonic cavities acoustical resonance may occur, as shown by Charwat. In these cases, resonant cavities, the heat transfer is drastically altered. One must check carefully for the presence of such unsteady conditions.

W. Wyborny

We have not observed acoustical reasonance till now.

T. N. Canning

The tests show the performance of a single cavity in changing the net heat flux to the body. The performance of a series of consecutive cavities might be very different.

W. Wyborny

It may be so; probably it will be, I don't know yet, because the tests are being made in the near future, and I hope we can present these results within a few months in comparison with drag measurements.

Discussion of the Paper
SOLUTION OF THE TIME DEPENDENT NAVIER STOKES EQUATIONS FOR THE FLOW OF DISSOCIATING GAS OVER A CIRCULAR CYLINDER

presented by

M. Scala (Speaker) and P. Gordon, USA

A. Eschenroeder

(i) How much computer time is required to achieve a steady-state solution to the problem treated here?

(ii) Have you attempted comparisons with solutions to the steady-state formulation of the equations?

M. Scala

(i) The amount of computer time required to achieve a steady state in the class of problems treated here is of the order of five hours of CDC 6600 computer time. This corresponds to approximately 20 microseconds of elapsed time in the physical problem.

(ii) Yes, we have. By using the same transport properties as Becker did (i.e. Prandtl number = 0.75), we were able to match his analytical solution to the one-dimensional steady-state shock wave structure problem to within one percent. The accuracy we achieve depends on the fineness of the computational mesh used. Hence, we can achieve solutions which are arbitrarily close to the earlier classical steady-state solutions of the Navier-Stokes equations by reducing our mesh size until two successive computations produce results which are within ε of each other. It must be noted that, when the spatial mesh is reduced at a certain rate, the temporal mesh must be reduced at a faster rate in order to satisfy the conditions required for convergence.

L. Lees

(i) How can you apply a boundary condition on radial velocity in the "wake" behind the body at a finite distance?

(ii) Why don't you pick up the growing unstable waves for the dynamically unstable flow?

M. Scala

(i) The mathematical character of the system of governing non-linear partial differential equations is parabolic-hyperbolic. In order to have a well-posed problem, this necessitates the specification of initial conditions throughout the entire computational domain of interest, and the specification of boundary conditions on velocity, temperature and density along the boundaries. In particular, for the

problem treated here, along the entire outer boundary on the downstream side, where $\pi/2 < \phi < \pi$, one must specify both components of velocity and the temperature. One would like to specify these boundary conditions at infinity, where these quantities are known precisely; but, due to practical machine-storage considerations, one has no choice but to specify these boundary conditions at a finite distance from the body. In fact, unless these conditions are specified at a finite distance from the body, one cannot proceed with the computations. Thus, although our numerical solution is "exact", it is also "approximate" to the extent of the arbitrary choice of boundary conditions invoked at the outer boundary on the downstream side. In our work we have arbitrarily chosen to apply boundary conditions which are absolutely correct as R_2 goes to infinity from R_1, the surface of the cylinder. Since we place R_2 beyond the sonic surface which envelopes the body, we expect the upstream influence of the approximate boundary condition to be small. We have verified this in a computation in which the radius R_2 was taken twice as large and found that the flow field structure remained the same except in the immediate vicinity of the boundary, where the supersonic flow must adjust itself to the outer boundary conditions. It has been suggested that we use an approximate solution of the wake problem to specify the downstream boundary conditions. This, however, would be just as arbitrary as what we have done and does not appear to be worth while, due to the absence of a significant upstream effect introduced at the downstream boundary.

(ii) In our computations, we do not introduce an artificial viscosity which would result in artificial damping but rather we use the actual molecular transport properties derived from kinetic theory. Moreover, the time step we utilize is of the order of 10^{-8} seconds; hence only oscillations of extremely high frequency would be neglected in our computations. Consequently, we must infer that the Reynolds number used ($Re \simeq 25 - 50$) is sufficiently small so that the flow is dynamically stable and no vortices are shed.

M. Giddens

Is your mesh size flexible enough over the field so that details of shock structure can be determined, even at very high Reynolds numbers?

M. Scala

The spatial mesh size that we have used is variable over the entire flow field rather than fixed. Thus, we use a fine mesh near the body, where more detail is required, including the structure of the shock wave and of the viscous layer, and a coarse mesh at larger distances from the body. It is noted that, near the shock wave, the spatial mesh size used must be comparable to the local mean free path and preferably smaller, in order to obtain the desired accuracy. Up to the present time, the maximum Reynolds number that we have used in our calculations is approximately 50. Thus, we do not yet know how large a Reynolds number we can achieve. In principle, however, if the storage capacity of the digital computer is sufficiently large, there should be no limit to the Reynolds number that can be achieved with the present numerical formulation.

Discussion of the Paper
MASS DENSITY MEASUREMENTS IN HYPERSONIC WAKES
presented by
J.G.G.Dionne (Speaker), C.M.Sadowski, L.Tardiff and J.E.H.Vanoverschelde, Canada

R.Legendre

You underlined that the spectrum of density fluctuation does not contain high frequencies. Even if the beam is narrow, I suppose that there is some mean value, eliminating the high frequencies.

J.G.G.Dionne

The beam diameter does contribute to the high frequency cut-off. However this does not seem sufficient to explain the rapid cut-off.

S.M.Bogdonoff

It was not clear to me why the density fluctuation data presented were averaged over four runs. Data for a single run would provide information on the actual density, while the averaging process seems to me to destroy the value of any data point (one axial position). Is single-run data available?

J.G.G.Dionne

From the single-firing data, it was noticed that the density variation around the mean density can be any value from 0 to 20-25%. So the data were averaged over the four firings available in order to get an approximation to the density variations one can expect at various axial distances. Nevertheless the original information for each firing is available and the actual density measured for each firing is shown in Figure 3.

W.Merzkirch

Would an optical method, e.g. an interferometer system, be sensitive enough for mass density measurements under these conditions?

J.G.G.Dionne

I would think that the interferometer techniques can measure density down to ambient pressures of a few torr. However these techniques give an integrated density value unless the density profile is already known. The electron beam technique described here can provide a point-to-point density measurement.

Discussion of the Paper
TURBULENCE CHARACTERISTICS IN THE HYPERSONIC WAKE OF A SHARP SLENDER CONE
presented by
A.G.Boyer (Speaker) and E.P.Muntz, USA

K.E. Slattery

Please discuss the statistical significance of the relative root mean square values you have presented, in the light of the limited sample presented by your method.

A.G.Boyer

The sampling time of the particular traces shown is ½ msec and approximately 10 density fluctuations are recorded in this time. I agree this is rather limited from a statistical viewpoint. However, let me point out that longer sampling times, up to 2 milliseconds, which recorded about 40 fluctuations, gave approximately the same r.m.s. value. Also, the r.m.s. values shown in the flow-field plot represent the average of 3 runs, the individual results all agreeing to within 10%. At each of these axial locations in the wake the density fluctuations are reasonably uniform and the r.m.s. values do appear statistically significant.

J. Fox

(i) The finding of maximum turbulent density fluctuations of an off-axis position correlates with the ideas available from low-speed incompressible turbulent shear flows, where the peak production of turbulence occurs near the maximum velocity gradient. Did you attempt to relate the peak density fluctuation with the velocity gradient?

(ii) In the presentation, you described the changing of one large fluctuation into smaller fluctuations as the "decay" of an eddy as it moves downstream. It seems more likely that we are seeing the development of turbulence in the near wake, where a single eddy is breaking down into many eddies with a range of sizes.

A.G.Boyer

(i) No, not yet. We intend to look at this, however, particularly when we obtain mean velocity measurements. I would expect to find a dependency or correlation of the density fluctuations with the velocity gradient, as you suggested.

(ii) Precisely. I have described this breaking-down process with respect to scale or size as a decay. In other words the average size of the fluctuations, averaged over our sampling time at each location, decreases as one proceeds downstream in the axial wake direction.

L. S. G. Kovasznay

At your station, X/D = 15 , the intensive pulses are highly correlated across the flow. Is this really turbulence?

A. G. Boyer

I do not pretend to interpret these density fluctuations as being indicative of fully-developed turbulence. Certainly they represent the initial development of turbulence. These particular measurements extend to 20 base diameters only, which is in the mid-wake or transitional region, as Dr Eschenroeder pointed out and discussed in his paper.

A. Eschenroeder

In answer to Dr Kovasznay's question, I would like to say that the high degree of radial correlation over relatively large radial distances is consistent with the observations by means of schlieren photography of wakes in free-flight ranges. In these first few tens of diameters of sharp cones, any laminar instabilities which may occur persist as periodic large scale disturbances for considerable distances at comparable Mach numbers and Reynolds numbers. Thus, the pattern observed is not likely to be representative of fully developed turbulence, as pointed out by J. Fox.

Discussion of the Paper
STUDIES OF THE TURBULENCE IN THE WAKE OF HYPERSONIC SPHERES UNDER SIMULATED RE-ENTRY CONDITIONS
presented by
D. Ellington (Speaker) and G. Trottier, Canada

R. Legendre

Is it possible to use either a shock tube or the shock in the tunnel itself for calibration?

D. Ellington

It would appear that the use of the bow shock itself to calibrate the probe would, in fact, be a good method to employ. Some information may also be obtained in this way on the frequency response of the probe.

Discussion of the Paper
STATISTICAL PROPERTIES OF TURBULENT WAKES
presented by
J.H.Herrmann (Speaker), W.G.Clay and R.E.Slattery, USA

E.P.Muntz

I would like to know from what volume the probe gathers signal or current. If the sheath size is large, then the probe may miss small-scale fluctuation, where the important dimension determines the volume from which the wake collects current and not the probe size itself.

J.H.Herrmann

In the range of electron density encountered in this work the probe size and the Debye length are approximately the same. Both are very much smaller than the measured correlation length. However, the speaker is quite correct in that Debye length and/or sheath volume constitutes the limit on the smallest size fluctuations which can be detected.

L.S.G.Kovasznay

How did you transform the statistical results obtained on the photographic plate into statistical data of the gas density fluctuations? What assumptions did you use? Did you think of a hollow model of the wake?

J.H.Herrmann

Statistical results from the film contrast may be transformed by the techniques described in detail in Reference 2. In effect the measured correlation lengths are unaffected by this transformation and hence are unchanged. The transformation assumes a homogeneous isotropic wake. Evidence for this is presented in Reference 2. The possibility of a "hollow" wake seems extremely unlikely on the basis of the experimental evidence.

Discussion of the Paper
RADAR INVESTIGATION OF THE WAKES OF BLUNT AND SLENDER HYPERSONIC VELOCITY PROJECTILES IN THE BALLISTIC RANGE
presented by
S. Zivanovic (Speaker), P.E. Robillard and R.I. Primich, USA

D. Ellington

Your curve of distance to break through as a function of $Re_\infty D$ shows a discontinuous derivative at $Re_\infty D \simeq 10^5$. The scatter on the data does not seem to justify the nature or existence of such a discontinuity. If such a physical discontinuity does in fact exist, what is the reason for it?

S. Zivanovic

The black curve is representative of many schlieren measurements. It is borrowed from References 10 and 11 with the author's permission. The schlieren results, as given in Figure 9, are selected points which correspond to radar measurements. The number of observed radar transitions was smaller than the number of schlieren transitions because the schlieren was put in operation earlier than the radar.

Discussion of the Paper
ELECTROSTATIC PROBE MEASUREMENTS IN THE TURBULENT WAKE OF HYPERSONIC SPHERES FIRED IN A BALLISTIC RANGE

presented by

A.Kirpatrick, A.Cantin (Speaker) and D.Heckman, Canada

P.Muntz

I am somewhat concerned about the effects of the probes on the isolated wake plasma in the range. My concern is principally with the effect on plasma potential, and the region of operation of the wake; i.e., whether the probe is put in some sort of retarding field region where the measurement would be sensitive to plasma potential fluctuations.

A.Cantin

The plasma associated with the wake is thermally generated and should be floating at zero potential. The large metallic plate, which both supports and serves as an electrical return for the probes, is, at ground potential, in electrical contact with the range. Once the wake has grown over this plate, its potential may become very slightly positive with respect to ground. We have not yet thoroughly investigated the characteristic V-I curve of our probes in a wake plasma, but from the work done we know that, in contrast to ion collection, the electron collection region does not appear to truly "saturate" in accordance with theoretical prediction for collision-dominated plasmas. However, we are quite sure we are operating above the "retardation" region and should not be overly sensitive to potential fluctuations. Our program for the near future includes some investigations of these matters.

S.M.Bogdonoff

Have you made any studies with the probes at other distances from the flight axis, so that some information on radial distributions could be found?

A.Cantin

Up to now, a total of ten firings have permitted us to make measurements at radial distances between 0.6 to 1.8 body diameters. The low electron density precludes measurements at large radial distances. Soon, an array of probes mounted perpendicular to the flight axis will permit us to compare axial and radial corrective velocities. Also, measurements have been performed in the wakes of 25.4 mm diameter spheres and the results obtained will be compared with those obtained in the wakes of 68.6 mm diameter spheres.

M.Taillet

(i) How far from the envelope is the probe nose?

A. Cantin

(i) The nose is 1.3 mm from the end of the envelope.

M. Taillet

(ii) Are the electronic density fluctuations correlated with the neutral density fluctuations?

A. Cantin

(ii) The comparison cannot be made at present, as we do not have neutral fluctuations measurements yet. At pressures ranging from 20 to 76 torr, such measurements will be provided by means of the experiment using the Rayleigh diffusion of a Laser beam. This experiment, however, has not reached its final stage of development.

Discussion of the Paper
WAKE ELECTRON DENSITY MEASUREMENTS BEHIND HYPERSONIC SPHERES AND CONES

presented by
R. A. Hayani (Speaker) and R. I. Primich, USA

J. Cresswell

For the case of the cone in nitrogen gas at a pressure of 75 torr, the electron density exceeds the case of air at the same pressure. Since there is much less oxygen present, what is the positive ion which serves as the source for electrons? It cannot be nitric oxide because of the oxygen deficiency.

R. A. Hayani

The electrons in the nitrogen wakes arise from ionization of nitrogen atoms and molecules. The levels of electron density are higher than those in air for the same flight condition because flow field temperature levels are higher than in air. This occurs because the higher dissociation energy of N_2 suppresses the absorption of energy into the chemical mode. Consequently temperatures are high enough to ionize N and N_2, despite their high ionization potential in comparison with nitric oxide, for example.

Discussion of the Paper
UTILISATION DES SOUFFLERIES A ARC BREF POUR L' ETUDE DES SILLAGES IONISES
presented by
Jacques Dorey and Didier Compard (Speaker), France

A. Eschenroeder

It would be possibly even more effective if the SF_6 were injected in colder parts of the flow. Both the 45° location on the nose and the arc chamber are high temperature regions where the SF_6 dissociates. The electron density decreases are likely to be caused by attachment to free fluorine.

The off-axis electron density peaks near the base flow are consistent with measurements in the free-flight range reported previously.

Regarding arc-heated facilities, I have reservations about the impurity effects and nozzle non-equilibrium influence on ionisation experiments. Your measured test section electron concentrations are consistent with calculations we made for pure air some years ago at Cornell. This tends to indicate that impurity effects are not too serious. Have you any measurements of impurity levels?

D. G. Compard

To answer the first point, our experiments seem to show that the reduction of density is due to the following mechanism:

First, dissociation of SF_6 in the hot gas region.

Secondly, attachment of electrons of fluorine with an increasing efficiency as the local gas temperature decreases.

(As a matter of fact, the relative reduction of electron density is greater for probe 3 than for probe 2, which is located in a higher gas temperature region). This is in agreement with what Good observed (Reference 23 of my paper). Actually, it will also be very interesting to try to inject in the base region, to investigate the possibility of attachment to SF_6 alone.

About your second comment, I think it is very important that our respective measurements agreed on the fact that the wake can be "hollowed".

About the third comment, I will say that this impurity problem is under investigation at ONERA (Ref. 19). But I must recall that the measured plasma characteristics in the free stream are low ($\simeq 10^7$ to 10^8 for electron density, less than 0.1 eV for electron temperature). As you say, this tends to indicate that impurity effects are not too serious. On the other hand, I would like to add that our hot-shot has a long run duration ($\simeq$ 100 ms) and that the data are taken from the less perturbed part of the flow. Moreover, an intermediate chamber (Ref. 19) will be used and should give very interesting results.

Discussion of the Paper
MATERIAL EFFECTS OF LOW TEMPERATURE ABLATORS ON HYPERSONIC WAKE PROPERTIES OF SLENDER BODIES

presented by

James D. Cresswell (Speaker), Brent Kaplan, Raymond P. Porter and Constantine P. Sarkos, USA

A. Eschenroeder

This work illustrates the concluding remark in my paper about the need to include realistic effects such as ablation, and I believe it is a significant advance in that direction. Based on recent observations, two possible areas of improvement seem to be appropriate: (i) The sudden jump of transport coefficients at the wake transition point could be replaced by a transitional diffusion formulation, such as that suggested by K. S. Wen. (ii) The oxygen negative ion kinetics should include some of the additional steps mentioned in Dr Sutton's comment to my paper; namely, negative ion charge transfer from molecular to atomic, ion associative detachment which returns electrons to the system, and attachment to oxides of nitrogen or carbon as chain-termination steps. These effects may be so dominant that we may even be able to simplify the ablation chemistry.

J. D. Cresswell

My response to both comments is "yes". In particular, the suggestion of incorporating the additional chemical processes governing the ultimate electron population decay in the far turbulent wake, as suggested by Dr Sutton in commenting on your paper, is attractive in a practical sense, since the wake flow computer program permits incorporation of more reactions, whereas computer-storage limitations preclude much extension to the chemical system for the boundary-layer analysis. It is fortunate that these reactions are important only in the wake.

Discussion of the Paper
BALLISTIC RANGE MEASUREMENTS OF WAKE ELECTRON DENSITY AND SPECTRAL EMISSION
presented by
C.F. Infosino (Speaker), R.R. Gastrock and R.A. Leverance, USA

R. Sedney

For the situation where the shock reflection had a large effect on the wake, was the wake turbulent?

C.F. Infosino

I do not know whether the wake was turbulent or not. We were not concerned with this in these tests.

I think it worth mentioning at this point that, in addition to the luminosity records, we set up an experimental microwave interferometer in the range and noticed an increase in the phase shift (or electron density) when the shock wave crossed the wake.

S.M. Bogdonoff

You showed some excellent pictures of the interaction of reflected waves from the walls with the wake in some special experiments. Have you ever observed such interactions in the large range where your main data were taken.

C.F. Infosino

The range is large enough so that any reflections would appear much too far back in the wake to be of any consequence. The results that I have indicated here were a result of reflections in a 5 in. diameter range. I would like to emphasise, however, my statement that reflections, even in a large range where there are a lot of obstructions, may indeed influence the wake measurement, but I do not have any direct experimental evidence to support this.

Discussion of the Paper
BOUNDARY LAYER PHENOMENA OBSERVED ON THE ABLATED SURFACES OF CONES RECOVERED AFTER FLIGHTS AT SPEEDS UP TO 7 KM/SEC
presented by
Michael Tauber, Thomas N. Canning (Speaker) and Max E. Wilkins, USA

R. E. Wilson

You showed a photograph of waves in the sand on a beach. I would suggest that these correspond to shock waves which existed in a supercritical water flow.

T. N. Canning

I agree that this may be the case through the influence of the free surface in setting up a standing-wave system. On the other hand this spatially fixed type of pattern has appeared without the presence of an obviously free surface. Professor Lees has suggested that an eigenwave may exist, which should explain the observed patterns as well.

The principal reason for describing these observations is to demonstrate further the high degree of two- and perhaps three-dimensional order that appears to exist in laminar transitional and turbulent flows.

M. Laug

A similar work is being done at ISL by Luneau. He fires metal projectiles, because metals ablate more than plastics at such high pressures. Do you have a particular reason to choose plastic projectiles?

T. N. Canning

We used plastics because the models changed shape only slightly during the flight. When we tested metal spheres, they eroded more deeply and achieved a sharp-pointed nose, indicating static stability and complicated heat transfer.